THESIS FOR THE DEGREE OF DOCTOR OF PHILOSOPHY

Effects of deep excavations in soft clay on the immediate surroundings

Analysis of the possibility to predict deformations and reactions against the retaining system

Anders Kullingsjö

Department of Civil and Environmental Engineering
Division of GeoEngineering
Geotechnical Engineering
CHALMERS UNIVERSITY OF TECHNOLOGY
Göteborg, Sweden 2007

Effects of deep excavations in soft clay on the immediate surroundings

Analysis of the possibility to predict deformations and reactions against the retaining system

ANDERS KULLINGSJÖ

ISBN 978-91-7385-002-5

© Anders Kullingsjö, 2007

Doktorsavhandlingar vid Chalmers tekniska högskola
Ny serie Nr 2683
ISSN 0346-718X

Department of Civil and Environmental Engineering
Division of GeoEngineering
Geotechnical Engineering
CHALMERS UNIVERSITY OF TECHNOLOGY
SE-412 96 Göteborg
Sweden
Telephone + 46 (0)31-772 1000

Reproservice, Chalmers University of Technology
Göteborg, Sweden 2007

Effects of deep excavations in soft clay on the immediate surroundings -
Analysis of the possibility to predict deformations and reactions against the retaining system

ANDERS KULLINGSJÖ

Department of Civil and Environmental Engineering
CHALMERS UNIVERSITY OF TECHNOLOGY

ABSTRACT

When excavating in an urban environment, the evaluation of the magnitude and distribution of ground movements is an important part of the design process, since excessive movements can damage adjacent buildings and utilities. In order to minimize movement of the surrounding soil, a retaining wall support system is used for deep excavations to provide lateral support.

This dissertation describes different methods of evaluating ground movements adjacent to a deep excavation in soft clay and how to estimate the lateral earth pressure acting on the retaining wall system. A review is presented regarding:

- Soil characteristics that are important for evaluation of deformations and earth pressure.
- Current empirical methods of estimating ground surface settlements
- Different classic methods of calculating lateral earth pressure
- Various soil modelling methods, with focus on the theory of elasto-plasticity.

This review is followed by an extensive case study performed at the Göta tunnel project, in the centre of Gothenburg, Sweden.

Back analyses were performed in order to predict and interpret ground deformations and the development of stress changes against the retaining wall system. These analyses took the form of non-linear finite element analyses with three different constitutive models (an isotropic linear elastic Mohr-Coulomb model, *e-ADP*, a total stress based model capable of modelling anisotropic undrained shear strength as well as non-linearity in shear, and *MIT-S1*, a bounding surface model based on effective stresses. The different outcomes of these three models are compared and discussed. Special focus has been on evaluating the parameters to the *MIT-S1* model and to evaluate the response of this model compared against advanced laboratory tests.

The outcome of the analyses shows the advantage, compared to simpler models, of using finite element methods in combination with an advanced soil model, such as the *MIT-S1*, capable of simulating small strain stiffness, non-linear elasticity, non-linearity in shear and the development of shear induced excess pore water pressure. The analyses also show the importance of combining *FE*-analyses with empirical methods for estimating ground surface settlements.

The field monitoring also demonstrated that deformations obtained by shear strength mobilization may be overshadowed by other engineering activities and poor workmanship. Close collaboration between the contractor and geotechnical consultant is of paramount importance.

Keywords: Case history, Constitutive models, Deep excavation, Earth pressure, Finite element method, Ground surface settlement, Retaining wall, Sheet pile wall, Soft Clay, Soil-structure interaction, *e-ADP*, *MIT-S1*, Analysis, Anisotropy, Deformation, Elastoplasticity, Laboratory tests, Plane strain, Pore pressure, Factor of safety, Shear strength, Shear stress, Shear test, Stiffness, Stress, Strain

PREFACE

The work presented in this dissertation has been carried out at the Division of GeoEngineering, Department of Civil and Environmental Engineering at Chalmers University of Technology. This research project has been financially supported by:

- Skanska with support from SBUF
- Vägverket (the Swedish National Road Administration)
- The VBT- consortium (an industrial consortium financed by Vinnova, SBUF and the universities and companies where the project took place).

This work was performed as an industrially financed project and I am very grateful to my employer, Skanska Sverige, for giving me the opportunity to devote the past two years to the project.

I wish to thank my supervisor Professor Göran Sällfors for his great interest and for guiding me through my work as well as for his critical examination of my manuscript. I would like to thank my colleagues at the Division for a valuable and stimulating time, both at the coffee table and in the laboratory. Ingemar Forsgren should be mentioned for all his work at the Göta tunnel and Peter Hedborg for his work in the laboratory.

Special thanks to all my colleagues at Skanska Teknik for their great interest in my work, especially Ingmar Svensk and Mats Ekenberg who initiated the support from Skanska.

The work could not have been performed without the invaluable support of all those taking part in the Götatunneln project in Gothenburg.

I am also grateful to Professor Andrew Whittle, MIT, who provided me with theoretical support and the tools to perform the analyses. The exchange with Professor David Potts of Imperial College was also very stimulating and provided guidance about how to perform this research project.

Finally, I would like to express my gratitude to my wife Ann-Louise for her great support and encouragement over these years and to our son Elmer, who always helps me to see the important things in life.

Göteborg, September 2007
Anders Kullingsjö

TABLE OF CONTENTS

1 INTRODUCTION 1
1.1 Background 1
1.2 The need for research 2
1.3 Research objectives 3
1.4 Scope of work 4
2 LITERATURE SURVEY 6
2.1 Introduction 6
2.2 Some important characteristics of undrained clay behaviour 6
2.2.1 Stress history 6
2.2.2 Stress paths adjacent to an excavation 9
2.2.3 Shear behaviour 11
2.2.4 Characterization of soil properties according to the *SHANSEP* concept 22
2.3 Empirical relations for the prediction of ground movements 23
2.3.1 Peck (1969) 24
2.3.2 O´Rourke (O'Rourke, 1981) 26
2.3.3 Bowles (1988) and Caspe (1966) 27
2.3.4 Clough and O´Rourke (1990) 28
2.3.5 Hsieh and Ou (1998) 29
2.3.6 A simplified model by Kung *et al.* (2007), the *KJHH* model 33
2.3.7 Distribution of ground movements parallel to the excavation 35
2.3.8 Displacement flexibility number 36
2.3.9 Artificial and self learning methods 37
2.4 Soil structure interaction 37
2.5 Soil modelling 39
2.5.1 Overview of different methods of analysis 40
2.6 Classical earth pressure theory 44
2.6.1 Coulomb 45
2.6.2 Rankine 46
2.6.3 Adhesion between the soil and the retaining wall. 47
2.6.4 Swedish practise 48
2.6.5 Mobilizable strength design (Osman and Bolton, 2004) 52
2.6.6 Arching effects 52
2.7 Stability 53
2.7.1 Overall stability. 53
2.7.2 Hydraulic uplift 54
2.7.3 Basal heave 54
2.7.4 Role of anisotropy 60
2.7.5 Three dimensional effects 62
2.8 Construction failures 62
2.9 Numerical calculations by means of the *FE*-method 62

2.9.1 Constitutive models 63
2.9.2 Interfaces and structural elements in *FE*-analysis 64
3 SOIL MODELLING: THEORY OF ELASTO-PLACTICITY FOR SOILS 65
3.1 Introduction 65
3.2 Continuum mechanics 65
3.2.1 Stresses 65
3.2.2 Principal stresses 66
3.2.3 Mean and deviatoric stress 67
3.2.4 Stress invariants 68
3.2.5 Principal stresses derived from deviatoric stresses 69
3.2.6 Shear stress 70
3.2.7 Strain invariants 72
3.2.8 Elasticity 73
3.3 Theory of elasto-plasticity 75
3.4 Elastic visco-plasticity 78
3.5 Perfect linear elasto-plastic behaviour or ideal elasto-plastic behaviour 79
4 THE GÖTA TUNNEL, WESTERN PART 82
4.1 Introduction 82
4.2 Soil conditions 82
4.3 Excavation sequence and design of the retaining wall system 83
4.4 Soil exploration 84
5 FIELD MEASUREMENTS 86
5.1 Introduction 86
5.2 Instrumentation 86
5.2.1 Horizontal deformation 86
5.2.2 Vertical deformation 86
5.2.3 Pressures 87
5.3 Section 1/430 north 88
5.3.1 Soil profile 90
5.3.2 Working sequence 90
5.3.3 Engineering deformations existing prior to excavation 91
5.3.4 Deformations caused by excavation 94
5.3.5 Deformations developed during tunnel construction 96
5.3.6 Deformations over time 98
5.3.7 Pore water pressure over time 100
5.3.8 Earth pressure over time 102
5.3.9 Strut forces over time 106
5.4 Section 1/470 south 106
5.4.1 Working sequence 108
5.4.2 Deformations and stress changes during the different phases of the work 110

5.4.3 Time dependent deformation 120
5.4.4 Pore water pressure and horizontal earth pressure over time 121
5.4.5 Monitored anchor forces over time 126
5.5 Complementary monitoring within the project 126
6 CHARACTERIZATION OF SOIL PROPERTIES 128
6.1 Introduction 128
6.2 Field Tests 128
6.3 Routine Laboratory Tests 128
6.4 Compression tests 129
6.5 Shear tests 131
6.6 Section 1/430 north 131
6.7 Section 1/470 south 135
6.8 Undrained triaxial tests 139
6.9 Undrained direct simple shear tests 144
6.10 Oedometer tests 145
7 FORMULATION OF THE *MIT-S1* CONSTITUTIVE MODEL 149
7.1 Introduction 149
7.2 Formulation of the *MIT-S1* model 149
7.2.1 Incrementally linearized elasto-plasticity 152
7.2.2 Incremental Effective Stress-Strain Relations, elastic responce 153
7.2.3 Bounding surface plasticity 153
7.3 Yield surface and Failure surface 154
7.4 Hardening laws and flow rules 160
7.5 Bounding surface plasticity 162
7.6 Input parameters 162
7.7 Compressibility, (ρ_c, $\boldsymbol{K}_0^{nc}$) 163
7.8 Unloading – reloading 172
7.8.1 Swelling behaviour 173
7.8.2 Reloading 175
8 EVALUATION OF INPUT PARAMETERS TO *MIT-S1* 178
8.1 Introduction 178
8.2 Evaluation procedure 178
8.3 Evaluation of compressibility behaviour, (ρ_c, $\boldsymbol{K}_0^{nc}$) 181
8.4 Evaluation of small strain compressibility, (C_b) 191
8.5 Evaluation of Poisson's ratio, (μ'_0 and ω) 196
8.6 Evaluation of non-linearity in volumetric response, (D and r) 200
8.7 Evaluation of the initial bounding surface, (ϕ'_m, m) and the failure surface (ϕ'_c) 204
8.8 Rate of evolution of the anisotropy of the boundary surface (ψ) and non linearity in shear (ω_s) 206
8.9 Irrecoverable plastic strain due to an unload reload cycle 211

8.10 Observed behaviour related to the *MIT-S1* formulation and the parameters fitted to the Järntorget site 213
8.10.1 Direct simple shear behaviour 214
8.10.2 Undrained behaviour 216
8.10.3 Unloading moduli 219
8.10.4 Reloading modulus 221
8.11 Summary of evaluated Swedish clay parameters 223
9 NUMERICAL ANALYSES OF TWO IDEALIZED EXCAVATIONS IN CLAY 225
9.1 Introduction 225
9.2 Formulation and input parameters to *e-ADP* 225
9.3 Comparison between the *e-ADP* model based on total stress and some effective stress based models 228
9.4 Soil profile used in reference calculations 233
9.5 Excavation 1 234
9.5.1 Comparison between the different calculations for excavation 1 239
9.5.2 Summary of design values from the different calculations for excavation 1 246
9.6 Excavation 2 248
9.6.1 Effect of vertical support spacing 250
9.6.2 Comparison of different soil models, h=2.5 257
9.7 Evaluation of empirical methods for estimating ground surface settlement 264
9.7.1 Excavation 1 264
9.7.2 Excavation 2 266
9.7.3 Empirical ground surface settlements adjacent to a deep excavation, considering three-dimensional effects 270
10 NUMERICAL ANALYSES OF DEEP EXCAVATIONS AT THE GÖTA TUNNEL 272
10.1 Introduction 272
10.2 Class A calculations 273
10.3 Class B calculations 276
10.4 Section 1/430 north 277
10.4.1 Class A 278
10.4.2 Class B calculations 280
10.5 Calculated vs. monitored deformations and earth pressure in section 1/430 north 284
10.6 Section 1/470 south, class A 290
10.7 Section 1/470 south, class B 291
10.8 Calculated vs. monitored deformations and earth pressure in section 1/470 south 295
10.9 Brief comparison between calculated forces on the retaining system 299
11 CONCLUSIONS AND PRACTICAL ASPECTS 302

11.1 Overall conclusion 302
11.2 Crucial aspects in soil behaviour 302
11.2.1 Laboratory study 304
11.3 Capability of different soil modelling approaches 305
11.3.1 Failure criterion 305
11.3.2 Short comments of the *MIT-S1* model 305
11.3.3 Short comments of the *e-ADP* model 306
11.4 Empirical methods 306
11.5 Deformation pattern adjacent to an temporary excavation in soft clay 306
11.5.1 Ground surface settlements 307
11.5.2 Wall deflection 308
11.5.3 Developed strain 308
11.6 Earth pressure 309
11.7 Appropriate requirements and restrictions on deformations 309
11.7.1 Wall in need of embedment support 310
11.7.2 Walls supported, not only by earth pressure, below the excavation grade 310
11.8 Short guidelines for the use of *FE*-calculations in the study of deep excavations 311
11.9 Theoretical behaviour vs. real behaviour 313
11.10 Practical outcome 314
12 FUTURE RESEARCH 315
12.1 Numerical analyses 315
12.2 Constitutive modelling 315
12.3 Laboratory testing 315
12.4 Field monitoring 316
REFERENCES 317

APPENDICES 329
Statistical analysis of the data presented by the builder 329

LIST OF NOTATION

Roman letters

a	Attraction ($=c'\cdot cot(\phi')$)
a_s	Swelling index
b	Normalized vertical stress where the vertical strain equals 0 for a closed unloading reloading cycle under oedometer conditions
b	Normalized effective vertical stress where the swelling effect equals the secondary compression when unloading from the *VCL*-line or the *LCC*-line.
$\mathbf{b}$	Transformed Measures used by *MIT-S1* model, tensor containing bounding surface anisotropy
b_1-b_5	Transformed Measures used by *MIT-S1* model, anisotropy
C_b	Small strain elastic compressibility (at load reversal)
C_c	Compression index for normally consolidated clay
D	Transitional compression behaviour
E'	Effective Young´s modulus
e_0	The void ratio *in situ*.
E_1-E_5	Transformed Measures used by *MIT-S1* model, strains
E_{eod}	Oedometer modulus
$e_{p'=1}$	The void ratio along the *LCC* or the *VCL* when the effective mean stress equals 1
E_u	Undrained Young´s modulus
e_{LCC}	Void ratio on the *LCC*
e_{VCL}	Void ratio on the *VCL*
$e_{\sigma'=1}$	The void ratio along the *LCC* or the *VCL* when the vertical effective stress equals 1
G	Shear modulus or modulus of rigidity
G_0	Initial shear modulus
G_{50}	Shear modulus secant modulus, from ε_q=0 to ε_q where 50% of the shear strength has been utilized
G_b	The secant shear modulus normalized in relation to the inverse of the porosity multiplied with the mean effective stress to the power of 1/3.
G_{max}	Shear modulus for small strain
G_{sec}	Shear modulus secant modulus, from ε_q=0 where nothing else is mentioned
h	Controls the irrecoverable plastic strain for unload reload cycle
I	Moment of inertia
$\mathbf{I}$	Identity matrix
K	Bulk modulus
K_a	Lateral earth pressure ratio in the active case, the lowest ratio possible.
K_0^{nc}	Lateral earth pressure ratio in the *LCC* regime

$K_{0,ul}$	Lateral earth pressure ratio when 1D unloaded from the *LCC* regim
$K_{0,rl}$	Lateral earth pressure ratio when 1D reloaded from stress situation obtained by 1D unloading from the *LCC* regim
K_p	Lateral earth pressure ratio in the passiv case, the highest ratio possible.
K_w	Bulk modulus of water
m	Shape of bounding surface
m	Power constant used to estimate the K_0-vlaue due to overconsolidation.
M	Oedometer modulus, Swedish denotation
M_0	Constant constrained modulus below the effective vertical preconsolidation pressure, Swedish method.
M_L	Constant constrained modulus between the stresses σ'^{precon}_{vert} and σ'_L, Swedish method.
M_{rl}	Oedometer modulus, reloading
M_s	Oedometer modulus, swelling
n	Porosity (=e/(1+e))
N	Number of load cycles
N_b	Stability number
N_{cb}	Stability factor
OCR_{max}	Maximum *OCR* during a closed unloading reloading cycle under oedometer conditions
OCR_{max}	Previous maximum *OCR*.
P	Transformed Measures used by *MIT-S1* model, tensor containing plastic flow directions
P	Transformed Measures used by *MIT-S1* model, plastic flow direction
P'_1-P'_5	Transformed Measures used by *MIT-S1* model, plastic flow direction
$p'_{e=1}$	The effective mean stress along the *VCL* when the void ratios equals 1
Q	Transformed Measures used by *MIT-S1* model, tensor containing yield surface gradients
Q	Transformed Measures used by *MIT-S1* model, yield surface gradient
Q'_1-Q'_5	Transformed Measures used by *MIT-S1* model, yield surface gradient
r	Non-linear volumetric swelling and volumetric hysteresis response
r	Wall adhesion or wall roughness ratio
R_m	The ratio between the minimum mean effective stress and the mean stress at *VCL* in a closed unloading reloading cycle.
s	the average value of σ_y and σ_x or the average value of σ_1 and σ_3 or the average value of $\sigma_{vert.}$ and $\sigma_{hor.}$ in the axial symmetric case.
s'	the average value of σ'_y and σ'_x or the average value of σ'_1 and σ'_3 or the average value of $\sigma'_{vert.}$ and $\sigma'_{hor.}$ in the axial symmetric case.
S_1-S_5	Transformed Measures used by *MIT-S1* model, effective stresses
s_u	Undrained shear strength
$s_{u\,X}$	Undrained shear strength, obtained from test X or in the X rotation of the principal stresses

t	The difference between σ'_y and σ'_x divided by two where σ'_z equals σ'_2 or the difference between $\sigma'_{vert.}$ and $\sigma'_{hor.}$ divided by two in the axial symmetric case.
w_L	Liquid limit

Greek letters

Δ^p	Normalized residual strain. Permanent strain as an effect of a closed unloading reloading cycle.
Δu	Excess pore water pressure
$\Delta\varepsilon_p$	Irrecoverable plastic strain for an unload reload cycle
δ	Rotation angle of principal stresses
$\boldsymbol{\varepsilon}$	Transformed Measures used by *MIT-S1* model, tensor containing strains
ε_p	Volumetric strain
ε_q	Distortional strain
ε_x	Strain in the x-direction (horizontal, free direction under *PS* conditions)
ε_y	Strain in they-direction (vertical)
ε_z	Strain in the z-direction (horizontal, constrained direction under *PS* conditions)
ϕ'_{cs}	Large strain (critical state) friction angle
ϕ'_m	Apex angle of the bounding surface
γ	Shear strain
γ	Unit weight of the soil
γ'	Effective unit weight of the soil
γ_{ij}	Shear angle for side i in the j direction
γ_w	Unit weight of water
μ'	Poisson's ratio
μ'_0	Poisson's ratio at load reversal
μ'_{rl}	Poisson's ratio during 1D reloading
$\mu'_{un\,sec}$	Secant value of Poisson's ratio during 1D unloading
μ_u	Undrained Poisson's ratio
ρ_c	Compressibility of sand in the *LCC* regime and *LCC* and/or *VCL* for sedimented clay
ρ_r	Inclination of the swelling curve in a lg e – lg p' space diagram.
$\boldsymbol{\sigma}$	Transformed Measures used by *MIT-S1* model, tensor containing effective stresses
σ'_1	Major principal effective stress
σ'_2	Intermediate principal effective stress
σ'_3	Minor principal effective stress
$\sigma'_{e=1}$	The vertical effective stress along the *VCL* and/or *LCC* when the void ratio equals 1
$\sigma'_{hor.}$	Horizontal effective stress

$\sigma'_{vert.}$	Vertical effective stress
σ'^{precon}_{vert}	Vertical preconsolidation pressure
σ'^{precon}_{hor}	Horizontal preconsolidation pressure
$\sigma'^{precon}_{\delta}$	Preconsolidation pressure in an arbitrary plane defied by the angle δ
σ'_x	Effective stress in the x-direction (horizontal, free direction under *PS* conditions)
σ'_y	Effective stress in the y-direction (vertical)
σ'_z	Effective stress in the z-direction (horizontal, constrained direction under *PS* conditions)
σ_1	Major principal total stress
σ_2	Intermediate principal total stress
σ_3	Minor principal total stress
$\sigma_{hor.}$	Horizontal total stress
$\sigma_{vert.}$	Vertical total stress
σ_y	Total stress in the y-direction (vertical)
σ_z	Total stress in the z-direction (horizontal, constrained direction under *PS* conditions)
τ	Shear stress
τ_f	Defining shear stress failure line in the s' - t space
τ_h	Horizontal shear stress
τ_{ij}	Shear stress on the i side acting in the j direction
τ_{max}	Equals the difference between σ'_1 and σ'_3 divided by two.
τ_{mob}	Mobilized shear stress
ω	Non-linearity in Poisson's ratio
ω_s	Small strain non-linearity in shear
ξ	Dimensionless distance in stress space along the hydrostatic axis
ξ_s	Amount of shear during a specified stress path, internal variable used in the *MIT-S1* model
ψ	Anisotropy evolution rate due to stress history

Abbreviations

CK_0UC	K_0 consolidated samples compressed under undrained conditions
CK_0UDSC	Undrained shearing in Directional Shear Cell, where the clay sample is consolidated under K_0 conditions.
CK_0UDSS	K_0 consolidated samples exposed to direct simple shear under undrained conditions
CK_0UE	K_0 consolidated samples exposed to extension under undrained conditions
CK_0UPSC	K_0 consolidated samples compressed under undrained plane strain conditions

CK_0UPSE	K_0 consolidated samples exposed for extension under plane strain undrained conditions
CRS	Constant rate of strain
ESP	Effective stress path
KJHH	A model for estimating ground surface settlements by Kung G. T. C., Juang, C. H., Hsiao, E C. L. and Hashash, Y. M. A.
LCC	Limit Compression Line
MC	Mohr-Coulomb.
MN	Matsuoka Nakai
NSP	Normalized soil parameter
OCR	Overconsolidation ratio. The ratio between the vertical preconsolidation pressure and the actual vertical effective stress.
PLEP-MC	Perfectly linear elasto-plastic *MC*-model. Linear elastic behaviour within the yield/failure surface defined by *MC´*s failure criteria
PS	Plane strain ($\varepsilon_z=\gamma_{xz}=\gamma_{yz}=\tau_{xz}=\tau_{yz}=0$)
SHANSEP	Stress history and normalized soil engineering properties
SPW	Sheet pile wall
TSP	Total stress path
USDM	User defined model
VCL	Virgin Compression Line

1 INTRODUCTION

When deep excavations are carried out in an urban environment, it is important to accurately predict the deformations inside and around the excavation. If the excavation is to be made adjacent to a building, it is necessary to evaluate the consequences of different ground movements and to investigate the likelihood of damage. It is also very important that the earth pressure against the retaining wall can be reliably calculated to yield the required level of safety against failure. A thorough understanding of the constitutive modelling of soft clay is of great importance when numerical tools, such as the finite element method, are used.

> "There is an urgent need for reliable means to estimate the extent and nature of the movements and disturbances associated with an excavation. The engineer needs to estimate the magnitude of the settlements and their pattern of distribution outside the excavation." (Peck, 1969)

The subject of deep excavations has been studied by many researches over a number of years. However, during the last decade the understanding of soil behaviour has increased substantially. This, in combination with an increased ability to use new technology to describe soil structure interaction, has resulted in the need to reconsider the present design methods for retaining structures for new underground constructions.

Ground movements around excavations were not of great importance a century ago. However, as urban areas have become denser, the risk of damage to existing buildings increases, thus making the prediction of ground movements a major issue when deep excavations are required.

When temporary retaining structures, i.e. steel sheet pile walls, are designed the safety of the support is the first priority. The demands on cost effective construction has increased, resulting in more slender sheet pile walls as well as an increased risk of damage to the surroundings.

This has led to the need for more accurate predictions of ground movements and increased knowledge of the design of temporary retaining structures.

1.1 Background

As long as urbanization continues, the need for underground constructions will increase, urged by financial and environmental aspects. The available ground for new structures are in many cases not very suitable for exploration. However, deep excavations within urban areas, which often consist of deep deposits of soft

clay and/or reclaimed ground with ongoing settlements, are almost unavoidable when new buildings or infrastructures are built.

Two main issues are associated with deep excavation in an urban environment:
1) the design of a temporary or permanent support system has to fulfil safety demands
2) the prevention and/or minimization of damage to adjacent constructions.

This project studies the effects caused by the excavation work. Other activities such as wall installation, piling, ground water lowering etc, also have a major impact on the surroundings, but will not be addressed here.

In soft clay, the design of sheet pile walls is relatively straightforward for excavations down to a depth of 5 – 6 metres. The design solution is often based on empirical knowledge and local experience. However, if the excavation depth exceeds the limit for which the sheet pile wall was designed, the methods for predicting the lateral earth pressure and deformation become unreliable. Certain design methods may be unsuitable when the excavation exceeds the depth for which the methods have been developed. Acceptable deformation relative to the excavation depth will decrease in line with increased depth and also due to increased restrictions on the effects on the surroundings. This decrease in tolerated relative deformation may lead to less utilization of the shear strength of the soil, which increases the need for a stronger support system such as combined sheet pile walls, SPW, and diaphragm walls.

For many geotechnical engineers the solution to the difficulties associated with deep excavation is the finite element method (*FE*-method). However, this tool is still rarely used and when it is, skill and understanding are often limited.kill in using this method and the understanding of it is often limited.

1.2 The need for research

A retaining system for deep excavations in the midst of existing structures is a highly complex soil/structure interaction problem affected by a combination of many factors. Many authors have addressed this issue (e.g. Peck, 1969; Mana and Clough, 1981; Wong and Broms, 1989; Clough and O'Rourke, 1990; Hashash and Whittle, 1996) and some identified factors are listed below.

- Soil behaviour
- Sequence of excavation and the quality of workmanship
- The stiffness of the support system
- The geometry of the excavation (width, length and excavation depth)
- Distance to firm stratum

- Length of embedment
- Distance to adjacent structures
- Type of foundation of adjacent structures
- The roughness between the soil and the structures
- Pore water pressure changes and accompanying consolidation in the surrounding soil

Of the identified factors that affect the behaviour caused by deep excavation, soil response is the most complex. Some important characteristics are non-linear stress strain response, anisotropy, rate effects and hysteretic behaviour. However, at present, everyday engineering work does not take all of these effects into account when designing retaining systems for deep excavations. In most cases, the design is made based on empirical design charts combined with a simplified numerical analysis. The excavation work is often performed in line with the observational method (Peck, 1969) to ensure that the rough predictions agree with the actual behaviour. However, this method relies on worst-case scenarios and knowledge of handling such situations. Design charts may be used for calibration if the conceptual model agrees with the monitored response during the excavation. However, the non-linear response in the system may not be observed if the modelling used is too course.

1.3 Research objectives

The objectives of this thesis are to deepen the knowledge and understanding of how deep excavations affect the surroundings and to highlight the complex connection between stress changes and developed deformations adjacent to deep excavations. How is the stress field in the soil adjacent to an excavation affected by the work? And what will the deformation pattern look like? Below, the main objective is broken down into sub areas

- Deepen the knowledge of the material parameters related to deformation in soft clay that is caused by deep excavations within sheet pile walls.
- Compare and evaluate the use of simple numerical methods for describing soil behaviour in relation to the results of more advanced constitutive relations.
- Compare empirical methods for the prediction of ground surface deformation with calculated ones
- Deepen the knowledge and understanding of how lateral pressure develops against a sheet pile wall
- Increase the knowledge of what the strain distribution looks like adjacent to an excavation.

In order to accomplish this:

- The existing empirical methods of predicting ground surface deformation have been compiled and compared
- Some important soil characteristics were identified.
- A reference project was used to monitor and study the behaviour of the soil structure interaction during an excavation. The monitoring was extensive
- A large number of laboratory tests were conducted in order to establish the clay behaviour for several stress paths.
- Back calculations of the monitored sections were performed
- The behaviour of two idealized excavations has been studied for different degrees of complexity in the methods used to describe the soil response

A secondary objective was to increase the knowledge of how to use numerical tools such as the *FE*-method for excavation work. This was accomplished by collaboration with the department of Civil & Environmental Engineering at Massachusetts Institute of Technology as well as at Imperial Colleges where some of the world's leading groups in numerical modelling are located. This collaboration resulted in the use of one of the most advanced constitutive models available for soil modelling in this project.

1.4 Scope of work

The prediction of ground movement caused by excavation and the required strength of the retaining system is a huge subject. As this prediction depends on a large number of factors, an attempt was made to limit the work as follows:

- The behaviour of the support system and soil response was restricted to that caused by the excavation. Other factors such as workmanship, adjacent constructions and certain engineering activities also affect the behaviour but were not considered in spite of their huge impact.
- The studied excavation as well as the idealized ones took place in a highly plastic, almost normally consolidated clay.
- All parameters used in the calculations were allocated best guess values or values provided by the builder. The degree of safety was not studied in this work, although it is mentioned briefly in the following.
- Undrained soil response was assumed
- Rate dependent behaviour, consolidation and creep were not taken in to account.
- The ways of describing the clay behaviour were limited to three different models: a very simple model, a total stress based model capable of modelling anisotropic shear strength behaviour and an advanced model based on effective stresses.

- Only two-dimensional plane strain conditions were considered. As deficiencies will always occur in geometry, soil characteristics, workmanship etc, the use of three-dimensional analysis is in most cases unlikely to improve the accuracy of the predictions. However, 3D effects preventing deformations were observed adjacent to the corners of an excavation and between the corners when the ratio between the length of the excavation and the excavation depth dropped below 6 (Ou and Shiau, 1998; Finno *et al.*, 2007).
- Failure mechanisms due to failure within the support system were not studied. The failure mechanisms taken into account are dependent on the strength of the soil and not on that of the structures, e.g. stability problems.

2 LITERATURE SURVEY

2.1 Introduction

This chapter provides a short description of undrained clay behaviour followed by a review of the empirical methods used for the prediction of ground surface deformation adjacent to an excavation. Soil structure interaction and different methods of soil modelling are presented and discussed. Lateral earth pressure can be calculated in various ways, and some of the classic methods are presented as well as the method based on the stability factor used in Sweden.

Failure mechanisms associated with supported excavations as well as some design charts for incorporating soil structure interaction into the classic methods are presented, as is an example of the incorporation of anisotropic strength into the stability factor calculation.

Finally, the use of numerical tools is briefly presented and discussed and the discussion will be continued in the following chapters.

In addition to the information in this Chapter, several other references were used in the evaluation of soil properties, descriptions of soil behaviour etc. These studies and their findings are presented next to the analyses made at a later stage of this work.

2.2 Some important characteristics of undrained clay behaviour

2.2.1 Stress history

The behaviour of a specific clay is exclusively connected to its stress history. This is valid for the stress-strain relationship associated with all kinds of loading as well as for the shear strength observed under undrained conditions (Ladd and Foott, 1974). When analysing an excavation it is crucial to know the stress history of the soil strata.

The actual stress state is a result of the situation under which the soil was deposited, the amount of erosion in the area and engineering activities, e.g. adjacent constructions, fills or excavations. All these factors affect the soil structure interaction as well as the degree of mobilized strength in the soil. Most soils have a stress memory corresponding to the previous maximum stress and the length of time the stress was active. This stress memory is often referred to as preconsolidation pressure, σ'^{precon}_{vert}, and it affects the behaviour of the soil in combination with the actual stress state.

The relation between σ'^{precon}_{vert} and actual vertical stress σ'_{vert} is denoted the overconsolidation ratio, *OCR*. It has been found that, if the soil deposit is unaffected by engineering activities, there is a coupling between mobilized shear strain, τ_{mob}, and the *OCR* (e.g. Schmidt, 1966; Mayne and Kulhawy, 1982). The relation given in Equation (2.1) was presented by Schmidt (1966) for 1D unloading (erosion or large excavations). This relation has been modified on several occasions, mostly in relation to the exponent 1.2 $\sin\phi'$. One proposed relation during reloading is given in Equation (2.2) (Mayne and Kulhawy, 1982).

$$K_{0,ul} = K_0^{nc} \cdot OCR^{1.2\cdot\sin\phi'} \tag{2.1}$$

$$K_{0,rl} = \left(1-\sin\phi'\right)\cdot\left(\frac{OCR}{OCR_{\max}^{(1-\sin\phi')}} + \frac{3}{4}\cdot\left(1-\frac{OCR}{OCR_{\max}}\right)\right) \tag{2.2}$$

As can be seen there is no correlation between these two relations and therefore a slight modification of these relations is here suggested in Equations (2.3) and (2.4) which will guarantee that the stress reversal point coincide for the two expressions. The reason for introducing *m* is to make the expressions more general. The expression given in Equation (2.3) has been used by many authors while the modification of Equation (2.2) is presented here for the first time.

$$K_{0,ul} = K_0^{nc} \cdot OCR^{m} \tag{2.3}$$

$$K_{0,rl} = K_0^{nc} \cdot \left(\left(\frac{OCR}{OCR_{\max}^{(1-m)}}\right) + \frac{3}{4}\cdot\left(1-\frac{OCR}{OCR_{\max}}\right)\right) \tag{2.4}$$

The relation in Equation (2.2) was originally derived mainly for sand in an attempt to generate a straight line in the *s´ - t* stress space[1], which was in line with previous findings (Wroth, 1975). However, the relation for reloading has poor agreement with the clay behaviour observed in this work, therefore two new relations were established and are presented in Equation (2.5) and Equation (2.6). The first expression employs a constant value of Poisson´s ratio, μ', during the reloading, thus generating a straight line. Depending on the expected hysteresis effect during an unloading-reloading cycle, the value of μ'_{rl} can be

[1] This stress space e, which was first introduced by Lambe (1967), is a very powerful way of expressing stress changes and estimating shear induced pore water pressure in a shear test etc. It is similar to the one in which Mohr's circles are defined but here only the top point of the circle is expressed, thus the shear strength is defined as $t_f=(s'+\cot\phi')\cdot\sin\phi'$.
$s'=\frac{\sigma'_{vert}+\sigma'_{hor}}{2}$, $s=\frac{\sigma_{vert}+\sigma_{hor}}{2}$, $t=\frac{\sigma'_{vert}-\sigma'_{hor}}{2}$ A stress change in the *s´-t* space is known as effective stress path (*ESP*) and in the *s-t* space is called a total stress path (*TSP*). *s´* and *s* can also be expressed by the major and the minor principal stress.
Author's note: In plane strain (*PS*) conditions it is more convenient to retain σ'_{vert} and σ'_{hor} and use a third dimensional axis defined by τ_{hor}, cf. Figure 2.5.

chosen, using the presented $\mu'_{un\,sec}$ (Figure 8.20b) as a guideline. The second expression was derived by fitting some unloading-reloading tests and has been tested over the range of m=0.4-0.7 and OCR=1.0-10.0 with good agreement, although a method that expresses μ'_{rl} as a function of (OCR/OCR_{max}) would be preferable.

$$K_{0,rl} = K_0^{nc} \cdot \left(\frac{OCR}{OCR_{\max}^{(1-m)}} \right) + \frac{\mu'_{rl}}{1-\mu'_{rl}} \cdot \left(1 - \frac{OCR}{OCR_{\max}} \right) \tag{2.5}$$

$$K_{0,rl} = K_0^{nc} \cdot \left(\left(\frac{OCR}{OCR_{\max}^{(1-m)}} \right) + \frac{3}{4} \cdot \left(1 - \left(\frac{OCR}{OCR_{\max}} \right)^{(1-m)} \right) \right) \tag{2.6}$$

The stress paths from Equation (2.3)-(2.6) are presented in Figure 2.1 for two different values of OCR_{max} (=2.0 and 10) and for K_0^{nc}=0.55 and m=0.6. These values are evaluated to best describe the unloading behaviour observed in this work. In the reloading stress path using Equation (2.5), μ'_{rl} is set to the secant value obtained from the unloading path.

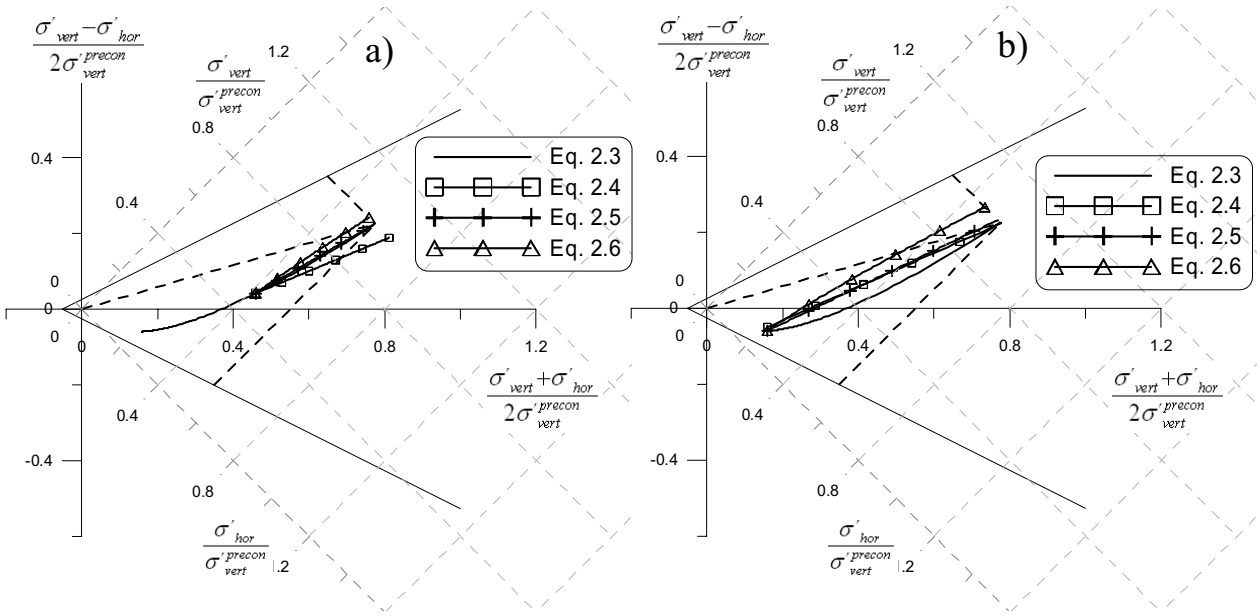

Figure 2.1: Stress paths for 1D unloading and reloading.
a) OCR=2.0 *b) OCR=10*

It is quite clear that the three different expressions in Eq. (2.4)-(2.6) differ from each other. Using Eq. (2.4) will generate the same result as Eq. (2.5) for high OCR-values. However, for low OCR-values, Poisson's ratio is too high from Eq. (2.4) compared to that from the unloading stage. Note that this is only valid for 1D unloading and reloading and that only horizontal layers exit in the stratum.

Other factors that affect the actual stress situation in-situ, e.g. previous engineering work, non-horizontal layers etc., have to be incorporated in the subsequent analysis.

2.2.2 Stress paths adjacent to an excavation

Stress changes will occur in the soil adjacent to the retaining structure as a result of the excavation. During the excavation, the soil on the retained side will lose some of its lateral support and the horizontal stress will decrease, while the soil beneath the excavation will be vertically unloaded. These two changes are the main phenomena that occur and affect the total stresses. Because of the difference in the drainage situation around an excavation, the effective stresses change in different ways. The drainage situation can be divided into three categories: 1) Drained situation, with no generated excess pore water pressure; 2) Undrained conditions, where the volume change in the soil is constrained and excess pore water pressure develops, reflecting the changes in mean total stress; 3) Partly drained, where excess pore water pressures initially develop but dissipate over time. All excavations theoretically fall into category three but the drainage requires a shorter or longer time due to the variation in hydraulic conductivity in the soil. A temporary excavation contained within a sheet pile wall in clay is assumed to behave in an undrained way until the final excavation stage. Any drainage during the excavation is considered to be due to time-delayed deformations. A coupled analysis that takes consolidation into account is necessary in order to observe this behaviour.

The stress changes surrounding an excavation have been compiled into two typical stress paths by Lambe (1970) and are presented in Figure 2.2. Lambe considered that the steady state pore water pressure changed after completion of the excavation; this makes the visualization quite cumbersome but also more accurate. In order to briefly explain the visualisation, the stress path for soil element B will be outlined here.

Element B: Initially the effective stresses σ'_{hor} and σ'_{vert}, had a relation of K_0. During unloading the effective stress path (*ESP*) went from point $\bar{B}_0$ to $\bar{B}_{ss}$, following almost the same behaviour as presented in Figure 2.1 for 1D unloading, the only difference being that the horizontal stress is slightly higher on account of the inward movement of the retained soil. Because of the constrained volume change as well as the assumed boundary condition, plane strain, the effective stress path, *ESP*, is only allowed to move vertically in the diagram. As a result of the stress history, the stress path is sketched slightly curved due to the fact that shear induced positive excess pore water pressure develops, thus counteracting the negative excess pore water pressure obtained from the boundary conditions and the constrained volume change. In order to

obtain this *ESP*, the initial *OCR* should be approximately 1.5[2]. The resulting excess pore water pressure is denoted Δu in Figure 2.2. This excess pore water pressure will dissipate over time, causing a decrease in both σ'_{hor} and σ'_{vert}. These stress changes will result in heave at the bottom of the excavation (the horizontal extension is constrained) and a slight decrease in s_u. The factor of safety related to basal heave therefore decreases. However, this is not a major problem, since most excavations experience some load on the excavation bottom shortly after completion.

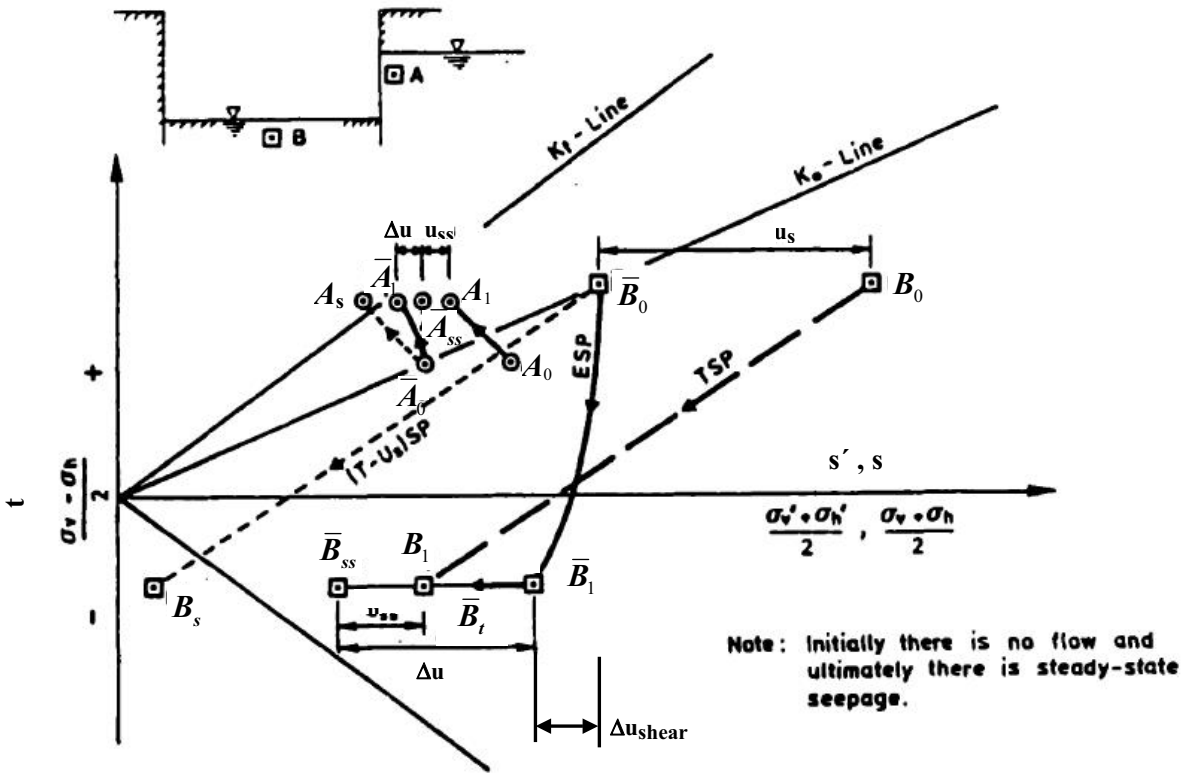

Stresses and strains for soil elements near an excavation	Soil element A	Soil element B
Initial (static) pore pressure, u_s	$A_0\bar{A}_0$	$B_0\bar{B}_0$
Pore pressure at steady-state flow, u_{ss}	$A_1\bar{A}_{ss}$	$B_1\bar{B}_{ss}$
Pore pressure upon unloading	Decreases	Decreases
Pore pressure during consolidation	Increases	Increases
Strain upon unloading	Vertical compression	Vertical extension
Strain during consolidation	Vertical compression	Vertical extension
Undrained shear strength during consolidation	Increases	Decreases

Figure 2.2: Stress paths for soil elements near an excavation (Lambe, 1970)

[2] Lower *OCR* will give a more curved undrained *ESP* while higher *OCR* will not bend at all. Dilatancy may even occur for a very high *OCR*, pushing the *ESP* in the other direction, but in that case, failure within the soil takes place when the excess pore water pressure dissipates.

The behaviour of soil element A can be described in a similar way, but this description is not included here. It should be noted that Lambe assumed a small drawdown of the water table at the location of soil element A.

In the stress path method presented here, s' and s are defined by the vertical and horizontal stresses but there are also large shear stresses, especially underneath the retaining wall as well as on the retained side, as can be seen in Figure 2.3. It is obvious that there are large areas where stress rotation occurs, which makes it crucial to know the soil behaviour associated with different kinds of loading.

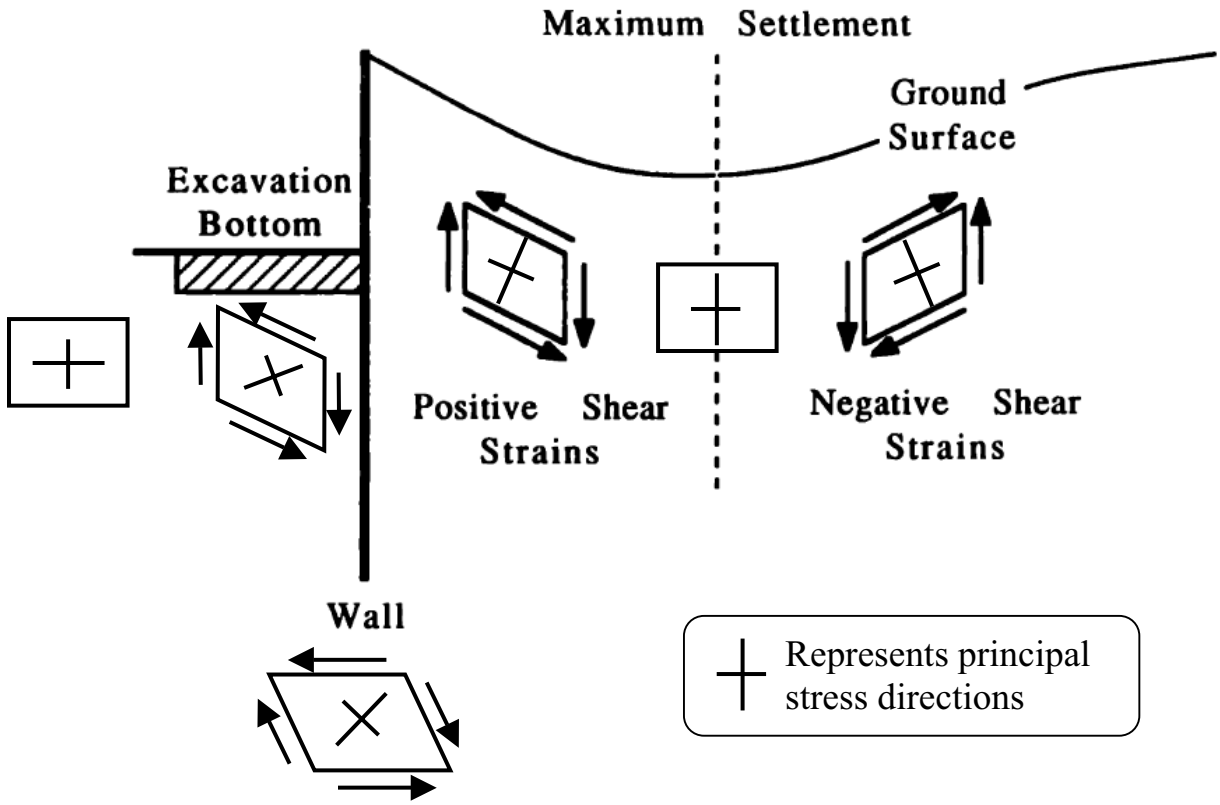

Figure 2.3: Schematic direction of soil shearing forces and rotation of the principal stresses, modified from Hashash, Figure 4.3-16 (1992)

2.2.3 Shear behaviour

When dealing with temporary excavations in soft clay, one of the most important factors is the shear strength. Under undrained conditions, which are the most common in these kinds of excavations, this is often expressed as the undrained shear strength, s_u. In most soil modelling applications, this strength is treated as a constant value, independent of the different ways of loading. However, most soft clays exhibit undrained strength anisotropy due to their

K_0-consolidation history (Larsson, 1977; Ladd, 1991). In the laboratory there are several different ways of evaluating s_u for different modes of shearing. An overview of these techniques can be found in Ladd (1991) and the most common is presented in Figure 2.4. These tests are performed in triaxial or shear cells.

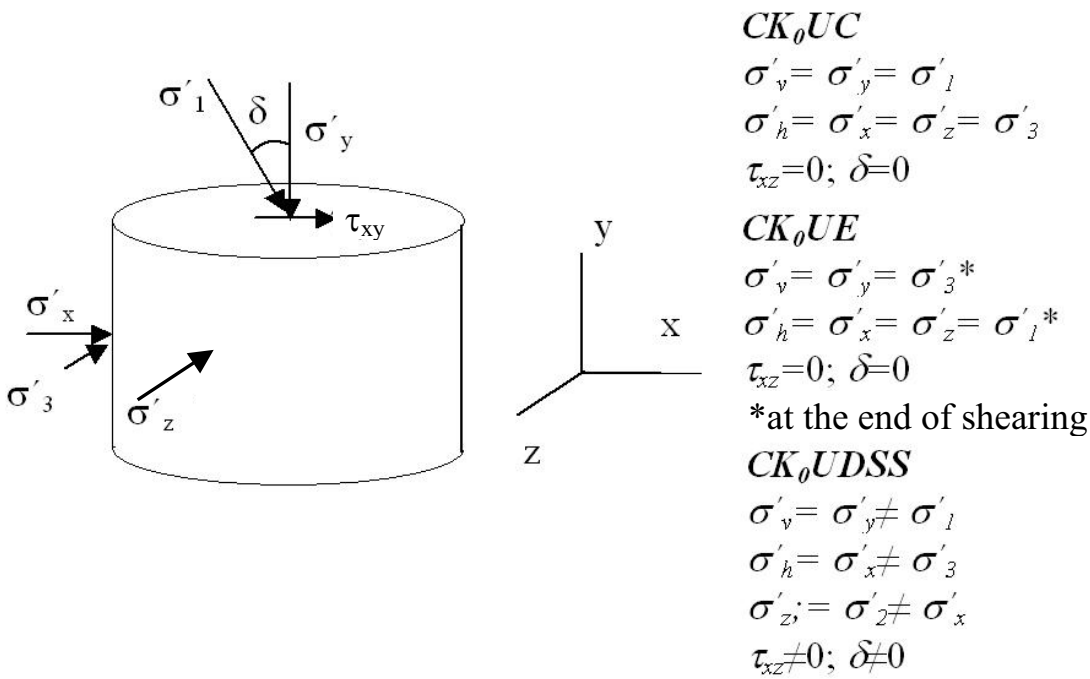

Figure 2.4: Definition of different undrained shear tests[3]

The boundary conditions for the different undrained shear tests are described in Figure 2.4. Standard laboratory tests are severely limited in terms of the range of stress paths that can be applied to the sample. The conditions for the different shear tests, such as degree of freedom and the stress situation depicted in Figure 2.4, indicate that the *CK$_0$UC* and *CK$_0$UE* tests are performed under axi-symmetrical conditions and the *CK$_0$UDSS* under semi-plane strain conditions. Because of the limitation associated with a triaxial test, the stress rotation is either 0º or 90º (when $\sigma'_h > \sigma'_v$), which makes it impossible to evaluate the shear strength for the other directions of the principal stresses. In the *CK$_0$UDSS* tests, the principal stresses are free to rotate but there is no way of controlling how they rotate, making it impossible to measure the anisotropical behaviour of the undrained shear strength, s_u, due to stress rotation. Highly advanced equipment,

[3] Active shear test: *CK$_0$UC*-Consolidated for a K_0 stress situation and sheared Undrained by Compression.
Passive shear test: *CK$_0$UE*- Consolidated for a K_0 stress situation and sheared Undrained by Extension.
Direct simple shear test: *CDSS*-Consolidated for a vertical stress and exposed for Direct Simple Shear undrained.

such as the Directional Shear Cell (*DSC*), the Hollow Cylinder apparatus (Jamiolkowski *et al.*, 1985) and the true triaxial cell, is necessary in order to create more sophisticated stress paths capable of measuring s_u at a specified stress rotation angle.

Assuming that the ground surface and all soil layers are horizontal, one can study a horizontal plane within in the soil strata. This plane has been prestressed to σ'^{precon}_{vert} and the orthogonal plane to $K_0^{nc} \cdot \sigma'^{precon}_{vert}$. An arbitrary plane-rotated δ from the horizontal one will, according to Larsson (1977), have the preconsolidation pressure given in equation (2.7).

$$\frac{\sigma'^{precon}_{\delta}}{\sigma'^{precon}_{vert}} = \left(\cos^2\delta + K_0^{nc}\sin^2\delta\right) \tag{2.7}$$

During undrained shear, excess pore water pressure develops in such a way that $\sigma'^{precon}_{\delta}$ is not exceeded. The maximum shear stress occurs on a plane rotated 45-$\phi'/2$ from the major principal stress, σ'_1. The maximum undrained shear stress (the undrained shear strength, s_u) can be calculated from equation (2.9) using the expression given in equation (2.8).

$$\left(\sigma'_{1\delta}+a\right) = \left(\sigma'_{3\delta}+a\right)\cdot\frac{1+\sin\phi'}{1-\sin\phi'} \qquad where \quad a=\frac{c'}{\tan\phi'} \tag{2.8}$$

$$s_{u\delta} = \frac{\sigma'_{1\delta}-\sigma'_{3\delta}}{2} \approx \frac{\sigma'^{precon}_{\delta}}{3} \qquad if\ c'\ is\ neglected\ and\ \phi'=30^\circ \tag{2.9}$$

The relation given in equation (2.9) is visualized in Figure 2.5 where s_u is given as the radius, $s_u = \sqrt{\left(t^2+\tau^2\right)}$.

The stress paths OA and OB in Figure 2.5 show axi-symmetrical behaviour, which does not occur in most geotechnical problems. If these stress paths were sketched under plane strain conditions, *PS*, the maximum s_u would depend on the failure criteria used. According to Mohr-Coulomb, the failure criteria should produce the same results as those illustrated in Figure 2.5. However, when applying the failure criteria proposed by Matsuoka and Nakai (1974) or Lade (1975) the undrained shear strength will increase due to the intermediate principal stress. In a laboratory test, Vaid and Campanella (1974) found an increase in s_u of about 10% for compression and 25% for extension. These effects are presented on the right hand side of Figure 2.5 as stress paths OA′ and OB′. On the basis of the sketched OC path, it cannot be established that the CK_0UDSS test gives the maximum shear stress within the soil sample. The *DSS* tests only give the strength when it is assumed that the stress rotation is 45º. This can have a great influence on the results of *FE*-analyses made by using a constant undrained shear strength value. Figure 2.5 shows the results from a CK_0UDSS test where it was assumed that peak strength develops when the

principal stresses have rotated by 30º. The path has a peak strength of $0.26\sigma'^{precon}_{vert}$ and a residual strength of $0.22\sigma'^{precon}_{vert}$. These values correspond well with empirical values from normal consolidated Gothenburg clay (w_L=75%). Figure 2.6 a and b are complemented by information about the effect of using a constant s_u without taking account of anisotropy. These values are often evaluated as peak or residual strength from a τ_{xy} - γ_{xy} plot, see Figure 2.6c. As can be seen in Figure 2.6a and b, the residual strength underestimates the strength when δ is less than 65º. By using these strengths in an *FE*-analysis, the relative shear strength, τ/s_u, will be approximately 100% for K_0=0.6. A minor overestimation of the strength will occur for δ>65º. The use of peak strength leads to an overestimation of the strength of δ >45º and an underestimation of the strength of δ <45º.

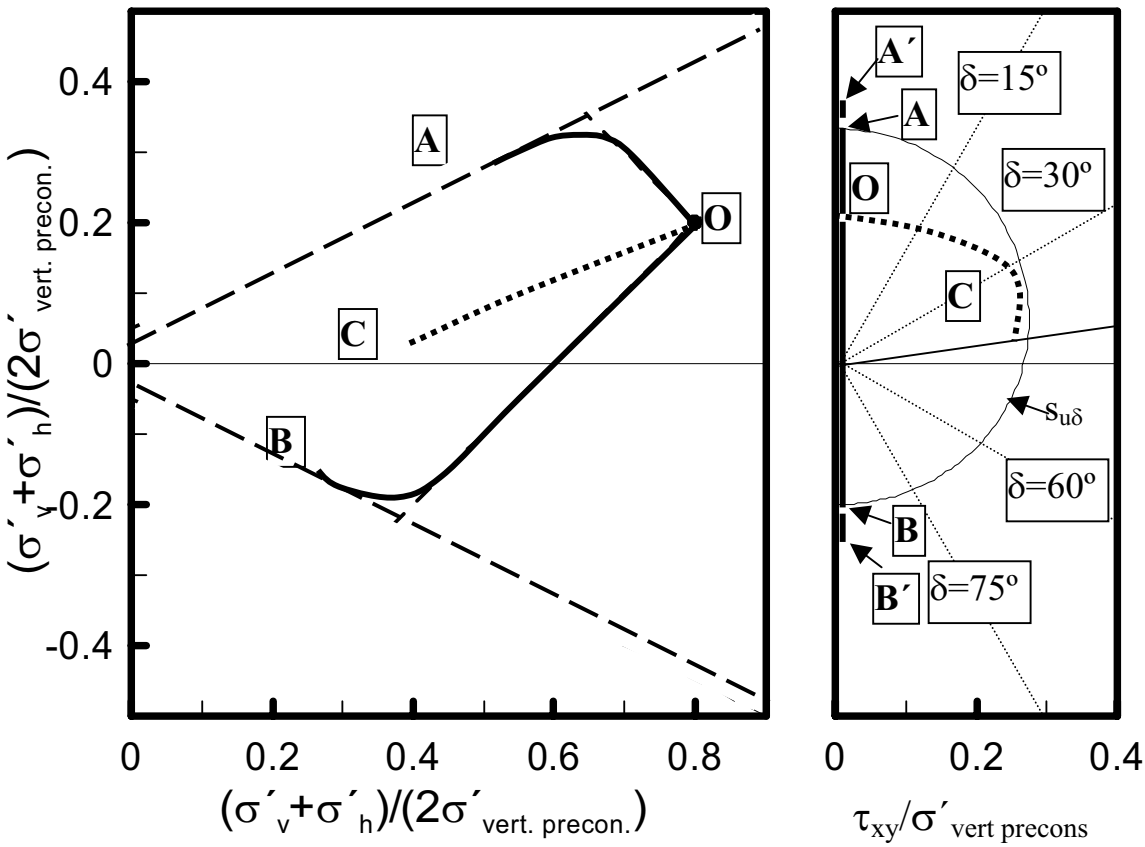

Figure 2.5: Idealized behaviour of undrained shearing of normal consolidated clay. The stress paths for the CK_0UC, CK_0UE and CK_0UDSS tests (OA, OB and OC) are sketched for a clay with ϕ'=30º, $c'/\sigma'^{precon}_{vert}$=0.03 and K_0^{nc}=0.6 .

The CK_0UDSS test sample is exposed to shear stresses higher than τ_{xy}. The sketched path indicates a shear strength that is about 20% higher than that usually evaluated. If the CK_0UDSS test corresponds to the horizontal slip plane in a slope stability problem, the use of $s_{u,\,DSS}$ will underestimate the safety factor.

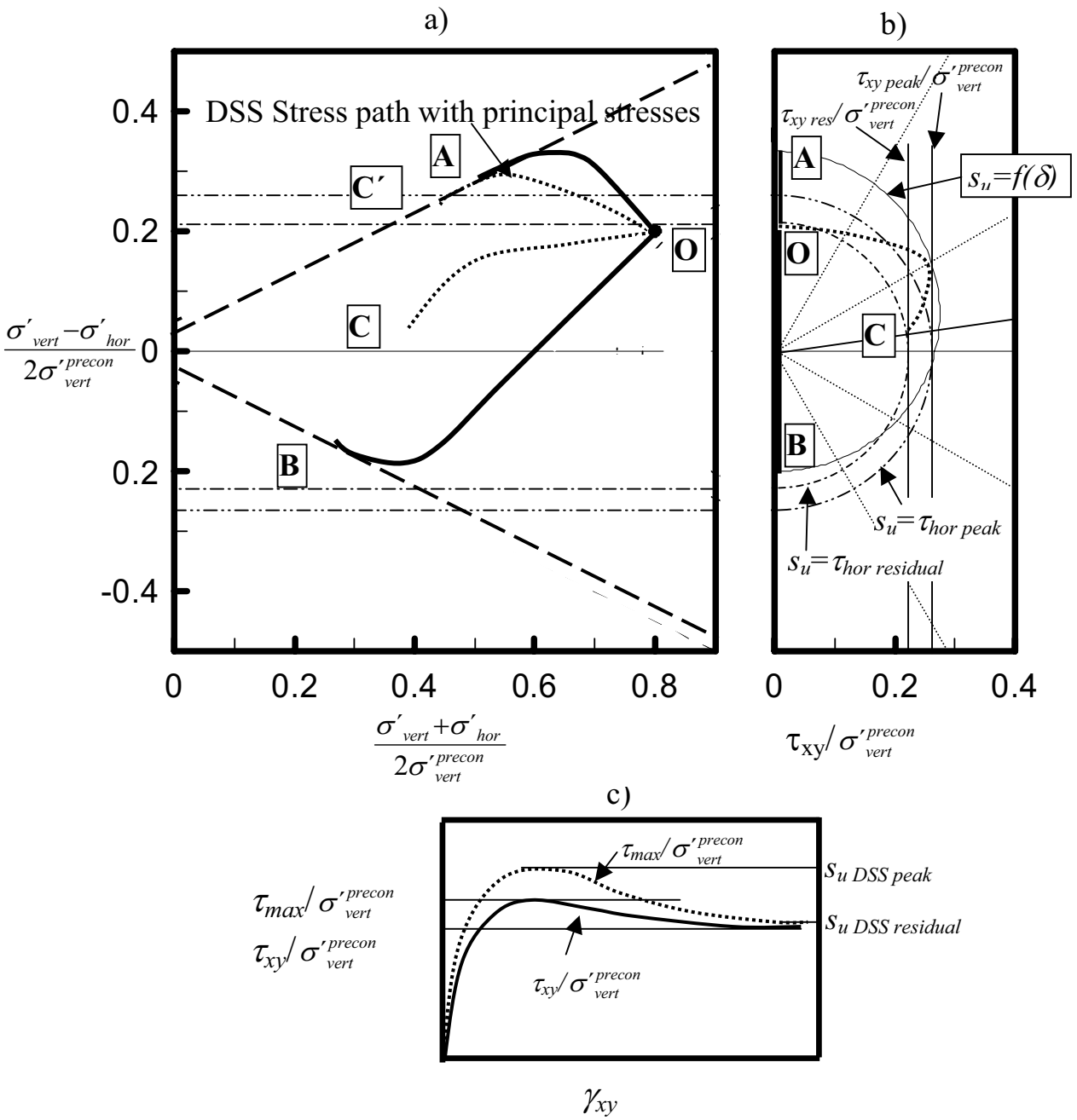

Figure 2.6: Idealized behaviour of a CK_0UDSS test for a clay with $\phi'=30^o$, $c'/\sigma'^{precon}_{vert}=0.03$ and $K_0^{nc}=0.6$.
a) Stress paths: OA-CK_0UC, OB-CK_0UE, OC-CK_0UDSS (vertical and horizontal stresses) and OC′-CK_0UDSS (principal stresses)
b) Visualisation of stress rotation during a CK_0UDSS test combined with the effect of using a constant undrained shear strength value.
c) Comparison of "true" undrained shear strength with that usually evaluated estimated from a CK_0UDSS test.

However, the evaluation of s_u is dependent of time effects: the time allowed for consolidation and the strain rate (or rate of load application). The time allowed for consolidation will affect the amount of "creep", which is a major issue in cases of low overconsolidation ratios. Developed creep leads to an aging effect

and consequently an increase in preconsolidation pressure, thus generating an increase in s_u for all shear modes. The strain rate affects s_u in that, for high strain rates, the evaluated s_u is higher than for low strain rates. This is in line with the observation that clay shows a unique relation between stress and strain when loaded (Mesri and Castro, 1987; Claesson, 2003). High strain rates generate higher preconsolidation pressure values than low ones. Temperature effects on the clay behaviour follow the same pattern as strain rates; a decrease in temperature generates the same effect on the preconsolidation pressure and s_u as an increased strain rate and vice versa. The surface in the stress space that defines the preconsolidation pressure is therefore unique for every combination of temperature and strain rate, cf. different shells in an onion.

In order to obtain consistent answers when the aim is to investigate a specific feature of clay, it is crucial to adhere to a strict method when performing laboratory tests (Ladd, 1991; Sällfors, 2003). The practice followed by many of the leading consulting and research laboratories is: an axial strain rate of 0.5%-1.0% per hour for undrained compression and extension; a shear strain rate of 5% per hour for direct simple shear tests (Ladd, 1991).

The application of different shear tests has been presented by many authors e.g. Clough and Hansen (1981) and Kulhawn (1992), and it is clear that extensive shear testing has to be carried out in order to accurately describe soil behaviour.

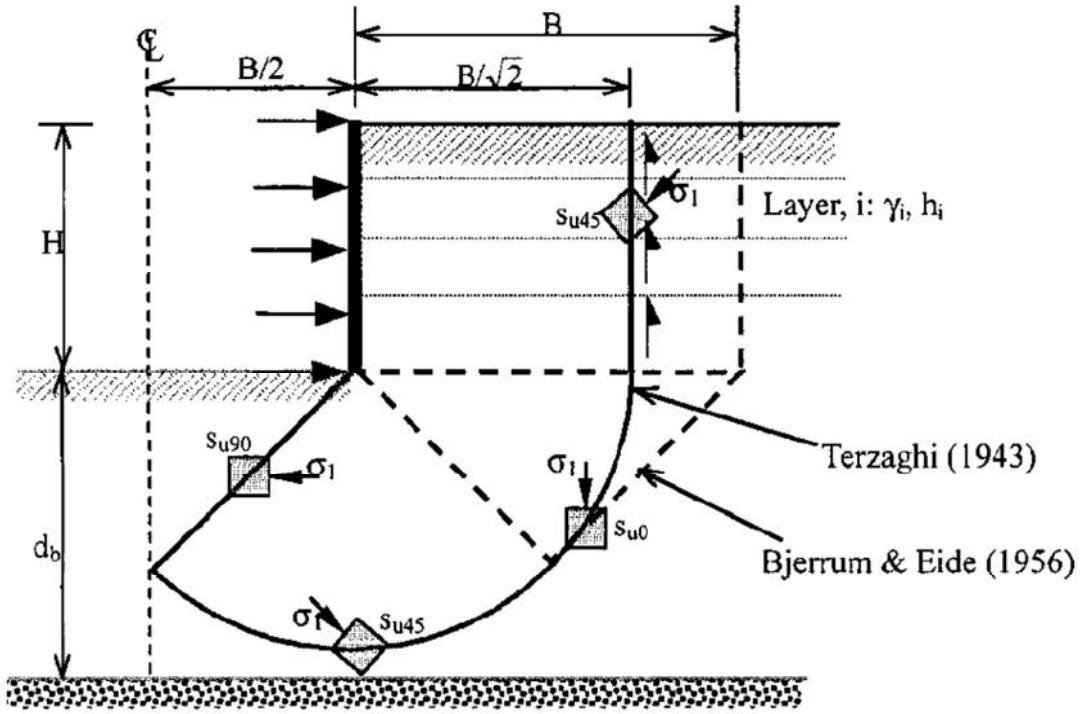

Figure 2.7: Principal stress directions developed for a basal stability mechanism, from Clough and Hansen (1981)

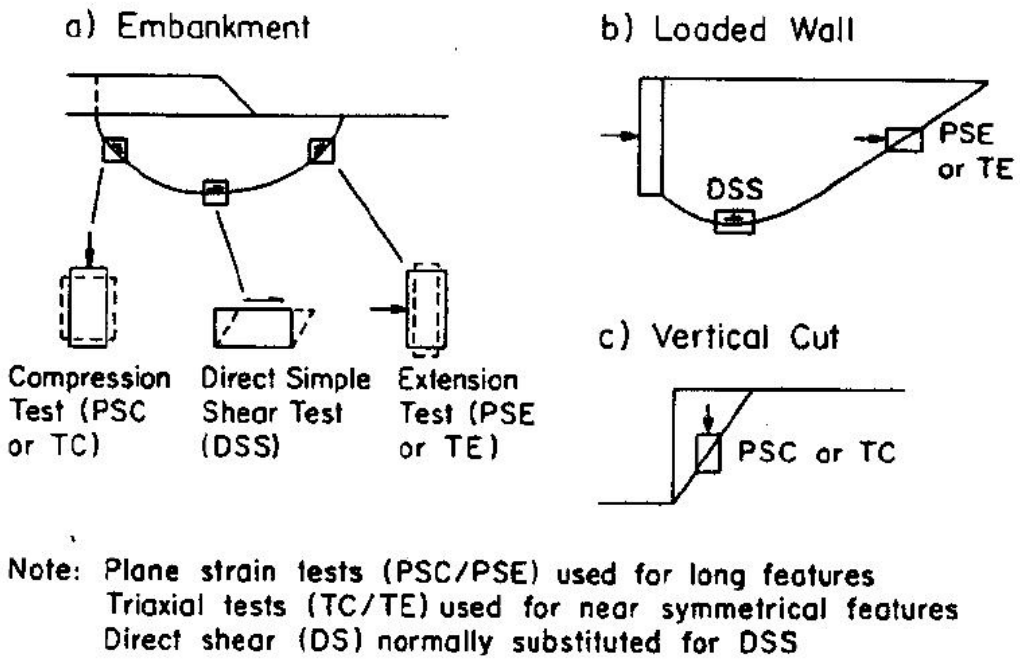

Figure 2.8: Overview of different stress situations in practice compared to a proper shear test, from Kulhawn (1992)

The σ'^{precon} can be estimated from undrained compression and/or extension triaxial tests but requires that shearing starts within a specified *OCR* range[4]. The preconsolidation pressure is considered to be the maximum stress obtained during undrained shearing. The idealized yield surface of a typical inorganic clay from the Gothenburg area is shown in Figure 2.9. If the sample is consolidated to a stress situation that fulfils the empirical relation given by Schmidt (1966) in Equation (2.10), with *m*=0.6, and a truly elastic response within the yield surface, the stress path will follow the ones in Figure 2.9. In order to estimate σ'^{precon}_{vert}, the *OCR* must be in the range of 1.0 to 1.7, while for σ'^{precon}_{hor} the range should be between 1.0 and 2.0.

$$K_0 = K_0^{nc} OCR^m \tag{2.10}$$

[4] The preconsolidation pressure is here reefered to as a surface in stress space and not only as the maximimum vertical stress. The compression tests will yield σ'^{precon}_{vert} while the extensions tests yields σ'^{precon}_{hor}.

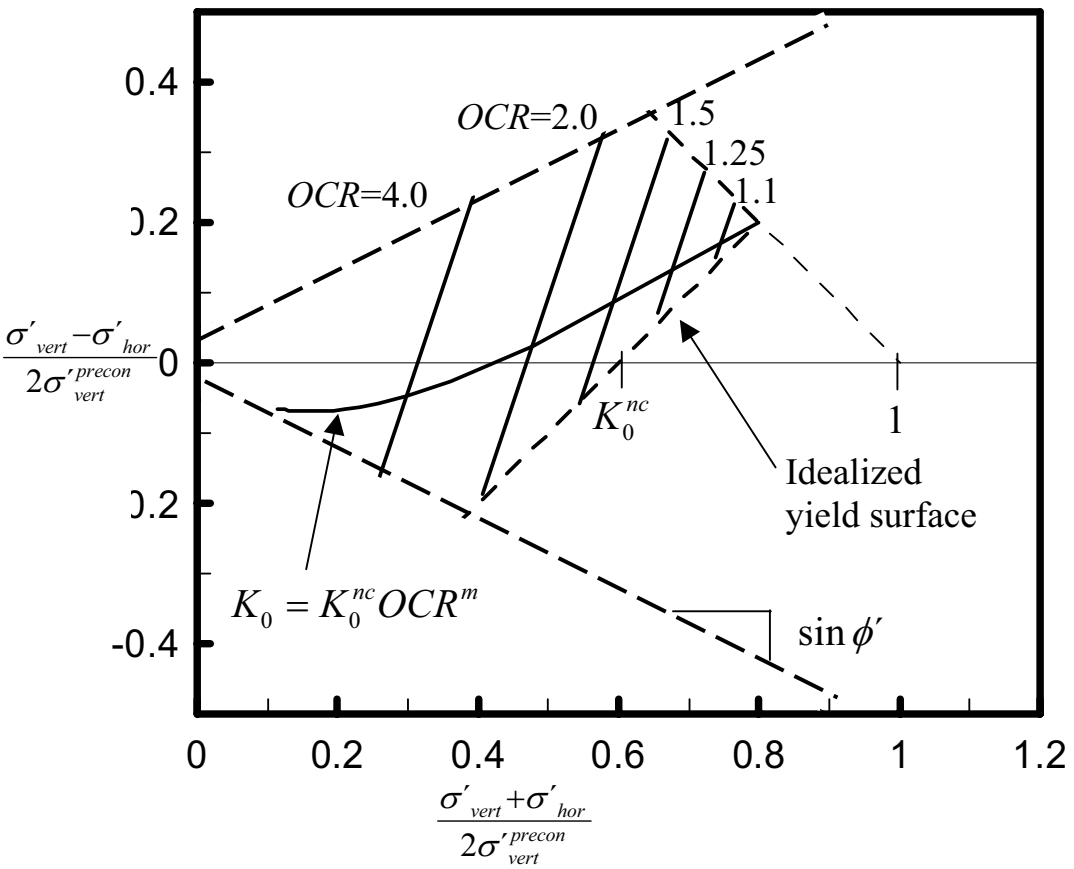

Figure 2.9: Idealized yield surface indicated by the dotted line, presented by Larsson and Sällfors (1981) is used here to illustrate a cohesive soil with ϕ'=30°, $c'/\sigma'^{precon}_{vert}$ =0.03 and K_0^{nc} =0.6. The empirical relation of K_0 as a function of OCR (Schmidt, 1966; Schmidt, 1967; Mayne and Kulhawy, 1982) is used with m=0.6 to visualize the ideal stress paths for undrained shearing in the triaxial cell.

Real soil behaviour will differ from that in Figure 2.10, as shear induced pore water pressure develops, causing the stress path to bend. This behaviour is related to the soil characteristics and stress history (*OCR*). The stress paths maximum absolute value on the ordinate represents the undrained shear strength. Empirical relations of undrained shear strength (Larsson, 1984) show that it is a function of w_L for an *OCR* value of 1.0. In the state of the art report by Ladd *et al.* (1977), a relation between s_u for an overconsolidated clay is represented as a function of *OCR* and s_u for *OCR*=1.0.

$$\left(\frac{s_u}{\sigma'^{precon}_{vert}}\right)_{OC} = \left(\frac{s_u}{\sigma'^{precon}_{vert}}\right)_{NC} OCR^{-0.25} \tag{2.11}$$

In Figure 2.10, the stress paths for undrained shearing in the triaxial test take both the shear induced pore water pressure and the change in maximum shear strength into account. In order to estimate σ'^{precon} the *OCR* must be less than 1.5 for vertical and 1.7 for horizontal preconsolidation pressure, Figure 2.11.

Various stress paths for undrained compression and extension tests performed with different *OCR*s are sketched in Figure 2.10 and Figure 2.11 where the former depicts the stress path without the degradation in shear strength due to the *OCR*. Figure 2.11 shows the stress paths when the *OCR* is taken into account. It should be noted that the soil strength is actually greater for a high *OCR* despite degradation, as it is related to σ'^{precon}_{vert} or $\sigma'^{in\ situ}_{vert}$.

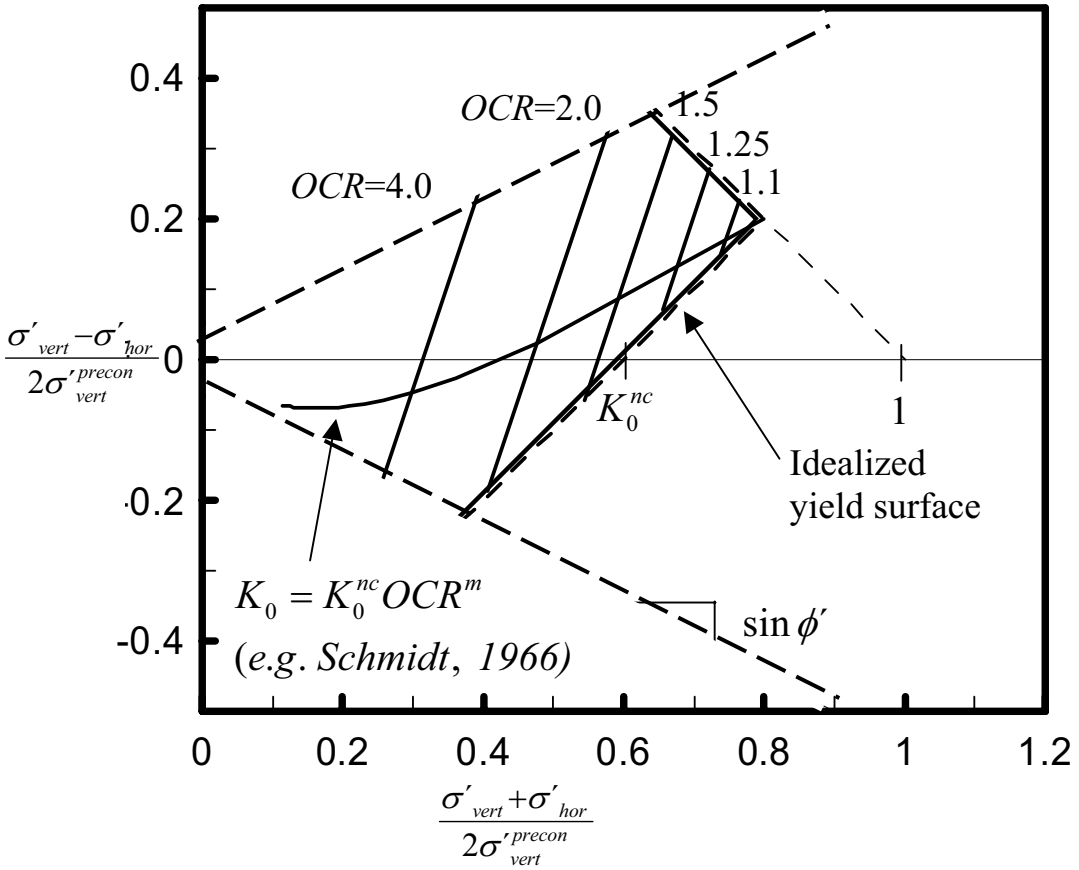

Figure 2.10: Idealized yield surface indicated by the dotted line, presented by Larsson and Sällfors (1981), for a cohesive soil with $\phi'=30^o$, $c'/\sigma'^{precon}_{vert}=0.03$ and $K_0^{nc}=0.6$. The empirical relation of K_0 is given as a function of the OCR (Schmidt, 1966; Schmidt, 1967; Mayne and Kulhawy, 1982) and used with m=0.6 in order to illustrate the ideal stress paths for undrained shearing in a triaxial cell.

In Figure 2.11 the degradation in s_u is given by the expression contained in the recommendations for slope stability analysis in Sweden (Skredkommissionen, 1995).

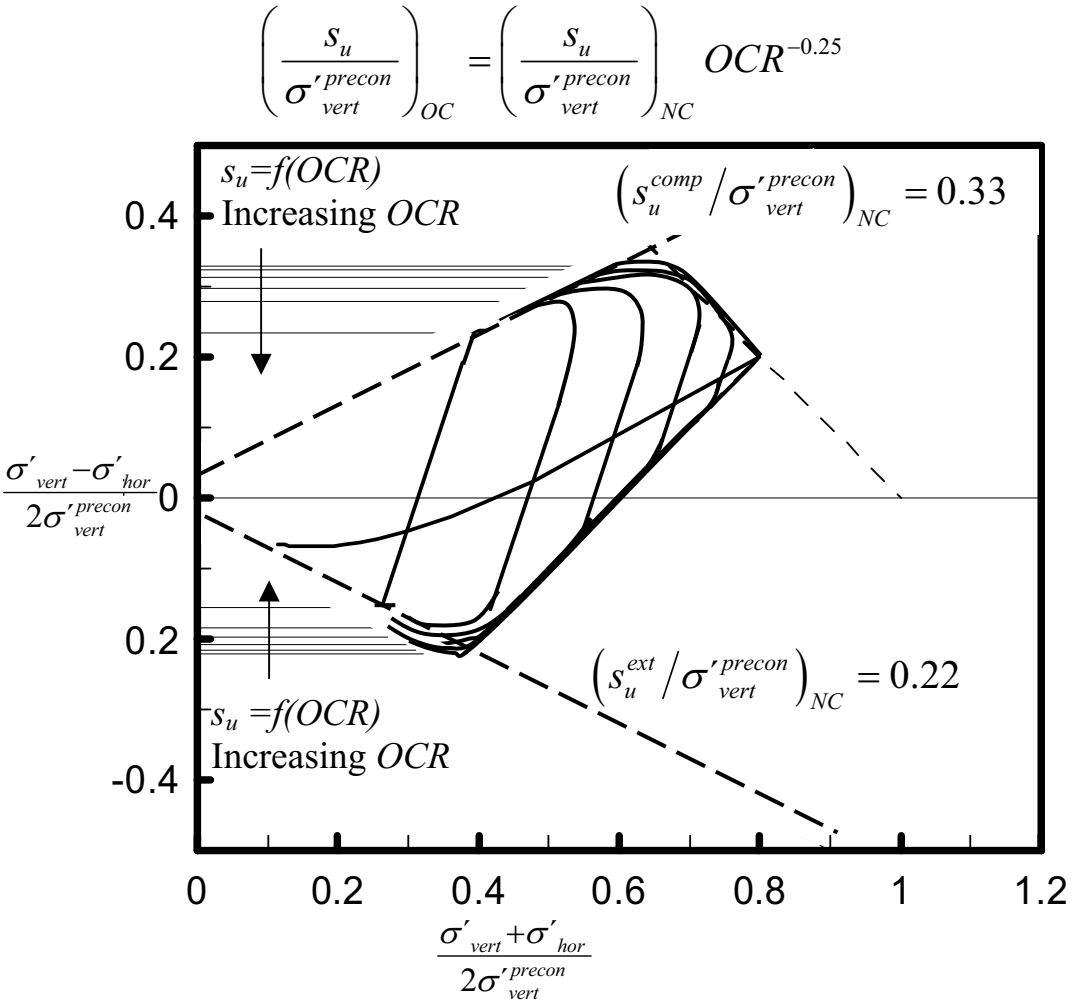

Figure 2.11: Idealized yield surface, ϕ'=30°, $c'/\sigma'^{precon}_{vert}$ =0.05 and K_0^{nc} =0.6. The empirical relations of the undrained shear strength (Larsson, 1984) combined with the effect of the OCR on shear strength (Ladd et al., 1977). Idealized stress paths for undrained shearing in a triaxial cell are presented for OCR 1.0, 1.1, 1.25, 1.5, 2.0 and 4.0. The liquid limit, w_L, of 70% was used to estimate the shear strength.

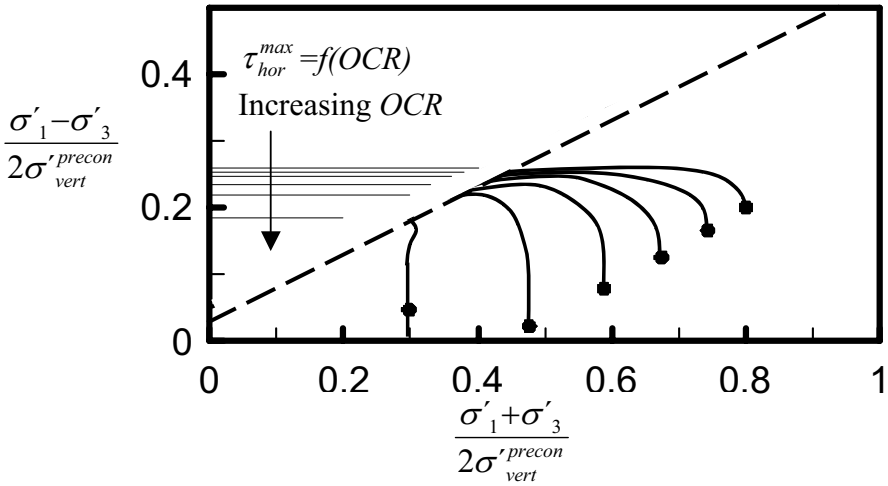

Figure 2.12: Idealized stress paths in CK_0UDSS tests for OCR 1.0, 1.1, 1.25, 1.5, 2.0 and 4. The undrained shear strength empirical relations (Larsson, 1984) combined with the effect of OCRs on shear strength (Ladd et al., 1977) for, $\phi'=30^o$, $c'/\sigma'^{precon}_{vert}=0.03$, $K_0^{nc}=0.6$ and $w_L=70$ %.

How σ'_v, σ'_h and δ develop under shearing is depicted in Figure 2.13.

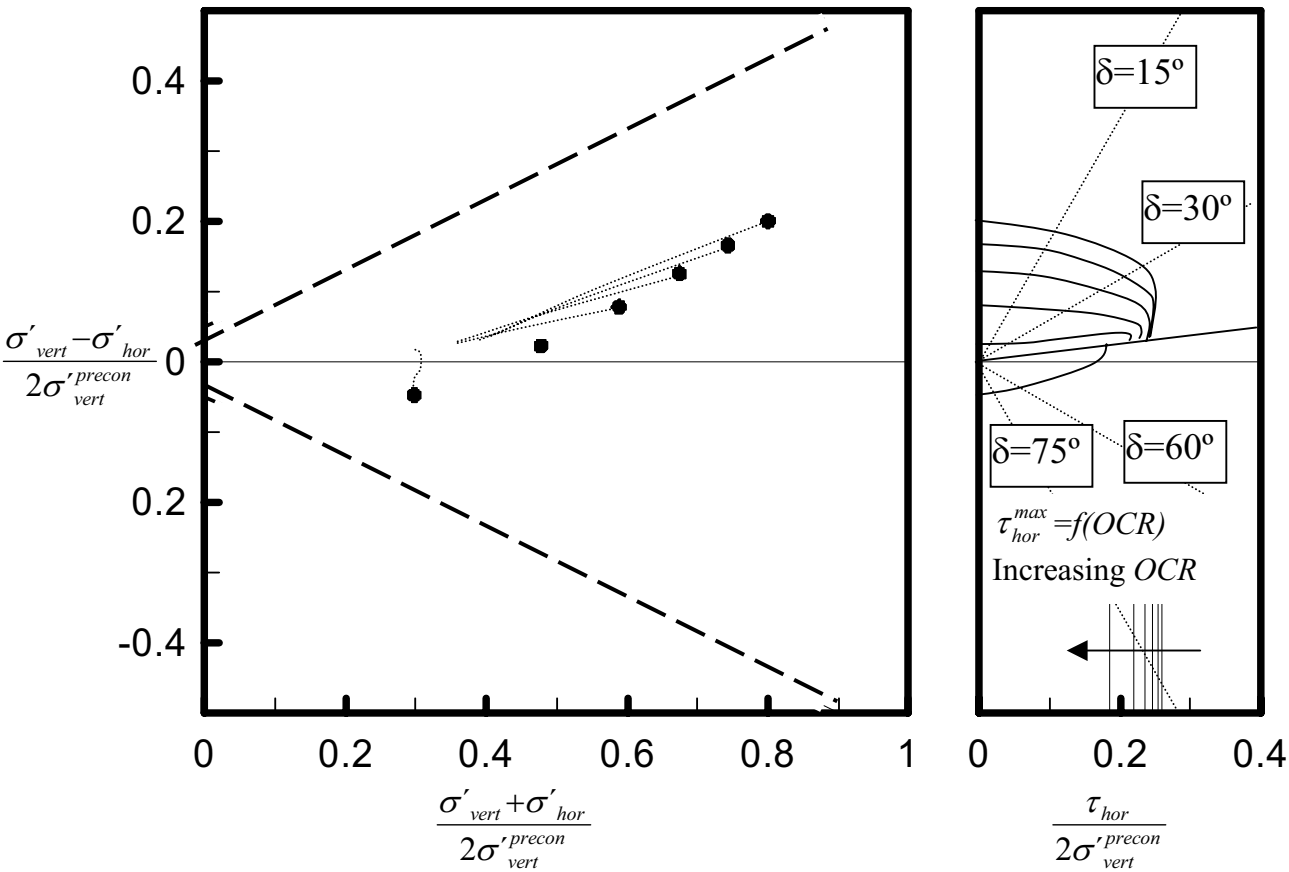

Figure 2.13: Idealized stress paths in CK_0UDSS tests in the s′-t space for OCR 1.0, 1.1, 1.25, 1.5, 2.0 and 4. The empirical relations of undrained shear strength (Larsson, 1984) combined with the effect of OCRs on the shear strength (Ladd et al., 1977) for, $\phi'=30^o$, $c'/\sigma'_{vert.\ precon.}=0.03$, $K_0^{nc}=0.6$ and $w_L=70\%$.

2.2.4 Characterization of soil properties according to the *SHANSEP* concept

Normalizing the different test results against the preconsolidation pressure yields almost the same results for the same *OCR*. This concept *NSP*, normalized soil parameter concept, is widely used and is the background to *SHANSEP.* It has been shown that using *NSP* gives a very good prediction of the shear strength profile.

The *SHANSEP* (Stress History And Normalized Soil Engineering Properties) concept was first presented by Ladd and Foott (1974) and has since been widely used. However, the method has been the subject of some scepticism in Sweden. The concept is based on observed behaviour indicating that soil properties can be estimated, implying that, for a homogeneous soil deposit, the properties are only dependent on the stress history. Homogeneous in this context means the same mineralogy, grain distribution and conditions that prevailed when the deposit took place.

The procedure is to consolidate test samples beyond the preconsolidation pressure and thereafter unload them to the *OCR* value *in-situ*. The consolidation and unloading are performed with the same boundary conditions as those to which the soil is naturally exposed. The engineering properties are thereafter estimated. The idea is that the estimated characteristics can be scaled down linearly using the ratio between the true and created preconsolidation pressure.

One of the main advantage of the *SHANSEP* method is that disturbance effects due to soil sampling are eliminated when creating a preconsolidation pressure and unloading to the same *OCR* as that of the soil in situ.

The concept is very useful in practical terms, as it provides the engineer with a tool to interpolate some properties from mere knowledge of the stress history, σ'^{precon}_{vert}.

This method has, however, been questioned by many engineers, e.g. (Tavenas, 1979), on the ground that the soil structure is broken down, leading to the loss of many characteristics.

Criticism has been levelled at the method but one procedure that makes use of the advantages of the method is performing an oedometer test within the triaxial cell. The test should be compressed to a vertical strain of approximately 15% followed by unloading to an *OCR* higher than 10. Thereafter the sample is compressed to a vertical strain of approximately 25%. The first compression stage ensures that the soil has a K_0 equal to K_0^{nc}. The stress path obtained by the

unloading stage yields a ratio between σ'_{hor} and σ'_{vert} for different *OCR* values in the profile. This relation is then used when the remaining tests are consolidated for in situ stresses. Complementing the oedometer test by another within the triaxial cell yields information on the agreement between the stress path obtained by unloading from the true and created preconsolidation pressure. Information about how the CRS-test can be performed to obtain knowledge such as the unloading-reloading modulus and how best to consolidate samples within the *DSS*-equipment can also be evaluated.

After establishing the stress history by means of the standard CRS-test and dividing the soil profile into different sub layers in terms of differences in e.g. liquid limit, water content and unit weight, a limited number of tests are required within each sub layer to determine the characteristics of the overall profile. It is not necessary to test each *OCR* in the profile since the relation between e.g. shear strength in normal consolidated and overconsolidated clay has been empirically stated (Ladd *et al.*, 1977)

2.3 Empirical relations for the prediction of ground movements

When excavating next to a building or some kind of existing infrastructure it is important to understand how the constructions will behave.

There are many ways of estimating ground movement based on empirical knowledge. Some of these methods are listed by Hsieh and Ou (1998), Tefera (2004) and by Kung *et al* (2007). The ground surface settlement adjacent to an excavation is often divided into two categories depending on its shape. The first type, spandrel, has the maximum settlement next to the wall and is the normal case in non-cohesive soils and when cantilever deformations are quite large. The second is called “Concave type”, which means that the maximum settlements will occur some distance away from the wall, in most cases within a distance corresponding to the excavation depth. The two types are presented in Figure 2.14.

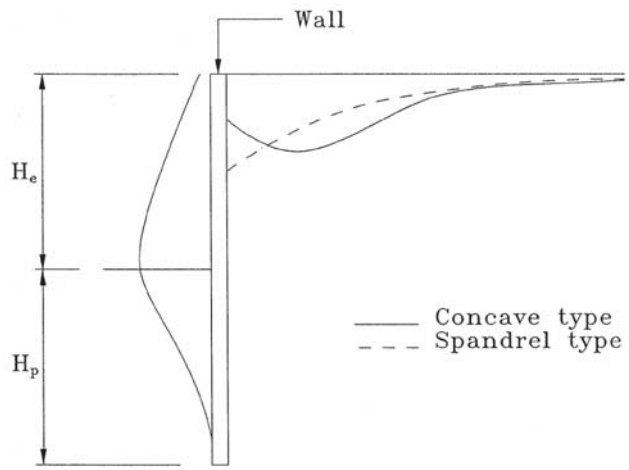

Figure 2.14: Types of settlement profile. (Hsieh and Ou, 1998)

The following sections will briefly describe some of the methods presented in the literature for predicting deformation adjacent to excavations. Note that, as each of these methods uses different notations, they will be explained in connection with each method and not listed in "List of notation". There are other methods which are not discussed here (e.g. Hamza *et al.*, 1999; Wang *et al.*, 2005; Leung and Ng, 2007).

2.3.1 Peck (1969)

Peck (1969) presented an empirical method with a major impact on the prediction of ground movement adjacent to an excavation. In his state of the art report, Peck analysed observations from different excavations regarding soil conditions, excavation depths, measured settlements next to the excavation, deformations of and forces in the lateral support system. Based on these case studies he proposed a method for estimating ground surface settlements.

Peck defines excavations as pits with vertical sides. These sides require some sort of lateral support.

The ground movement caused by an excavation in soft clay is often divided into three different groups related to causes:

1) Workmanship, deformation caused by the work procedure.
2) Unloading of the soil beneath the excavation. Poor safety against base failure leads to ground surface subsidence around the cut.
3) The soil along the supported sides tends to move inwards, even below the excavation level as a consequence of the equilibrium of a flexible wall. The inward movement causes settlements outside the excavation.

According to Peck, the most effective way of reducing settlements near a cut is to substantially reduce the inward movement of the sheeting. This can be done by a stiff and/or prestressed support system.

Recommendations regarding how deep the top anchor/strut can be placed in order to prevent large ground movements are also made in the report. These recommendations have previously been presented by Peck (1943) and Ward (1955), see equation (2.12).

$$H = \frac{2 \cdot s_u}{\gamma} \tag{2.12}$$

Base failure will occur if (e.g. Peck, 1943; Bjerrum and Eide, 1956)

$$N_b = \frac{q + \gamma \cdot H}{s_u} > N_{cb} \tag{2.13}$$

The stability factor, N_{cb}, and the stability number, N_b, are discussed in Section 2.6.4 and 2.7.3.

In Figure 2.15 all data analysed by Peck have been compiled into categories of expected ground subsidence next to an excavation.

Note: The data on which these categories are based were taken from excavations supported by sheet pile walls or soldier pile walls with lagging. Newer techniques (e.g. diaphragm walls, increased possibility to install stiff *SPW*, preinstalled soil improvement or sprayed concrete for lagging between the soldier piles) mean that the maximum settlements are often smaller than those predicted by Peck's method.

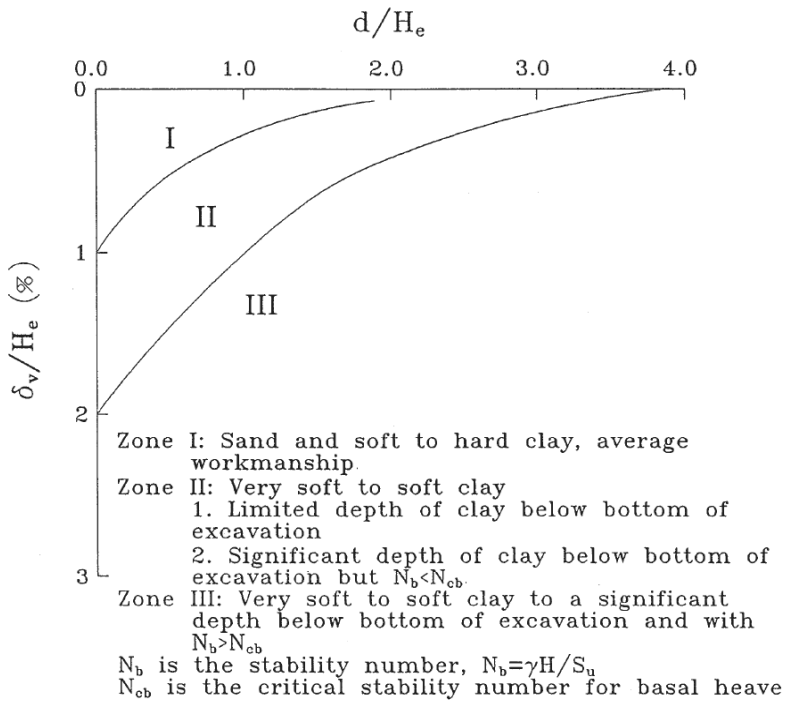

Figure 2.15: Summary of settlements adjacent to open cuts in various Soils, as function of Distance from Edge of Excavation, (Peck, 1969)

In his report, Peck also analysed the available data from different projects regarding earth pressure and loads on the lateral support system such as struts and anchors and concluded that the behaviour of the soil and the bracing system depends on the stability number, N_b, see equation (2.13). For an excavation in soft clay, it is not unusual for N_b to increase to a value of about 6 to 7. A suggestion as to how the earth pressure can be estimated for bracing and sheet pile design is provided in Figure 2.16. The *m* value can decrease down to 0.4 for cuts where soft clay extends to a considerable depth below the bottom of the excavation. The earth pressure in Figure 2.16c can be seen as a minimum pressure during the excavation procedure, due to the fact that it is negative for

an *m* value of 1 and a stability number of less than 4. This is always the case at the beginning of an excavation.

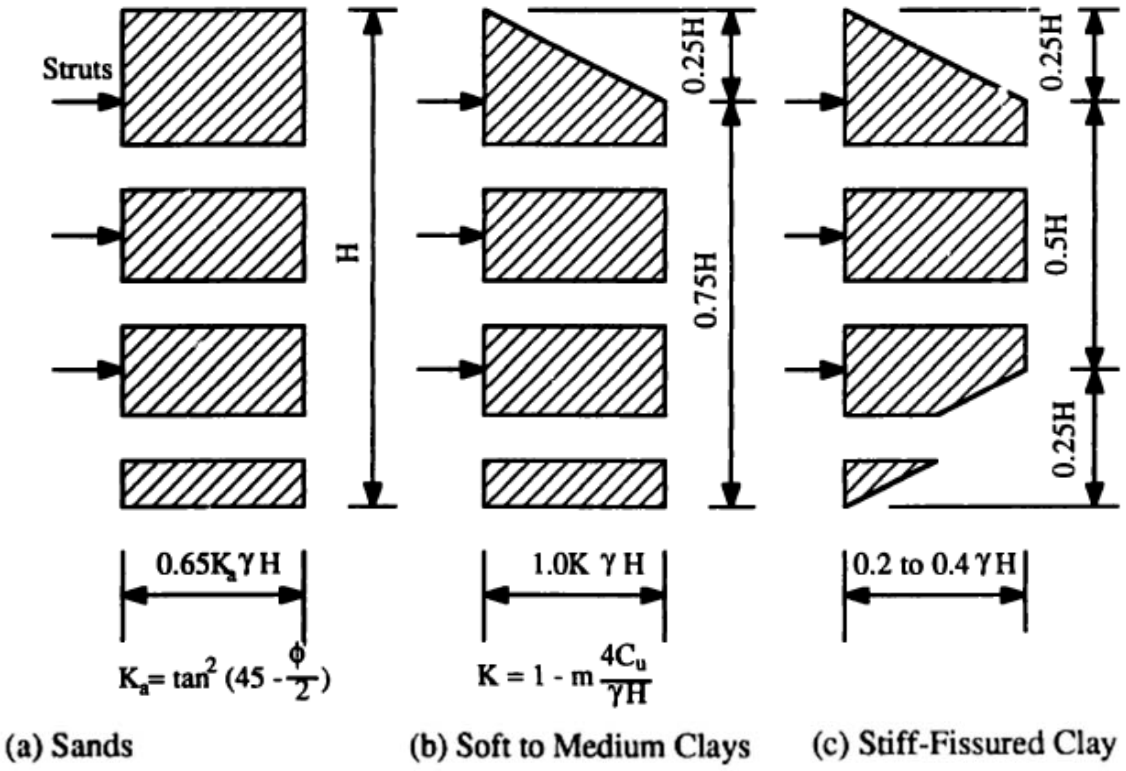

Figure 2.16: Apparent pressure diagrams suggested by Terzaghi and Peck (1967) for computing strut loads in braced cuts.

An excavation with a stability number greater than 6 develops extensive plastic zones, and therefore an assumption of a state of plastic equilibrium is valid.

2.3.2 O´Rourke (O'Rourke, 1981)

O'Rourke summarises case histories of braced excavations in both sand and clay and provides recommendations regarding expected ground movement due to the excavation and construction processes.

The wall deflections are expressed by two parameters (see Figure 2.17)*;* lateral cantilever movement, s_w, and inward bulging, s'_w. A coefficient of deformation*,* C_D*,* is defined from these deflections. The author emphasised that this coefficient should only be used as an approximate measure of relative deformation.

$$C_D = \frac{S_W}{S_W + S'_W} \tag{2.14}$$

In the paper the ratio of horizontal displacement of the wall to ground settlements next to the cut is plotted versus the coefficient of deformation, see Figure 2.17.

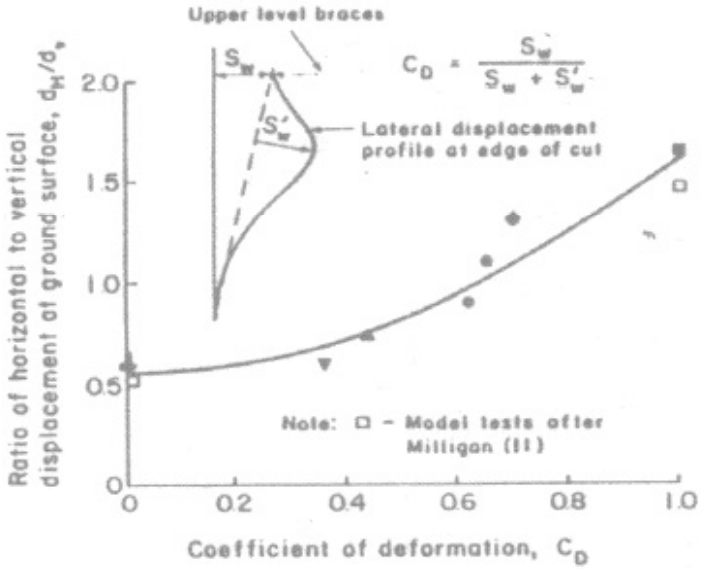

Figure 2.17: Ratio of horizontal to vertical displacement of ground surface as a function of deformation for fixed-end walls (O'Rourke, 1981)

The following conclusions can be drawn from Figure 2.17. The ratio between horizontal and vertical displacement is 1.6 for a cantilever and 0.6 if the top of the wall is fixed laterally.

The author also observed the effect of brace stiffness, pre-stressing of braces and timing of brace placement. The case studies revealed that brace stiffness could be as low as two percent of effective ideal stiffness (AE/L) due to lack of contact between the wall and the struts.

2.3.3 Bowles (1988) and Caspe (1966)

Caspe (1966) presented a method for estimating ground surface settlements from expected lateral wall deflection, which is an effective approach for sheet pile walls designed using beam spring theory. The following steps are employed to calculate the settlements.

- Estimating the lateral deflection by means of empirical relations or by representing the soil with springs.
- Integrating the lateral wall deflection in order to estimate the amount of soil volume moving laterally, V_s.
- Estimating the lateral distance of the settlements influence.

$$D = \left(H_w + H_p\right) \cdot \tan\left(45 - \phi'/2\right) \tag{2.15}$$

D=influence zone
H_w=final excavation depth

Under undrained conditions H_p=B, where B is the width of the excavation, while under drained conditions H_p=0.5·B·tan(45+ϕ'/2)

– The maximum settlement, assuming that it occurs next to the wall.

$$\delta_{vm} = \frac{4 \cdot V_s}{D} \tag{2.16}$$

– The settlements distribution is assumed to be parabolic.

$$\delta_v = \delta_{vm} \cdot \left(\frac{D - x}{D} \right)^2 \tag{2.17}$$

where x is the distance from the wall.

The lateral wall deflection is not only caused by strength mobilization of the soil as a result of the excavation but also comprises ground movements due to "workmanship". This method can therefore be used to identify ground surface settlements caused by factors other than lateral movement, e.g. material contraction due to vibrations or material transportation as a result of hydraulic gradients.

2.3.4 Clough and O´Rourke (1990)

In (Clough and O'Rourke, 1990), the authors summarize case histories of ground movements, which are divided into two categories: 1) Movements caused by the excavation and the support process. 2) Movements caused by auxiliary construction activities. The recorded movements were categorised and presented in a plot where the relative lateral displacement was plotted against the stiffness of the support system, Figure 2.18.

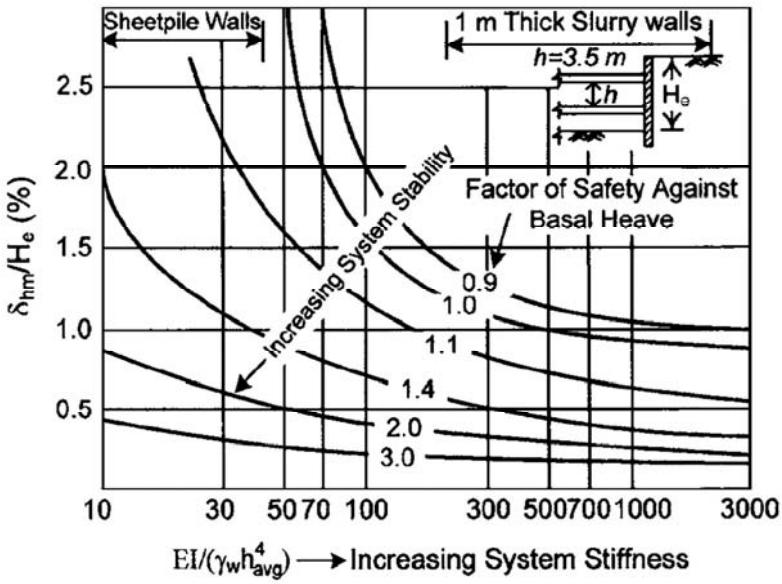

Figure 2.18: Design curves used to obtain maximum lateral wall movement (soil settlement) in soft to medium clays (Clough and O'Rourke, 1990).

Based on the case study, the authors suggested three different settlement profiles next to the excavation. For excavations in sand and stiff clay, the typical settlements profile seems to have a triangular distribution, while in the case of soft clay, the best match of the measured settlements appears to be a trapezoid, Figure 2.19.

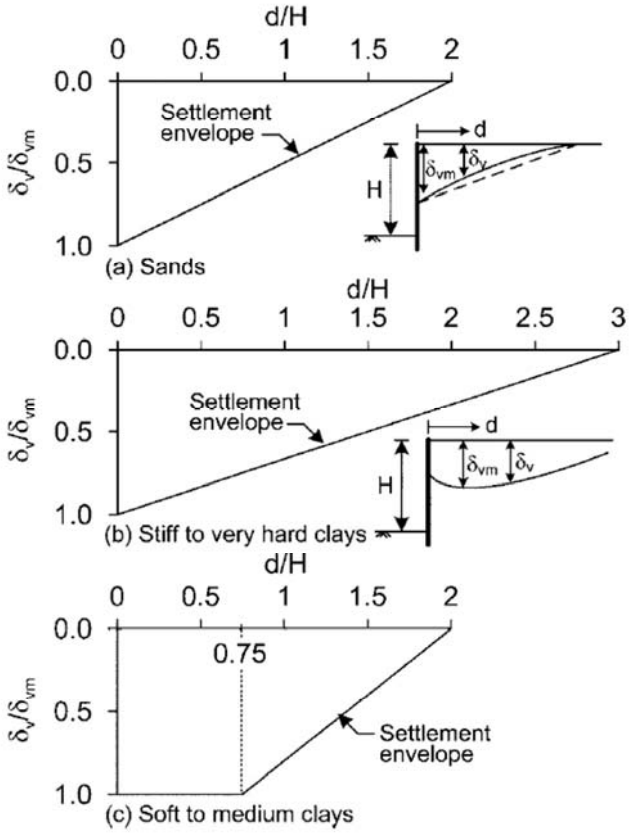

Figure 2.19: Dimensionless settlement profiles recommended for estimating the distribution of settlements adjacent to excavations in different soil types (Clough and O'Rourke, 1990).

2.3.5 Hsieh and Ou (1998)

In this paper the authors present two different methods of prediction for settlements adjacent to an excavation, the first for a settlement profile similar to the sprandrel type and the second for an expected concave type.

In order to establish which profile can be expected, the lateral wall deformation must be known or estimated. The lateral wall deformation is therefore divided into two components, cantilever component A_c, and a component caused by the bending of the wall, deep inward component A_s. The area A_c is defined in Equation (2.18).

$$A_c = \max\left(A_{c1}, A_{c2}\right) \tag{2.18}$$

The two components are illustrated in Figure 2.20.

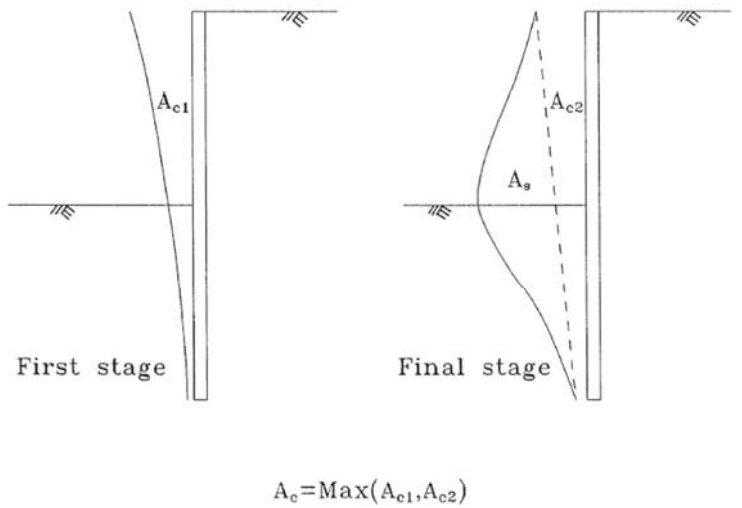

Figure 2.20: Areas of the cantilever and deep inward components.

Several studies clearly indicate that the settlement profile will be of the concave type if $A_s \geq 1.6 \cdot A_c$ Figure 2.21.

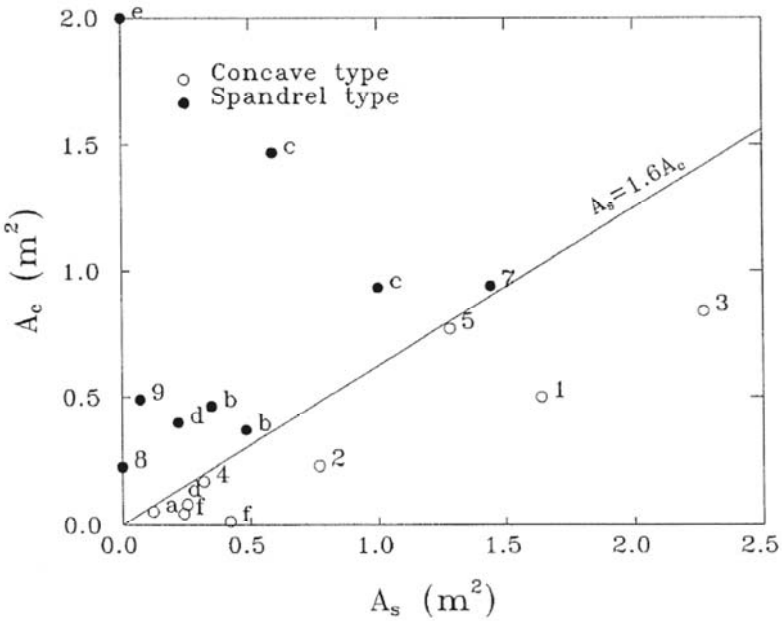

Figure 2.21: Relationship between the area of the cantilever component and the deep inward component of the deflected wall.

The case study performed in the paper and a study by Mana and Clough (1981) appear to show a relation of approximately 0.5 to 1.0 between maximum ground settlements and the maximum lateral wall deflection, Figure 2.22.

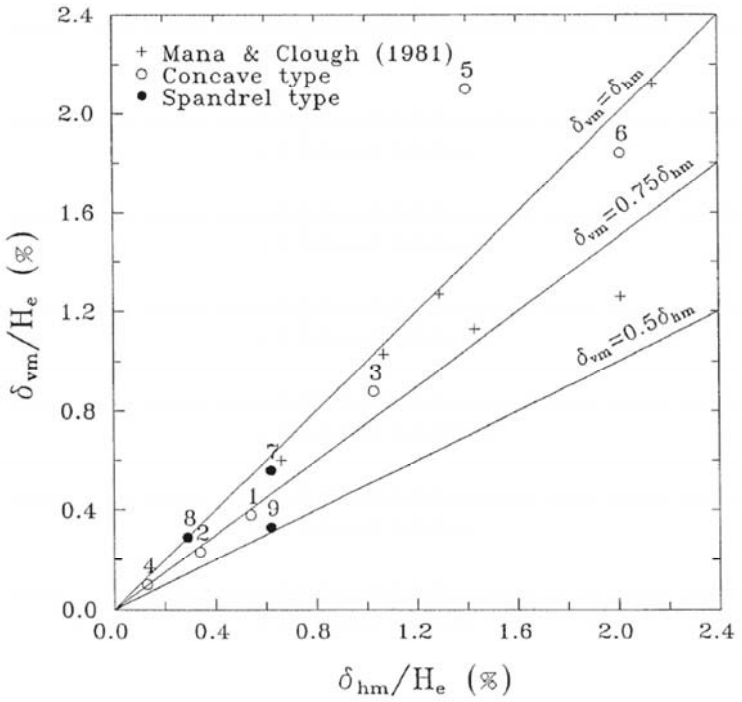

Figure 2.22: Relationship between maximum wall deflection and maximum ground surface settlement.

The prediction procedure is as follows:

- Predict the lateral wall deflection by means of either a finite element method or a spring beam model.
- Determine the type of settlement profile, either spandrel or concave.
- Estimate the maximum ground surface settlement, see Figure 2.22.
- Calculate the surface settlement at various distances from the wall in accordance with the information contained in the following sections.

If no satisfactory predictions of the lateral deformations are available, the method proposed by Clough and O'Rourke (1990) can be used, although it does not provide any information about the settlement profile. However, the final settlement profile is the same type as that in the earlier excavation step, which means that the critical ground settlements in the final excavation step can be predicted using the observational method in the earlier stages of the excavation

2.3.5.1 Sprandrel settlement profile

The following pattern was suggested by Hsieh and Ou (1998) based on a number of observed settlement profiles, see Figure 2.23.

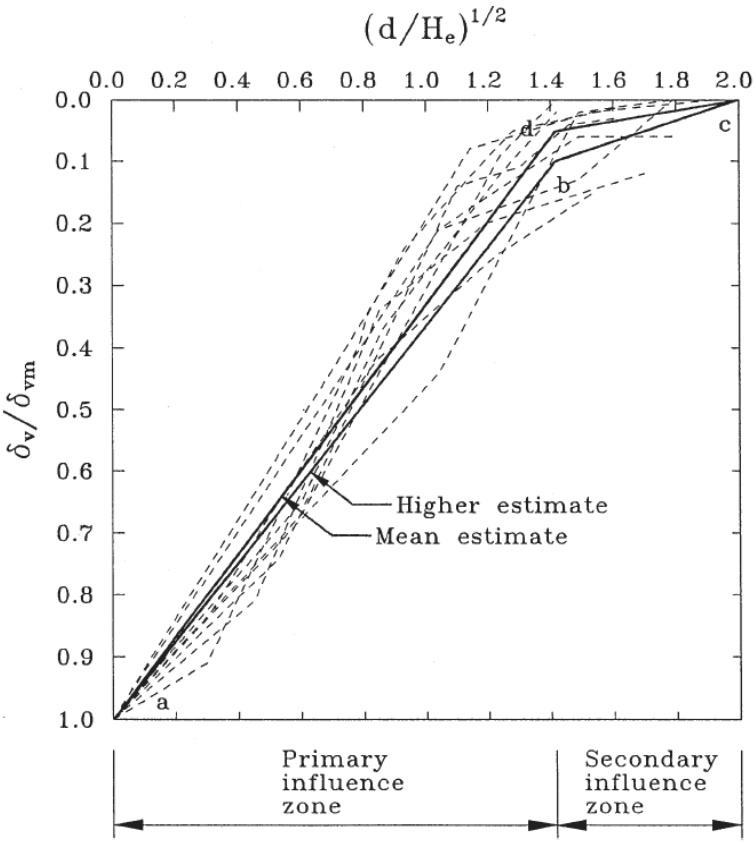

Figure 2.23: Proposed method for predicting spandrel settlement profile. Each broken line represents a case history.

The mean estimate line is based on a regression analysis while the higher estimate line is the mean line plus one standard deviation, as expressed in equation (2.19).

$$\delta_v = \left(-0.636 \cdot \sqrt{\frac{d}{H_e}} + 1\right) \cdot \delta_{vm} \qquad if\ d/H_e \le 2$$
$$\delta_v = \left(-0.171 \cdot \sqrt{\frac{d}{H_e}} + 0.342\right) \cdot \delta_{vm} \qquad if\ d/H_e > 2 \tag{2.19}$$

H_e is the excavation depth and d equals the distance from the wall. As can be seen in Figure 2.23, line a-b has a relatively steep slope. This area is referred to as the "primary influence zone". Within this $d/H_e \le 2$ zone, the settlements can have a negative effect on adjacent buildings. Outside of this zone the settlements seem to be insignificant. The maximum settlement outside the primary influence zone is about 10% of the settlement next to the wall.

2.3.5.2 Concave settlement profile.

This kind of settlement profile will occur if the deformations during the first excavation step, prior to the installation of the first support level, are small compared to those during the subsequent excavation steps. In order to predict

these settlement profiles, it is important to know where the maximum lateral deformation will occur. In most cases it will be at or near the bottom of the excavation and a number of studies indicate that the maximum ground settlement will develop at a distance of half the excavation depth from the wall (Nicholson, 1987; Ou *et al.*, 1993). Other cases studies (Clough and O'Rourke, 1990) show that the settlement next to the wall appears to be in the range of 50-70% of the maximum settlement. In the profile type presented by the authors, 50% of the maximum settlements are assumed to be next to the wall. Even in the case of these kinds of profiles, the settlements are deemed to be negligible at a distance of $4H_e$, and 10% of the maximum settlements are at a distance of $4H_e$ from the wall. Figure 2.24 shows a simplified linear relationship between the turning points

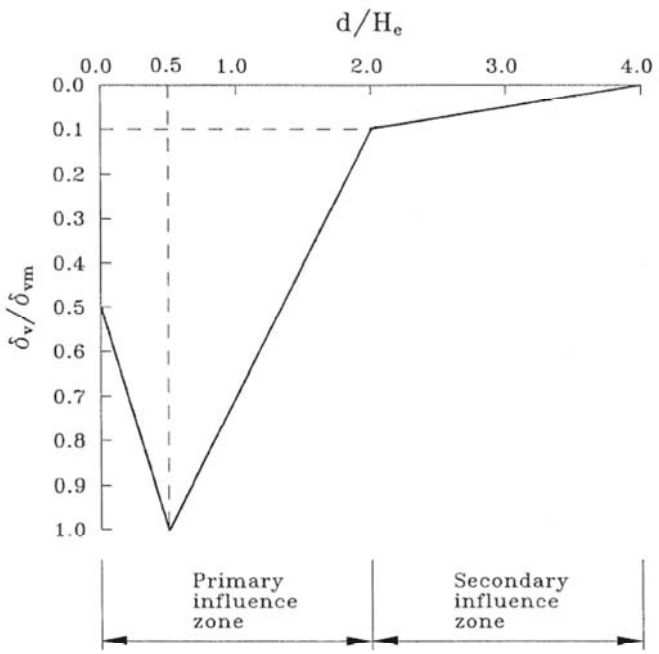

Figure 2.24: Proposed method for predicting concave settlement profile (Hsieh and Ou, 1998).

2.3.6 A simplified model by Kung *et al.* (2007), the *KJHH* model

A semi-empirical model was recently presented by Kung *et al. (2007)* entitled "Simplified Model for Wall Deflection and Ground-Surface Settlement Caused by Braced Excavation in Clays.

The model is based on

1. Good quality excavation case histories (33)
2. FE analysis using a small-strain soil model
3. Isolation of the most important factors affecting maximum wall deflection
4. A large amount of artificial data on excavation-induced wall and ground responses in the form of *FE* calculations

The authors identified the following parameters as the most important for the inward movement of the retaining wall

- Excavation height, H_e
- Support system stiffness, $EI/(\gamma h_{avg}^4)$
- Width of excavation, B
- Relative undrained shear strength, s_u/σ'_{vert}
- Relative soil stiffness, E_i/σ'_{vert}

A transformation function[5] was established for each of these parameters in order to study the relation between them and maximum wall deflection. Based on the transformation functions, a regression analysis was performed as a means of studying the influence of each of the five parameters.

$$X_i = a_{1i}x_i^2 + a_{2i}x_i + a_{3i} \tag{2.20}$$

$$\begin{aligned}\delta_{h\,max}^{no\ hard\ stratum} &= b_0 + b_1X_1 + b_2X_2 + b_3X_3 + b_4X_4 \\ &\quad + b_5X_5 + b_6X_1X_2 + b_7X_1X_3 + b_8X_1X_5\end{aligned} \tag{2.21}$$

The coefficients of Equation (2.20) can be found in Table 2.1 and those of Equation (2.21) in Table 2.2. Having established $\delta_{h\,max}^{no\ hard\ stratum}$, an adjustment is made to account for the presence of a hard stratum

$$\delta_{h\,max} = \frac{\delta_{h\,max}^{no\ hard\ stratum}}{K} \tag{2.22}$$

Where $K=1.5(T/B)+0.4$ for $(T/B) \leq 0.4$ and 1.0 otherwise, T is the distance from the excavation grade to the firm layer.

Table 2.1: Coefficients for linear transformation of five variables

i	x_i	a_{1i}	a_{2i}	a_{3i}	Applicable range of x_i
1	H_e	-0.4	24	-50	0-30
2	$ln(EI/(\gamma h_{avg}^4))$	11.5	-295	2000	≤0
3	$B/2$	-0.04	4	90	0≤B≤100 (m)
4	s_u/σ'_{vert}	3225	-2882	730	0.2-0.4
5	E_i/σ'_{vert}	0.00041	-1	500	200-1200

[5] Kung *et al.* are aware of the limitations of the KJHH model when using a polynomial function. However, it has been found to be suitable within an applicable range for each of the five parameters.

When the $\delta_{h\,max}$ has been established the ratio between $\delta_{h\,max}/\ \delta_{v\,max}$ is found by using Equation (2.23) where $Y_1=\Sigma H_{clay}/H_e$ (the amount of clay to the excavation grade), $Y_2= s_u/\sigma'_{vert}$ and $Y_2= E_i/\ \sigma'_{vert}/1000$. The coefficients c_0-c_8 are listed in Table 2.2

$$R = c_0 + c_1Y_1 + c_2Y_2 + c_3Y_3 + c_4Y_1Y_2 + c_5Y_1Y_3 + c_6Y_2Y_3 + c_7Y_3^3 + c_7Y_1Y_2Y_3 \qquad (2.23)$$

Table 2.2: Coefficients for Equation (2.21) and (2.23)

i	0	1	2	3	4	5	6	7	8
b_i	-13.4197	-0.49351	-0.09872	0.06025	0.23766	-0.15406	0.00093	0.00285	0.00198
c_i	4.55622	-3.40151	-7.37697	-4.99407	7.14106	4.60055	8.74863	0.38092	-10.5896

The predicted ground surface profile follows the pattern presented by Hsieh and Ou (1998) for the concave settlement profile and can be found in Equation (2.24). However, small adjustments have been made compared to the settlement profile presented by these authors.

$$\delta_{vert}(x) = R \cdot \delta_{h\,max} \begin{cases} 1.6\ {}^{x}\!/_{H_e} + 0.2 & for \quad 0 \le {}^{x}\!/_{H_e} \le 0.5 \\ -0.6\ {}^{x}\!/_{H_e} + 1.3 & for \quad 0.5 \le {}^{x}\!/_{H_e} \le 2.0 \\ -0.05\ {}^{x}\!/_{H_e} + 0.2 & for \quad 2.0 \le {}^{x}\!/_{H_e} \le 4.0 \end{cases} \qquad (2.24)$$

Kung *et al*. compared the results of the *KJHH* model with the 33 cases and the *FE* simulations (144 different combinations) and calculated the model bias as well as its standard deviation. They demonstrated that the model bias for horizontal deformation can be expressed by $\mu_{hor}=1.0$ with $\sigma_{hor}=0.25$ and for maximum vertical deformation by $\mu_{vert}=1.0$ with $\sigma_{hor}=0.13$.

2.3.7 Distribution of ground movements parallel to the excavation

There are several empirical and semi-empirical methods for predicting the settlement distribution at various distances from the retaining wall, some of which have been presented here. However, in many cases the three-dimensional effects caused by the relatively high stiffness at the corners of an excavation lead to smaller ground movements near the corners and larger movements towards the centre of the retaining wall. Roboski and Finno (2006) presented an erfc fitting function for describing these differences in ground movement parallel to an excavation wall. The function in question (see Equation (2.25)) was derived from well documented excavations and the work by Schmidt (1969).

$$\delta(x) = \delta_{max}\left[1 - \frac{1}{2}\operatorname{erfc}\left(\frac{2.8\left(x + L\left(0.015 + 0.035 \cdot \ln\left(\frac{H_e}{L}\right)\right)\right)}{0.5 - L\left(0.015 + 0.035 \cdot \ln\left(\frac{H_e}{L}\right)\right)}\right)\right] \tag{2.25}$$

where x is the distance from the corner, L the length of the excavation, H_e the excavation depth and δ_{max} the deformation at the centre of the excavation. The latter can be approximately derived from two-dimensional *FE*-calculations or an empirical method and can describe both horizontal and vertical deformation, see Figure 2.25

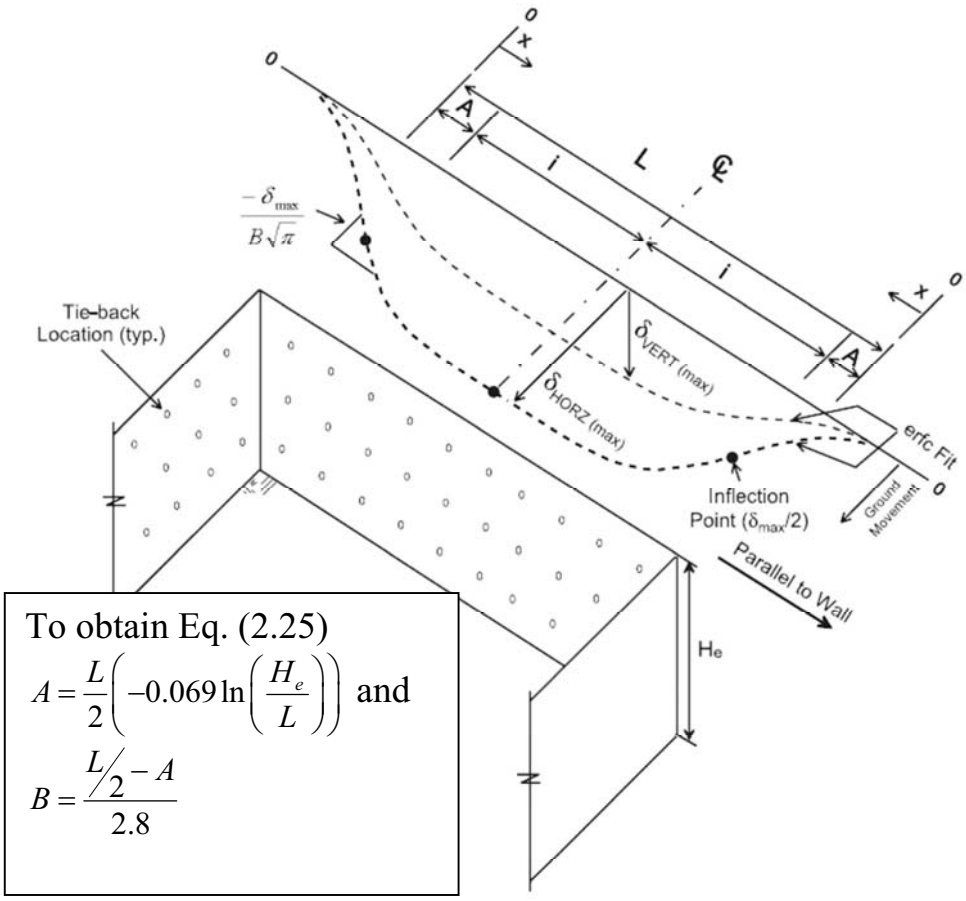

Figure 2.25: Empirical deformations parallel to the excavation, from Roboski and Finno (2006).

This method is not recommended when adjacent constructions have deep foundations or for very stiff constructions, since these affect the distribution. However, the authors recommended it for shallow foundations, which is the case in many old buildings.

2.3.8 Displacement flexibility number

Most of the prescribed empirical or semi-empirical settlement prediction methods described previously assume that similar behaviour can be expected

when using the same support system stiffness ($EI/\gamma_w h_{avg}^4$). However, this is only based on maximum lateral deflection and not on the shape of the deflection. The support system stiffness resembles the flexibility number $H^4/(EI)$ presented by Rowe (1952), where H is equal to the wall height. Addenbrooke *et al.* (2000) extended the relation developed by Rowe to make it applicable to a multipropped retaining wall and introduced a displacement flexibility number, $EI/\ h_{avg}^5$, assuming plane strain conditions.

Addenbrooke *et al.* (2000) performed many non linear *FE* analyses capable of describing small strain behaviour and came to the conclusion that, for a given initial stress situation and prop stiffness, a support system with the same flexibility number generates practically the same maximum lateral wall deformation and the same ground surface settlement profile.

2.3.9 Artificial and self learning methods

In recent years computer capacity has increased, thus making it possible to create self-learning programs. When it comes to predicting ground surface settlements from an excavation carried out in many steps, field monitoring, e.g. lateral wall deflection, support loads and observed settlements, can be used as input variables to obtain a prognostication for forthcoming excavation stages. The code will automatically update the constitutive model parameters that describe soil behaviour, so that the monitored deformations and loads are obtained in the calculation (Jan *et al.*, 2002; Hashash *et al.*, 2006).

Parameters have been manually updated for many years and the risk associated with automatic updating is that it may generate unrealistic soil parameter combinations. Some upper and lower parameter ranges must be incorporated into the automatic updating code.

2.4 Soil structure interaction

Deep excavations in soft clay involve interaction between the soil and the retaining system, which makes the geo-structures more complex than in many other engineering structures. The retaining system, e.g. an embedded sheet pile wall supported by struts or anchors, is both supported and loaded by the soil. Load and support depend on the deformation within the soil mass. This is true for the anchors and struts as well, but the deformation needed to produce full support is much smaller than in the soil mass.

The support of an embedded sheet pile wall, *SPW*, is not only related to the embedded length but also to the mobilized shear strength in the soil on the retained (active) side. Small deformations generate low mobilization of the strength, leading to high loads on the retaining system, while large deformations

utilize the strength of the soil, thus generating less pressure. However, the deformation necessary for full utilization of the soil capacity is dependent on the relative deformation between the retaining wall and the soil. In the active case, where the wall moves away from the soil, the deformation needed to utilize the full capacity of the soil strength is, as a rule of thumb, 0.1% of the height of the structure. The soil strength counteracts the movement of the soil. In the passive case, where the wall moves against the soil, the strength is utilized in a way that counteracts the deformation in the wall. A deformation of approximately 1% is required to develop full strength utilization in the passive case.

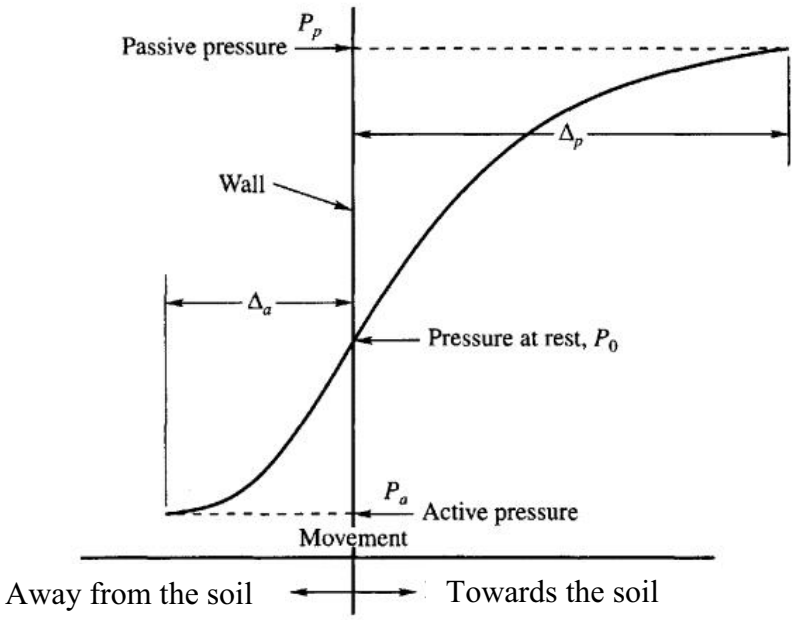

Figure 2.26: Principles of the link between lateral deformation and the force acting on the retaining wall. $\Delta_a \approx 0.1\%$ of H and $\Delta_p \approx 1.0\%$ of H. H indicates the height of the wall.

This rule of thumb cannot be directly transferred to the situation adjacent to a supported embedded *SPW*. On the retained side, the active pressure develops quickly in the unsupported areas (no struts or pre-stressed anchors). During the subsequent excavation phases, the wall may move against the soil in some areas, depending on the support system. This movement will generate the pressure at rest for a smaller deformation required for the development of active pressure. On the excavated side of the wall, the decrease in vertical stress affects the relation between horizontal and vertical stress. Consequently, the capacity to develop full strength utilisation decreases.

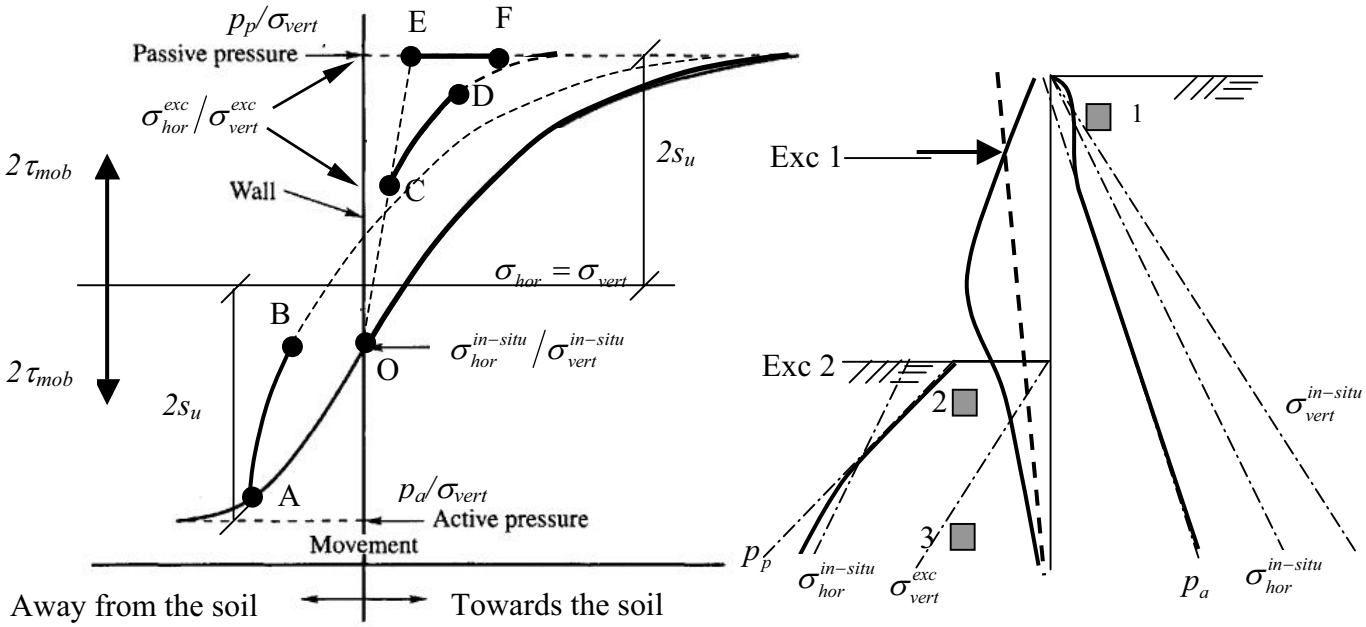

Point	Stress deformation path	Comment
1	0-A-B	Inward deformation followd by a backward deformation due to rotation
2	0-E-F	Inward movements followed by a decrease in the ability to develop passive pressure. Full plasticity is reached due to the fact that $\sigma_{hor}^{in-situ} > p_p$
3	0-C-D	Inward movements followed by a decrease in the ability to develop passive pressure. Full passive pressure has not developed, $\sigma_{hor}^{in-situ} < p_p$

Figure 2.27: Sketch of the relation between developed lateral pressure due to the initial stress state and the deformation in the sheet pile wall.

2.5 Soil modelling

A model in this context is a simplification used to describe the real soil behaviour. When modelling soil it is important to use the proper level of simplification. In some cases, a rough estimate of the behaviour of a structure will be adequate and there is no benefit to be gained from trying to model the soil behaviour in detail. However, if there is a need for more reliable estimations, a more advanced model has to be used. When modelling the problem in a more complex way, the need for proper input parameters increases and in most cases the effort involved in obtaining them increases as well.

The challenge is to use the appropriate level of effort in order to obtain the desired accuracy in the results. “The skill in modelling is to spot the appropriate level of simplification – to recognise those features which are important and those which are unimportant” (Wood, 2004).

Classical soil modelling can roughly be divided into two groups: 1) Limit equilibrium methods and 2) Linear elastic solutions, (Nordal, 2004).

In limit equilibrium methods, a complete soil mass, e.g. slope stability, is studied. In classic slope stability analysis, a safety factor is calculated for a given geometry and soil strength. Classic earth pressure theory is also based on limit equilibrium assumptions.

The second group consists of a coupling between stresses and strains at each individual point in the soil mass. Historically, a linear elastic relation between stress and strain has been assumed. When this approach is used, the problem is often solved by the finite element method. During recent decades, the capacity of computers have increased, making it possible to solve problems with more and more unknown parameters. An effect of the growing use of computers is the development of many constitutive models.

Soil modelling is a way of exploring the relation between cause and effect on a soil mass, e.g. a mathematical relationship between stresses and strains or stress increments and strain increments. The relationship is often referred to as the constitutive or material law.

However, soil modelling involves more than just using an appropriate constitutive model. The constitutive model provides the right relation between stresses and strains in a certain point, but in order to analyse a soil mass, the equilibrium, compatibility and constitutive equations must be combined and used with the proper boundary conditions (Nordal, 2004).

2.5.1 Overview of different methods of analysis

The short introduction to soil modelling above states that, for an exact theoretical solution, the *equilibrium*, *compatibility*, *material behaviour* and *boundary condition requirements* must be satisfied. Both forces and displacements have to be taken into account. Potts and Zdravkovic (1999) presented an overview of different methods. These methods can be grouped into categories and are here presented in Table 2.3 and Table 2.4. The first table summarizes how well the different approaches fulfil the requirements of an exact theoretical solution, while the latter summarizes the capacity of the various approaches to provide design information.

Closed form solutions

Closed form solution refers to analytical expressions that are theoretically correct. This kind of solution may be found for a particular geotechnical issue, but will still remain approximate, since it was developed for idealized conditions. If a closed form solution can be established, it is the best way of

analysing the problem at hand. Because of the complexity of soil behaviour, there are only two groups of closed form solutions, one assuming isotropic linear elastic behaviour in the soil, while the other employs geometric symmetry to reduce the problem to one dimension.

Limit equilibrium
This is probably the most common way of analysing geotechnical problems such as stability. A failure surface with the soil at failure over its whole length is assumed. Examples of these kinds of solution are the Coulomb wedge analysis and the method of slices used for overall stability problems.

Stress field solutions
The soil is assumed to be at failure in the complete soil mass. Equilibrium is obtained by combining the failure criterion with the equilibrium equations. One example of this kind of solution is the active and passive stresses proposed by Rankine (1857).

Limit analysis (lower and upper bound)
These methods assume that the soil behaves in a perfectly plastic fashion when the stresses reach a single yield surface. Neither hardening nor softening effects are taken into account. Associated flow is assumed and, even at failure, deformations are deemed to be small.

An upper bound solution can be found by selecting any kinematically, possible failure mechanism and performing an appropriate work rate calculation. This solution in this case will be unsafe or true (Chen, 1975).

A lower bond solution is dependent on the identification of a statically admissible stress field, which at no point violates the yield condition. The loads in equilibrium will provide a safe or a true solution (Chen, 1975).

For example, the critical height of a vertical cut in undrained clay (Potts and Zdravkovic, 1999) is $4 \cdot s_u/\gamma$ for the upper and $2 \cdot s_u/\gamma$ for the lower bound solution

When the upper and the lower bound solutions coincide, the true solution is obtained.

Results from upper and lower bound solutions are presented by Ukritchon *et al.* (2003) for undrained stability of braced excavations in clay. These results are presented as ranges for the stability number, *N*, for different braced excavations. The influence of wall adhesion, distance to firm layers and the effect of wall embedment are presented.

Numerical analysis

A common way of modelling the soil-structure interaction is to use a beam-spring model. In these kinds of analysis, the soil is represented by springs, and the retaining structure is analysed using either finite element or finite difference techniques. Any support, e.g. struts or anchors, is also represented by springs (Pappin *et al.*, 1986; Borin, 1989). The soil behaviour is reduced to a spring coefficient, often represented as a simplified model of the behaviour presented in Figure 2.26. A difficulty associated with this method is the establishment of the spring coefficient[6], $k=f(\delta)$, which cannot be directly estimated from the soil modulus. Converting a stress strain relation in the soil to a force deformation relation requires assumptions about the strain field next to the excavation. To take account of phenomena such as preserved lateral stresses at the excavated side of the wall, cf. Figure 2.27, the relation describing the soil-structure interaction must be fairly complex. The beam-spring method has difficulties producing reliable results for complex geometries, e.g. berms, and neglects the influence of adjacent structures.

In a full numerical analysis, the soil mass is modelled with a constitutive relation, and the interaction between soil and structure is thereafter obtained by either the finite element method or the finite difference method. The constitutive relation can be more or less complicated. A suitable level of complexity for the problem studied has to be established in these relations. Constitutive relations require good input data as well as parameters describing the strength and the stress-strain relation. For more complex constitutive relations capable of simulating true soil behaviour, a greater number of properties describing the soil have to be established. The routine investigation of the soil properties may have to be complemented by other kinds of tests. This is often incorrectly referred to as a shortcoming of the method. The only true shortcoming of the method is the user's skill in modelling the problem, e.g. establishing the proper boundary conditions and understanding the effect of some simplifications in the model. The user also has to be familiar with the effect of approximations in the algorithm used to solve the non-linear numerical analysis and errors associated with the chosen discretisation of the problem (Potts and Zdravkovic, 1999).

[6] Also called the coefficient of subgrade reaction.

Table 2.3: Basic solution requirements satisfied by the various methods of analysis (Potts and Zdravkovic, 1999, table 1.1)

Method of analysis		Required solution				
		Equilib-rium	Compab-itility	Constitutive behaviour	Boundary conditions	
					Force	Disp.
Closed form		S	S	Linear elastic	S	NS
Limit equilibrium		S	NS	Rigid with failure criterion	S	NS
Stress field		S	NS		S	NS
Limit analysis	Lower bound	S	NS	Ideal plasticity with associated flow rule	S	NS
	Upper bound	NS	S		NS	S
Beam-Spring approaches		S	S	Soil modelled by springs or elastic interaction factors	S	S
Full numerical analysis		S	S	Any	S	S

S – Satisfied; NS – Not Satisfied

Table 2.4: Design requirements satisfied by the various methods of analysis (Potts and Zdravkovic, 1999, table 1.2)

Method of analysis		Design requirements						
		Stability			Wall and supports		Adjacent structures	
		Wall and support	Base heave	Overall	Structural force	Displacement	Structural force	Displacement
Closed form		No	No	No	Yes	Yes	Yes	Yes
Limit equilibrium		Yes	*	*	Yes			
Stress field		Yes	*	*	Yes	No	No	No
Limit analysis	Lower bound	Yes	*	*	**	No	No	No
	Upper bound	Yes	*	*	**	**	No	No
Beam-Spring approaches		Yes	No	No	Yes	Yes	No	No
Full numerical analysis		Yes	Yes	Yes	Yes	Yes	Yes	Yes

* Separate calculation needed

** Crude estimate

Non-linear full numerical analysis makes it possible to evaluate the stress distribution as well as the deformation of a retaining wall and soil. Different construction activities can be incorporated into the analysis. However, finite element calculations are rarely used as a primary source of information for stability analyses or calculating lateral earth pressure. Simpler methods such as limit equilibrium are still very common when designing the required retaining system.

Apart from being easy to handle, one of the main reasons for continuing to use the simpler methods is the uncertainty related to designing a structure with an adequate factor of safety. The commonly used method for obtaining a factor of safety using the finite element is the stepwise reduction of shear strength until the deformations get out of hand. This method of determining the factor of safety raises questions, e.g. about correlations between strength and modulus. Such uncertainties have not been studied by means of the limit equilibrium method, maybe with the assumption of studying progressive failure, thus the factor of safety obtained from the *FE*-analysis is often questioned, in spite of the fact that it may be more accurate than the method with different kinds of partial factors. However, the demands on the factor of safety are based on empirical knowledge and should not be disregarded. Basic methods such as limit equilibrium still merit use when to establish the factor of safety.

2.6 Classical earth pressure theory

There are many methods for estimating the lateral pressure against a retaining wall. An overview of such methods was presented by Dellatre (2001) and can be seen in Figure 2.28. All of these methods will, however, not be discussed here, only some of the classic ones.

All these methods were developed for the serviceability limit state, with the exception of that proposed by Brinch-Hansen.

Historically, the theory of plasticity has been used to calculate lateral earth pressure. In this theory, a zone of soil is assumed to reach plastic equilibrium so that plastic collapse occurs. A wedge of soil will slip relative to the rest of the soil mass. Full mobilization of the peak soil strength is assumed along this slip surface. The collapse load is calculated from this assumption after reducing the peak strength values by a factor of safety. The reduction is introduced to allow uncertainties and limit movements, thus ensuring that the actual stresses are far from their ultimate values.

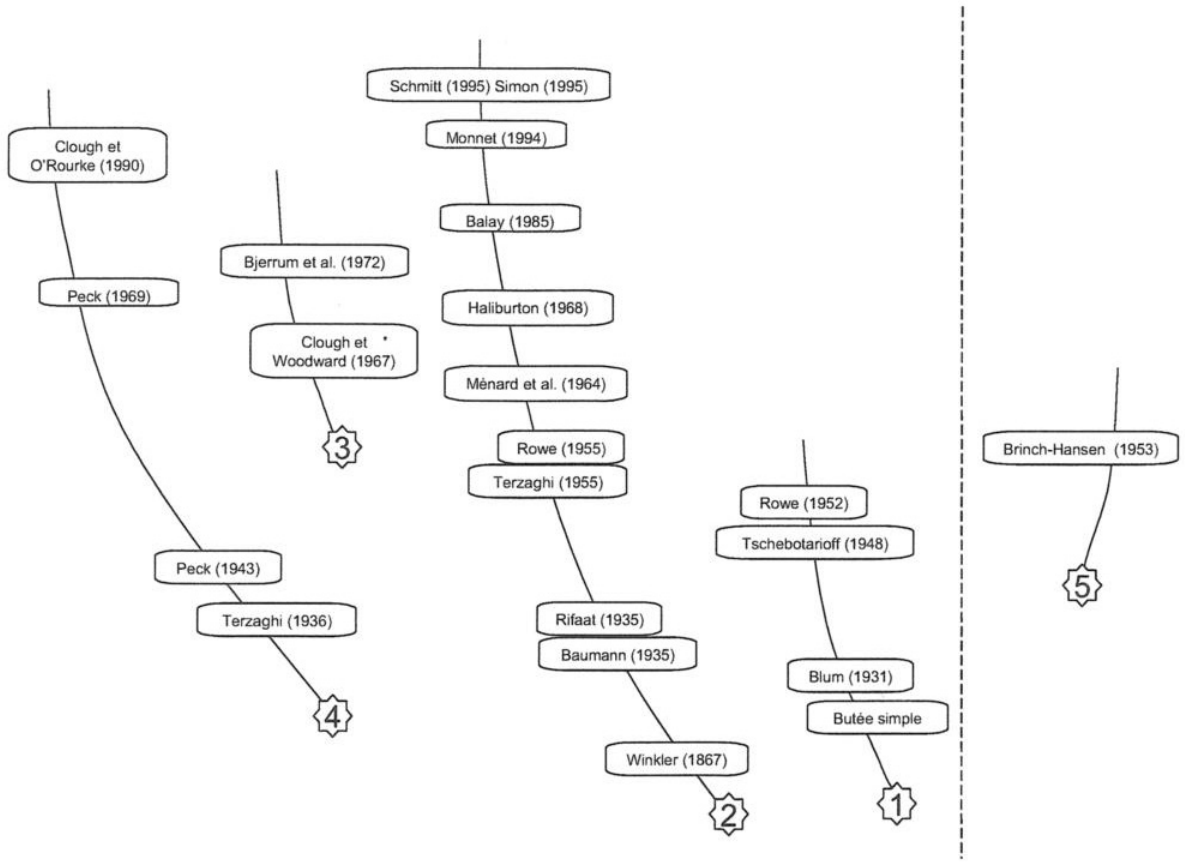

Figure 2.28: Major directions and principal stages in the development of design methods for retaining walls. The left side of the diagram shows serviceability limit analysis methods and the right side the ultimate limit state analysis method.
1) classical methods 2) subgrade reaction methods 3) finite element methods 4) empirical methods 5) ultimate limit state analysis methods
(Dellatre, 2001; also presented by Tefera, 2004)

2.6.1 Coulomb

Charles Augustin Coulomb was probably the first author to address the subject of "soil mechanics". Coulomb is often believed to have defined shear strength, but in reality he did not and in his "Essay" (Coulomb, 1776) mentions a Monsieur Amontons. In his wedge method where he assumed the wedge to be a rigid body, he used the shear strength in Equation (2.26) but in fact he did not write the equation himself.

$$s = c' + \sigma' \cdot \tan(\phi') \tag{2.26}$$

Coulomb sketched the wedge slightly curved but in his equation he used straight failure surfaces. Many textbooks state that Coulomb did not include cohesion in his equation, but in fact he did. The equation known as "Coulomb's lateral earth coefficients" was not written by Coulomb but derived using the same relation as Coulomb, although without considering cohesion (Oner, 1997). This coefficient defines the limits of the relationship between effective vertical stress and effective horizontal stress, Equation (2.27).

$$\sigma'_{hor} = \gamma' z K \tag{2.27}$$

where γ' is the effective unit weight, z the depth and K the lateral coefficient. The limits of K are given in Equations (2.28) and (2.29).

$$K_a = \frac{\sin^2(\alpha+\phi')}{\sin^2(\alpha)\sin(\alpha-\delta)\left[1+\sqrt{\frac{\sin(\phi'+\delta)\sin(\phi'-\beta)}{\sin(\alpha-\delta)\sin(\alpha+\beta)}}\right]} \tag{2.28}$$

$$K_p = \frac{\sin^2(\alpha-\phi')}{\sin^2(\alpha)\sin(\alpha+\delta)\left[1-\sqrt{\frac{\sin(\phi'+\delta)\sin(\phi'-\beta)}{\sin(\alpha-\delta)\sin(\alpha+\beta)}}\right]} \tag{2.29}$$

In Equation (2.28) and (2.29) α defines the inclination of the wall against the vertical and β defines the inclination of the ground surface. The friction angle between the wall and the soil is defined by δ.

2.6.2 Rankine

According to Rankine, earth pressure limits was defined based on the assumption that the whole soil mass is in a state of plastic equilibrium. Contrary to Coulomb, Rankine did not consider wall friction. The relations for the lateral earth pressure coefficients are given by Equation (2.30) and (2.31).

$$K_a = \cos(\beta)\frac{\cos(\beta)-\sqrt{\cos^2(\beta)-\cos^2(\phi')}}{\cos(\beta)+\sqrt{\cos^2(\beta)-\cos^2(\phi')}} \tag{2.30}$$

$$K_p = \cos(\beta)\frac{\cos(\beta)+\sqrt{\cos^2(\beta)-\cos^2(\phi')}}{\cos(\beta)-\sqrt{\cos^2(\beta)-\cos^2(\phi')}} \tag{2.31}$$

where β defines the inclination of the ground surface.

Cohesion was first introduced as a parameter, as we know it today, by Bell (1915), Equations (2.32) and (2.33).

$$p_a = \gamma' z K_a - 2c'\sqrt{K_a} + p_w \tag{2.32}$$

$$p_p = \gamma' z K_p + 2c'\sqrt{K_p} + p_w \tag{2.33}$$

where K_a and K_p are functions of ϕ' and c' is shear strength when the compression forces equal zero, cf. Equation (2.26). In order to obtain the total stress, the stationary pore water pressure, p_w, must be added. In the undrained total stress analysis, $c'=s_u$ and $\phi'=0$. It should be noted that in most design situations, negative values of p_a cannot be taken into account.

2.6.3 Adhesion between the soil and the retaining wall.

Rankine neglected adhesion between the soil and the retaining wall in his derivation of the earth pressure limits. However, adhesion does exist and the amount is dependent on the roughness between the structure and the soil. The roughness ratio, *r*, is defined in Equation (2.34)

$$r = \frac{\tau_{wall\ soil}}{\tau_{soil}}$$

$$\begin{aligned} &\textit{Cohesionless soil} && r = \frac{\tan(\delta)}{\tan(\phi')} \ \textit{(at failure)} \\ &\textit{Cohesive soil (undrained)} && r = \frac{\tau_{wall}}{s_u} \ \textit{(at failure)} \end{aligned} \qquad (2.34)$$

According to the findings by Janbu (1957; 1972), roughness plays the most important role in the development of active and passive earth pressure and it is of utmost importance to adopt a consistent sign convention for *r*. Janbu's definition of the signs is presented in Figure 2.29, where cases a and b are the most common for retaining walls. However, case b may occur when the vertical support is insufficient, e.g. prestressed non-horizontal tie-backs. Case d can occur when the wall is used as an anchor.

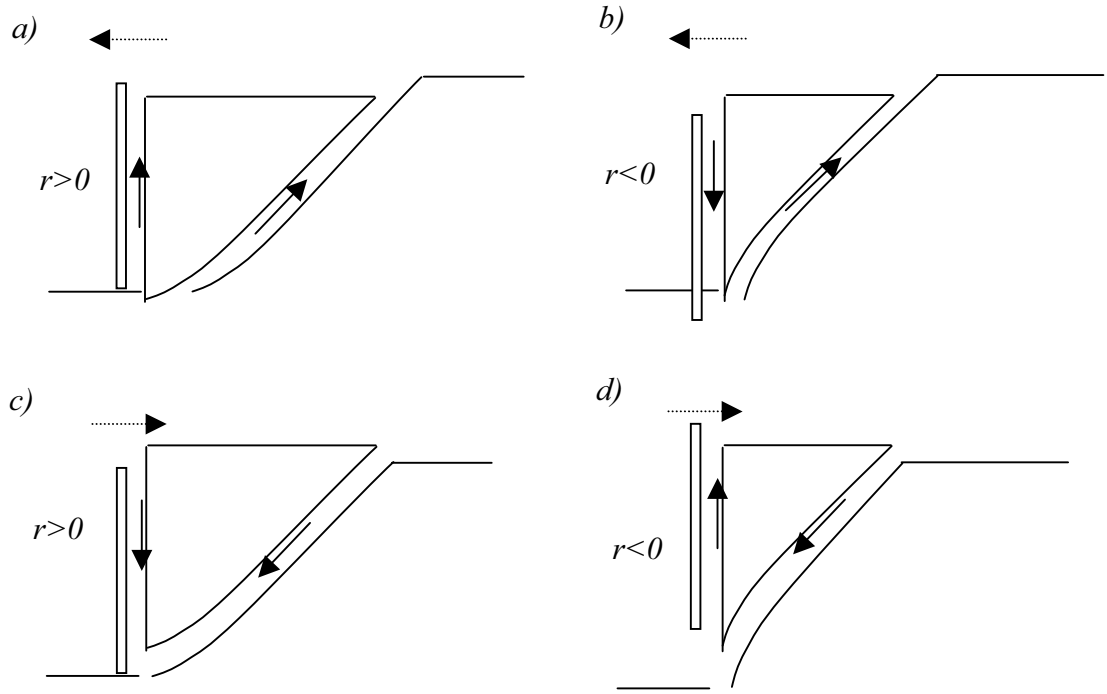

Figure 2.29: Definition of the sign convention for active and passive earth pressure together with developed shear forces on the active and passive wedges.
a) Active pressure, sufficient vertical support of the wall
b) Active pressure, insufficient vertical support of the wall
c) Passive pressure, sufficient vertical support of the wall
d) Passive pressure, when the wall is dragged out of the ground

According to Janbu the developed lateral earth pressure can be derived from the expression in Equation (2.35)

$$p_a = \sigma_{vert} - N_{ap} \cdot s_u \qquad p_p = \sigma_{vert} + N_{ap} \cdot s_u \tag{2.35}$$

where N_{ap} is defined in Equation (2.36). The restrictions on N_{ap} are due to the fact that, when assuming plane failure surfaces, accuracy declines to close to 1 or –1.

$$\begin{aligned} &N_{ap} = 2\sqrt{1+r} \quad \textit{with the restriction on} \\ &\frac{1}{2}(\pi - 2) < N_{ap} < \frac{1}{2}(\pi + 2) \end{aligned} \tag{2.36}$$

For example, the net pressure below the excavation grade will correspond to a stability factor of 5.14 for r=1, cf. Equation (2.40).

2.6.4 Swedish practise

The method commonly used for sheet pile wall design in Sweden is primarily based on Rankine's theory and on a method presented by Bjerrum & Eide (1956), as well as assumptions based on empirical observations (Stille, 1976; Fredriksson and Stille, 1979; Sahlström, 1979; Ryner *et al.*, 1996). Bjerrum's method mainly concerns safety against base failure for excavations in clay. The capacity of the soil to withstand the unbalanced forces of cohesive soils below the excavation grade is derived using the stability factor, N_{cb}.

The assumptions are based on earth pressure monitoring as well as calculations made using the *FE*-method, which attempt to describe the earth pressure distribution against the sheet pile wall (Fredriksson and Stille, 1979; Sahlström, 1979; Ryner *et al.*, 1996).

Compared to Rankine's theory that only deals with earth pressure, Bjerrum’s method for braced excavations and the empirical assumptions for anchored walls make it possible to incorporate the effects of the dimensions of the excavation as well as the preloading in the anchors.

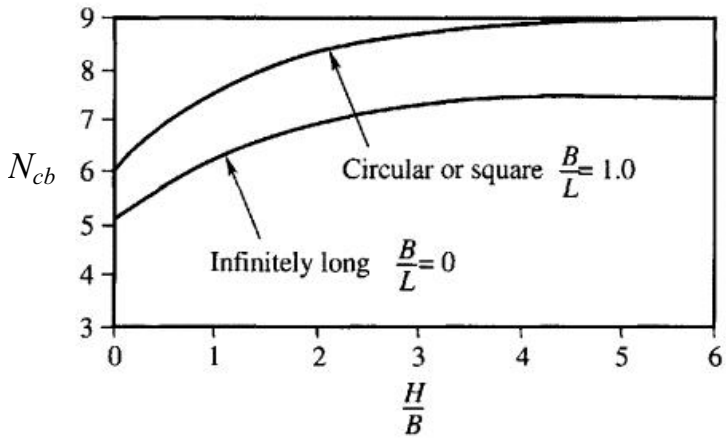

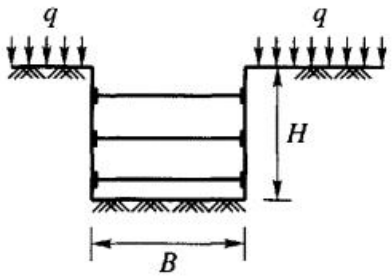

$$N_{cb\ rect} \approx \left(0.84 + 0.16 \cdot B/L\right) \cdot N_{cb\ square}$$

Figure 2.30: Stability factor for braced excavations (Bjerrum and Eide, 1956). Values of N_{cb} after Skempton (1951).

The factor of safety against basal heave was defined by Bjerrum and Eide (1956) and is given by Equation (2.37)

$$F = \frac{N_c}{N_b} \tag{2.37}$$

$$N_b = \frac{\gamma H + q}{s_u} \tag{2.38}$$

where N_c is the stability factor that corresponds to the bearing factor proposed by Skempton (1951) and N_b the stability number. s_u is the undrained shear strength; $\gamma H+q$ equals σ_{vert} at the retained side of the wall at a depth of H metres.

The method used in Sweden assumes that the embedded length of a *SPW* has to carry a load corresponding to $F=1.0$. In cases where $F>1.0$, the soil has the capacity to carry the loads from the retained side. The ability to carry load is defined as the difference between using the stability number, N_b, and the stability factor, N_{cb}.

$$\gamma H + q = N_b \cdot s_u \tag{2.39}$$

$$\gamma H + q + p_{net} = N_{cb} \cdot s_u \tag{2.40}$$

where p_{net} is the capacity to carry additional vertical load without base failure.

Combining Equations (2.39) and (2.40) indicates that the ability of the soil to carry additional load is positive for $F>1.0$ and negative for $F<1.0$. In the Swedish method, the ability to carry additional load is back-calculated from the factor of safety against basal heave. Figure 2.31a shows the failure mechanism assumed by Bjerrum and Eide (1956). Since the forces acting on a plane have to be in balance, a reaction p_{net}* is also shown in Figure 2.31a.

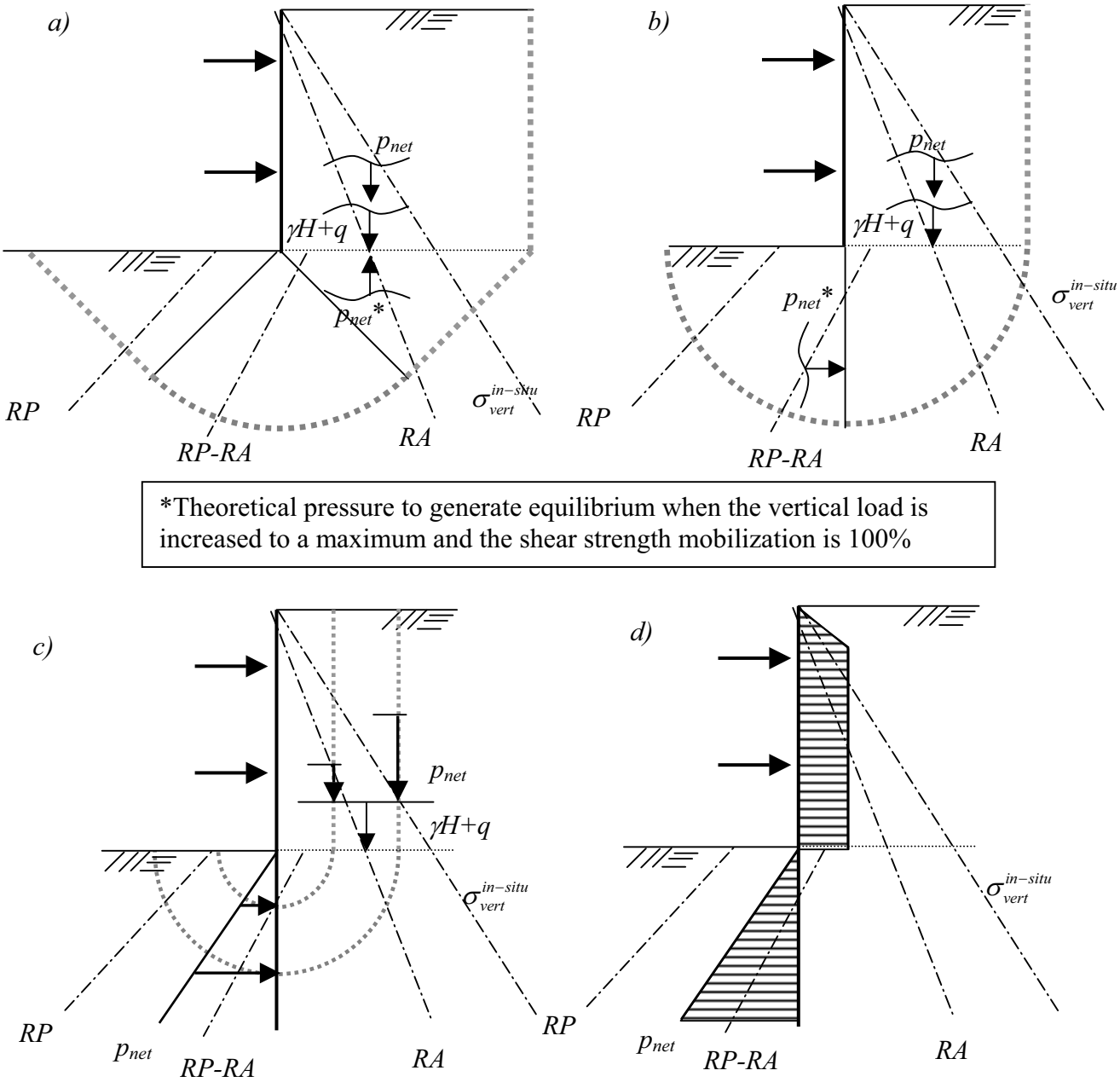

Figure 2.31: Loads acting on a sheet pile wall according to the Swedish method (Ryner et al., 1996) based on the ability to withstand basal heave
a) Failure mechanism for basal heave (Bjerrum and Eide, 1956) and the ability to carry additional load, p_{net}.
b) Simplified failure mechanism similar to that proposed by Terzaghi (1943). The ability to carry higher load is rotated around the centre of the failure surface.
c) Sketch over the ability to carry higher load for different failure surfaces, assuming the same stability factor.
d) Resulting earth pressure affecting the wall, where the pressures above the bottom of the excavation are redistributed due to the effect of prestressed anchors or constrained deformation in rigid struts. Note that p_{net} does not develop if it is not required to carry unbalanced forces.

Based on the assumption that the soil mass beneath the excavation grade rotates as a rigid body, the reacting forces, p_{net}* can be rotated around the centre of the assumed failure surface. The method appears to be safe, because the rotation of the ability to carry load does not follow the failure mechanism for which N_{cb} is derived. However, a reduced stability factor would be better for the failure mechanism employed, cf. (Terzaghi, 1943). Another approach to dealing with the forces acting on the embedment is to treat p_{net} as the required capacity of the wall to redistribute the forces in a way that makes the excavation safe against basal heave.

When using the relation for basal heave as a base for the lateral earth pressure, the calculation assumes the same adhesion between the soil and the wall as in the assumed rigid body. Aas (1985) and Karlsrud and Aas (1995) proposed a similar method to calculate the net pressure from the base stability number. In their work the amount of adhesion were included and the net earth pressure could be calculated from Equation (2.41)

$$p_{net} = f \cdot N_{cb} \cdot s_u - (\gamma H + q) \tag{2.41}$$

where f was found to be 0.9 for a roughness value of 0.5 (Aas, 1985).

The assumption of the adhesion and shape of the failure surface yields the different critical failure surfaces derived by Coloumb (1776), Bjerrum and Eide (1956) and Janbu (1957).

Stille (1976) studied the effect of the vertical component from the anchor forces and the shear forces acting along the inside and outside face of an anchored sheet pile wall in clay and assumed a constant value of s_u and lateral pressure in agreement with Janbu. The stability factor was calculated on the basis of the horizontal and vertical equilibrium of the wall. The results are plotted as functions of the dimensionless force ($R \cdot \cos(\alpha)/s_u/H$) for various degrees of roughness on the excavated side and for different ratios between the embedding and the excavation depth. Note that $R \cdot \cos(\alpha)$ is the horizontal component of the anchor reaction with no pre-stress at horizontal equilibrium and active lateral pressure on the retained side as well as passive lateral pressure against the embedded length. The effect of various degrees of roughness on the respective sides is also presented. All these calculations resulted in recommended design values for the stability factor, N_{cb}, (Ryner *et al.*, 1996)

For anchored walls with sufficient vertical stability, the recommended value of N_{cb} is 5.7 but it can be as low as 4.1 when the vertical stability is insufficient or 3.6 in highly sensitive clays.

2.6.5 Mobilizable strength design (Osman and Bolton, 2004)

Due to the differences between safety requirement and displacement calculations, Osman and Bolton (2004) suggested a new design method for retaining walls in clay entitled the "Mobilizable strength design (MSD) method".

This method is based on the stress-strain behaviour in the soil. A kinimatically admissible deformation mechanism with distributed plastic strains is assumed, and the mobilized strength needed for equilibrium is calculated according to the principle of virtual work. Satisfactory agreement has been found both with non-linear *FE*-analyses and field measurements (Osman and Bolton, 2004; Osman and Bolton, 2007) . However, the method has to be carried out in the form of an iterative procedure in order to verify that the proper stiffness is used.

2.6.6 Arching effects

Arcing effects have been seen in many cases affecting the support loads and the bending moments within the retaining wall. Bjerrum *et al.*(1972) stated that arching effects is to be seen in most cases where a flexible retaining wall is used and supported by struts. The observed support loads exceed the one obtained by classical earth pressure calculations, while the observed bending moments seems to be less then predicted with classical calculations. Bjerrum *et al.* (1972) also showed that the arching effect could be seen when using continuum finite element method. The arching effect is illustrated in Figure 2.32.

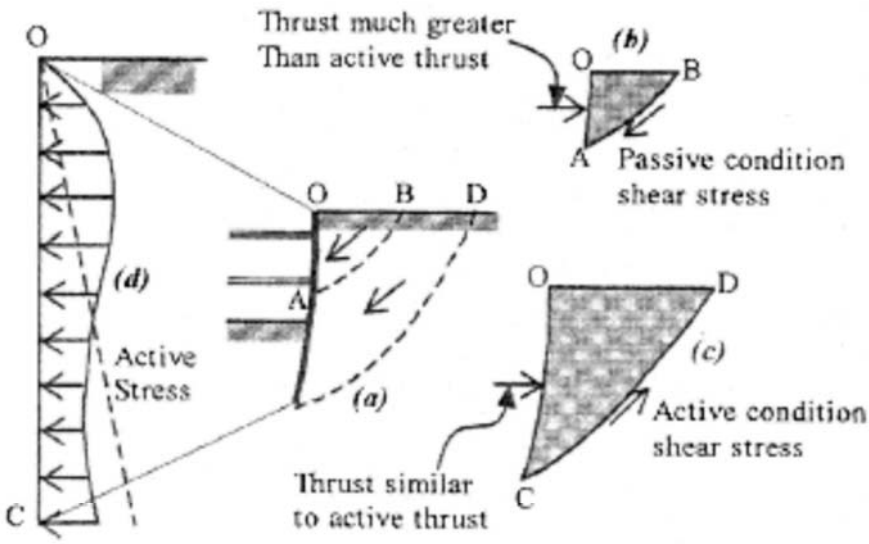

Figure 2.32: Illustration of arcing effects due to deep seated movements (Lambe and Whitman, 1969; Hashash and Whittle, 2002; Karlsrud and Andresen, 2005)

Using *FE* is is probably the only way to realistically simulate the complex interaction between soil and support system and to provide realistic results of

lateral earth pressure as well as support loads and bending moments within the wall. Several studies have shown the arching effects (e.g. Hashash and Whittle, 2002; Karlsrud and Andresen, 2005).

2.7 Stability

When performing an excavation, it is not only the lateral pressure or deformation that requires attention, as there are other failure mechanisms, e.g. overall stability, basal heave and hydraulic uplift. In this section, these phenomena will be briefly discussed.

2.7.1 Overall stability.

In this context overall stability refers to the same problem that usually occurs in slope stability. However, in this case the slip surface is partially controlled by the geometry of the support system. The factor of safety can be expressed in different ways depending on how the overall stability is analysed. When using a limit equilibrium method, it is often expressed as the ratio between average shear strength and average mobilized shear stress. When using numerical methods, the factor of safety is usually shear strength reduced in a way that leads to failure, *phi/c*-reduction(Brinkgreve and Bakker, 1991; Brinkgreve, 2002) or shear strength reduction (e.g. Faheem *et al.*, 2003).

When studying the stability by means of limit equilibrium, the effect of support loads may have to be taken into account, especially in cases where prestressed anchors are used, e.g. anchors fixed in the bedrock act as an external load on the assumed failure mechanism. Anchors fixed in the soil (or in deadmans) exhibit mechanisms that develop in a way that involves the complete anchor system. In such cases the support works as an internal force within the rigid body that defines the failure mechanism. The way in which it is taken into account by the various methods of vertical slices differs between approaches. A review of popular limit equilibrium techniques can be found in many textbooks, e.g.(Nash, 1987). It is, however, often difficult to assess the accuracy of these solutions due to the assumptions made regarding: Shape of failure surface; Procedure to locate the critical surface; Approximations used to solve the equilibrium (i.e. interslice force assumptions); Interaction with different structures.

Studying the overall stability using the limit analysis technique will improve the accuracy of the obtained factor of safety. Results from using limit analysis as opposed to limit equilibrium methods have been presented by several authors, e.g. (Yu *et al.*, 1998; Kim and Salgado, 1999; Chen *et al.*, 2004). The findings from these studies reveal that the limit equilibrium methods agree well, from a practical point of view, with the results obtained from limit analysis. Unfortunately, none of these studies investigated the effect of a retaining structure.

Full numerical analyses study all possible failure mechanisms simultaneously; no separate calculation for overall stability is necessary. With a proper constitutive relation for soil behaviour effects, such as anisotropy, hardening and softening can be included. No extra consideration of the support loads and/or the stiffness of the embedded retaining wall is required. Effects such as progressive failure are included in the sense that the forces will be redistributed when failure occurs in some parts of the soil mass. Full progressive behaviour can be modelled when using a constitutive model capable of describing softening behaviour. To obtain a factor of safety, a shear strength reduction can be made. However, the outcome will only be the failure mechanisms with the lowest factor of safety. In order to study other mechanisms, changes must be made in the conceptual model.

2.7.2 Hydraulic uplift

Hydraulic uplift may occur when a low permeable (undrained) layer overlies a permeable (drained) one. When the pore water pressure within the drained layer exceeds the total weight of the undrained layer, uplift may occur. The failure mechanism studied due to hydraulic uplift is the soil within the excavation treated as a rigid body. Some shear forces act on this body and prevent uplift. Care has to be taken if these forces have to be incorporated in order to prevent uplift, as other failure mechanisms may invalidate them. In such cases it is crucial that the hydraulic pressure within the drained layers is known and that knowledge of possible drained layers is sufficient.

The problem of interacting failure mechanisms will be solved by a full numerical analysis.

2.7.3 Basal heave

The base stability associated with deep excavation in soft clay can be analysed using either the slip surface method or a method related to bearing capacity. The slip surface method is the same as that used for overall stability while the latter is identical to basal heave.

Several limit equilibrium methods have been presented for different failure mechanisms. These methods may or may not incorporate effects of embedding, distance to firm layer, adhesion and wall stiffness. The two best known methods are presented in Figure 2.33 (Terzaghi, 1943; Bjerrum and Eide, 1956). Figure 2.33 has been complemented by the principal stress directions (Clough and Hansen, 1981)

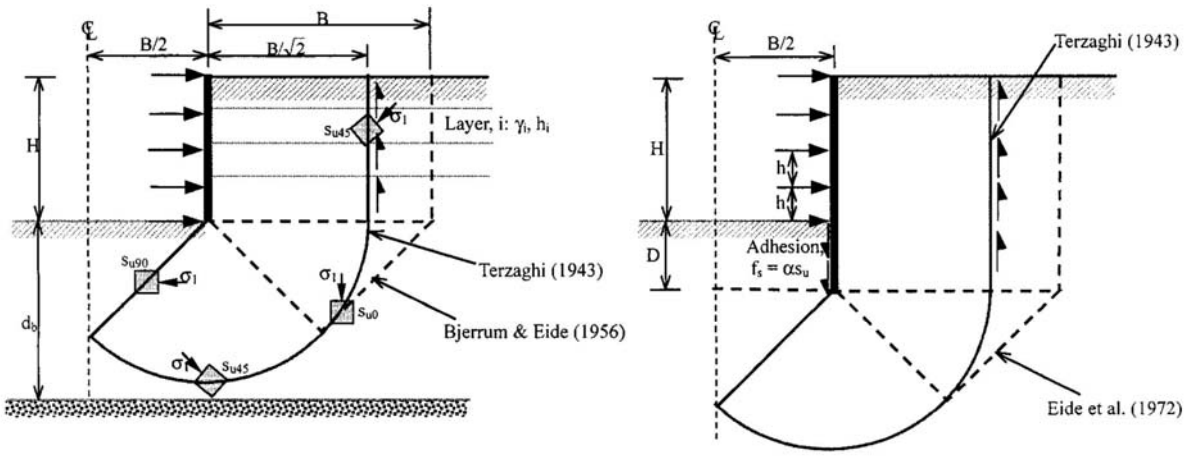

Figure 2.33: Examples of failure mechanisms without embedment and with wall embedment (Ukritchon et al., 2003)

The basal stability is often expressed by the stability number, N_b, Equation (2.38). The stability number at failure (stability factor) is denoted N_{cb}. Different methods for calculating N_b are presented in Table 2.5, where γ and s_u are the average values of the unit weight and the undrained shear strength of the retained soil.

Table 2.5: Stability number from limit equilibrium calculations of basal stability (Ukritchon et al., 2003)

Case	Stability number, N	Notes	Reference
1	$\frac{\gamma H}{s_u}=N_{c1}+\sqrt{2}\left(\frac{H}{B}\right)$	Base case—homogeneous deep clay $N_{c1}=5.7;\ d_b \geqslant B/\sqrt{2}$	Terzaghi (1943)
2	$\frac{\gamma H}{s_u}=N_{c2}$	Base case—homogeneous deep clay $N_{c2}=f(H/B)=5.1->7.5$	Bjerrum and Eide (1956)
3	$\frac{\gamma H}{s_u}=N_{c1}+\left(\frac{H}{d_b}\right)$	Effect of underlying bearing layer $d_b<B/\sqrt{2}$	Terzaghi (1943)
4	$\frac{\gamma H}{s_{uu}}=N_{c1}\left(\frac{s_{ub}}{s_{uu}}\right)+\sqrt{2}\left(\frac{H}{B}\right)$	Two clay layers: s_{uu}, s_{ub}—strengths in retained soil and below excavated grade	Terzaghi (1943)
5	$\frac{\gamma H}{s_{u45}}=N'_c\frac{1}{2}\left(\frac{s_{u0}+s_{u90}}{s_{u45}}\right)+\sqrt{2}\left(\frac{H}{B}\right)$	Anisotropic shear strengths in clay s_{u0}, s_{u45}, s_{u90}—strengths at $\delta=0°$, 45°, 90°, Fig. 1 $N'_c=f(s_u[\delta])=4.0->5.5$	Clough and Hansen (1981)
6	$\frac{\gamma H}{s_u}=N_{c1}+\sqrt{2}\left(\frac{H+D}{B}\right)+2\left(\frac{D}{B}\right)$	Effect of embedment—rigid wall	Terzaghi (1943)
7	$\frac{\gamma H}{s_u}=N_{c2}+2\alpha\left(\frac{D}{B}\right)$	Effect of embedment—rigid wall α—adhesion between interior soil plug and wall	Eide et al. (1972)
8	$\frac{\gamma H}{s_u}=N_{c2}+x\frac{\pi^2 M_y}{D(D+h)s_u}$	Effect of embedment—elastic strain energy for bending of wall: M_y—yield moment of wall; h—excavation depth below lowest support (Fig. 1b); and $x=1/8$, 9/32, 1/2 for free, sliding, and fixed-end conditions	O'Rourke (1993)

Note: Bearing capacity factors N_{c2} and N'_c obtained from Skempton (1951) and Davis and Christian (1971).

The stability factor can be assessed by using a non-linear numerical analysis, e.g. finite element, with either excavation to a depth where failure occurs or by the shear strength reduction method. However, this requires a skilful user and a

constitutive model capable of capturing the important phenomena adjacent to an excavation. An alternative method of calculating the stability of an excavation is by means of limit analyses. The calculations involved are very useful for creating design charts regarding e.g. the use of an embedment wall to increase *N*. Several design charts have been developed by Ukritchon *et al.* (2003) , where the stabilizing effect of wall embedment has been studied. Design charts pertaining to the effect of introducing adhesion without embedment of the wall and the influence of the distance to firm layers are reproduced in Figure 2.34. These design charts are obtained by solving the limit analysis numerically, using finite element methods, which combine the advantages of the finite element for handling complex problems with the power of limit analysis for bounding the exact collapse load. In order to isolate the failure mechanism, which is important for basal heave, the support system above the excavation grade is assumed to be rigid. The limit analyses are performed with a Tresca failure criterion where s_u defines the shear strength. Figure 2.34a demonstrates that the assumptions made by Bjerrum and Eide (1956) are conservative and that the relation for basal stability given by Terzaghi's (1943) relation for basal stability corresponds to the upper limit for wide excavations but overestimates the stability factor for narrow ones. It is obvious from Figure 2.34b that the distance only affects the stability factor when the width of the excavation exceeds the distance from the excavation grade to the firm layer. In this case, it is clear that the relation presented by Terzaghi (1943) agrees with the results of the lower bound analyses.

When introducing a wall embedment, the stiffness of the wall has to be considered in the limit analysis. This is done for a given ratio between the width and the depth of the excavation and the results are reproduced in the design chart presented in Figure 2.35. The limit analyses are compared with the results using case 8 in Table 2.5. Please note that free end conditions have been employed and that the form factor, η, is set to 1.5, which is valid for a rectangular section (diaphragm wall). The Figure has been complemented by the stability number when η =1.0, which comes closer to the behaviour of an *SPW*. Typical ranges for three cases have also been added to the original Figure: Excavation to 20 m with a 33.3 metre flexible *SPW*; Excavation to 20 m with a 33.3 metre stiff combined *SPW*; Excavation to 10 m with a 16.7 metre flexible *SPW*. The design chart in Figure 2.35 is valid for r=1.0 (full adhesion). The method for estimating N_{cb} proposed by Eide *et al.* (1972) takes adhesion into account and treats the wall as rigid. The stability factor presented by Eide *et al.* (1972) for the two relations between embedment and excavation depth is also included in Figure 2.35.

It is clear that the method proposed by Terzaghi (1943) matches the upper bound and that the method by Eide *et al.* (1972) exceeds the findings from the limit

analyses, especially for short embedment. The method presented by O'Rourke (1993) is shown to be inaccurate compared to the limit analyses and does not yield higher values for N_{cb} when the embedment is increased relative to the excavation depth and significantly over predicts the stability factor for rigid walls.

The limit analyses show that the retaining wall has a minor effect on the stability factor in the case of flexible walls. However, when dealing with a large embedment and rigid walls, the effect increases quickly to a maximum value where $M_p/(s_u D^2)>4.0$. This limit represents the failure mechanism when soil movements occur under the end of the retaining wall, known as classic basal heave. For lower values, the wall embedment deforms into the excavated area and plastic hinges develop. The lower bound analyses show that two hinges develop in very flexible walls, $M_p/(s_u D^2)=0.05$, one on the excavation grade and the second approximately 0.2B metres below it. In the case of ordinary SPW design, $M_p/(s_u D^2)=0.5$, only one hinge develops at the excavation grade. Note that this mechanism assumes a rigid strut at the bottom of the excavation. In practice, this is not true during the construction process and the hinge probably develops at the lowest support level, which appears to result in the relative strength parameter in Figure 2.35 being expressed as $M_p/(s_u(h_e+D)^2)$, where h_e defines the distance between the lowest support and the excavation grade.

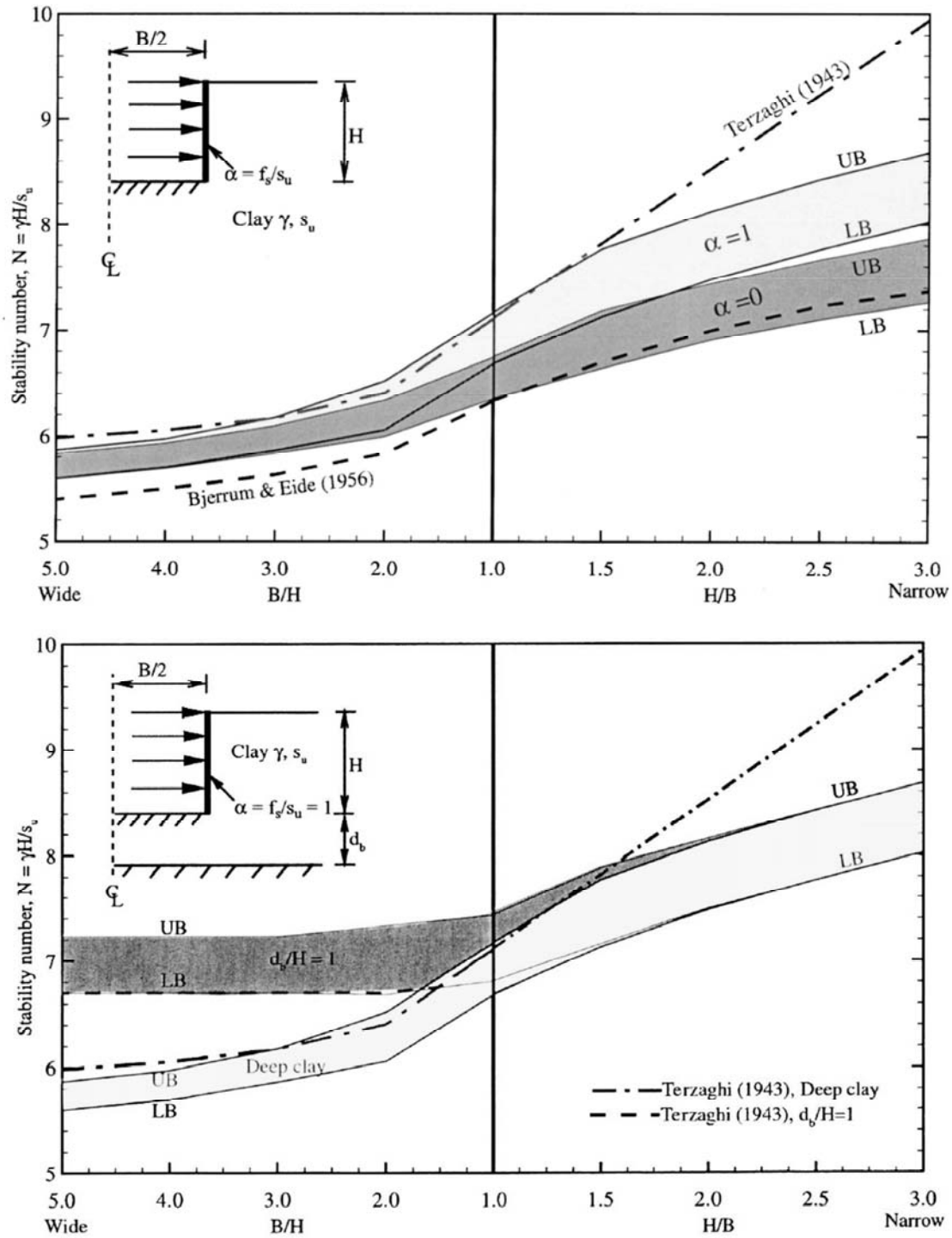

Figure 2.34: Comparison between classic assumptions pertaining to the stability number combined with limit analyses (Ukritchon et al., 2003)
a) Effect of introducing wall adhesion for a braced excavation in clay.
b) Effect of closeness to firm layer for a braced excavation in clay.

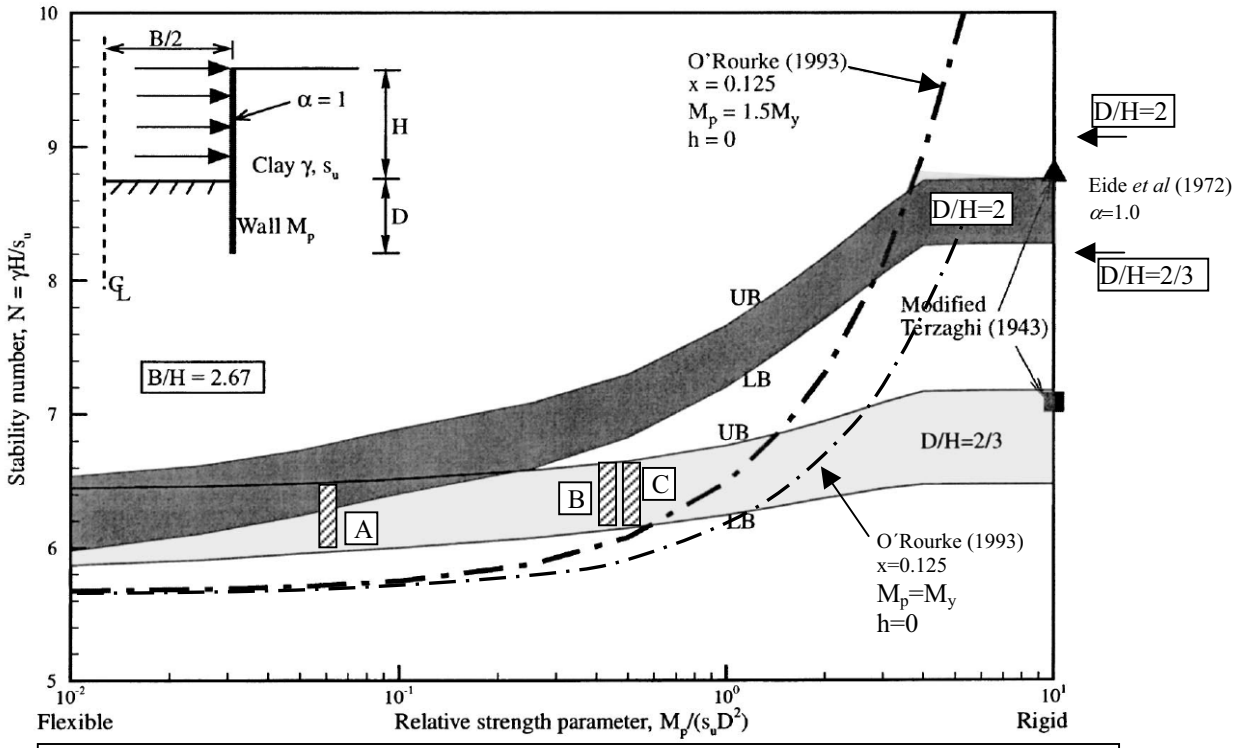

A: Representative range for a *SPW* with M_{pl}=680 kNm/m; H=20 m
B: Representative range for a *SPW* with M_{pl}=4200 kNm/m; H=20 m
C: Representative range for a *SPW* with M_{pl}=680 kNm/m; H=10 m

Figure 2.35: Comparison between the method proposed by O'Rourke (1993) for the stability number combined with limit analyses (Ukritchon et al., 2003). The effect of wall stiffness has been taken into account. The original figure has been complemented with the stability number based on O'Rourke (1993) for an SPW and with three representative ranges for deep excavations in normal consolidated clay.

A quite cumbersome relation for establishing N_{cb} as a function of B/H, D/H and $M_p/(s_uD^2)$ has been presented and covers the limit analyses over the range of B/H=0.33-5, D/H=0-2 and $M_p/(s_uD^2)=10^{-3}$-6. This relation assumes complete adhesion between the soil and the wall.

$$\frac{\gamma H}{s_u}=\frac{(2+\pi)\left(\frac{B}{H}\right)+b_2+b_3\sqrt[4]{\frac{M_p}{s_uD^2}}\left(\frac{D}{H}\right)^2\left\{c_2\left(\frac{D}{H}\right)\left(\frac{H}{B}\right)^2+c_3\sqrt{\frac{(D/H)}{(H/B)}}\right\}}{\frac{B}{H}+a_2+\sqrt{\frac{M_p}{s_uD^2}}\left\{a_3\left(\frac{D}{H}\right)+a_4\sqrt{\frac{D}{H}}\right\}} \tag{2.42}$$

where the seven coefficients have been estimated by curve fitting. In cases when the excavation is performed with zero-embedment, the relation is simplified to

$$\frac{\gamma H}{s_u} = \frac{(2+\pi)\left(\frac{B}{H}\right)+b_2}{\frac{B}{H}+a_2} \tag{2.43}$$

where a_2=0.608, a_3=0.208, a_4=-0.224, b_2=6.102, b_3=2.082, c_2=0.147 and c_3=0.172.

Results from a parallel study to that by Ukritchon *et al.* (2003) have been presented by Faheem *et al.* (2003) and contain several closed form equations for calculation of the stability number; different failure mechanisms were studied and the effect of wall embedment taken into account. These equations were derived from upper bound analysis theory. In combination with these calculations, *FE*-calculations were performed to study the effects of embedment, the presence of hard stratum and wall stiffness.

2.7.4 Role of anisotropy

It is well known that anisotropy is an important factor in stability problems. However, it is not easy to introduce these effects into a stability analysis of a supported structure. The strain levels needed for mobilization of the peak strength will vary for different principal stress rotations, thus the actual stress state has to be considered. In an undrained excavation sequence, the amount of developed shear has to be taken into account when studying a specific stage in terms of stability. An isotropic situation was assumed in the limit analyses discussed in the previous section. Hashash and Whittle (1996) presented results from non-linear finite element analyses using the *MIT-E3* model, which is capable of describing the anisotropic behaviour of clay. They studied an idealized excavation with different geometries, Figure 2.36, and continued excavating until failure occurred. Back calculation of the stability factor obtained from their analyses is presented in Figure 2.37. The reason for the interval given in Figure 2.37 is that the excavation was performed in 2.5 metre steps.

The incorporation of anisotropy increases the stability factor by up to 40%. As expected, the effect of anisotropy is highest for a short embedment in relation to an excavation where the embedment has relatively stiff walls. Short walls have a failure surface with a higher degree of active failure than an excavation with a deep embedment. The results showing a decrease in the stability factor when anisotropy is taken into account concern a relatively low stiffness. The reason for this is probably due to the different failure mechanisms described previously.

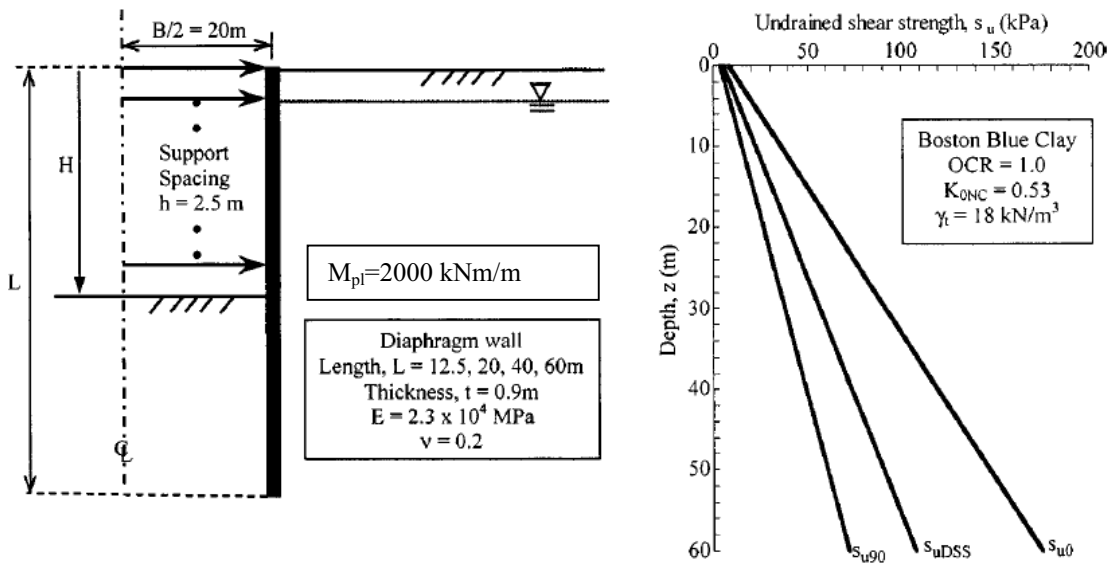

Figure 2.36: Non-linear analyses of an idealized excavation using the MIT-E3 model (Hashash and Whittle, 1996)

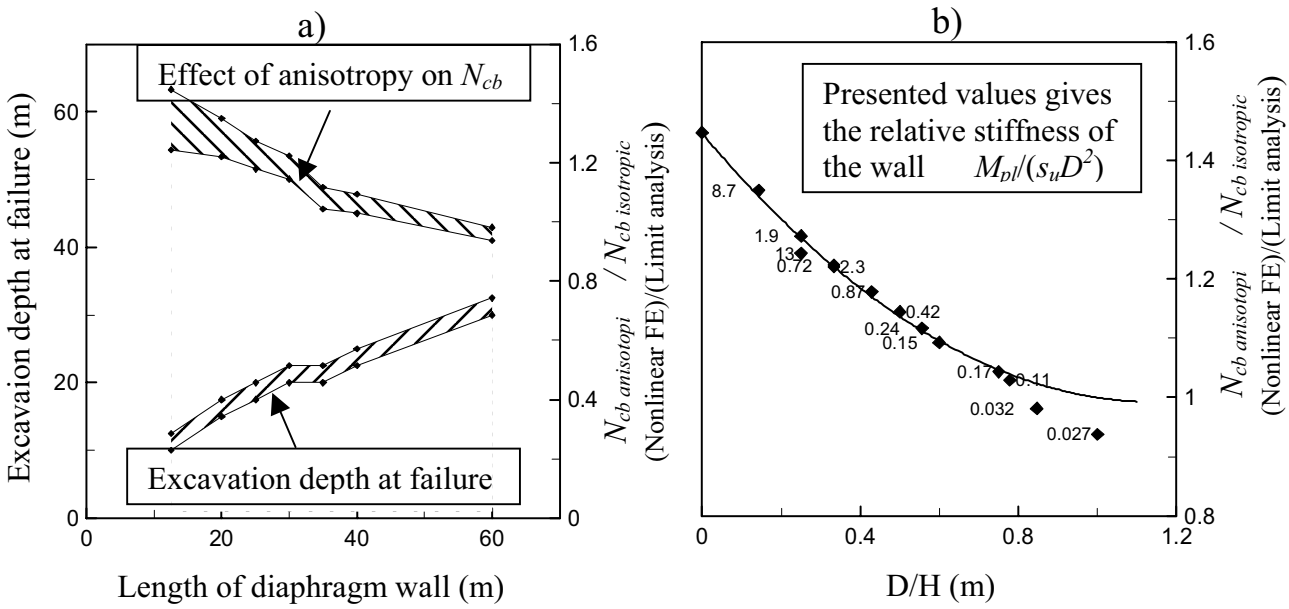

Figure 2.37: Comparison between stability factors using non-linear finite element analyses with the MIT-E3 model (Hashash and Whittle, 1996) and using the limit analyses (Ukritchon et al., 2003)

There are a couple of constitutive models capable of handling anisotropic behaviour in undrained clay. *MIT-E3* and *MIT-S1* are examples of available models suitable for undrained coupled analyses of excavations. There are also some total stress based models capable of describing this behaviour under undrained conditions, e.g. *Anisoft* and *e-ADP*.

Compared to the undrained shear strength obtained from direct shear tests, anisotropic effects will always numerically increase the factor of safety.

2.7.5 Three dimensional effects

Taking the three-dimensional effect into account increases the stability factor. According to Terzaghi (1943) , the increase in the stability factor can be obtained by multiplying the two-dimensional stability factor by the shape factor, $\lambda_s=1+0.2\cdot(B/L)$, where B is the width of the excavation and L is the length. This shape factor has also been applied to Bjerrum and Eide's stability factor. Faheem et al. (2004) studied the effect by performing a large number of three-dimensional *FE*-calculations for various geometries and using the reduced shear strength technique until failure occurred. They found that the shape factor proposed by Terzaghi is valid within the range of $0\leq B/L\leq 4.0$, irrespective of embedding. They also presented a critical value of stiffness for the embedment, by which it can be treated as rigid, $\rho_s=EI/(\gamma D^4)>55$.

2.8 Construction failures

Other failure mechanisms primarily depend on the construction elements in the retaining system, e.g. the support system and the retaining wall. Such failure mechanisms may develop when the load from the retained soil is underestimated. This underestimation is mainly due to insufficient knowledge about the hydraulic situation and other engineering activities adjacent to the wall, e.g. piling. These failure mechanisms will, however, not be discussed in detail in this work as the focus here is on the deformation caused by an excavation and the interaction between the retaining system and the soil, which is dependent on the stiffness and capacity to carry the load.

2.9 Numerical calculations by means of the *FE*-method

During recent decades there has been great progress in the area of numerical simulations, both in terms of computer power and constitutive soil models. The increased computer capacity has opened the way for more complex conceptual models that describe the problem not only in 2D but also in 3D.

In order to perform a numerical analysis of e.g. an excavation and to be confident about the outcome, the user has to have knowledge of:

- Simplifications made in the conceptual model, describing the actual problem
- Influence of chosen boundary conditions
- Limitations of the constitutive model, describing the soil behaviour
- Soil structure interaction

- The accuracy and suitability of the algorithm for solving non-linear analysis
- Influence of incremental size, iteration and convergence criteria, e.g. acceptable errors, on the solution.

The focus here is on constitutive models and not on the *FE*-method itself. Further information about the *FE*-method can be found in the literature (e.g. Nordal, 1983; Potts and Zdravkovic, 1999; Zienkiewicz and Taylor, 2000; Potts and Zdravkovic, 2001; Potts *et al.*, 2002; Altabba and Whittle, 2003; Smith and Griffiths, 2004.).

2.9.1 Constitutive models

Constitutive relations describe mathematically how stresses and strains will interact. These relations can be more or less complicated depending on the behaviour they attempt to describe. True soil behaviour is complex and requires a sophisticated constitutive soil model. However, it is sufficient to use fairly simple models for most problems. The choice of constitutive model involves estimating the value of using a complex model (compared to a simple one) as well as the cost of finding the input parameters to the complex model, compared to the simple one.

Different groups of constitutive models are compiled in Table 2.6. This table is not complete, thus for a more detailed overview of the different constitutive models used for describing soil behaviour, see the overview by Lade (2005)

Table 2.6: Different groups of constitutive models and their characteristics related to use in practice

	Type of constitutive relation	Example of models	
Easy to use and to analyse. Simple description of true soil behaviour ↑	Linear elastic	Hook's law	↓ Complex, with many input parameters. Increased possibility to describe true soil behaviour
	Non-linear elastic	Duncan and Chang (1970)	
	Elastic perfectly plastic,	Drucker and Prager (1951)	
	Hardening models	Druckers's Cap (Drucker *et al.*, 1957) *e-ADP* (Grimstad *et al.*, 2006)	
	Bounding surface models	*MIT-E3* (Whittle, 1987) *MIT-S1* (Pestana, 1994)	
	Multi surface models	Bubble model (Al-Tabbaa and Wood, 1989)	

The ability to describe true soil behaviour varies between each of these categories, and sometimes even within categories. For example, the hardening *e-ADP* model, which is based on total stresses and comprises only one yield surface and a failure criterion, is capable of describing anisotropy during undrained conditions, while the Bubble-model by Stallebrass and Taylor (1997) is not. On the other hand, the latter model is capable of reproducing the small strain behaviour under undrained as well as drained conditions.

There are hardening models with one or more yield surfaces and either isotropic hardening, kinematic hardening or a mix of these. The elastic behaviour within the yield surface may be non-linear or linear. These differences will affect the outcome as well as the number of parameters (input parameters as well as internal variables) required.

Bounding surface models are based on a concept presented by e.g. Dafalias and Popov (1975). The bounding surface generates plastic strains even for reloading. Bubble models are an improvement of the bounding surface concept, as they are extended by the inclusion of an inner kinimatic yield surface, which generates some plastic strain when unloaded to a specific extent.

Models are available for describing time effects such as strain rate dependent strength and creep. These models can be based on visco-plasticity (e.g. Runesson, 1978; Zhou *et al.*, 2005) or elasto-plasticity with an assumed loading unloading cycle related to time, for the generation of creep deformations (Vermeer and Neher, 2000). However, neither of these models are included in this work. It was assumed that the studied excavations would be completely undrained, although that is never completely true. Ou *et al.* (2000) revealed that excavations in silty clay, performed over the course of a year, exhibit partially drained behaviour.

2.9.2 Interfaces and structural elements in *FE*-analysis

Different structural elements are available for modelling e.g. retaining wall systems. The wall can be modelled by a plate element and its supports, either anchors and/or props, can be modelled by spring or beam elements. The true coupling between the wall and the supports indicates which modelling approach is most suitable. In order to define the properties characterising the interaction between the soil and the structural element, the soil-structure interaction can be described by introducing interface elements. This work does not contain information about how to define these various elements. However, the behaviour of the elements relevant to this work can be found in Brinkgreve (2002).

3 SOIL MODELLING: THEORY OF ELASTO-PLACTICITY FOR SOILS

3.1 Introduction

Soil modelling is often understood as a way of describing a specific situation or problem involving soil. Soil modelling includes everything from idealization of the problem to constitutive relations of the soil. However, in this section, soil modelling refers to the constitutive relations between stress and strain or the stress increment and strain increment.

3.2 Continuum mechanics

3.2.1 Stresses

Soil is a complex material comprising mineral grains, pore fluid and gas in the voids between the solid particles. The isotropic pressure in the pore fluid is called pore water pressure, u. The stiffness and strength of a soil is dependent on the stresses between the grains. These stresses are called effective stresses, σ_{ij}', and the relationship between total stress, effective stress and pore water pressure for a saturated soil is described in Equation (3.1).

$$\sigma_{ij} = \sigma_{ij}' + u \cdot \delta_{ij} \qquad \delta_{ij}=1 \text{ if } i=j \text{ otherwise } 0 \tag{3.1}$$

where i defines the surface on which the stress is applied and j the direction of the stress.

All constitutive models should be based on effective stresses, as both stiffness and strength are dependent on them. However, there are also soil models based on total stresses which can, in some cases, be more user friendly due to the fact that effective soil parameters or stresses may be difficult to determine. The reason for using models based on total stresses is the difficulty in describing how pore water pressure develops for different kinds of loading but also the fact that the most commonly available soil characteristics for clay are derived from undrained tests. For materials with very low hydraulic conductivity, such as clay, this can be a good way of describing some of the soil behaviour.

The stress state of a material point can be described by stress components on an infinitesimal cube, Figure 3.1.

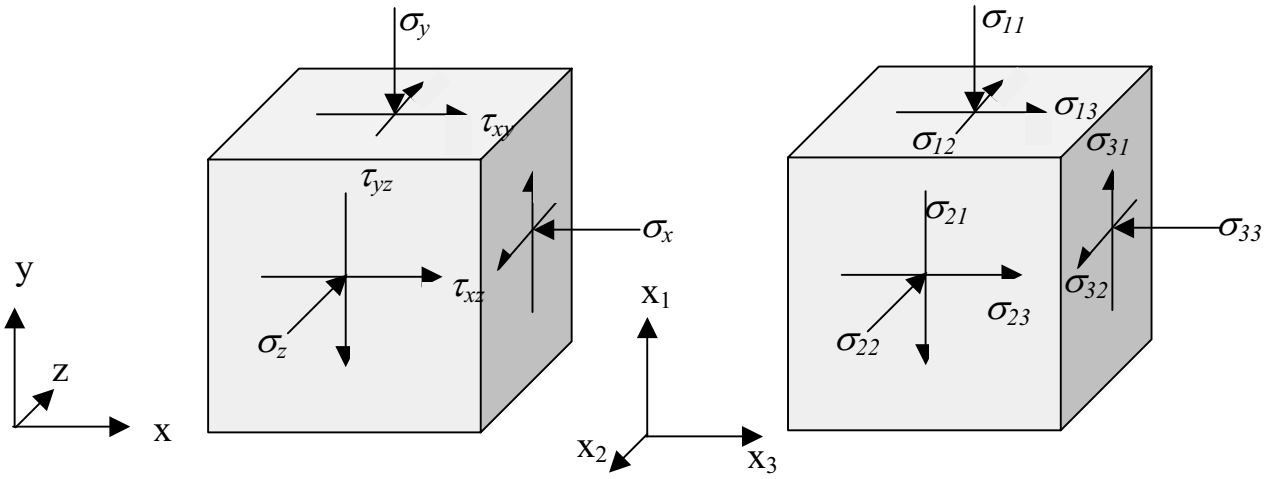

Figure 3.1: Stress state for a material point for two different coordinate system.

The stress components are often presented in matrix form, Eq.(3.2), or in a second order tensor, Eq. (3.3). Due to moment equilibrium, it is obvious that $\sigma_{ij} = \sigma_{ji}$ this reduces the stress components from 9 to 6.

$$\boldsymbol{\sigma} = \begin{pmatrix} \sigma_{11} & \sigma_{12} & \sigma_{13} \\ \sigma_{21} & \sigma_{22} & \sigma_{23} \\ \sigma_{31} & \sigma_{32} & \sigma_{33} \end{pmatrix} \; and \; \boldsymbol{\sigma}' = \begin{pmatrix} \sigma'_{11} & \sigma'_{12} & \sigma'_{13} \\ \sigma'_{21} & \sigma'_{22} & \sigma'_{23} \\ \sigma'_{31} & \sigma'_{32} & \sigma'_{33} \end{pmatrix} \tag{3.2}$$

$$\boldsymbol{\sigma} = \begin{pmatrix} \sigma_{11} \\ \sigma_{22} \\ \sigma_{33} \\ \sigma_{12} \\ \sigma_{13} \\ \sigma_{23} \end{pmatrix} \; and \; \boldsymbol{\sigma}' = \begin{pmatrix} \sigma'_{11} \\ \sigma'_{22} \\ \sigma'_{33} \\ \sigma'_{12} \\ \sigma'_{13} \\ \sigma'_{23} \end{pmatrix} \tag{3.3}$$

3.2.2 Principal stresses

For a given stress state it is always possible to find a plane where no shear stresses exist. According to Caucy´s law the internal stresses, Figure 3.1, will cause surface traction on an arbitrary plane defined by **n**.

$$\mathbf{t} = \boldsymbol{\sigma}^{\mathbf{t}}\mathbf{n} = \boldsymbol{\sigma}\mathbf{n}: \quad \mathbf{n}^{\mathbf{t}} = \left(\cos\theta_1, \cos\theta_2, \cos\theta_3\right) \tag{3.4}$$

If no shear stresses exist on plane **n**, the traction t equals $\sigma\mathbf{n}$. This will lead to an eigenvalue problem with the non-trivial solution presented in Equation (3.5). The definition of the stress invariants is valid for effective stresses.

$$det\left(\boldsymbol{\sigma}'\text{-}\sigma'\mathbf{I}\right)=0$$

which can be expressed in terms of

$$\sigma'^{3}-I_1\cdot\sigma'^{2}-I_2\cdot\sigma'-I_3=0$$

where I_1, I_2 and I_3 are stress invariants. (3.5)

$$I_1=\sigma'_{11}+\sigma'_{22}+\sigma'_{33}$$

$$I_2=-\sigma'_{11}\sigma'_{22}-\sigma'_{11}\sigma'_{33}-\sigma'_{22}\sigma'_{33}+\sigma'_{12}{}^{2}+\sigma'_{13}{}^{2}+\sigma'_{23}{}^{2}$$

$$I_3=det\left(\boldsymbol{\sigma}'\right)$$

Equation (3.5) yields three roots of σ. These roots represent a principal stress denoted σ'_1, σ'_2, σ'_3,, where $\sigma'_1\geq\sigma'_2\geq\sigma'_3$. The directions of the principal stresses are perpendicular to each other and can be obtained by Eq. (3.6).

$$\left(\boldsymbol{\sigma}'\text{-}\sigma'_i\mathbf{I}\right)\mathbf{n_i}=0:\ i=1,2,3 \tag{3.6}$$

If the principal stresses and their directions are known, the stresses in any orthogonal coordinate system can be calculated using the spectral theorem.

3.2.3 Mean and deviatoric stress

The deviatoric stresses, s_{ij}, express the deviation from isotropic mean stress, Equation (3.7).

$$\mathbf{s}=\boldsymbol{\sigma}'\text{-}\boldsymbol{\sigma}'_{\mathbf{m}}$$

or

$$\begin{pmatrix} s_{11} & s_{12} & s_{13} \\ s_{21} & s_{22} & s_{23} \\ s_{31} & s_{32} & s_{33} \end{pmatrix}=\begin{pmatrix} \sigma'_{11} & \sigma'_{12} & \sigma'_{13} \\ \sigma'_{21} & \sigma'_{22} & \sigma'_{23} \\ \sigma'_{31} & \sigma'_{32} & \sigma'_{33} \end{pmatrix}-\begin{pmatrix} \sigma'_m & 0 & 0 \\ 0 & \sigma'_m & 0 \\ 0 & 0 & \sigma'_m \end{pmatrix} \tag{3.7}$$

where

$$\sigma'_m=p'=\left(\sigma'_{11}+\sigma'_{22}+\sigma'_{33}\right)/3=\left(\sigma'_1+\sigma'_2+\sigma'_3\right)/3=I_1/3=I_1/3$$

The deviatoric principal stresses, s_1, s_2, s_3, are defined in a similar way to the principal stresses.

$$det\left(\mathbf{s}\text{-}s\mathbf{I}\right)=0$$

which can expressed in terms of

$$s^3-J_1\cdot s^2-J_2\cdot s-J_3=0$$

where J_1, J_2 and J_3 are deviatoric stress invariants.

$$J_1=s_{11}+s_{22}+s_{33}=0 \tag{3.8}$$

$$J_2=-s_{11}s_{22}-s_{11}s_{33}-s_{22}s_{33}+s_{12}{}^{2}+s_{13}{}^{2}+s_{23}{}^{2}=I_2+I_1^2/3$$

$$J_3=det\left(\mathbf{s}\right)=I_3+\left(1/3\right)\cdot I_2\cdot I_1+\left(2/27\right)\cdot I_1^3$$

$$J_3=\left(\sigma'_{11}-p'\right)\left(\sigma'_{22}-p'\right)\left(\sigma'_{33}-p'\right)+2\sigma'_{12}\sigma'_{13}\sigma'_{23}$$

$$-\left(\sigma'_{11}-p'\right)\sigma'_{23}{}^{2}-\left(\sigma'_{22}-p'\right)\sigma'_{13}{}^{2}-\left(\sigma'_{33}-p'\right)\sigma'_{12}{}^{2}$$

When combining Equations (3.5)-(3.8) it is obvious that $s_i = \sigma'_i - \sigma'_m$ and that the principal directions are similar for principal stresses and principal deviatoric stresses.

3.2.4 Stress invariants

Stress invariants are convenient for describing the stress situation in a stress point. If the stress tensor, see Equation (3.3), is given for a specified coordinate system, the values of the tensor will change if the coordinate system is changed This does not mean that the actual stress situation changes, as the principal stresses and the principal stress directions are the same, Equations (3.5) and (3.6). What it means is that any expression dependent on the principal stresses will be invariant to the choice of coordinate system. It is very useful if the constitutive relationship is expressed in terms of stress invariants.

There are several definitions of stress invariants in the literature, but the three most commonly used are p', q and θ. The mean effective stress is given by p', q is the distortional or deviatoric stress, while θ is referred to as Lode's angle. From a geometrical point of view, p' describes how far out the stress state is along a hydrostatic axis, $\sigma'_1 = \sigma'_2 = \sigma'_3$. Deviatoric stress indicates the distance from the hydrostatic axis of a particular stress situation along a plane specified by the hydrostatic axis, called the π-plane. A constant deviator stress will give a cylinder centred around the hydrostatic axis. Lode's angle describes the location of the current stress state on the circle in the π-plane.

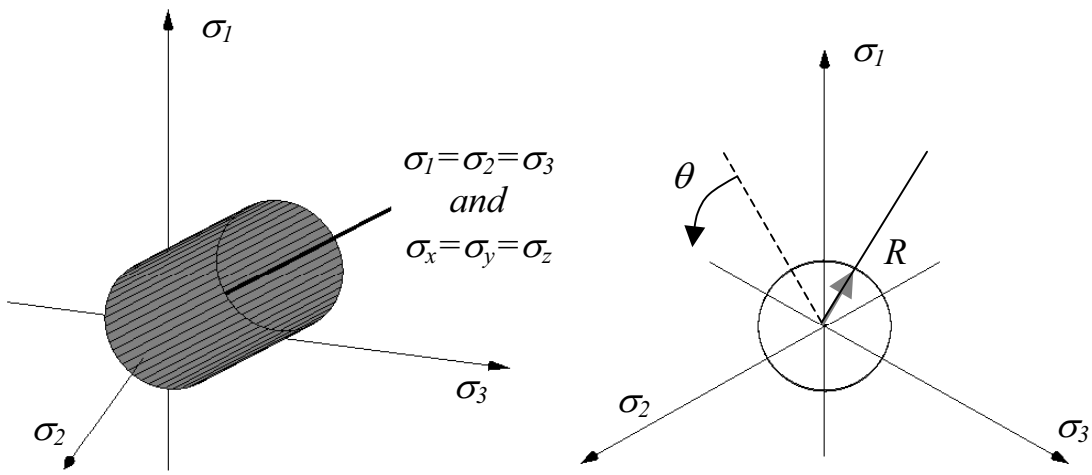

Figure 3.2: The constant value on the second deviatoric invariant defines a cylinder in the pricipal stress space. The stress point has to be in the sector defined by $-30^o \leq \theta \leq 30^o$ when $\sigma_1 \geq \sigma_2 \geq \sigma_3$.

The relationship between the radius, R, in the π-plane, J_2 and q is obvious from Eq. (3.9). Please note that this expression is valid for total stresses as well effective stresses.

$$R=\sqrt{s_1^2+s_2^2+s_3^2}=\sqrt{(\sigma_1-\sigma_m)^2+(\sigma_2-\sigma_m)^2+(\sigma_3-\sigma_m)^2}=$$
$$\sqrt{2}\cdot\sqrt{\frac{1}{6}\left\{(\sigma_1-\sigma_3)^2+(\sigma_1-\sigma_2)^2+(\sigma_2-\sigma_3)^2\right\}}=\sqrt{2}\cdot\sqrt{J_2} \tag{3.9}$$
$$q=\sqrt{3\cdot J_2}=\sqrt{\frac{1}{2}\left\{(\sigma_1-\sigma_3)^2+(\sigma_1-\sigma_2)^2+(\sigma_2-\sigma_3)^2\right\}}$$

If the stresses are expressed in an arbitrary coordinate system, the distortional stress and the second deviatoric stress invariant can be expressed according to Eq. (3.10). This expression is valid for total as well as effective stresses.

$$q=\sqrt{\frac{1}{2}\left\{(\sigma_{11}-\sigma_{33})^2+(\sigma_{11}-\sigma_{22})^2+(\sigma_{22}-\sigma_{33})^2+6\cdot\left(\sigma_{12}{}^2+\sigma_{21}{}^2+\sigma_{31}{}^2\right)\right\}}$$
$$J_2=\frac{1}{3}\cdot q^2=\frac{1}{6}\left\{(\sigma_{11}-\sigma_{33})^2+(\sigma_{11}-\sigma_{22})^2+(\sigma_{22}-\sigma_{33})^2+6\cdot\left(\sigma_{12}{}^2+\sigma_{21}{}^2+\sigma_{31}{}^2\right)\right\} \tag{3.10}$$
$$R=\sqrt{\frac{2}{3}}\cdot q=\sqrt{\frac{1}{3}\left\{(\sigma_{11}-\sigma_{33})^2+(\sigma_{11}-\sigma_{22})^2+(\sigma_{22}-\sigma_{33})^2+6\cdot\left(\sigma_{12}{}^2+\sigma_{21}{}^2+\sigma_{31}{}^2\right)\right\}}$$

3.2.5 Principal stresses derived from deviatoric stresses

An explicit expression can be obtain for the principal stresses from Eq. (3.8), by using a trigonometrical identity and by substituting s for $r\cdot\sin\theta$, (Nordal, 2004).

$$\begin{pmatrix}\sigma_1\\ \sigma_2\\ \sigma_3\end{pmatrix}=2\cdot\sqrt{J_2/3}\cdot\begin{pmatrix}sin(\theta+2\cdot\pi/3)\\ sin(\theta)\\ sin(\theta+4\cdot\pi/3)\end{pmatrix}+I_1/3\cdot\begin{pmatrix}1\\1\\1\end{pmatrix}$$
$$\begin{pmatrix}\sigma_1\\ \sigma_2\\ \sigma_3\end{pmatrix}=\frac{2}{3}\cdot q\cdot\begin{pmatrix}sin(\theta+2\cdot\pi/3)\\ sin(\theta)\\ sin(\theta+4\cdot\pi/3)\end{pmatrix}+p\cdot\begin{pmatrix}1\\1\\1\end{pmatrix} \tag{3.11}$$

Different relations for θ are given in Eq. (3.12).

$$\theta = \frac{1}{3}\cdot\arcsin\left(-\frac{3\cdot\sqrt{3}\cdot J_3}{2\sqrt{J_2^{\,3}}}\right) = \frac{1}{3}\cdot\arcsin\left(-\frac{3\cdot\sqrt{3}\cdot J_3}{2\cdot\left(\sqrt{\left(\frac{q^2}{3}\right)}\right)^3}\right)$$

$$= \frac{1}{3}\cdot\arcsin\left(-\frac{3\cdot\sqrt{3}\cdot J_3}{2\cdot\frac{q^3}{3\cdot\sqrt{3}}}\right) = \frac{1}{3}\cdot\arcsin\left(-\frac{27\cdot J_3}{2\cdot q^3}\right) = \tag{3.12}$$

$$= \arctan\left(\frac{1}{\sqrt{3}}\left(2\cdot\frac{\sigma_2-\sigma_3}{\sigma_1-\sigma_3}-1\right)\right)$$

3.2.6 Shear stress

Shear stresses occur if a point in a medium is affected by non-isotropic pressure. The ability of the material to withstand shear stresses is often referred to as the strength of the material.

If the stresses are defined by the principal stresses, σ'_1, σ'_2 and σ'_3, the stress traction, **t**, on an arbitrary plane defined by **n** is obtained from Eq. (3.13)

$$\mathbf{t} = \boldsymbol{\sigma}'^T\mathbf{n} \qquad \boldsymbol{\sigma}' = \begin{pmatrix} \sigma'_{11} & \sigma'_{12} & \sigma'_{13} \\ \sigma'_{21} & \sigma'_{22} & \sigma'_{23} \\ \sigma'_{31} & \sigma'_{32} & \sigma'_{33} \end{pmatrix} \qquad \mathbf{n} = \begin{pmatrix} n_1 \\ n_2 \\ n_3 \end{pmatrix} \tag{3.13}$$

The normal stress and the shear stress on this plane is obtained by means of Eq. (3.14)

$$\begin{aligned} \sigma'_n &= \mathbf{t}^T\mathbf{n} \\ \tau &= \sqrt{\mathbf{t}^2 - \sigma'^{\,2}_n} \end{aligned} \tag{3.14}$$

In some studies, these stresses are referred to as octahedral stress, σ'_{oct}, and octahedral shear stress, τ_{oct}. The octahedral is defined with its corners in the midpoint at each side of a cube in the principal coordinate system. Octahedral stresses act on each side of the octahedral, Figure 3.3, and are defined in Equation (3.15)

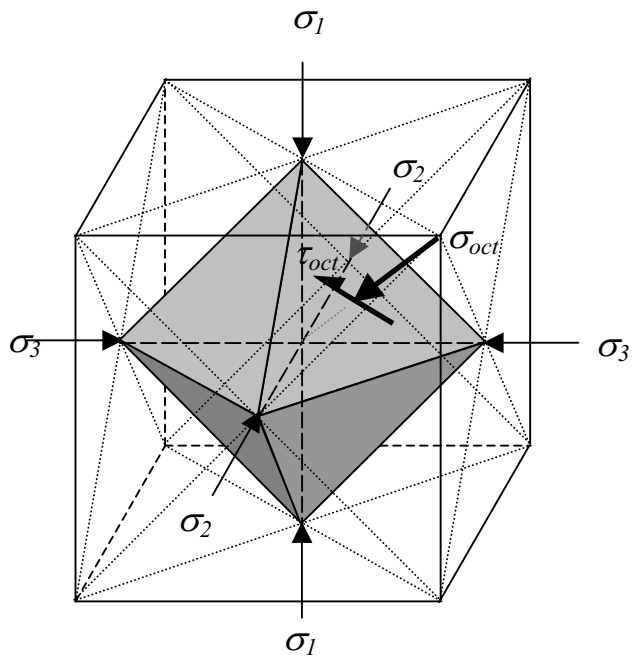

Figure 3.3: Octrahedral planes and octadreal stresses.

$$\sigma'_{oct} = \mathbf{t}^T\mathbf{n} = \left(\boldsymbol{\sigma}^T\mathbf{n}\right)^T\mathbf{n} = \sigma'_1 \cdot n_1^2 + \sigma'_2 \cdot n_2^2 + \sigma'_3 \cdot n_3^2 = \frac{\left(\sigma'_1 + \sigma'_2 + \sigma'_3\right)}{3} = p'$$

$$\tau_{oct} = \sqrt{\mathbf{t}^2 - \sigma'^2_n} = \sqrt{\left(\sigma'_1 \cdot n_1\right)^2 + \left(\sigma'_2 \cdot n_2\right)^2 + \left(\sigma'_3 \cdot n_3\right)^2 - \left(\sigma'_1 \cdot n_1^2 + \sigma'_2 \cdot n_2^2 + \sigma'_3 \cdot n_3^2\right)^2} \quad (3.15)$$

$$= \sqrt{\frac{1}{9} \cdot \left\{\left(\sigma'_1 - \sigma'_2\right)^2 + \left(\sigma'_2 - \sigma'_3\right)^2 + \left(\sigma'_1 - \sigma'_3\right)^2\right\}} = \sqrt{\frac{2}{3} \cdot J_2} = \frac{R}{\sqrt{3}} = \frac{\sqrt{2}}{3} \cdot q$$

The important question is in which plane the shear stress reaches its maximum. If Eq. (3.14) is used for obtaining the shear stress on an arbitrary plane, the maximum value of the shear stress can be obtained by

$$\frac{\delta\tau^2}{\delta n_1} = 0 \qquad \frac{\delta\tau^2}{\delta n_3} = 0 \quad (3.16)$$

and by using

$$n_2^2 = 1 - n_1^2 - n_3^2 \quad (3.17)$$

The relevant solution is

$$\mathbf{n} = \begin{pmatrix} 0 \\ \pm 1/\sqrt{2} \\ \pm 1/\sqrt{2} \end{pmatrix} \quad (3.18)$$

This exercise can be done in three different ways by switching the places of n_1, n_2 and n_3 in Eq. (3.16) and (3.17) in order to arrive at the same kind of solution

as in Eq. (3.18). This solution involves a 45 degree rotation around one of the principal axes. The absolute maximum shear stress will be for a plane rotated 45 degrees around the second principal axis, since $\sigma'_1 \geq \sigma'_2 \geq \sigma'_3$.

$$\tau_{\max} = \frac{1}{2} \cdot \left(\sigma'_1 - \sigma'_3\right) = \frac{q}{2} \text{ for axisymm. conditions. Lode's angle equals } \pm \pi/6 \tag{3.19}$$

3.2.7 Strain invariants

When a stress change occurs, the material will become deformed. The relative deformations are generally called strains.

Strains are defined as

$$\varepsilon_{ij} = -\frac{1}{2} \cdot \left(\frac{\partial u_i}{\partial x_j} + \frac{\partial u_j}{\partial x_i} \right) \quad i,j=1,2,3 \tag{3.20}$$

and are often given in the same form as stresses, i.e. in the form of a matrix or second order tensor.

$$\boldsymbol{\varepsilon} = \begin{pmatrix} \varepsilon_{11} & \varepsilon_{12} & \varepsilon_{13} \\ \varepsilon_{21} & \varepsilon_{22} & \varepsilon_{23} \\ \varepsilon_{31} & \varepsilon_{32} & \varepsilon_{33} \end{pmatrix} \tag{3.21}$$

$$\boldsymbol{\varepsilon}^T = \begin{pmatrix} \varepsilon_{11} & \varepsilon_{22} & \varepsilon_{33} & 2\varepsilon_{12} & 2\varepsilon_{13} & 2\varepsilon_{23} \end{pmatrix} = \begin{pmatrix} \varepsilon_{11} & \varepsilon_{22} & \varepsilon_{33} & \gamma_{12} & \gamma_{13} & \gamma_{23} \end{pmatrix} \tag{3.22}$$

The deformation of a medium involves work, which is defined as the product between the applied force and the deformation in the direction of the force. Thus, work within a continuum is defined as the sum of the product of the stress increment and the strain increment where the stresses have an identical direction. Note that here incremental strain and stress have the same notation.

$$W = \boldsymbol{\sigma} : \boldsymbol{\varepsilon} = \sum_{i,j=1,2,3}^{n} \sigma_{ij} \cdot \varepsilon_{ij} \tag{3.23}$$

If the work is divided into two separate parts, volumetric and deviatoric, it would be convenient if the former was dependent on the mean stress, p, multiplied by the volumetric strain, ε_p, and the latter was dependent on the deviatoric stress, q, multiplied by the distortional strain, ε_q.

$$W = \boldsymbol{\sigma} : \boldsymbol{\varepsilon} = p \cdot \varepsilon_p + q \cdot \varepsilon_q \tag{3.24}$$

where ε_p is defined in Eq. (3.25). It can be shown that the distortional strain, ε_q, is the same as in Eq. (3.26)

$$\varepsilon_p = \varepsilon_{11} + \varepsilon_{22} + \varepsilon_{33} \tag{3.25}$$

$$\varepsilon_q = \frac{2}{3} \sqrt{\frac{1}{2} \left\{ \left(\varepsilon_{11} - \varepsilon_{22}\right)^2 + \left(\varepsilon_{11} - \varepsilon_{33}\right)^2 + \left(\varepsilon_{22} - \varepsilon_{33}\right)^2 + 6 \cdot \left(\varepsilon_{12}^{\ 2} + \varepsilon_{13}^{\ 2} + \varepsilon_{23}^{\ 2}\right) \right\}} \tag{3.26}$$

3.2.8 Elasticity

Stresses and strains are coupled to each other by a constitutive relationship.

Assuming that the relation between stresses and strains is the same for loading and unloading, we have a true elastic relation.

$\boldsymbol{\sigma} = \mathbf{D}\boldsymbol{\varepsilon}$

$$\begin{pmatrix} \sigma_{11} \\ \sigma_{22} \\ \sigma_{33} \\ \sigma_{12} \\ \sigma_{13} \\ \sigma_{23} \end{pmatrix} = \begin{pmatrix} D_{11} & D_{12} & D_{13} & D_{14} & D_{15} & D_{16} \\ D_{21} & D_{22} & D_{23} & D_{24} & D_{25} & D_{26} \\ D_{31} & D_{32} & D_{33} & D_{34} & D_{35} & D_{36} \\ D_{41} & D_{42} & D_{43} & D_{44} & D_{45} & D_{46} \\ D_{51} & D_{52} & D_{53} & D_{54} & D_{55} & D_{56} \\ D_{61} & D_{62} & D_{63} & D_{64} & D_{65} & D_{66} \end{pmatrix} \begin{pmatrix} \varepsilon_{11} \\ \varepsilon_{22} \\ \varepsilon_{33} \\ \gamma_{12} \\ \gamma_{13} \\ \gamma_{23} \end{pmatrix} \tag{3.27}$$

$\boldsymbol{\varepsilon} = \mathbf{D}^{-1}\boldsymbol{\sigma}$

$$\begin{pmatrix} \varepsilon_{11} \\ \varepsilon_{22} \\ \varepsilon_{33} \\ \gamma_{12} \\ \gamma_{13} \\ \gamma_{23} \end{pmatrix} = \begin{pmatrix} D_{11}^{-1} & D_{12}^{-1} & D_{13}^{-1} & D_{14}^{-1} & D_{15}^{-1} & D_{16}^{-1} \\ D_{21}^{-1} & D_{22}^{-1} & D_{23}^{-1} & D_{24}^{-1} & D_{25}^{-1} & D_{26}^{-1} \\ D_{31}^{-1} & D_{32}^{-1} & D_{33}^{-1} & D_{34}^{-1} & D_{35}^{-1} & D_{36}^{-1} \\ D_{41}^{-1} & D_{42}^{-1} & D_{43}^{-1} & D_{44}^{-1} & D_{45}^{-1} & D_{46}^{-1} \\ D_{51}^{-1} & D_{52} & D_{53}^{-1} & D_{54}^{-1} & D_{55}^{-1} & D_{56}^{-1} \\ D_{61}^{-1} & D_{62} & D_{63}^{-1} & D_{64}^{-1} & D_{65}^{-1} & D_{66}^{-1} \end{pmatrix} \begin{pmatrix} \sigma_{11} \\ \sigma_{22} \\ \sigma_{33} \\ \sigma_{12} \\ \sigma_{13} \\ \sigma_{23} \end{pmatrix} \tag{3.28}$$

D is the stiffness matrix and $\mathbf{D}^{-1}$ the flexibility matrix. The components can be either stress dependent or stress path dependent. Constant components result in linear elastic material.

Since no work should be generated during closed loop loading and unloading, the **D** matrix must be symmetric, (Nordal, 2004).

Full isotropy

If a material has the same elastic properties in all directions it is denoted full isotropy and the stiffness matrix changes into

$$\mathbf{D} = \begin{pmatrix} D_{11} & D_{12} & D_{12} & 0 & 0 & 0 \\ & D_{11} & D_{12} & 0 & 0 & 0 \\ & & D_{11} & 0 & 0 & 0 \\ & & & \frac{1}{2}(D_{11} - D_{12}) & 0 & 0 \\ & SYM & & & \frac{1}{2}(D_{11} - D_{12}) & 0 \\ & & & & & \frac{1}{2}(D_{11} - D_{12}) \end{pmatrix} \tag{3.29}$$

This can be shown by means of coordinate transformation in different steps. In the same way the flexibility matrix can be defined as

$$\mathbf{D}^{-1} = \begin{pmatrix} D^{-1}_{11} & D^{-1}_{12} & D^{-1}_{12} & 0 & 0 & 0 \\ & D^{-1}_{11} & D^{-1}_{12} & 0 & 0 & 0 \\ & & D^{-1}_{11} & 0 & 0 & 0 \\ & & & 2\left(D^{-1}_{11} - D^{-1}_{12}\right) & 0 & 0 \\ & SYM & & & 2\left(D^{-1}_{11} - D^{-1}_{12}\right) & 0 \\ & & & & & 2\left(D^{-1}_{11} - D^{-1}_{12}\right) \end{pmatrix} \tag{3.30}$$

In the case of an isotropic linear relationship, the constitutive matrix must be specified by two independent parameters, namely the elastic modulus, E, and Poisson´s ratio, μ', or the shear modulus, G, and the volumetric modulus, K. The components of Eq. (3.30) will be as presented in Equation (3.31).

$$\begin{aligned} D_{11} &= \frac{E}{(1+\mu')\cdot(1-2\cdot\mu')}\cdot(1-\mu') = K + \frac{4}{3}\cdot G = M \\ D_{12} &= \frac{E}{(1+\mu')\cdot(1-2\cdot\mu')}\cdot\nu = K - \frac{2}{3}\cdot G = M - 2\cdot G \\ D^{-1}_{11} &= \frac{1}{E}\cdot 1 = \frac{1}{9\cdot K} + \frac{1}{3\cdot G} = \frac{M-G}{G\cdot(3\cdot M - 4\cdot G)} \\ D^{-1}_{12} &= \frac{1}{E}\cdot(-\mu') = \frac{1}{9\cdot K} - \frac{1}{6\cdot G} = \frac{M - 2/3\cdot G}{G\cdot(6\cdot M + 8\cdot G)} \end{aligned} \tag{3.31}$$

where M (or E_{eod}) is denoted oedometer modulus. Some relations between the different parameters are given below.

$$K = \frac{E}{3\cdot(1-2\cdot\mu')} \tag{3.32}$$

$$G = \frac{E}{2\cdot(1+\mu')} \tag{3.33}$$

$$E = \frac{9\cdot K}{1+3\cdot K/G} \tag{3.34}$$

$$\mu' = \frac{1}{2}\cdot\left(1 - \frac{1}{K/G + 1/3}\right) \tag{3.35}$$

$$M = \frac{E\cdot(1-\mu')}{(1+\mu')\cdot(1-2\cdot\mu')} = 2\cdot G\cdot\frac{(1-\mu')}{(1-2\cdot\mu')} = K + \frac{4}{3}\cdot G \tag{3.36}$$

The reason for using K and G is that Eqs. (3.7) and (3.27)-(3.31) give

$$\begin{aligned} p &= K\cdot\varepsilon_v \\ s_{ij} &= 2\cdot G\cdot e_{ij} \end{aligned} \tag{3.37}$$

which is a powerful and commonly used expression.

The oedometer modulus, *M*, is convenient if oedometer tests are available. The modulus evaluated from these test will be *M*.

$$M = \frac{\partial \sigma'_{vert}}{\partial \varepsilon_{vert}} \qquad when \quad \varepsilon_{hor} = 0 \tag{3.38}$$

If stress dependent components are used in **D,** more of the real soil behaviour can be incorporated than is the case with linear elasticity. The decrease in shear modulus with increasing deviatoric stress can be simulated, while a stiffer response can be simulated for unloading and reloading than for loading. This kind of model is relatively simple due to the small number of input parameters (Duncan and Chang, 1970). such models have the following limitations (Nordal, 2004).

- If loading is almost neutral[7], different loading and unloading-reloading components lead to a variation in response and a smooth transition is required.
- The principal directions of the strain increments coincide with those of the stress increments.

The elasto-plasticity theory can be used to overcome the shortcomings of an elastic model.

3.3 Theory of elasto-plasticity

When using the theory of elasto-plasticity, the strains are divided into two parts, elastic and plastic.

The elastic strains are calculated in the same manner as described in the previous section, while the plastic strains are irrecoverable and controlled by a) the yield criterion, b) flow rule and c) hardening rule.

$$d\boldsymbol{\varepsilon} = d\boldsymbol{\varepsilon}^e + d\boldsymbol{\varepsilon}^p \tag{3.39}$$

$$d\boldsymbol{\varepsilon}^e = \mathbf{D}^{-1} d\boldsymbol{\sigma} \tag{3.40}$$

Yield criteria

The yield criterion defines an area in the stress space, within which all load increments lead to elastic strains. If the stress state is located on the boundary of the yield criterion, both elastic and plastic strains will occur when the stress point is loaded. The yield criterion is expressed by Eq. (3.41)

[7] Neutral loading is defined as loading parallel with the mobilized strength in the soil. Minor deviations from this line will generate either loading or unloading, with great differences in the modulus.

$$f(\boldsymbol{\sigma},\kappa)=0 \tag{3.41}$$

where $\boldsymbol{\sigma}$ represents the stress state and κ hardening parameters. Depending on the model, $\boldsymbol{\sigma}$ and κ represent different parameters.

Examples of the yield criterion are presented for two classic constitutive models:

– The classic elasto-perfectly plastic Mohr-Coulomb model is represented by p´ and q, representing the yield criterion coinciding with the failure surface represented by Mohr-Coulumb´s failure cone. No hardening parameter is used, which means that no plastic strains occur before the stress state reaches failure. If the model is complemented by a hardening parameter, i.e. a yield cone within the failure cone, it will be able to describe plastic behaviour without failure. An example of a hardening parameter is mobilized friction.

– In the widely used Cam-Clay model, the hardening parameter is void ratio, e, or the isotropic preconsolidation stress, p_0.

When loading occurs, the hardening parameter is changed in a way that expands the yield surface, fulfilling the requirement that the stress state must be on the yield surface. Loading, unloading and reloading are defined according to Eq. (3.42)

$$\begin{aligned} &f(\boldsymbol{\sigma},\kappa)=0 \ \textit{loading} \\ &f(\boldsymbol{\sigma},\kappa)<0 \ \textit{unloading or reloading} \end{aligned} \tag{3.42}$$

Since the yield surface expands during loading $f(\boldsymbol{\sigma},\kappa)=0$, the consistency equation must be fulfilled.

$$df=\left\{\frac{\partial f}{\partial \boldsymbol{\sigma}}\right\}^T d\boldsymbol{\sigma}+\frac{\partial f}{\partial \kappa}d\kappa=0 \tag{3.43}$$

Flow rule

Plastic strains will develop when loading occurs on the yield surface, $f(\boldsymbol{\sigma},\kappa)=0$. During loading the yield surface is pushed outwards, $f(\boldsymbol{\sigma}+\Delta\boldsymbol{\sigma},\kappa+\Delta\kappa)=0$. The stress increment, $\Delta\boldsymbol{\sigma}$, can be divided into two parts, elastic, which creates elastic strains, and plastic, which generates plastic strains. The flow rule is introduced, Eq. (3.44), to describe the development of plastic strains.

$$d\boldsymbol{\varepsilon}^p=\mu\cdot\left\{\frac{\partial g}{\partial \boldsymbol{\sigma}}\right\} \tag{3.44}$$

where μ is a scalar and g a potential function. The plastic strains develop perpendicular to the surface described by the potential function, g. When g coincides with f, the flow is said to be associated, otherwise it is described as non-associated.

In the classic elasto-perfectly plastic Mohr-Coulomb model the yield surface is expressed as a function dependent on the friction angle, ϕ', and the attraction, a. The dilatancy angle, ψ, describes the potential function. If ϕ' equals ψ the flow is associated.

The modified Cam-Clay model proposed by Roscoe and Burland (1968) is another example of a model with associated flow.

Hardening rule
The hardening rule controls the amount of plastic strain caused by the plastic stress increment. This rule links the amount of plastic strains with the increased size of the yield surface, thus giving a coupling between κ and μ. In the general hardening plasticity models, it is assumed that κ is a function of the plastic strains.

$$\kappa = \kappa\left(\boldsymbol{\varepsilon}^p\right) \tag{3.45}$$

Combining Eq. (3.43) and Eq. (3.44) will give

$$\begin{aligned} df &= \left\{\frac{\partial f}{\partial \boldsymbol{\sigma}}\right\}^T \delta\boldsymbol{\sigma} + \frac{\partial f}{\partial \kappa} d\kappa = \left\{\frac{\partial f}{\partial \boldsymbol{\sigma}}\right\}^T d\boldsymbol{\sigma} + \frac{\partial f}{\partial \kappa}\frac{d\kappa}{d\boldsymbol{\varepsilon}^p} d\boldsymbol{\varepsilon}^p \\ &= \left\{\frac{\partial f}{\partial \boldsymbol{\sigma}}\right\}^T d\boldsymbol{\sigma} + \mu \cdot \frac{\partial f}{\partial \kappa}\frac{d\kappa}{d\boldsymbol{\varepsilon}^p}\frac{\partial g}{\partial \boldsymbol{\sigma}} = \left\{\frac{\partial f}{\partial \boldsymbol{\sigma}}\right\}^T d\boldsymbol{\sigma} - \mu \cdot A = 0 \end{aligned} \tag{3.46}$$

$$\mu = \frac{1}{A} \cdot \left\{\frac{\partial f}{\partial \boldsymbol{\sigma}}\right\}^T d\boldsymbol{\sigma}$$

The elasto plastic constitutive matrix.
In order to calculate the stress and strain response, expressions similar to those in Eq. (3.27) and Eq. (3.28) are required.

<u>The flexibility matrix:</u>
The flexibility matrix is obtained by combining Eq. (3.39), (3.40), (3.44) and (3.46).

$$\begin{aligned} d\boldsymbol{\varepsilon} &= d\boldsymbol{\varepsilon}^e + d\boldsymbol{\varepsilon}^p = \mathbf{D}^{-1} d\boldsymbol{\sigma} + \mu \cdot \left\{\frac{\partial g}{\partial \boldsymbol{\sigma}}\right\} \\ &= \mathbf{D}^{-1} d\boldsymbol{\sigma} + \frac{1}{A}\left\{\frac{\partial g}{\partial \boldsymbol{\sigma}}\right\}\left\{\frac{\partial f}{\partial \boldsymbol{\sigma}}\right\}^T d\boldsymbol{\sigma} \\ d\boldsymbol{\varepsilon} &= \mathbf{D}_{ep}^{-1} d\boldsymbol{\sigma} \\ \mathbf{D}_{ep}^{-1} &= \mathbf{D}^{-1} + \frac{1}{A}\left\{\frac{\partial g}{\partial \boldsymbol{\sigma}}\right\}\left\{\frac{\partial f}{\partial \boldsymbol{\sigma}}\right\}^T \end{aligned} \tag{3.47}$$

<u>The stiffness matrix:</u>
The stiffness matrix is obtained by Combining Eqs. (3.39), (3.40), (3.44) and (3.46)

$$\left\{\frac{\partial f}{\partial \boldsymbol{\sigma}}\right\}^T d\boldsymbol{\sigma} - A \cdot \mu = 0$$

$$d\boldsymbol{\varepsilon} = d\boldsymbol{\varepsilon}^e + d\boldsymbol{\varepsilon}^p = \mathbf{D}^{-1} d\boldsymbol{\sigma} + \mu \cdot \left\{\frac{\partial g}{\partial \boldsymbol{\sigma}}\right\}$$

$$\textit{multiply by } \left\{\frac{\partial f}{\partial \boldsymbol{\sigma}}\right\}^T \mathbf{D}$$

$$\left\{\frac{\partial f}{\partial \boldsymbol{\sigma}}\right\}^T \mathbf{D} d\boldsymbol{\varepsilon} = \left\{\frac{\partial f}{\partial \boldsymbol{\sigma}}\right\}^T \mathbf{D}\mathbf{D}^{-1} d\boldsymbol{\sigma} + \left\{\frac{\partial f}{\partial \boldsymbol{\sigma}}\right\}^T \mathbf{D} \left\{\frac{\partial g}{\partial \boldsymbol{\sigma}}\right\} \mu$$

$$\left\{\frac{\partial f}{\partial \boldsymbol{\sigma}}\right\}^T \mathbf{D} d\boldsymbol{\varepsilon} = \left\{\frac{\partial f}{\partial \boldsymbol{\sigma}}\right\}^T \mathbf{D} d\boldsymbol{\varepsilon} + \left\{\frac{\partial f}{\partial \boldsymbol{\sigma}}\right\}^T \mathbf{D} \left\{\frac{\partial g}{\partial \boldsymbol{\sigma}}\right\} \mu = A \cdot \mu$$

$$\mu = \frac{\left\{\frac{\partial f}{\partial \boldsymbol{\sigma}}\right\}^T \mathbf{D} d\boldsymbol{\varepsilon}}{A - \left\{\frac{\partial f}{\partial \boldsymbol{\sigma}}\right\}^T \mathbf{D} \left\{\frac{\partial g}{\partial \boldsymbol{\sigma}}\right\}}$$

$$d\boldsymbol{\sigma} = \mathbf{D} d\boldsymbol{\varepsilon} - \mu \cdot \mathbf{D} \left\{\frac{\partial g}{\partial \boldsymbol{\sigma}}\right\}$$

$$d\boldsymbol{\sigma} = \mathbf{D} d\boldsymbol{\varepsilon} - \mathbf{D} \left\{\frac{\partial g}{\partial \boldsymbol{\sigma}}\right\} \frac{\left\{\frac{\partial f}{\partial \boldsymbol{\sigma}}\right\}^T \mathbf{D} d\boldsymbol{\varepsilon}}{A - \left\{\frac{\partial f}{\partial \boldsymbol{\sigma}}\right\}^T \mathbf{D} \left\{\frac{\partial g}{\partial \boldsymbol{\sigma}}\right\}}$$

$$d\boldsymbol{\sigma} = \left(\mathbf{D} - \mathbf{D} \left\{\frac{\partial g}{\partial \boldsymbol{\sigma}}\right\} \frac{\left\{\frac{\partial f}{\partial \boldsymbol{\sigma}}\right\}^T \mathbf{D}}{A - \left\{\frac{\partial f}{\partial \boldsymbol{\sigma}}\right\}^T \mathbf{D} \left\{\frac{\partial g}{\partial \boldsymbol{\sigma}}\right\}} \right) d\boldsymbol{\varepsilon} = \mathbf{D}_{ep} d\boldsymbol{\varepsilon} \tag{3.48}$$

3.4 Elastic visco-plasticity

The visco-plasticity theory can be used to incorporate visco-plastic and strain rate dependent behaviour. This theory follows the same concept as presented in the earlier section about elastic-plasticity with consideration of the strain rate. The stains are given by Equation (3.49)

$$d\boldsymbol{\varepsilon} = d\boldsymbol{\varepsilon}^e + d\boldsymbol{\varepsilon}^p + d\boldsymbol{\varepsilon}^{vp} \tag{3.49}$$

The flow rule is defined in the same way as for the theory of elasto-plasticity, although the scalar, μ, is changed to μ_2 which is a function of the strain rate (Perzyna, 1963). A couple of models based on this theory are suitable for

modelling effects such as creep and strain rate dependent stiffness in soils (Runesson, 1978; Zhou *et al.*, 2005).

Since strain rate dependency and consolidation were assumed to be a minor problem related to temporary excavations in clay, this phenomenon was not included in this work, and therefore the theory of visco-plasticity is not discussed in detail.

3.5 Perfect linear elasto-plastic behaviour or ideal elasto-plastic behaviour

In this work a simple but commonly used model will be employed as well as more advanced models. The simple model is a perfectly linear elastoplastic model, with a yield criterion based on Mohr-Coulomb's failure criterion. The plastic behaviour is controlled by a non-associated flow rule. However, as the model is used in this project the plastic strains will develop as if the flow rule was associated.

The elastic behaviour is governed by the input parameters E (Young´s modulus) and μ' (Poisson´s ratio) or by G and E_{oed} (Shear and Oedometer modulus respectively). The Mohr-Coulumb failure criterion depends on the shear strength, c_{ref}, and the friction angle, ϕ', while ψ controls the dilatancy.

The theory of elasto-plasticity was described in the previous sections. For a linear elasto perfectly plastic model some simplifications are made.

- there is no hardening parameter
- the yield surface coincides with the failure surface

The failure surface is defined by Mohr-circles and expressed as six planes in the stress spaces (e.g. Brinkgreve, 2002; Nordal, 2004). Each failure plane is associated with a plastic potential surface. But since $\sigma'_1 \geq \sigma'_2 \geq \sigma'_3$, only one of these planes is important.

The constitutive relation between stresses and strains can be expressed in stress invariants, see the previous section. This yields a failure surface as in Equation (3.50)

$$
\begin{aligned}
f(\boldsymbol{\sigma}) &= q - M \cdot (p' + a) = q - M \cdot p' - M \cdot c' / \tan\phi' \\
f(\boldsymbol{\sigma}) &= \sigma'_1 - \sigma'_3 - \sin\phi' \cdot (\sigma'_1 + \sigma'_3 + 2a) \\
f(\boldsymbol{\sigma}) &= t - \sin\phi' \cdot (s' + a)
\end{aligned}
\tag{3.50}
$$

and with a potential surface of

$$g(\boldsymbol{\sigma}) = q - M^* \cdot p' + k_1$$
$$g(\boldsymbol{\sigma}) = \sigma'_1 - \sigma'_3 - \sin\psi \cdot (\sigma'_1 + \sigma'_3 + 2a) + k_2 \tag{3.51}$$
$$g(\boldsymbol{\sigma}) = t - \sin\psi \cdot (s' + a) + k_2$$

The inclination, M, in a p'-q plot is used to calculate the strength of the soil in a specified condition. Since Mohr-Coulomb provides different deviatoric stress depending on the intermediate principal stress, σ_2, M changes in line with the stress path in the stress space.

For axial symmetric compression

$$M_{comp} = \frac{6 \cdot \sin\phi'}{3 - \sin\phi'} \tag{3.52}$$

and for axial symmetric extension

$$M_{ext} = \frac{6 \cdot \sin\phi'}{3 + \sin\phi'} \tag{3.53}$$

In intermediate cases, M can be expressed by Equation (3.54)

$$M(\theta) = \frac{3 \cdot \sin\phi'}{\sqrt{3}\cos\theta + \sin\theta\sin\phi'} \tag{3.54}$$

The same exercise is valid for M^*.

$$M^*(\theta) = \frac{3 \cdot \sin\psi}{\sqrt{3}\cos\theta + \sin\theta\sin\psi} \tag{3.55}$$

The constitutive relationship described in Equation (3.48) is here expressed by the invariants p' and q.

$$\begin{pmatrix} \delta p' \\ \delta q \end{pmatrix} = \begin{pmatrix} K & 0 \\ 0 & G \end{pmatrix} \begin{pmatrix} \delta\varepsilon_p \\ \delta\varepsilon_q \end{pmatrix} \textit{ in the elastic region}$$
$$\textit{and} \tag{3.56}$$
$$\begin{pmatrix} \delta p' \\ \delta q \end{pmatrix} = \frac{3 \cdot G \cdot K}{K \cdot M \cdot M^* + 3 \cdot G} \cdot \begin{pmatrix} 1 & M^* \\ M & MM^* \end{pmatrix} \begin{pmatrix} \delta\varepsilon_p \\ \delta\varepsilon_q \end{pmatrix} \textit{ on the failure surface}$$

As can be seen in Equation (3.56), there is no flexibility matrix on the failure surface, the determinant of the elasto perfectly plastic stiffness matrix equals zero. This means that there are infinite strains without any stress changes. The $\delta\varepsilon_p / \delta\varepsilon_p$ ratio is $-M^*$, cf. Equation (3.44). If the stress element situated on the failure surface is only exposed by the presence of deviatoric stains, there will be a stress change along the failure surface, denoted neutral loading.

Figure 3.4 illustrates the yield surface according to Mohr-Coulomb for a constant value on p'. The dotted lines in the figure illustrate how the stress path

develops under PS conditions for different Poisson's ratio values, starting from q equals 0, isotropic.

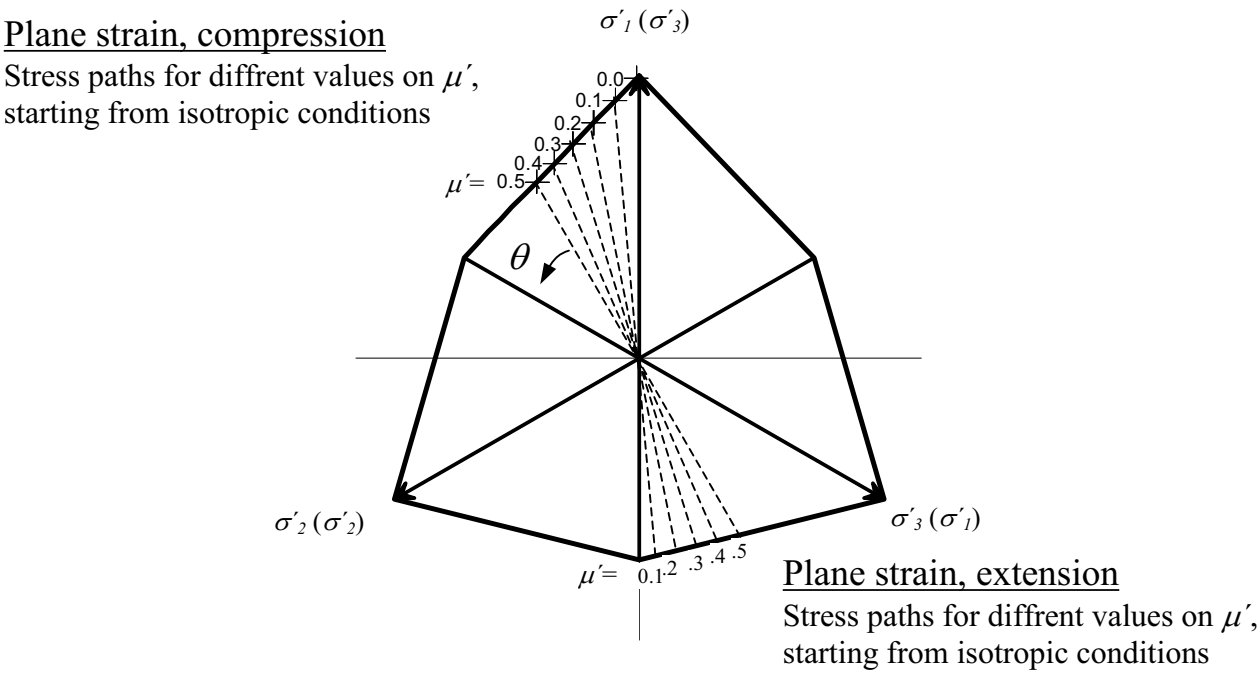

Figure 3.4: Loading under plane strain conditions. Plot showing the points of impact on the failure surface in relation to different Poisson's values. The loading starts from an isotropic state. The pricipal stresses within brackets are valid for extension.

4 THE GÖTA TUNNEL, WESTERN PART

4.1 Introduction

In Gothenburg, a large tunnel project was carried out between 2001 and 2006. The project involved deep excavations in soft clay at both ends of the tunnel, while the central section was located in bedrock (Figure 4.1). The excavations in soft clay took place to a depth of 18 metres below the original ground surface and 16 metres below sea level. In some places the excavations were carried out next to and under existing buildings.

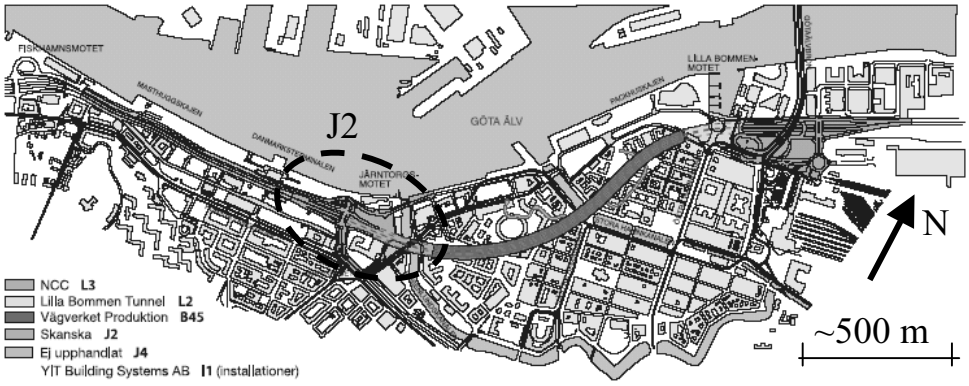

Figure 4.1: Plan of the tunnel project. The studied site, contract J2, is at the western end of the tunnel (www.vv.se).

The excavations at the J2 site were performed in soft clay. The area is situated along the Göta River and the clay layer was 20 metres in most places and over 40 metres at the western part of the site, while at the eastern part there is an outcrop of bedrock.

The main part of the J2 site is located on ground reclaimed from the river during the 18th and 19th centuries. The original water depth was approximately 0.5 to 1.0 metres. During the extension of Gothenburg harbour, some parts of the area were dredged 2.5 to 4.5 metres below sea level, and in some places old quay constructions can be found. When the tunnel project started, the area was filled to 2 to 3 metres above the mean water level of the river. Effects of secondary consolidation are still visible. The progressive settlements are in the order of 0-3 mm/year in the eastern and 3-8 mm/year in the western part.

4.2 Soil conditions

The fill consists of material that was available at the time the land was reclaimed and includes material dredged from the river and excavated from other parts of the city as well as different kinds of waste products from the period during which the area was filled. Because of its varied composition, the fill has fairly

high hydraulic conductivity and the pore water pressure is in direct contact with the water in the river.

The soft clay under the fill is very homogeneous with a water content of approximately 70 % and a similar liquid limit. The shear strength, mainly estimated from field vane tests, is about 15 kPa at the top of the clay layer with an increase of approximately 1.0 kPa/m. The clay is normally consolidated in the main part of the site. However, areas with an *OCR* of slightly less than two do exist. The progressive ground surface settlement is mainly due to consolidation and creep in the clay, although some of the settlements can also be attributed to compaction in the fill layer. Some variation in clay properties occurs because of the different stress histories in the area. Beneath the clay layer are 0 – 2 (in some parts up to 5) metres of cohesionless material, mainly sand but also weathered bedrock.

4.3 Excavation sequence and design of the retaining wall system

The excavation was performed within sheet pile walls supported by anchors fixed backwards into the bedrock or by struts. Anchors were used when the vertical stability of the wall was adequate and where the contractor found it economical to use such a support system. Struts were employed in other parts where the distance to the bedrock was too great. An overview of the excavation pit can be seen in Figure 4.2, where the nearest part is the eastern section of the J2 contract. The photo is taken from the top of the intersection between the concrete tunnel and the tunnel blasted out of the bedrock. The construction work has been presented by Liedberg *et al.* (2003) and Ekenberg (2004).

The excavation was performed as follows (from west to east):

- as an open excavation, with a final excavation grade 0-2 metres below the ground surface
- within *SPW*s supported by berms, which were excavated stepwise after the installation of struts against a concrete slab cast in the centre of the excavation. The final excavation grade was 2-6 metres below the original ground surface.
- within *SPW*s with props between the two sides. Berms were used with a stepwise excavation of an inner section where a concrete slab was placed. Temporary struts were placed against the concrete before the berms were excavated. The concrete slab was extended to support the walls and the temporary struts were removed. The final excavation grade was 6-10 metres below the original ground surface.
- underwater supported by a top level of struts and a concrete slab cast on the excavation grade. This slab was anchored to the bedrock for vertical

stability. The final excavation grade was 10-12 metres below the original ground surface.

– within *SPW*s driven down to the bedrock. These walls were supported by anchors installed backwards and fixed into the bedrock. Up to 5 rows of anchors were used in some parts, with three rows in the main section. The groundwater within the pit was lowered to prevent hydraulic uplift. The final excavation grade was 12-18 metres below the original ground surface.

Several kinds of sheet piles were used, from AZ13 S355 to HZ975C S355, and the wales were designed for loads of up to approximately 500 kN/m.

Figure 4.2. Overview of the excavation, March 2004

4.4 Soil exploration

Before the Göta tunnel project started, an extensive field investigation was carried out by the builder, the Swedish National Road Administration. Four sub-areas with different strength properties were identified at the J2 site.

The undrained shear strength was evaluated from field vane tests as well as from some fall-cone tests. The undrained shear strength obtained from various bore holes and depths were analysed statistically in order to arrive at a design value and to be able to present representative values of partial factors to be used in ultimate limit and serviceability limit design. All data from one of these sub-areas have been analysed statistically and the results presented in Table 4.1. For further details, see Appendix A.

Table 4.1: Shear strength estimated by the Swedish Road Administration in sub-area JE-JF north.

Layer	Depth	$s_{u,\ trend}$ (kPa)	Number of tests	Standard deviation (kPa)	$s_{u,\ trend\ reduced}$ (kPa)	$s_{u\ presented}$ (kPa)
Upper	4	17.5	121	2.0	16.3	16
part	13	28.9			28.1	27,5
Lower	13	28.5	130	2.5	27.6	27,5
part	25	37.3			35.5	35

Additional soil characteristics provided by the builder will be presented in connection to where they are used.

5 FIELD MEASUREMENTS

5.1 Introduction

This research project included an extensive field study, which was carried out at the Järntorget site, one part of the Göta tunnel project in Gothenburg. The aim of the field study was to increase knowledge, understanding and the empirical base of how deep excavation in soft clay within steel sheet pile walls affects surrounding areas. Extensive instrumentation was installed in three sections, where the effect of existing ground constructions was expected to be insignificant. The horizontal and vertical deformations were measured at different depths and distances from the sheet pile wall and surface settlements monitored every 4 metres from the sheet pile wall, to a distance of 32 metres. Furthermore, the pore water pressure was measured at different levels and distances from the wall. Finally, the earth pressure and the forces in the anchors and/or struts were measured.

5.2 Instrumentation

5.2.1 Horizontal deformation

The horizontal deformations in the sections were measured both by gauges welled at the sheet pile wall at different levels of the sheet pile wall and by inclinometers installed behind the wall. The wall gauges were part of the contractor's monitoring program and was measured in three dimensions. Inclinometers installed as part of this research project were used to measure horizontal movements next to the sheet pile wall and in the soil at specified distances behind the wall. The inclination was measured in two perpendicular directions, thus yielding the deformation both towards the excavation and along the sheet pile wall. The accuracy of the measurements was 0.02% (± 2mm/m). The tilt of the inclinometer was measured by strain gauges. Due to the fact that the guide tube did not have any keyways, the measurements were insensitive to the rotation of the tube during installation (Hanna, 1985). The inclination was measured manually at every metre, after which the horizontal movements were calculated.

5.2.2 Vertical deformation

As part of the mandatory monitoring program at the site, the vertical deformations of the ground surface were kept under surveillance at different locations up to a distance of 32 metres behind the wall. For logistic reasons, several of these gauges were damaged and new ones installed during the project, with some interpolation made to cover the loss of data. In order to deepen the understanding of how the vertical deformations developed in the soil strata, bellow hose settlement devices for the measurement of settlement at different

depths were installed at varying distances from the wall. This type of equipment has been used successfully in Sweden for about 30 years and the accuracy is approximately ± 1 mm. The method is described by e.g. (Wager, 1972; Sällfors, 1975; Bozozuk and Fellenius, 1979; Persson, 2004).

5.2.3 Pressures

The horizontal earth pressure adjacent to the sheet pile wall was measured with GLÖTZL: PE/P 10/20 KF 10 no. 16.02.11 type earth pressure cells, see Figure 5.1

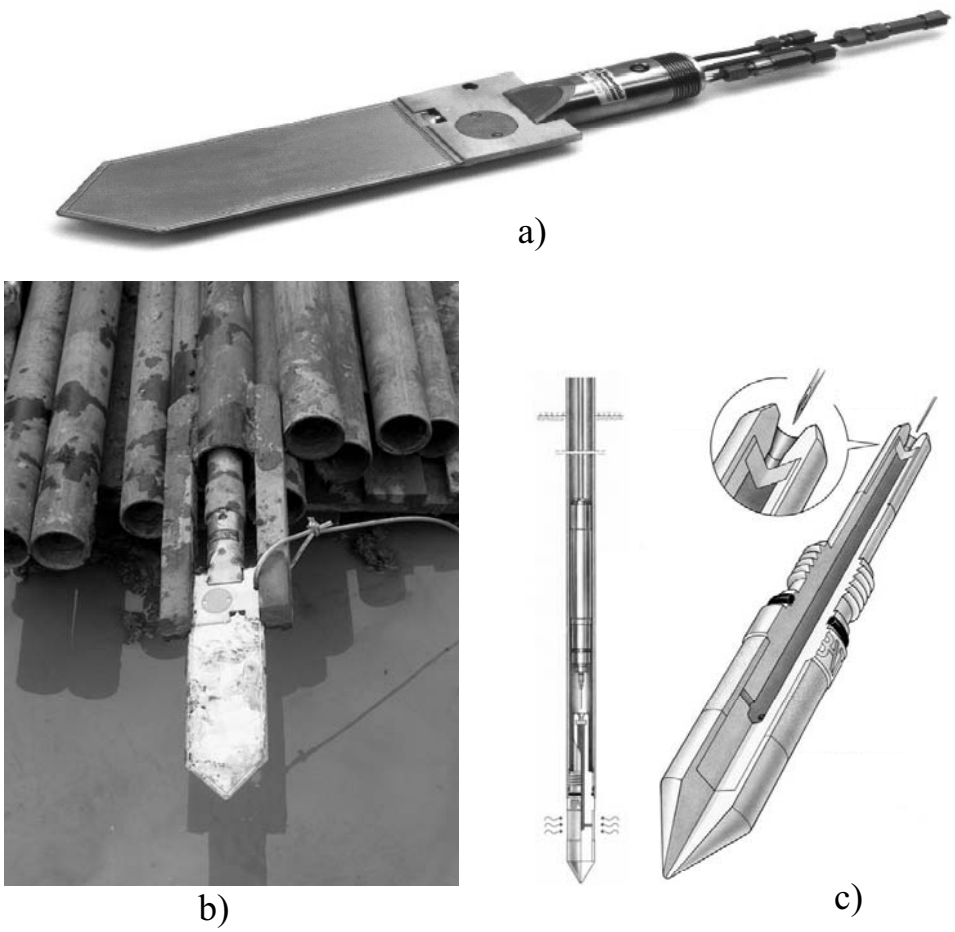

Figure 5.1. Instrumentation devices for measuring earth pressure and pore water pressure.
a) Earth pressure cell, type PE/P 10/20 KF 10 nr 16.02.11 manufactured by Glötzl.
b) Installation tool for the earth pressure cells
c) The principle behind the BAT MK II piezometer.

The earth pressure cells used have, according to the manufactory, an accuracy of ± 2 kPa. The literature reports that due to some effects such as arching and/or disturbance, the earth pressure cells often yield lower values than expected but the relative stress changes seem to be accurate (Edstam and Jendeby, 1992; Persson, 2004).

The pore water pressure was measured at different locations on the site, in order to obtain an overview of the stress changes adjacent to an excavation. The devices installed by Chalmers were of the BAT: Mk II type. The principles of this system are presented in Figure 5.1c

As part of the contactor's monitoring program, the loads in supporting struts and anchors were measured close to sections of special interest, including those monitored in this project.

5.3 Section 1/430 north

The excavation was carried out inside a strutted sheet pile wall, to a depth of 10.5 metres.

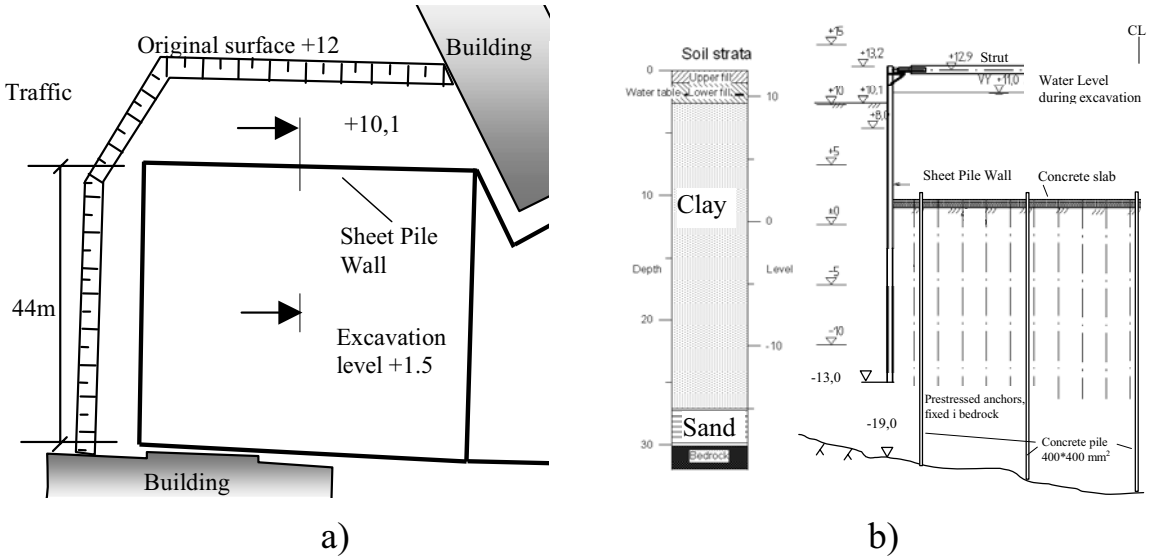

Figure 5.2: Test section 1/430 north.
a) Plan *b) Section (right)*

The deformations in the section were measured with inclinometers at various distances behind the sheet pile wall and with extensometers at two different distances from the wall.

Inclinometer 1 (I1) was installed in a pipe welded to the sheet pile wall. Inclinometers 2 and 3 (I2 and I3) were located 8.9 and 18.9 metres behind the wall.
Extensometers (bellow hoses) 1 and 2 (B1 and B2) were located at a distance of 5.4 and 11.8 metres behind/ the wall.

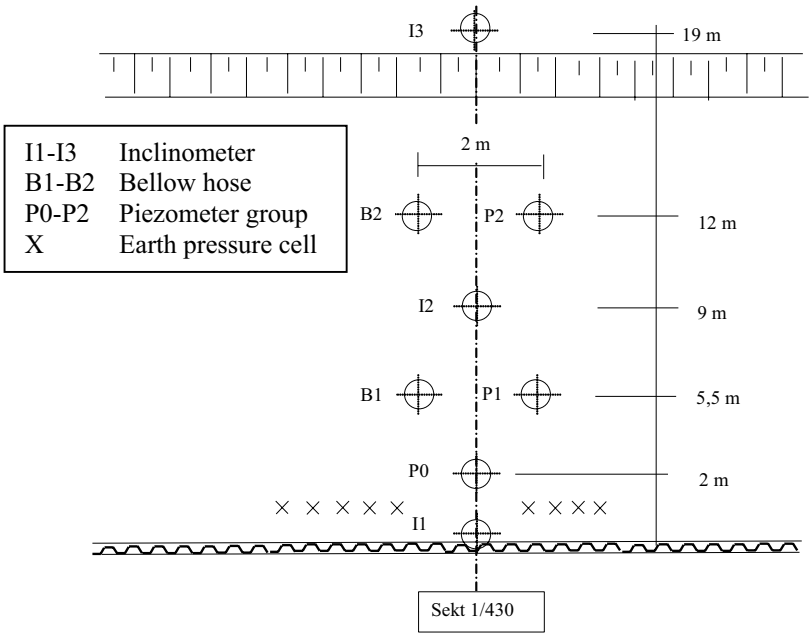

a)

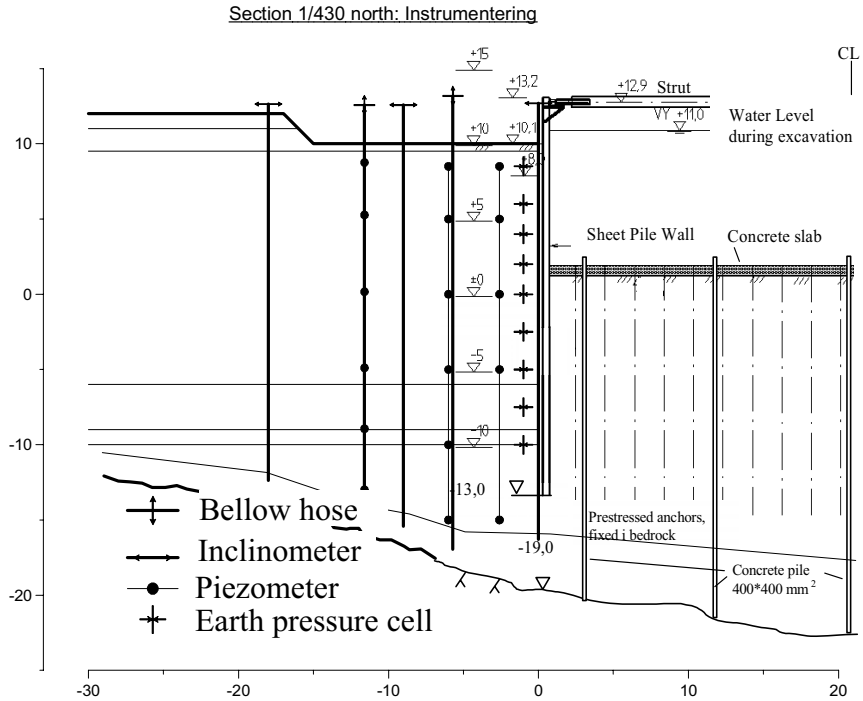

b)

Figure 5.3: Instrumentation in test section 1/430 north.
a) Placement of measuring instruments
b) Section showing the monitoring

The inclinometers were installed down to the depth of the cohesionless material on top of the bedrock. The thickness of the cohesionless material varied between 1 and 3 metres. Horizontal movement was measured at every metre of depth.

The bellow hoses were installed to the same depth and the vertical movement was measured at every metre. The reference date for the inclinometers and bellow hoses is presented in Table 4.1 below.

Table 5.1: Installation date and date of reference monitoring of the inclinometers and the bellow-hoses

Gauge	Installation date	Date of zero setting
I1	2002-08-15	2002-10-18
I2	2002-07-01	2002-07-09
I3	2002-07-01	2002-07-09
B1	2002-07-01	2002-07-14
B2	2002-07-01	2002-07-14

The pore pressure distribution with depth was determined at different distances from the wall. The pore pressure at each distance was measured at 5 to 6 levels. The earth pressure was measured at 9 different levels on the retained side of the sheet pile wall. The earth pressure cells measured both the total horizontal stress and pore pressure.

The measurements described above were carried out within this project, in addition to which the contractor had an extensive measurement programme.

5.3.1 Soil profile

The ground at this location is 2 metres above sea level, +12.0. The area was filled between 1790 and 1860. The depth of the fill is around 2.5 metres. Below the fill the soil stratum consists of a 25 metre clay layer. The clay is soft and highly plastic and situated above a 0 to 5 metre sand layer.

5.3.2 Working sequence

The excavation was carried out in well-defined sequences, which are presented in Figure 5.4. The individual steps are listed in Table 5.2.

Table 5.2: Working sequence in section 1/430 north

1. Installation of Sheet Pile Wall.
2. Excavation to a level of +10.1 inside and outside the wall.
3. Excavation to a level of +9.5 inside the wall.
4. Pile driving.
5. Placement of fill inside the wall to a level of +11.0.
6. Gradual underwater excavation and assembly of the struts.
7. Concrete casting.
8. Installation of anchors.
9. Dewatering to a level of +10.0.
10. Dewatering to a level of +9.0.
11. Dewatering to a level of +6.0.
12. Dewatering

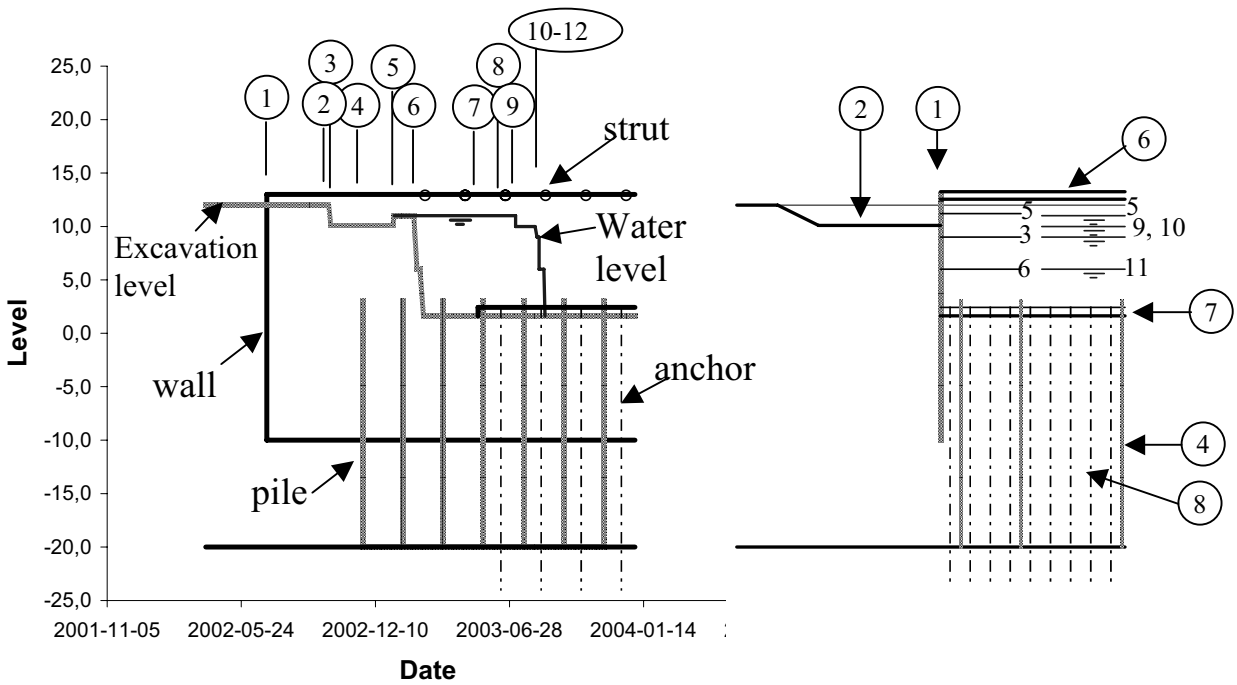

a) b)

Figure 5.4: Visualisation of the working sequence in section 1/430 north
a) Chronological working sequence
b) Working sequence in a simplified section

5.3.3 Engineering deformations existing prior to excavation

In order to decrease the loads on the sheet pile wall and limit future settlements, a 2 m excavation was made outside the location of the planned tunnel. This excavation was carried out in steps. In August 2002, the excavation east of

section 1/428 was carried out, but only to a distance of 12 metres from the wall, although 17 metres had been recommended. During this first excavation, a heave of 40 mm was registered by the bellow hose B1 (B2 was located in the edge of the excavation and registered a heave of 10 mm). The excavation west of section 1/428 took place during December 2002. The deformation caused by this excavation could not be distinguished from the movements due to the installation of piles within the pit. The piles were installed in rows to carry the loads from the tunnel. They were mainly installed from southeast to northwest, in order to minimize the effect on a building located opposite the monitored section. Pile rows A to D were installed during November 2002, and row E was installed in the first weeks of December 2002. The location of the pile rows can be seen in Figure 5.5, row A and B who are symmetrical around the centre line.

In order to keep the displacement at minimum during piling, a volume compensation were made by pressing an open-ended steal tube into the clay. This tube was then retrieved and because of the applied vacuum pressure within the tube and the cohesion, the clay within the tube was removed. This phenomenon can be compared with the process known as “plugging” which, due to its simplicity, is commonly used for highly plastic clays in Sweden. The method has, however, a disadvantage compared to e.g. pre-drilling, in that clay can only be removed down to a depth of 10-15 metres, depending on the size of the tube and cohesion of the clay.

The piles were installed from level +10 with a follower to bring the pile head down to level +3. The attempt to remove the clay was generally successful down to level ±0 with the result that, after installing the piles, an increase in volume occurred below level ±0 and a volume decrease above level +3.0. The rate of volume decrease corresponds to the same volume per metre of depth as that of the increase below level ±0. The effect of this procedure can be seen in Figure 5.5b.

The unloading excavation resulted in a heave of approximately 4 cm on the surface. The heave took place in the upper 15 metres of the clay layer. Part of this uplift could be an effect of piling in row A, more than 40 metres from the monitoring area.

During piling the wall was pressed outwards and the uplift outside the wall increased, especially in the unloaded area. When installing the piles next to the wall, it was pressed outwards in sections where the piles pressed the clay to the side and inwards where some of the clay was removed to balance the volume. Piling caused approximately the same amount of outward movement as vertical uplift.

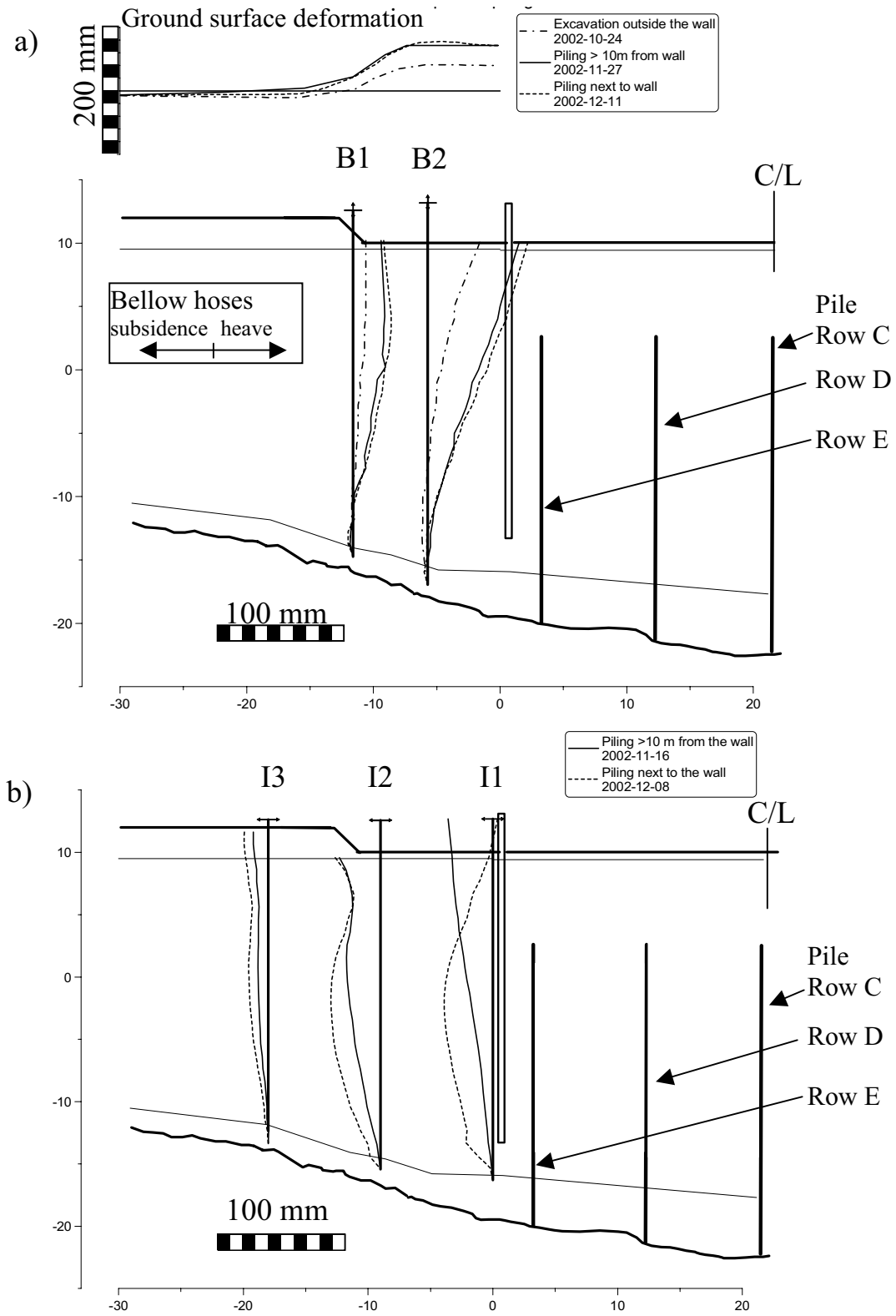

Figure 5.5: Deformations in section 1/430 north prior to the main excavation
a) Vertical deformation (The gauges show heave due to unloading and volume displacement due to the piling)
b) Horizontal displacement

5.3.4 Deformations caused by excavation

After the piling was finished, the excavation work began. To obtain sufficient safety in terms of overall stability, bottom heave and hydraulic uplift, the excavation was performed under water. The water level was kept at +11, and the clay was removed by an excavator standing in the pit on a temporary fill to +11.0.The excavation was made in strips, with successive installation of struts as soon as the final depth was reached, see Figure 5.6.

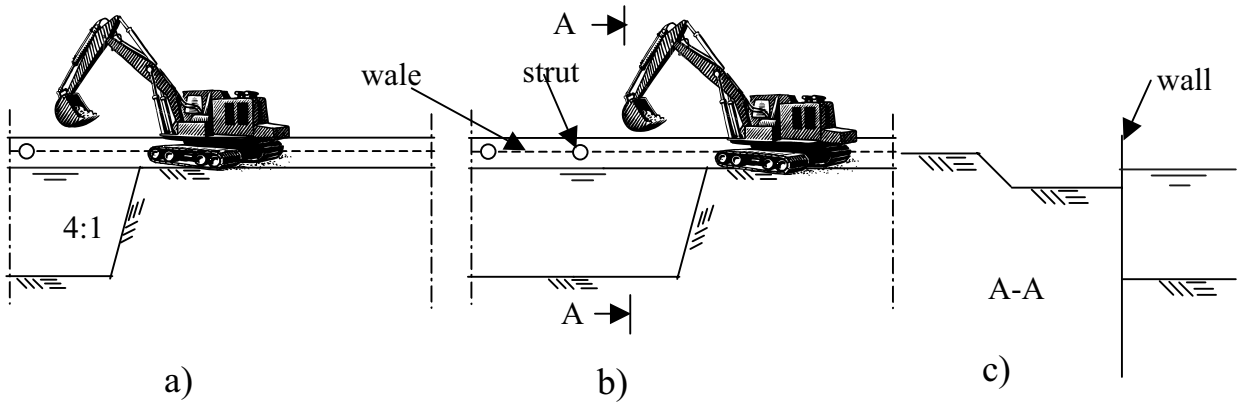

Figure 5.6: Underwater excavation sequence
a) excavation strip i b) excavation strip i+1
c) section A-A. Cantilever

This excavation method was chosen for practical reasons. To keep the wall deflection as low as possible, the struts should have been installed before instead of after the excavation. This excavation method left one part of the wall without support, with the exception of water pressure, which had a cantilever height of approximately 10 metres. The design considered 3D effects. Figure 5.7 shows the deformation during the excavation, the installation of a concrete slab and the dewatering of the pit. The result of the partly unsupported stepwise excavation is shown in Figure 5.7b. The cantilever movement was in the order of 2-4 cm. The differences between the registered deformations obtained on 2003-04-14 and 2003-08-03 are mainly an effect of the fact that the stepwise deformation was complete in the neighbouring sections, although the installation of the concrete slab and the anchors also had some impact. During the excavation, some subsidence obviously occurred and the soil moved towards the pit. Some of these movements may have been caused by consolidation as a consequence of piling. Case studies in the literature indicate that the initial effect adjacent to piling is heave, although in most cases the heave decreases over time as a consequence of consolidation, and on some occasions the net movement can be settlement (Dugan and Freed, 1984; Johansson and Jendeby, 1998; Johansson and Jendeby, 1999; Jonsson and Kristiansson, 2004). The subsidence was approximately 2-4 cm. During the excavation phase the wall moved inwards by approx. 4 cm. The settlement and the inward movement corresponded well with each other.

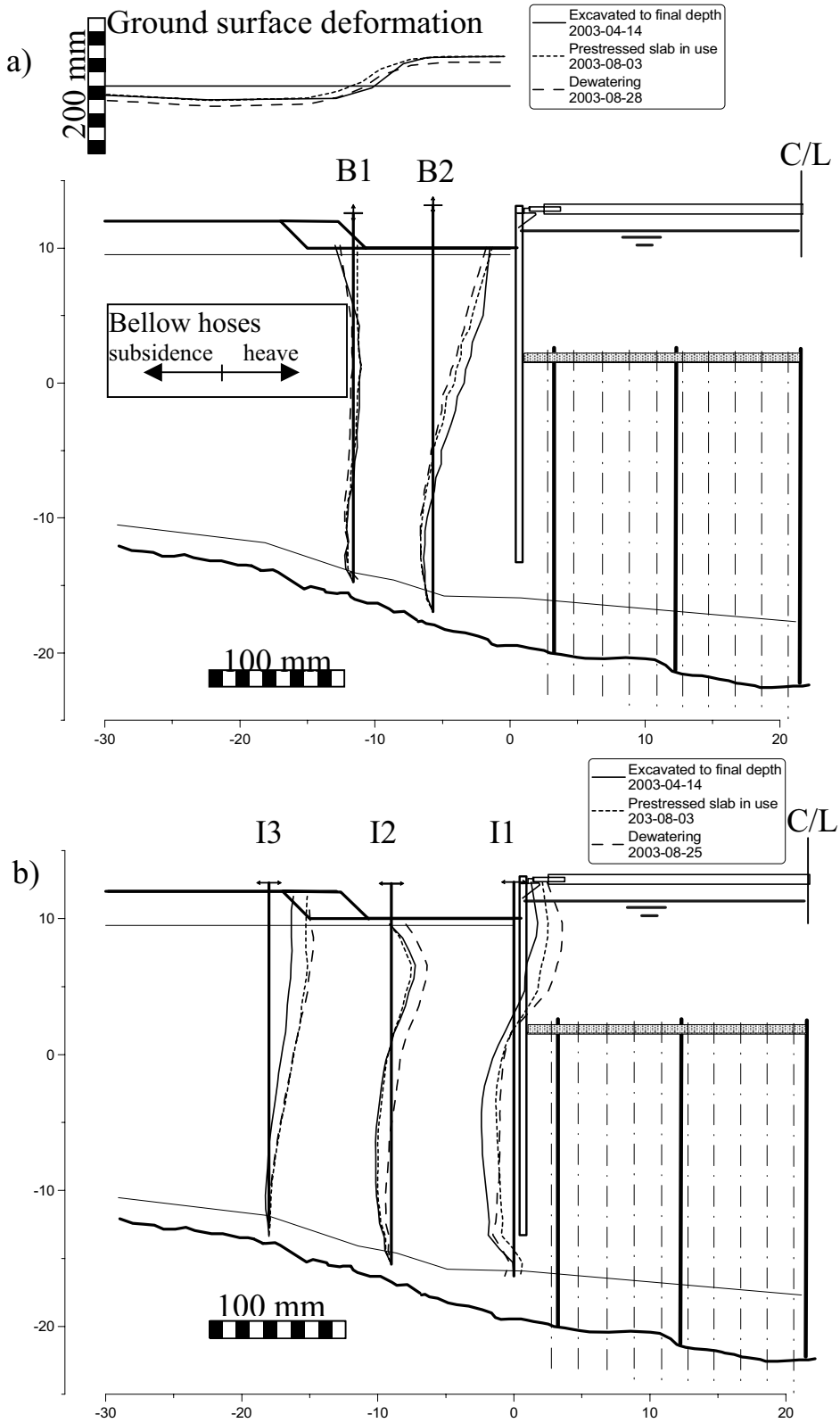

Figure 5.7: Deformations developed in section 1/430 north during excavation
a) Vertical deformation
b) Horizontal displacement

Before dewatering the pit, the unloading excavation outside the wall was increased, as can be seen in Figure 5.7a, this resulted in the form of a heave between 2003-04-14 and 2003-08-03. During dewatering the wall moved inwards by another cm and subsidence also increased.

5.3.5 Deformations developed during tunnel construction

Deformations are shown in Figure 5.8 for two dates after completion of the excavation. These two measurements reveal that the settlements continued after the tunnel section was cast and the area between the tunnel and the wall refilled with sand. The horizontal displacement mainly continued underneath the tunnel and inclinometer I1 moved by 3 cm. Inclinometers I2 and I3 showed increasing deformations of the same magnitude as I1. The reason for this may be relaxation in the anchors, consolidation effects, or the dissipation of negative pore water pressure underneath the tunnel. All of these effects would cause a decrease in the horizontal pressure, perpendicular to the direction of the tunnel.

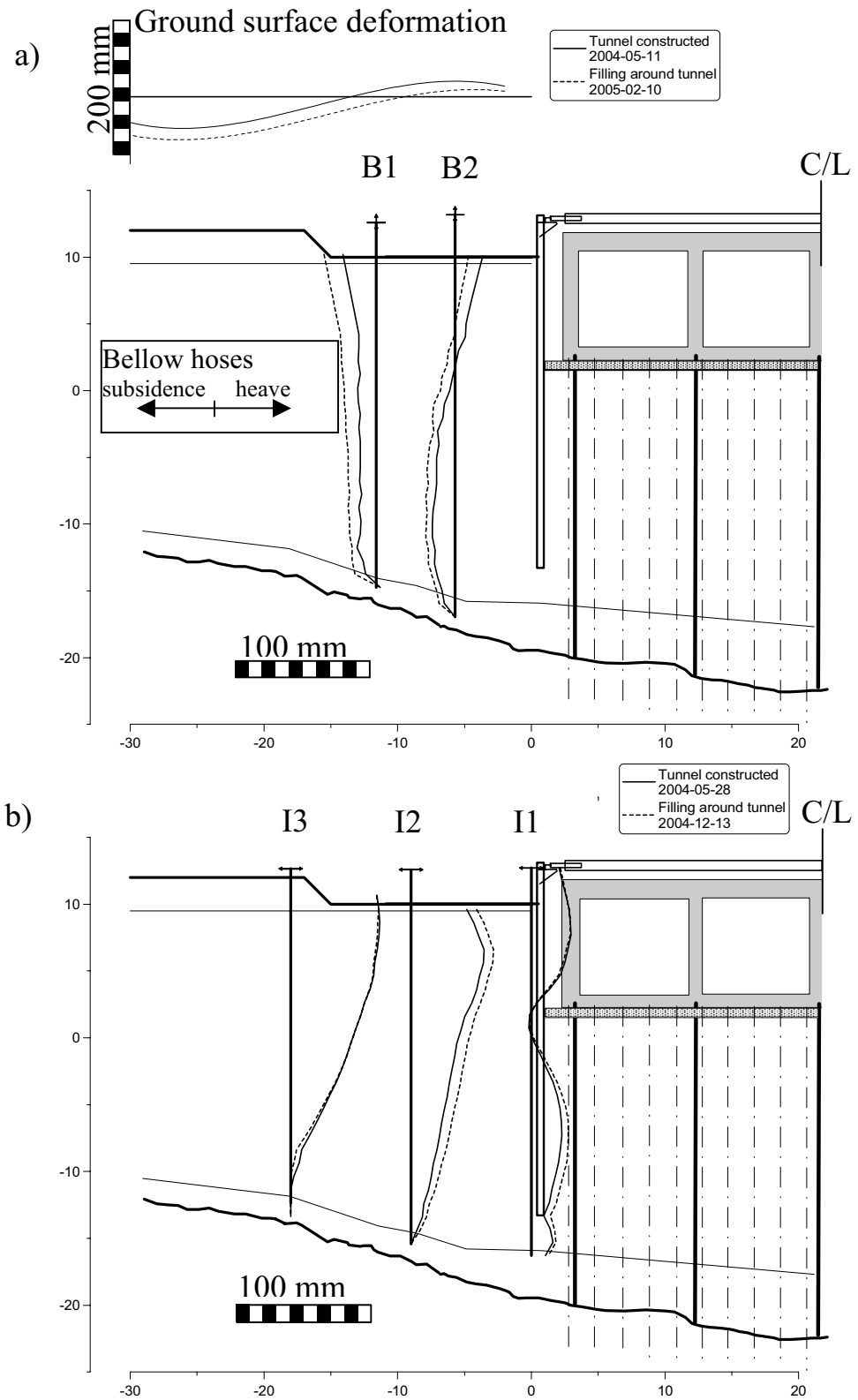

Figure 5.8: Deformations developed in section 1/430 north after excavation
a) Vertical deformation
b) Horizontal displacement

5.3.6 Deformations over time

In previous sections, the deformations are presented for different specific dates. During the excavation work, measurements were made to record the deformation at every working phase and the time delay between the different phases. In Figure 5.9 the vertical deformations measured by the bellow-hoses are presented for every 5th metre. The horizontal deformations are presented in Figure 5.10. To make it legible, only some important levels are presented, e.g. top of the wall, midspan between the strut and slab etc. To elucidate how the deformation developed, Figure 5.9 and Figure 5.10 are complemented by details of the working sequence.

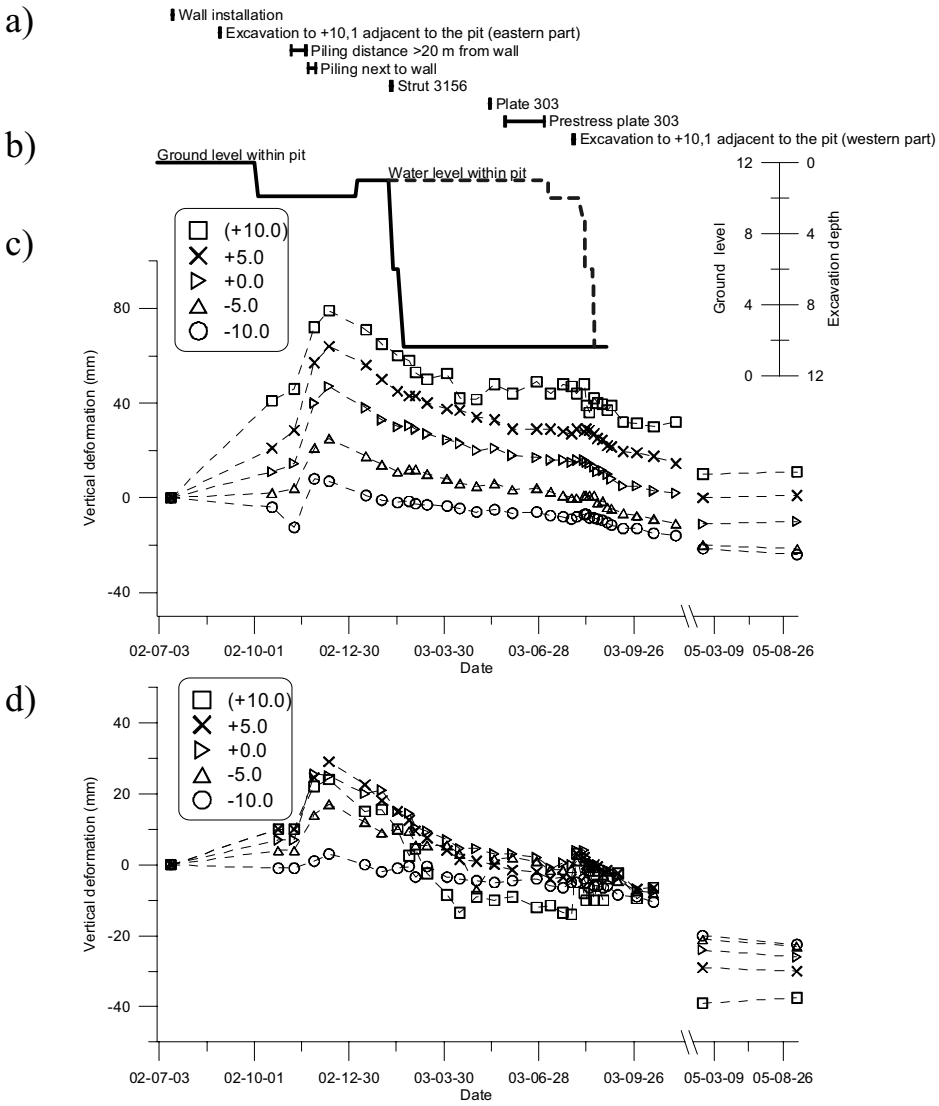

Figure 5.9: Vertical displacement over time
a) Working sequence
b) Excavation and water level within the pit
c) Bellow-hose B1 d) Bellow-hose B2

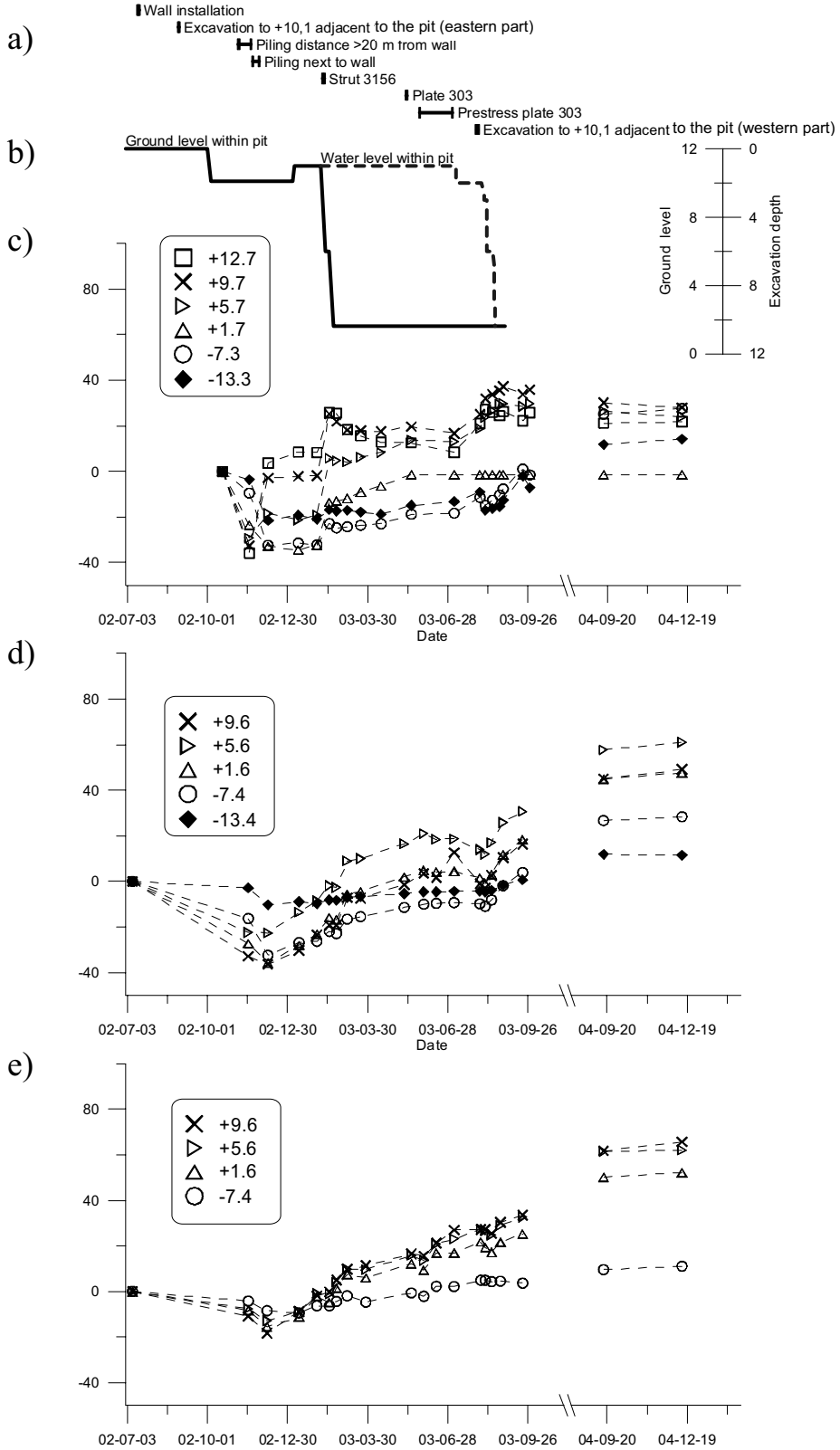

Figure 5.10: Horizontal displacement over time
a) Working sequence
b) Excavation and water level within the pit
c) Inclinometer I1 d) Inclinometer I2 e) Inclinometer I3

5.3.7 Pore water pressure over time

The pore water pressure was measured by means of standard piezometers and a piezometer built into the earth pressure cells. The location of these gauges is shown in Figure 5.3 and the variation in measured pore water pressure is presented in Figure 5.11 and Figure 5.12. These figures are complemented by the stationary pore water pressure as an initial value.

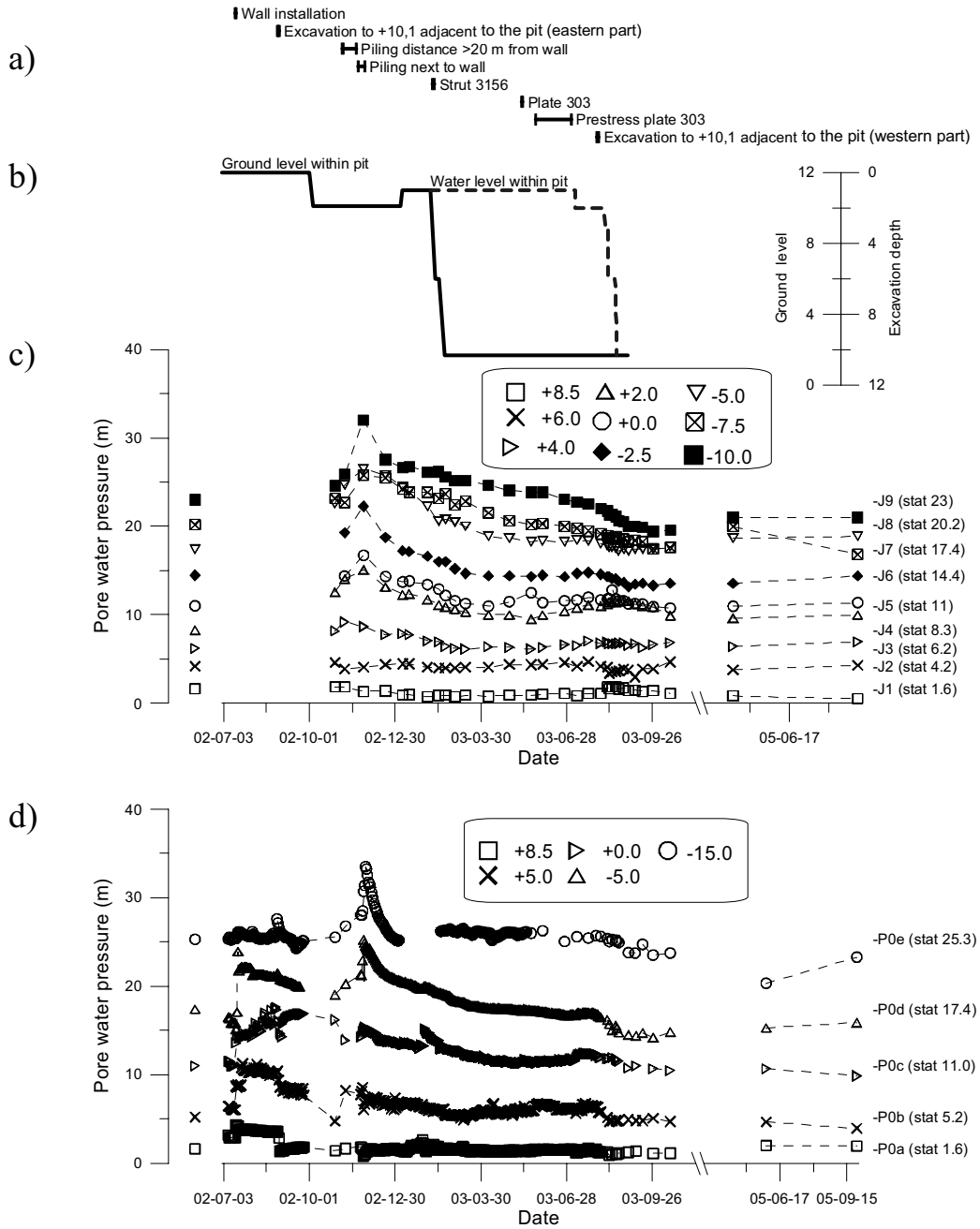

Figure 5.11: Pore water pressure over time
a) Working sequence
b) Excavation and water level within the pit
c) Earth pressure cells (0.5 m behind the wall)
d) Piezometer group P0 (2.0 m behind the wall)

The earth pressure cells were installed after the sheet pile wall and the excavation outside the pit. The effect from installing the wall is quite clear from the piezometer P0 group, as the pore water pressure increased for a short time between 3 and 15 m, with the smaller increase in the upper layer. The wall was installed down to a level of -13.0 and for that reason the pore water pressure at level –15.0 remained unchanged.

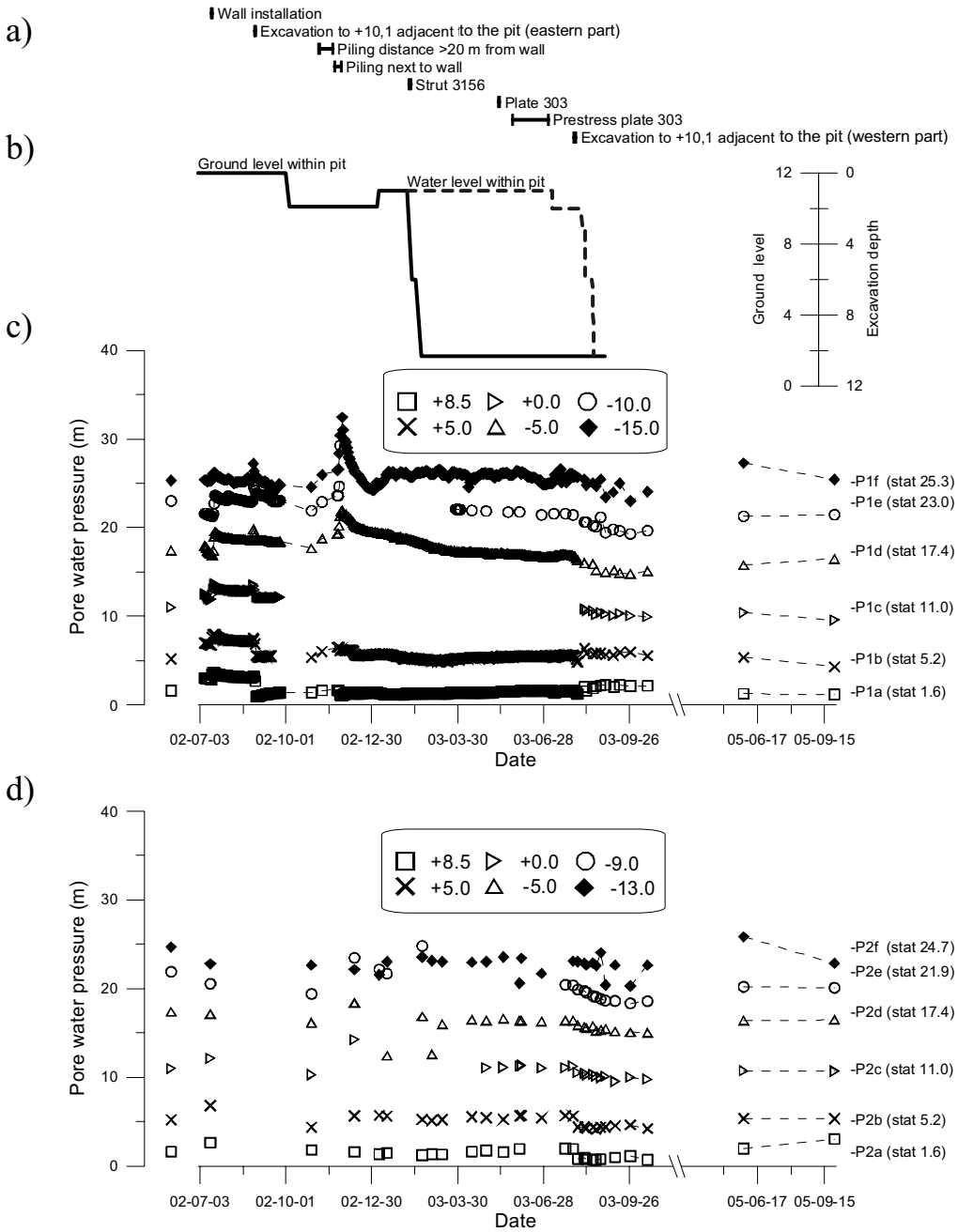

Figure 5.12: Pore water pressure over time
a) Working sequence
b) Excavation and water level within the pit
c) Piezometer P1 group (5.5 m behind the wall)
d) Piezometer P2 group (12.0 m behind the wall)

During the excavation outside the pit, the pore water pressure decreased in the upper layers by approximately 20 *kPa*. The vertical unloading was 2 metres of fill (≈36 *kPa*). The drop in pore water pressure should be almost the same as the decrease in p', which yields a secant value of μ' of 0.25. At the +8.5 level the *OCR* value increases to approx 5. Based on Figure 8.20, this unloading behaviour will be fitted to the formulation with the power m=0.6 proposed by Schmidt (1966). This value is identical to that in laboratory tests.

During piling next to the wall, the lower part of the wall was pressed outwards while the upper part rotated inwards, see Figure 5.5 and Figure 5.10. At the same time the pore water pressure increased for a short period by 30-40 *kPa* between level –5 and –15. In the upper part the pore water pressure decreased by up to 25 *kPa*. The rotation point seems to be at level +3.0, which corresponds to the monitored decrease and increase in the pore water pressure at a distance of 2 metres from the wall.

The excess pore water pressure that developed during the piling was not completely eliminated before the start of the underwater excavation, although by that stage the decrease in pressure over time had accelerated, generating negative excess pore water pressures. This was a consequence of unloading the clay horizontally.

The next dramatic change in pore water pressure occurred when the pit was dewatered, which led to an increase in negative excess pore water pressure. The monitoring was continued for a long time after the excavation ended and revealed that due to time and the load generated within the pit, the pore water pressure returned to that corresponding to stationary pressure.

5.3.8 Earth pressure over time

The monitored earth pressures are presented in Figure 5.14 and Figure 5.15, where the latter contains data adjusted for reasonable stress changes and the fact that in some cases, the gauges yield values that are too low for total horizontal stress, σ_h.

The measured earth pressure follows the same pattern, over time, as the pore water pressure, e.g. an increase in σ'_h for the lower gauges and a decrease in σ'_h for the upper gauges when the piles in row E were installed (Figure 5.5). During the pre-stressing of the anchors that hold the slab, an increase in the horizontal stress in the surrounding area was observed. This was also expected, in spite of the fact that no outward movements were registered by the inclinometer.

During dewatering a decrease in σ_h was obvious at all levels except level +2.0. This was also expected due to the monitored movements of the wall at this phase

of the work. Unfortunately, the two deepest cells did not produce reliable results after a while, probably due to fatigue caused by the high pressure during monitoring.

Under undrained conditions, the total stress change generates alterations in pore water pressure, Δu. Irrespective of the influence of preconsolidation pressure, this change equals that in the total mean stress. For example, during the excavation outside the pit a decrease in σ_{vert} with $\Delta\sigma_{vert}$ yielded $\Delta u = \Delta\sigma_{vert}/3$, $\Delta\sigma'_{vert} = \Delta\sigma_{vert}\cdot 2/3$ and $\Delta\sigma'_{hor} = -\Delta\sigma_{vert}\cdot 1/3$ under elastic conditions.

Stress changes $\Delta\sigma_{hor}$ $(=\Delta\sigma_x)$ were generated during the piling and excavation. During these stages, the behaviour of the wall corresponded to plane strain, *PS*, and Δu became 1/2 of $\Delta\sigma_x$. It follows from this that $\Delta\sigma'_{vert} = -\Delta\sigma_{hor}\cdot 1/2$ and $\Delta\sigma'_x = \Delta\sigma_{hor}\cdot 1/2$ under elastic conditions. If the ratio between $\Delta\sigma_{hor}$ and Δu becomes greater than 0.5, the stress path (s'-t space) bends to the left if $\Delta\sigma_{hor}>0$ and to the right where $\Delta\sigma_{hor}<0$. For ratios of less than 0.5 the stress path will bend in the opposite direction.

Studies of the behaviour during piling next to the wall clearly revealed that, for the lower part of the wall, $\Delta\sigma_{hor} \geq \Delta u\cdot 2$. This indicates that plastic deformations occurred within the soil. The part of the inward wall rotation showed $\Delta\sigma_{hor} \leq \Delta u\cdot 2$ which also indicated plastic strains. This can be seen in Figure 5.13, where the effective stress path, *ESP*, downwards represents the behaviour of the lower part of the wall and the *ESP* upward reveals the behaviour of the upper part.

A study of level +6.0 during dewatering revealed that the monitored stress changes yielded $\Delta\sigma_{hor} \leq \Delta u\cdot 2$ and in the later stages $\Delta u \approx 0$. This indicates that the stress path seems to follow a yield surface to the left of the s'-t space.

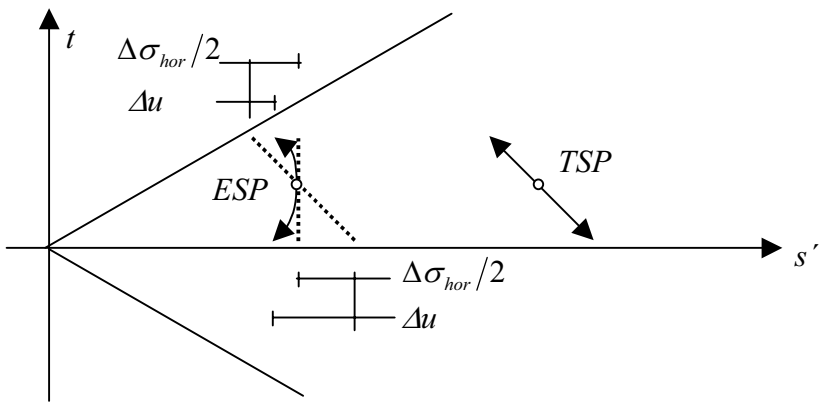

Figure 5.13: Sketch of stress paths based on the monitored earth pressures

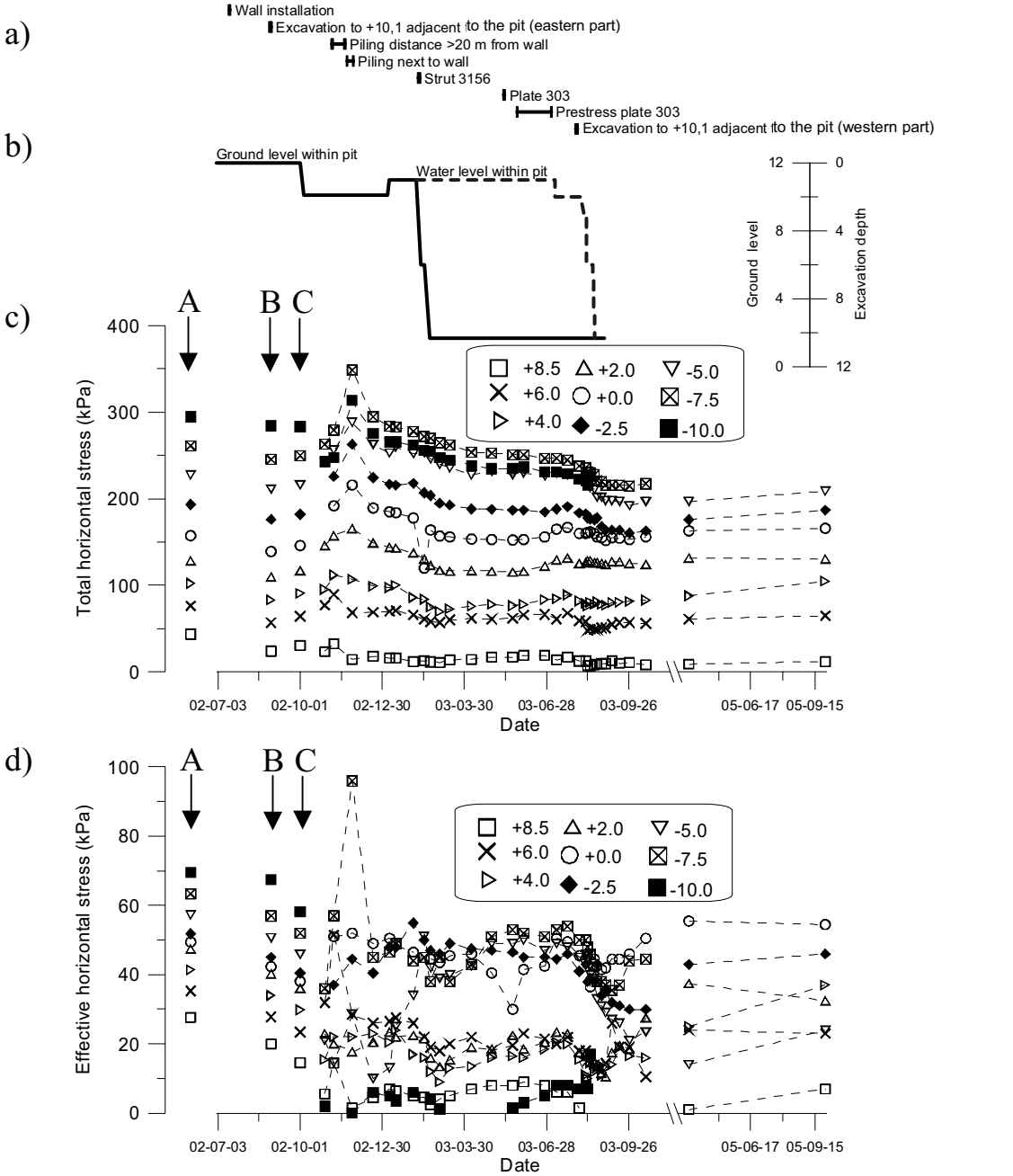

A: Assumed initial stress (K_0=0.6)
B: Assumed stress situation after excavation outside the pit (undrained)
C: Assumed stress situation after excavation outside the pit (drained)

Figure 5.14: Earth pressure over time
a) Working sequence
b) Excavation and water level within the pit
c) Earth pressure cells (0.5 m behind the wall)
d) Effective earth pressure cells (0.5 m behind the wall)

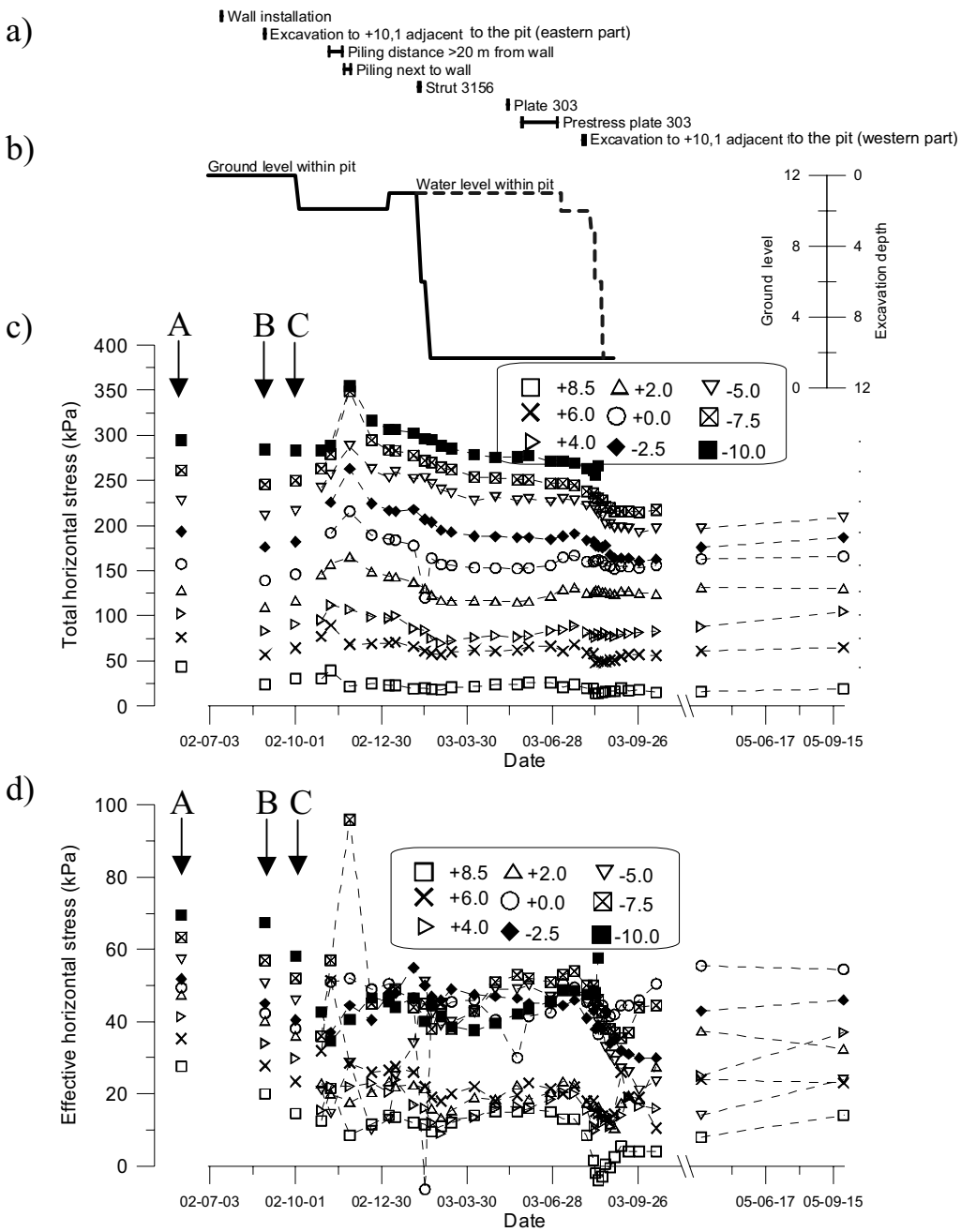

A: Assumed initial stress (K_0=0.6)
B: Assumed stress situation after excavation outside the pit (undrained)
C: Assumed stress situation after excavation outside the pit (drained)

The first monitored data have been adjusted in a way that yields reliable results. The same adjustment for a specific cell has been used in all pressure readings.

Figure 5.15: Earth pressure over time, adjusted data.
a) Working sequence
b) Excavation and water level within the pit
c) Earth pressure cells (0.5 m behind the wall)
d) Effective earth pressure cells (0.5 m behind the wall)

After completion of the excavation work the earth pressures appeared to increase slightly, which could be an effect of the fact that the sheet pile wall prevented the horizontal movements measured in inclinometer I2 and I3.

5.3.9 Strut forces over time

The monitored strut forces is presented in Figure 5.16, the force was automatically registered four times per day. Studying the different monitoring times, it is obvious that the temperature had a crucial effect on the strut force. The results presented in Figure 5.16 are for 6 am. However, the strut foces monitored at noon or 6 pm was 50 to 100 kN higher than the ones presented here.

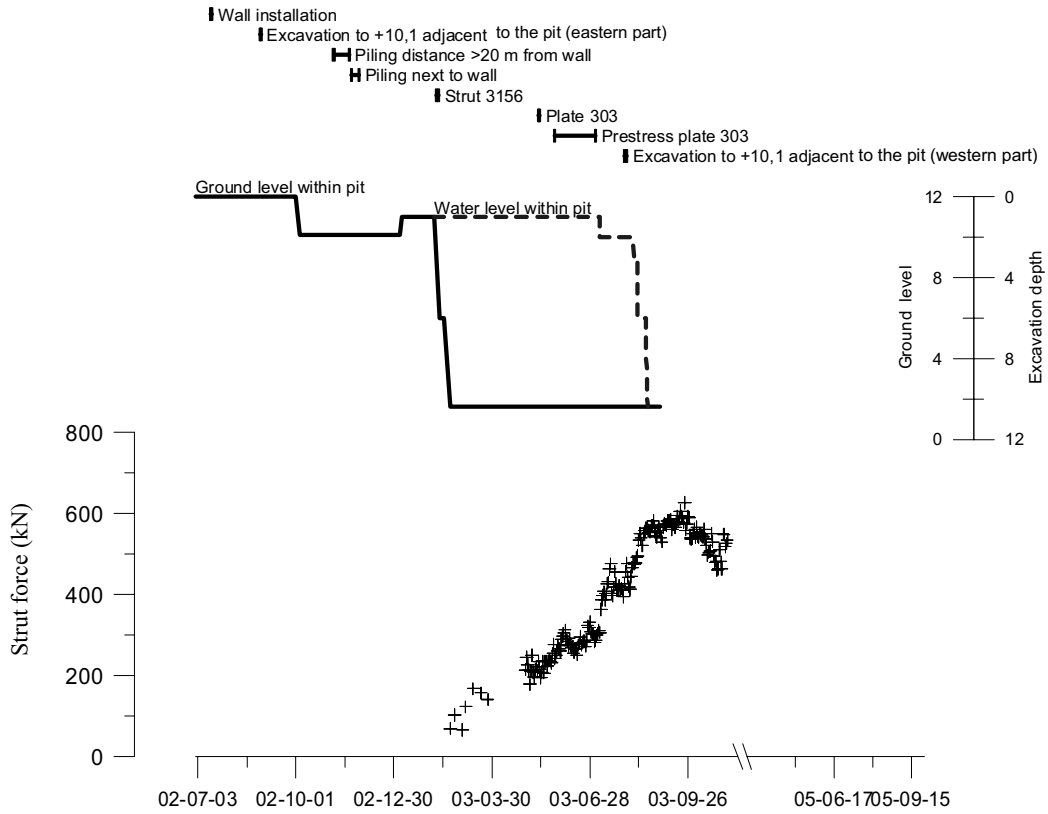

Figure 5.16: Monitored strut force in section 1/430 north.

5.4 Section 1/470 south

The sheet pile wall was installed down to the bedrock. In order to prevent hydraulic uplift, the base of the sheet pile wall was sealed against groundwater flow. The ground water pressure in the pit was decreased continuously when the clay was excavated, and the sheet pile wall was anchored backwards in the bedrock at three levels.

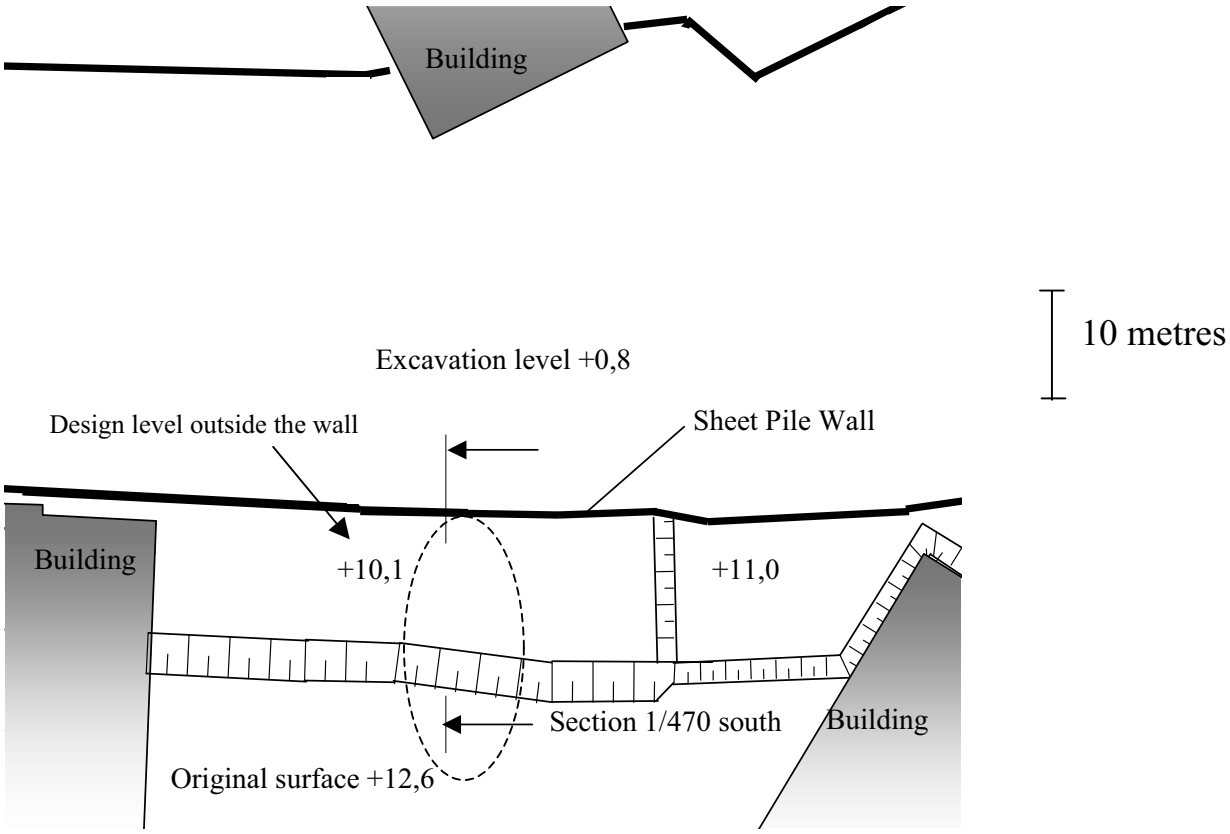

Figure 5.17: Plane: part of the J2 contract in the Göta tunnel project.

The horizontal deformations in the section were measured with inclinometers at different distances behind the sheet pile wall while vertical deformations were measured by means of bellow hoses at two different distances from the wall.

Inclinometer 1 (*I1*) was installed next to the sheet pile wall and inclinometers 2 and 3 (*I2* and *I3*) were located 9 and 19 metres behind the wall respectively. Bellow hose 1 and 2 (*B1* and *B2*) were located 5.5 and 12 metres behind the wall.

The inclinometers were installed to the level of the cohesionless material overlaying the bedrock and the thickness of cohesionless material varied between 0 and 2 metres. The inclinometers measured at every metre of depth. The bellow hoses were installed to the same depth and measured the vertical movement at every metre.

The pore pressure distribution was determined at various distances from the wall at five levels. The earth pressure was measured at eight different levels on the retained side of the sheet pile wall and at three on the excavated side. The earth pressure cells measured both total horizontal stress and pore pressure.

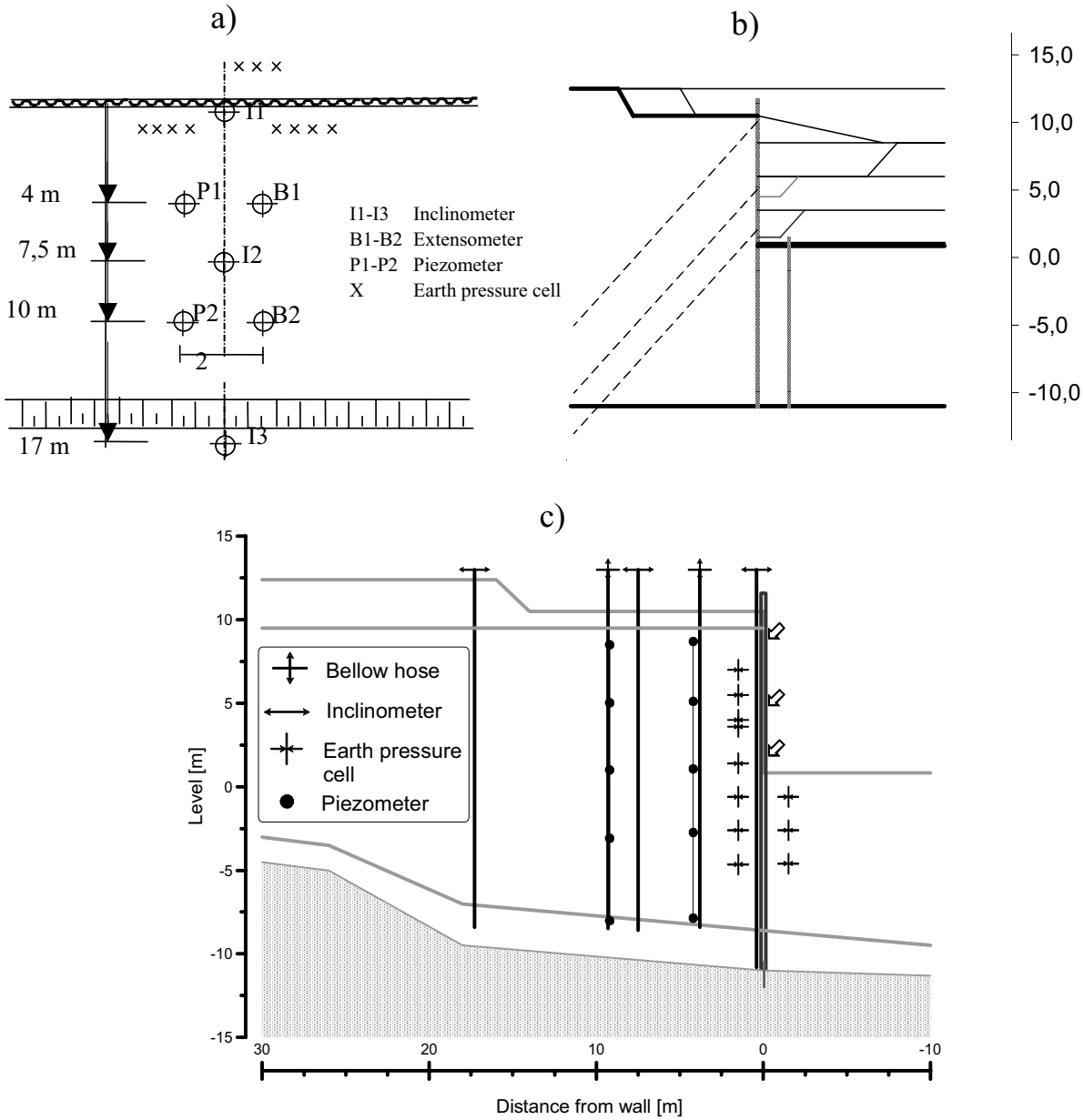

Figure 5.18: Instrumentation of section 1/470 south
a) Overview of the monitoring
b) Section 1/470 south with different excavation steps
c) Section showing the various gauges

The measurements described above were carried out by Chalmers University of Technology. In addition, the contractor had an extensive program for monitoring the effects on the surroundings due to the excavation.

5.4.1 Working sequence

The construction of the retaing system (sheet pile wall, waling and anchors) took place in a stepwise manner. During excavation, the support for the wall had to be installed before the deformation became too large. The working sequence for this phase is described below.

Table 5.3: Working sequence in section 1/470 south.

1. Installation of Sheet Pile Wall.
2. Excavation to a level of +10.5 inside and behind the wall.
3. Excavation to a level of +8.5 inside the wall.
4. Installation of wales and anchors at level +9,0.
5. Excavation to a level of +6.0 inside the wall and to a level of +4.0 locally beside the wall.
6. Installation of wales and anchors at level +5.0.
7. Fill of temporary road in and up from the shaft.
8. Excavation to a level of +3.5 inside the wall and to a level of +1.0 locally beside the wall.
9. Installation of wales and anchors at level +2.0.
10. Excavation to a level of +0.8 inside the wall.
11. Piling
12. Concrete casting.

The working sequence is illustrated in Figure 5.19.

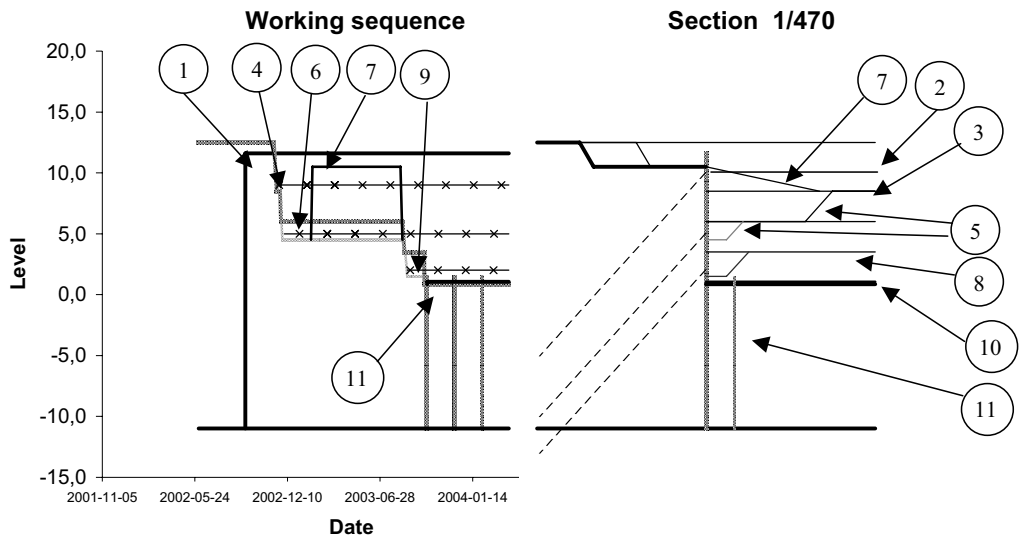

(a) (b)

Figure 5.19: Working sequence in section 1/470 south.
a) Excavation and anchoring versus time. b) Section 1/470 south
The numbers indicate the working stages listed in Table 5.3.

5.4.2 Deformations and stress changes during the different phases of the work

The deformations were monitored manually in connection with every phase of the work, in order to capture the undrained response. The time effects were also measured at different points in time after completion of each phase of the work.

The deformations measured during the different phases of the work are presented in Figure 5.20 to Figure 5.23. The ground surface deformations are fitted to all data obtained within a distance of 10 metres from section 1/470 south. The deformation in the 2 metre area closest to the wall is only an interpolation, since the nearest gauge was installed at a distance of 2 metres from the wall. The monitored deformation in inclinometer I3 is shown as relative deformations from level -5.4. The reason for not presenting the data below this level is that the inclinometer in question was affected by the installation of anchor row 1.

Figure 5.20 shows the monitored deformations in the section during the early phases of the excavation. The vertical deformation during these phases was small, as the heave caused by the unloading outside the wall was almost negligible due to limited extension. The top of the wall moved inwards by one centimetre before the installation of the first row of anchors. The installation of the anchors at level +9.0 forced the inclinometer outwards. During the excavation for anchor row two, the wall moved inwards with the maximum deformations occurring at level +5.0, and the earth pressure in the pit decreased. A decrease was also observed outside the wall at level +3.7.

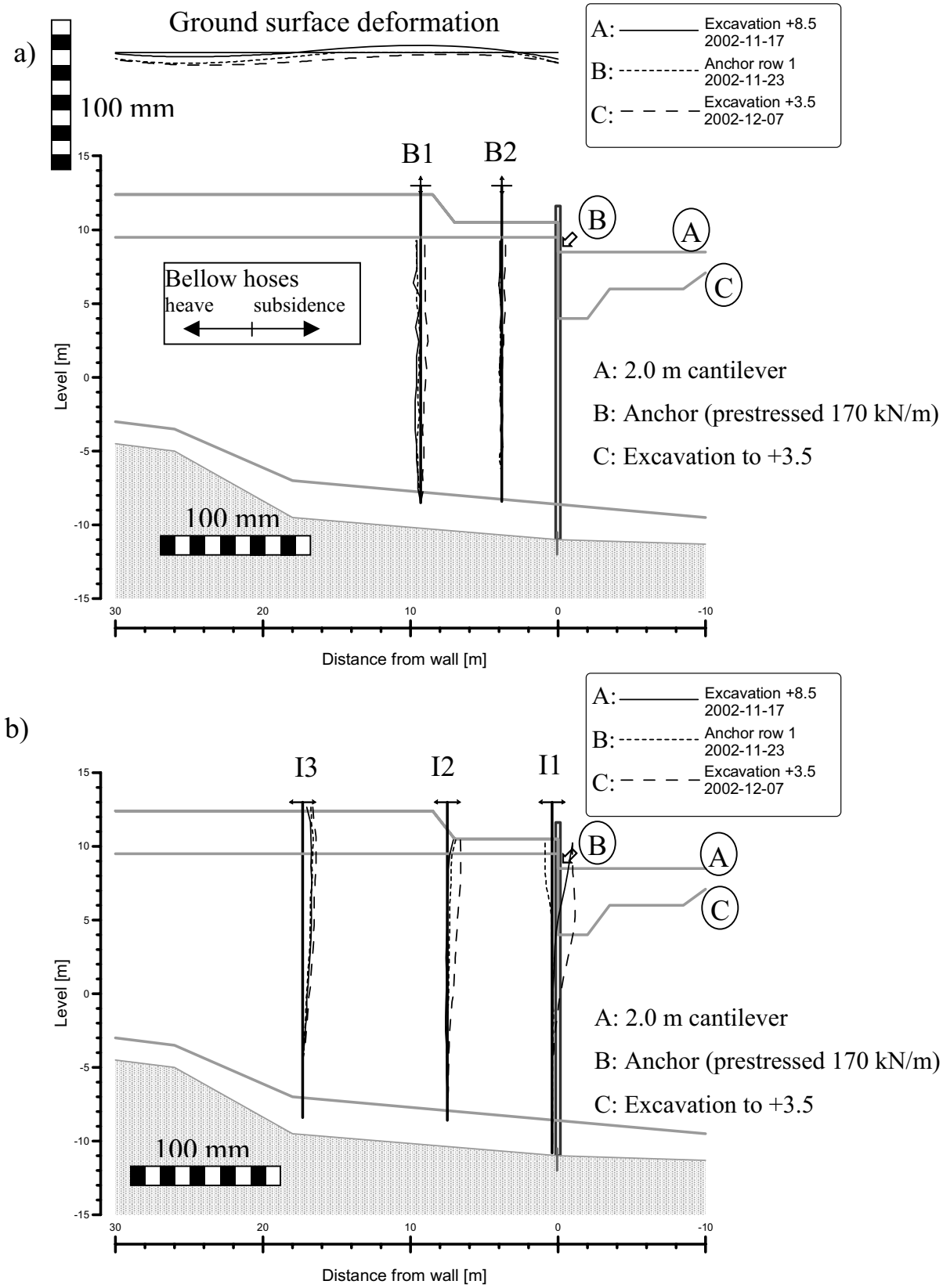

Figure 5.20: Deformations in section 1/470 south, during the first three excavation stages a) Vertical displacement b) Horizontal displacement

The anchors at level +5.0 were installed at two different periods. In section 1/470 and west of section 1/470 they were installed and prestressed on 2003-01-09, while those east of section 1/470 were installed on 2003-02-25. The reason for this was that the area west of section 1/470 was used as a road for transport to and from the pit and therefore the installation of the anchors at this location took place at an early stage. The road was built at the beginning of February 2003. The applied force decreased from 523 kN/m to 415 kN/m before the automatic monitoring system came into use.

For some reason the top of the wall developed a deformation of 2 cm inwards between 2003-01-02 and 2003-01-03 but this gradually reverted/declined between 2003-01-15 and 2003-01-20. This deformation was reflected in the rapid increase in anchor force between 2003-01-02 and 2003-01-03, when the force increased from 1125 kN (190 kN/m) up to 1325 kN for a short period, see Figure 5.30. This high anchor force was monitored approximately constant during one week, after which the anchors at level +5.0 were installed and the force at level +9.0 gradually decreased to 1150 kN in the course of the following week. At the same time the high anchor force led to the increase in total and effective stress monitored at level +7.0, see Figure 5.28. This sudden increase in pressure with an accompanying inward movement was probably caused by excavators and temporary fill placed next to the wall before the clay was removed from the site. During installation of anchor row two, the bellow hose, located in the area where the anchors were installed in the bedrock, showed a settlement in the lower part of the layer. During this period, the groundwater pressure, as well as the pore water pressure in the lower part of the clay, decreased by 2 m on average during a month. However, most of the subsidence was probably caused by volume loss during the installation of anchor row 2. The lowering of the groundwater should have affected both B1and B2 but no settlements were measured in the lower part of B1, see Figure 5.21, during this short period.

The construction of the road decreased the anchor reaction by a magnitude of 10 kN/m in both rows 1 and 2, although over time the anchor reaction increased beyond the value that pertained before the road was built. The construction of the road also increased the earth pressure behind the wall at level +3.6 although the earth pressure cell in the pit remained remarkably unchanged. During the lifetime of the road deformations developed inwards the pit and downwards.

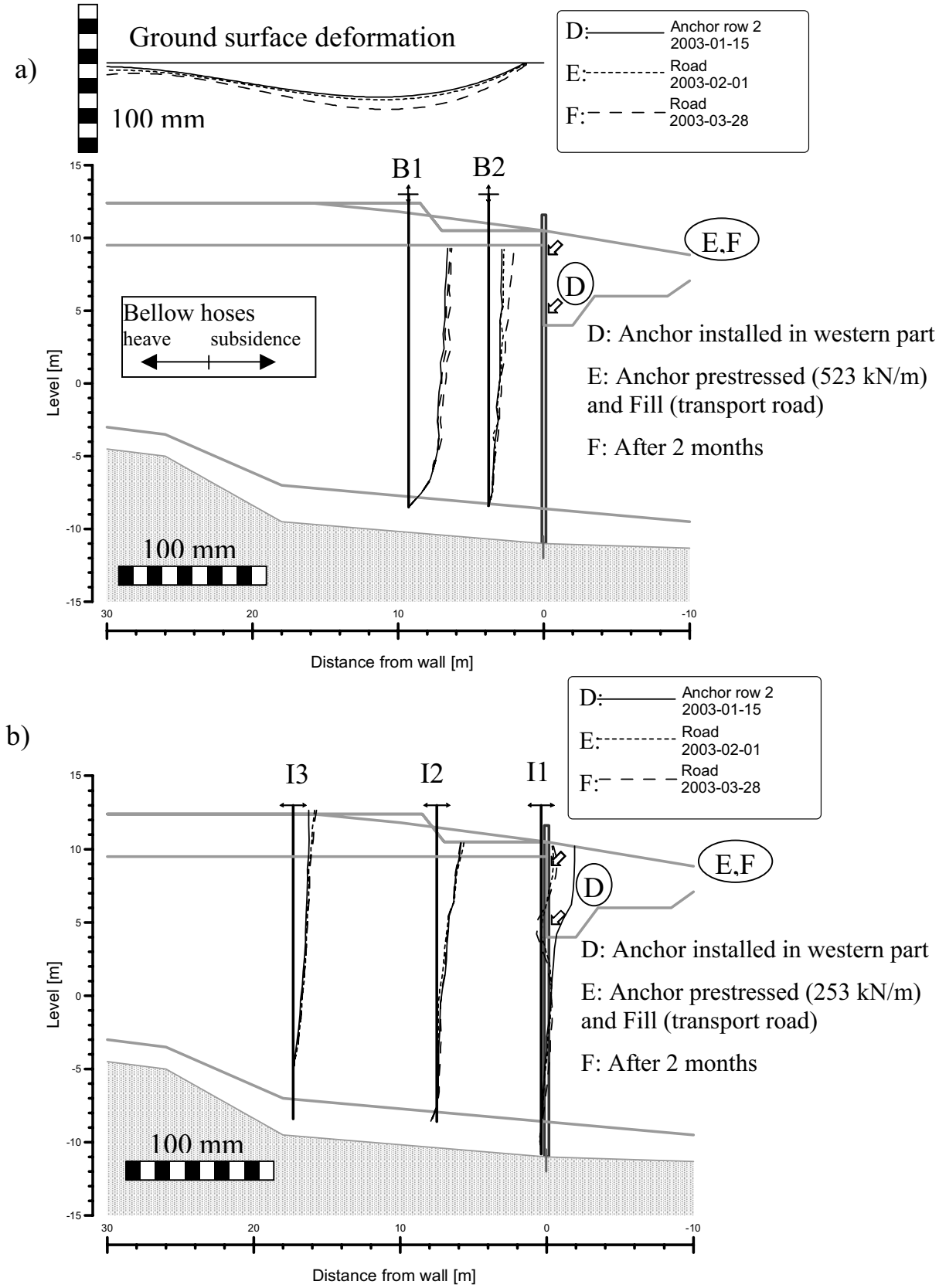

Figure 5.21: Deformations in section 1/470 south, during the installation of anchor row 2 and due to the temporary transport road
a) Vertical displacement
b) Horizontal displacement

The road was removed in August 2003 and excavation of the clay continued. Figure 5.22 shows how the deformation developed during excavation for anchor row 3 and how the anchor installation affected the deformation pattern behind the wall. Before the excavation in the pit, the excavation outside the wall was extended to cover a distance of 16 instead of only 8 metres, in order to decrease the load. The anchors were installed at the end of August and prestressed on 10th of September. As can be seen in Figure 5.22a, the vertical deformation within the lower soil layer increased due to the installation work. During this period the pore water pressures remained high, which confirms that the volume loss could be due to either compaction in the friction layer below the clay or to an effect of material loss caused by drilling. During excavation for anchor row 3, the wall moved inwards. This movement is clear from inclinometer I2. The increased excavation outside the wall caused an inward movement in inclinometer I3, although no heave was measured.

During the excavation work for anchor row 3 the monitored total earth pressure behind the wall at level +3.6 decreased by 35 kPa with a 20 kPa decrease in effective stress. During the same period, the forces in anchor row 2 increased by 32 kN/m. The force in row 1 increased in the early stages due to excavation related to the deconstruction of the road, but when the excavation started below anchor row 2 the reaction in row 1 decreased slightly, probably due to some rotation around anchor row 2. These stress changes are summarized in Table 5.4.

When the anchors at level +2.0 were prestressed, the forces in anchor row 1 and 2 decreased by 3 kN/m and 23 kN/m respectively. Please note that the applied force decreased from 547 to 415 kN/m before the automatic monitoring system came into use. The monitored increase in earth pressure at level +3.6 was 30 kPa in terms of total stress and 20 kPa in effective stress, see Table 5.4. The observed stress changes below the bottom of the excavation are presented in Table 5.5. It was observed that, during the removal of the road, the total stress in the pit decreased, followed by an increase in σ_h, when the local trench along the wall was excavated. This increase correlates well with the observed movements in I1, cf. Figure 5.26c.

Table 5.4 Changes in anchor reactions and earth pressure cells above the excavation level.

	Reaction changes in anchor row (kN/m)		Changes in monitored pressure (kPa)	
	1	2	$\Delta\sigma_h^{+3.6}$	$\Delta\sigma'^{+3.6}_h$
Excavation for anchor row 3	-	+32	-30	-20
Prestressing of anchor row 3	-3	-23	+30	+20

Table 5.5: Monitored stress changes in the earth presseur cells below the final excavation grade.

	Changes in monitored pressure behind the wall (kPa)					
	$\Delta\sigma_h^{-0.6}$	$\Delta\sigma'^{-0.6}_h$	$\Delta\sigma_h^{-2.6}$	$\Delta\sigma'^{-2.6}_h$	$\Delta\sigma_h^{-4.6}$	$\Delta\sigma'^{-4.6}_h$
Excavation for anchor row 3	-30	-5	-30	0	-10	-4
Prestressing of anchor row 3	+30	+5	+20	0	0	0
	Changes in monitored pressure in the pit (kPa)					
	$\Delta\sigma_h^{-0.6}$	$\Delta\sigma'^{-0.6}_h$	$\Delta\sigma_h^{-2.6}$	$\Delta\sigma'^{-2.6}_h$	$\Delta\sigma_h^{-4.6}$	$\Delta\sigma'^{-4.6}_h$
Removal of transport road	-40	0	-25	*	-30	*
Local trench along the wall	+10	0	+20	*	*	+5
Prestressing of anchor row 3	-20	+5	+15	0	+20	0

* relevant data are missing.

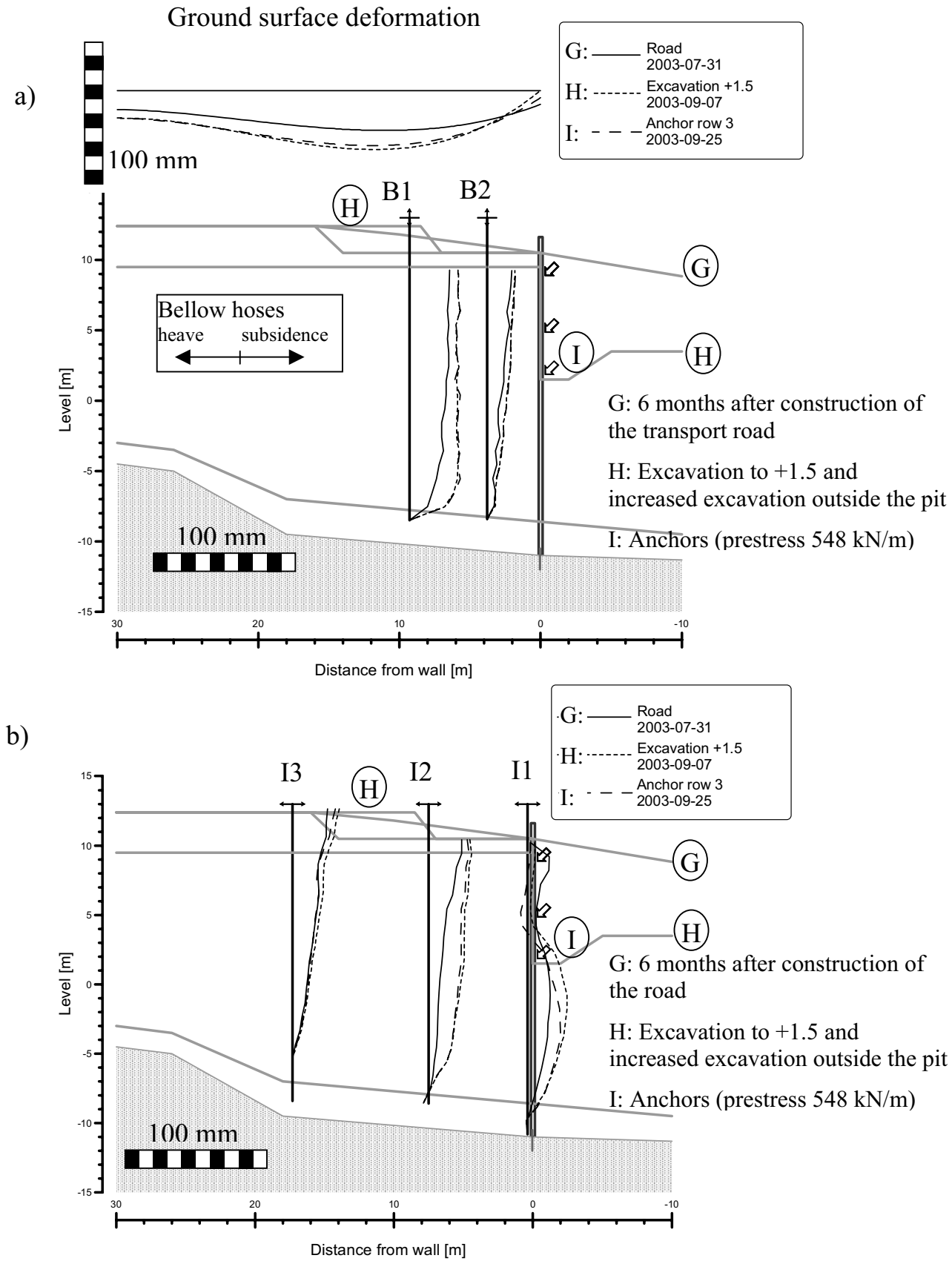

Figure 5.22: Deformations in section 1/470 south, deformations due to the transport road and the installation of anchor row 3.
a) Vertical displacement
b) Horizontal displacement

The final excavation to the +0.9 level increased the deformations even further. Several days after completion of the excavation, the measured maximum inward movement was approximately 4 cm in the midspan between anchor row 3 and the dowel, see Figure 5.23. The anchor reaction increased by 19 kN/m in row 3 during the excavation. At the same period the reactions in row 1 decreased slightly while those in row 2 remained almost constant. The monitored lateral total stress changes in the pit, during the final excavation phase, were –25 kPa, -20 kPa and –20 kPa at levels –0.6, -2.6 and –4.65 respectively. The same stress changes were observed outside the pit, with a sudden drop in σ_h from 15 to 20 kPa immediately after the start of excavation, although the stresses recovered within 2 weeks. During this period horizontal effective stresses were almost constant.

After completion of the excavation work, piles were installed in the location of the planned tunnel walls. The piling seems to have had only a minor effect in this section, in contrast to the behaviour observed in section 1/430 north. In the pit, the observed total and effective horizontal stresses decreased after piling. The stress changes were in the order of 20 kPa for total stresses and between 10 and 40 kPa for the effective ones, where the higher value was obtained in the lower part of the clay. The anchor force in row 3 increased from 460 to 520 kN/m, at which point the concrete slab (20 cm) was cast on the ground.

The work on the tunnel continued and the space between the finished tunnel and the wall was refilled during the Spring of 2005. During this period, the deformations in the section increased, see Figure 5.23 and Figure 5.24, to a maximum wall deformation of 6 cm and a maximum subsidence of 7 cm. The monitored total horizontal stress was approximately constant, with the exception of level +3.6, which decreased by 20 kPa around the turn of the year 2003-2004. This decrease was correlated to the inward movements at this level during the same period.

The tunnel slab was cast in the Spring of 2004 and there was a clear response in the earth pressure measured 1.5 metres below the tunnel, which increased by 15 kPa.

The anchors at level +2.0 and +5.0 were cut on 9th February and 29th April respectively. When anchor row 3 was cut, an increase of 20 kN/m in the anchor reaction at level +2.0 was observed and when row 2 was cut, the reaction at level +9.0 increased by 10 kN/m. During the Spring 2005 the total earth pressure increased below the tunnel by 40 kPa, 20 kPa and 10 kPa at levels -0.6, -2.6 and -4.6 respectively.

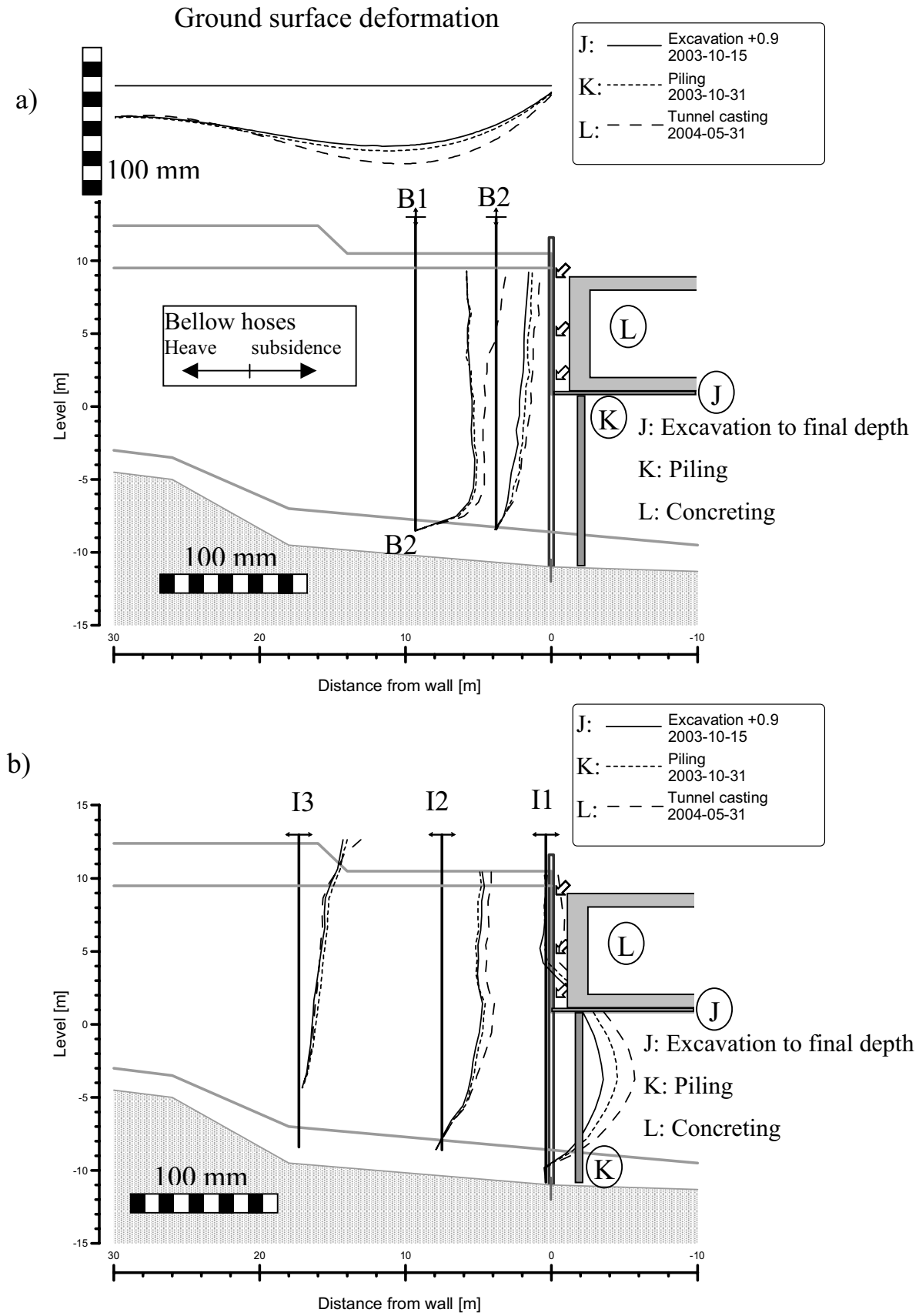

Figure 5.23: Deformations in section 1/470 south, due to the final excavation and during the first construction phases.
a) Vertical displacement
b) Horizontal displacement

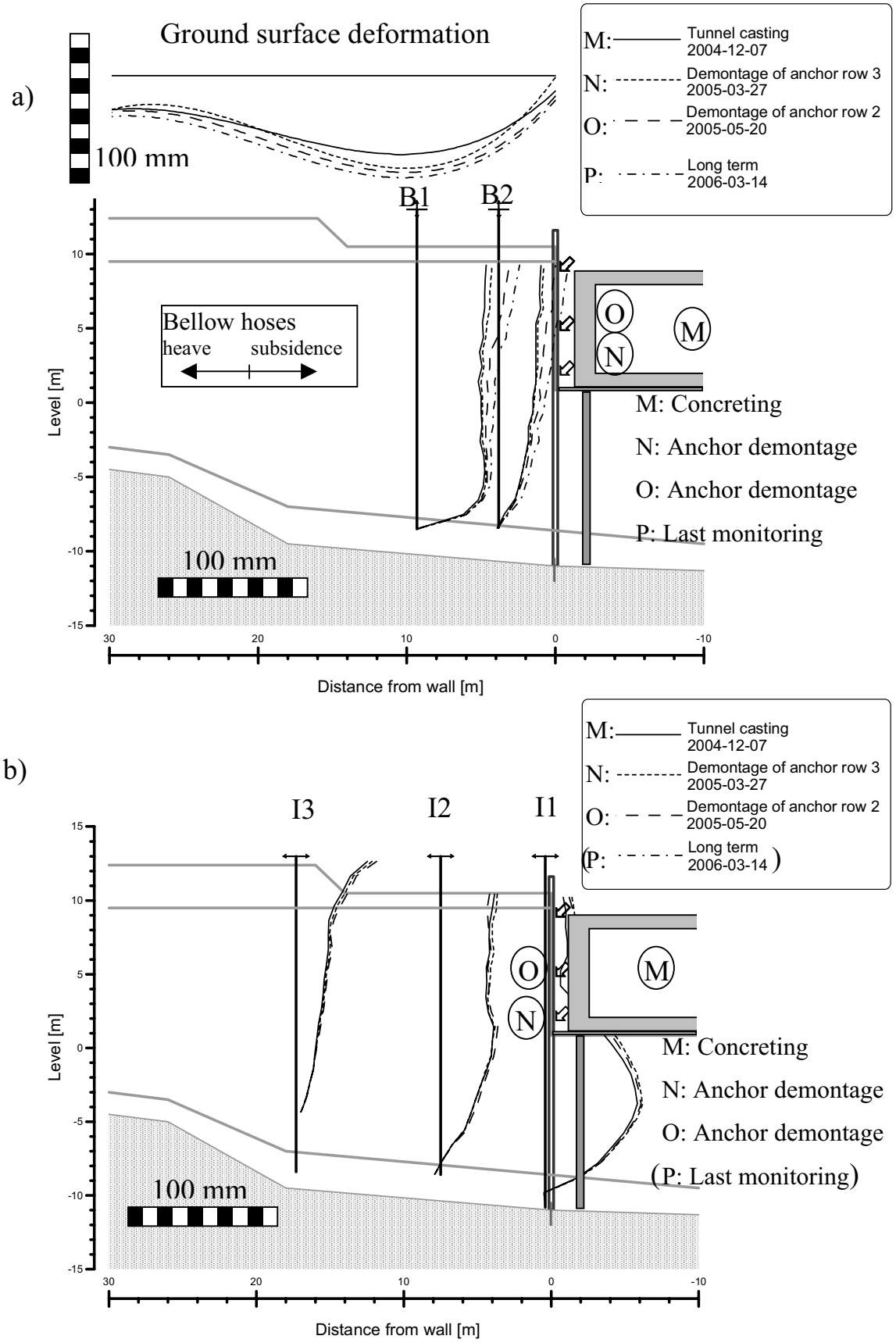

Figure 5.24: Deformations in section 1/470 south, due to completion of the tunnel section and cutting of anchor rows 3 and 2.
a) Vertical displacement b) Horizontal displacement

5.4.3 Time dependent deformation

In Figure 5.25, the observed vertical deformations within the soil profile are presented for some of the levels. The figure is complemented by information about the progress of work and the excavation level in the pit. The correlation between the subsidence monitored by bellow hose B2 and the anchor installation is obvious. The horizontal deformations are presented in Figure 5.26.

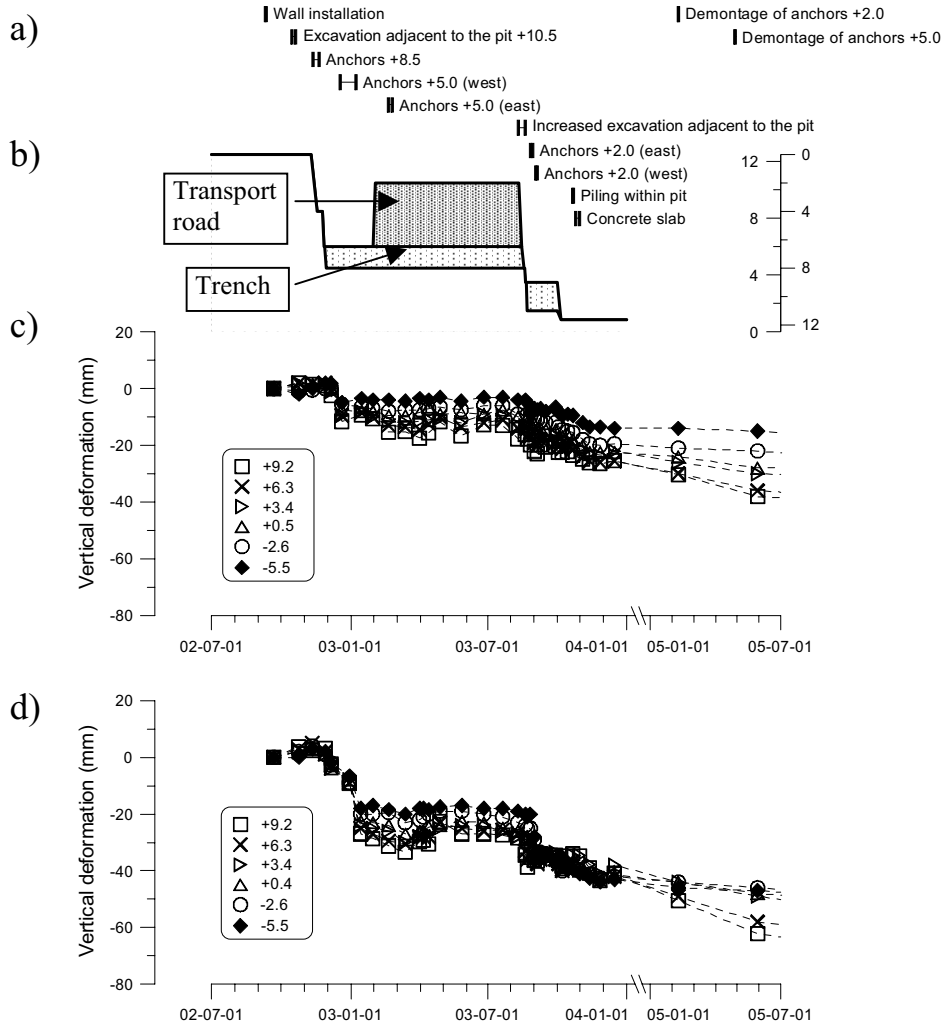

Figure 5.25: Vertical displacement over time
a) Working sequence
b) Excavation level in the pit
c) Bellow-hose B1 d) Bellow-hose B2

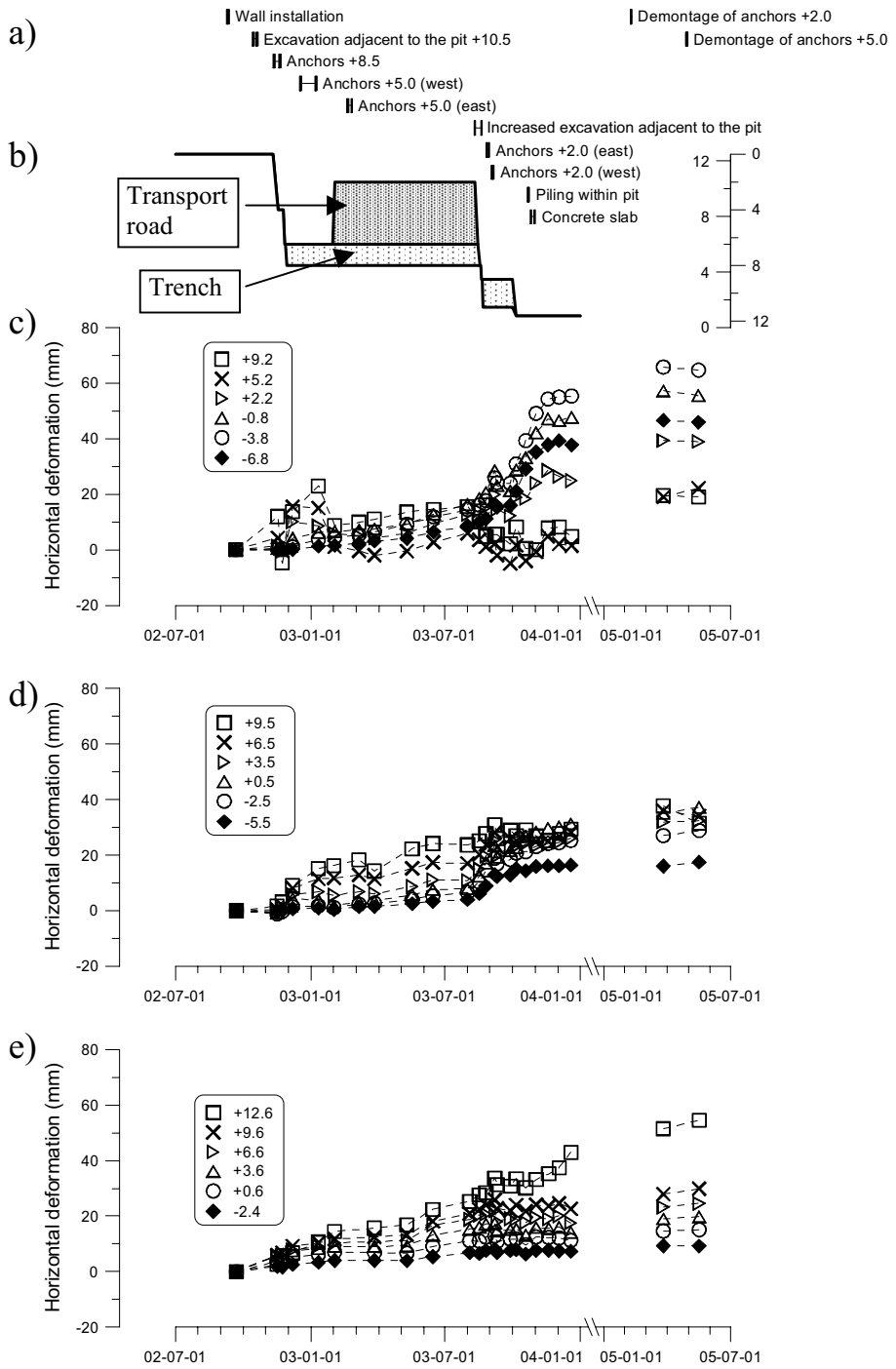

Figure 5.26: Horizontal displacement over time
a) Working sequence
b) Excavation level in the pit
c) Inclinometer I1 d) Inclinometer I2 e) Inclinometer I3

5.4.4 Pore water pressure and horizontal earth pressure over time

In Figure 5.27, the observed pore water pressure behind the wall is presented over time. The two piezometers at levels -7.9 and -8.0 clearly correlate with the observed ground water pressure in an adjacent piezometer within the sand layer. The latter piezometer was part of the contractor's monitoring program, which is

not included in this work. This correlation can also be partly observed in the P2 piezometer group at level -3.1.

The monitored lateral total and effective stress behind the sheet pile wall is presented in Figure 5.28. The results from the spade cells in the pit are presented in Figure 5.29. Unfortunately, the connection to the piezometer incorporated into two of the cells was temporarily lost during some of the excavation work and after commencing the fill between the tunnel and the wall.

In order to allow comparison of the monitored pressures, Figure 5.27 to Figure 5.29 are complemented by details of the stationary pressure (A). The spade cell results are also complemented by the theoretical pressures due to the excavation level +10.5, B for an assumed undrained response and C for a drained response.

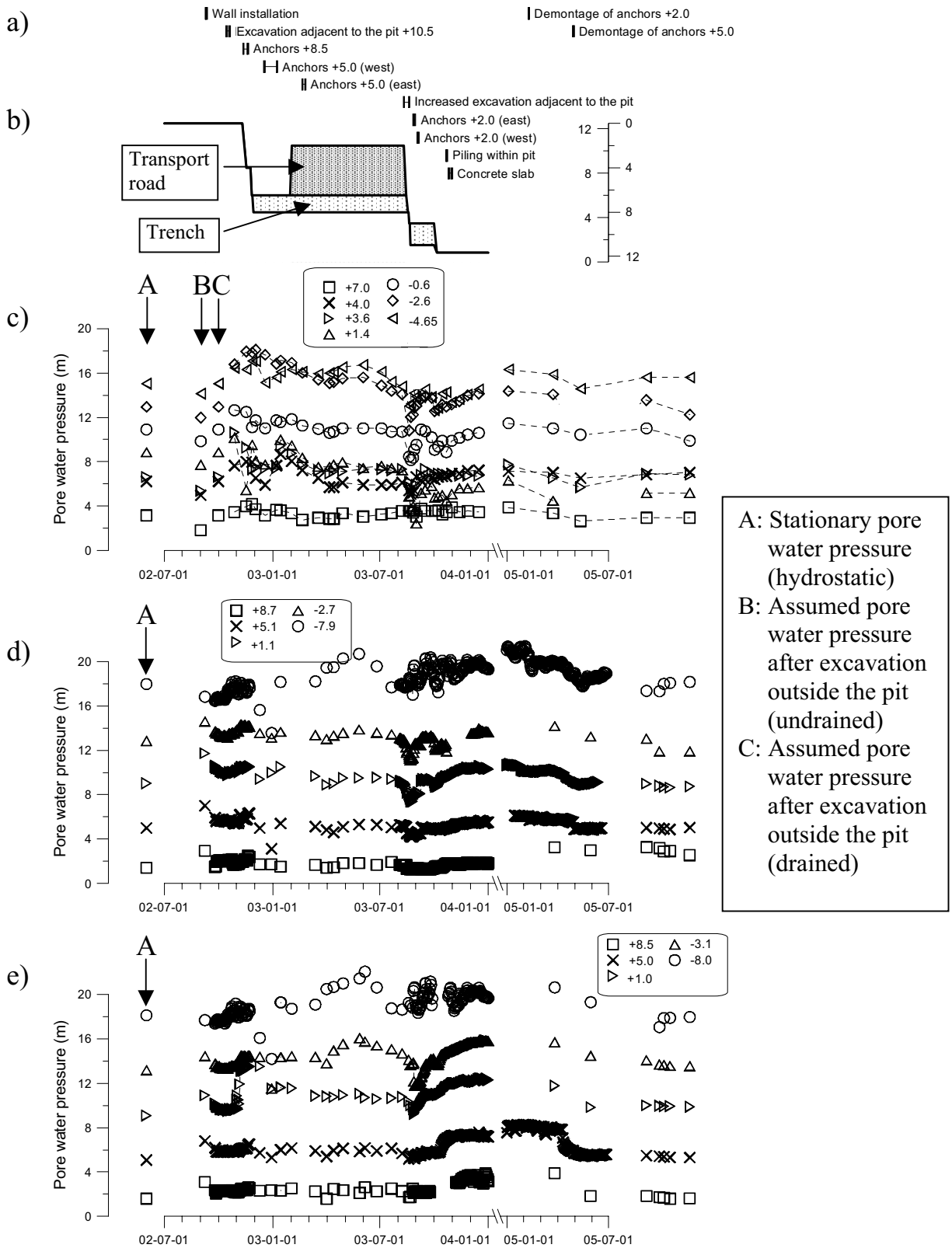

Figure 5.27: Pore water pressure over time
a) Working sequence
b) Excavation level in the pit
c) Earth pressure cells (0.5 m behind the wall)
d) P1 Piezometer group (2.0 m behind the wall)
e) P2 Piezometer group (2.0 m behind the wall)

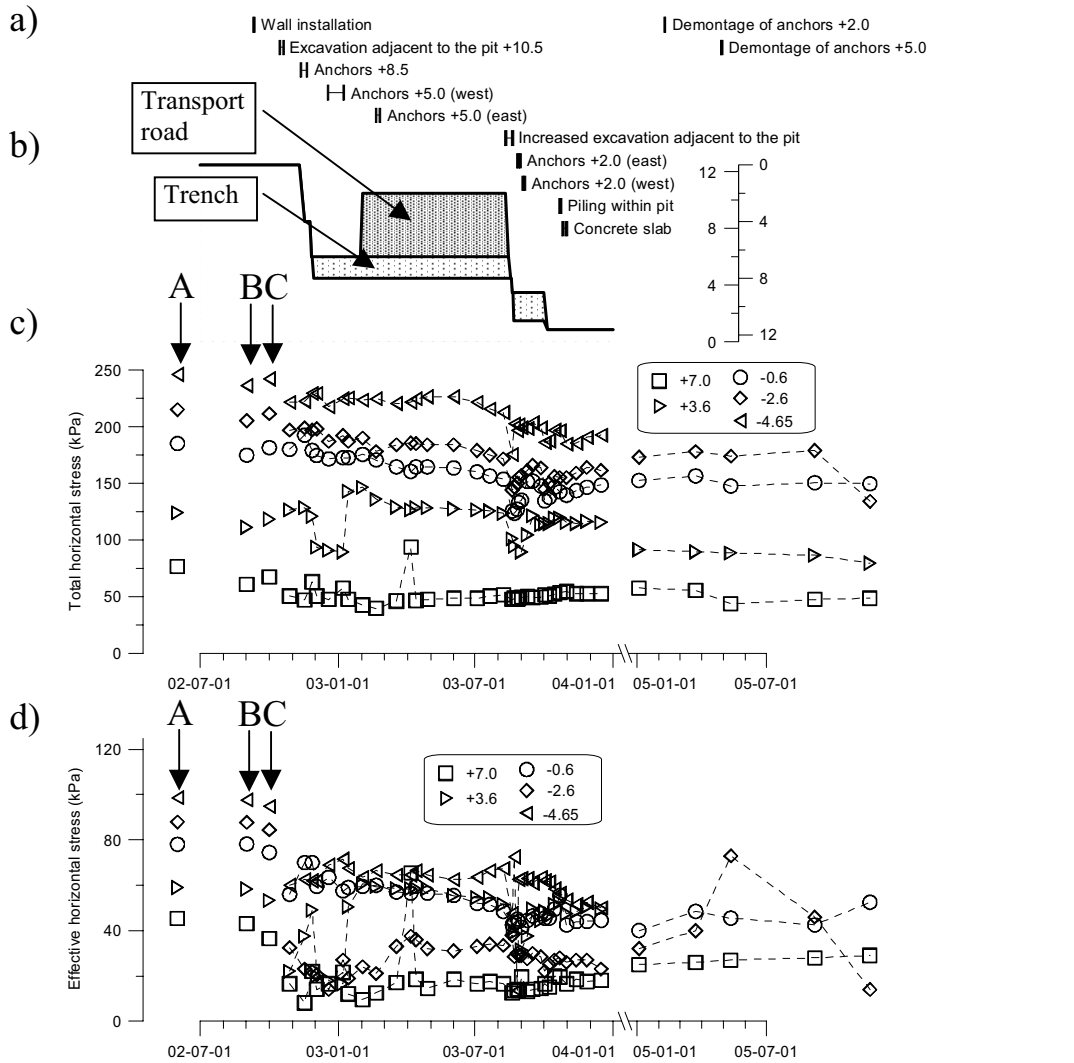

A: Assumed initial stress (K_0=0.7)
B: Assumed stress situation after excavation outside the pit (undrained)
C: Assumed stress situation after excavation outside the pit (drained)

Figure 5.28: Earth pressure over time, earth pressure cells outside the pit
a) Working sequence
b) Excavation level in the pit
c) Total earth pressure 0.5 m behind the wall
d) Effective earth pressure 0.5 m behind the wall

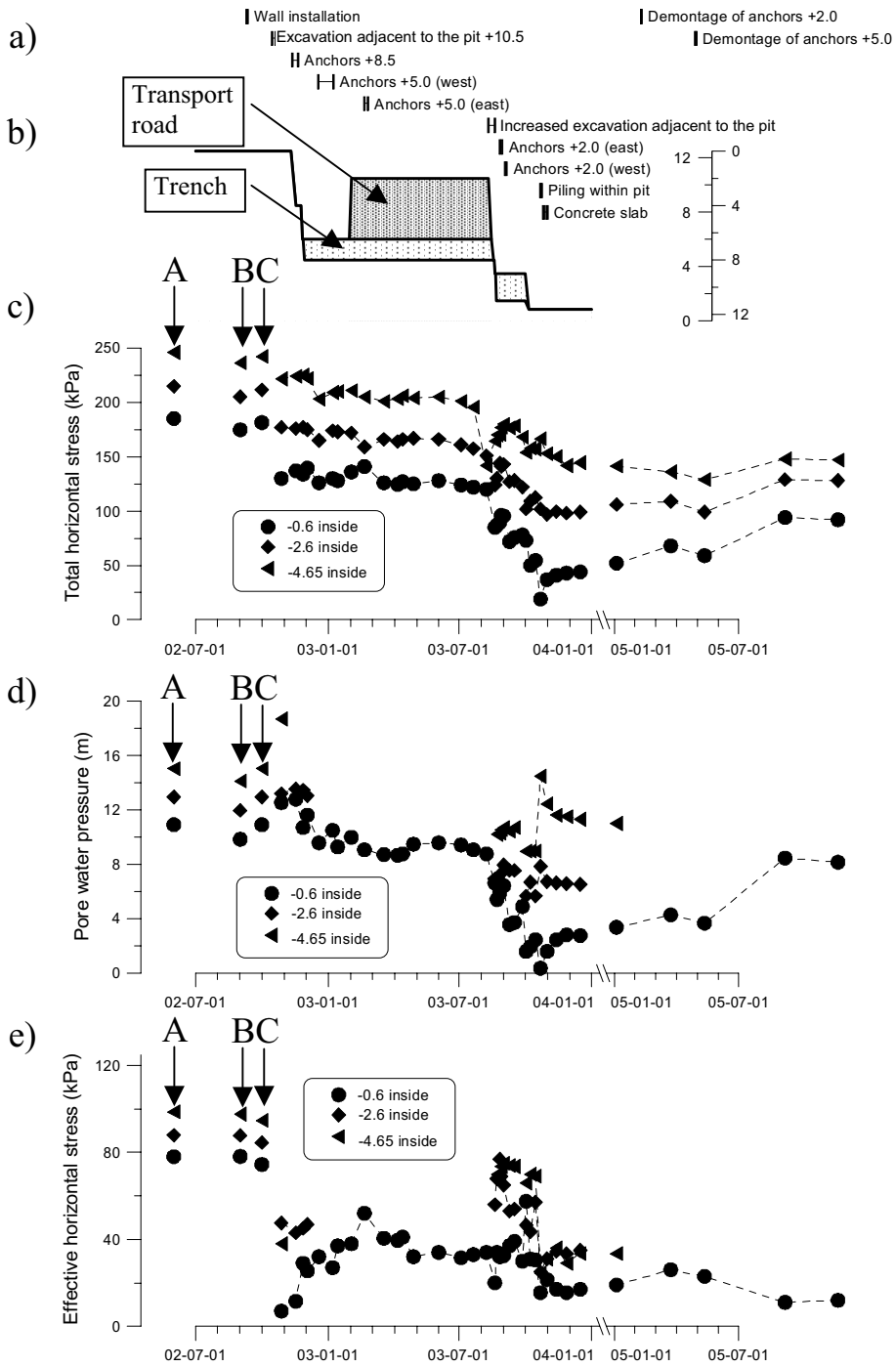

A: Assumed initial stress (K_0=0.7)
B: Assumed stress situation after excavation outside the pit (undrained)
C: Assumed stress situation after excavation outside the pit (drained)

Figure 5.29: Earth pressure over time, earth pressure cells in the pit
a) Working sequence
b) Excavation level in the pit
c) Total earth pressure 0.5 m in front of the wall
d) Pore water pressure cells 0.5 m in front of the wall
e) Effective earth pressure cells 0.5 m in front of the wall

5.4.5 Monitored anchor forces over time

The contractor's monitoring program for the behaviour of the sheet pile wall measured the anchor force by one gauge per row. The result is presented over time in Figure 5.30. The automatic logging of the anchor forces started a couple of weeks after the prestressing of the anchors. During this period the actual forces are unknown, but the force in the gauge at level 1 increased at this time, probably due to the inward movement and the difference between working phases B and C in Figure 5.20. After anchor rows 2 and 3 had been prestressed, the forces decreased. This could be an effect of relaxation in the anchors and/or time effects in the clay.

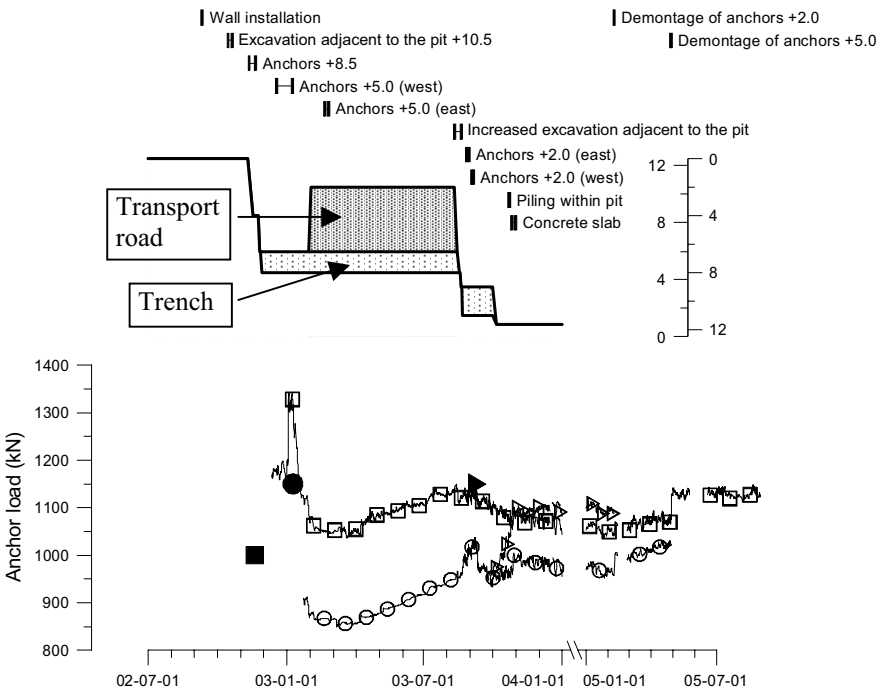

Figure 5.30: Monitored anchor force in section 1/470 south. (Solid symbols represent the initial force applied on the anchors)

When anchor rows 3 and 2 were cut, there was a clear increase in force in the anchor row above.

5.5 Complementary monitoring within the project

Within this research project, two further sections were monitored, 1/390 north and 1/550 south. Results from these two sections have partly been presented in two master theses supervised by the author (Lindström and Matsoukatidis, 2003; Oskarsson and Thorén, 2004).

Section 1/390 was studied by Oskarsson and Thorén (2004) with the aim of investigating the 3D-effects of stepwise excavation. The excavation was carried out in two main steps. Firstly, excavation of the main tunnel and secondly excavation of the ramps. The excavation was made between two rows of sheet

pile walls. The soil strata consisted of 30 metres of clay and the depth of the excavation was 10 m.

The thesis by Oskarsson and Thorén (2004) presents the monitoring of the excavation of the main tunnel, which comprised:

- Two groups of piezometers, one inside the excavation area and the other outside the inner sheet pile wall.
- Two Bellow hoses, down to and fixed into firm layer underlaying the clay, within the excavated area, one 6.5 m and the other 12.5 m from the wall.
- Four Bellow hoses installed down to the the final excavation level.

Apart from the monitoring presented by Oskarsson and Thorén (2004), the vertical deformations outside the outer sheet pile wall, pore water pressure and lateral stresses were monitored by the author during all phases of the work. The results from these measurements are, however, not included in this thesis.

The section studied by Lindström and Matsoukatidis (2003) was within the canal, which passes through the site. The retaining wall consisted of a sheet pile wall installed to the bedrock and anchored at four levels. The work by Lindström and Matsoukatidis presents a comparison between calculated wall movements and the measured ones at an excavated depth of 9 metres of the total 15.5 metres.

This section was monitored by one inclinometer next to the wall while the anchor force was monitored at three of the four levels. The monitoring continued after Lindström and Matsoukatidis (2003) presented their master thesis, but the results are not presented here.

6 CHARACTERIZATION OF SOIL PROPERTIES

6.1 Introduction

An extensive laboratory study was performed in order to establish the soil characteristics needed for the numerical analyses of the excavations. Classical tests as well as a number of special tests were carried out, the objective of which was to contribute to a deeper understanding and to explain the response to different kinds of loadings and the connection to stress history. The test results presented in this chapter are utilized in subsequent chapters to evaluate the input parameters for various calculations.

The clay in the Göteborg area is quite well documented, especially by the work performed at Chalmers over recent decades. The results from the laboratory tests in this study have been continuously compared with empirical experience and previous test results.

6.2 Field Tests

The clay was tested in situ by means of field vane and CPT tests. Undrained shear strength and preconsolidation pressure can be roughly estimated from the CPT (Cone Penetration Test), although the main purpose of such tests is to investigate whether any layer has higher hydraulic conductivity. Other penetration tests were performed to ascertain the depth to firm layers such as sand and bedrock.

6.3 Routine Laboratory Tests

Undisturbed samples from the analysed sections were investigated and the following parameters determined routine tests: density, ρ, natural water content, w_N, liquid limit, w_L, sensitivity, S_t and undrained shear strength, s_u.

The clay in Gothenburg is fully saturated and the specific gravity, G_s, was evaluated to 2.74 ton/m^3. A slight discrepancy was observed when comparing these values with back calculated values of G_s based on density and water content.

Water content, density, void ratio and porosity are different ways of expressing the degree of compaction of uniformly saturated clay. In the case of a uniform clay layer, compaction is dependent on both grain size distribution and stress history. Relations between the various expressions of compaction can be found in Jumikis (1962) or in many other textbooks.

There are a number of models available for describing the properties of a soil as a function of its density, mostly in terms of void ratio, e. According to these

relations, different sub layers within the clay can be identified by studying the water content or the densities in combination with the preconsolidation pressure, σ'^{precon}_{vert}.

In order to describe the soil strata, 1D compression tests were employed to back calculate the initial void ratio, as there is a direct link between densities, water content, grain size distrubution and the stress history of a clay layer.

6.4 Compression tests

Compression tests were performed in order to determine the response of the clay to loading. The most practical way to do this is to run oedometer tests.

During these tests the stress or strain is controlled in one direction while preventing deformation in other directions. If the direction of the controlled stress or strain is similar to the vertical direction in situ, these load case will correspond to the actual sedimentation behaviour of the clay. If the sample is loaded beyond the preconsolidation pressure, the response will provide an accurate description of the behaviour of the soil when loaded.

The preconsolidation pressure is often defined as the maximum load to which the soil has been exposed. This is a simplification due to the fact that estimations of preconsolidation pressure also contain aging and creep effects. A more accurate definition is the maximum load that the clay can carry without a decrease in the constrained modulus as a result of a constant increase in stress or strain. Due to creep effects and visco-elastic behaviour, a quick test will generate a higher preconsolidation pressure value than a slow one.

Compression tests can also be performed in a triaxial cell in different ways. The two most common methods comprise either loading the soil sample isotropically or increasing cell and vertical pressure in such a way that the radius remains constant, as in ordinary oedometer tests. The advantage of using triaxial cells is that both the horizontal and vertical stresses are known and that there is no ring friction present.

Several oedometer tests, with some complementary 1D compression tests in the triaxial cell, were performed in order to evaluate vertical preconsolidation pressure and investigate the response of the clay to compression.

The preconsolidation pressure was estimated according to Swedish practice (Sällfors, 1975; Larsson, 1981; Larsson, 1986). The tests were performed with a deformation rate of 0.0024 mm/min, although there are other methods of estimating preconsolidation pressure (Casagrande, 1936) (Becker *et al.*, 1987). If the methods referred to above by Casagrande and Becker are used on CRS

tests, the estimated preconsolidation pressure has a slightly higher value than that obtained by use of the Swedish method. This will however not be accurate for the Casagrande method since that was developed for 24 hours stepwise loading tests, and in that case the agreement between evaluated preconsolidation pressure from the Swedish method performed with a deformation rate of 0.0024 mm/min and the method by Casagrande is excellent. The method developed by Becker have not been used and verified for highly plastic clays found at the west coust of Sweden. This makes the method inappropriate to use.

The preconsolidation pressure was estimated according to Swedish practice (Sällfors, 1975; Larsson, 1981; Larsson, 1986). The tests were performed with a deformation rate of 0.0024 mm/min.

In this thesis the method proposed by Sällfors (1975) is used, since the influence of the strain rate on highly plastic clay is considerable, even in the case of very low strain rates. At a deformation rate of 0.0024 mm/min, the method shows good agreement with tests run at lower speeds in which the preconsolidation pressure is estimated as the effective stress at the highest curvature in the stress-strain curve. CRS-tests, on highly plastic clay, evaluated according to the Swedish method have been shown to have practically identical stress-strain curves to those from conventional 24-hour standard incremental tests (Larsson, 1985).

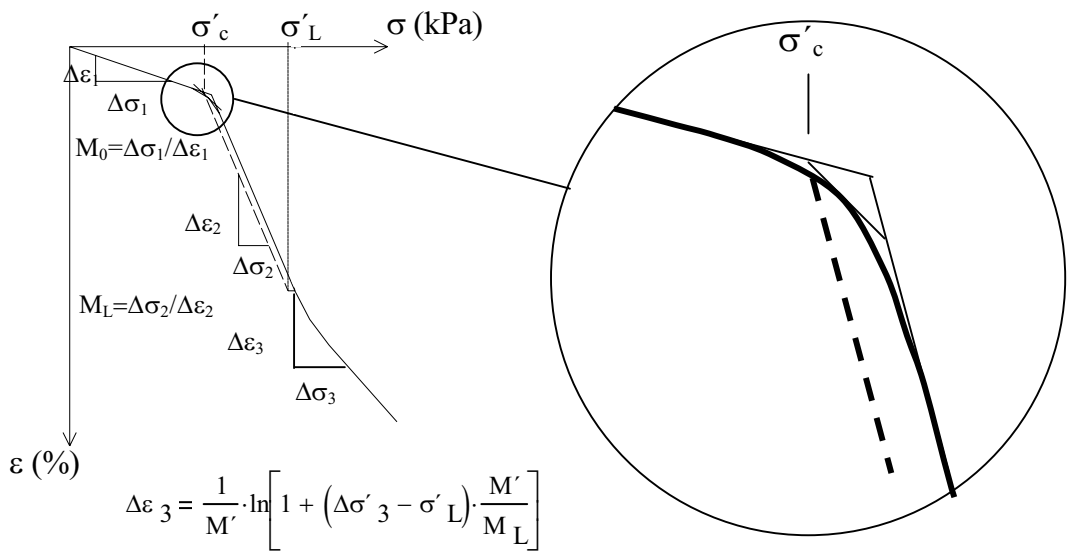

Figure 6.1: Estimation of preconsolidation pressure, σ'^{precon}_{vert} $(=\sigma'_c)$, and the constrained modulus, M_0 and M_L. The constrained modulus at stress levels higher than σ'_L is expressed as a function of the radius of the curvature (second order differential coefficient for $\sigma=f(\varepsilon)$, $M'=\frac{\partial^2\sigma'}{\partial\varepsilon^2}$).

It has been established that the modulus M_0 from a CRS test is less than the unloading reloading modulus, and therefore the CRS test was complemented by ordinary oedometer tests with stepwise loading and unloading as well as CRS tests in which the deformation direction was changed. Three different types of CRS unloading reloading tests were performed, details of which are presented below.

First. The unloading and reloading tests in the CRS equipment were modified in terms of the deformation rate in order to ensure that the loading rate would remain fairly constant ($M_{ur} \approx 4 * M_0 \rightarrow 0.0024/4 = 0.006$ mm/min).
Second. The unloading was controlled in terms of stress. The vertical stress was decreased linearly with time, which led to vertical compression for *OCR* less than 1.25 as a result of creep effects. When the *OCR* value exceeded 1.25, the sample started to swell, which was expected (Larsson, 1981).
Third. In order to prevent creep deformation during the initial unloading, the strain was kept constant over a three to five-hour period, which meant that the effective vertical stress decreased to a point where *OCR* equalled approximately 1.25. After that the vertical stress was decreased linearly with time. In these tests the samples were unloaded to a given *OCR* value before being reloaded to the strain level from which the unloading started. The reloading was followed by another unloading reloading cycle to a different *OCR* value. After three cycles the samples were loaded beyond the previous maximum stress level to guarantee that the samples were situated on the virgin compression line before another unloading reloading sequence was performed.

6.5 Shear tests

Several undrained and drained triaxial tests were also performed, some of which were consolidated to an assumed K_0 value, while others were consolidated by keeping the radius constant. The 1-D compression tests discussed previously were, after loading beyond the preconsolidation pressure, exposed to undrained shear. These tests are also known as oedotriaxial tests (Janbu, 1973). The result of these tests was analysed in accordance with *SHANSEP*, (Ladd and Foott, 1974).

Simple direct shear tests characterized by a constant change in the distortion of the sample were also performed in various sections and at different depths.

6.6 Section 1/430 north

This area is a part of the old quay built between 1790 and 1860. The fill in this area is approximately 2.5 metres, while the clay layer is about 30 metres thick.

In order to illustrate the homogeneity of the clay, the results of a Cone Penetration Test (CPT) performed by the Swedish Road Administration as part of an investigation prior to construction of the tunnel are presented in Figure 6.2. This is just one of the many tests conducted.

Undisturbed samples from this section was studied regarding water content, liquid limit and density, see Figure 6.3a. The water content in the profile decreased from 80% at 5 metres to 40% at a depth of 25 metres. The water content at the top of the clay layer was as high as 90%, which is also indicated by the reduced shear strength and preconsolidation pressure, cf. Figure 6.3b and Figure 6.4. Thin silt layers were observed at the bottom of the clay layer, which probably causes the decrease in pore water pressure. The density increased with depth, as was expected in cases of a decrease in water content. The coupling between density and water content resulted in a specific gravity, G_s, of 2.8-2.9 ton/m^3. This was larger than expected compared to previous measurements. According to the Swedish classification system, the clay is medium sensitive. The sensitivity varies between 10-30 with the higher values in the upper part, see Figure 6.3b. This kind of clay is classified as highly sensitive to quick in the United States (Holtz and Kovacs, 1981).

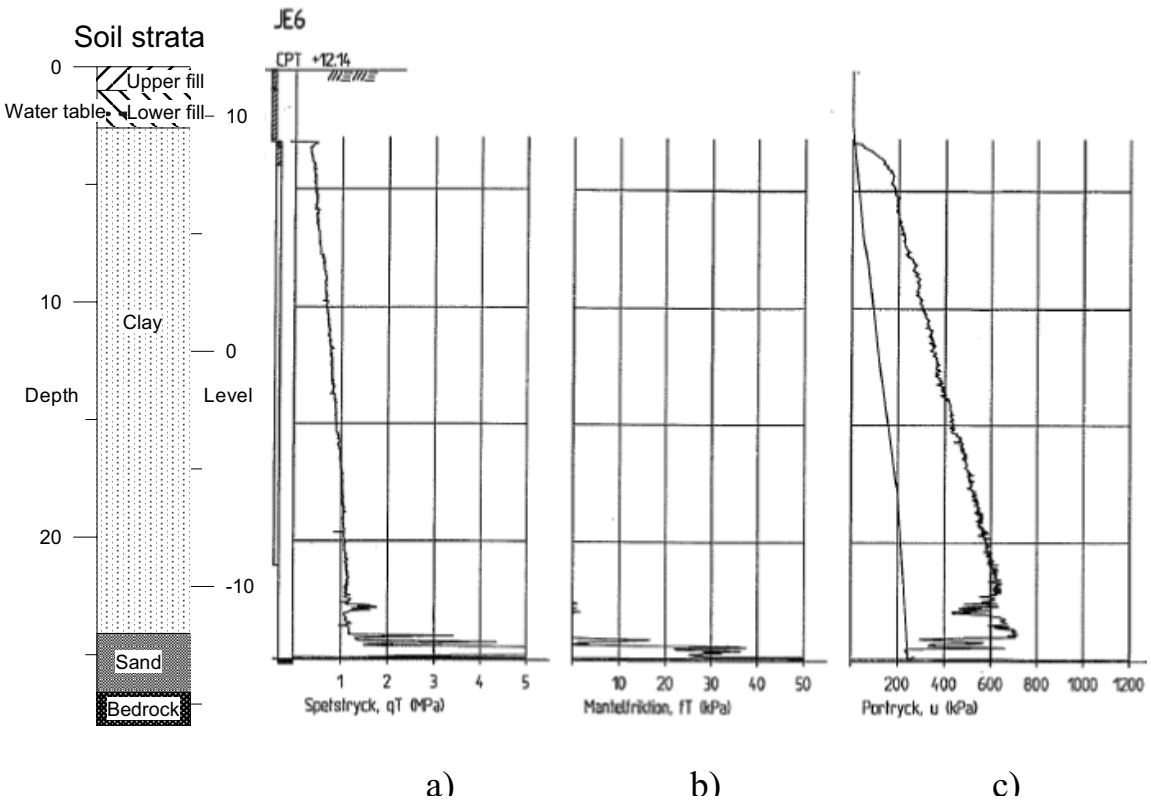

Figure 6.2: Results from the CPT-test JE6 showing a) tip resistance b) friction against the shaft c) pore water pressure.

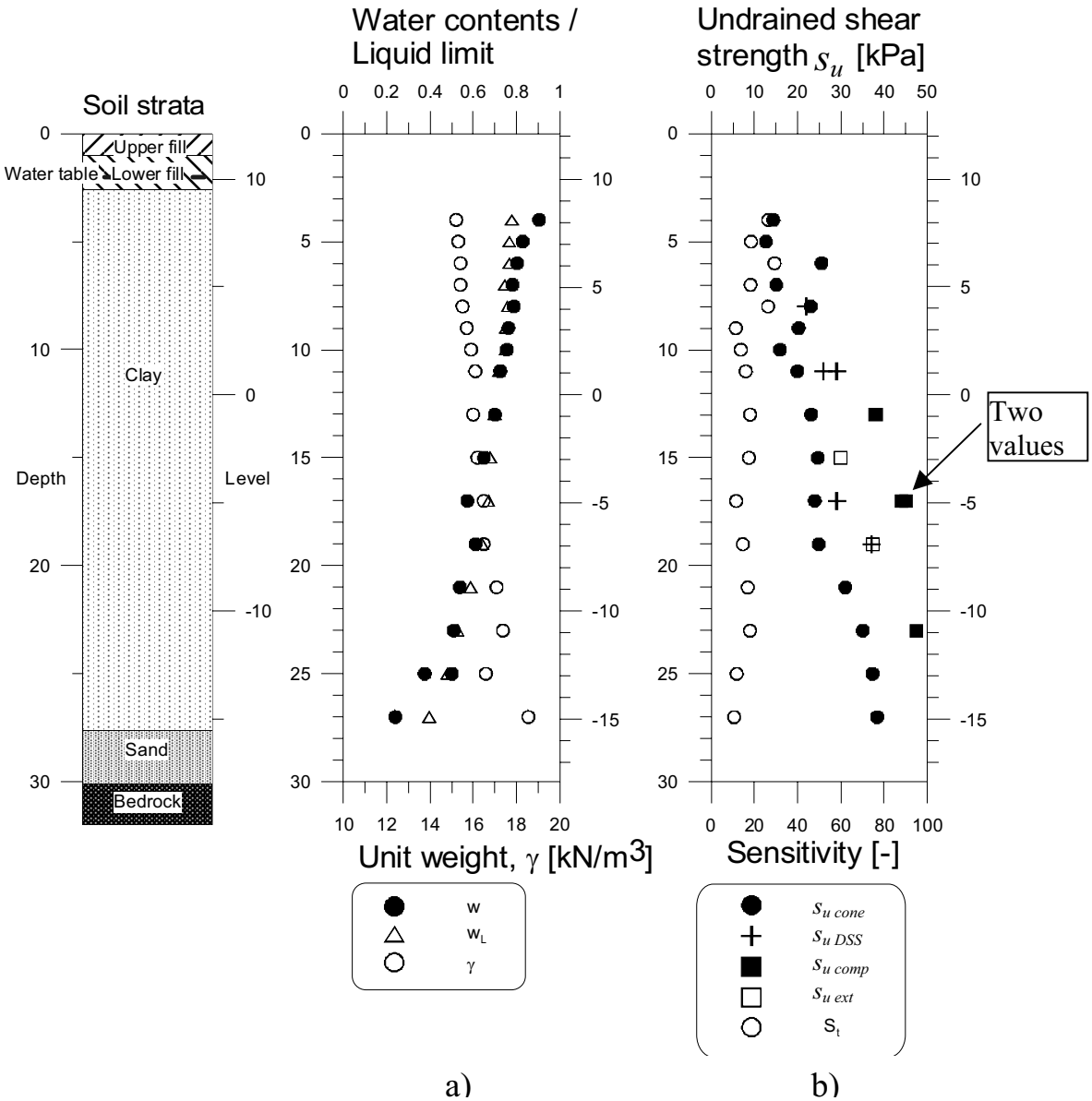

Figure 6.3 Bore hole 1/430 north. a) Water content, liquid limit and unit weight. b) Shear strength and sensitivity.

The shear strength measured in different kinds of tests is presented in Figure 6.3b. In the three active tests, the samples were consolidated to a stress greater than the assumed in situ stress. The consolidation pressure also exceeded the preconsolidation pressure from the CRS tests, see Table 6.1.

Table 6.1: *Stress conditions for the undrained shear tests.*
CK_0UC-Consolidated for a K_0 stress situation and sheared Undrained by Compression, active shear test.
CK_0UE- Consolidated for a K_0 stress situation and sheared Undrained by Extension, passive shear test
CDSS-*Consolidated for a vertical stress and exposed for Direct Simple Shear undrained, simple direct shear test.*

Depth	Type	$\sigma'^{in-situ}_{vert}$	σ'^{cons}_{vert}	$K_{0\ cons}$	σ'^{precon}_{vert} from CRS
13	*CK_0UC*	91	109	0.63	98
17	*CK_0UC*	106	133	0.62	117
23	*CK_0UC*	141	89	0.62	154
15	*CK_0UE*	96	97*	0.7	103
19	*CK_0UE*	117	109	0.57	130
8	*CDSS*	72	74	-	100
11	*CDSS*	86	88	-	110
11	*CDSS*	86	88	-	110
17	*CDSS*	106	104	-	127
19	*CDSS*	117	117	-	132

*The sample was first consolidated for $\sigma'_v=120$ and $K_0=0.62$ and unloaded before shearing.

Based on the 1D-compression tests, the vertical preconsolidation pressure, referred to as σ'^{precon}_{vert}, was estimated in accordance with Swedish standard practice described earlier. The vertical effective stress in situ, $\sigma'^{in-situ}_{vert}$, was estimated from the measured unit weight and pore water pressure in the clay, which were evaluated from field measurements. These measurements were compared with those obtained by the Swedish Road Administration as well as with the estimated preconsolidation pressure. Note that the upper 7 metres contained lots of shells which is reflected in poor quality samples and a wide scatter in the estimated preconsolidation pressures.

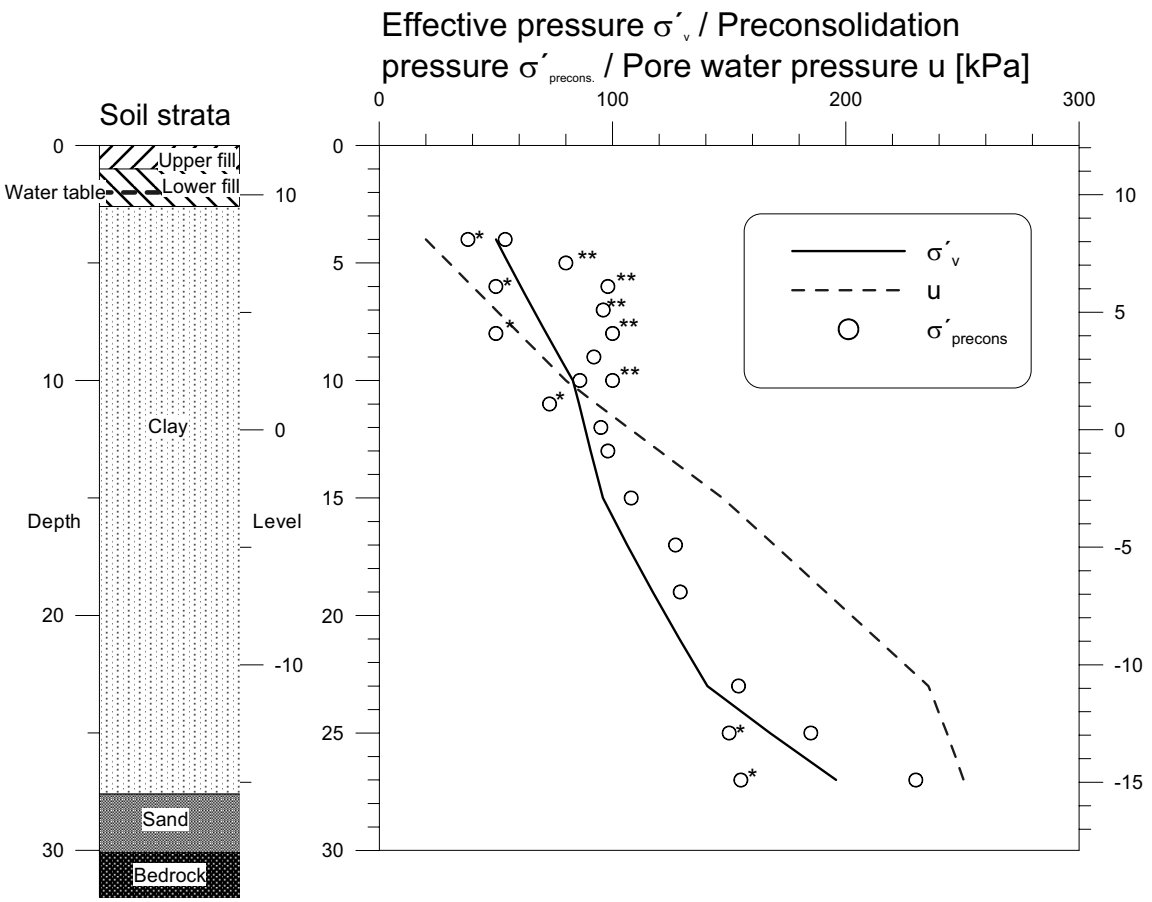

Figure 6.4: Evaluated preconsolidation pressure from CRS-tests compared with the stress situation of the clay.
** The evaluated preconsolidation pressure is below the actual vertical effective stress. This is probably due to sample disturbance.*
*** These tests show a jagged stress-strain response, which is probably due to the presence of small shells in the clay.*

6.7 Section 1/470 south

This section is located within the same area as section 1/430 north, although the load history differs somewhat. This part of the old quay was probably used for storage of the iron, which was shipped from the harbour. The fill layer is slightly thicker than that in the previous section and situated on top of 19 m of clay.

Undisturbed samples from this section were studied and the water content, liquid limit and density determined, see Figure 6.5a. The water content in the profile decreased from just below 80% at 4 m to 45% at a depth of 20 m. Compared to the test results from section 1/430 north, the water content is slightly lower at corresponding levels. The density increases with depth and is higher than that measured in section 1/430 at the same level. This indicates that the preconsolidation pressure could be higher than in section 1/430. The coupling between density and water content produces a specific gravity, G_s, of 2.8-3.0 ton/m^3. This is greater than expected compared to laboratory results. According

to the Swedish classification system, the clay is medium sensitive, and its sensitivity is more or less constant at 20 through the profile, see Figure 6.5b.

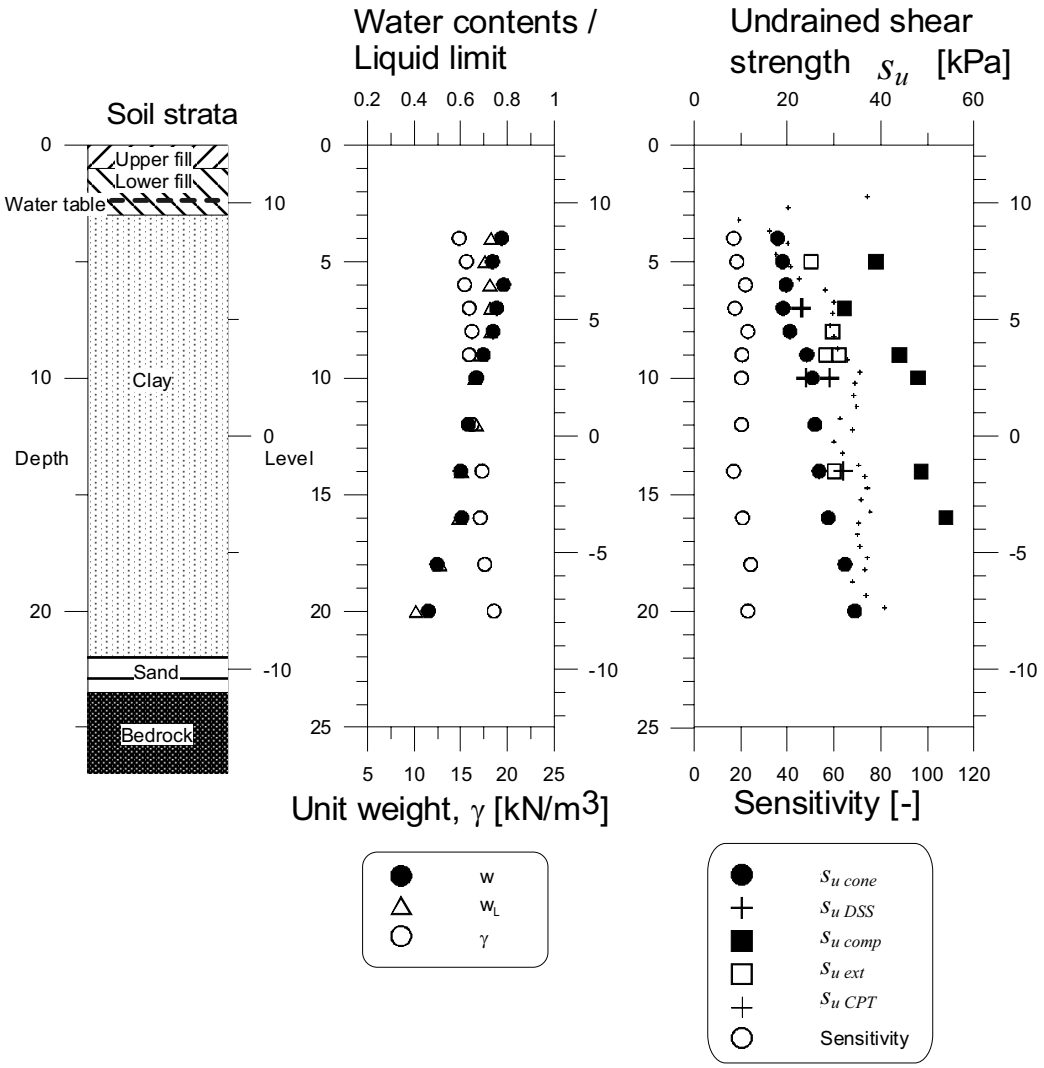

a) b)

Figure 6.5: Bore hole 1/470 north. a) Water content, liquid limit and unit weight. b) Shear strength and sensitivity.

The determined undrained shear strength is presented in Figure 6.5b. The undrained shear strength from a cone penetration test, $s_{u\ CPT}$, was estimated by means of semi-empirical relations (Larsson, 1995). The undrained shear test was performed under different stress conditions, in an attempt to capture different stress behaviours related to variations in the stress situation (Table 6.2). Some of these results will be analysed in the following chapters.

Table 6.2: Stress condition in the undrained shear tests.

Depth	Type	$\sigma'^{in-situ}_{vert}$	σ'^{cons}_{vert}	$K_{0\ cons}$	σ'^{precon}_{vert} from CRS
5[1)]	CK_0UC	60	60	0.78	127
7	CK_0UC	74	61	0.89	153
9[2)]	CK_0UC	83	84	0.74	130
14[4)]	CK_0UC	116	116	0.70	169
16	CK_0UC	130	111	0.73	175
5[1)]	CK_0UE	60	60	0.78	127
8	CK_0UE	71	70	0.79	133
9[2)]	CK_0UE	83	85	0.75	130
9[3)]	CK_0UE	83	182	0.59	130
16[5)]	CK_0UE	130	132	0.61	175
7	*CDSS*	71	71	-	142
10	*CDSS*	89	89	-	131
10	*CDSS*	89	145	-	131
14	*CDSS*	116	116	-	170

1) The sample was first consolidated for $\sigma'_v=60$ and $K_0=0.60$
2) The sample was first consolidated for $\sigma'_v=84$ and $K_0=0.55$
3) The sample was exposed for a K_0 test until $\varepsilon_{vert}=8.4\%$ ($\sigma'_v=184$ and $K_0=0.57$) after which it was left without any strain changes, which resulted in a decrease in stress ($\sigma'_v=160$ and $K_0=0.66$). Before shearing, the K_0 test was loaded again to $\sigma'_v=184$ which yielded $\varepsilon_{vert}=8.8\%$.
4) The sample was first consolidated for $\sigma'_v=119$ and $K_0=0.56$
5) The sample was first consolidated for $\sigma'_v=133$ and $K_0=0.55$

The vertical preconsolidation pressure was estimated from CRS-tests and is presented in Figure 6.6. The results differ from what was expected and the trend also appears higher than in other areas along the Göta River. Based on experience, the *OCR* is around 1.3 with higher values in the upper part. The ratio of 1.3 is most likely an effect of creep. In the filled areas, the expected *OCR* is 1.0-1.3 due to progressive creep deformation, compare Figure 6.4

In order to verify whether there were any layers within the clay layer that could explain the scatter in the evaluated preconsolidation pressures, a CPT test was performed in the section, 15 metres south of the sheet pile wall, but no clearly visible layers were detected (Figure 6.7).

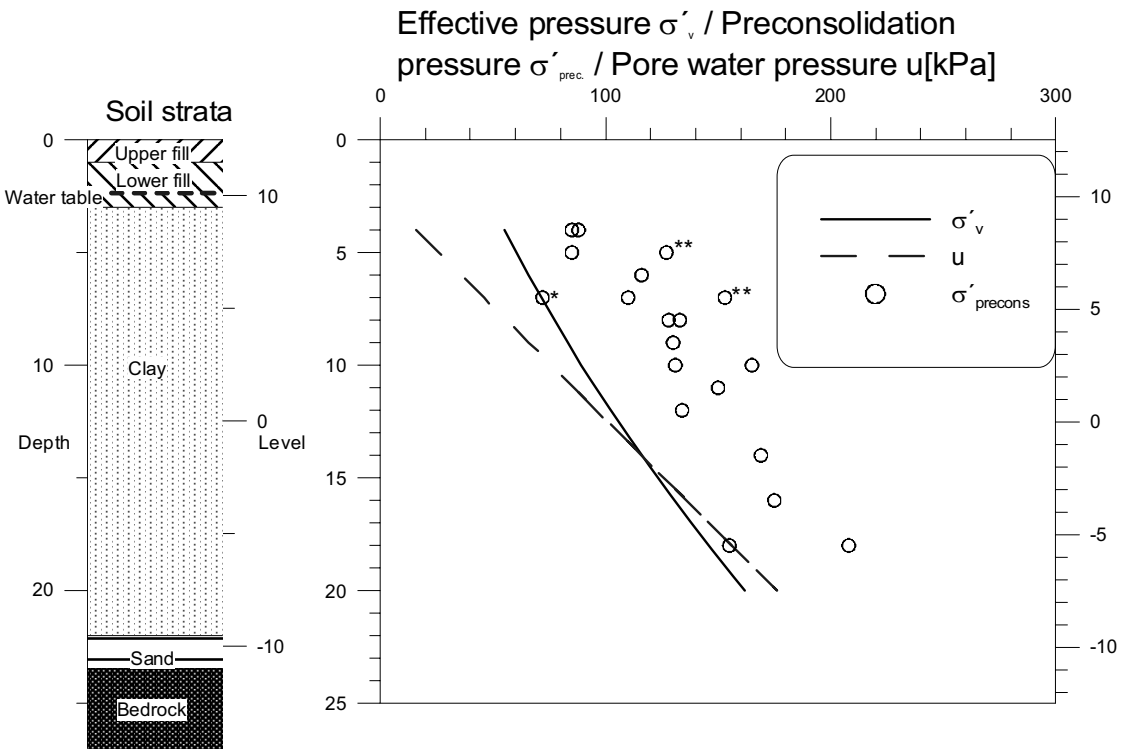

Figure 6.6: Estimated preconsolidation pressure from CRS-tests compared with the stress situation in the clay.
** The estimated preconsolidation pressure is below the actual vertical effective stress. This is probably due to some sample disturbance.*
*** These tests show a jagged stress-strain response, probably caused by the presence of small shells in the clay.*

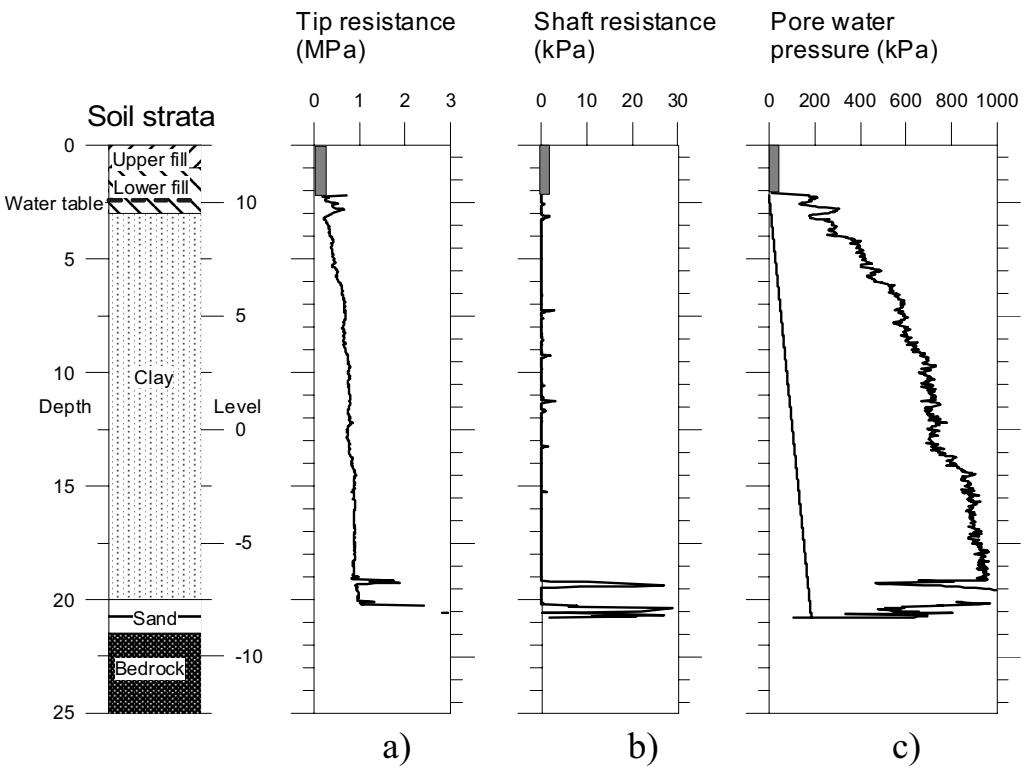

Figure 6.7: Results from a CPT-test at bore hole 1/470b showing
a) tip resistance b) friction against the shaft c) pore water pressure.

The shear strength, $s_{u\ CPT}$, exceeds the strength obtained in the fall cone and direct simple shear test (Figure 6.5b). The estimated preconsolidation pressure agrees very well with the results of the oedometer tests, see Figure 6.8, which have been complemented by results from borehole JE9 in section 1/460 south.

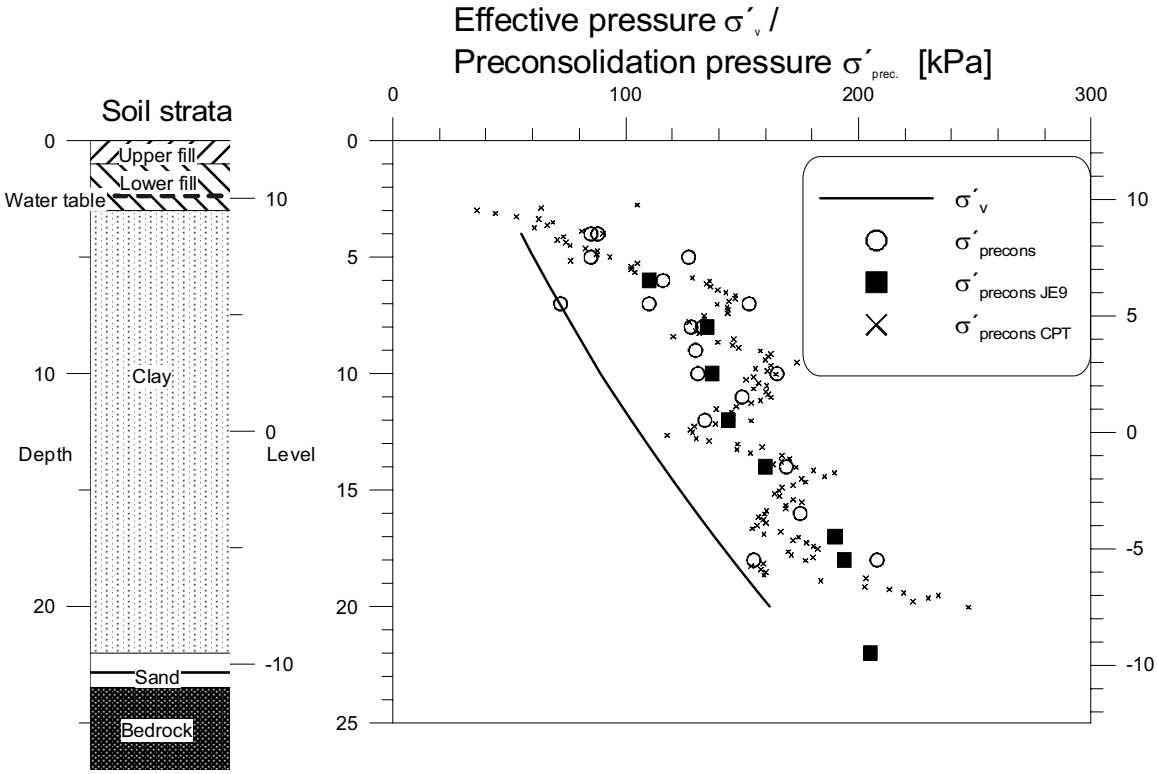

Figure 6.8: Evaluated preconsolidation pressure from CRS-tests compared with data from bore hole JE9 and CPT tests.

6.8 Undrained triaxial tests

Undrained triaxial tests are mainly used to obtain the shear strength for different loading situations, although the stress strain response can also be evaluated. There are two ways of determining the active shear strength, $s_{u\ active}$, as well as two ways of determining the passive shear strength, $s_{u\ passive}$. In all these cases the shearing starts from a specified stress situation, preferably the in situ stress but other stresses can also be employed, depending on the aim of the test. During the undrained phase, no volume change in the sample is permitted.

Active tests were performed either by increasing σ_{vert} and maintaining σ_{hor} constant or by decreasing σ_{hor} and maintaining σ_{vert} constant. Where σ_{hor} remains constant and where an increase of σ_{vert} creates an increase in the mean stress, Δp, excess pore pressure is generated in the sample, thus leading to an increase in σ'_{vert} and a decrease in σ'_{hor}. If active tests are performed by decreasing σ_{hor} and maintaining σ_{vert} constant, Δp will become negative and thus

generate negative excess pore pressure, which will lead to the same changes in effective stresses as in the first case.

Passive tests are performed by either decreasing σ_v and maintaining σ_h constant or by increasing σ_h and maintaining σ_v constant. The same logic that applied to active tests means that the changes in effective stress are equal, irrespective of the approach used when performing passive tests.

If the stress changes are not affected by the stress history, the ratio between $\Delta\sigma'_v$ and $\Delta\sigma'_h$ is –2 and the stress path in the s'-t stress space follows an inclination of 3:1. However, if effective stresses are increased in such a way that the preconsolidation pressure are getting close, the structure of the clay will start to break down, resulting in shear induced excess pore water pressure and plastic strains. The changes in pore pressure will differ from those keeping the in mean stress constant and the stress path in the s'-t stress space will divagate from the inclination 3:1.

According to the *NSP* method and the *SHANSEP* concept the behaviour of a cohesive soil is proportional to the vertical preconsolidation pressure, thus making it practical to normalize the stresses regardning σ'^{precon}_{vert}. Soil samples with identical *OCR* will exhibit the same response, even if there are differences in consolidation pressure. It should be noted that this is only valid if the soil has been sedimented under similar conditions and has the same mineralogy and grain-size distribution. This is demonstrated by two undrained compression tests, which were consolidated for a relation between σ'_h and σ'_v representing the assumed stresses in situ, see Figure 6.9 and Figure 6.10. As can be seen, the match is excellent both regarding the stress path and stress-strain relations. However, this method requires that the preconsolidation pressure is known. In this case, the actual preconsolidation pressure in situ was exceeded slightly and therefore the normalization was simple, although in most cases the exact preconsolidation pressure is unknown, which can be a problem if σ'^{precon}_{vert} scatters. The σ'^{precon}_{vert} can be determining from the CK_0UC test but it presupposes that shearing starts within a specified *OCR* range.

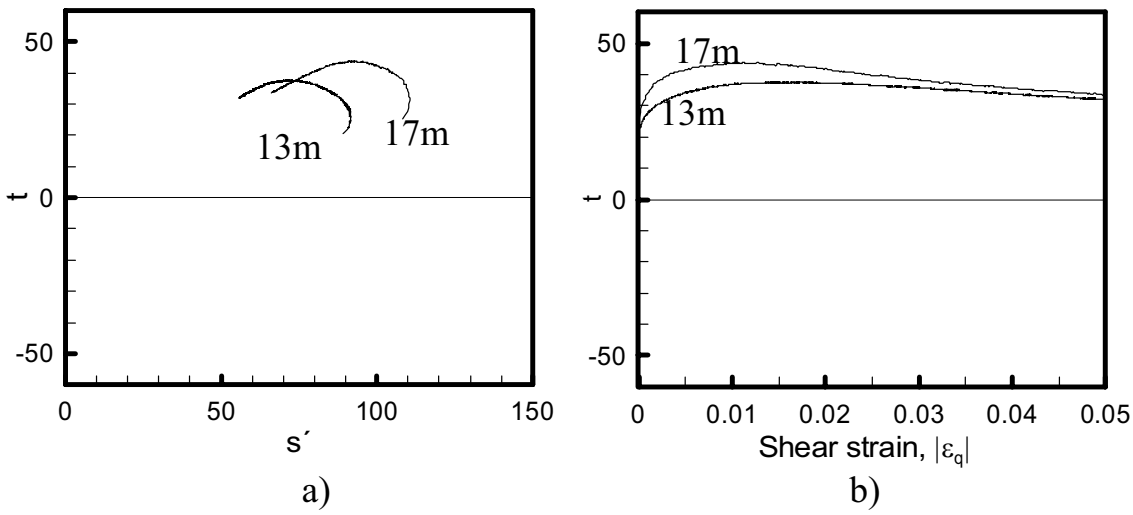

Figure 6.9: *CK_0UC test for depths of 13 and 17 metres consolidated for a K_0 value of 0.6 and an OCR of 1.0.*
a) Stress path in the s´-t space.
b) Shear strain vs. maximum shear stress, t, in the sample.

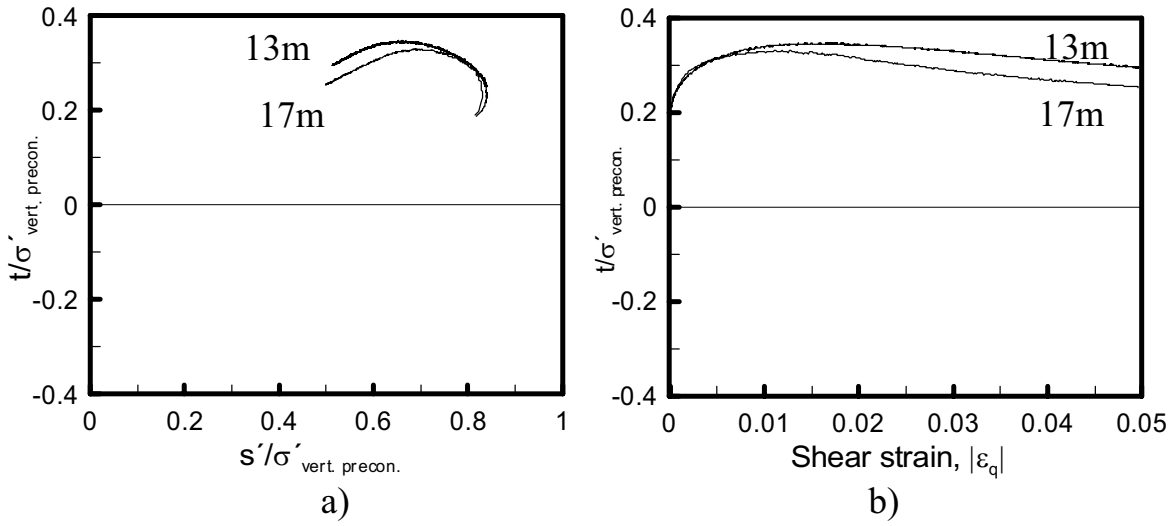

Figure 6.10: *Normalized CK_0UC test for depths* of *13 and 17 metres consolidated for a* K_0 *value of 0.6 and an OCR of 1.0.*
a) Stress path in the $s'/\sigma'^{precon}_{vert}$ - $t/\sigma'^{precon}_{vert}$ *space.*
b) Shear strain vs. normalized maximum shear stress, $t/\sigma'^{precon}_{vert}$*, in the sample.*

Results from the *CK_0UC* and *CK_0UE* tests performed for in situ stresses from section 1/470 south are presented in Figure 6.11. Undrained compression tests and the extension tests performed at *OCR*≈1.0, some of which were consolidated according to the original *SHANSEP* concept, are presented in Figure 6.12. These two figures show that the normalization against the preconsolidation pressure yields consistent s_u, for consolidation far above the actual preconsolidation pressure in situ. However, the excpected increase in stiffness did not occur, see, curves 3,4 and 8 in Figure 6.12

Some undrained shear tests from section 1/470 south are presented in Figure 6.11 in order to visualize the stress paths and the stress strain response. The shear tests were performed at estimated in situ stresses based on the evaluated true K_0 tests with both loading and unloading. The true K_0 tests yielded the K_0^{nc} value as well as the stress path during unloading for a specific *OCR* value. The consolidation is performed in two steps. First with a stress situation corresponding to $\sigma'^{in\ situ}_{vert}$ and K_0^{nc} and then with a stress situation corresponding to $\sigma'^{in\ situ}_{vert}$ and a K_0 value corresponding to Equation (2.10).

Ladd and Foott (1974) proposed the use of the *SHANSEP* method (Stress History And Normalized Soil Engineering Properties) in order to normalize soil behaviour, whereby the modulus is proportional to the maximum vertical stress, Equation (6.1).

$$G_{in\ situ} = \frac{\sigma'^{precon}_{vert\ in\ situ}}{\sigma'^{max\ consolidation}_{vert}} G_{in\ situ} \tag{6.1}$$

In order to verify that the true K_0 consolidation lies on the virgin curve (coinciding with the K_0^{nc} line) the vertical stress has to exceed the level σ'_L, which is defined in Figure 6.1. This corresponds to approximately 10-15% of vertical strain. Tests were performed using *SHANSEP* and the results compared with tests run on samples consolidated to the K_0 value and approximately the same *OCR*. The match in stress paths was excellent but for the stress strain response the *SHANSEP* method was to soft. This can be due to the fact that the 24 hours during which the sample was allowed to consolidate was insufficient. It has also been observed that samples that were given no time to consolidate no or limited increase in s_u occured. Use and non-use of the *SHANSEP* method is compared in Figure 6.12.

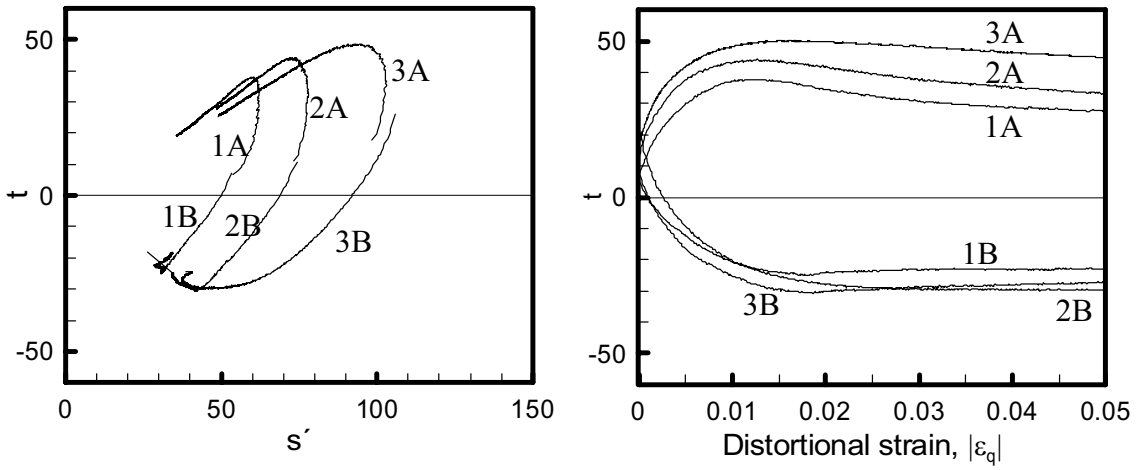

a) b)

Test	Section	Depth	Type	$\sigma'^{in\text{-}situ}_{vert}$	σ'^{cons}_{vert}	$K_{0\ cons}$	τ_{fu}	σ'^{precon}_{vert}
1A	1/470	5	CK_0UC	60	60	0.78	39	115
2A	1/470	9	CK_0UC	83	84	0.74	44	137
3A	1/470	14	CK_0UC	116	116	0.70	49	150
1B	1/470	5	CK_0UE	60	60	0.78	25	115
2B	1/470	9	CK_0UE	83	85	0.75	31	137
3B	1/470	16	CK_0UE	130	132	0.61	30	145

c)

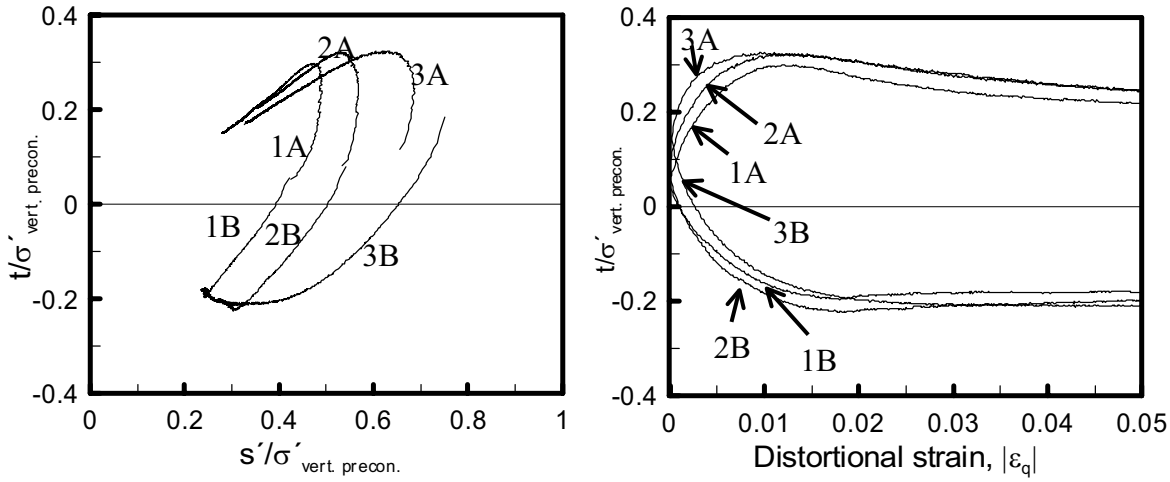

d) e)

Figure 6.11: Undrained triaxial shear tests for section 1/470, consolidated for in situ stresses.
a) Stress paths in the s´-t space
b) Shear stain vs. maximum shear stress, t
c) Stress situation for each test
d) Normalized stress paths in the s´-t space
e) Shear stain vs. normalized maximum shear stress, $t/\sigma'^{precon}_{vert}$

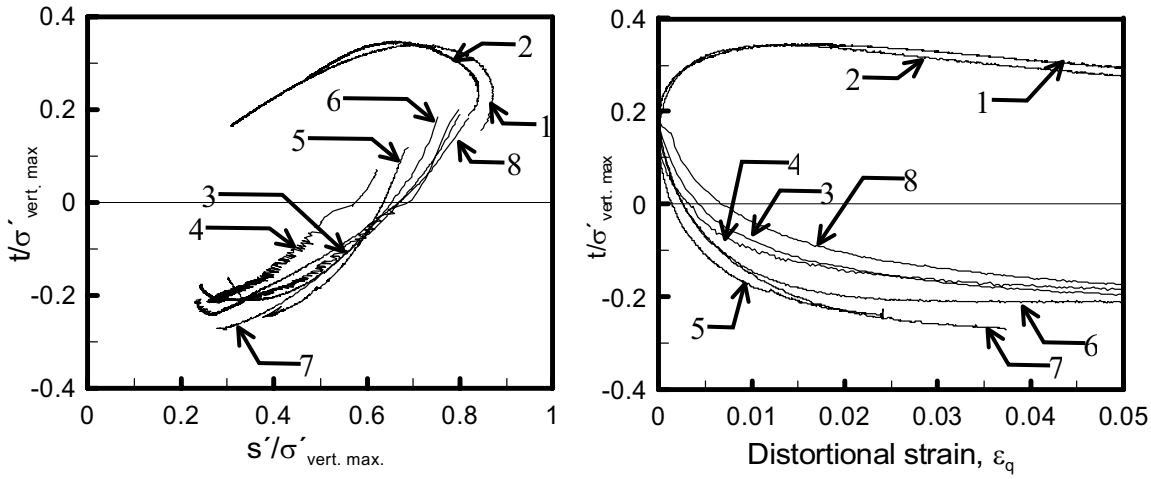

a) b)

Test	Section	Depth	$\sigma'^{precon\ in\ situ}_{vert}$	σ'^{cons}_{vert}	σ'^{max}_{vert}	*OCR*	$\varepsilon^{cons}_{vert}$	$\tau_{fu}/\sigma'^{max}_{vert}$
1	1/430	13		109	109	1.00	2.2	0.35
2	3/180	14		104	105	1.01	3.5	0.29
3	1/470	9		182	182	1.00	9.3	0.24
4	1/406	12		132	163	1.23	10.4	0.23
5	1/430	15		97	120	1.24	2.3	0.25
6	1/470	16		132	141	1.07	3.2	0.21
7	3/180	18		130	130	1.00	3.4	0.32
8	1/430	19		224	224	1.00	8.6	0.17

c)

Figure 6.12: Undrained triaxial shear tests on normal consolidated samples.
a) Normalized stress paths in the s´-t space
b) Shear stain vs. normalized maximum shear stress, $t/\sigma'^{precon}_{vert}$
c) Stress situation for each test

6.9 Undrained direct simple shear tests

Undrained direct simple shear tests were performed at both SGI and Chalmers on clay from different depths taken from Järntorget. In most cases the samples were consolidated to in situ stresses (vertical) but some tests were performed at different *OCR*s from the same tube. The CK_0UDSS tests were carried out using equipment developed at SGI. The applied shear force generates a rotation of the principal stresses. The principals of the test are shown in Figure 2.4. The limitation of the method is described in section 2.2.3.

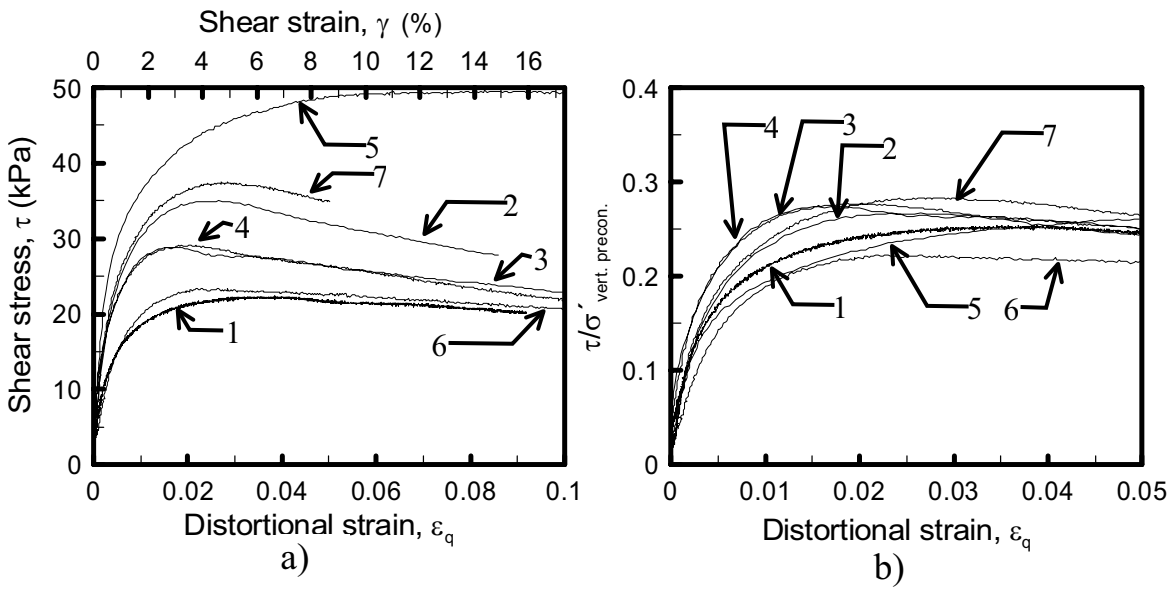

Test	Section	Depth	$\sigma'^{\,in\ situ}_{v\ precon}$	$\sigma'_{v\ cons}$	OCR	$\varepsilon^{cons}_{vert}$	$\tau_{fu}/\sigma'_{v\ max}$
1	1/430	8	81	75	1.08	3.06	0.28
2	1/470	10	131	89	1.47	3.38	0.27
3	1/430	11	105	88	1.19	3.04	0.27
4	1/430	11	105	88	1.19	-	0.28
5	1/430	11	105	168	1.12	9.25	0.27
6	1/430	11	105	44	2.39	1.69	0.22
7	1/430	19	132	89	1.12	3.44	0.28

c)

Figure 6.13: Results from CK_0UDSS tests
a) Shear stress vs. distortional strain
b) Normalized shear stress vs. distortional strain
c) Stress situation for each test

Results from the CK_0UDSS tests are shown in Figure 6.13. Even in the case of the *DSS* test it appears that the stress strain response ($G_{tan}=\delta\tau/\ \delta\gamma$) cannot be normalized in accordance with the *SHANSEP* method. However, the measured shear stress seems to follow the *SHANSEP* concept.

6.10 Oedometer tests

The most usual way of performing these tests in Sweden is to run a CRS test with the deformation rate 0.0024 mm/min. However, there are other ways of running these kinds of test, e.g. different deformation rate, stepwise loading or true K_0 tests in the triaxial cell. Each of these tests is performed during drained conditions with monitoring of the excess pore water within the sample. The CRS test is the most economical test for evaluating standard parameters, but if focus is on the creep behaviour, the stepwise oedometer test is preferable. In order to fully control the stresses the oedometer case must be simulated in the triaxial cell. This can be achieved in two ways; either by calculating the average radial

strain by controlling the volume change within the sample as well as that in the liquid which regulates the radial pressure or by means of internal gauges directly attached to the sample.

Typical results from ordinary CRS test shown in Figure 6.14. From the test the following parameters were evaluated:

σ'^{precon}_{vert} — Vertical preconsolidation pressure.
σ'_L — The effective stress above σ'^{precon}_{vert} where the constrained modulus starts to increase.
M_0 — The constrained modulus below σ'^{precon}_{vert}.
M_L — The constrained modulus between σ'^{precon}_{vert} and σ'_L.
M' — The increase in the constrained modulus above σ'_L.
k — The hydraulic conductivity at σ'^{precon}_{vert}.
c_v — The coefficient of consolidation at σ'^{precon}_{vert}.
β — The decrease in k dependent on the strain.

There are other parameters that could also be evaluated as well depending on how the stress deformation curve is presented. One way of expressing the stress deformation relationship is to plot the effective vertical stress, $\sigma'_{vert,}$ vs. void ratio, e, which reveals whether the soil behaviour at different depths is merely an effect of the stress history. The stress strain relation can be described as a function of e and σ'^{precon}_{vert} if the curves merge into a single curve when σ'^{precon}_{vert} has been exceeded, thus making it easier to describe changes in the constrained modulus due to the soil density. The same tests shown in Figure 6.14 are presented as $\sigma'_{vert,}$ vs. e in Figure 6.15. From the stress strain curves presented in Figure 6.14 and Figure 6.15 it is obvious that the three tests have a response that can be described as a function of e and σ'^{precon}_{vert} which is a great advantage when trying to model the soil profile.

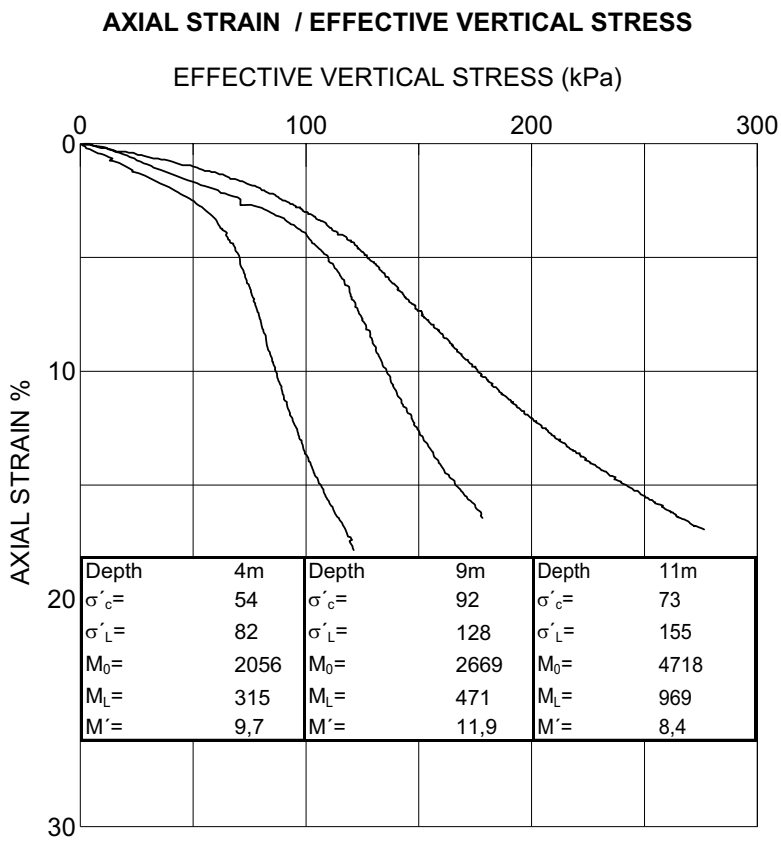

Figure 6.14: Stress strain response from the CRS tests. $\sigma'_{vert,}$ vs. ε_{vert}.

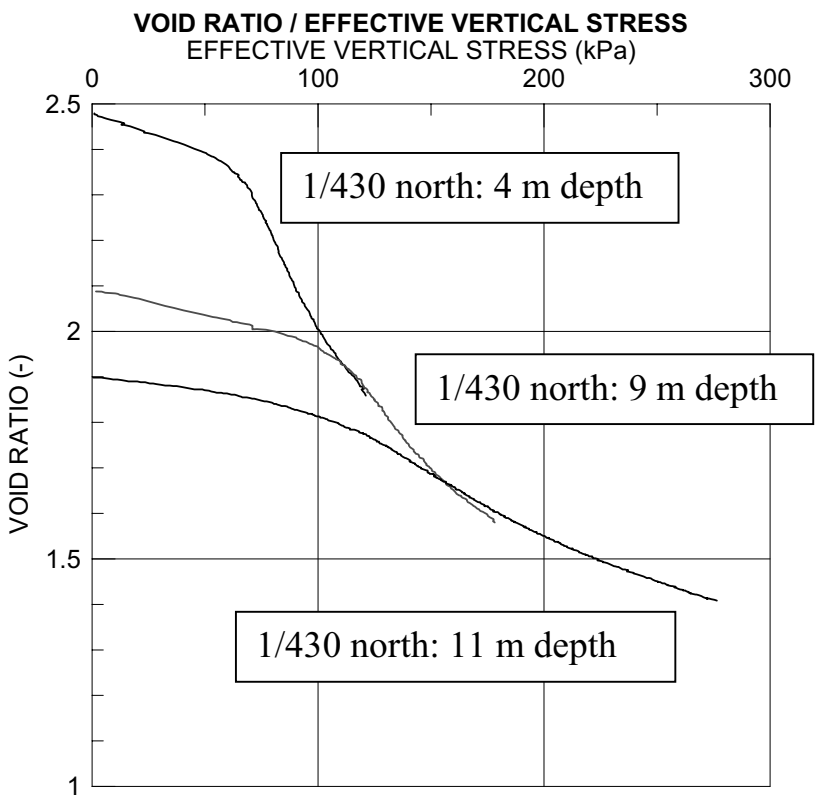

Figure 6.15: Stress strain response from the CRS tests. $\sigma'_{vert,}$ vs. e.

7 FORMULATION OF THE *MIT-S1* CONSTITUTIVE MODEL

7.1 Introduction

The *MIT-S1* is a constitutive model presented by Pestana (1994) that is capable of describing the effective stress-strain-strength behaviour of uncemented soils. The model contains two separate sets of parameters for cohesive or non-cohesive soils. This thesis focuses on the capability of the model to describe the behaviour of saturated cohesive soil, in particular that of highly plastic clay such as that in Gothenburg. The model is an extension of previous work carried out at MIT[8] (Kavvadas, 1982; Whittle, 1987).

The model has three basic components:
1) An elasto-plastic model with a single yield surface defined as a function of a normally consolidated soil. The plasticity is described by a non-associated flow rule, while hardening rules describe the evolution of anisotropic stress-strain properties.
2) Small strain stiffness is described by a non-linear relation and the hysteretic effects caused by an unload-reload cycle are incorporated.
3) A bounding surface that controls the plasticity of overconsolidated soils. The surface location is dependent on the stress path and the stress history.

The difference between a bounding surface model and a traditional elasto-plastic model is that elasto-plastic deformations occur due to all loading, even within the bounding surface. Mapping rules control the magnitude of the plastic deformations within the bounding surface. The amount of plastic behaviour depends on the proximity of the current stress state to the bounding surface.

7.2 Formulation of the *MIT-S1* model

This section briefly summarizes the formulation of the *MIT-S1* model, for further information see Pestana (1994)

The use of standard invariants e.g. p', q and θ, ends up in an isotropic formulation. When dealing with such a formulation it is impossible to simulate anisotropy. In order to enable the *MIT-S1* model to describe the anisotropic behaviour of the soil, the standard stress and strain invariants have to be abandoned. Therefore all six components in the stress and strain tensor has to be addressed. In the *MIT-S1*, as well as *MIT-E3*, these stresses and strains are expressed in transformed variables, see Table 7.1. Some of the stress measures employed are illustrated in Figure 7.1

[8] MIT – Massachusetts Insitute of Technology

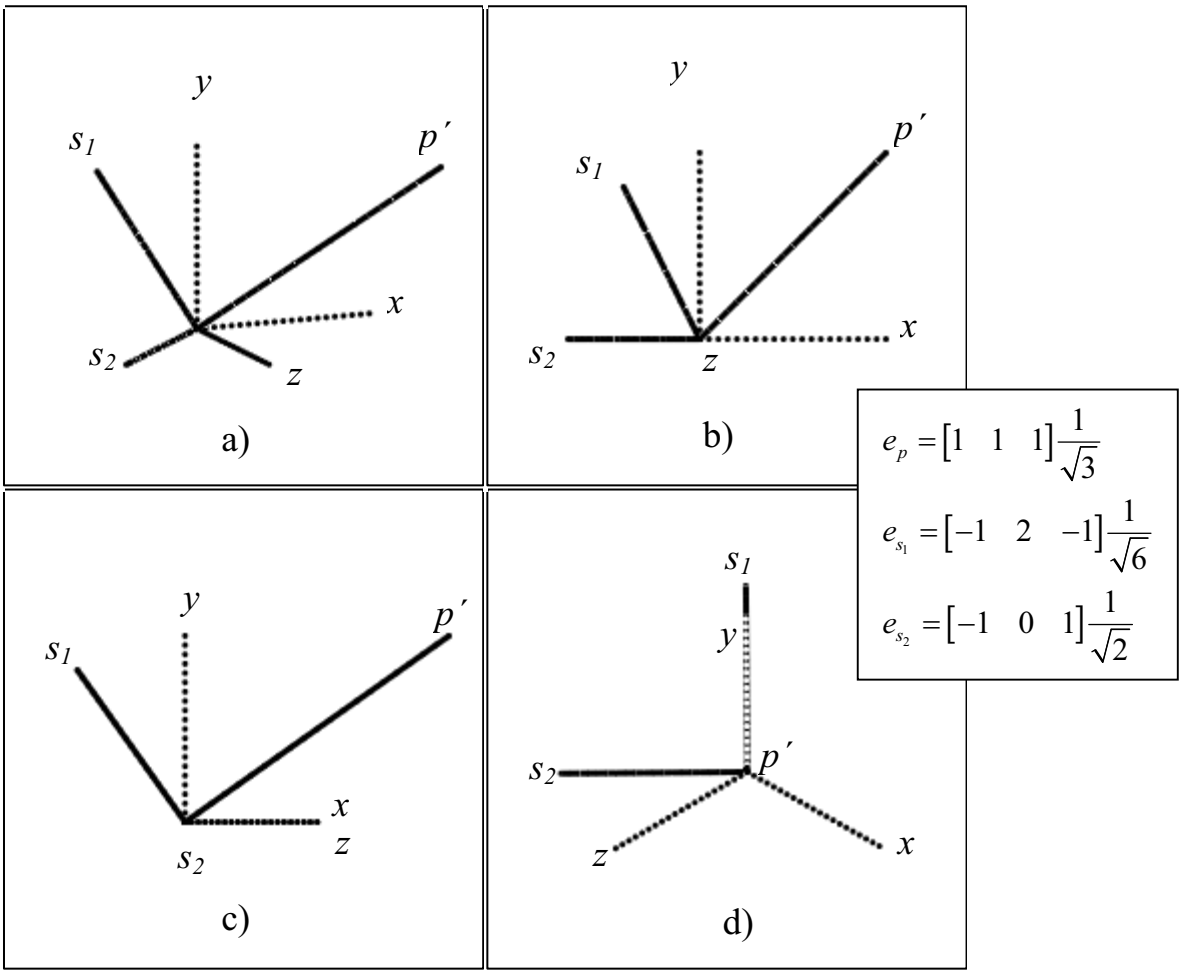

Figure 7.1: Illustration of some of the measures used in the MIT-S1. The y-axis represents the vertical axis. Axes x and z represent the two different horizontal axes. p´ represents the mean stress, s_1 defines the magnitude of the vertical stress compared to the horizontal stresses when x equals z, while s_2 defines the stress difference in the two horizontal directions.
a) An overview of the two-coordinate system
b) z-view (in this view the s´-axis coincides with p´ and the t-axis is perpendicular to p´, thus defining a plane[9])
c) s_2-view (this view represents the axisymmetric case)
d) p´-view (a plane perpendicular to the p-axis are often referred to as the deviatoric plane)

[9] *s´* and *t* is here defined without any influence of any shear forces. The stress measure s_1 does not coinside with the defined plane.

Table 7.1: Transformed Measures used by the MIT-S1 Model (Whittle and Kavvadas, 1994)

Effective Stress $\boldsymbol{\sigma} = (p', \mathbf{s})$	**Stress ratio*** $(1, \boldsymbol{\eta})$	**Strain** $\boldsymbol{\varepsilon} = (\varepsilon_{vol}, \mathbf{e})$	**Yield Surface Gradient** $\mathbf{Q} = (Q, \mathbf{Q}')$	**Plastic Flow Direction** $\mathbf{P} = (P, \mathbf{P}')$	**Anisotropy**** $(1, \mathbf{b})$
$p' = \frac{\sigma'_x + \sigma'_y + \sigma'_z}{3}$	1	$\varepsilon_{vol} = \varepsilon_x + \varepsilon_y + \varepsilon_z$	$Q = Q_x + Q_y + Q_z$	$P = P_x + P_y + P_z$	1
$s_1 = \frac{2\sigma'_y - \sigma'_x - \sigma'_z}{\sqrt{6}}$	$\eta_1 = \frac{2\eta_y - \eta_x - \eta_z}{\sqrt{6}}$	$E_1 = \frac{2\varepsilon_y - \varepsilon_x - \varepsilon_z}{\sqrt{6}}$	$Q'_1 = \frac{2Q_y - Q_x - Q_z}{\sqrt{6}}$	$P'_1 = \frac{2P_y - P_x - P_z}{\sqrt{6}}$	$b_1 = \frac{2b_y - b_x - b_z}{\sqrt{6}}$
$s_2 = \frac{\sigma'_z - \sigma'_x}{\sqrt{2}}$	$\eta_2 = \frac{\eta_z - \eta_x}{\sqrt{2}}$	$E_2 = \frac{\varepsilon_z - \varepsilon_x}{\sqrt{2}}$	$Q'_2 = \frac{Q_z - Q_x}{\sqrt{2}}$	$P'_2 = \frac{P_z - P_x}{\sqrt{2}}$	$b_2 = \frac{b_z - b_x}{\sqrt{2}}$
$s_3 = \sqrt{2} \cdot \tau_{xy}$	$\eta_3 = \sqrt{2} \cdot \eta_{xy}$	$E_3 = \sqrt{2} \cdot \varepsilon_{xy}$	$Q'_3 = \sqrt{2} \cdot Q_{xy}$	$P'_3 = \sqrt{2} \cdot P_{xy}$	$b_3 = \sqrt{2} \cdot b_{xy}$
$s_4 = \sqrt{2} \cdot \tau_{yz}$	$\eta_4 = \sqrt{2} \cdot \eta_{yz}$	$E_4 = \sqrt{2} \cdot \varepsilon_{yz}$	$Q'_4 = \sqrt{2} \cdot Q_{yz}$	$P'_4 = \sqrt{2} \cdot P_{yz}$	$b_4 = \sqrt{2} \cdot b_{yz}$
$s_5 = \sqrt{2} \cdot \tau_{xz}$	$\eta_5 = \sqrt{2} \cdot \eta_{xz}$	$E_5 = \sqrt{2} \cdot \varepsilon_{xz}$	$Q'_5 = \sqrt{2} \cdot Q_{xz}$	$P'_5 = \sqrt{2} \cdot P_{xz}$	$b_5 = \sqrt{2} \cdot b_{xz}$

* $\eta_i = s_i / p'$ ****b** contains state variables defining the orientation of the tip of the bounding surface in stress space, cf. Equation (7.21) and Figure 7.4. For a normal consolidated clay, with $\sigma'_x = \sigma'_x$ and $\tau_{xy} = \tau_{yz} = \tau_{xz} = 0$, b_1 becomes $\frac{2}{\sqrt{6}}\left(1 - K_0^{nc}\right)$ and b_2-b_5 =0.

7.2.1 Incrementally linearized elasto-plasticity

The strain increment in the S1 model is divided into two separate parts, one for recoverable and one for irrecoverable strains.

$$\dot{\boldsymbol{\varepsilon}} = \dot{\boldsymbol{\varepsilon}}^{e} + \dot{\boldsymbol{\varepsilon}}^{pl} \tag{7.1}$$

The elastic stress change due to elastic incremental strains is written as

$$\dot{\boldsymbol{\sigma}} = \begin{Bmatrix} \dot{p}' \\ \dot{\boldsymbol{s}} \end{Bmatrix} = \begin{Bmatrix} K\dot{\varepsilon}_{vol}^{e} \\ 2G\dot{\boldsymbol{e}}^{e} \end{Bmatrix} \tag{7.2}$$

Flow rule

$$\dot{\boldsymbol{\varepsilon}}^{pl} = \begin{Bmatrix} \dot{\varepsilon}_{vol}^{pl} \\ \dot{\boldsymbol{e}}^{pl} \end{Bmatrix} = \dot{\Lambda} \begin{Bmatrix} P \\ \boldsymbol{P}' \end{Bmatrix} \tag{7.3}$$

P and $\mathbf{P}'$ are volumetric and deviatoric components of the potential function. Λ is a scalar defining the strain increment.

Load direction

$$KQ\dot{\varepsilon}_{vol} + 2G\boldsymbol{Q} : \dot{\boldsymbol{e}} = \begin{cases} \geq 0 \ \textit{Loading} \\ < 0 \ \textit{Unloading} \end{cases} \tag{7.4}$$

Q defines the loading direction. In classical soil mechanics this is the gradient of the yield surface f($\boldsymbol{\sigma}$, e, α', $\boldsymbol{b}$). Where $\boldsymbol{\sigma}$ and e are state variables, i.e. current stress and void ratio respectively and α' and $\boldsymbol{b}$ are internal variables defining the size and orientation of the bounding surface.

Observe that the symbol ":" is used instead of $\sum_{i=1}^{5} Q_i \dot{e}_i$. The general expression is found in Equation (7.5).

$$\boldsymbol{A} : \boldsymbol{B} = \sum_{i=1} A_i B_i \tag{7.5}$$

7.2.1.1 Incremental Effective Stress-Strain Relationship

$$\begin{Bmatrix} \dot{\sigma} \\ \dot{\boldsymbol{s}} \\ \dot{e} \end{Bmatrix} = \begin{Bmatrix} K\left(\dot{\varepsilon}_{vol} - \dot{\Lambda}P\right) \\ 2G\left(\dot{\boldsymbol{e}} - \dot{\Lambda}\boldsymbol{P}'\right) \\ \left(1+e\right)\dot{\varepsilon} \end{Bmatrix} \tag{7.6}$$

$$\dot{\Lambda} = \frac{KQ\dot{\varepsilon} + 2G\boldsymbol{Q}' : \dot{\boldsymbol{e}} + \frac{\partial f}{\partial e}\left(1+e\right)\dot{\varepsilon}}{H + KQP + 2G\boldsymbol{Q}' : \boldsymbol{P}'}$$

H is the elasto-plastic modulus, defining hardening of the yield surface.

7.2.2 Incremental Effective Stress-Strain Relations, elastic responce

$$\dot{\sigma} = K\dot{\varepsilon}_{vol} \qquad \dot{\boldsymbol{s}} = 2G\dot{\boldsymbol{e}} \tag{7.7}$$

Dimensionless Distance Measures (in stress space)

$$\xi = \begin{cases} p'/p'_{rev} & for\ \ p' < p'_{rev} \\ p'_{rev}/p' & for\ \ p' \geq p'_{rev} \end{cases} \tag{7.8}$$

$$\xi_s = \sqrt{(\boldsymbol{\eta} - \boldsymbol{\eta}_{rev}) : (\boldsymbol{\eta} - \boldsymbol{\eta}_{rev})} \tag{7.9}$$

where the subscript "rev" refer to the latest stress reversal point, which are treated as internal variables.
Definition of Tangential Elastic Moduli

$$\frac{K}{p_{atm}} = \frac{(1+e)}{e\rho_r}\left(\frac{p'}{p_{atm}}\right) \ where\ \rho_r = D(1-\xi^r) + \frac{1+\omega_s\xi_s}{C_b}\left(\frac{p'}{p_{atm}}\right)^{2/3} \tag{7.10}$$

$$\frac{2G}{K} = \begin{cases} \dfrac{2\,G_{\max}/K_{\max}}{1+\omega\xi_s} & for\ p' < p'_{rev} \\ \dfrac{2\,G_{\max}/K_{\max}}{1+\omega\xi\xi_s} & for\ p' \geq p'_{rev} \end{cases} \quad ; \quad \frac{2G_{\max}}{K_{\max}} = 3\left(\frac{1-2\mu_0}{1+\mu_0}\right) \tag{7.11}$$

where C_b and μ_0 are elastic parameters and D, r, ω and ω_s material constants defining the hysteresis response, cf. Section 7.8 and Chapter 8.
Strain amplitudes

$$\chi^2 = \begin{cases} {}^{\Delta l}\varepsilon_{vol}{}^2 & for\ \dot{\boldsymbol{\varepsilon}} \neq 0\ drained\ conditions \\ {}^{\Delta l}e : {}^{\Delta l}e & for\ \dot{\boldsymbol{\varepsilon}} = 0\ undrained\ conditions \end{cases} \tag{7.12}$$

Loading Conditions and Stress Reversal Point (SRP)

$$\chi\dot{\chi} = \begin{cases} {}^{\Delta l}\varepsilon_{vol}\dot{\varepsilon}_{vol} & for\ \dot{\boldsymbol{\varepsilon}} \neq 0 \\ {}^{\Delta l}e : \dot{e} & for\ \dot{\boldsymbol{\varepsilon}} = 0 \end{cases} \tag{7.13}$$

7.2.3 Bounding surface plasticity

Loading conditions

$$KQ_I\dot{\varepsilon} + 2G\boldsymbol{Q}_I : \dot{\boldsymbol{e}} \begin{cases} \geq 0\ Loading \\ < 0\ Unloading \end{cases} \tag{7.14}$$

where $\mathbf{Q}_I$ is the gradient of the bounding surface at the image point, I.

Elasto-plastic modulus and Flow Rule

$$\begin{aligned} \boldsymbol{P} &= \boldsymbol{P}_I(1-g_1) + \boldsymbol{P}_0 g_1 \quad ; 0 \leq g_1 \leq 1 \\ H &= \langle H_I \rangle + H_0 g_2 \quad ; g_2 \geq 1 \end{aligned} \tag{7.15}$$

where $\boldsymbol{P}_0$ is the value of $\boldsymbol{P}$ at first yield. H_0 defines transition to the Limited Compression Curve, *LCC*, and g_1 and g_2 are mapping functions describing the relative position of the current stress and image stress state. <> are the Macuaulay brackets. i.e. $\langle A \rangle = A$ if $A>0$ and 0 otherwise.

Mapping rules

$$P_0 = -2\left|\boldsymbol{\eta} - \boldsymbol{b}\right|\left|\frac{\boldsymbol{s}}{\alpha}\right| \quad ; \quad \boldsymbol{P}'_0 = \boldsymbol{P}'_I \tag{7.16}$$

$$H_0 = \left(\frac{\rho_r}{\boldsymbol{\rho}_c - \rho_r}\right) hK_{\max I}\left|\boldsymbol{Q}_I\right|\left|\boldsymbol{P}_I\right| \tag{7.17}$$

$$g_1 = \frac{\alpha' - \alpha'_0}{\alpha' - \alpha'_{0i}} \tag{7.18}$$

$$g_2 = \frac{g_1}{1 - g_1}\left(1 - \frac{\boldsymbol{\eta} : \boldsymbol{\eta}}{c^2}\right)^{1/2} \tag{7.19}$$

where h is a material property, α' is the size of the bounding surface and α'_0, α'_{0i} are the sizes of the current load surface and the load surface at first yield, respectively.

7.3 Yield surface and Failure surface

Failure conditions in *MIT-S1* are represented by an isotropic function proposed by Matsuoka and Nakai (1974). If the stresses are transformed to principal stresses, this surface can be visualized, Figure 7.2. The failure surface is denoted *MN* and compared with Mohr-Coulomb's failure surface, *MC*.

The failure surface is given by the Equation

$$f = I_3 + \frac{\cos^2 \phi'_{cs}}{9 - \sin^2 \phi'_{cs}} I_1 I_2 = 0 \tag{7.20}$$

where I_1, I_2 and I_3 are stress invariants previously described in section 3.2.4. A detailed description how this expression is transfeered to the measures used in the *MIT-S1* model is given by Kavvadas (1982).

As can be seen in Figure 7.2, the shear strength from an axi-symmetric case is lower than if all three principal stresses are different, e.g. plane strain conditions or non-horizontal soil layers. The *MN* surface encloses the *MC* surface, and the two only coincide when two principal stresses are identical.
Note: The definition of Mohr-Coulomb's failure criteria is that the shear strength is constant, regardless the intermediate principal stress. The axi-symmetric case defines the shear strength in the corners of the *MC* hexagon. In both the *MC*- and *MN*- failure surface, $\phi'_{cs,\,comp}$ equals $\phi'_{cs,ext}$.

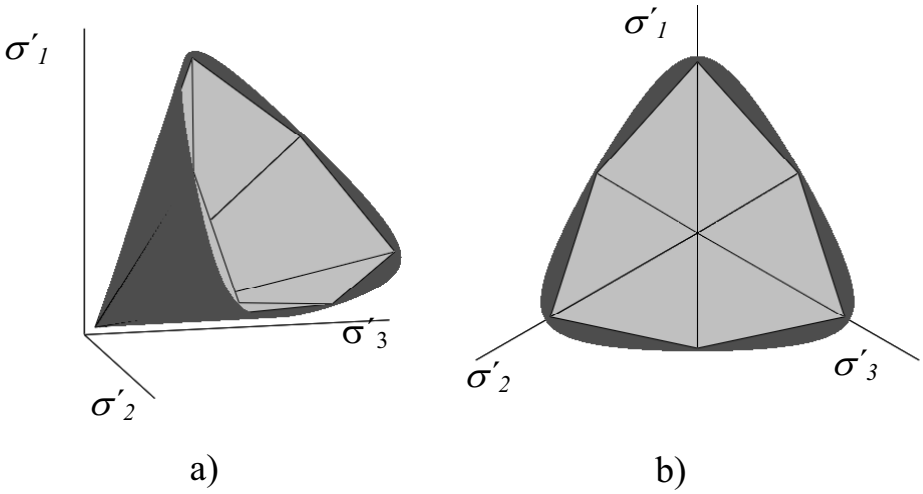

Figure 7.2: Visualisation of the failure surface used in the MIT.S1 model. (Dark grey failure surface in MIT-S1, Light grey failure surface in accordance with Mohr-Coulomb)
a) 3D plot
b) Deviatoric shear plane

For deviatoric loading under plane strain conditions, starting from isotropic conditions, the stress path will reach the failure surface at different locations, depending on the value of Poission´s ratio, Figure 7.3 a).

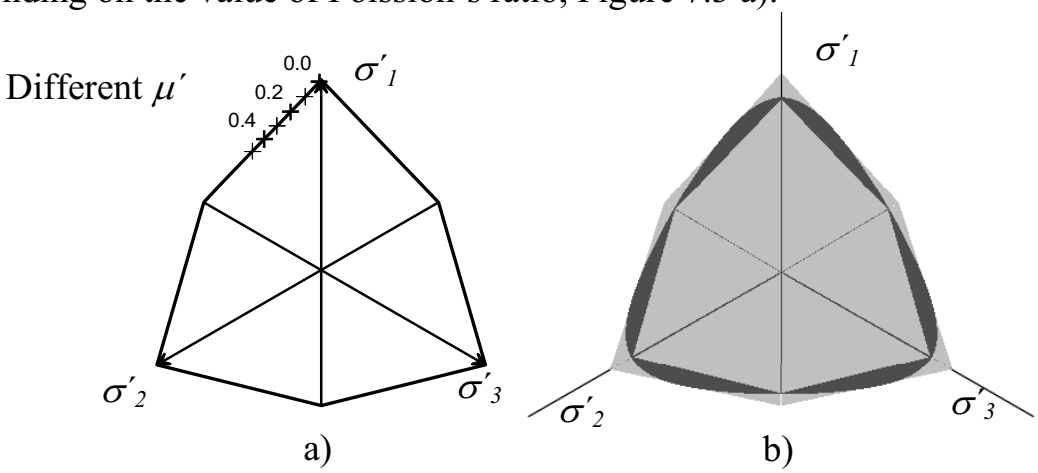

Figure 7.3: Visualization of the increase in shear strength during plane strain conditions.
a) Stress paths in the deviatoric plane during shear with plane strain conditions. The shear loading starts from isotropic conditions. Plot showing the points of impact on the failure surface in relation to different Poisson's values, when exposed for compression.
b) The Inner Mohr-Coulomb surface and the MIT-S1 failure surface have the same ϕ'_{cs} (30°) and the outer MC- surface, which is tangential to the failure surface used in MIT-S1, has a ϕ'_{cs} of 34° which is an increase in shear strength of 12%.

The *MIT-S1* model is capable of capturing the increase in shear strength caused by the stress paths differing from those developed under axi-symmetric conditions, which is an effect of the intermediate principal stress. Vaid and Campanella (1974) showed that the ϕ'_{cs} increase in Haney Clay is 6% in compression and 1.5% in extension under plane strain conditions relative to axi-symmetric conditions. Please note that $\phi'_{cs\ ext.}$ is 13% higher than $\phi'_{cs\ comp}$. In the case of sands, the ϕ'_{cs} increase is in the order of 10% if plane strain conditions are compared to the results from axi-symmetrical tests (Ochiai and Lade, 1983).

In clay exposed to shear the increase in ϕ'_{cs} is of minor significance. Instead, the effect of boundary conditions on the undrained shear strength, s_u, is important. In *MIT-S1*, s_u is governed primarily by the bounding surface, see Figure 7.4 and Figure 7.5. For plane strain conditions Vaid and Campanella (1974) reported a ratio between plane strain compression and axi-symmetrical compression, $s_{u,\ comp\ PS}/s_{u,\ comp\ axi\text{-}symm}$, of 1.10 and for extension, $s_{u,\ ext\ PS}/s_{u,\ ext\ axi\text{-}symm}$, where the ratio was 1.26. The bounding surface (yield surface for normally consolidated clays) is given by Equation (7.21).

$$
\begin{aligned}
f &= (\boldsymbol{s} - p'\boldsymbol{b}) : (\boldsymbol{s} - p'\boldsymbol{b}) - \zeta^2 p'^2 \left(1 - \left(\frac{p'}{\alpha}\right)^m\right) = 0 \\
\zeta^2 &= c^2 + \boldsymbol{b} : \boldsymbol{b} - 2\boldsymbol{\eta} : \boldsymbol{b} \\
c^2 &= c_a{}^2 + c_b{}^2 J_{3\eta} \\
c_a{}^2 &= \frac{8\sin^2 \phi'_m}{3 + \sin^2 \phi'_m} \\
c_b{}^2 &= 3 - c_a{}^2/2 \\
J_{3\eta} &= \det|\boldsymbol{\eta}| \\
\alpha &= \sigma'_{vert\ precons}\left(1 + K_0^{nc}\right)/2
\end{aligned}
\tag{7.21}
$$

where all parameters are described in Table 7.1 and Table 7.2 in section 7.2 and 7.6 respectively. The bounding surface is visualized for the stress situation where no external shear forces are present, $\tau_{xy} = \tau_{xy} = \tau_{xy} = 0$, Figure 7.4.

The bounding surface has the shape of a distorted lemniscate[10]. For high overconsolidation ratios the surface has a similar shape to that of the *MN* failure surface, which makes it better for describing the behaviour of highly overconsolidated clays compared to its predecessor, *MIT-E3*. For smaller *OCR* values the surface become more circular round the anisotropic axis, b, defined by the K_0^{nc}-value, this is highlighted in Figure 7.4d-f. In Figure 7.4 the axi-

[10] A lemniscate is a plane curve with a characteristic shape, consisting of two loops that meet at a central point. This shape is used as a mathematical symbol for infinity. Note that the bounding surface only cunists of one of these loops.

symmetric plane is visualized together with some of the stress invariants used in *MIT-S1*.

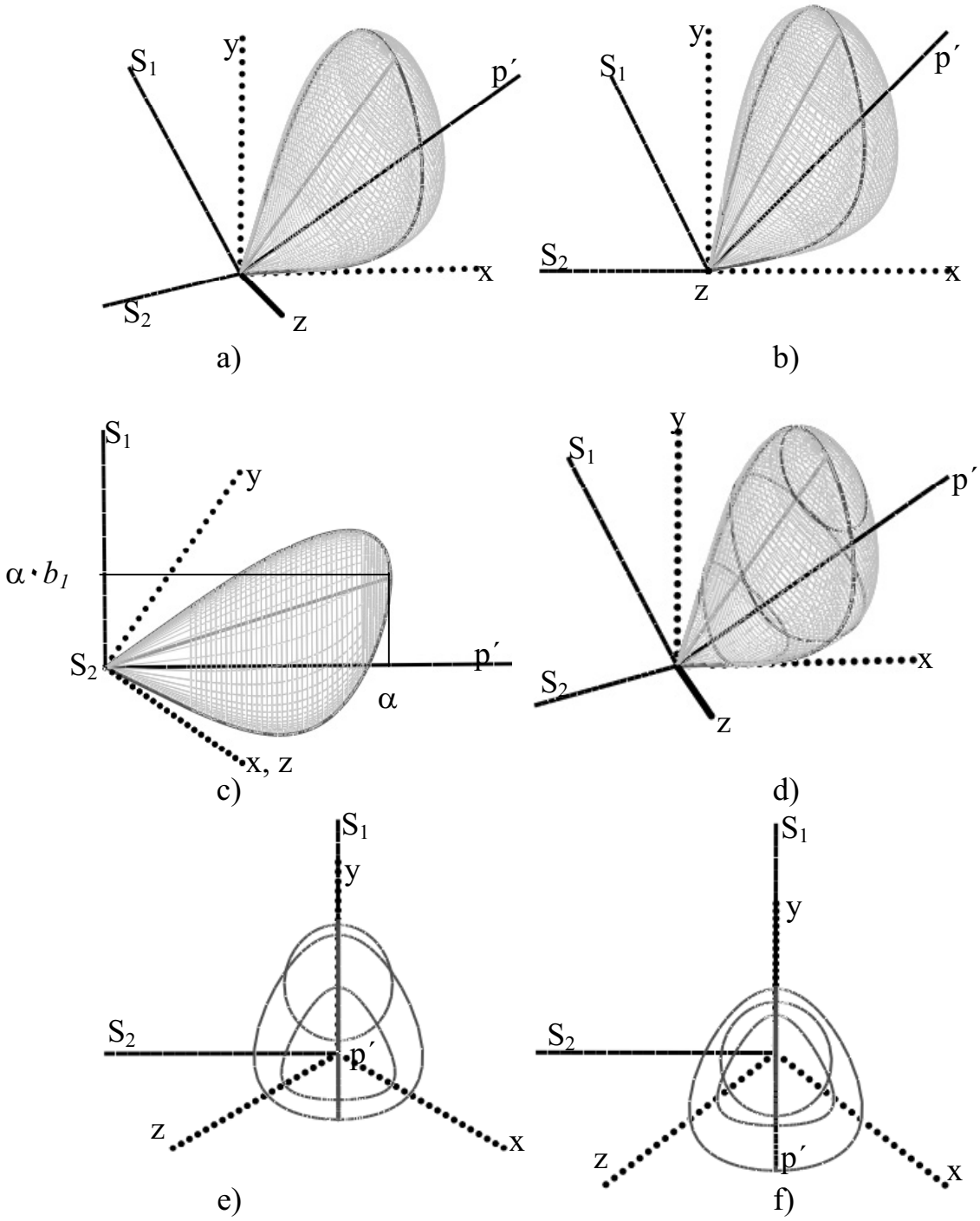

Figure 7.4: The bounding surface for a stress situation with one major vertical stress and two equal horizontal stresses.
a) 3D-plot *b) View along Z-axis*
c) View along S_2-axis (the axi-symmetric plane)
d) 3D-plot with accentuation of geometry for three different mean stresses, p'/p'_{tip} equals 0.3, 0.65 and 0.94.
e) Figure 7.4d along p-axis, (deviatoric plane)
f) Figure 7.4d along b-axis.

Due to practical reasons, the stress state is often presented in the s'-t space, from the perspective of the bounding surface along the z-axis, which can be achieved by a 45 degrees clockwise rotation. In this kind of visualization the z-stress often represents the intermediate principal stress. In Figure 7.5 the bounding surface is presented in s'-t space and the red line represents the shape of the surface in the axi-symmetrical plane. From this perspective it is obvious that the undrained shear strength is higher when $\sigma'_z > \sigma'_x$, e.g. plane strain conditions, for a comparison see Figure 7.3.

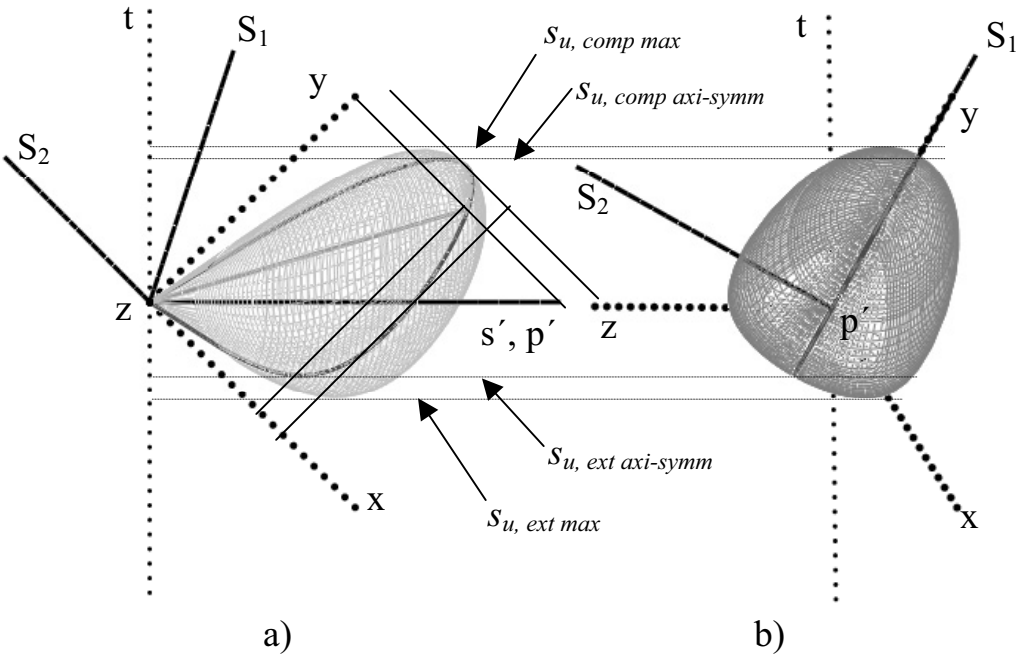

Figure 7.5: Undrained shear strength defined by the bounding surface. The Undrained shear strength from axi-symmetric conditions as well as maximum undrained shear strength dependent on the intermediate principal stress.
a) s'-t space
b) view along s'-axis.

The bounding surface in Figure 7.5 (ϕ_m=40º, m=3, K_0^{nc}=0.55) gives a ratio between $s_{u,comp\ max} / s_{u,comp\ axi\text{-}symm}$=1.08 and between $s_{u,ext\ max} / s_{u,ext\ axi\text{-}symm}$=1.26. These ratios should be compared to the ones found by Vaid and Campanella (1974), which were 1.10 and 1.26 respectively. One should bear in mind that the undrained shear strength is also affected by the location of the starting point within the bounding surface and the fact that the value of Poisson's ratio affects the stress path. Table 7.2 presents the ratio between undrained shear strength and vertical preconsolidation pressure, σ'^{precon}_{vert}, for different loading conditions.

Table 7.2: Ratio between undrained shear strength and vertical preconsolidation pressure for different loading conditions.

$s_{u,\ comp\ axi\text{-}symm} / \sigma'^{precon}_{vert}$	$s_{u,\ comp\ max} / \sigma'^{precon}_{vert}$	$s_{u,\ ext\ axi\text{-}symm} / \sigma'^{precon}_{vert}$	$s_{u,\ ext\ max} / \sigma'^{precon}_{vert}$
0.34	0.37	0.19	0.24

One should bear in mind with regard to Figure 7.5 that σ'^{precon}_{vert} differs from what we usually evaluate in laboratory tests. In the *MIT-S1* model, σ'^{precon}_{vert} together with K_0^{nc} defines α, which is the tip of the bounding surface. In laboratory tests the vertical and horizontal preconsolidation pressures are often evaluated as the vertical and horizontal stress tangent to the bounding surface in the *s´-t* space. This is illustrated in Figure 7.6.

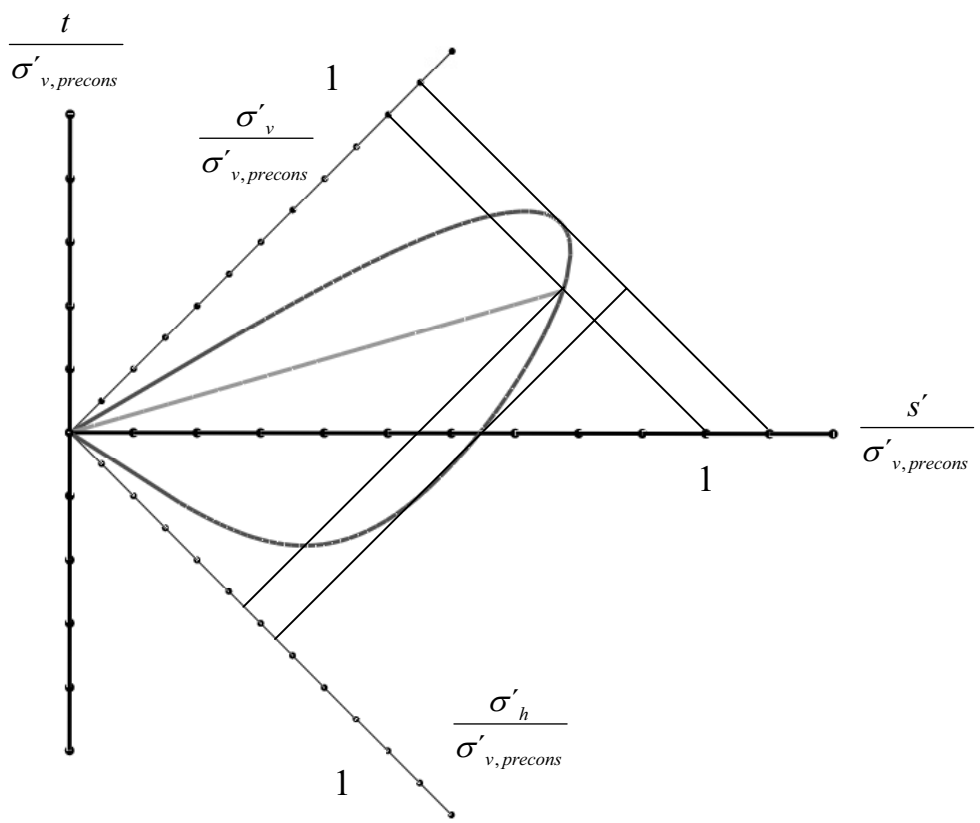

Figure 7.6: Visualization of the boundary surface in s´-t space. (ϕ_m=40°, m=3, K_0^{nc} =0.55)

If undrained compression and extension tests are simulated for a normally consolidated clay, with the input parameters ϕ_m=40°, m=3, K_0^{nc}=0.55, the stress path will follow the bounding surface. According to Swedish practice, the

evaluated vertical and horizontal preconsolidation pressure will be 10% and 18% higher than the given input values. The ratio between σ'^{precon}_{hor} and σ'^{precon}_{vert} will increase from 0.55 to 0.59.

When generating the initial stress situation in a soil profile, one should bear in mind that the stress path for undrained compression differs from what is expected from Swedish practice. As mentioned in Section 6.4, different methods of evaluating the preconsolidation pressure exits, (Casagrande, 1936; Becker *et al.*, 1987). These methods have to be used under the same conditions as they were developed and calibrated. The Swedish method for determining vertical preconsolidation pressure have to be made at a slow deformation rate calibrated against the clay behaviou and the method proposed by Casagrande (1936) requires 24 hours stepwise loading tests. The *MIT-S1* model, in common with most other constitutive models, was developed by people who are active in areas where the Casagrande tradition is very strong. On the other hand, the use of the CRS-equipment has spread, without using the Swedish method (Sällfors, 1975) for evaluation of σ'^{precon}_{vert} or other methods calibrated against field data. Using Casagrandes method (1936) for the estimation of σ'^{precon}_{vert} combined with *MIT-S1* model uncritically will lead to two differences, which augment one another, as illustrated in the following example.

According to Swedish practice σ'^{precon}_{vert} is evaluated to 100 kPa. If the same test result is evaluated according to the method proposed by Casagrande or by Becker, σ'^{precon}_{vert} may increase by a few percent. If this method is used for generating the stress situation with the *MIT-S1* model and the vertical preconsolidation pressure is evaluated as the maximum vertical stress during an undrained compression test, the value will rise by a further 10%. As can be seen from Figure 7.6 and Table 7.2, the empirical relations for Swedish clays, with w_L*=50-70%*, are almost fulfilled if the preconsolidation pressure evaluated from the Swedish practise is used as a start value in the *MIT-S1* model with $\phi_m=40^o$, $m=3$, $K_0^{nc}=0.55$ (Skredkommissionen, 1995).

7.4 Hardening laws and flow rules

The *MIT-S1* model contains two hardening laws, one controlling the size and the other the orientation of the bounding surface.

The rotational hardening law is described by equation (7.22). It is based on the general concept that the principal directions rotate towards the principal stresses.

$$\dot{\boldsymbol{b}} = \psi \frac{(1+e)}{e\alpha}\left(\frac{r_x}{m}\left\langle Q\dot{\varepsilon}^p\right\rangle + r_y\left|\boldsymbol{Q}':\dot{\boldsymbol{e}}^p\right|\right)(\boldsymbol{\eta}-\boldsymbol{b})$$
$$r_x = \left(k^2 + \boldsymbol{b}:\boldsymbol{b} - 2\boldsymbol{\eta}:\boldsymbol{b}\right)/k_a^{\,2}$$
$$r_y = \left(d^2 + \boldsymbol{b}:\boldsymbol{b} - 2\boldsymbol{\eta}:\boldsymbol{b}\right)\left(1-\left(\frac{\alpha}{p}-1\right)\right) \tag{7.22}$$
$$d^2 = d_a^{\,2} + d_b^{\,2} J_{3\eta}$$
$$d_b^{\,2} = 3 - c_a^{\,2}/2$$
$$d_a^{\,2} = \frac{2\left(1-K_0^{nc}\right)^2}{1+K_0^{nc}+\left(K_0^{nc}\right)^2}$$

In Equation (7.22) ψ is a material constant defining the rate of change in anisotropy and therefore the rate at which the soil erases the memory of its compression history. Q is the load direction for stresses located on the bounding surface and is given by the gradient, Equation (7.23).

$$\boldsymbol{Q} = \frac{\partial f}{\partial \boldsymbol{\sigma}} = \begin{Bmatrix} \dfrac{\partial f}{\partial p} \\ \dfrac{\partial f}{\partial \boldsymbol{s}} \end{Bmatrix} = \begin{Bmatrix} Q \\ \boldsymbol{Q}' \end{Bmatrix} \tag{7.23}$$

The change in size of the boundary surface is given by equation (7.24).

$$\frac{\dot{\alpha}}{\alpha} = \frac{(1+e)\dot{\varepsilon}^p}{e\left(\rho_c - \rho_r\right)} - \frac{2\cdot\boldsymbol{b}:\dot{\boldsymbol{b}}}{a^2 + \boldsymbol{b}:\boldsymbol{b}}$$
$$a^2 = 24\left(\frac{\sin\phi'_{cs}}{3-\sin\phi'_{cs}}\right)^2 \tag{7.24}$$

These two hardening laws control the size and shape of the bounding surface, e.g. if a soil sample with $K_0^{nc} \neq 1.0$ is loaded hydrostatically, the bounding surface will increase and become more and more symmetric round the hydrostatic axis (b_1 decreases from $6^{0.5}(1-K_0^{nc})/(1+2K_0^{nc})$ to 0). If the same sample is exposed to 1D compression after hydrostatic loading, the bounding surface will gradually revert to its original shape.

Plastic strains are described by a non-associated flow rule; this means that the developed plastic strains do not follow the direction of the boundary surface gradient, **Q**. The direction of the plastic flow is given in equation (7.25).

$$P = (k^2 - \boldsymbol{\eta} : \boldsymbol{\eta})\frac{p'}{\alpha}$$

$$\boldsymbol{P}' = xP\boldsymbol{\eta} + |\boldsymbol{\eta}|\varsigma^2 \frac{\boldsymbol{Q}'}{\alpha} \tag{7.25}$$

$$x = \left(\frac{\rho_c}{\rho_c - \rho_r}\right)\left(\frac{1}{3}\left(\frac{1+2K_0^{nc}}{1-K_0^{nc}}\right) - \frac{K}{2G}\left(\frac{\rho_r}{\rho_c}\right)\right)$$

This Equation fulfils two important criteria:

a. Shearing at the critical state leads to no further change in volume.

b. 1D compression of normally consolidated clay will develop plastic strains along the axis defined by K_0^{nc}.

7.5 Bounding surface plasticity

The use of a bounding surface will create plastic strains in all kinds of loading, even within the bounding surface. The distance to the bounding surface controls the amount of plastic strains, according to mapping rules Equation (7.14)-(7.19). The bounding surface is scaled down to pass through the actual stress point. This surface is often denoted “first yield surface”. The direction of the plastic strains is the same as if the stress point were located on the bounding surface. The big advantage of using a bounding surface instead of an ordinary yield surface is among other things:

- Shear induced pore water pressure is obtained for undrained shearing.
- The transition to normally consolidated behaviour is smooth.
- Effects such as hysteresis are simulated for a closed unloading reloading cycle.

7.6 Input parameters

To describe a cohesive soil the model contains 13 parameters, which are presented in Table 7.2 and described in the following sections. The model also contains state and internal parameters. For example, the stress situation (σ) and void ratio (e) are state parameters while the size and orientation of the bounding surface (α' and b) are internal parameters.

Table 7.2: An overview of the MIT-S1 parameters describing a saturated, cohesive soil. The tests from which the parameters were evaluated are also indicated.

Test type	Parameter	Physical contribution
Hydrostatic or 1-D compression	ρ_c	Compressibility of normally consolidated clay (log e vs. log σ'_v)
	D	Non linear volumetric swelling behaviour
	r	
	h	Irrecoverable strain
K_0 oedometer or triaxial	K_0^{nc}	K_0 for NC clay
	μ'_0	Poisson's ratio at stress reversal which controls $2G_{max}/K_{max}$
	ω	Non linear Poisson's ratio. Stress path during 1-D unloading
Undrained triaxial shear tests:	ϕ'_{cs}	Critical state friction angle in triaxial compression
OCR=1; CK_0UC	ϕ'_m	Geometry of Bounding Surface. Stress path of undrained CK_0UTC/TE tests (*OCR*=1.0)
OCR=1; CK_0UC	m	
CK_0UC; *OCR*>1	ω_s	Small strain non linearity in shear
	ψ	Rate of evaluation of anisotropy (rotation of bounding surface)
Shear wave velocity /Resonant Column	C_b	Small strain stiffness at load reversal

7.7 Compressibility, (ρ_c, K_0^{nc})

The compressibility, which is the relation between density and stress, of a normally consolidated saturated cohesive soil, is represented by the inclination, ρ_c, in the log p' - log e space. The definition of the Limiting Compression Curve, *LCC*, is based on the assumption that a soil exposed to first time loading, with the same boundary conditions as in the oedometer, has a stress path that follows a straight line defined by a constant value, K_0^{nc}. The mean effective stress is denoted p'. Since the model is rate independent, no effects from second order compression are taken into account.

Note: There are other models that deal with creep, although these effects are probably less significant when dealing with excavations. Due to this simplification care is recommended when creating the real initial stresses, since there is no possibility of calculating the increase in *OCR* caused by creep.

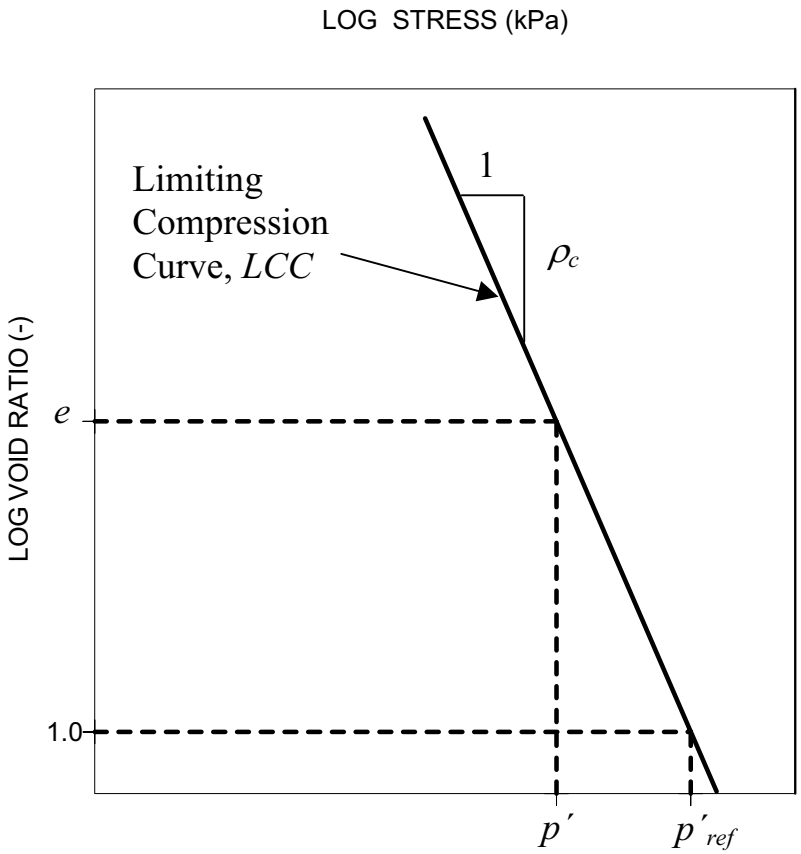

Figure 7.7: Conceptual model of the Limiting Compression Curve, LCC.

The *LCC* is defined as the inclination in a lg p' vs. lg e plot and since K_o^{nc} is defined as constant for virgin compression, the inclination in a lg σ'_{vert} vs. lg e plot will have the same inclination as the *LCC*.

$$\lg_{10}(e) = \rho_c \lg_{10}\left(\frac{p'_{ref}}{p'}\right) = \rho_c \lg_{10}\left(\frac{\sigma_v'_{ref}}{\sigma_v'}\right)$$
$$e = \left(\frac{p'_{ref}}{p'}\right)^{\rho_c} = \left(\frac{\sigma_v'_{ref}}{\sigma_v'}\right)^{\rho_c} \tag{7.26}$$

From an engineering point of view it can be more useful to treat the void ratio as a function of p' and the value when p' equals 1.

$$\lg_{10}\left(\frac{e_{p'=1}}{e}\right) = \rho_c \lg_{10}(p') \qquad \lg_{10}\left(\frac{e_{\sigma_v'=1}}{e}\right) = \rho_c \lg_{10}(\sigma_v')$$
$$e = \frac{e_{p'=1}}{p'^{\rho_c}} \qquad e = \frac{e_{\sigma_v'=1}}{\sigma_v'^{\rho_c}} \tag{7.27}$$

The following relations are then obtained.

$$\frac{e_{\sigma_v'=1}}{e_{p'=1}} = \left(\frac{3}{1+2K_0^{nc}}\right)^{\rho_c}$$
$$\frac{\sigma_{v\ ref}'}{p'_{ref}} = \left(\frac{3}{1+2K_0^{nc}}\right) \tag{7.28}$$

The change in void ratio can be expressed as volumetric strain, ε_{vol}, if the initial void ratio is known, Eq. (7.29)

$$\varepsilon_{vol} = \frac{e_0 - e}{e_0 + 1} \quad \textit{and in the oedometer} \quad \varepsilon_{vertical} = \frac{e_0 - e}{e_0 + 1} \tag{7.29}$$

The relation in Equation (7.27) can be used in combination with Eq. (7.29) to gain an understanding of how the strain will develop at a certain void ratio. In Equation (7.30) and Equation (7.31), σ' can either represent σ'_v or p' while ε represents ε_{vert} or ε_{vol}.

$$\varepsilon = \frac{e_0 - \left(\frac{\sigma'_{ref}}{\sigma'}\right)^{\rho_c}}{e_0 + 1} \tag{7.30}$$

$$\sigma' = \frac{\sigma'_{ref}}{\left(-\varepsilon e_0 - \varepsilon + e_0\right)^{1/\rho_c}} \tag{7.31}$$

The modulus in 1D compression is expressed by Equations (7.32), (7.33) and (7.34).

$$M = \sigma'_{vert} \frac{e_0 + 1}{\rho_c} \left(\frac{\sigma'^{ref}_{vert}}{\sigma'_{vert}}\right)^{-\rho_c} \tag{7.32}$$

$$K = p'_{vert} \frac{e_0 + 1}{\rho_c} \left(\frac{p'^{ref}_{vert}}{p'_{vert}}\right)^{-\rho_c} \tag{7.33}$$

$$G = \frac{1}{2} \sigma'_{vert} \frac{e_0 + 1}{\rho_c} \left(\frac{\sigma'^{ref}_{vert}}{\sigma'_{vert}}\right)^{-\rho_c} \left(1 - K_0^{nc}\right) \tag{7.34}$$

A 1D compression test is performed in the triaxial cell and evaluated according to Swedish practice, Figure 7.8. These tests start from an unloaded specimen. When the horizontal stress is known, the ratio between horizontal and vertical effective stress can be added to the stress – strain curve, Figure 7.9.

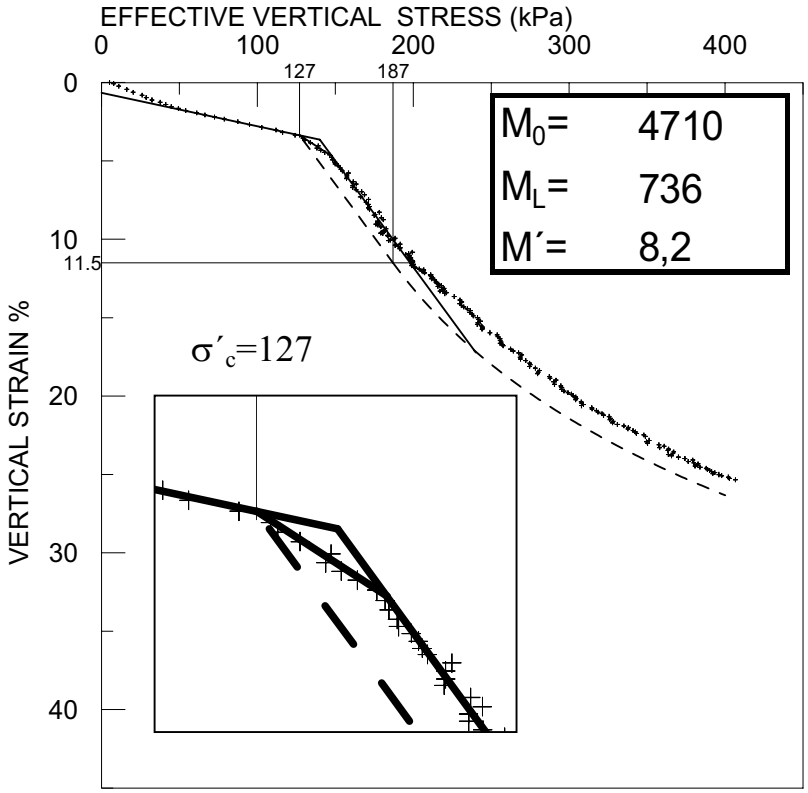

Figure 7.8: 1D compression tests performed in the triaxial cell. Borehole 1/470b, depth 8 metres (Test 1470b 8).

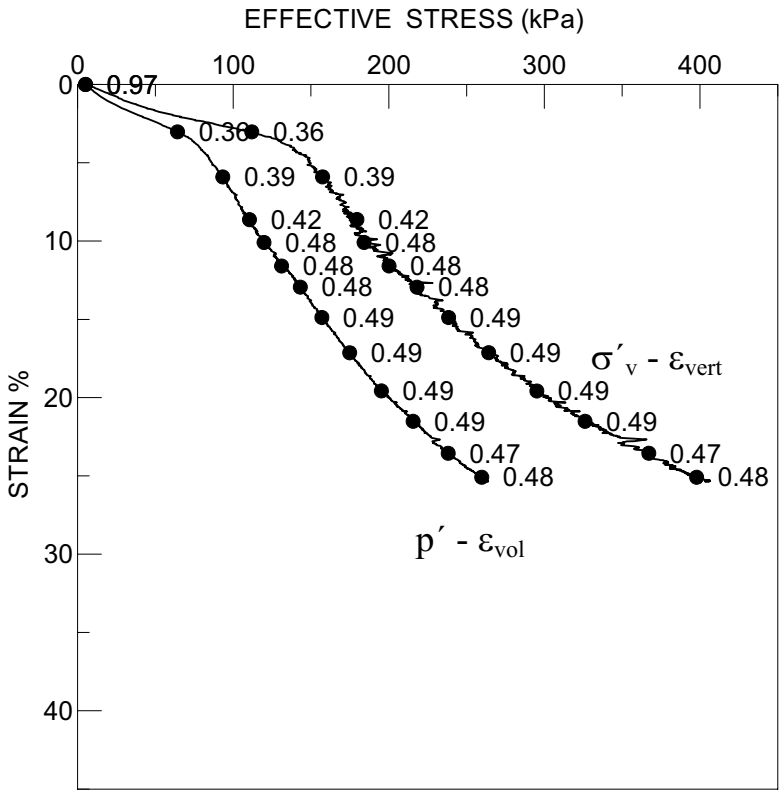

Figure 7.9: Ratio between σ'_h and σ'_v presented as values in stress – strain space for an 1D compression test (Test 1470b 8).

The same test can be presented as a stress path in s' - t space, see Figure 7.10, where the coupling between σ'^{precon}_{vert}, σ'_L and σ'_{hor} is clearly illustrated.

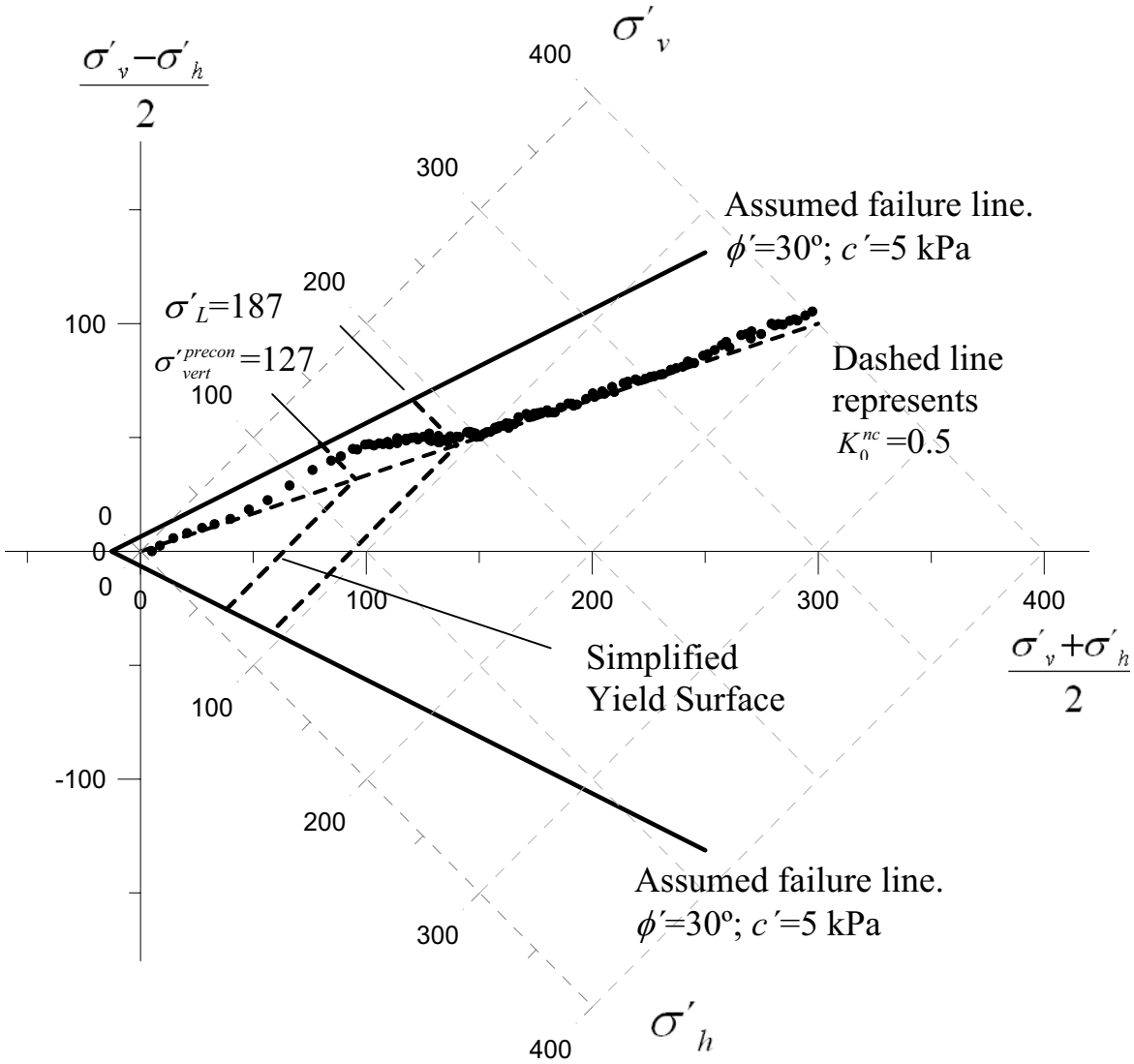

Figure 7.10: 1D compression test (Test 1470b 8) visualized in s' - t space. A simplified yield surface expressed by σ'^{precon}_{vert} and $\sigma'^{precon}_{hor} = \sigma'^{precon}_{vert} K_0^{nc}$ is also illustrated in the figure. The evaluated σ'_L is visualized. As can be seen, σ'_L represents the point at which the stress path reaches the K_0^{nc}-line.

The disadvantage of standard CRS tests becomes quite obvious when the stress path is studied, as the latter will not cross the stress point that is present under field conditions. This will also affect the development of the strain during compression and may contribute to that the evaluated constrained modulus below the preconsolidation pressure being too low compared to the one evaluated in field tests. During the standard CRS test the shear stress ratio is higher than under field conditions. It can also be the reason for the constrained modulus being almost constant before the stress path coincides with the virgin compression line, M_L (Figure 7.11).

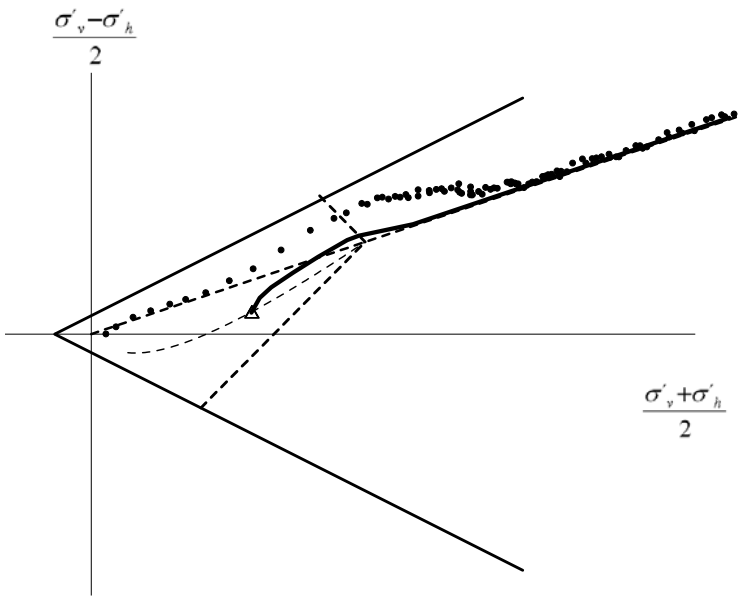

a)

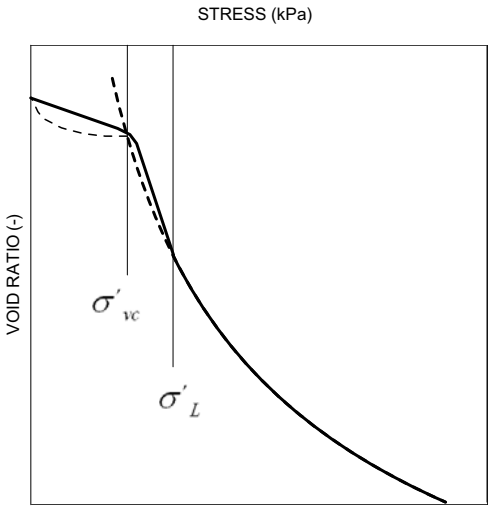

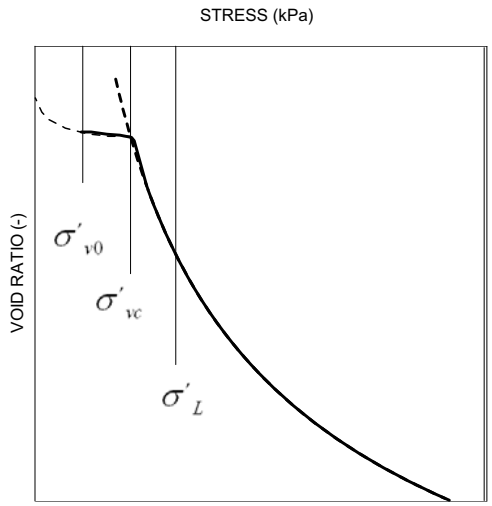

b) c)

Figure 7.11: Differences between an 1D compression test starting from fully unloaded conditions[11] or consolidated to in situ stresses.
a) Stress path from a fully unloaded sample compared with a sketch of a stress path loaded from in situ conditions.
b) Stress vs void ratio for an oedometer test starting from fully unloaded conditions.
c) Stress vs. void ratio for an oedometer test starting from in situ stresses

[11] Complete unloading is probably quite rare, since some negetive pore water pressure always will exit in the sample kepping σ'_{vert} above zero.

If the relation between mean stress and void ratio as described in Equation (7.26) is applied in this test, the following conformity will be obtained, see Figure 7.12.

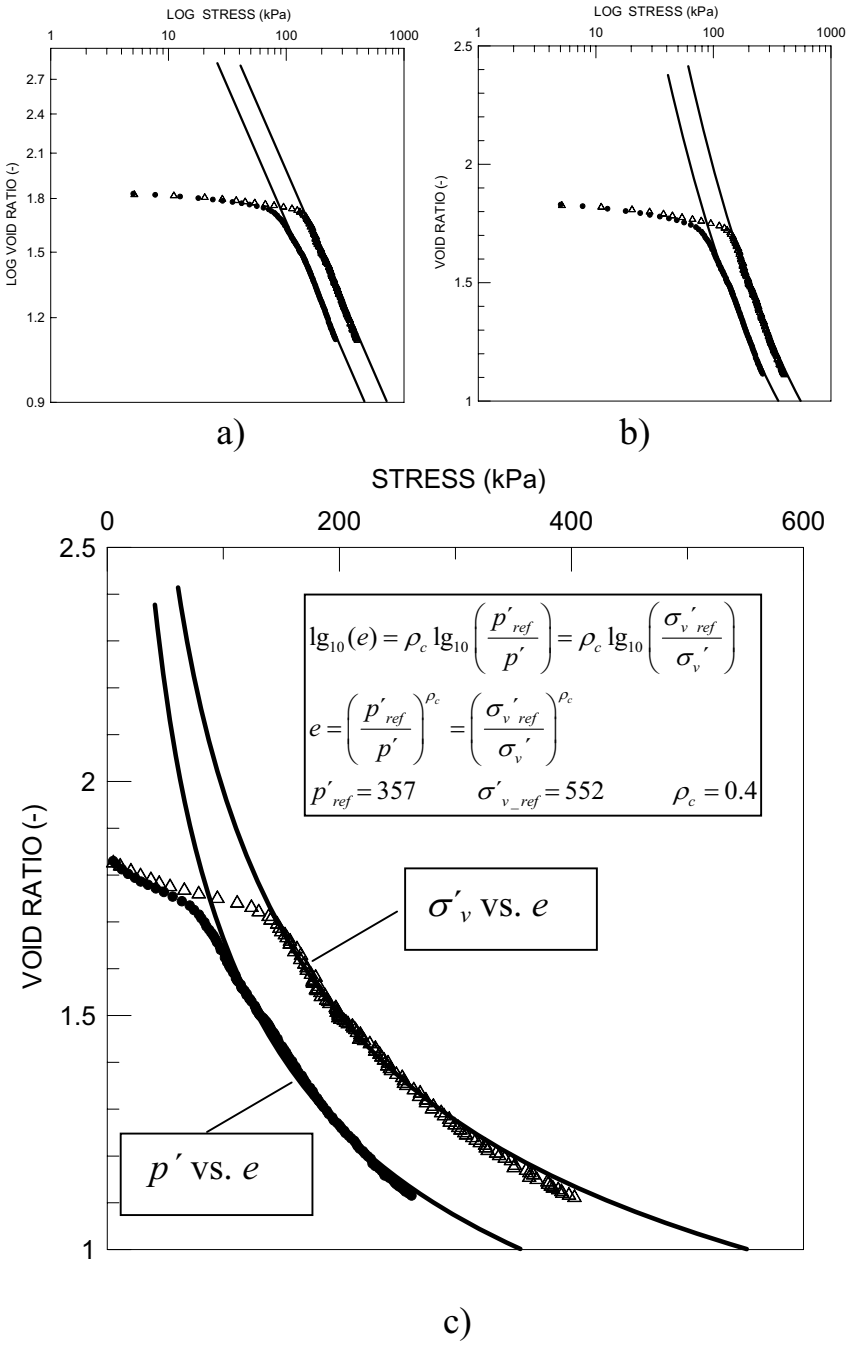

Figure 7.12: Stress vs void ratio from test 1470b_8 is presented in different scales. a)log –log, b) log-lin, c) lin-lin.

In order to predict e.g. the settlement of an embankment, it is easier to visualize how the strain will develop when the load increases. Presented as stress vs. strain we obtain the behaviour seen in Figure 7.13.

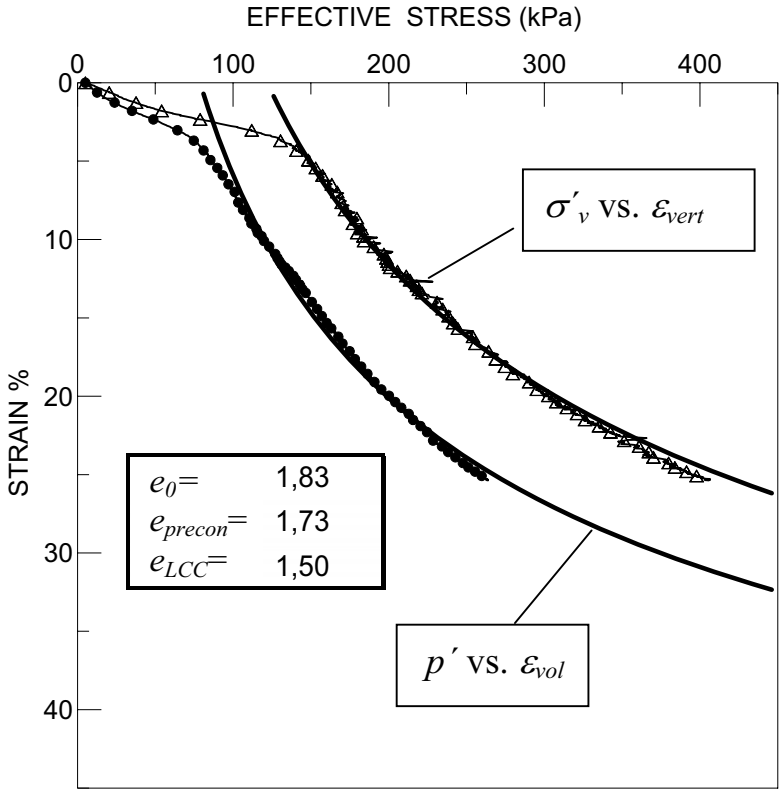

Figure 7.13: Relation between stress –strain from laboratory test 1/470b_8 and the prediction of the MIT-S1 model.

The constrained modulus, *M*, and the compression modulus of the studied example are presented in Figure 7.14 and Figure 7.15.

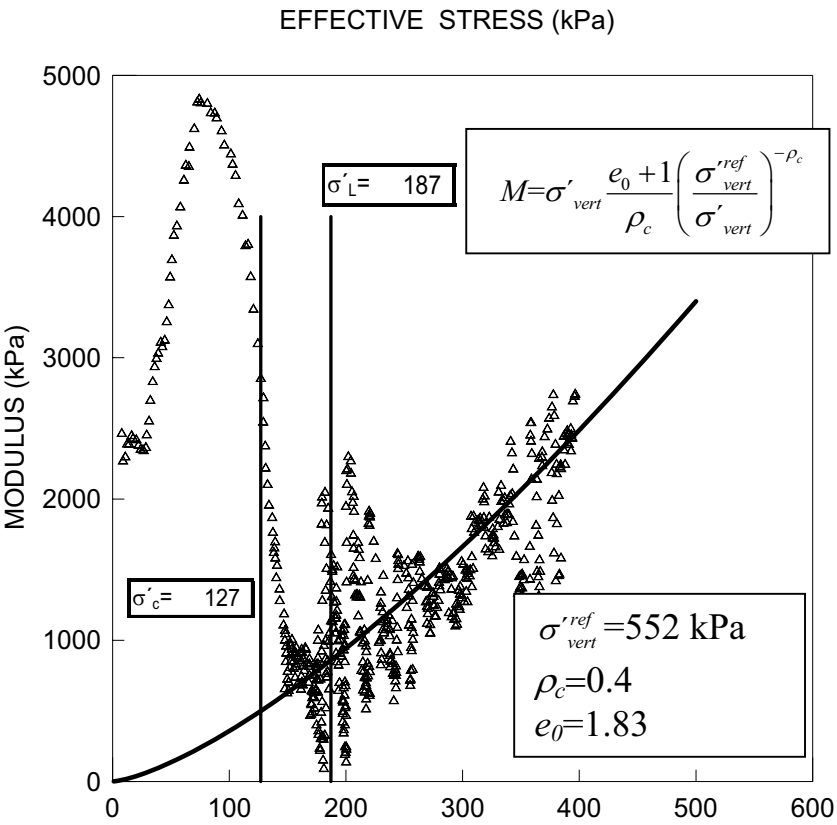

Figure 7.14: Constrained modulus vs. effective vertical stress.

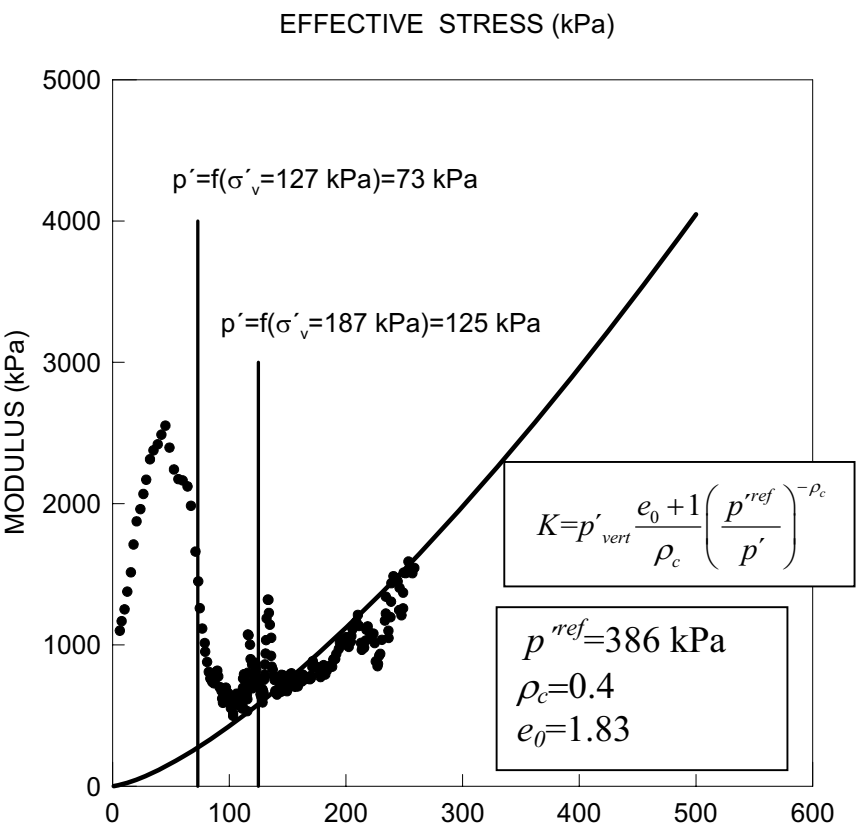

Figure 7.15: Compression modulus vs. mean effective stress.

The modulus can also be expressed as a function of void ratio

$$M=\sigma'^{ref}_{vert}\frac{e_0+1}{\rho_c}e^{\frac{-(1+\rho_c)}{\rho_c}} \tag{7.35}$$

If the soil stratum is homogenous in a way that can be expressed by the same input parameters, Equations (7.32) and (7.35) will yield identical results. This means that the actual preconsolidation pressure and modulus for first time loading can be predicted by studying the water contents or densities.

7.8 Unloading – reloading

Loading and unloading below the preconsolidation pressure are to a great extent dependent on how the actual stress situation has been reached. This is visualized in Figure 7.16 (Note that Pestana (1994), in this figure, uses σ' instead of p' for the mean stress). If a soil sample is unloaded from point D′ it will show a stiffer response compared to one unloaded from point D′′. The opposite is the case for loading.

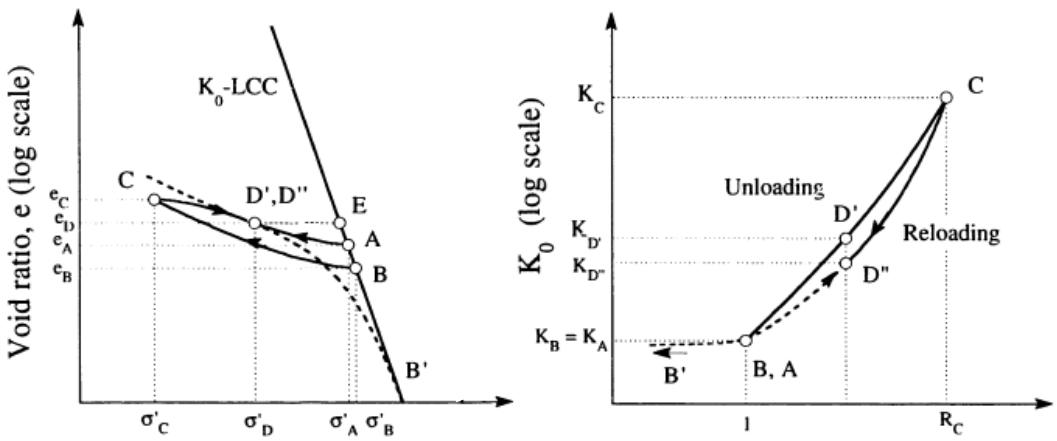

	State Variables at D			Internal Variables at D			
Path	σ'	K_0	e	α'	σ'_{rev}	$^{\Delta l}\varepsilon$	$\alpha'_{\omega i}$
BCD"	σ'_D	$K_{D''}$	e_D	σ'_E	σ'_C	$^{D}\varepsilon - {}^{C}\varepsilon$	σ'_C
A-D'	σ'_D	$K_{D'}$	e_D	σ'_E	σ'_D	$^{D}\varepsilon - {}^{A}\varepsilon$	σ'_D

$R=\sigma'_A/\sigma'$ for path AD′′ and
$R=\sigma'_B/\sigma'$ for path BCD′

Figure 7.16: Initial Values of State Variables for the MIT-S1 model as a function of Past Stress history for K_0-Consolidated Soil, figure 4.29 (Pestana, 1994).

In Figure 7.17 this is illustrated as stress paths in the *s′-t* stress space.

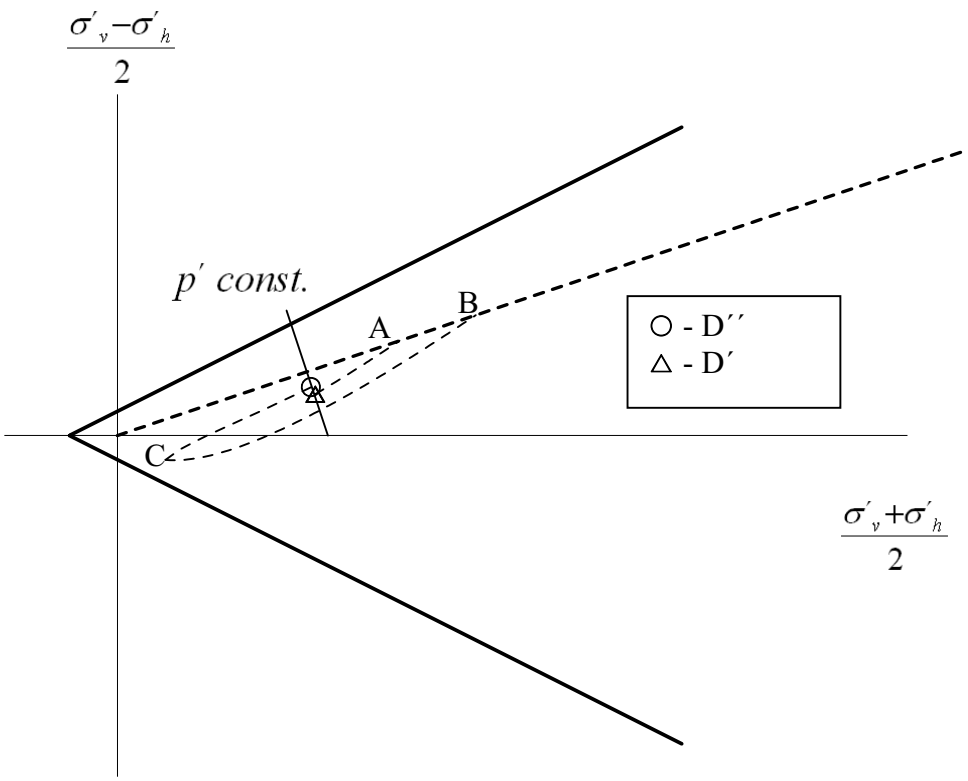

Figure 7.17: Visualization of how different stress paths can yield the same mean stress and void ratio. Please note that the loading and unloading response from point D´ and point D´´ are very different.

In order to keep track of the stress path the *MIT-S1* model contains internal and state variables. Depending on the stress history, this makes it possible to capture the different behaviour at point D. Figure 7.16 can be rearranged to show vertical stress, with the same boundary conditions as in the oedometer, and the result will be almost identical to that shown Figure 7.16, in spite of the fact that the K_0 value differs between point D´ and D´´.

7.8.1 Swelling behaviour

The most widely used compression models for cohesive soils are presented in Equation (7.36) and Equation (7.37) (Casagrande, 1936)

$$\Delta e = C_s \Delta \log_{10}(\sigma'_v) = \frac{C_s}{2.3} \frac{\Delta \sigma'_v}{\sigma'_v} \tag{7.36}$$

$$\Delta e = \kappa \Delta \ln(p') = \kappa \frac{\Delta p'}{p'} \tag{7.37}$$

The parameters are usually evaluated from swelling over one log-cycle. For hydrostatic swelling, Equation (7.36) and Equation (7.37) can be rearranged to

$$C_s = 2.3 \cdot \kappa \tag{7.38}$$

For 1D swelling, the relation in Equation (7.38) is not valid. In order to translate κ to C_s one has to use a given relation between the K_0-value and the *OCR*. In most cases it is convenient to use the expression proposed by Schmidt (1967)

$$K_0 = K_0^{nc} OCR^m \tag{7.39}$$

In this case we can obtain the relation between κ and C_s in Eq. (7.40) where A can usually be set in the range of 1.1 – 1.5. Assuming that Poisson's ratio is constant during swelling, the factor A will be in the range of 1 to 2.

$$\begin{aligned} C_s &= \frac{2.3}{A} \cdot \kappa \\ A &= \frac{\left(1+2K_0^{nc}\right)\left(OCR-1\right)}{OCR\left(1+2K_0^{nc}\right)-1-2K_0^{nc}OCR^m} \end{aligned} \tag{7.40}$$

If the swelling behaviour is assumed to be linear in $\log_{10}(e)$ - $\log_{10}(p')$ the following relations are obtained.

$$\begin{aligned} \frac{\Delta e}{e_{revUL}} &= \left(\frac{\Delta p'}{p_{revUL}'}\right)^{\rho_r} \\ \Delta\varepsilon_{vol} &= -\frac{\Delta e}{e+1} = \frac{e_{revUL}}{e+1}\left(\frac{\Delta p'}{p_{revUL}'}\right)^{\rho_r} \end{aligned} \quad \text{hydrostatic} \tag{7.41}$$

$$\begin{aligned} \frac{\Delta e}{e_{revUL}} &= \rho_{rv}\left(\frac{\Delta\sigma'_v}{\sigma'_{v_revUL}}\right)^{\rho_{rv}} \\ \Delta\varepsilon_{vert} &= -\frac{\Delta e}{e_0+1} = \frac{e_{revUL}}{e_0+1}\rho_{rv}\left(\frac{\Delta\sigma'_v}{\sigma'_{v_revUL}}\right)^{\rho_{rv}} \end{aligned} \quad \text{1D swelling} \tag{7.42}$$

The ratio between ρ_{rv} and ρ_r is in the range of 0.6 to 0.9 and the typical value of the ratio between ρ_{rv} and ρ_c reported in the literature is 0.15 – 0.25, but extreme values 0.08 (Mexico City Clays) and 0.45 (Na-montmorillonite) have also been found. The assumption that the swelling is a straight line in $\log_{10}(e) - \log(p')$ is quite rough. To increase the accuracy the inclination in $\log_{10}(e) - \log(p')$, ρ_r, is described by the function

$$\begin{aligned} \rho_r &= \frac{1}{C_b}\left(\frac{p'}{p_{atm}}\right)^{2/3} + D(1-\xi^r) \\ \Delta\varepsilon_{vol} &= -\frac{\Delta e}{e_0+1} = \frac{e_{revUL}}{e_0+1}\left(\frac{\Delta p'}{p'_{revUL}}\right)^{\left(\frac{1}{C_b}\left(\frac{p'}{p_{atm}}\right)^{2/3}+D(1-\xi^r)\right)} \end{aligned} \tag{7.43}$$

When unloading takes place in an 1D swelling test, additional swelling will occur due to changes in the ratio between shear and mean effective stress. This is incorporated in Equation (7.44)

$$\rho_r = \frac{1+\omega_s \xi_s}{C_b}\left(\frac{p'}{p_{atm}}\right)^{2/3} + D(1-\xi^r) \tag{7.44}$$

$$\xi_s = \frac{3\sqrt{6}\left(K_0 - K_0^{nc}\right)}{\left(1+2K_0\right)\left(1+2K_0^{nc}\right)} \tag{7.45}$$

C_b, D and r are material constants and $\xi = p'/p'_{revUL}$. Parameter C_b controls the stiffness immediately after load reversal.

In Equation (7.44) ω_s is a material constant describing small strain non-linearity in shear. The relation for K_0 in Equation (7.39) can be used to estimate the swelling in a 1D test.

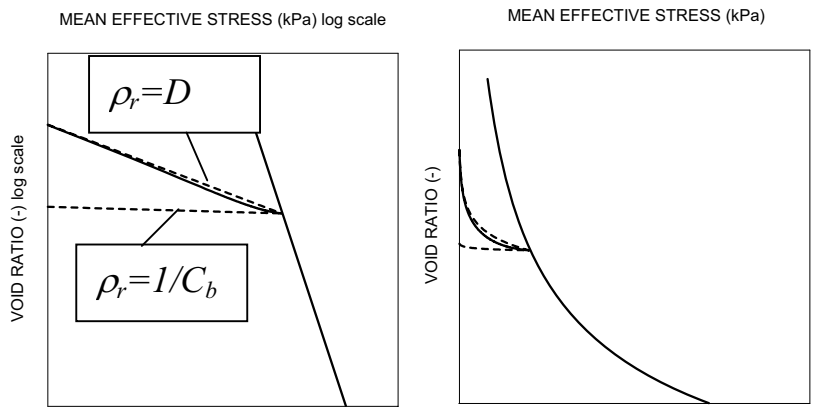

Figure 7.18: Sketch of the Swelling behaviour in two different scales. Dotted lines show the effect of the different terms in Eq. (7.43).

7.8.2 Reloading

During reloading both elastic and plastic strain will occur. The elastic deformations will depend on

$$\frac{\Delta e}{e_{revRL}} = \left(\frac{\Delta p'}{p_{revRL}'}\right)^{\rho_r}$$

$$\Delta\varepsilon_{vol} = -\frac{\Delta e}{e_0+1} = \frac{e_{revRL}}{e_0+1}\left(\frac{\Delta p'}{p_{revRL}'}\right)^{\rho_r} \qquad \text{hydrostatic} \tag{7.46}$$

$$\rho_r = D(1-\xi^r) + \frac{1+\omega_s \xi_s}{C_b}\left(\frac{p'}{p_{atm}}\right)^{2/3} \tag{7.47}$$

In the case of hydrostatic reloading the internal variables ξ and ξ_s will be p'/p'_{revUL} and 0 respectively, see Equation (7.8) and (7.9).

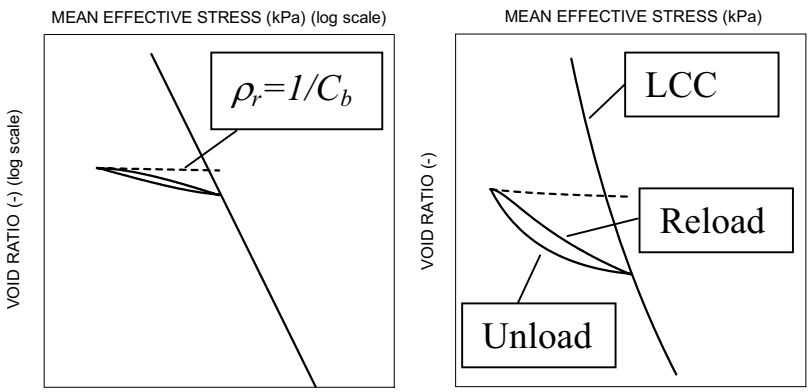

Figure 7.19: Sketch of the Reloading behaviour, elastic part, in two different scales. Dotted lines show the tangent at the point in time at which the reloading starts.

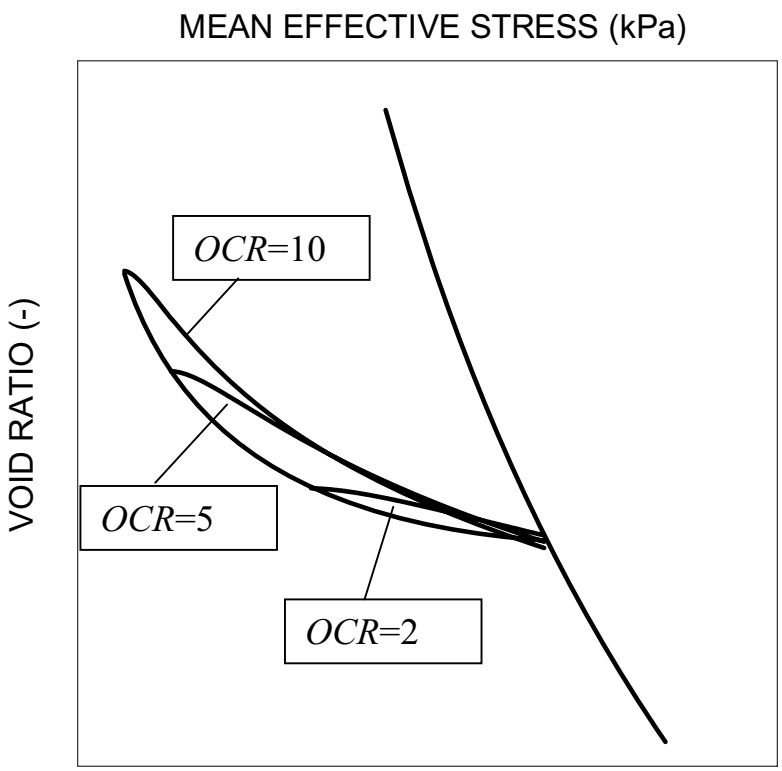

Figure 7.20: Visualization of the impact of the overconsolidation ratio on reloading behaviour.

Incorporation of the bounding effect will yield plastic deformation with an increased ratio between plastic and elastic strain close to the bounding surface. This effect is controlled by Equations (7.6) and (7.15) combined with the mapping rules (7.16) to (7.19). The parameter h controls the plastic strain, Δ^p, developed during a closed unload – reload cycle, see Figure 7.21. The amount of plastic strain decreases in line with an increase of h, h>0.

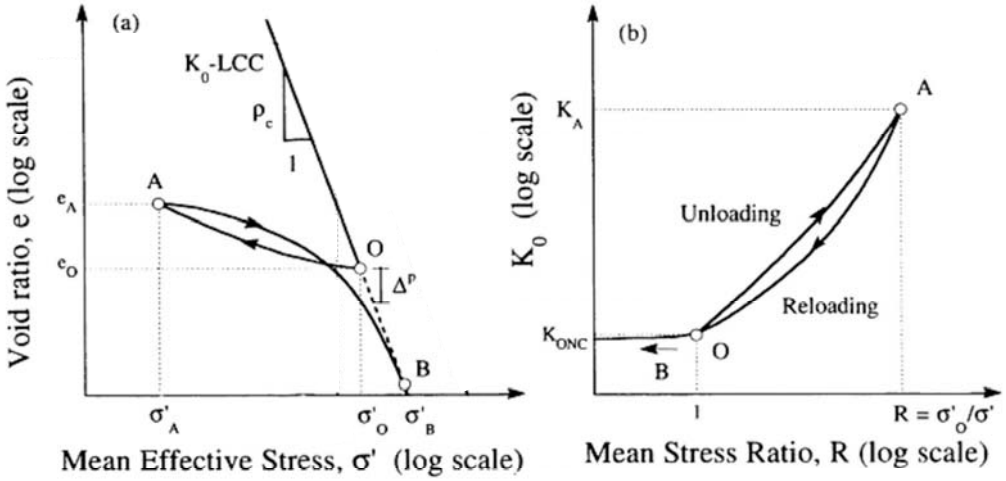

Figure 7.21: Conceptual Model of First Load and Unload Reload used in MIT-S1 for 1-D Compression, figure 4.2 (Pestana, 1994)

8 EVALUATION OF INPUT PARAMETERS TO *MIT-S1*

8.1 Introduction

This section describes the evaluation of the parameters for the *MIT-S1* constitutive model. The Järntorget clay parameters, which were described in Chapters 7 where the formulation of the model is presented, will be evaluated in accordance with the procedure described by (Pestana, 1994; Pestana and Whittle, 1999; Pestana *et al.*, 2002)

8.2 Evaluation procedure

Pestana and Whittle (1999) described the different parameters of the model and how they can be obtained, see Table 8.1. Some of the parameters are quite easy to evaluate, while others need to be fitted in pairs to the laboratory test results.

Table 8.1: Summary of the MIT-S1 model input parameters (Pestana and Whittle, 1999)

Parameter	Physical meaning	Suggested method of evaluation
ρ_c	Compressibility of sand in the *LCC* regime and *VCL* for sedimented clay	Obtain from the NC clay (C_C) standard compressibility index
D	Transitional compression behaviour	Measure 1-D swelling curve
r	Non-linear volumetric swelling and volumetric hysteresis response	Measure 1-D swelling curve
h	Irrecoverable plastic strain for unload-reload cycle	Calibrate from 1-D reload curve
K_0^{nc}	Lateral earth pressure ratio in the *LCC* regime	Measure for *NC* clays following *SHANSEP* consolidation (Ladd *et al.*, 1977)
C_b	Small strain elastic compressibility (initially after load reversal)	Derive from elastic wave velocity measurements, e.g. bender elements
μ'_0	Poisson's ratio at load reversal	Measure effective stress path during 1-D swelling from *LCC* state (to *OCR* 5-10)
ω	Non-linearity in Poisson's ratio	Measure effective stress path during 1-D swelling from *LCC* state (to *OCR* 5-10)
ϕ'_{cs}	Large strain (critical state) friction angle	Measure in undrained triaxial compression shear tests

Parameter	Physical meaning	Suggested method of evaluation
ϕ'_m	Apex angle of bounding surface, shown in Figure 8.30.	Undrained strength ratios in triaxial compression and extension tests at *OCR*=1
m	Shape of bounding surface	Shape of effective stress paths in CK_0UC, CK_0UE tests at *OCR*=1
ω_s	Small strain non-linearity in shear	Local measurement of small strain (0.001%≤γ≤0.1%) shear stiffness or modulus degradation
ψ	Rate of evolution of anisotropy due to stress history	Measure undrained stress strain behaviour in undrained shear (CK_0UE and/or CK_0UC) at moderate to large shear strains (5%≤γ≤20%)

The parameters in the *MIT-S1* are linked and should therefore be evaluated in a specific order. Figure 8.1 shows how these parameters are linked and the laboratory tests from which they were evaluated. The following sections are in the same order as the outline presented in Table 8.2

Table 8.2: Procedure for the evaluation of the MIT-S1 parameters.

- 1D compression test, CRS, will yield ρ_c
- 1D compression test, triax, will yield K_0^{nc}
- Bender element test will yield C_b
- 1D unloading test, triax, will yield μ'_0, ω
- 1D unloading test, triax and/or CRS, will yield D and r.
- The stress path from CK_0UC and CK_0UE at *OCR*=1.0 will yield ϕ'_{cs}, ϕ'_m and m
- The stress strain relation from CK_0UC and CK_0UE at different *OCR* will yield ω_s and ψ
- 1D reloading test, triax and/or CRS, will yield h

Having evaluated all the soil parameters at the Järntorget test site, the model was used to verify the known behaviour revealed by the UK_0DSS-test. The model was thereafter employed to increase knowledge of how stress rotation occurs in a UK_0DSS-test and to verify how well it matches the Swedish empirical data for undrained shear strength and 1D unloading and reloading.

In Sweden most empirical relations of clay behaviour are linked to the liquid limit, w_L, which is not an *MIT-S1* input parameter. Swedish clay shows e.g. $s_{u\,DSS}$ and $s_{u\,ext}$ decreases in line with a decrease in w_L (note that this is not the cases for

$s_{u\ comp}$). The final section provides some brief comments on the evaluated parameters as well as several recommended values for other Swedish clays.

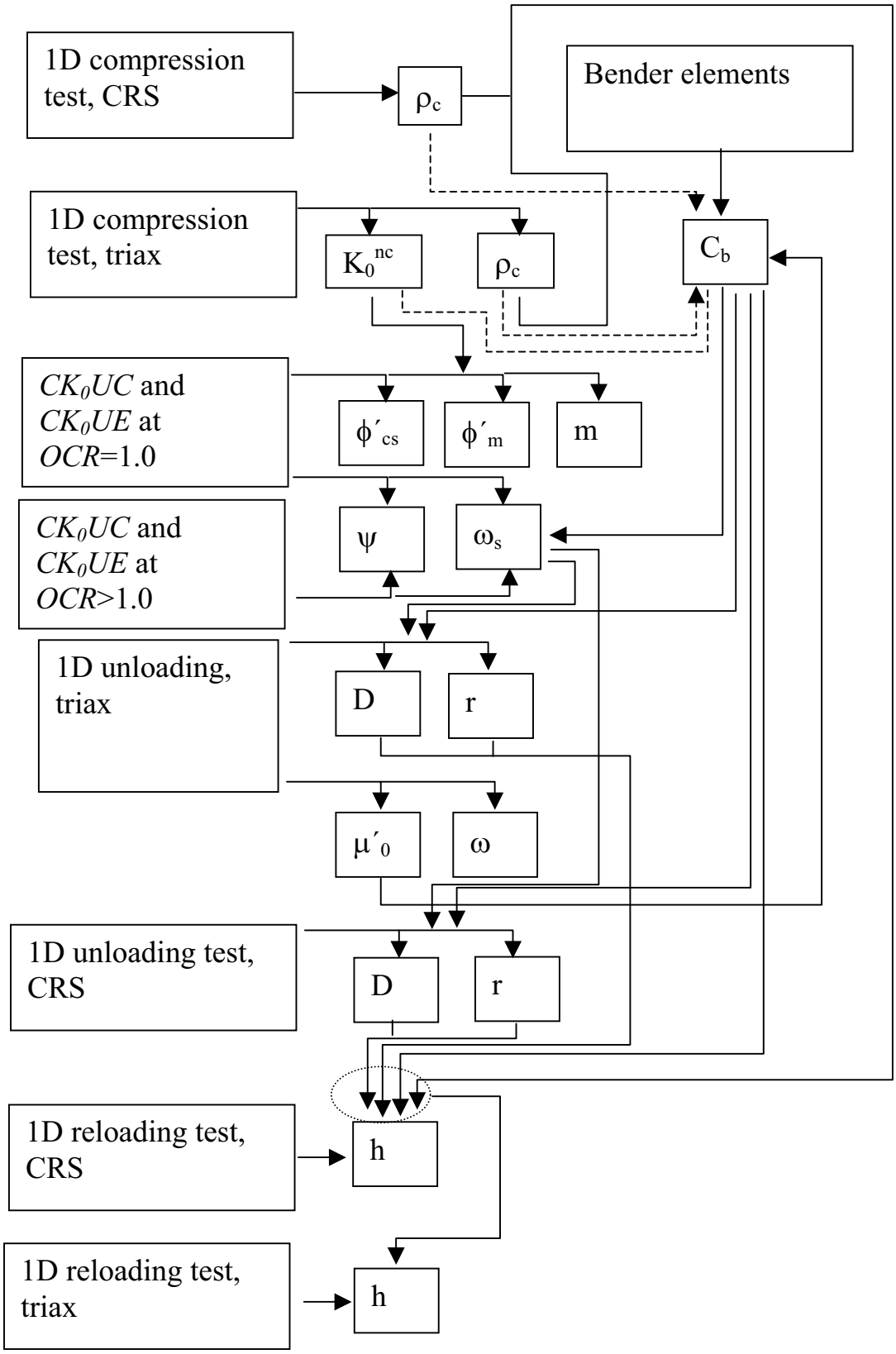

Figure 8.1: Block diagram showing the different tests and the parameters derived from them.

8.3 Evaluation of compressibility behaviour, (ρ_c, K_0^{nc})

Oedometer tests and K_0-test in the triaxial were performed to evaluate compression characteristics. As a consequence of the result, the soil strata were divided into two layers. The change in characteristics was chosen to begin at level +0.5 at an average depth of approximately 12 meters at the site. Based on Figure 8.2-Figure 8.6, the inclination of ρ_c was set at 0.4 for the upper and 0.35 for the lower layer. K_0^{nc} was verified to be in the range of 0.45 to 0.55, based on Figure 8.7-Figure 8.12. This agrees with the result presented by Sällfors (1975) for Bäckebol clay, which comes from a site 10 km north of Järntorget. The value obtained by Sällfors (1975) was 0.53. In the following, K_0^{nc} is set at 0.55.

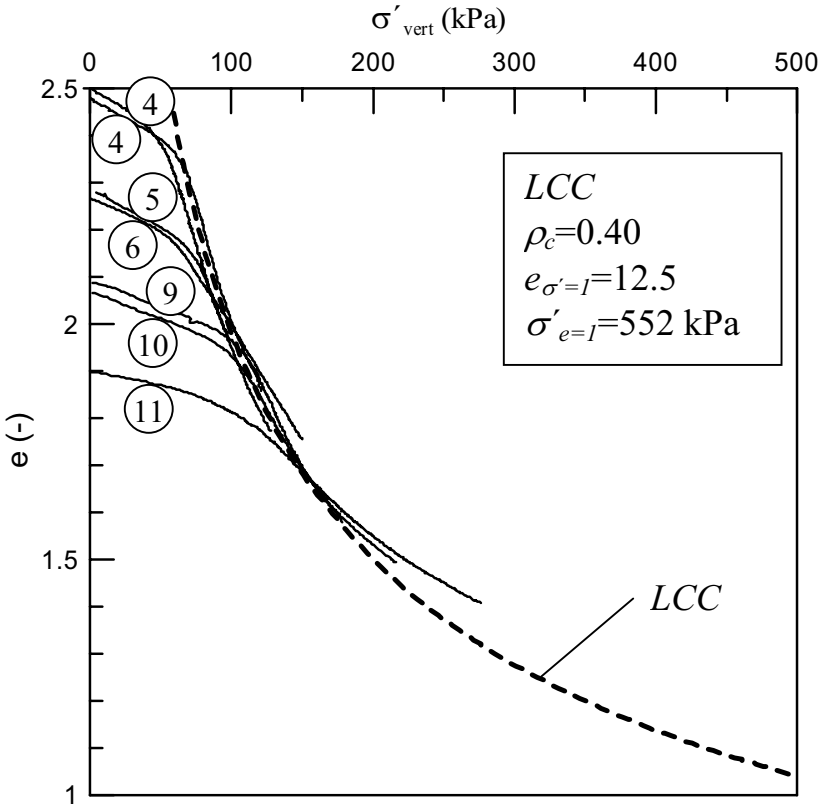

Figure 8.2: 1D compression results from CRS tests above the +0.5 level in section 1/430 north, linear scale.
Circles in the graph denote the depth from which each sample was taken.
Dashed line: best fit for LCC according to Eq. 7.26.

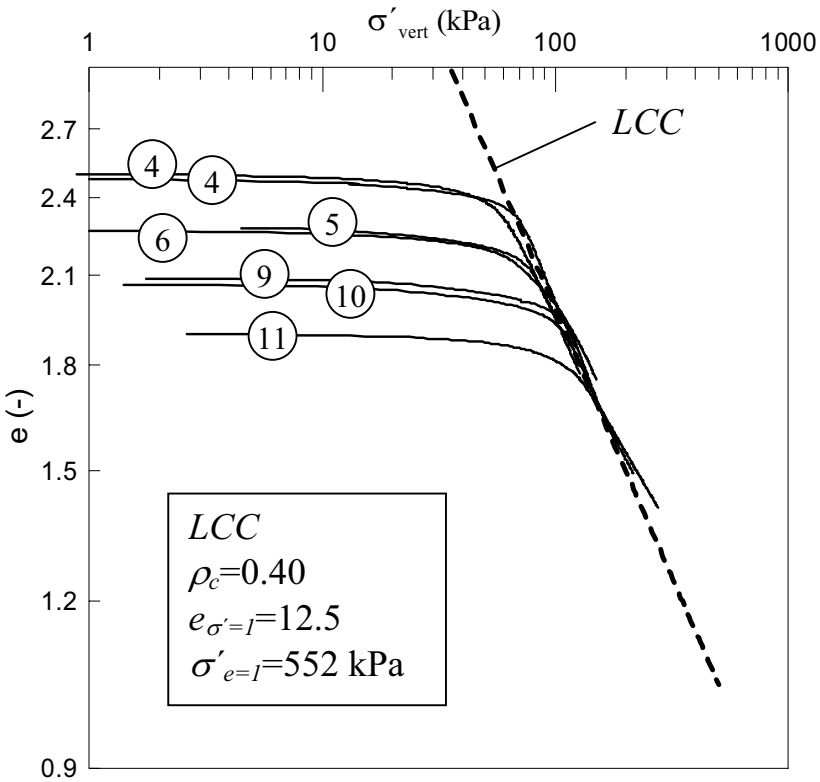

Figure 8.3: 1D compression results from CRS tests above the +0.5 level in section 1/430 north, lg/lg scale.
Circles in the graph denote the depth from which each sample was taken.
Dashed line: best fit for LCC according to Eq. 7.26.

As can be seen in Figure 8.4, the results from tests at 25 and 27 m differ from those at other depths. Firstly, the 27 m sample has a higher w_n compared to the one from 25 m. These two samples seem to belong to another "family" than the rest. Ocular testing revealed that the clay from a depth of 25 m contained thin layers of silt, which is probably the reason for the difference in behaviour.

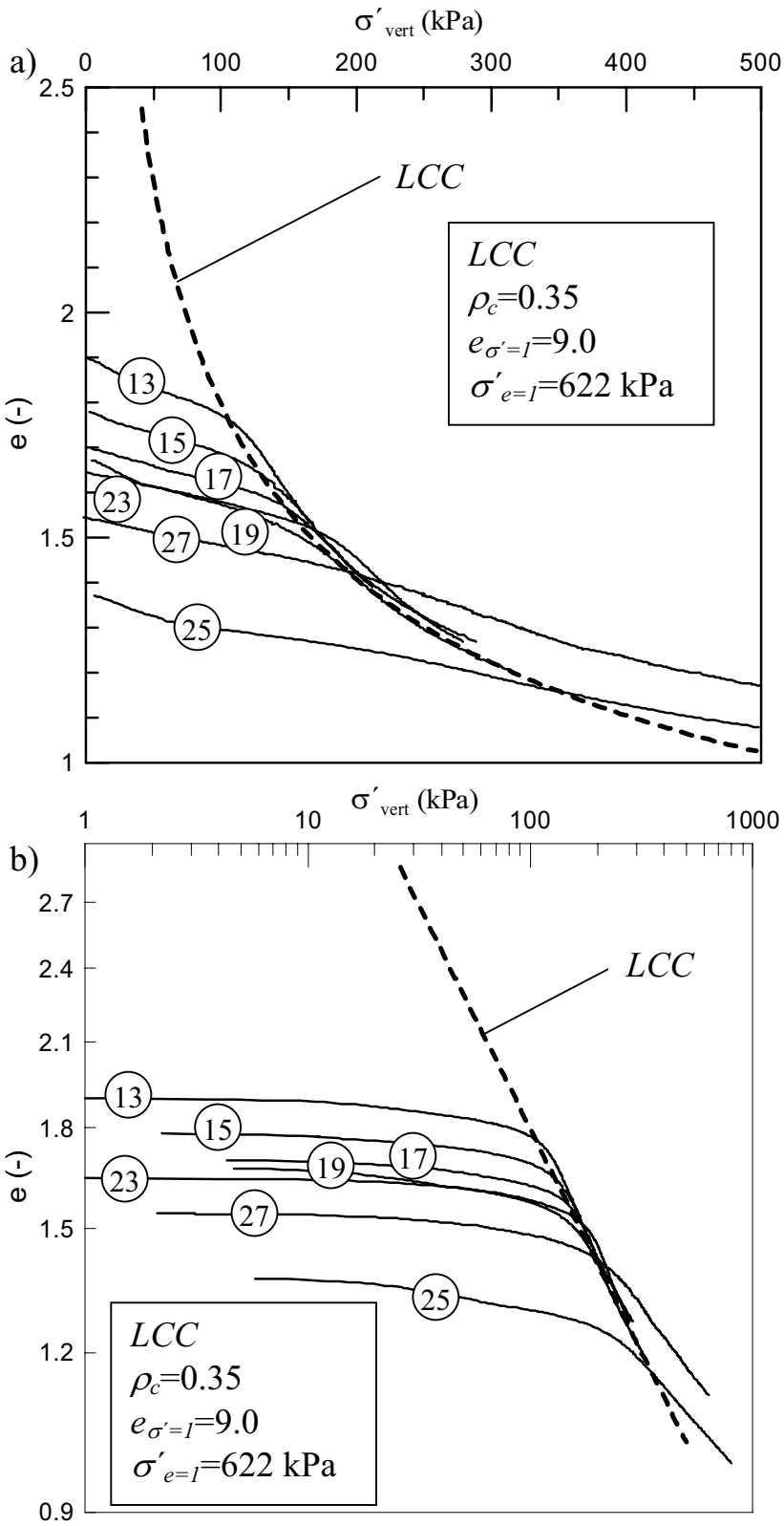

Figure 8.4: 1D compression results from CRS tests below the +0.5 level in section 1/430 north. a) linear scale a) lg/lg scale.
Circles in the graph denote the depth from which each sample was taken.
Dashed line: best fit for LCC according to Eq.7.26.

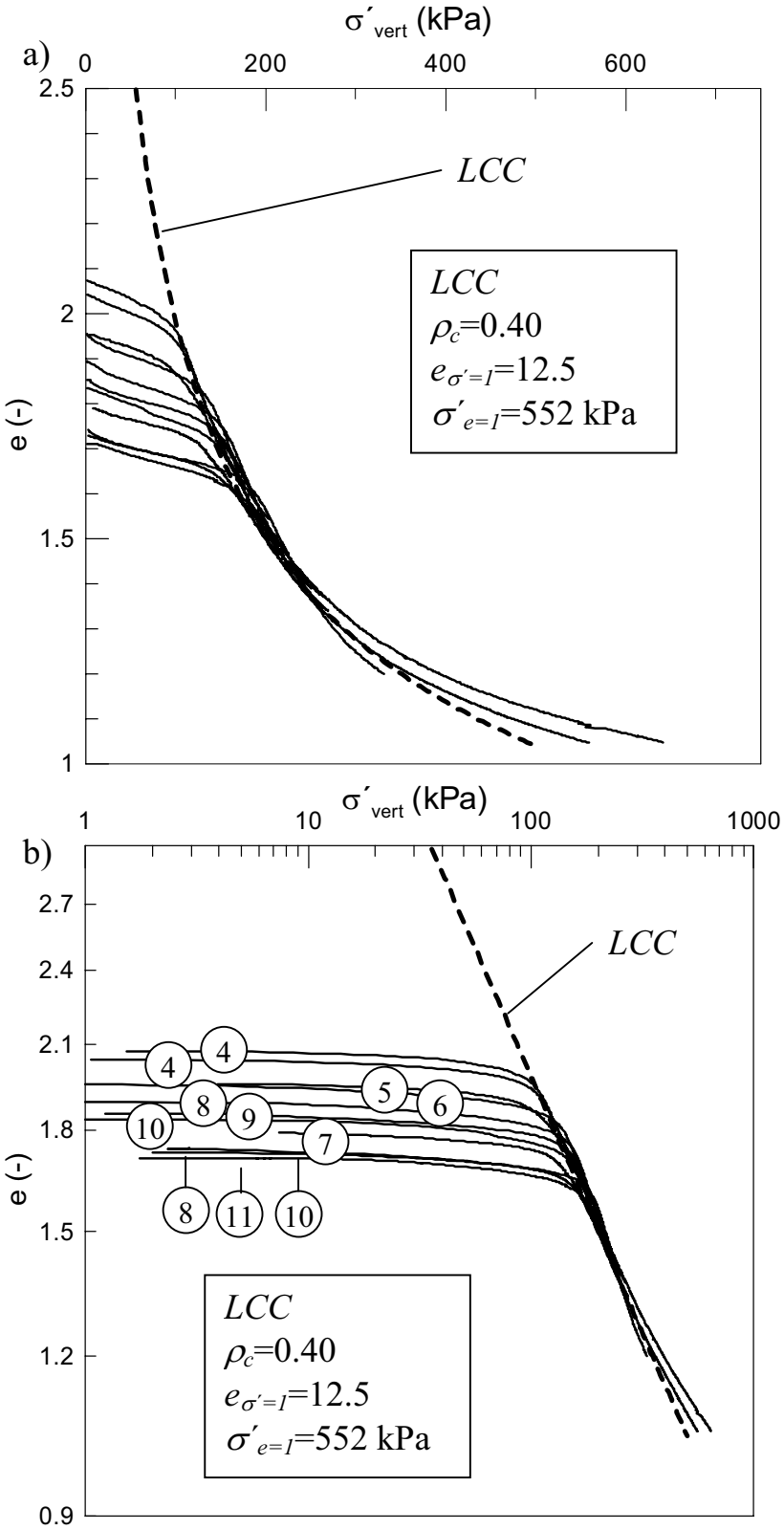

Figure 8.5: 1D compression results from CRS tests above the +0.5 level in section 1/470 south a) linear scale a) lg/lg scale.
Circles in the graph denote the depth from which each sample was taken.
Dashed line: best fit for LCC according to Eq.7.26.

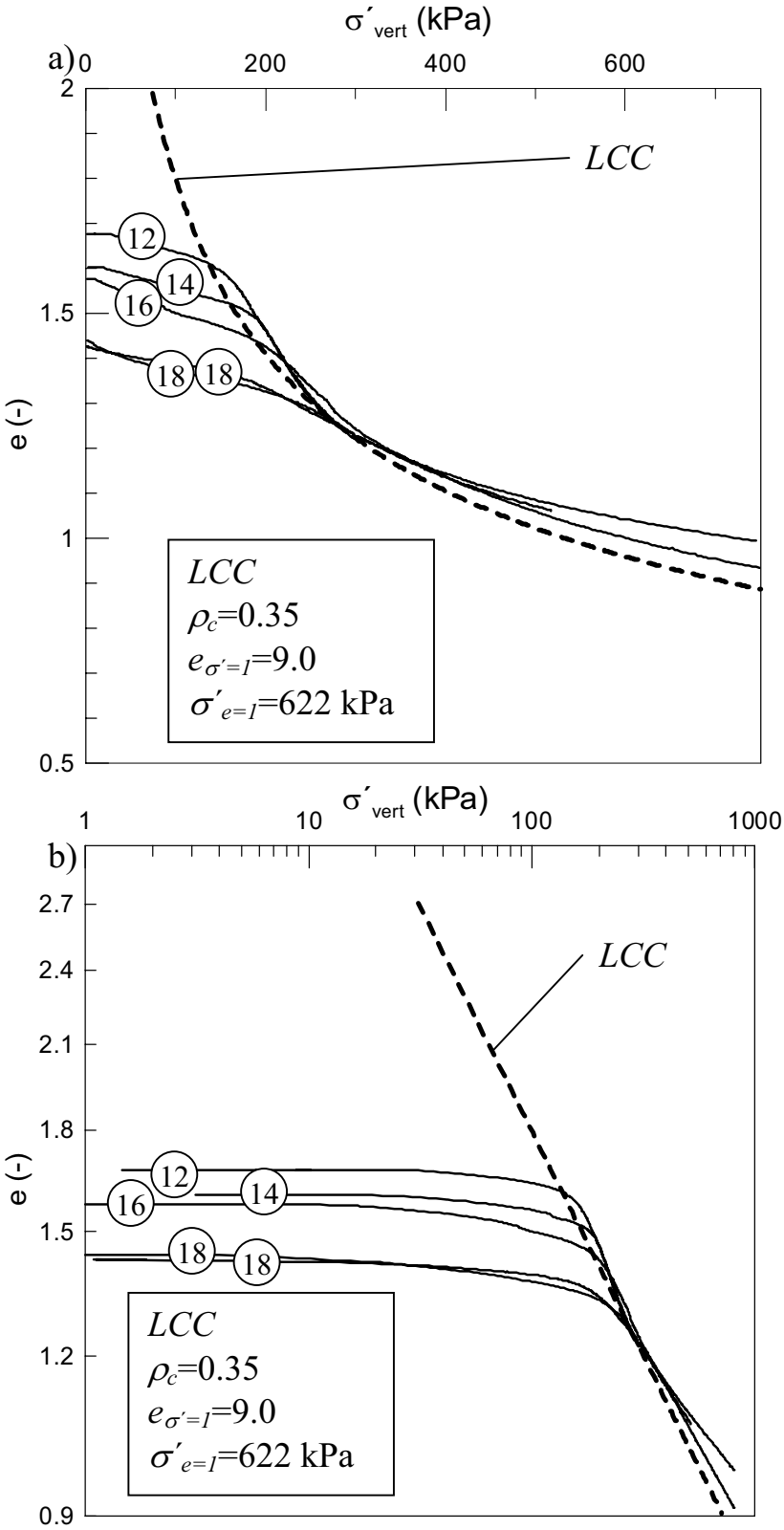

Figure 8.6: 1D compression results from CRS tests below the +0.5 level in section 1/470 south, a) linear scale a) lg/lg scale.
Circles in the graph denote the depth from which each sample was taken.
Dashed line: best fit for LCC according to Eq.7.26.

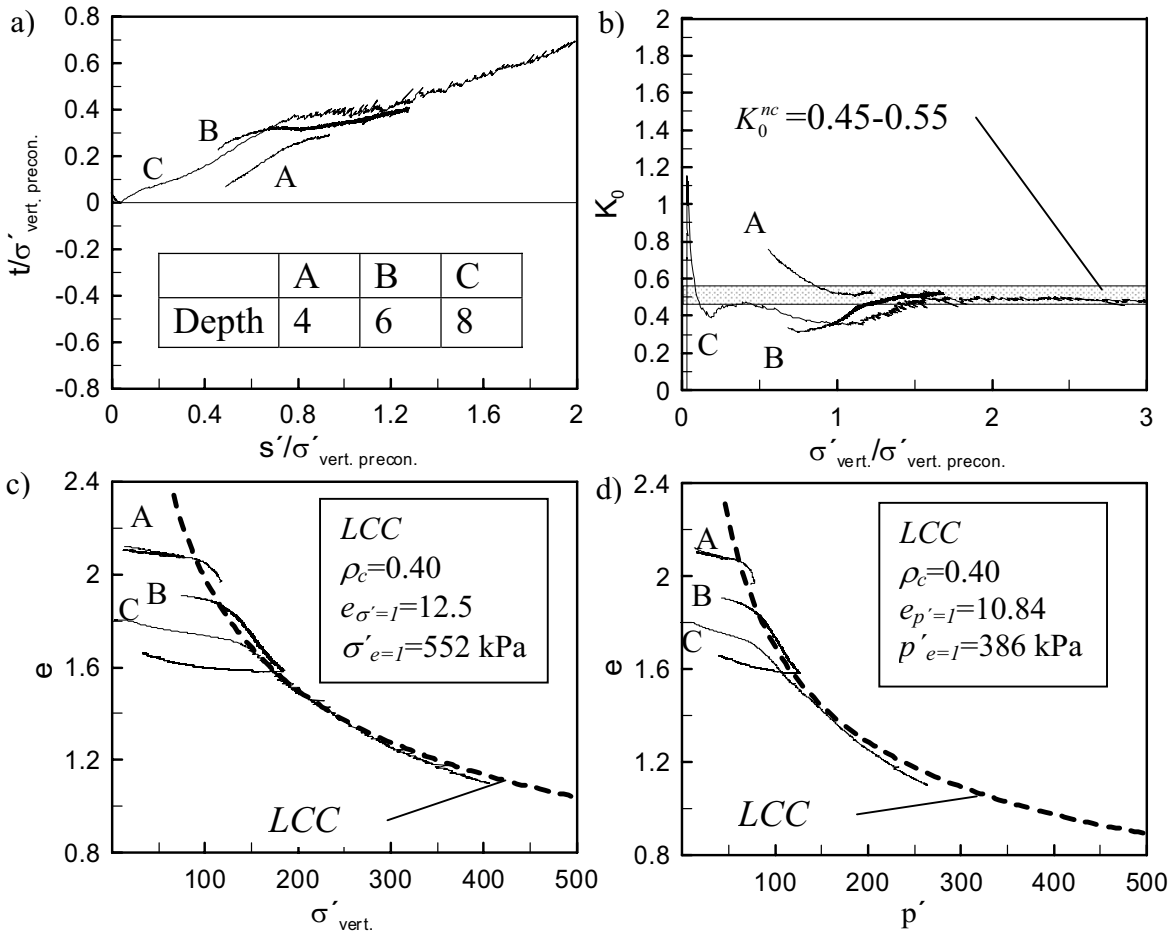

Figure 8.7: Test results from triaxial K_0 tests. Depth 4, 6 and 8 m in section 1/470.
a) Normalized stress paths during loading in the s´-t space
b) K_0 values obtained during loading
c) Void ratio vs. vertical effective stress
d) Void ratio vs. mean effective stress

The reason for starting from different locations is both previous unloading and reloading in order to create different loacations in the *s´-t*-space and to study how the starting point affects the length of time required to reach the *LCC*-line. The soil below preconsolidation pressure has an almost constant Poission ratio, which is lower than that corresponding to K_0^{nc}. When the stress path reaches the preconsolidtion pressure it bends and becomes almost horizontal ($\mu'\approx 0.5$) until it reaches the K_0^{nc} line, after which it follows that line. The K_0^{nc} line is the same as the *LCC*-line, compare Figure 7.13 and Figure 7.15. This means that in order to properly evaluate K_0^{nc}, the compression has to be set to at least ε_{vert}=10%.

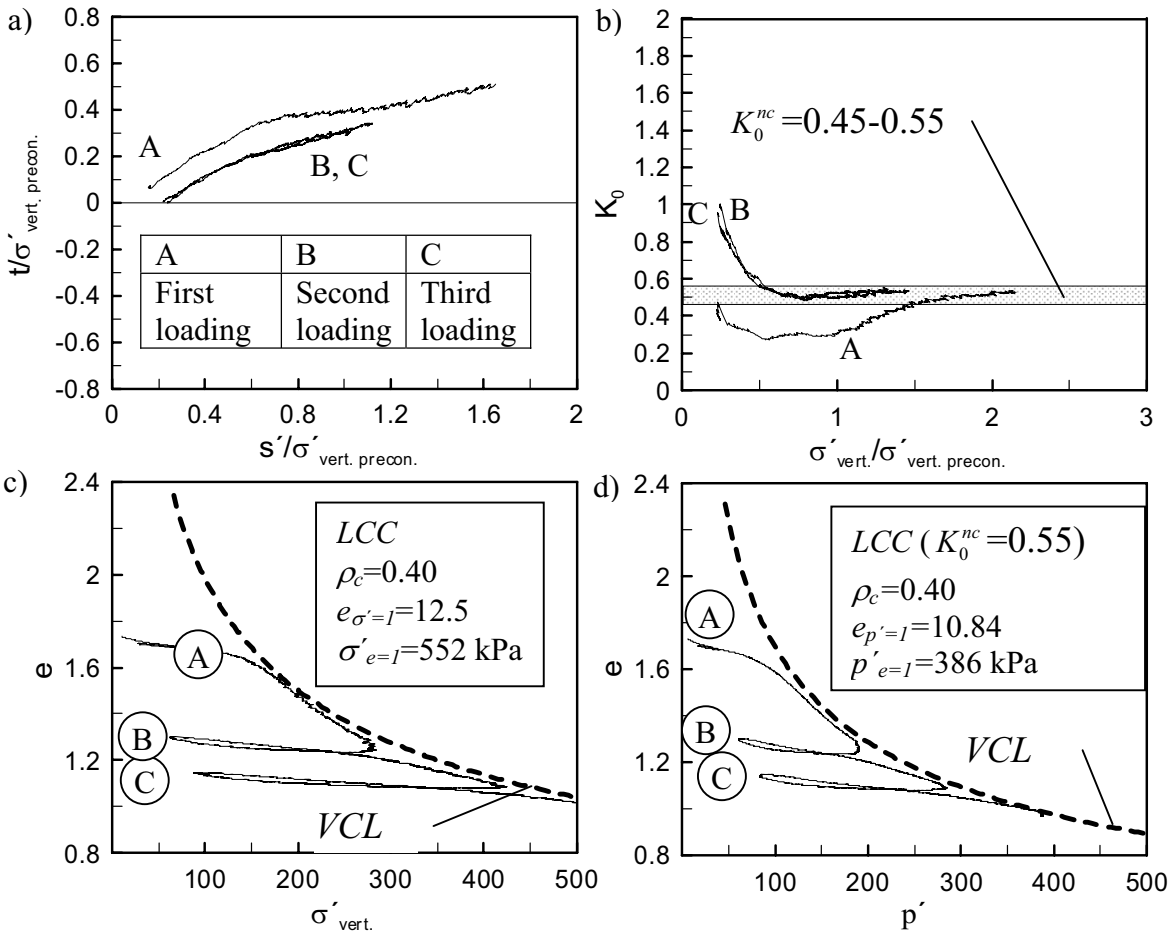

Figure 8.8: Test results from the triaxial K_0 test. Depth 8 m, section 1/470 loading in cycles.
a) Normalized stress paths during loading in the s´-t space
b) K_0 values obtained during loading
c) Void ratio vs. vertical effective stress
d) Void ratio vs. mean effective stress

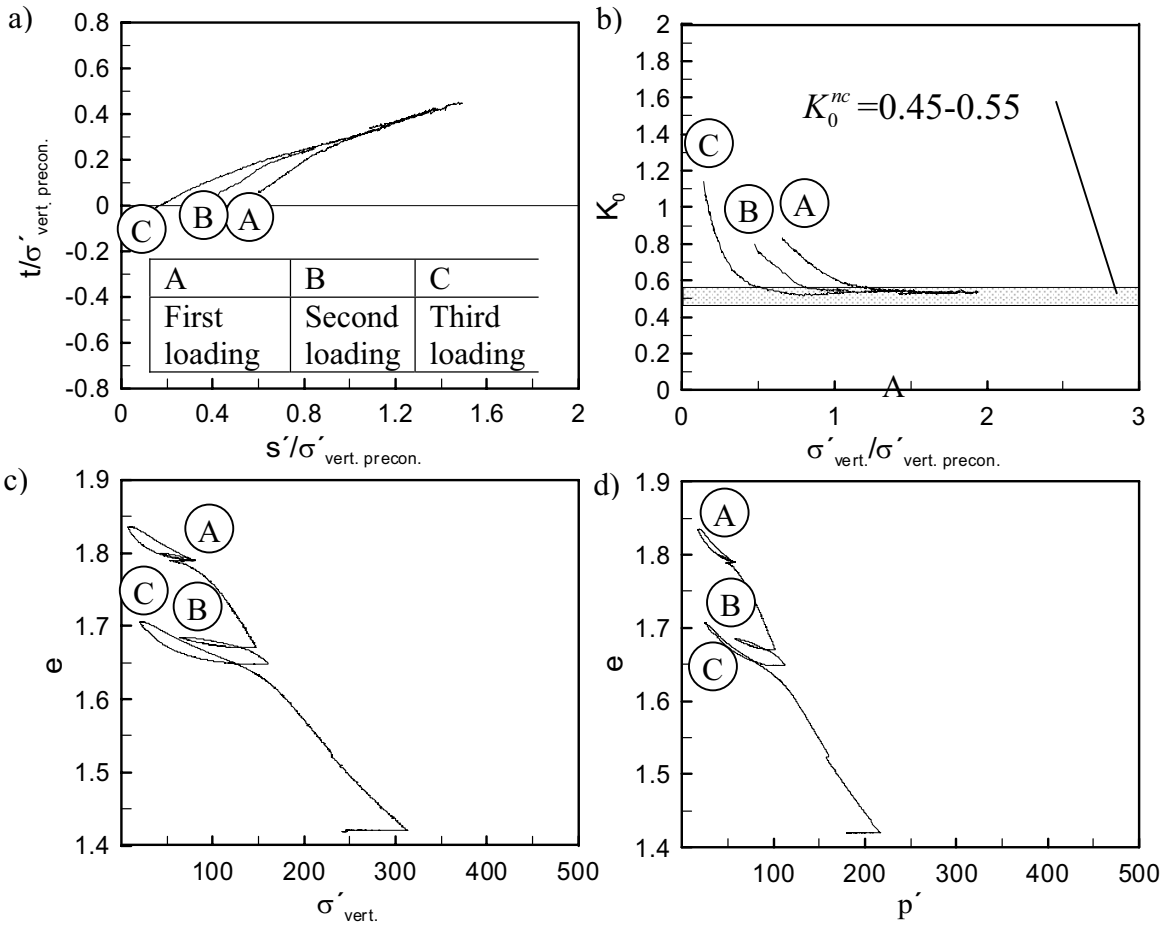

Figure 8.9: Test results from the triaxial K_0 test. Depth 10 m, section 1/430 loading in cycles. The samples contained small pieces of shell.
a) Normalized stress paths during loading in the s´-t space
b) K_0 values obtained during loading
c) Void ratio vs. vertical effective stress
d) Void ratio vs. mean effective stress

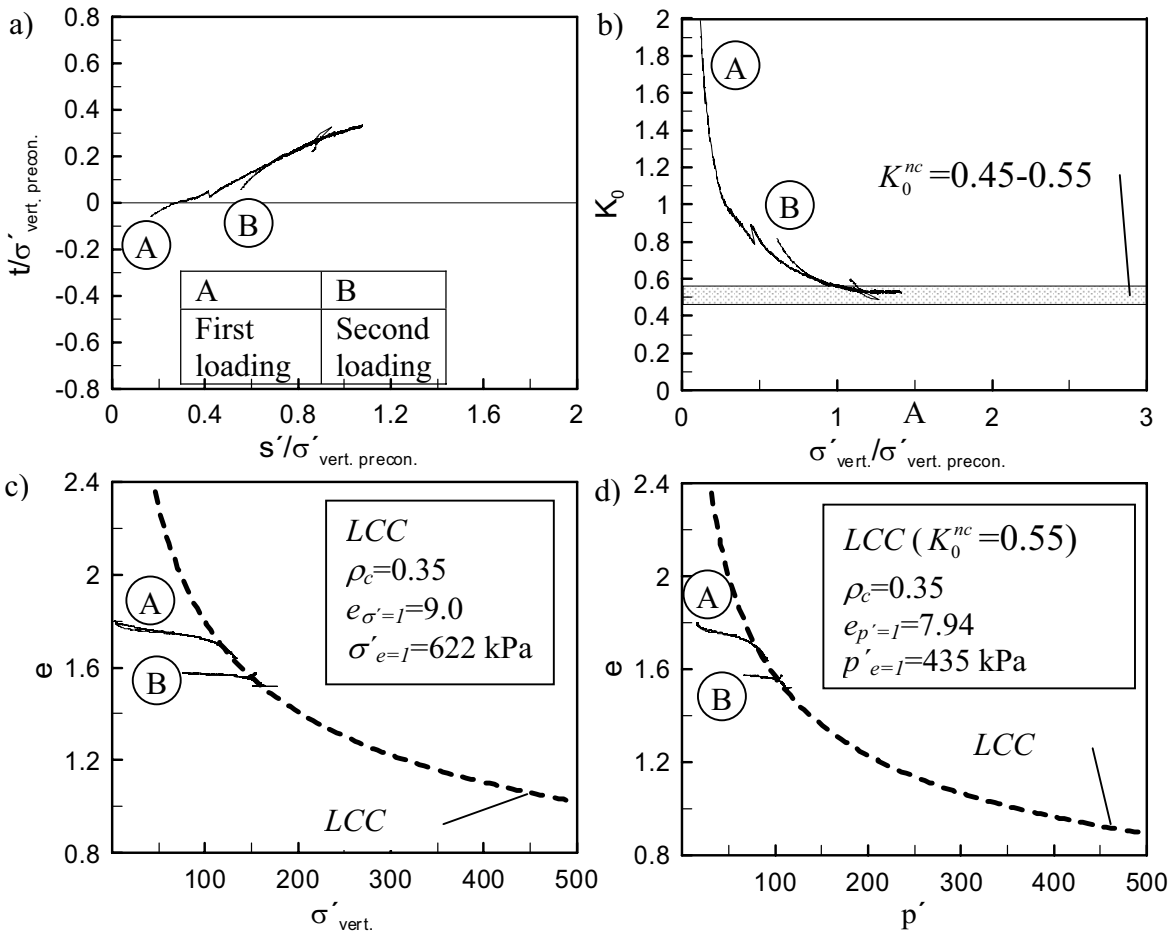

Figure 8.10: Test results from the triaxial K_0 test. Depth 12 m, section 1/430 loading in cycles.
a) Normalized stress paths during loading in the s´-t space
b) K_0 values obtained during loading
c) Void ratio vs. vertical effective stress
d) Void ratio vs. mean effective stress

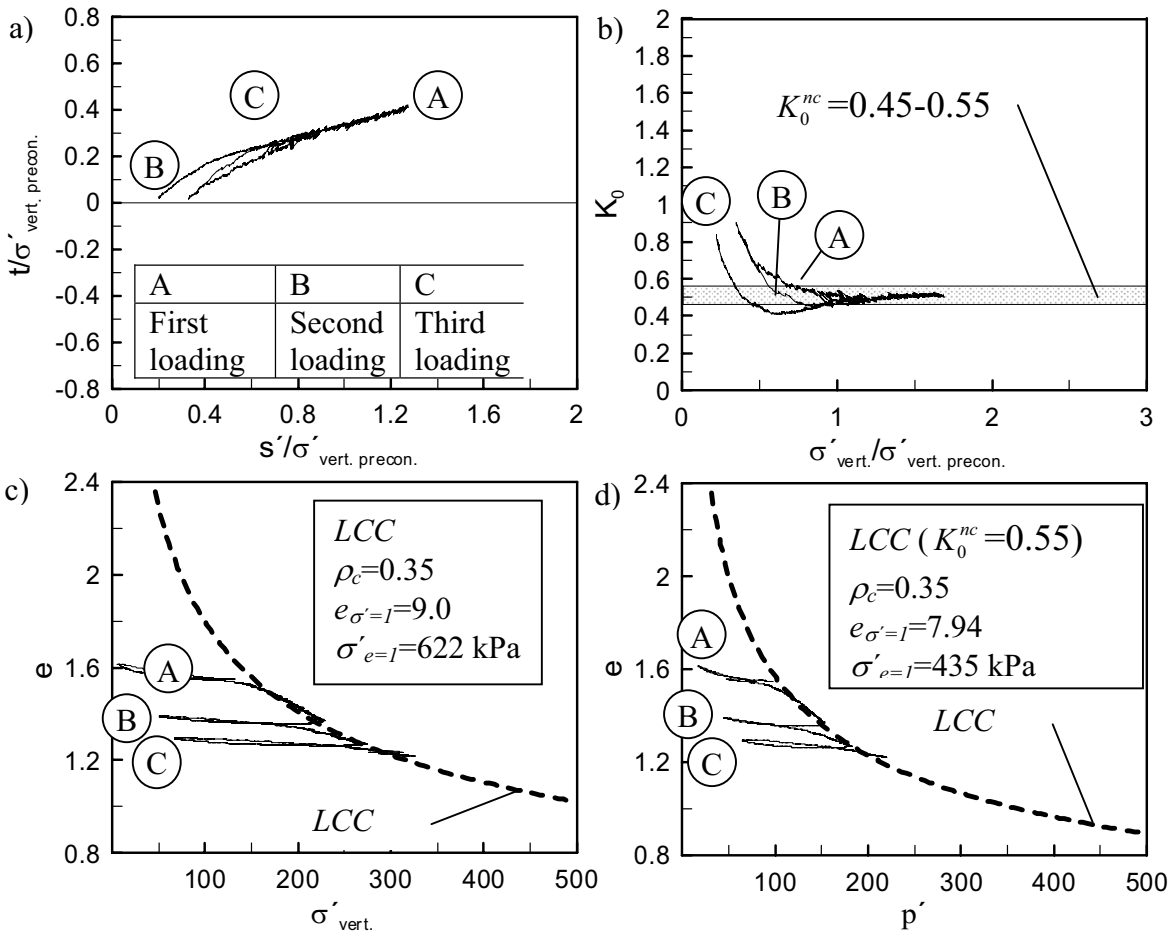

Figure 8.11: Test results from the triaxial K_0 test. Depth 14 m, section 1/470 loading in cycles.
a) Normalized stress paths during loading in the) s´-t space
b) K_0 values obtained during loading
c) Void ratio vs. vertical effective stress
d) Void ratio vs. mean effective stress

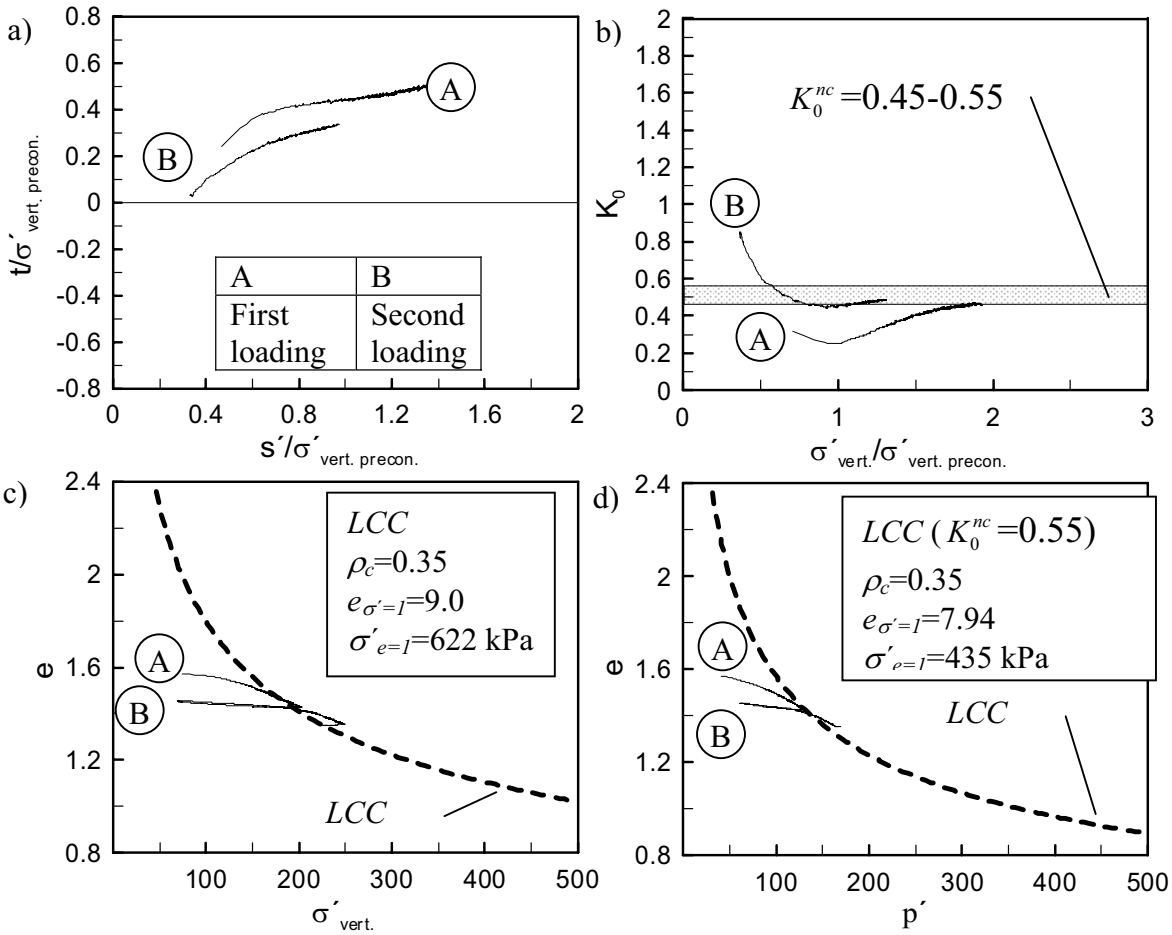

Figure 8.12: Test results from the triaxial K_0 test. Depth 19 m, section 1/430 loading in cycles.
a) Normalized stress paths when loaded in the s´-t space
b) K_0 values obtained during loading
c) Void ratio vs. vertical effective stress
d) Void ratio vs. mean effective stress

8.4 Evaluation of small strain compressibility, (C_b)

The parameter C_b controls the stiffness of the soil immediately after load reversal and is most reliably evaluated by means of the small strain shear modulus, G_{max}. In this thesis, small strain elastic compressibility is evaluated using the bender element test. The C_b parameter can also be evaluated from other tests, but reliable data from very small strains is required. C_b is a function of G_{max}, μ_0, e and p'_0, Equation (8.1).

$$C_b = \frac{1}{1.5}\frac{G_{\max}}{p'^{1/3}}\frac{e}{1+e}\frac{1+\mu'_0}{1-2\mu'_0}$$

$$= \frac{1}{1.5}G_b\frac{1+\mu'_0}{1-2\mu'_0} \qquad (8.1)$$

with G_{max} and p' given in atmospheres

Results from bender element tests are presented in Figure 8.13. Results from Persson (2004) and from new laboratory tests are also provided. In the study by Persson (2004)the initial shear modulus is compared with the empirical values used in Sweden, see Figure 8.14.

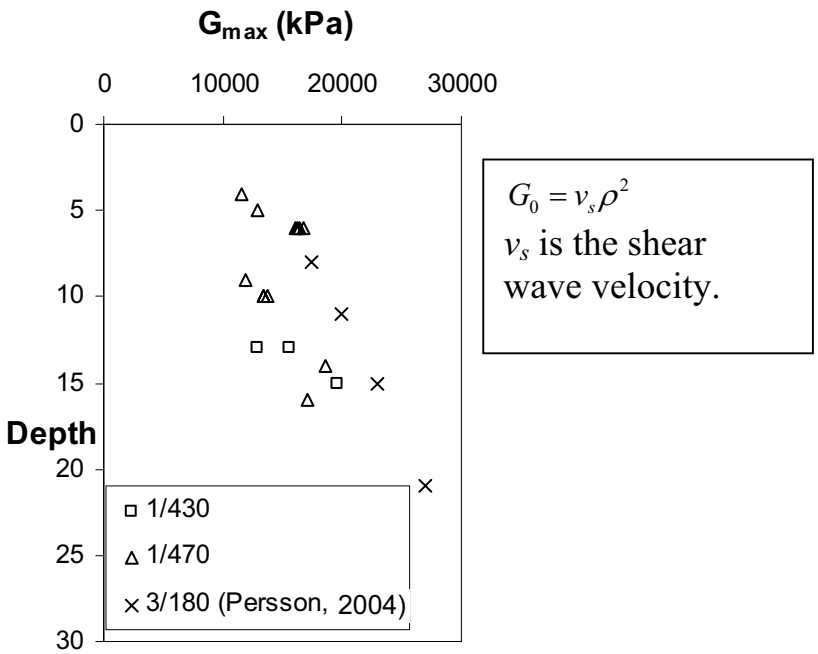

Figure 8.13: The initial shear modulus evaluated from shear wave tests.

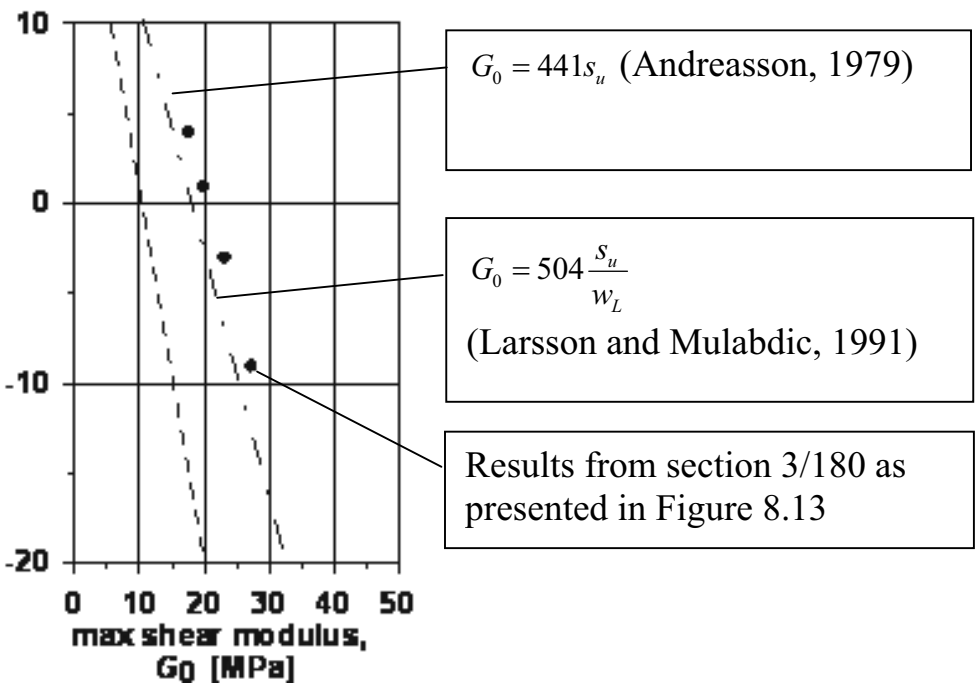

Figure 8.14: Initial shear moduli evaluated by shear wave velocity from section 3/180 compared with empirical relations (Persson, 2004)

Evaluating C_b in accordance with the relation in Equation (8.1) yielded the results illustrated in Figure 8.15 and Figure 8.16. Note that the same *LCC*-line has been assumed for section 3/180 with $\mu'_0=0.15$ and K_0^{nc} =0.55.

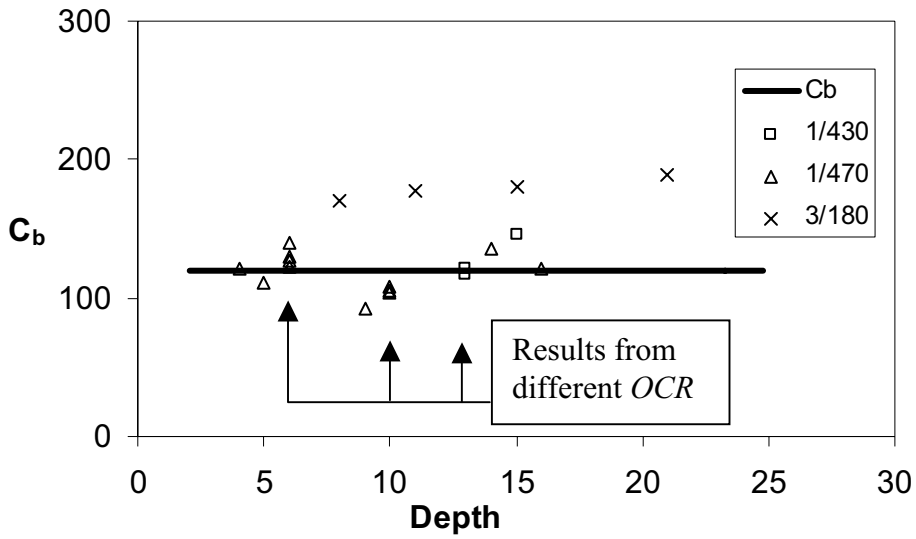

Figure 8.15: Small strain elastic compressibility C_b evaluated from bender element tests. A C_b value of 120 was chosen as a representative value for the Järntorget site.

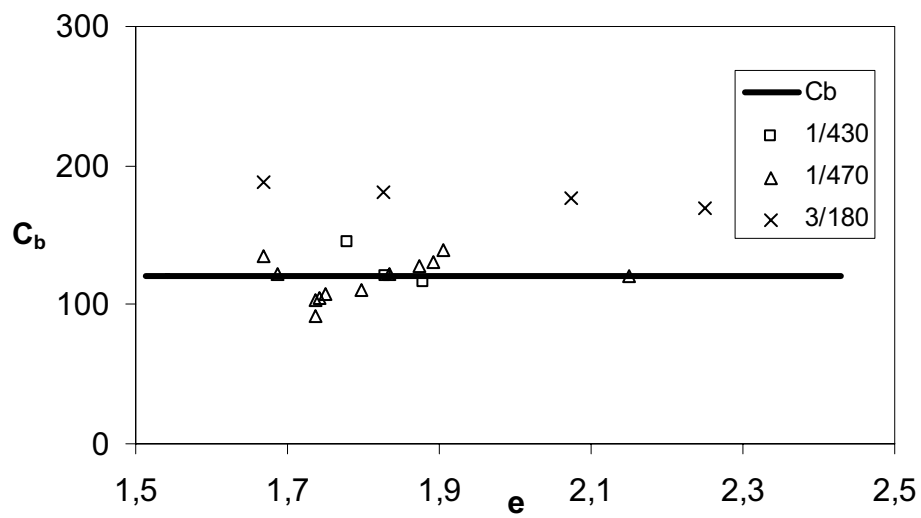

Figure 8.16: Small strain elastic compressibility C_b vs. void ratio.

The method of expressing the initial shear modulus, G_{max}, in terms of small strain elastic compressibility, C_b, has no empirical meaning for most engineers. Back calculated values of G_{max} are therefore presented in Figure 8.17. The back calculation was performed with a trend line for σ'^{precon}_{vert} and for two different *OCR* values. As a comparison, the empirical G_{max}, Equation (8.2) (Larsson and Mulabdic, 1991) is also presented.

The way of expressing the initial shear modulus, G_0, in terms of small strain elastic compressibility, C_b, has no empirical meaning to most engineers. Therefore back calculated values of G_{max} is presented in Figure 8.17. The back calculation is performed with a trend line for σ'^{precon}_{vert} and for two different *OCR* values. As a comparison the empirical G_0 , equation (8.2), (Larsson and Mulabdic, 1991) is also presented.

$$G_0 = \mu \cdot 504 \frac{\tau_{fu}}{w_L} \qquad \mu = 1 - 0.4 \lg_{10} OCR \tag{8.2}$$

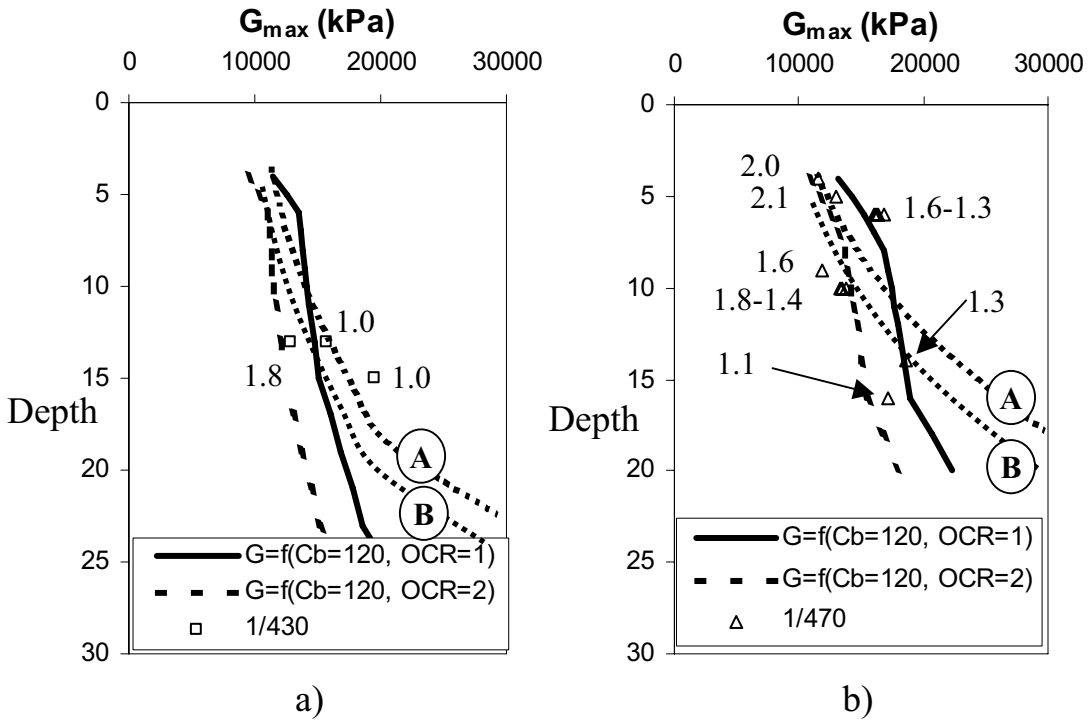

*Figure 8.17: Measured G_{max} for different OCR values in the two sections compared with the G_{max} given by MIT-S1 (C_b=120) for OCR 1.0 and 2.0. The empirical relation, Eq. (8.2), is given for in **A** for OCR=1 and in **B** for OCR=2.*
a) Section 1/430 b) Section 1/470

The match is excellent in section 1/430 and the scatter in preconsolidation pressure explains the small scatter in section 1/470. In section 1/470 the results are better represented with the *MIT-S1* model and the empirical relation, especially at large depths were the liquid limit, w_L, increases.

From Figure 8.13 and Figure 8.16 it is obvious that the initial shear moduli is higher in section 3/180, 1.7 km upstream the river. To match the measured values in this section a C_b value of 180 can be used,

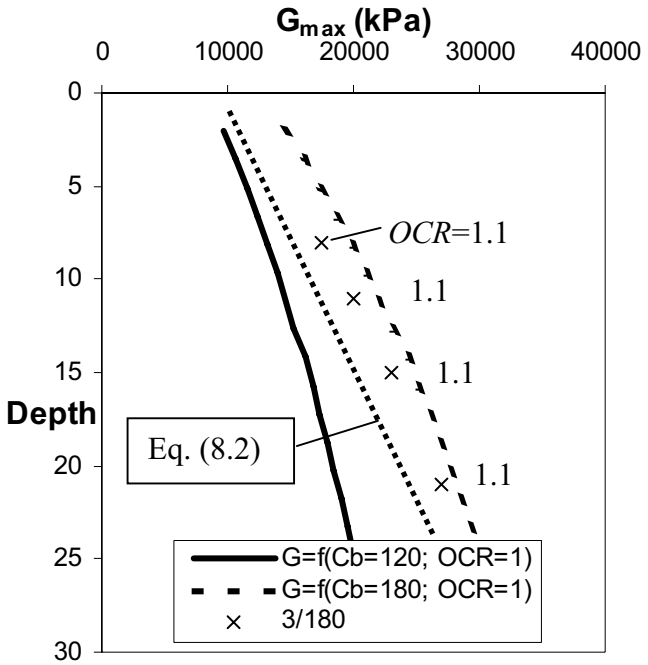

Figure 8.18: Calibration of the C_b value for section 3/180 and empirical relation from Eq. (8.2) for OCR=1.0.

The initial shear modulus obtained by seismic methods shall also be compared with results from other tests. In Figure 8.19 the secant shear modulus obtained by CK_0UC and CK_0UE test are given as well as results from the proposed method by Pestana (1994). The G_{max} or G_b given by the bender element tests show a value between the initial value from the CK_0UC and CK_0UE test. Where the results from the CK_0UE test show a stiffer response than the CK_0UC test. It can also be seen that the response is quite stiffer in section 3/180 even for the undrained shear test.

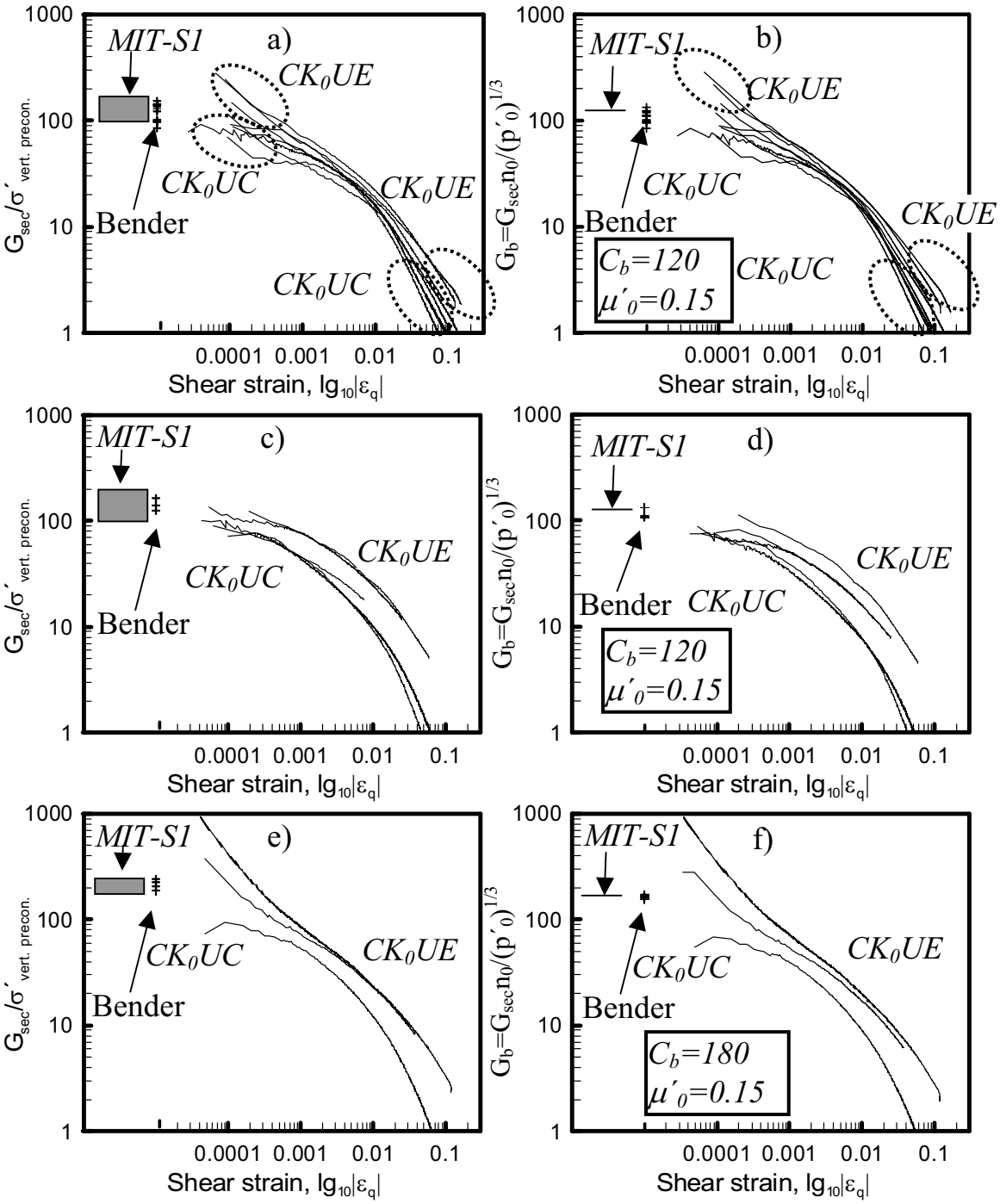

Figure 8.19: Result from CK_0UC and CK_0UE compared with the results from the bender element test
Section 1/470 a) conventional approach b) proposed method
Section 1/430 c) conventional approach d) proposed method
Section 3/180 e) conventional approach f) proposed method

8.5 Evaluation of Poisson's ratio, (μ'_0 and ω)

The *MIT-S1* model uses a variable Poisson's ratio, μ', to describe the variation of K_0 during 1D-unloading and reloading. The variation of μ' is given in equation (8.3).

$$\mu' = \frac{\mu'_0 + \omega\xi_s/3}{1 + 2\omega\xi_s/3} \tag{8.3}$$

$$\xi_s = \sqrt{(\boldsymbol{\eta} - \boldsymbol{\eta}_{rev}) : (\boldsymbol{\eta} - \boldsymbol{\eta}_{rev})}$$

$\boldsymbol{\eta}$ *is the actual stress ratio and* (8.4)

$\boldsymbol{\eta}_{rev}$ *is the stress ratio at latest stress reversal point*

This variation can be used to approximately get the empirical relation given by Schmidt (1966), equation (8.5). Pestana (1994) also gives the relation for ω as a function of K_0^{nc}, μ'_0 and OCR_1, where OCR_1 is the preconsolidation pressure where σ'_{vert} equals σ'_{hor}

$$K_0 = K_0^{nc} OCR^m \tag{8.5}$$

$$\omega = \sqrt{\frac{3}{2}} \frac{1 + 2K_0^{nc}}{\left(1 - K_0^{nc}\right)^2} \left(K_0^{nc} - 1 + \frac{3\left(1 - 2\mu'_0\right)}{\left(1 + \mu'_0\right)} \left(\frac{1 + 2K_0^{nc}}{3} - \frac{1}{OCR_1} \right) \right) \tag{8.6}$$

If Schmidt's relation is used the actual Poisson's ratio during 1D unloading can be derived, Figure 8.20. In simple constitutive models, where a constant value of μ' is used a secant value of μ' should be used to model the 1D unloading, Figure 8.20b gives the secant value when unloading from *OCR*=1.0.

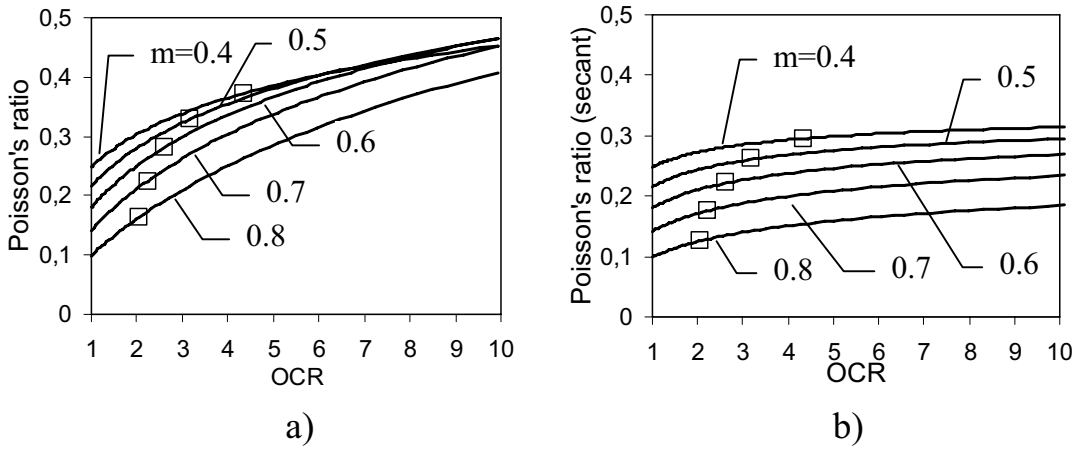

Figure 8.20: Variation of μ' according to Schmidt's empirical relation, K_0^{nc} =0.55. Squares indicate where K_0 equals 1.
a) Actual Poisson's ratio during 1D unloading for different m values
b) Secant value of Poisson's ratio during 1D unloading for different m values

Typical values of ω is given in Figure 8.21 if the stress path in 1D unloading follows Schmidt's relation.

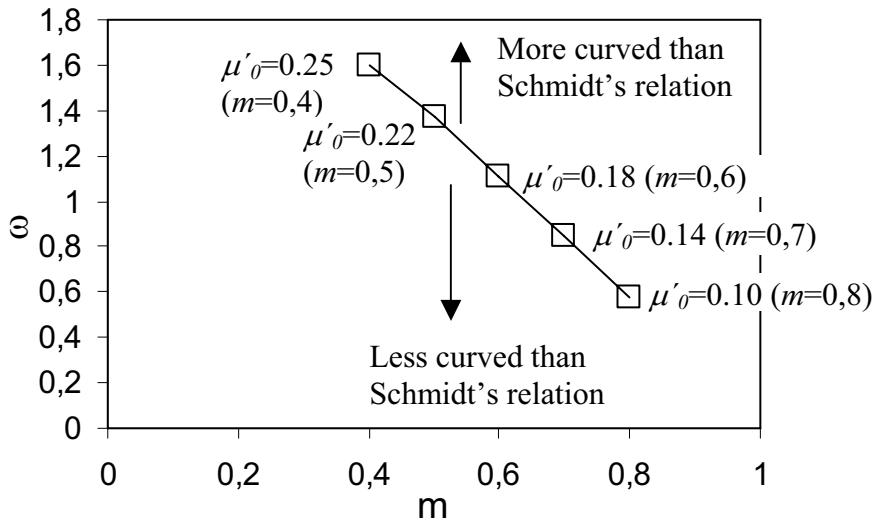

Figure 8.21: Derived values of ω using Schmidt's empirical relation.

Stress paths from 1D unloading test are visualized in Figure 8.22 combined with appropriate values of μ'_0 and m in Schmidt's relation. From the laboratory result μ'_0 is chosen to 0.15 and ω is chosen to 2.0. μ'_0=0.15 represents a value of m=0.7 (Schmidt, 1967) but most of the results are better matched with a stress path defined by a slightly smaller value of m. This means that the curvature of the unloading stress path has a higher curvature than obtained by Schmidt's relation with m=0.7. From Figure 8.21 ω shall be higher than 0.8. The relation given in equation (8.6) gives $\omega(K_0^{nc}=0.55, \mu'_0=0.15; OCR_1=2{,}8)\approx 2.0$. The sensitivity of the parameters μ'_0 and ω is shown in Figure 8.23 were the stress path for 1D unloading from the *VCL*-line is shown. The swelling will also be affected by these two parameters since the inclination of the stress path (depending on the actual μ' value) indirect controls the ratio between K and G. Figure 8.23 is also complemented with Schmidt's relation, just to compare how the empirical relation agrees with the one in *MIT-S1*.

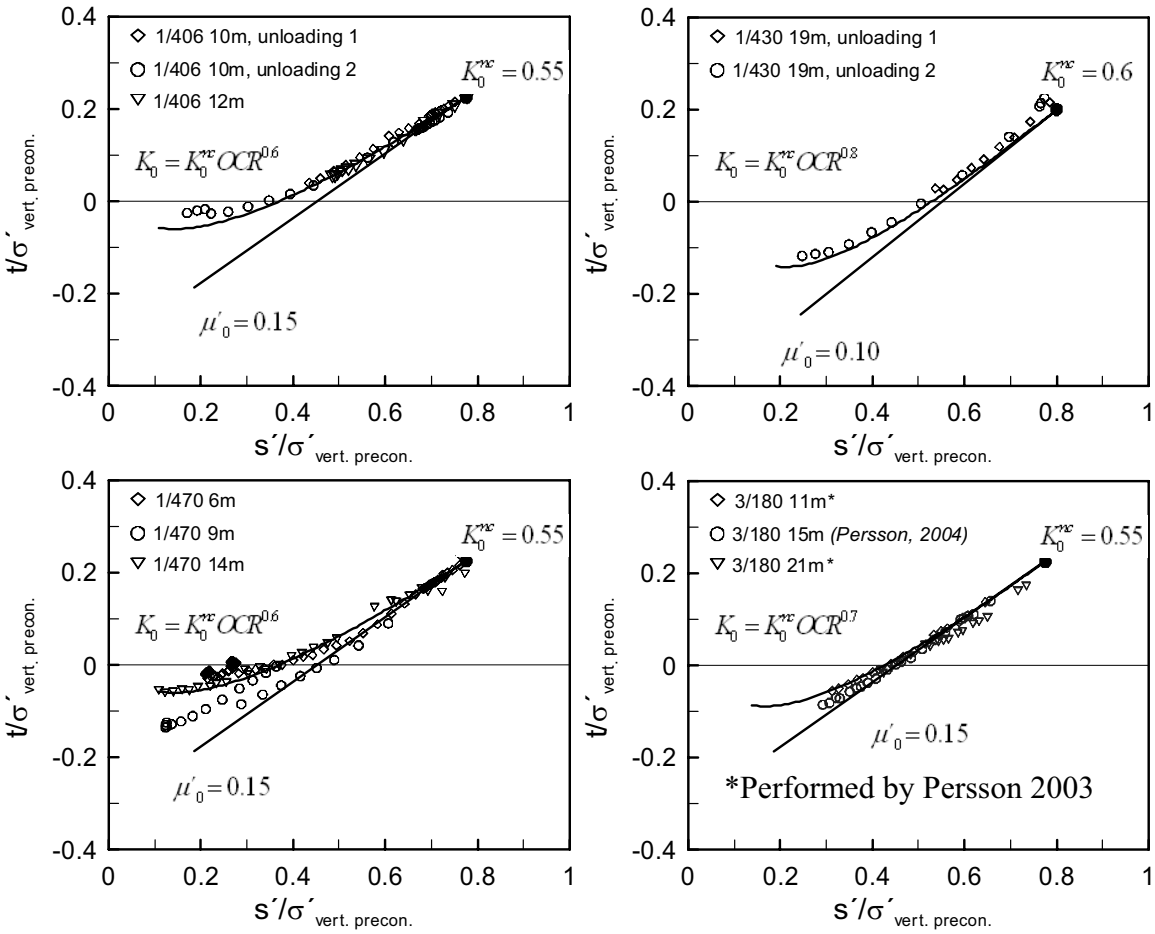

Figure 8.22: Stress paths from 1D unloading test.

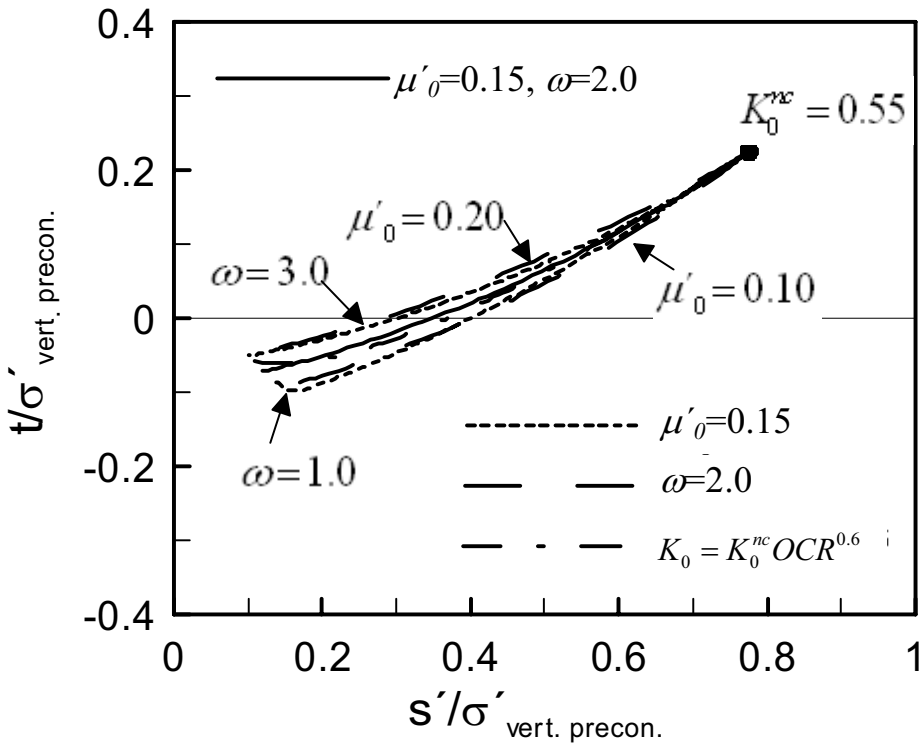

Figure 8.23: Effect of the MIT-S1 parameters ω and μ'_0 on the stress path for 1D-unloading from the LCC-line.

8.6 Evaluation of non-linearity in volumetric response, (*D* and *r*)

During 1D unloading the clay expands. For a saturated clay there has to be available water sucked into the clay, which keeps the excess pore water pressure at zero. The swelling is non-linear when plotted versus decrease in vertical stress as well as the decrease in mean stress. Several 1D-unloading tests have been performed within this project and some results are presented in this section, Figure 8.24.

The model *MIT-S1* uses two parameters to describe the non-linear behavior in the hydrostatic swelling, *D* and *r*. *D* defines the inclination of the swelling line at an *OCR* of about 10 if the unloading is plotted in log-scale. If 1D swelling is studied the strain due to shear has to be incorporated. This is done through the parameter ω and the amount of changes in relative shear stress during the swelling, ξ_s, previously defined. The initial volumetric strain will depend on the initial stiffness, which is a function of the parameters C_b and μ'_0. The transition between the intial modulus at unloading and the modulus at large *OCR*:s is highly controlled by the paramter *r*.

The volumetric strain during unloading will differ as a consequence from where on the *LCC*-line the unloading starts since the small strain modulus in *MIT-S1* depends on C_b. The initial shear stiffness depends on C_b, n and p', Equation (8.1), which leads to different strains for the same unloading ratio if the unloading starts from different loacations along the *LCC*-line. Figure 8.25 shows the 1D-swelling modeled by *MIT-S1* compared with laboratory results.

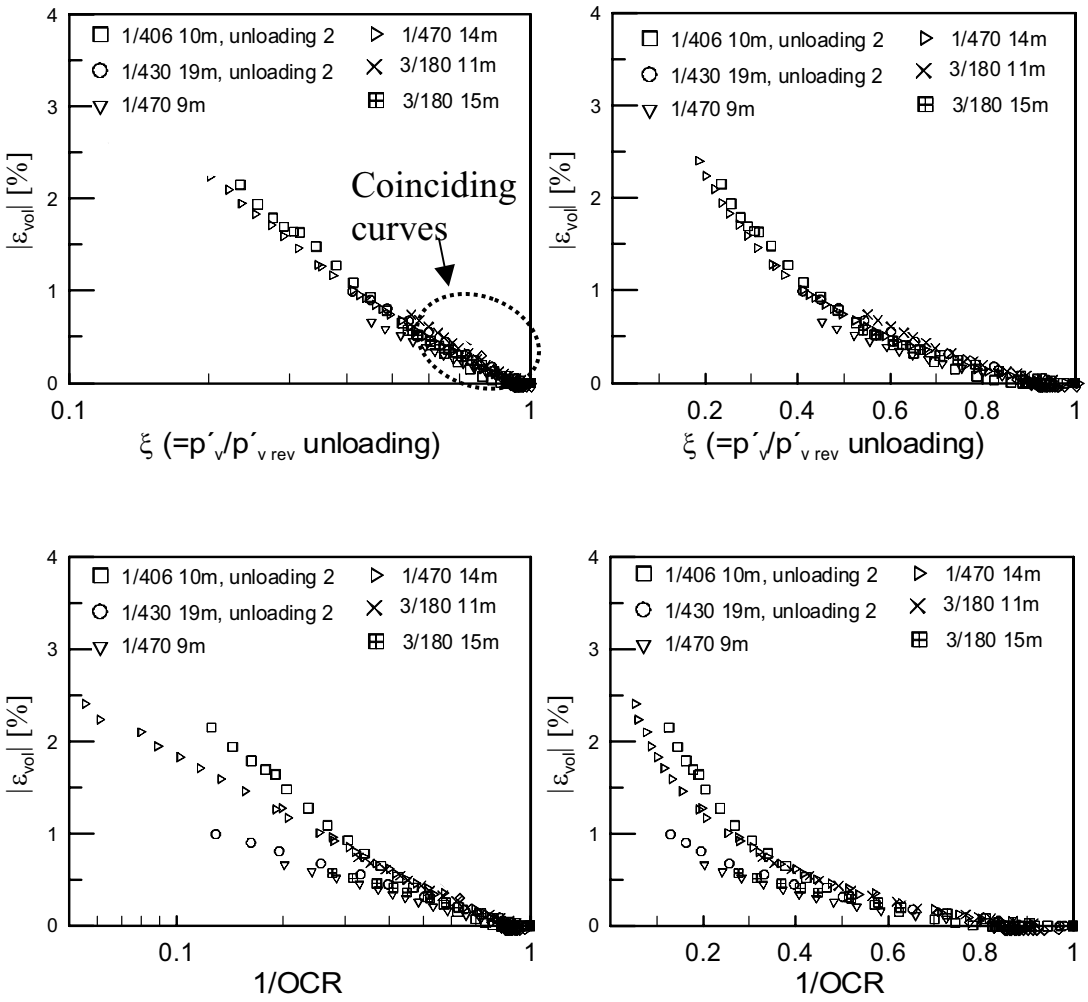

Figure 8.24: Swelling during 1D-unloading

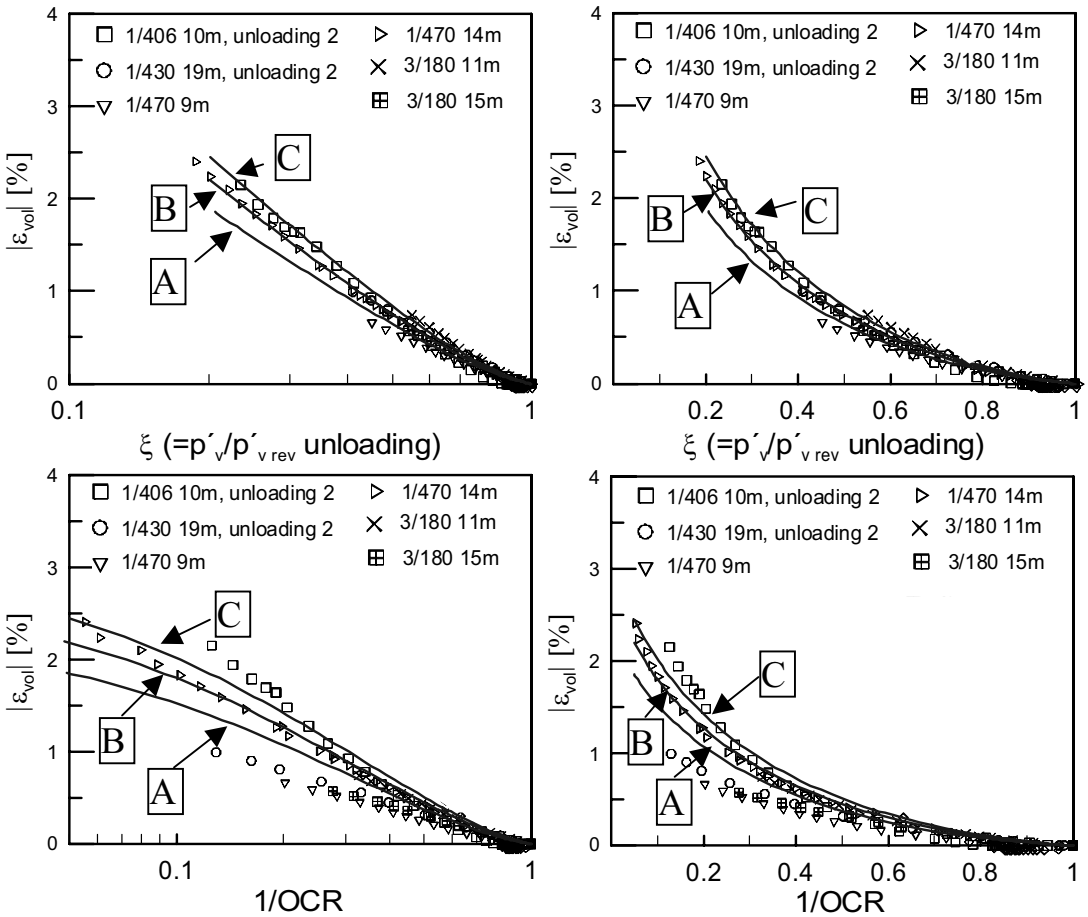

Test	σ'^{precon}_{vert}
1/406 10m	161 kPa
1/430 19m	117 kPa
1/470 9m	112 kPa
1/470 14m	135 kPa
3/180 11m	105 kPa
3/180 15m	135 kPa

MIT-S1 parameters			
ρ_c	0.4	ω_s	15
C_b	120	D	0.005
μ'_0	0.15	r	2.0
ω	2.0		
A:	$\sigma'^{precon}_{vert} =$	100	kPa
B:	$\sigma'^{precon}_{vert} =$	150	kPa
C:	$\sigma'^{precon}_{vert} =$	200	kPa

Figure 8.25: Swelling during 1D-unloading, comparison between simulated swelling from three different locations on the LCC-line (σ'^{precon}_{vert} =100, 150 and 200 kPa).

The sensitivity for parameters *D* and *r* is shown in Figure 8.26. As can be seen there is only negligible differences between the different combinations of *D* and *r* up to an *OCR* value of 2. Compare Equation (7.43) and Figure 7.18.

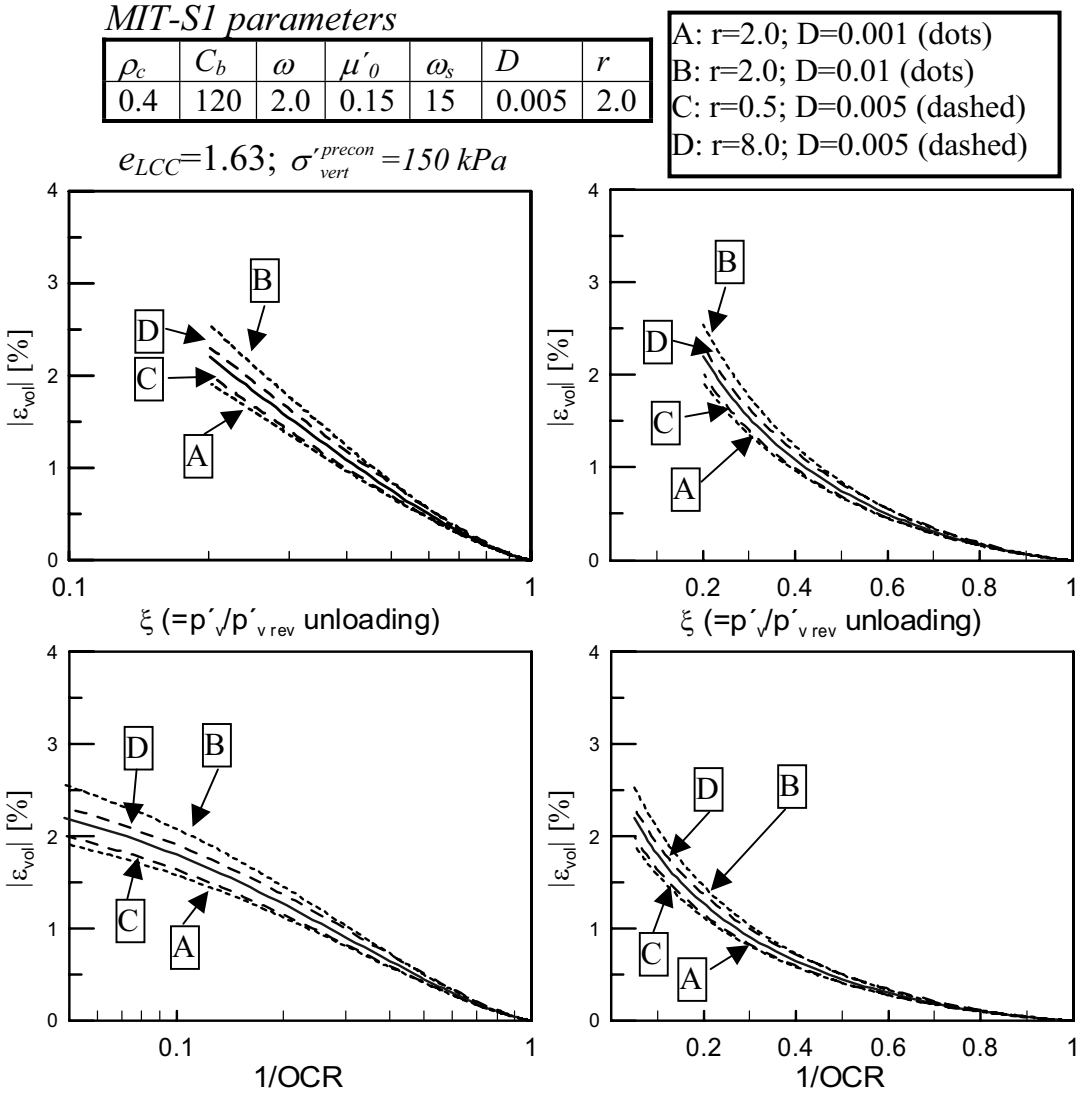

Figure 8.26: Effects of parameters D and r on 1D-swelling.

MIT-S1 parameters

ρ_c	C_b	ω	μ'_0	ω_s	D	r
0.4	120	2.0	0.15	15	0.005	2.0

	A	B	C
σ'^{precon}_{vert}	100	150	200

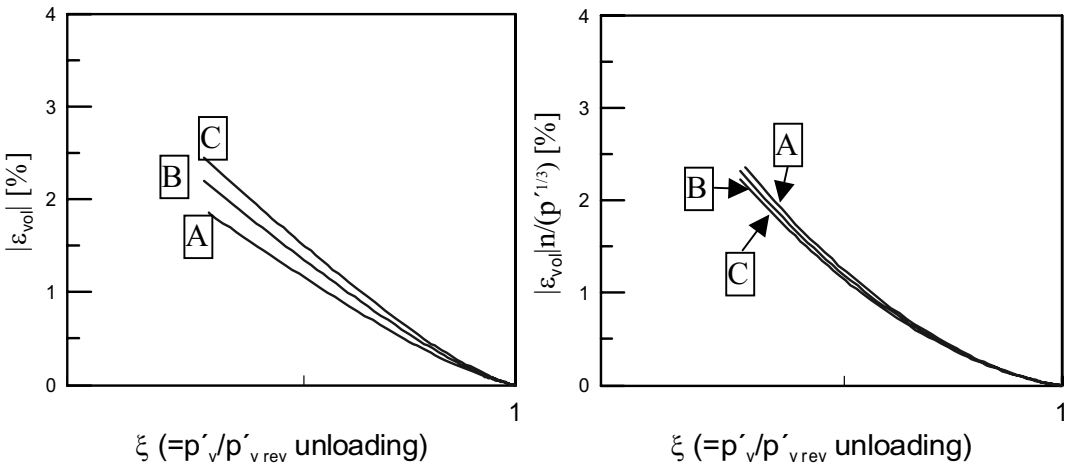

Figure 8.27: 1D swelling effect after normalization of the volumetric strain against the porosity divided by the mean stress to the power of 1/3.

8.7 Evaluation of the initial bounding surface, (ϕ'_m , m) and the failure surface (ϕ'_c)

The bounding surface has the shape of a distorted droplet/lemniscate, see Section 7.3, which is controlled by:

- ϕ'_m which controls the opening angle around the isotropic axis at very high *OCR* values
- the tensor **b** that defines the direction in the stress space around which the boundary surface is centred
- *m* which controls the distortion of the bounding surface

In sedimented soil the initial horizontal stresses, σ'_x and σ'_z, are usually equal while the shear stresses τ_{xy}, τ_{xz} and τ_{yz} are equal to zero. This implies that the boundary surface is symmetrical around the axi-symmetrical plane and can be visualized in the *s´-t* stress space, see Figure 8.28. The figure has been complemented by an empirical failure surface and empirical failure points for different *OCR*-values. The boundary surface is defined by K_0^{nc}=0.55, an opening angle of 40º and *m* equals 2.0. The parameter *m* defines the size of the abdomen of the bounding surface when *t* is negative, extension side. The chosen failure angle of 35º agrees well with the simplified failure surface defined by ϕ' 30º and an intercept of 3% of σ'^{precon}_{vert} as well as with the empirical failure point for different *OCR*-values (Equation (8.7)), marked as filled circles in Figure 8.28. The empirical value of $s_{u\ ext}$ for normal consolidated clay is dependent on the liquid limit, w_L. Where w_L=70%, $s_{u\ ext}$ will be 21% of σ'^{precon}_{vert}. The same ratio for $s_{u\ comp}$ is 33% independent of w_L.

$$\frac{s_u}{s_{u\ OCR=1.0}} = OCR^{-0.25} \quad \text{(Ladd } et\ al.\text{, 1977)} \tag{8.7}$$

Ladd *et al* (1977) comments that the power value used in Equation (8.7) might be –0.15 for low *OCR* values deacreasing down to –0.25 in line with an increase in *OCR*, however the value mainly used in Sweden is –0.25 independent of the *OCR* value (Skredkommissionen, 1995).

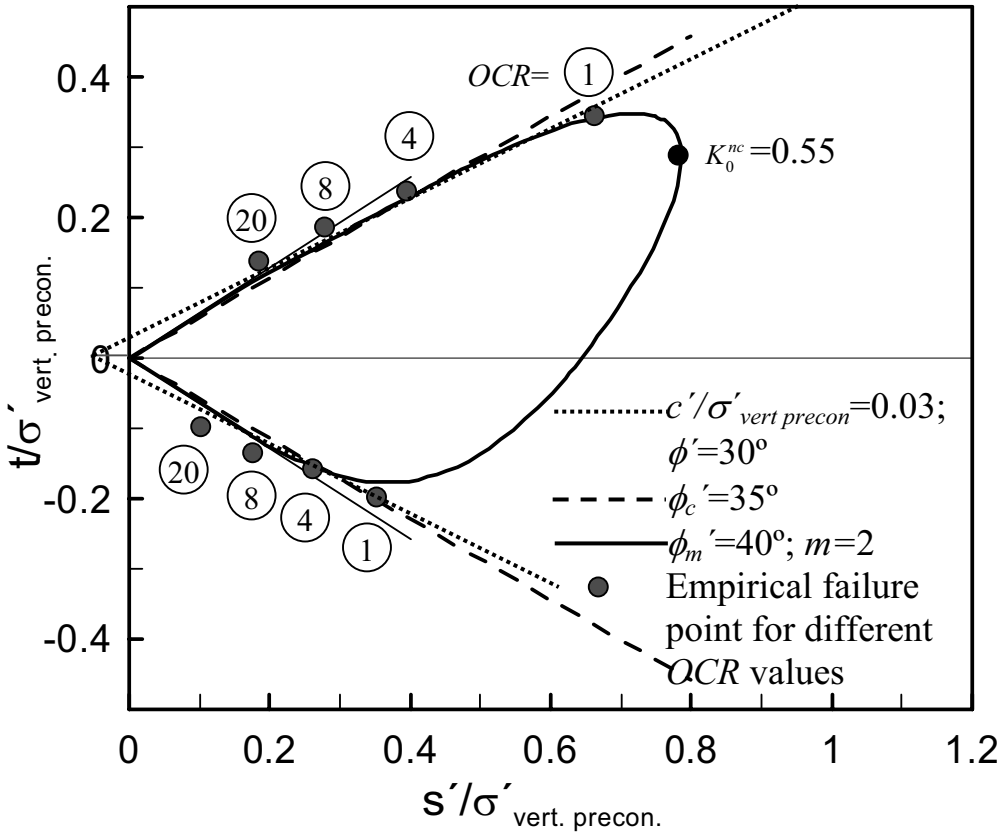

Figure 8.28: Yield and bounding surface in the MIT-S1 model compared with an empirical failure surface.

The sensitivity of the initial boundary surface due to variations in parameters ϕ'_m and m is shown in Figure 8.29. As can be seen, the parameter m greatly influences the undrained extensive shear strength.

The parameter ϕ'_c controls the failure surface which is in turn controlled by an isotropic function presented by Matsuoka and Nakai (1974). In the axisymmetric case this failure corresponds with the Mohr-Coulomb failure criterion. Since the model does not contain any intercept, this angle has to be slightly larger than the empirical value of 30º. For samples mainly exposed to τ_{xy}, τ_{xz} and τ_{yz} (s_3, s_4 and s_5) stresses, the failure criterion controls the strength while the bounding surface controls the shear induced excess pore water pressure.

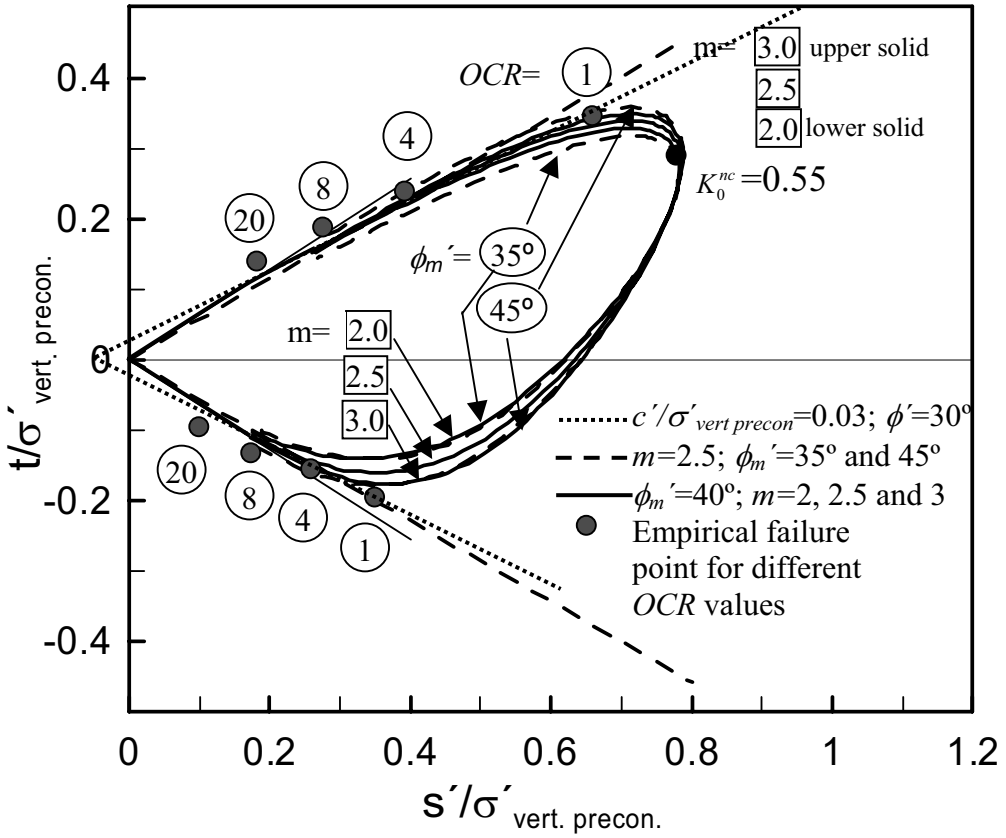

Figure 8.29: Influence of parameters ϕ'_m and m on the initial bounding surface.

8.8 Rate of evolution of the anisotropy of the boundary surface (ψ) and non linearity in shear (ω_s)

The *MIT-S1* model uses two hardening laws, rotational hardening and size changes of the boundary surface.

Rotational hardening is based on the concept that the principal directions of anisotropy rotate towards the main stress axis (Hashiguchi, 1977). The amount of rotational is described by the parameter ψ. The effect of this hardening law is shown in Figure 8.30, where the shape of the boundary surface is presented for different strains during a CK_0UC and a CK_0UE test. Both these tests were simulated for a stress situation of *OCR* equals 1.0 and a K_0 value of 0.55. The boundary surface is defined by ϕ_m'=40º and m=2. The squares in Figure 8.30 show the effective stress path in the s'-t space while the solid lines indicate the shape of the surface. As can be seen, the shape becomes more symmetric around the isotropic axis when large strains, b_1, decrease. The size, α, increases due to shearing. The effect of both these hardening rules is greater in extension than compression. The anisotropy, caused by stress history, is fully erased at an extension strain of 10%.

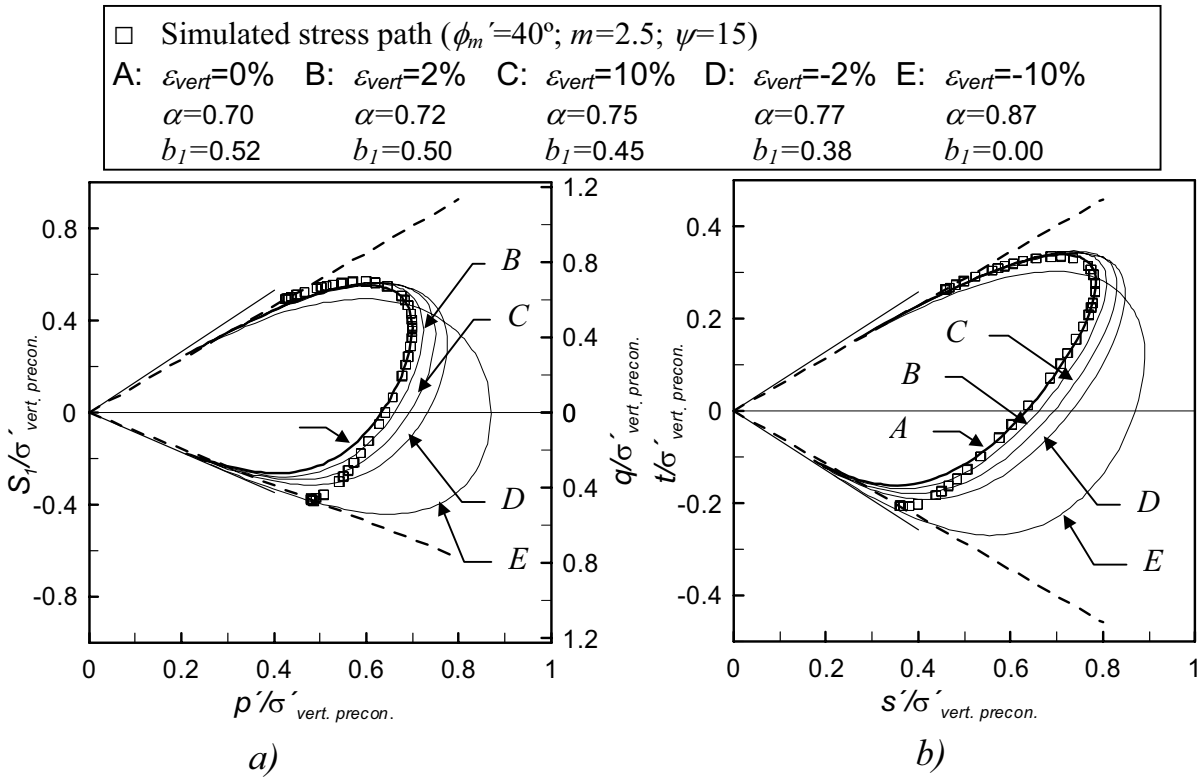

Figure 8.30: Change in the bounding surface during simulated CK_0UC and CK_0UE tests. a) p'-S_1 (q) space b) s'-t space

The sensitivity of parameter ψ is shown in Figure 8.31. According to Equation (7.22), there is no rotational hardening or changes in anisotropy for ψ=0. A high value of ψ erases the anisotropic memory more quickly than a low value and also has an effect on the stress path and undrained shear strength, especially in extension. During shearing, plastic strains develop as do changes in anisotropy, **b**, which alter the size, α, of the boundary surface (Equation (7.24)). The change in size increases for high values of ψ which is an effect of plastic strain occurring during rotational hardening.

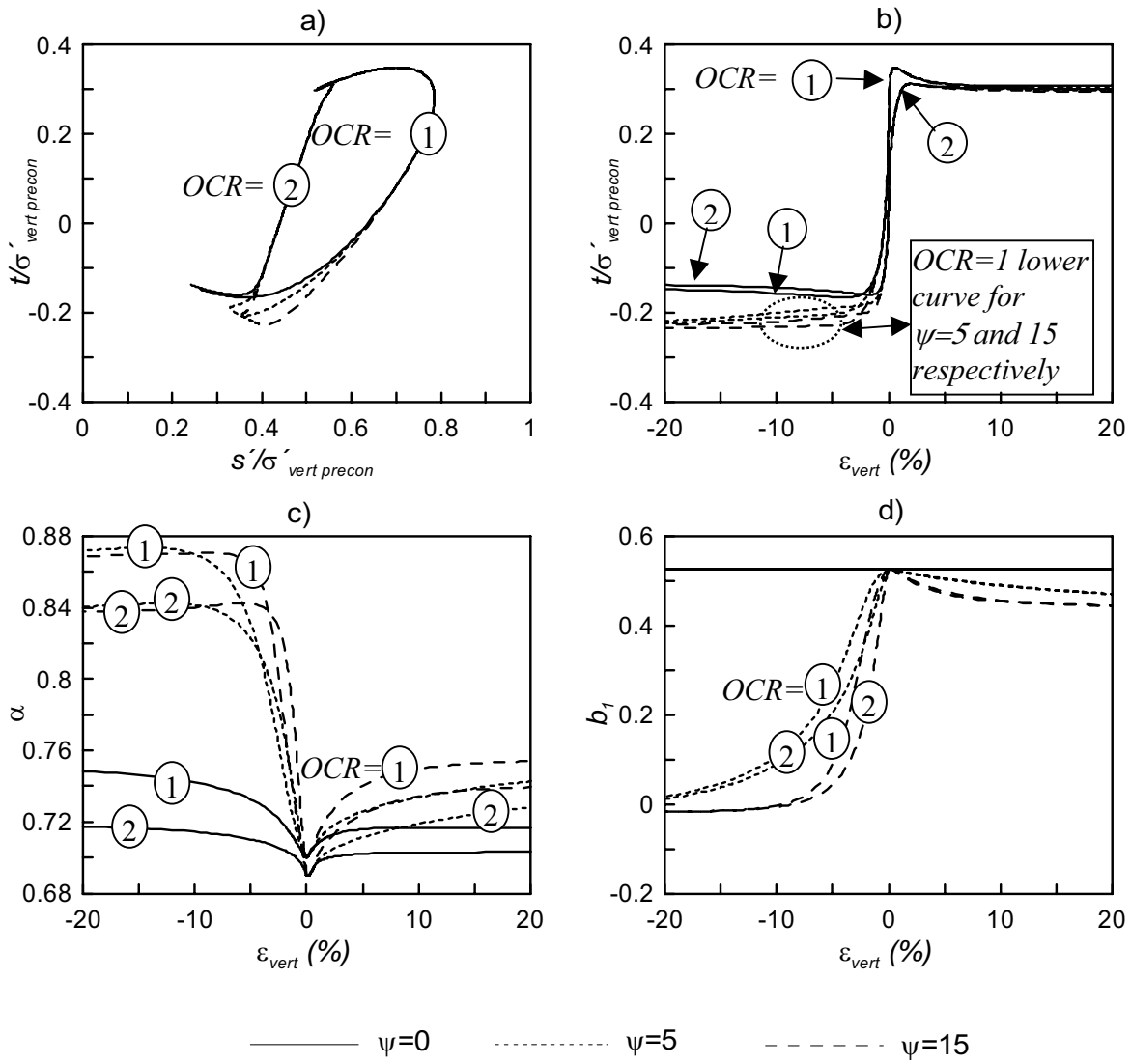

Figure 8.31 Visualisation of ψ's effect on the internal hardening parameters α and b_1 during simulated CK_0UC and CK_0UE tests for OCR 1.0 and 2.0.
a) stress path in the s´-t space *b) stress strain curve*
c) change in size, α *d) change in anisotropy*

The effect of these changes in the bounding surface, due to hardening, are important when complex stress paths occur, e.g. when different stress paths follow upon each other. When modelling a problem that does not relate to green field conditions, the effects of adjacent or former constructions influence the size and orientation of the boundary surface (preconsolidation pressure) and where a high degree of previous extensive strain is anticipated, it can indicate that the anisotropy may have been erased. If the green field anisotropy has been reduced it takes large strains, under constrained conditions, to re-establish the original anisotropy.

As shown above the parameter ψ has a major influence on the undrained shear strength in extension, although the parameter ω_s, which controls the small strain non-linearity in shear, also affects the undrained shear strength in extension. The

latter parameter influences the value of ρ_r, Eq. (7.44), which affects the hardening rules, Eq. (7.22) and Eq. (7.24).

The effect of varying these two parameters is shown in Figure 8.32 and Figure 8.33. The latter shows how these parameters affect the hardening rules. The parameters are fitted against the undrained laboratory tests presented in a previous chapter and excellent agreement can be observed in Figure 8.34.

□ *Laboratory tests 1/470 14m CK_0UC and 16 m CK_0UE*

MIT-S1 parameters (solid line)

ρ_c	C_b	μ'_0	D	r	ω	K_0^{nc}	ϕ'_{cs}	ϕ'_m	m	ω_s	ψ
0.35	120	0.15	0.005	2.0	2.0	0.55	35	40	2.5	5.0	15

Combinations of parameter ω_x and ψ.

A: ω_s= 0; ψ=15 (dashed)
B: ω_s=15; ψ=15 (dashed)
C: ω_s= 5; ψ= 0 (dots)
D: ω_s= 5; ψ=30 (dots)

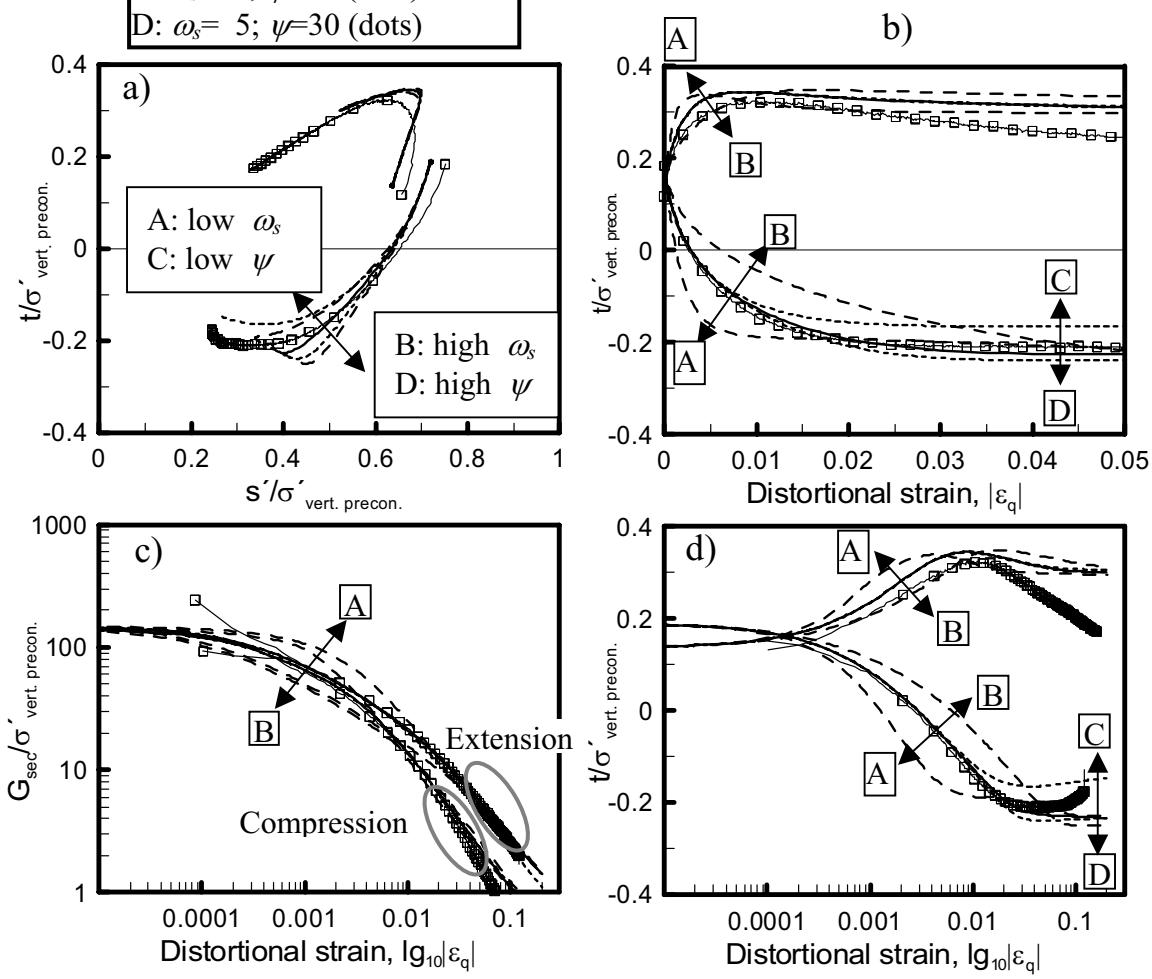

Figure 8.32: Influence of parameters ω_s and ψ in cases of undrained axisymmetric behaviour
a) stress path in the s´-t space *b) t vs. ε_q*
c) G_{sec} vs. $lg\varepsilon_q$ *d) t vs. $lg\varepsilon_q$*

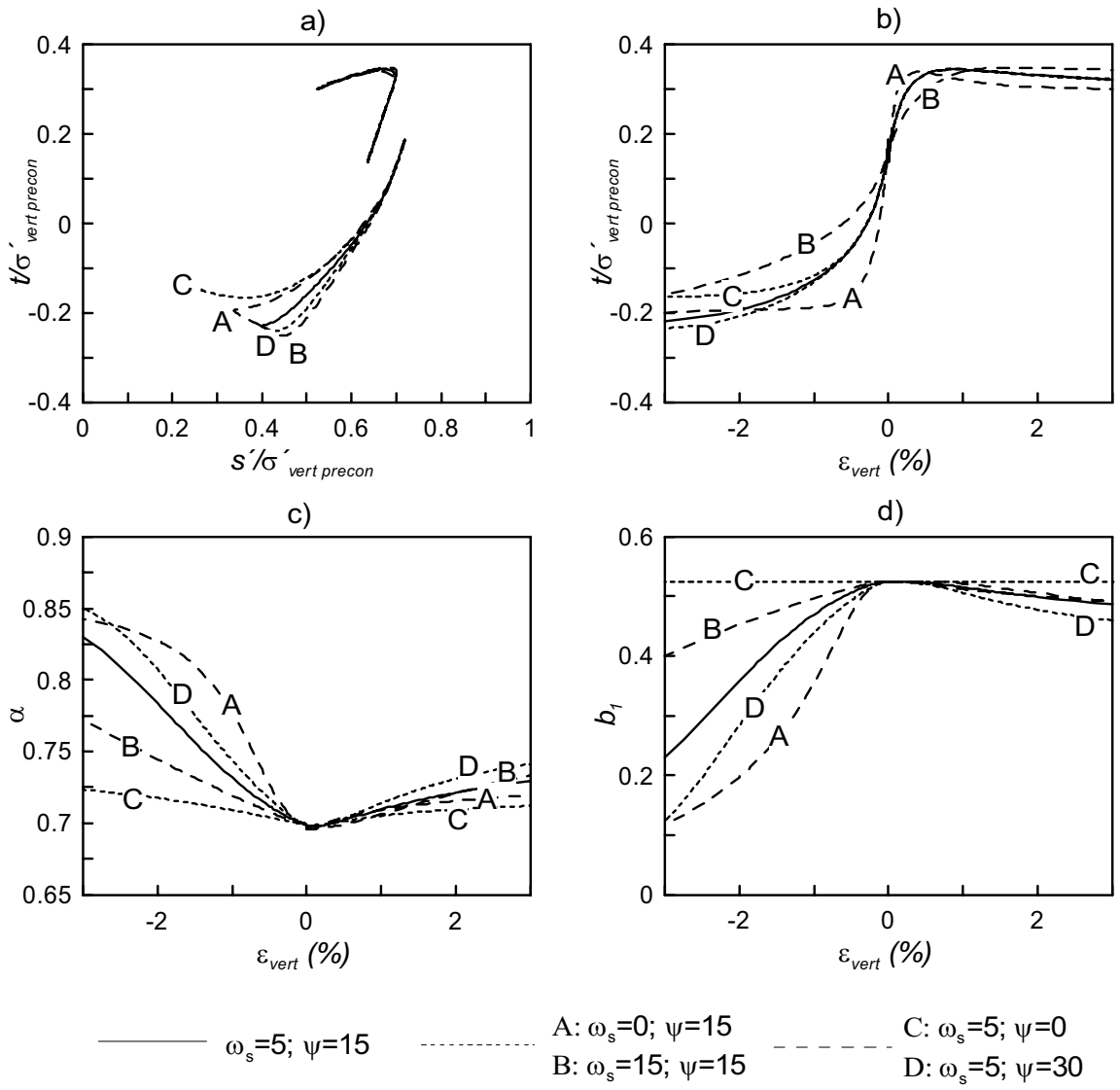

Figure 8.33: Visualisation of how parameters ω_s and ψ influence the hardening rules.

Laboratory tests from borehole 1/470 (thin solid lines) and the MIT-S1 parameters (wide solid line)

ρ_c	C_b	μ'_0	D	r	ω	K_0^{nc}	ϕ'_{cs}	ϕ'_m	m	ω_s	ψ
0.35	120	0.15	0.005	2.0	2.0	0.55	35	40	2.5	5.0	15

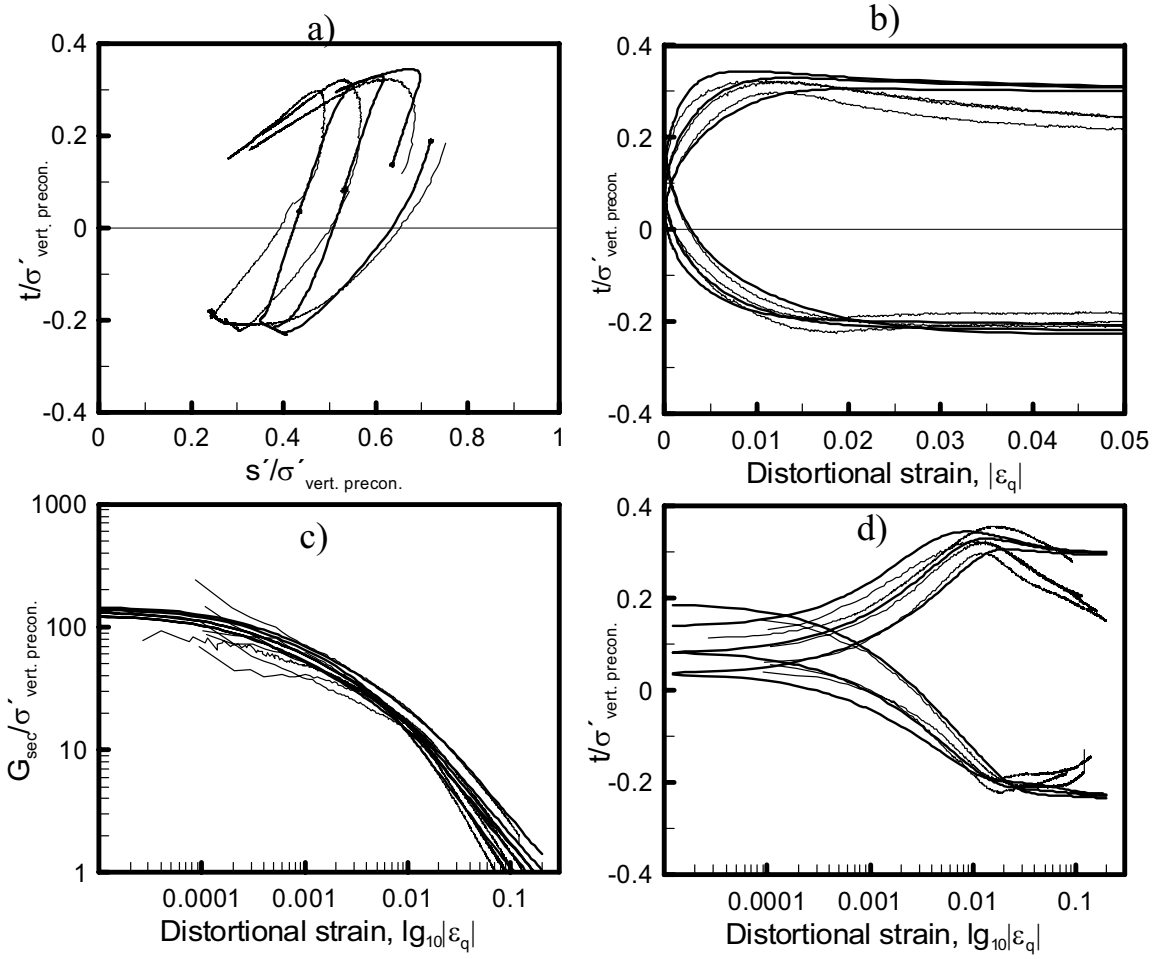

Figure 8.34: Model behaviour compared with test results from section 1/470.
a) stress path in the s´-t space *b) t vs. ε_q*
c) G_{sec} vs. $lg\varepsilon_q$ *d) t vs. $lg\varepsilon_q$*

8.9 Irrecoverable plastic strain due to an unload reload cycle

True soil behaviour exhibits plastic strains due to the unload reload cycle. This phenomenon is captured in the bounding surface formulation by mapping rules. The plastic strain of one closed unloading reloading cycle, $\Delta\varepsilon_p$, increases with the amount of maximum *OCR*. The influence of parameter *h* is shown in Figure 8.35.

MIT-S1 parameters

ρ_c	C_b	μ'_0	D	r	ω	K_0^{nc}	ϕ'_{cs}	ϕ'_m	m	ω_s	ψ
0.4	120	0.15	0.005	2.0	2.0	0.55	35	40	2.5	5.0	15

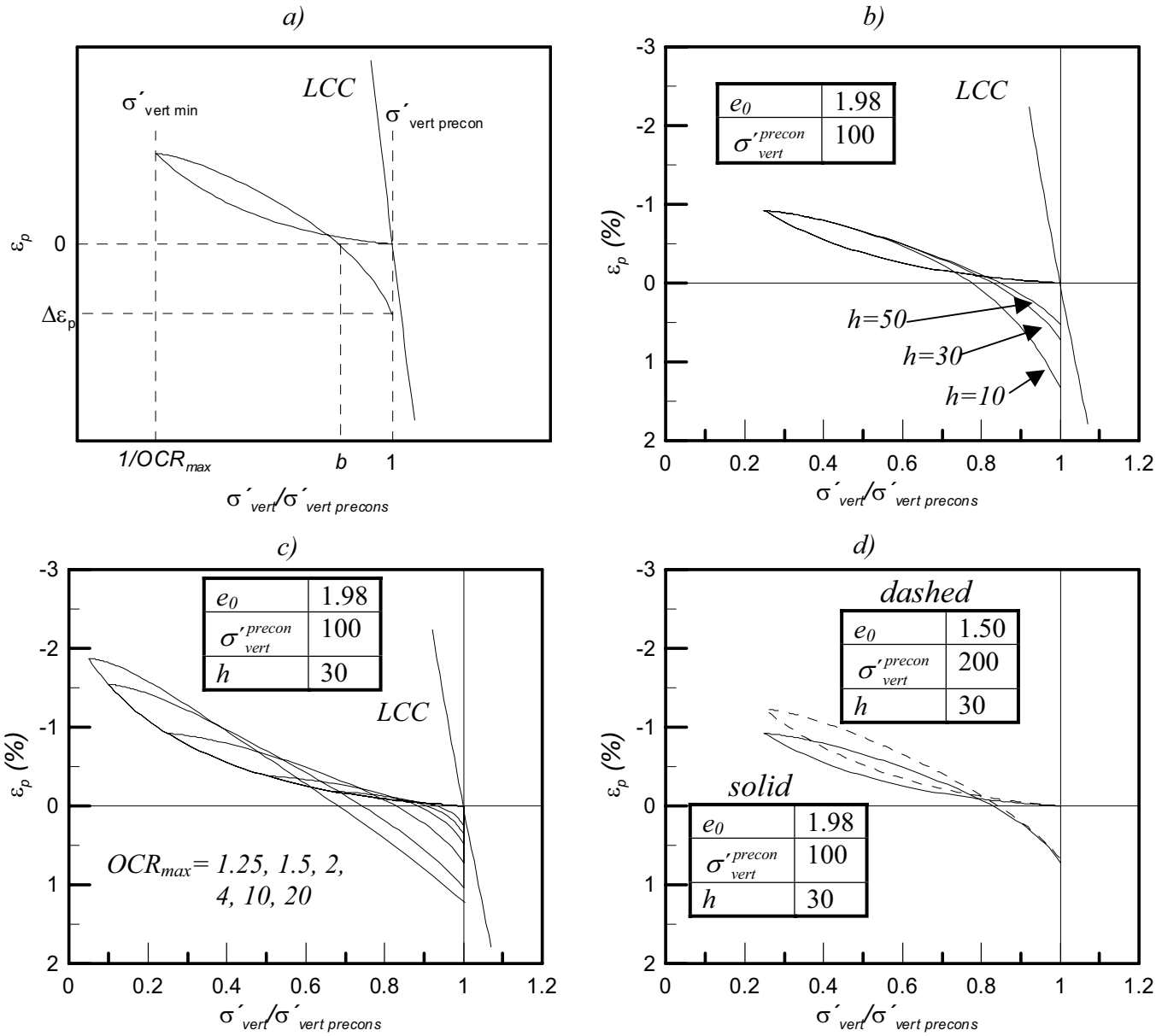

Figure 8.35: Influence of parameter h on the volumetric strain during an unloading reloading cycle under oedometer conditions.
a) definition of behaviour *b) Influence of h on $\Delta\varepsilon_p$*
c) reloading behaviour from different OCR_{max}
d) different volumetric responses related to the location along the LCC-line

For evaluation of h several unloading reloading loops have been performed in the laboratory. These test have been performed both as K_0 tests and as oedometer test. The results associated with $\Delta\varepsilon_p$ and b are presented in Figure 8.36. Parameter b is defined as the normalized vertical stress where ε_p equals 0.

Simulations of these two parameters were performed for h=10, 30 and 50 under two different initial conditions along the *LCC*-line, σ'^{precon}_{vert}=100 and 200 kPa. From Figure 8.36 it is obvious that the influence of σ'^{precon}_{vert} can be disregarded for moderate unloading ratios and therefore σ'^{precon}_{vert} was not considered in the test results. A value of 30 was chosen for parameter h. The reason for the introduction of parameter b was due to the fact that it has been used in the literature, to define both the stress ratio where the swelling equals the effects of secondary compression and the intersection between the unloading and reloading curve in a σ'_{vert}-ε_{vert} plot (Larsson, 1986). Both test results and simulations using the *MIT-S1* model reveal that the tangential reloading oedometer modulus, M_{rl}, is approximately constant in the σ'^{min}_{vert} to b•σ'^{precon}_{vert} stress range.

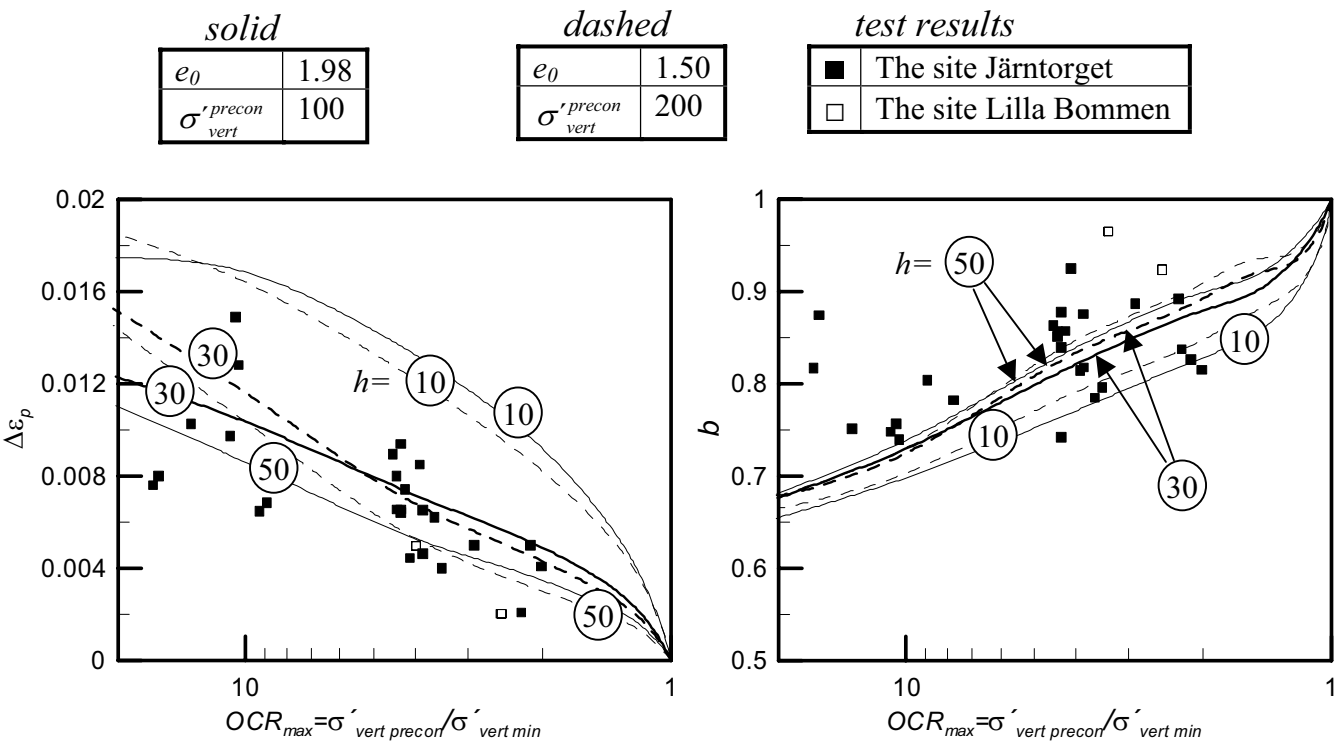

Figure 8.36: Determination of parameter h compared with test results.
a) Fitting of irrecoverable strains, $\Delta\varepsilon_p$
b) Comparison between simulated and observed values of b.

8.10 Observed behaviour related to the *MIT-S1* formulation and the parameters fitted to the Järntorget site

The *MIT-S1* formulation seems capable of simulating most of the behaviour observed in Swedish clay with the exception of time effects such as creep (secondary compression), different *LCC*-lines for various strain rates etc. This section provides a brief summary of observations made during different laboratory test simulations.

8.10.1 Direct simple shear behaviour

Direct simple shear, *DSS*, tests were simulated in order to compare the results with those obtained in the laboratory. In the laboratory test the shear stress, τ_{xy}, and distortional angle, γ_{xz}, were measured. Simulation also offers the possibility of visualizing how the test sample may behave, in terms of the development of excess pore water pressure, Δu, rotation of the principal stresses etc. The test results are presented in Section 6.9 but in Figure 8.37 below the normalized τ_{xy} and G_{sec} *vs.* ε_q., are compared with the simulated *DSS*-test, in which the data for the Järntorget site was applied. The visualization was made for a normally consolidated clay, *OCR*=1.0, and for a slightly overconsolidated clay, *OCR*=2.0. The range was chosen to fit that of the laboratory tests. As can be seen, the match is excellent in all but three cases, denoted 1, 5 and 6 in Figure 6.13. The *OCR* in the sample in test 5 exceeded 2.0 and is therefore logical according to Equation (8.7). The consolidation stress in test 6 represents a stress situation far in excess of the σ'^{precon}_{vert} found in the field, and the fact that it does not seem to agree with the *SHANSEP* assumption has been previously discussed.

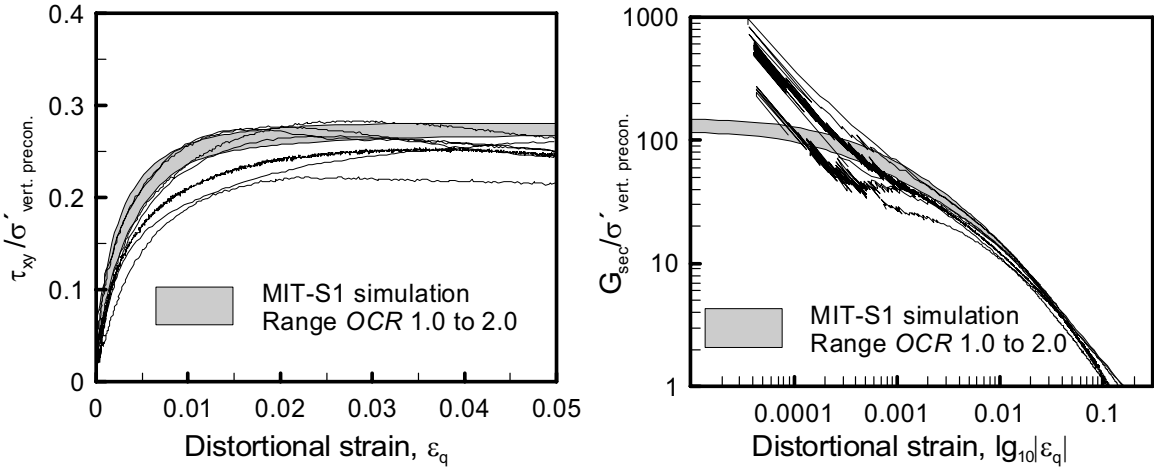

Figure 8.37: Simulated DSS-test compared with laboratory data
a) Shear stress vs. distortional strain
b) Shear module (secant) vs distortional strain

The shear modulus obtained shows excellent agreement with the laboratory results for strains larger than 0.01%, while the accuracy in monitoring small strain in the direct simple shear equipment is insufficient.

The *MIT-S1* formulation seems capable of simulating the behaviour observed in the *DSS*-tests. Limitations of the *DSS*-tests were discussed in a previous chapter, which also include a sketch of some of the stress paths. The following stress paths were obtained from the simulations, see Figure 8.38.

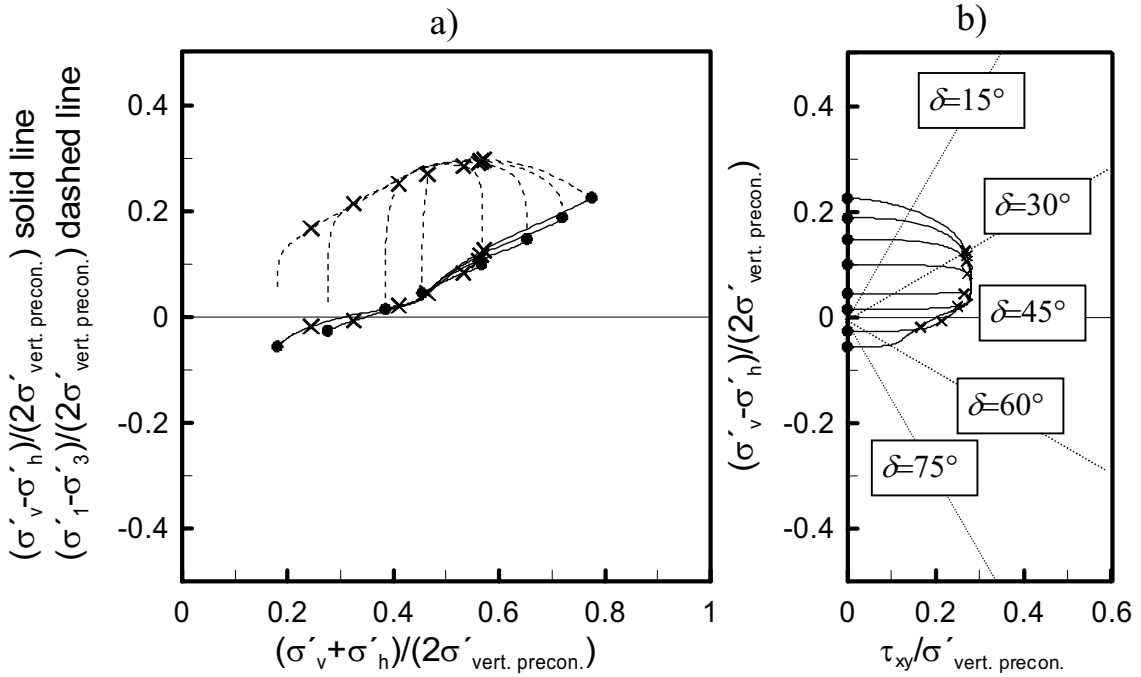

Figure 8.38: Stress paths from the simulated DSS-test, OCR=1.0, 1.1, 1.25, 1.5, 2.0, 2.5, 4.0 and 8.0.
a) Stress path in the s´-t and s´-τ_{max} space *b) τ_{xy}-t space*

In Figure 8.39 the stress paths have been complemented by the evaluated shear strength, $s_{u,\,DSS}$. This strength is not the peak value of shear stress in the sample, due to dilation, the model indicates increasing strength for overconsolidated clay, even in the case of non-acceptable strains. Instead of peak values, the strength was evaluated as shear stress at a specified value, where *G* is reduced to a certain value, in this case to the effective vertical preconsolidation pressure. In the model, dilation occurs when *OCR*>2.0. In the case of low *OCR* values, it is obvious that $s_{u,\,DSS}$ occurs at a stress rotation that is slightly higher than 30º and approximately 10% higher than the τ_{xy} measured in the *DSS*-test, see Figure 8.39.

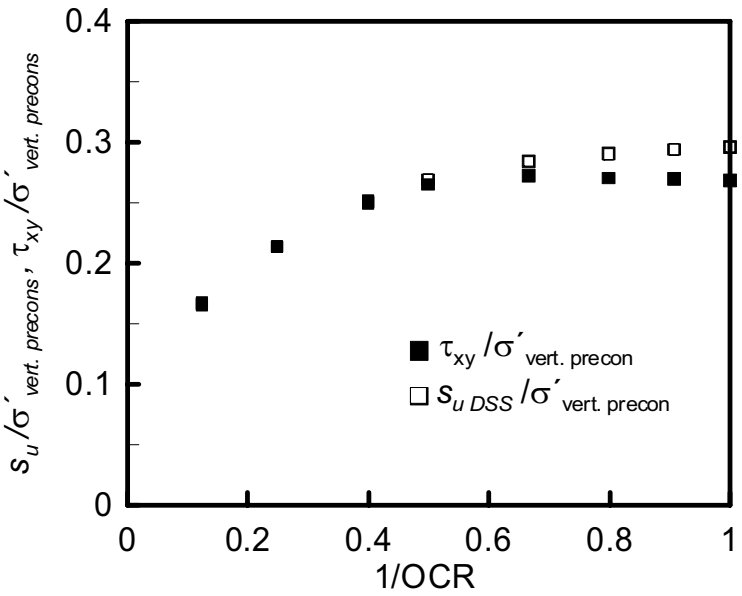

Figure 8.39: The dependence of maximum shear on OCR in the DSS-test. τ_{xy} is the applied shear stress at failure and $s_{u\ DSS}$ the maximum shear stress in the sample at failure.

In practice, it is not advisable to use the higher value in Figure 8.39 as a strength parameter in calculations were the actual stress rotation is not incorporated.

8.10.2 Undrained behaviour

Simulation of UK_oTC, UK_oTE and UK_oDSS tests has been presented in sections 8.8 and 8.10.1. These tests enable visualization of the *OCR* dependent undrained shear strength. The undrained shear strength, s_u, is evaluated as the shear stress when the strain changes become unacceptable for a deviatoric load increment. This level has here been defined as the shear stress when *G* becomes smaller than σ'^{precon}_{vert} [12]. In Figure 8.40b the evaluated shear strength is visualized by means of "x" in the stress strain curve. In this figure it is obvious that neither the peak value nor the residual strength can be used independently of the *OCR*-value. It is impossible to use a specified strain value in a stringent way for different *OCR* values. One should rather attempt to identify an acceptable strain for the problem on hand before choosing the strength. Figure 8.40a show*s* the undrained compression and extension stress paths for different *OCR* values under axi-symmetrical- and plane strain conditions. In the figure the evaluated s_u is denoted "x" under axi-symmeric conditions and "+" under plane strain.

[12] The reason for using $G=\sigma'^{precon}_{vert}$ as definition for failure may be questioned, however it produces reliable strength and there will still be some strength to mobilize. Evaluating the strength as the peak strength will yield large deformations for high *OCR*s. Using a constant strain level as a reference for the s_u yields that for low *OCR*s that the stess strain curve is beyond the peak and/or that for high *OCR*s that there still will be considerable strength to mobilize. The constant value on *G* could have any value as long as it is positive and that the tolerable strain is not exceeded.

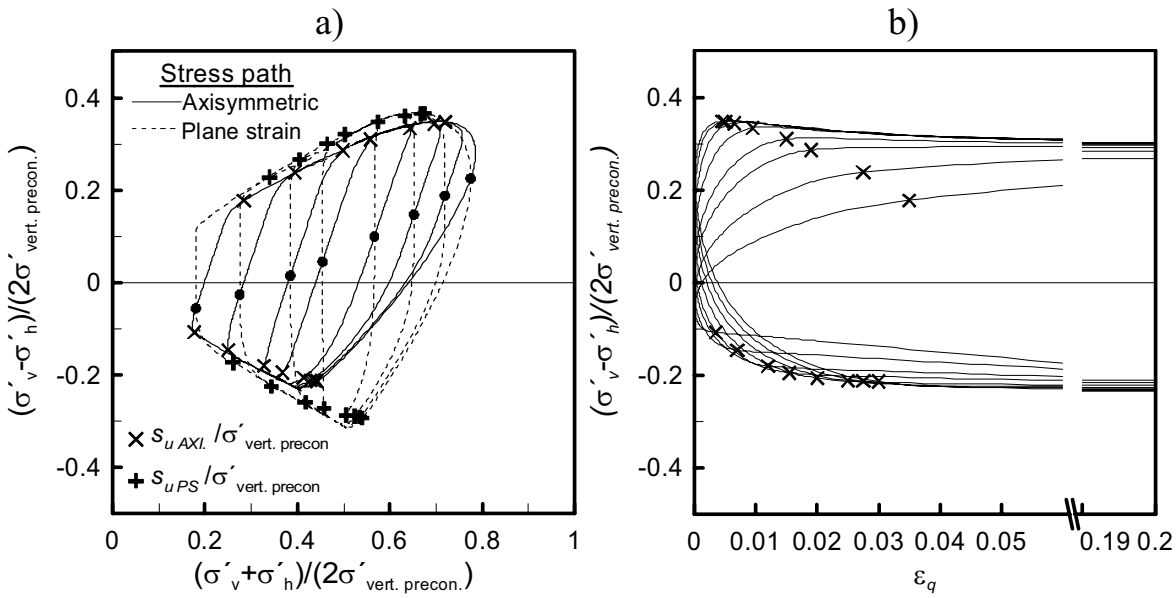

Figure 8.40: Undrained shear behaviour for OCR 1.0, 1.1, 1.25, 1.5, 2.0, 2.5, 4.0 and 8.0 a) stress paths in the s´-t space under axisymmetric conditions and plane strain. b) shear stress vs. distortional strain under axisymmetric conditions, complemented by estimated undrained shear strength.

Figure 8.40a clearly illustrates that plane strain increases s_u. In compression, the increase obtained by using the *MIT-S1* model is about 5% and in extension it is as high as 35%. The latter increase may not be appropriate for all *OCR* values, as it is dependent on the size of strain deemed acceptable.

The s_u values from the simulation of different laboratory tests with the *MIT-S1* model are shown in Figure 8.41 where a) presents the evaluated s_u for different *OCR* values and laboratory tests and b) shows the degradation of s_u as a function of the *OCR*. Figure 8.41b is complemented by the relation proposed by Ladd *et al.*, (1977) although the simulated undrained shear strengths are better approximated using the hyperbolic relation in Equation (8.8).

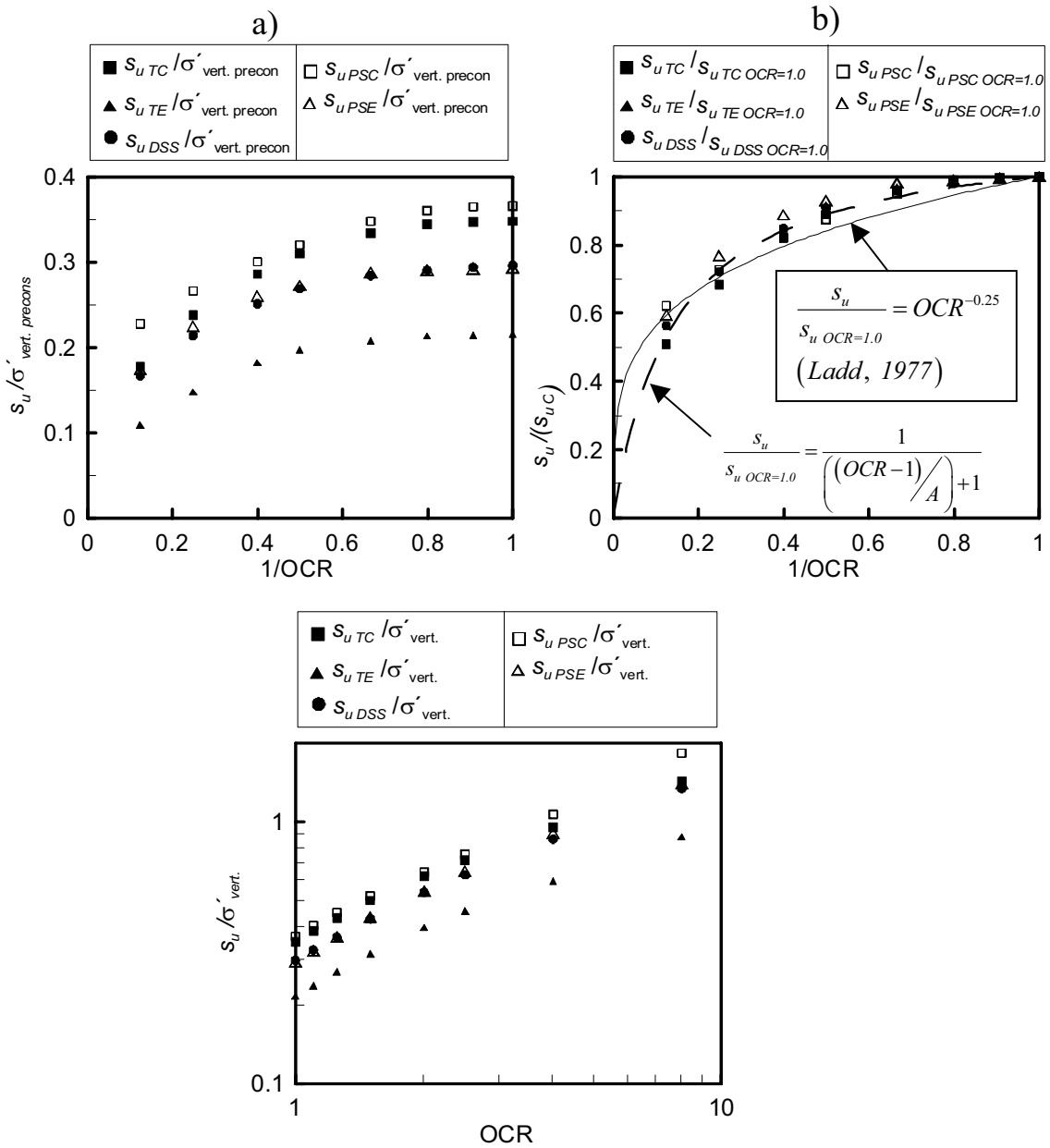

Figure 8.41: Evaluated undrained shear strength from MIT-S1 simulations
a) Normalized s_u vs. 1/OCR b) Degradation of s_u dependent on the OCR
c) Normalized s_u against σ'_{vert} vs. OCR

This new way of describing degradation seems to be more accurate for matching the simulated results than that presented by Ladd *et al.* (1977), particularly in the case of an *OCR* less than 4.0. The hyperbolic degradation presented in Figure 5.44b has an A value of 8.

$$\frac{s_u}{s_{u\,OCR=1.0}} = \frac{1}{\frac{(OCR-1)}{A}+1} \qquad \textit{A is in the range of 7-10} \qquad (8.8)$$

The simulated undrained shear tests have approximately the same shear modulus. The initial modulus, G_0, is the same for all directions and the degradation in G_0, shown in Figure 8.42a, is controlled by Equation (8.9).

$$G_0 = C_b \frac{1.5(1-2\mu_0)}{(1+2\mu_0)} \frac{p'^{1/3}}{n_0} \tag{8.9}$$

The stiffness decreases with increased ε_q and Figure 8.42b shows how G_{sec} decreased in a *DSS*-test due to undrained shear. Almost identical results were derived from the various types of shear test.

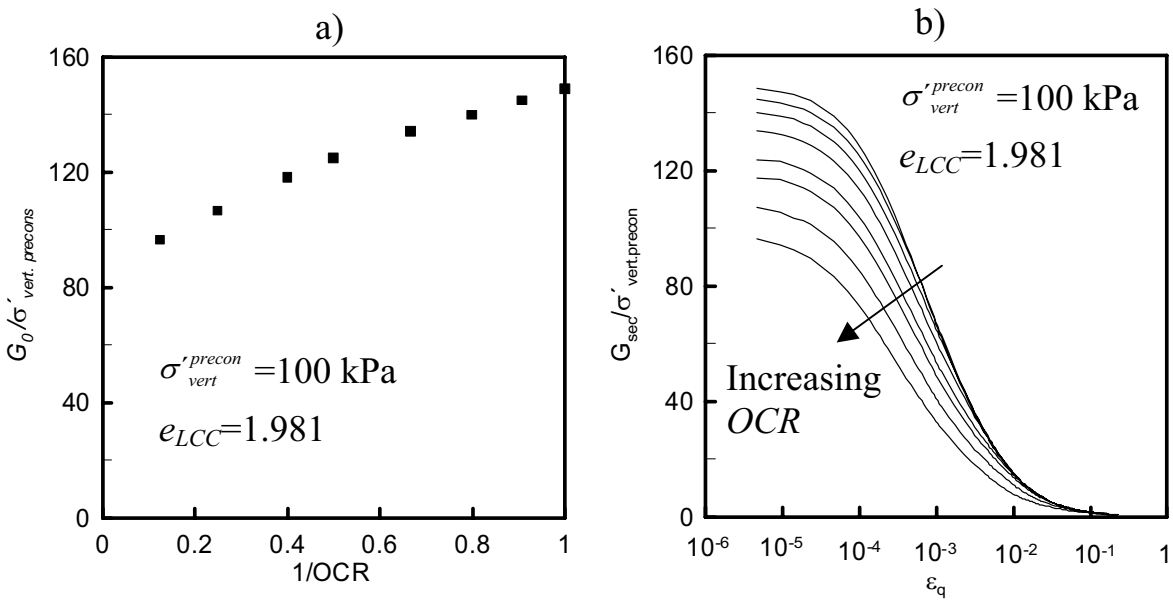

Figure 8.42: Visulaization of G_{sec} obtained from the MIT-S1 model
a) Degradation of G_0 with increased OCR
b) Degradation of G_{sec} with increased ε_q (CK_0DSS-test)

The initial modulus is identical and the degradation has the same shape although some differences occur due to plastic strains close to the bounding and/or failure surface.

8.10.3 Unloading moduli

There are different ways of unloading e.g. decreasing the shear and/or mean stress. However, in most cases unloading refers to a decrease in vertical stress under the same boundary conditions as in the oedometer. The swelling behaviour in this case is controlled by the unloading constrained modulus, M_{ul}. The observed behaviour, both from field measurements and laboratory tests, is that normal consolidated clay exposed to relatively low stress decreases exhibits a very stiff response. In young clays, the swelling can even be neutralized by time dependent compression. When unloading to higher *OCR* values, the modulus gradually decreases with increased swelling per load unit. Several studies have been performed on this phenomenon in Sweden, (Larsson, 1977;

Larsson, 1986; Alén and Jendeby, 1996; Karlsrud, 2003; Persson, 2004). All these reports propose a relation of M_{ul} directly proportional to σ'^{precon}_{vert}, which is not the case in the *MIT-S1* formulation.

$$M_{ul} = \frac{\frac{1}{b}\frac{\sigma'^{precon}_{vert}}{OCR}}{a_s} \qquad \text{(Larsson, 1986)} \qquad (8.10)$$

where the typical values for Swedish clay are b=0.8 and a_s=0.1. However, in a field study by Alén and Jendeby (1996), values of a_s in the range of 0.001 to 0.0025 were obtained, and the b value was slightly below 0.8.

$$M_{ul} = \max\begin{cases} \sigma'^{precon}_{vert} A\left(\frac{1}{OCR}\right)^4 \\ \frac{\frac{\sigma'^{precon}_{vert}}{OCR}}{a_s} \end{cases} \qquad \text{(Persson, 2004)} \qquad (8.11)$$

where the values A=1500 and a_s is in the range of 0.0025 to 0.005 evaluated from field tests on the site at Lilla Bommen. The changeover between the formulas is in the range of OCR=1.5 to 2.0.

$$M_{ul} = \sigma'^{precon}_{vert} B \cdot e^{\frac{C}{OCR}} \qquad \text{(Persson, 2007)} \qquad (8.12)$$

where the values B=35 and C=3.5 are derived from field tests on the site at Lilla Bommen

From the *MIT-S1* formulation a simplified expression of M_{ul} can be derived using Schmidt´s relation of how μ' changes during 1D-unloading.

By using Eq. (3.35) in combination with Eq. (7.11) the expression in Eq. (8.13) can be derived.

$$\mu' = \frac{1}{2} - \frac{1}{\left(\frac{2\left(\mu'_0 + \mu'_0\omega\xi_s + 1 + \omega\xi_s\right)}{-3\left(2\mu'_0 - 1\right)} + \frac{1}{3}\right)2} \qquad (8.13)$$

From Eq. (7.9) and from constrained 1D unloading Eq. (8.14) is obtained.

$$\xi_s = \frac{3\sqrt{6}\left(K_0 - K_0^{nc}\right)}{\left(1 + 2K_0\right)\left(1 + 2K_0^{nc}\right)} \qquad (8.14)$$

By using Eq. (2.3) in Eq. (8.14) and substitute into Eq. (8.13) an expression for μ' as a function of OCR is obtained. This expression contains the *MIT-S1*

parameters μ'_0, ω_s and K_0^{nc} and the curve fitting parameter m from Schmidt's expression of the unloading stress path.

The swelling behaviour is given in Eq. (7.10) and in combination with Eqs. (3.32) - (3.36) and the expression for μ' as a function of *OCR* a relation for the unloading oedometer modulus can be derived as a function of *OCR,* the state parameters e_{LCC} and the preconsolidation pressure. This relation contains the *MIT-S1* parameters μ'_0, ω_s, K_0^{nc}, C_b, D and r and Schmidt's parameter m.

The comparison between these different formulations of how the unloading moduli vary depending on *OCR* makes it obvious that those from field studies show a stiffer response than the ones obtained exclusively by means of laboratory tests, see Figure 8.43. As has been demonstrated, the initial stiffness at the Lilla Bommen site is higher than at Järntorget, C_b being 180 instead of 120. But even if C_b is increased to 180 and all other parameters in the *MIT-S1* formulation are kept constant, there will still be a factor of 2 to 4 between Persson´s results and those derived from the *MIT-S1* model.

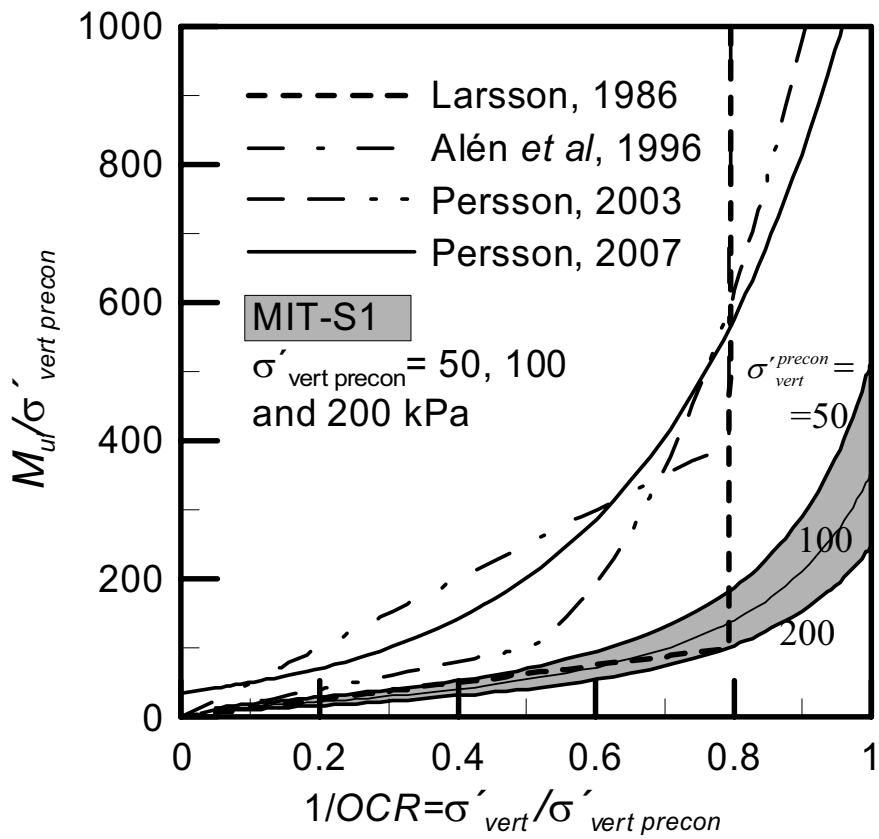

Figure 8.43: Comparison between different formulations for the unloading modulus.

8.10.4 Reloading modulus

The reloading modulus, M_{rl} is approximately constant until all strains due to swelling have been eliminated. This occurs at smaller stresses than those at the

point at which unloading started. The ratio between these stresses is denoted *b*. This simplification leads to the formula presented in Equation (8.15) where all swelling above the stress ratio *b* has been disregarded.

$$M_{rl} = \frac{\sigma'^{precon}_{vert}\left(b - \frac{1}{OCR_{\max}}\right)}{\int_{\sigma'^{precon}_{vert}/OCR_{\max}}^{b\cdot\sigma'^{precon}_{vert}} \frac{1}{M_{ul}\left(\sigma'_{vert}\right)} d\sigma'_{vert}} \tag{8.15}$$

In *MIT-S1* simulations the parameter *b* varies between 0.7 and 0.9 for OCR_{max} in the range of 20 to 1.25, c.f. Figure 8.36. However, when presenting approximate values of M_{rl} (secant modulus) the same *b* value (0.8) is used. The reloading moduli evaluated from different ways of expressing the swelling are presented in Figure 8.44. As discussed in a previous section, the results from the field data indicate stiffer behaviour.

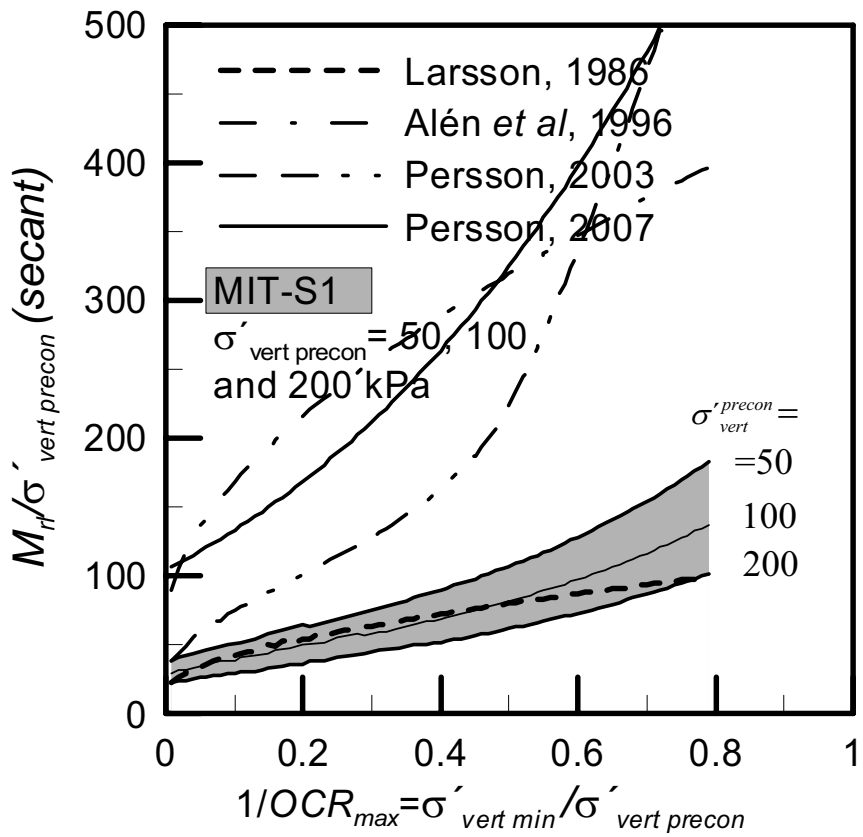

Figure 8.44: Illustration of the reloading modulus dependent on the OCR at which the reloading starts. The modulus is assumed to be constant and the crossing of the stress strain curve for a closed unloding reloding cycle is set to 80% of σ'^{precon}_{vert}

The diagram in Figure 8.44 presents a range of reloading modulus to be expected for reloading to a stress situation represented by *OCR* 1.25. Above this stress level the modulus decreases gradually to one represented by the *LCC*-line at *OCR* 1.0. In laboratory tests the constant modulus M_0 is estimated below

σ'^{precon}_{vert}. The M_0 modulus estimated from the oedometer is strongly affected by the stress changes caused by taking the sample from the ground and placing it in the laboratory equipment. If the disturbance (the swelling due to unloading) is kept low, the M_0 value will be higher than if the sample has been allowed to swell as a result of unloading.

8.11 Summary of evaluated Swedish clay parameters

Earlier in this chapter all the *MIT-S1* parameters were evaluated at the Järntorget test site in Gothenburg. The values were matched to laboratory results performed within this project.

Table 8.3: Summary of evaluated parameters and assumed possible ranges. The table also includes the values for Boston Blue Clay as a reference, (Pestana et al., 2002).

Test type	Parameter	Physical contribution	Järntorget	Possible range Järntorget	Possible range Sweden	BBC
Hydrostatic or 1-D compression	ρ_c	Compressibility of normally consolidated clay (lg e vs. lg σ'_{vert})	0.4 layer 1 0.35 layer 2	0.3-0.5	0.3-0.5	0.178
	D	Non linear volumetric swelling behaviour	0.005	0.001-0.01	0.001-0.01	0.04
	r		2.0	0.5-8.0[1]	0.5-8.0[1]	0.85
	h	Irrecoverable strain	30	20-40	5-50	6
K_0 oedometer or triaxial	K_0^{nc}	K_0 for *NC* clay	0.55	0.45-0.55	0.45-0.6	0.49
	μ'_0	Poisson's ratio at stress reversal controlling $2G_{max}/K_{max}$	0.15	0.1-0.2	0.1-0.2	0.24
	ω	Non linear Poisson's ratio. Stress path during 1-D unloading	2.0	1.0-3.0[2]	0.5-3.0[2]	1.0
Undrained triaxial shear tests: *OCR*=1; CK_0UC *OCR*=1; CK_0UC CK_0UC; *OCR*>1	ϕ'_{cs}	Critical state friction angle in triaxial compression	35.0°	33.0°-35.0°	28.0°-35.0°	33.5°
	ϕ'_m	Geometry of Bounding Surface. Stress path of undrained CK_0UTC/TE tests	40°	35°-45°	35°-45°	46.0°
	m		2.5	2.0-3.0	1.5-3.0	0.80
	ω_s	Small strain non linearity in shear	5	4-6[5]	3-8[5]	8.0
	ψ	Rate of evaluation of anisotropy (rotation of bounding surface)	15	5-15[4]	0-30[4]	15
Shear wave velocity	C_b	Small strain stiffness at load reversal	120	80-140[3]	80-250[3]	450

1) The higher value correspond with D=0.001 and vice versa
2) The higher value correspond with μ'_0=0.1 and vice versa
3) The higher value correspond with high values of D and/or r and vice versa
4) The higher value correspond with low values of m and vice versa
5) The higher value correspond with low values of ψ and vice versa

Changes in w_L must have a direct influence on parameter m. The empirical relation between the lower values of $s_{u\ ext}$ and low values of w_L can be obtained by using low values on m and vice versa. The strength $s_{u\ DSS}$ is affected by ϕ'_{cs} and the amount of generated excess pore water pressure, which is controlled by the bounding surface plasticity, mapping rules, which in turn is controlled by one of the hardening laws (ψ). A lower value of ϕ'_{cs} will decrease $s_{u,\ DSS}$ and is therefore suitable for a cohesive soil with a lower w_L.

The effect of high sensitivity can be partly modelled. High sensitivity leads to large differences in peak and residual strength which are partly controlled by parameters ω_s and ψ.

Previous research reveals that the observed response in the field is stiffer than that in the laboratory. Since all parameters were estimated from laboratory tests one can assume that the true value of C_b is in the range of 200 to 300 and that r or D should probably be in the lower range in Table 8.3.

In order to verify the values of the different parameters the following tests are needed in combination with the ranges presented in Table 8.3.

- CRS tests to establish the *LCC*-line. Some of these tests should be unloaded and reloaded from the *LCC*-line to different *OCR* values. Some should be unloaded to $OCR \geq 10$.
- UK_0UC and UK_0UE for $OCR=1.0$.
- UK_0UC and UK_0UE for $OCR \geq 1.5$.
- K_0 test compressed to $\varepsilon_{vert}>10\%$ stress path coinciding with the *LCC*-line. This test should be unloaded from the *LCC*-line to $OCR \geq 5$ and reloaded back again.

9 NUMERICAL ANALYSES OF TWO IDEALIZED EXCAVATIONS IN CLAY

9.1 Introduction

Since the field measurements at the site of the Göta tunnel are affected by more than just deformation caused by stress changes due to the excavation, e.g. piling, volume loss in the sand layer underlying the clay, temporary ramps used for work vehicles etc., some idealized examples of excavations are presented in this chapter. These examples are analysed by means of three different soil models in an attempt to predict the behaviour. The soil properties used are typical of the highly plastic clay in Gothenburg. The calculation results are thereafter compared with some empirical methods used for predicting ground surface settlements adjacent to an excavation.

The soil models employed comprise a simple, but widely used, *PLEP* model with *MC* failure criteria, the *MIT-S1* model described earlier and a total stress based model, *e-ADP*. The latter is briefly described in this chapter and more information can be found in the literature (Grimstad, 2005; Grimstad *et al.*, 2006).

The reason for introducing a total stress based model is that a model capable of capturing anisotropic behaviour under undrained conditions will require simpler constitutive relations than those of a model based on effective stresses. However, a total stress based model cannot perform a coupled analysis nor can it be used to study the behaviour under drained conditions.

In the comparison between these three types of models the need to take anisotropic behaviour into account will be elucidated, while in the comparison between the *MIT-S1* and *e-ADP* the increased knowledge derived from using an effective based formulation as opposed to the total stress based formulation will be demonstrated.

9.2 Formulation and input parameters to *e-ADP*

The formulation is limited to *PS* conditions and based on the work by Athanasiu (1999), who developed the constitutive equations capable of modelling the variation in s_u for different load directions (Bjerrum and Aitchison, 1973).

A total stress based model, *ANISOFT,* was developed and implemented in PLAXIS by Andresen and Jostad (1999). *ANISOFT* is formulated as an isotropic strain hardening/softening incremental elastoplastic model with an associated flow rule. The yield function is based on the Tresca criteria with different strengths dependent on the rotation of the principal stresses. A simplification of

ANISOFT called *NGI-ANI2,* that can be used in combination with *PLAXIS* is available (www.ngi.no) and consists of the same framework as *ANISOFT* but without any strain softening.

The *e-ADP* model developed at *NTNU* (Grimstad, 2005; Grimstad *et al.*, 2006) is approximately the same as *ANISOFT* but with no softening or inner elastic stress region. An elliptical yield surface is used and loading from the initial state will generates varying amounts of plastic strain depending on both the size and the direction of loading. There is a difference between the interpolation function for different load directions used in *e-ADP* and *ANISOFT*.

The *e-ADP* model uses $s_{u\ comp}$, $\tau_{xy\ DSS}^{max}$ and $s_{u\ ext}$ as direct input parameters for strength and the amount of engineering shear strain at failure based on the CK_0UC-, CK_0UC- and CK_0UEC- tests, in combination with an elastic shear modulus that defines the stress-strain response. The change in strength and shear modulus follows the same pattern as that in Equation (9.1) for $s_{u\ comp}$, which means that the initial σ'_{vert} is treated as an indirect input parameter within the constitutive formulation. The engineering strain is defined in Equation (9.2). In order to model the undrained behaviour, μ' is set slightly lower than 0.5, yielding 12 input parameters, 8 of which are true parameters, compared with the 13 used by the *MIT-S1*. An advantage is that the *e-ADP* parameters can be established by laboratory test more widely used than those needed to fit the *MIT-S1* parameters.

$$s_{u\ comp} = C_A + \kappa_A \cdot \sigma'_{vert} \qquad \textit{where } C_A \textit{ and } k_A \textit{ are input paramters} \tag{9.1}$$

$$\gamma = \sqrt{3} \cdot \varepsilon_q \tag{9.2}$$

$$\gamma_{comp}^p = \left|\varepsilon_y - \varepsilon_x\right|_{failure} \qquad \gamma_{DSS}^p = \gamma_{xy\ failure} \qquad \gamma_{ext}^p = \left|\varepsilon_y - \varepsilon_x\right|_{failure}$$

The *e-ADP* model uses a yield criteria shaped like an ellipse in the t'- τ_{xy} space defined by Equation (9.3) and visualized in Figure 9.1b. The failure surface is a symmetrical ellipse with its centre at $t=(s_{u\ comp}- s_{u\ ext})/2$ and $\tau_{xy}=0$, but defined on the basis of the initial stress mobilization, see Figure 9.1a.

$$F = r - \kappa \cdot R_f = 0 \tag{9.3}$$

where r, κ and R_f is defined in Figure 9.1.

Hardening is defined by the equation proposed by Vermeer and Borst (1984) and provides a smooth transition from initial mobilised shear stress to failure, Eq. (9.4), where γ_p^p is the plastic strain along the failure surface written as a function of θ. This function consists of an interpolation between the three input parameters γ_{comp}^p, γ_{DSS}^p and γ_{ext}^p, the outcome of which is sketched in Figure 9.1d.

This implies that a stress path tangential to a constant yield surface generates plastic strains if θ increases.

$$\kappa = \begin{cases} 2\dfrac{\sqrt{\gamma^p/\gamma_p^p}}{1+\gamma^p/\gamma_p^p} & \gamma^p \le \gamma_p^p \\ 1 & \gamma^p > \gamma_p^p \end{cases} \tag{9.4}$$

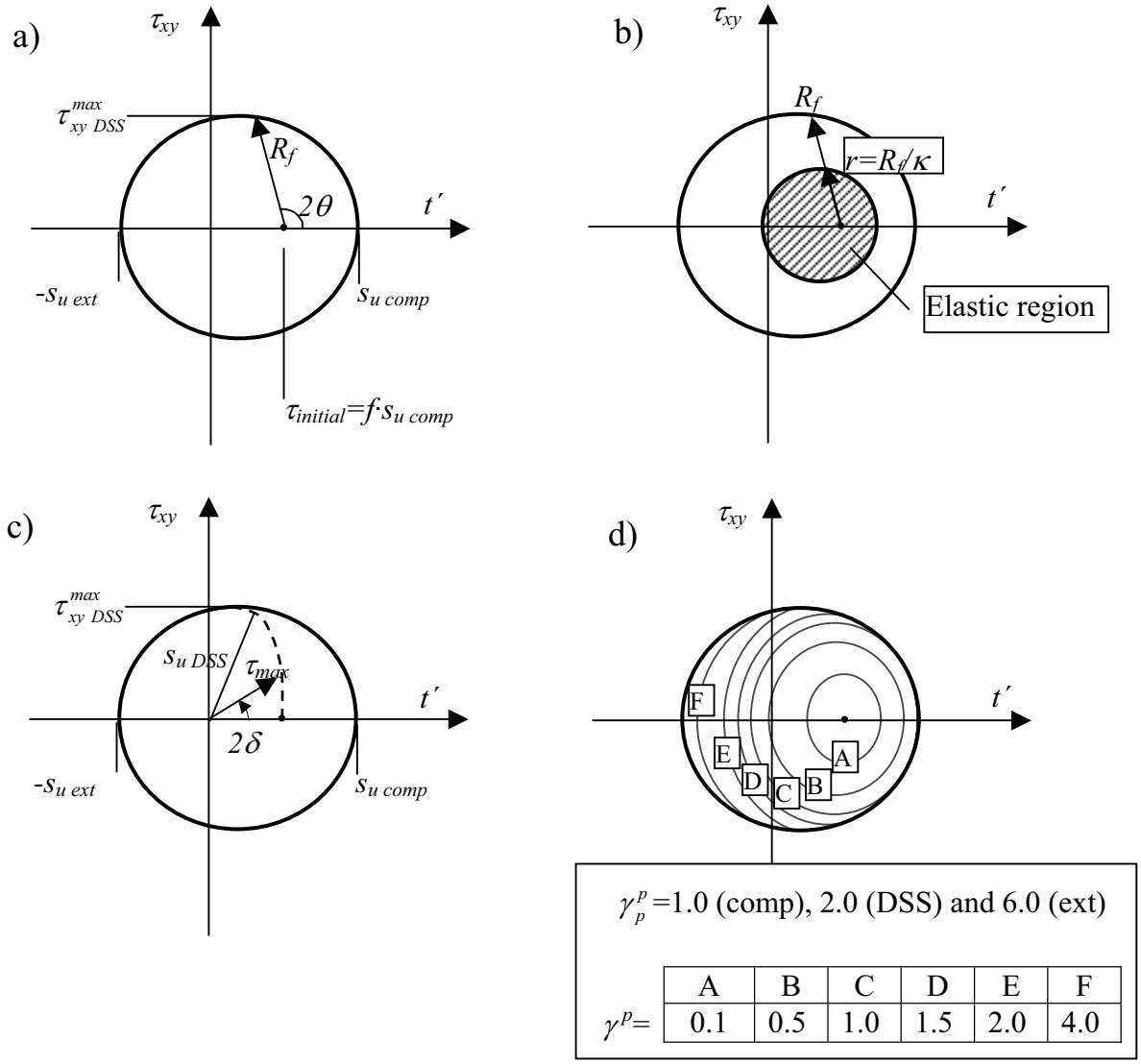

	A	B	C	D	E	F
γ^p=	0.1	0.5	1.0	1.5	2.0	4.0

Figure 9.1: The e-ADP model (in accordance with the Swedish empiric relations for w_L≈70% and f=50%)
a) Elliptic failure criteria b) Visualization of the hardening used in e-ADP
c) Sketched stress path for a CK_0UDSS-test
d) Sketch illustrating how γ_p develops in relation to different stress path directions from the initial stress state.

The accumulated plastic shear strain, γ_p, is to be integrated along the strain path,

$$\gamma^p = \int d\gamma^p = \int \sqrt{\left(d\varepsilon_x^p - d\varepsilon_y^p\right)^2 + \left(d\gamma_{xz}^p\right)^2} \tag{9.5}$$

The *e-ADP* model uses an associated flow role to calculate the direction of the developed strains.

9.3 Comparison between the *e-ADP* model based on total stress and some effective stress based models

Some discussions and comparison of the *e-ADP* model are presente by Grimstad et al. (2006). An example is the comparison between the capacity of the *e-ADP* to model s_u for different load directions and the result derived from the *MIT-E3* model *(Whittle, 1987; Whittle, 1993)*. These results are compared with those of laboratory tests in Figure 9.2. The same comparison was made by Pestana (1994) for the *MIT-S1*, and the result is also presented in Figure 9.2. The outcome from the *e-ADP* seems to match the test results well, but this is only true for undrained conditions. The two models developed at *MIT* consist of only one set of parameters describing the behaviour of all kinds of *OCR* values, while the *e-ADP* parameter set requires modification to cover different *OCR* values.

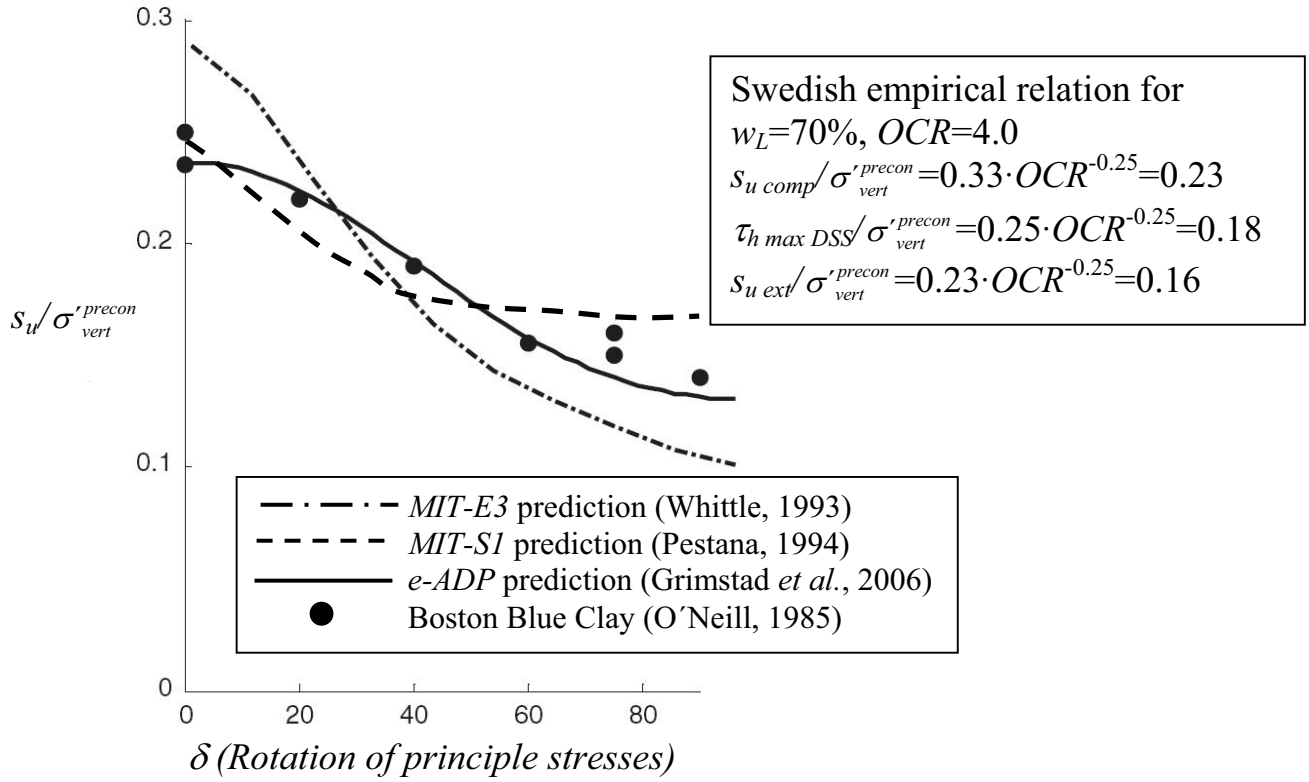

Figure 9.2: Comparison of the capacity of different models to reprocuce tests on Boston Blue Clay in a directional shear cell (O´Neill, 1985; Whittle, 1993; Pestana, 1994; Grimstad et al., 2006), OCR=4 in the test and in the MIT-E3 simulations as well as with MIT-S1.

The three models *e-ADP*, *NGI-ANI2* and *MIT-S1* have been compared in relation to different stress paths. The outcome from *MIT-S1* simulations, $\sigma'^{precon}_{vert}=100$ kPa, $K_0^{nc}=0.55$, $e=1.98$ and $OCR=1.0$, were chosen as input parameters to the

e-ADP and *NGI-ANI2*, see Table 9.1. The parameter set used by the *MIT-S1* is evaluated in Chapter 8. The use of results from the *MIT-S1* makes it possible to study the agreement between the different models. Note that the comparison refers to *PS*-conditions and that the elastic shear modulus used by the *e-ADP* and *NGI-ANI2* is set to 2/3 of G_{max} used by *MIT-S1*. G_{max} can be evaluated from Equation (8.1) and is in this case 14 600 kPa.

Table 9.1: Input parameters used by the e-ADP and NGI-ANI2.

		$s_u/\sigma'^{precon}_{vert}$ $\tau_{xy\ max}/\sigma'^{precon}_{vert}$	ε_q (%) when $G_{tan}<\sigma'^{precon}_{vert}$	γ^p_p
CK_0UC	OCR=1.0	0.37	0.375	0.65
CK_0UDSS	OCR=1.0	0.27	1.39	2.4
CK_0UE	OCR=1.0	0.29	3.75	6.5
G=9733 kPa				
μ'=0.495				

Four different laboratory tests were simulated and the stress paths studied in order to compare the three models; CK_0UPSC, CK_0UPSE, CK_0UDSS and CK_0UDSC[13] (Germaine, 1982). The latter test was performed by increasing τ_{xy} and maintaining t constant. The outcome of these simulations is presented in Figure 9.3. As a consequence of the formulation, only *MIT-S1* is capable of simulating the *ESP*. The agreement between the three models is excellent for the CK_0UPSC and CK_0UPSE tests. However, in the other two types of test the *NGI-ANI2* deviates from the other two models. The reason for this is probably the differences in the interpolation functions within these two models. As a consequence of these simulations, the total stress based *e-ADP* model appears capable of modelling the anisotropic behaviour under undrained *PS* conditions as well as *MIT-S1* in the case of first time loading. Some unloading tests were simulated to illuminate the differences between a bonding surface model with non-linear elastic behaviour (*MIT-S1)* and the formulation based on isotropic hardening (*e-ADP)*. Some special stress paths were simulated to visualize these differences and also the effect caused by changing stress path directions. The different stress paths are presented in Table 9.2, where the stress paths 2B and 2C approximately agree with a location on the active side, close to the foot of a sheet pile wall and the passive side respectively (Grimstad *et al.*, 2006). The outcome of these stress paths is presented in Figure 9.4.

[13] Undrained shearing in Directional Shear Cell, where the clay sample is consolidated under K_0 conditions

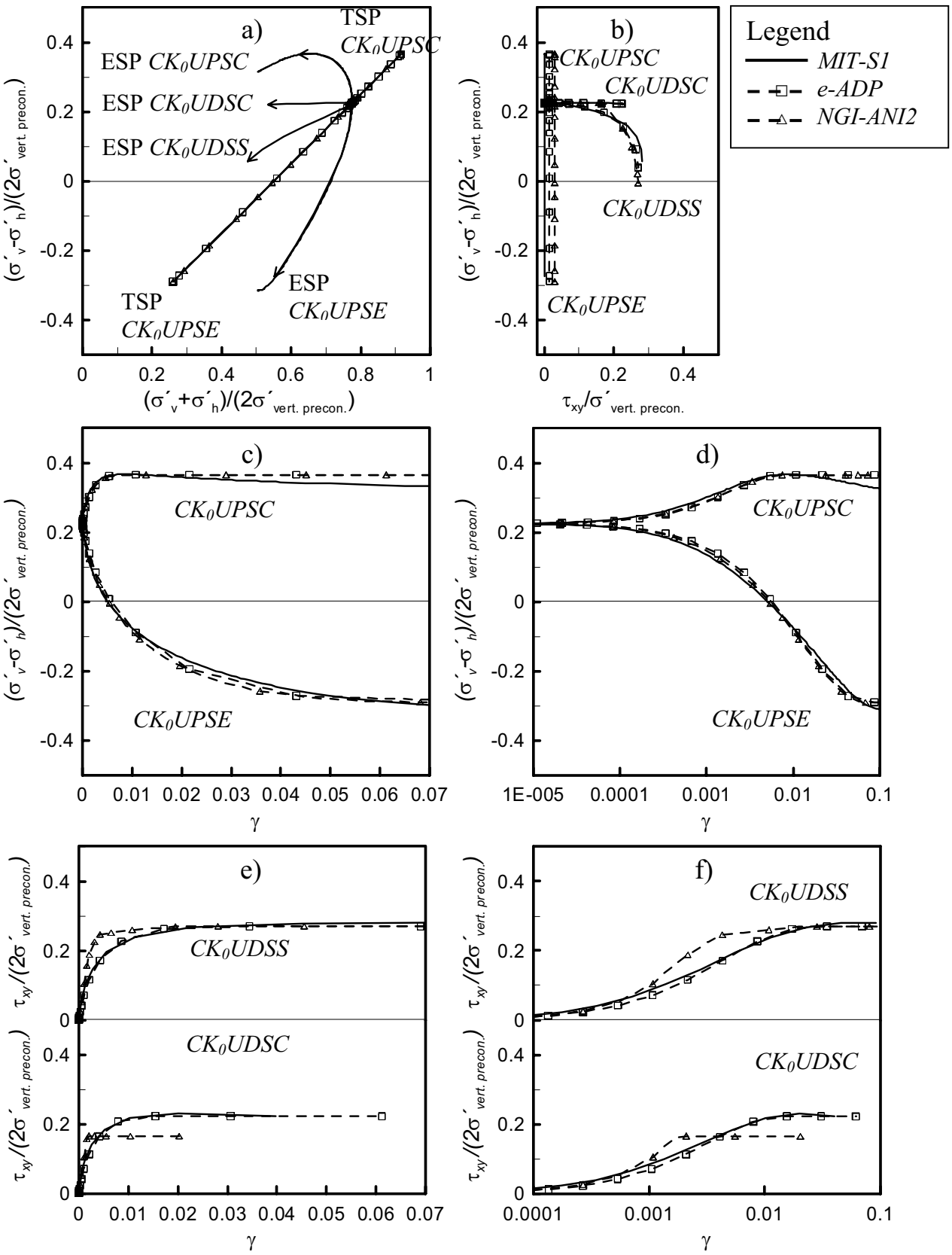

Figure 9.3: Comparison between the MIT-S1, e-ADP and NGI-ANI2 models in four well defined laboratory tests
a) Stress paths in the s´-t space b) Stress paths in the τ_{xy}-t space
c) Stress strain relations for CK_0UPSC and CK_0UPSE d) log scale
e) Stress strain relations for CK_0UDSS and CK_0UDSC f) log scale

Table 9.2: Different stress paths for illustration of the variation in behaviour of the MIT-S1 and e-ADP models.

Stress path	Point	t	τ_{xy}
1	0	22.5	0
	1	32	0
	2	22.5	0
1a	3	36	0
1b	4 (from 2)	-27	0
2	0	22.5	0
	5	*DSS* conditions	20
2a	6	*DSS* conditions	0
	7	*DSS* conditions	25
2b	8 (from 5)	*UC*	20
2c	9 (from 5)	*UE*	20

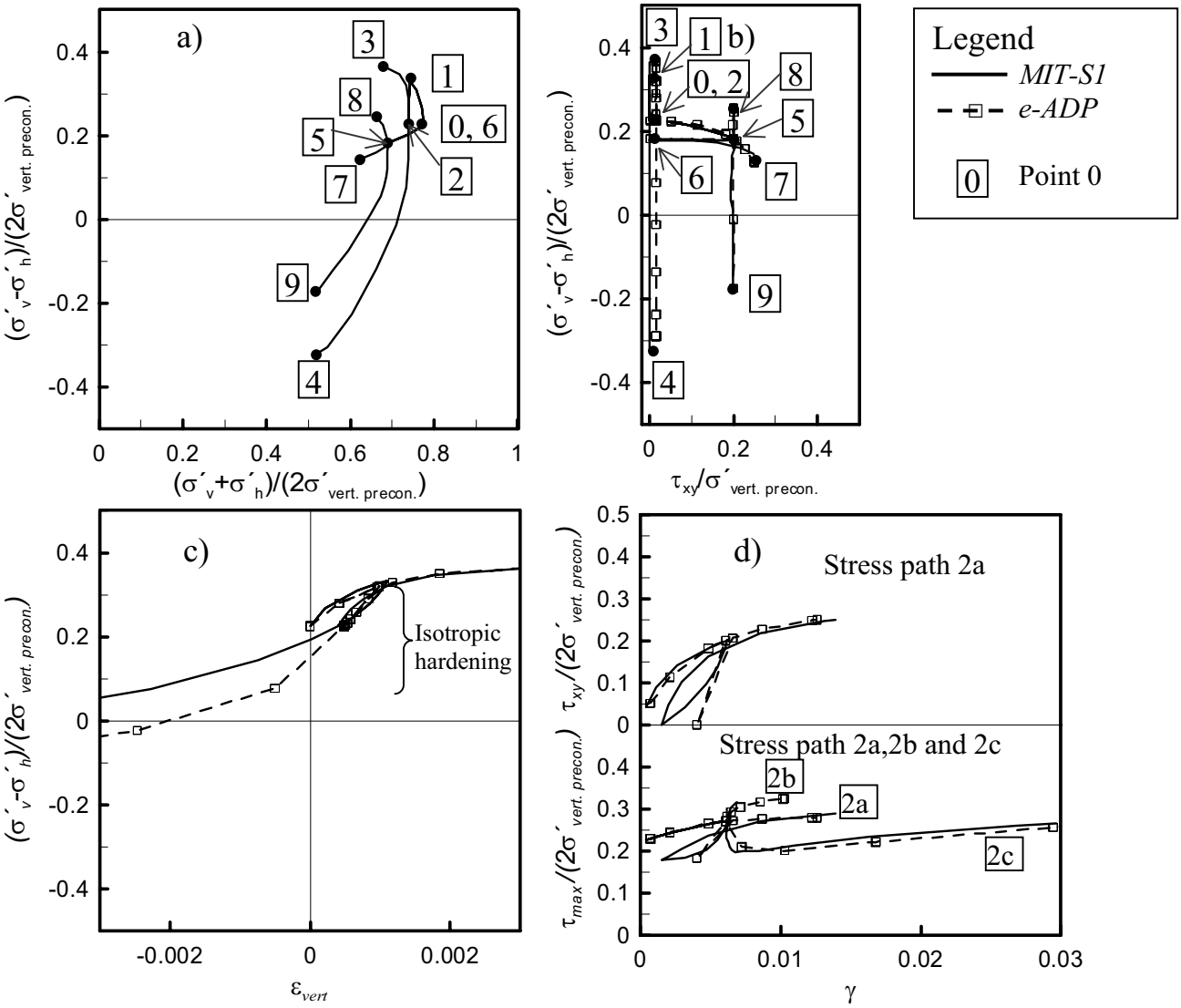

Figure 9.4: Comparison between the MIT-S1 and e-ADP models for different stress paths
a) Stress paths in the s´-t space b) Stress paths in the τ_{xy}-t space
c) ε_{vert} vs. t for stress path 1 d) γ vs. τ_{xy} and τ_{max} for stress path 2

The main differences occur when the stress path passes through the elastic region, see stress paths 1 and 2a. The agreement between the two models is excellent for changes in stress path direction, as long as Equation (9.3) equals zero.

The reduction of the elastic shear modulus, *G*, employed in the *e-ADP* model seems to fit the first time loading perfectly, but is questionable for unloading. When the amount of unloading is high, further reduction of *G* leads to better agreement between the two models. For practical problems, such as excavations with prestressed anchors, the amount of unloading will differ in the soil and therefore there will always be some deviation with a linear elastic model.

9.4 Soil profile used in reference calculations

A soil reference profile must be established in order to run reference calculations for a typical excavation. The chosen soil profile consisted of a 1 m fill upon a thick clay layer with a ground water table 1 m below the ground surface. The unit weight of the fill was set to 18 kN/m^3 and the clay to 16 kN/m^3. The water pressure was assumed hydrostatic. The preconsolidation pressure was established by means of *OCR*=1.25, which is a typical value for the clay deposits on the Swedish west coast, and a constant value on σ'^{precon}_{vert} in the upper 4 meters of the clay layer. The undrained strength parameters evaluated from *MIT-S1*, with the parameter set presented in Chapter 8 (page 223), were used in the numerical calculation involving the *e-ADP* model describing the clay behaviour. The elastic shear modulus used in the *e-ADP*, $G_{e\text{-}ADP}$, was set to G_{max}, in order to keep the deformations small. These parameters are dependent on the *OCR* value within the soil profile. Since the *e-ADP* uses constant values of the amount of strain at failure, the clay is divided into three sub layers. The stress situation and strength are presented in Figure 9.5, as is the amount of strain at failure and the sub division used by the *e-ADP*.

A comparison of a *PLEP-MC* model is also presented. The G_{sec} employed in these calculations, when small strains were expected, was set to one third of $G_{e\text{-}ADP}$, which corresponds well with the assumption using the relation for the oedometer modulus, E_{eod}, given in Equation (10.8) where A=2.5. When large strain is expected G_{sec} is reduced by another 2.5 times, to a value which corresponds to E_{eod}=250$\cdot \tau^{max}_{xy\ DSS}$.

The interaction between the sheet pile wall, *SPW*, and the clay is modelled with interfaces. These interfaces are modelled as a *PLEP-MC* material with a strength of 50% of $\tau^{max}_{xy\ DSS}$. The stiffness in the interface is set to 25% of the stiffness used when the clay is modelled as a *PLEP-MC* material.

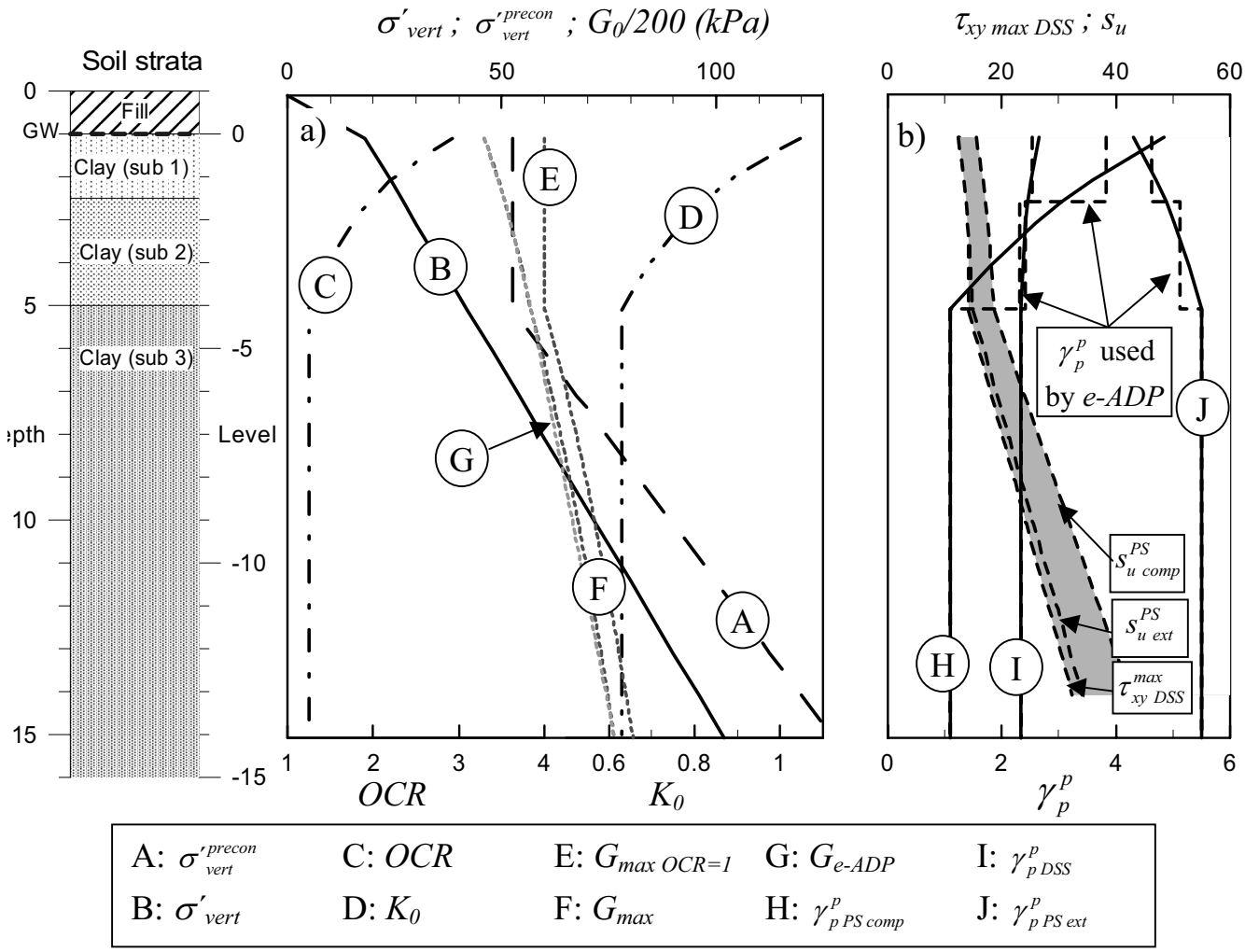

Figure 9.5: Stresses and strengths in the soil profile.
a) Stress situation in the soil profile
b) Undrained shear strength in the profile (grey area). The amount of γ at failure for stress path (the solid line represents the outcome from MIT-S1 and the dashed line the division used by the e-ADP).

Numerical analysis with soil models based on total stresses have to be performed in a slightly different way than those involving soil models based on effective stresses. The differences lies in how the water pressures are treated and care must be taken when changing between the two different approaches in soil modelling.

9.5 Excavation 1

A shallow excavation with only one anchor row was studied, Figure 9.6. The work sequence modelled is 1) installation of the sheet pile wall, *SPW*, in a dike excavated in the upper fill layer, 2) excavation to level –1.5, 3) installation of the anchor row, 4) excavation to level –4.5. Numerically the wall installation

was done as "wished in place". In order to study the different ways of modelling the clay behaviour the fill layer was treated without any strength, just acting as a load on the clay layer.

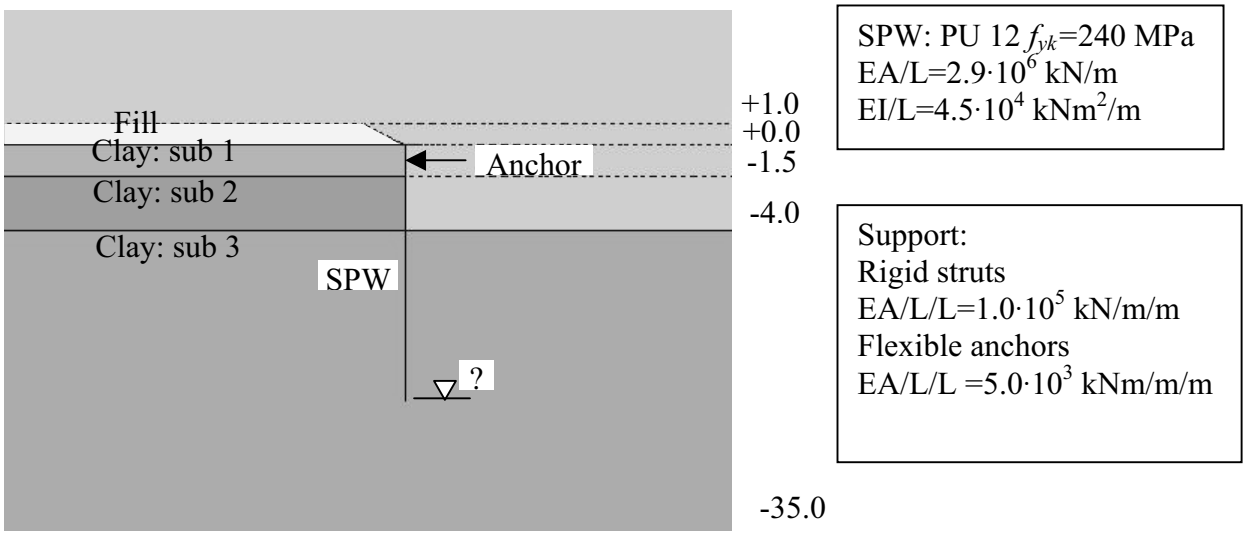

Figure 9.6: Plane strain model of the sheet pile wall

The results of several calculations will be presented in order to illustrate different ways of describing the clay and with two different kinds of support systems, rigid struts and flexible anchors. All calculations start from the stress situation described in Figure 9.5. First, the length of the SPW was established by simulating the excavation where the clay behaviour was described by the *PLEP-MC* formulation. The excavation was thereafter exposed to a *phi/c*-reduction (Brinkgreve, 2002), a stepwise decrease in shear strength until failure occurred. The ratio between the unreduced and reduced strength at failure is denoted F. The length of the wall was chosen so that $F \geq 1.4$ was fulfilled. After the required length was established, the section was studied with reference to the four different ways of describing clay behaviour. These calculations were followed by a calculation of the factor of safety for cases in which the clay was described by the *MIT-S1* and *e-ADP* formulations. An overview of the calculations, which were made with a rigid and a flexible support, is presented in Table 9.3.

Table 9.3: Calculation scheme

Calculation	Material model	Factor of safety	Outcome
A	*PLEP-MC* large strain	F≥1.4	The required length of the wall
B	*PLEP-MC* large strain	1.0 (L from A)	Deformation pattern etc.
C	*PLEP-MC* small strain	1.0 (L from A)	Deformation pattern etc.
D	*e-ADP*	1.0 (L from A)	Deformation pattern etc.
E	*MIT-S1*	1.0 (L from A)	Deformation pattern etc.
F	*PLEP-MC* small strain	*Phi/c*-reduction	Factor of safety
G	*MIT-S1*		Factor of safety
H	*e-ADP*		Factor of safety
I	*PLEP-MC* large strain	1.0	Required length of the wall
J	*MIT-S1*	1.0	Required length of the wall
K	*e-ADP*	1.0	Required length of the wall

When calculating the factor of safety in numerical analyses, the most common method is to incrementally reduce the strength of the soil. However, one should be aware that the purpose of reducing the strength is to cover natural variations within the soil strata as well as man made mistakes e.g. in calculations or the excavation. When reducing the strength it is important to remember that the initial stress mobilization cannot be more than 100%, a phenomena that has been discussed by Grimstad *et al.* (2006) and is described here in relation to the *MIT-S1* model. Three parameters within the *MIT-S1* formulation, ϕ'_{cs}, ϕ'_m and m, directly affect s_u. Following the standard procedure of reducing $\tan \phi'$ without changing any other parameter, the initial bounding surface and the failure cone will change as in Figure 9.7. The outcome of this method of strength reduction is that in the case of a normally consolidated clay, the reduction of $s_{u\ comp}$ will correspond to F_c=1.17 while for $s_{u\ ext}$ the corresponding factor of safety will be F_c=1.37. It should be noted that no effects of plane strain conditions or rotational hardening are taken into account in the model. The amount of change in mobilised shear strength, f_{mob}[14], also depends on the *OCR* within the soil, which is illustrated by the sketched 1D-unloading path, indicated by the dashed line in Figure 9.7. However, in the case of a clay with an *OCR*=1.0 the increase in f_{mob} ranges from 65% to 78%.

[14] f_{mob} is the ratio between the mobilized shear stress and the s_u, for the same rotation of the principal stresses. In normally consolidated clay deposit with horizontal layers $f_{mob}=\tau_{mob}/s_{u\ comp}=\sigma'_{vert}(1-K_0^{nc})/(2\cdot s_{u\ comp})$={Swedish empirical relation yields}= $3/2\cdot(1-K_0^{nc})$; δ=0°}

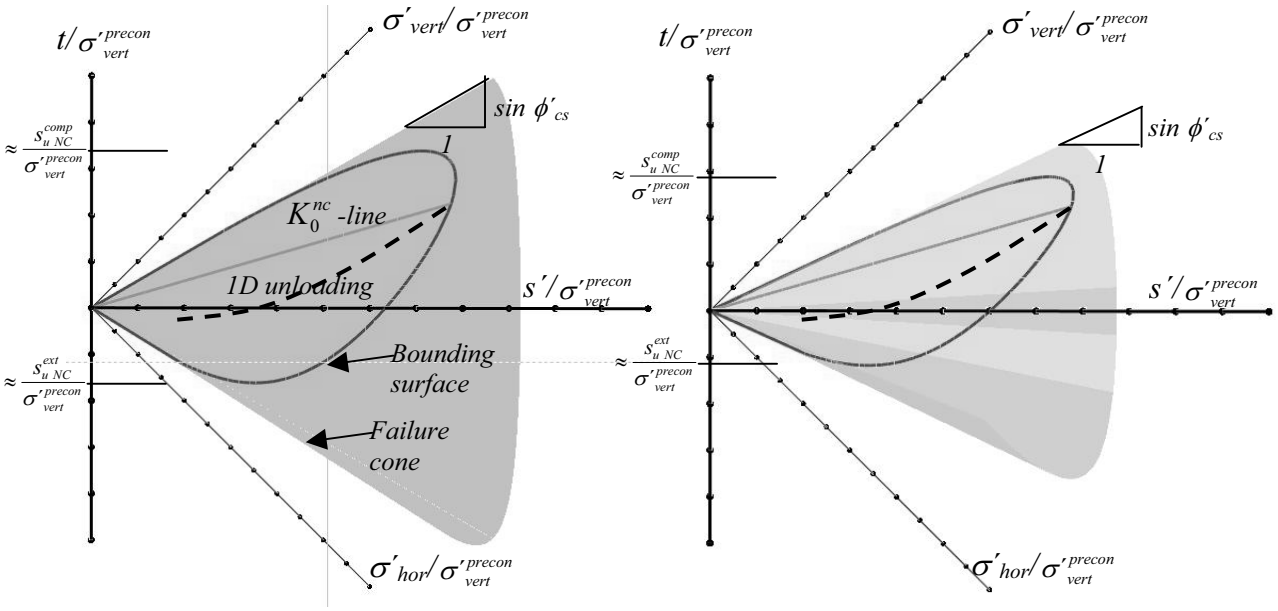

Figure 9.7: Effects of reducing ϕ'_m and ϕ'_c keeping K_0^{nc} constant.
a) m=2.5, ϕ'_m =40°, ϕ'_{cs} =35° and K_0^{nc} =0.55
b) m=2.5, ϕ'_m =30° and ϕ'_{cs} =25° and K_0^{nc} =0.55

If the strength parameter reduction is made in a way that keeps f_{mob} constant, several of the input parameters require adjustment, primarily the value of K_0^{nc} followed by μ'_0 and ω, which have to be changed in order to describe the stress situation for *OCR>1.0.* This is illustrated in Figure 9.8.

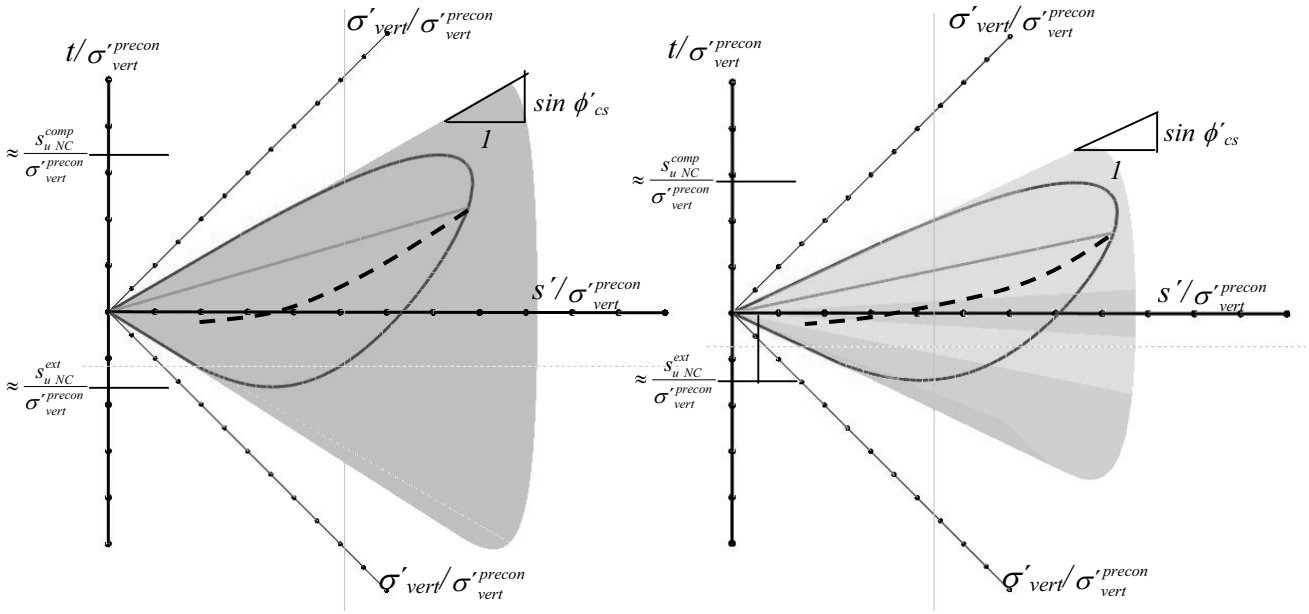

Figure 9.8: Effects of reducing ϕ'_m and ϕ'_c keeping f_{mob} constant.
a) m=2.5, ϕ'_m =40°, ϕ'_{cs} =35°, K_0^{nc} =0.55, μ'_0=0.15 and ω=2.0
b) m=2.5, ϕ'_m =30°, ϕ'_{cs} =30°, K_0^{nc} =0.65, μ'_0≈0.2 and ω≈4.0

The outcome of this way of reducing the strength is for a normal consolidated clay; $F_{c\ comp}$=1.17 and $F_{c\ ext}$=1.13. Reducing the parameter m, which controls the belly shape of the bounding surface in extension, can increase $F_{c\ ext}$. This latter method seems to be more accurate than the former but it is very time consuming to calibrate all the parameters for every incremental decrease in the strength. Therefore the first method is used in one calculation just to observe the effect. How the factors of safety, F_c, $F_{\phi'}$ and $F_{c\phi}$ are related to each other needs to be studied more in detail before any comparison between the absolute numbers can be made. It should be noted that the commonly used Hardening soil model within PLAXIS, which can be used with the *phi/c*-reduction function, generates the same pattern as *MIT-S1* between F_c and $F_{\phi'}$ for *OCR* values less than 2.0, provided the strength is defined by effective parameters.

One should bear in mind that the scatter in shear strength within a soil strata probably also results in a scatter in initial stress situation and stress strain response, since most of these parameters are more or less correlated to one another. This is not accounted for in the ordinary *phi/c*-reduction (Brinkgreve, 2002) where only the strength is reduced in the actual calculation phase, as if the properties suddenly change at a certain point. A better way to model the factor of safety is to use decreased values of the strength parameters, and proper stiffness correlated to the used strength, through the complete numerical analyses. The safety factors obtained from studying the problem with different reduction on parameters in *FE*-analyses can not directly be compared with the factors of safety that are obtained from limit equilibrium methods. The purpose of using factors of safety is to verify that the probability of failure is kept at a tolerable level, but when using reduced input parameters, no direct coupling to the probability of failure is made. Therefore, a sensitivity analysis where some properties are changed to see the influence on the analysis is recommended. To obtain a real factor of safety a probabilistic approach is recommended. In a probabilistic study of a deep excavation by Schweckendiek (2006), also briefly presented in (Schweckendiek and Courage, 2007), it has been shown that, for the section presented in Figure 9.9, the parameter with the greatest influence on the factor of safety for the *SPW* is the stiffness of the clay and for the rotation stability the unit weight (geometry) has the greatest influence. These results are of course depending on the material properties used, the correlation between the properties and the assumed statistical distribution of the parameters.

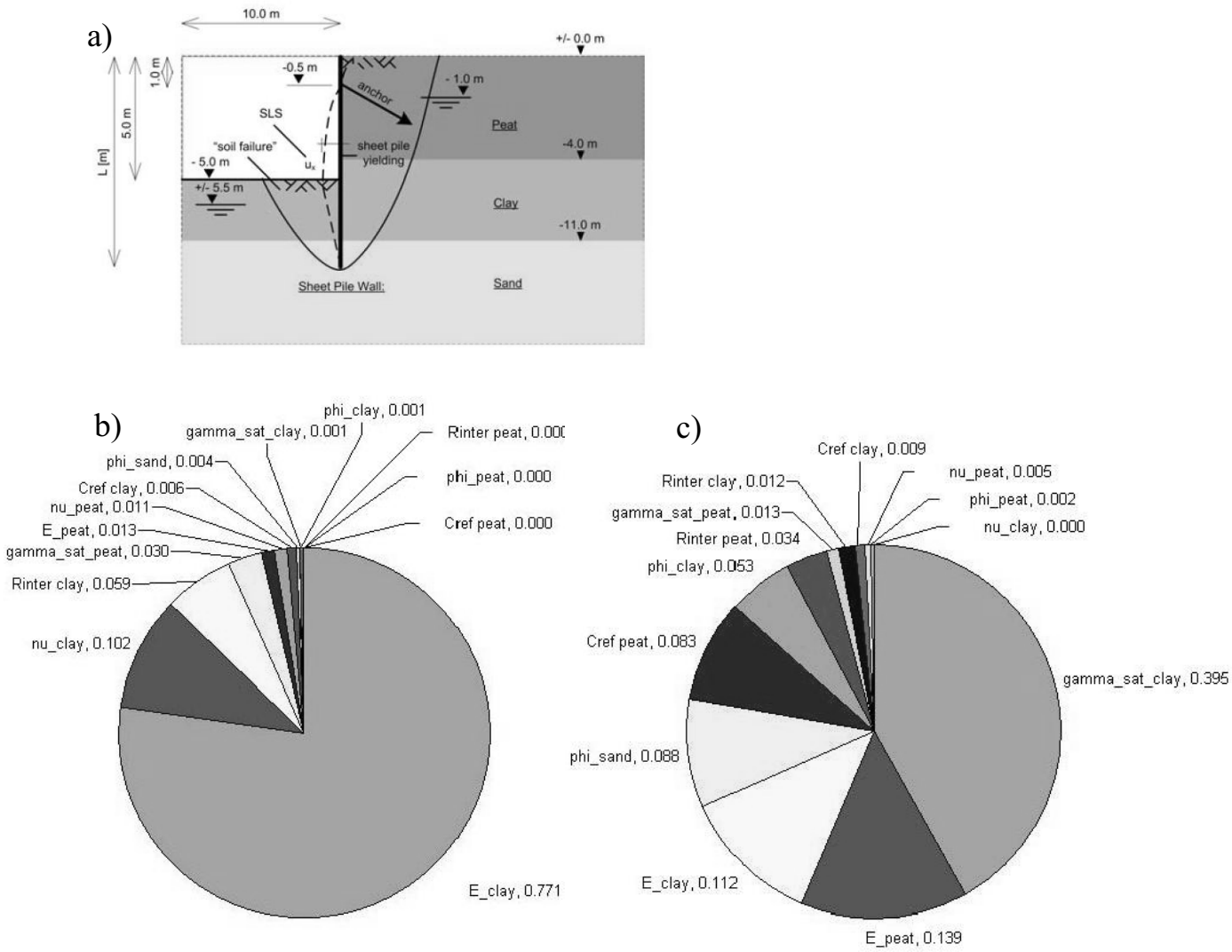

Figure 9.9: Case study for a probabilistic study of a deep excavation, (fig 9.1, 9.11 and 9.14 Schweckendiek, 2006)
a) Section studied
b) Factors that influence (α^2) in SPW failure in an FE-study
c) Factors that influence (α^2) in soil shear failure in a limit equilibrium study.

9.5.1 Comparison between the different calculations for excavation 1

In this section the results from the various calculations are compared.

As previously described, the required wall embedding was determined by a *phi/c*-reduction and found to be 5.0 metres. A traditional design in accordance with the method used in Sweden, (Ryner *et al.*, 1996) was also employed. This design method is based on the work by Bjerrum and Eide (1956) and used in combination with safety factors related to s_u. With the given geometry the N_c-factor (Bjerrum and Eide, 1956) was found to be 5.2, while an embedding of 5.0 metres and N_c=5.2 yielded a maximum decrease in s_u of a factor of 1.2. This demonstrates that numerical analyses differ from the empirically based method. In order to obtain a factor of safety as high as 1.4 the embedding has to be at

least 7.3 metres or the N_c-factor used in the calculation has to be increased to about 6.1.

The outcome from the different calculations regarding ground surface subsidence and wall movement due to excavation are presented in Figure 9.10 to Figure 9.11, from which the following can be observed:

- When using the stiff behaviour of the *PLEP-MC*-model, $E_{eod} \approx 625 s_u$, the deformation pattern corresponds well to the other models. This is valid for both rigid and flexible support. While a stiffness corresponding to $E_{eod} \approx 250 s_u$ gives deformations that are far too large.
- The deformation pattern of the first excavation step agreed extremely well with the *e-ADP* and *MIT-S1* models, but for the second excavation the wall movements from *e-ADP* coincided with the result obtained by using a *PLEP-MC* model with a stiff response.
- The ground surface movements from the *e-ADP* and *MIT-S1* models show the same pattern, the only difference being that *e-ADP* gives larger settlements. These patterns are a great improvement on the results obtained by using a *PLEP-MC* model.
- Varying the stiffness in the interface leads to only minor changes in the outcome.
- The *e-ADP* model reveals a load concentration around the wall support, which is also reflected in a larger load on the waling, see Table 9.4 and Table 9.5.

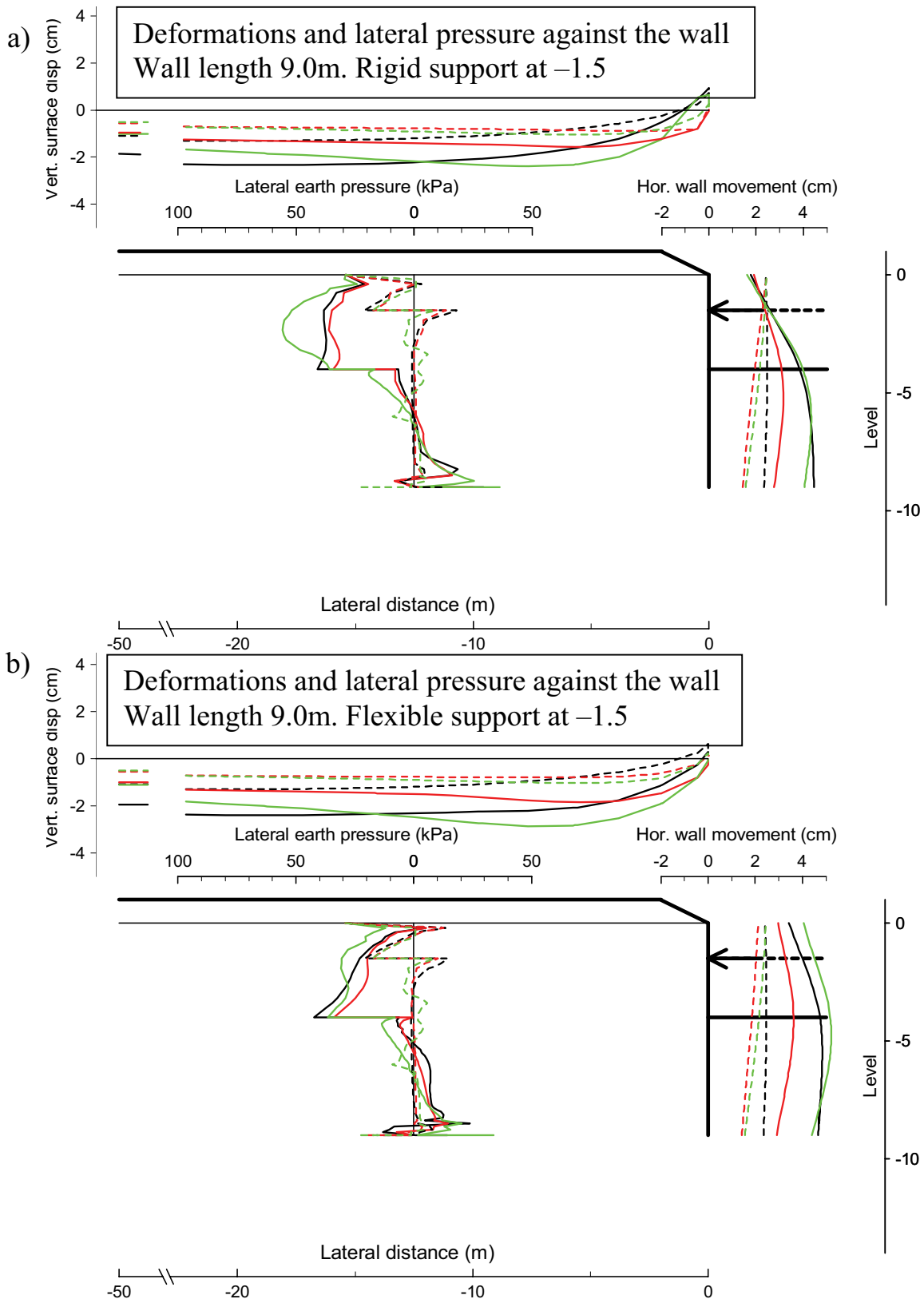

Figure 9.10: Comparison of the results from three different soil models. Embedding of the wall is 5 m
*a) with a **rigid** support. b) with a **flexible** support.*
Black line: PLEP-MC (small strains expected), Green line: e-ADP, Red line: MIT-S1. Dashed lines represent the response of excavation to –1.5 and solid lines the response of excavation to –4.0

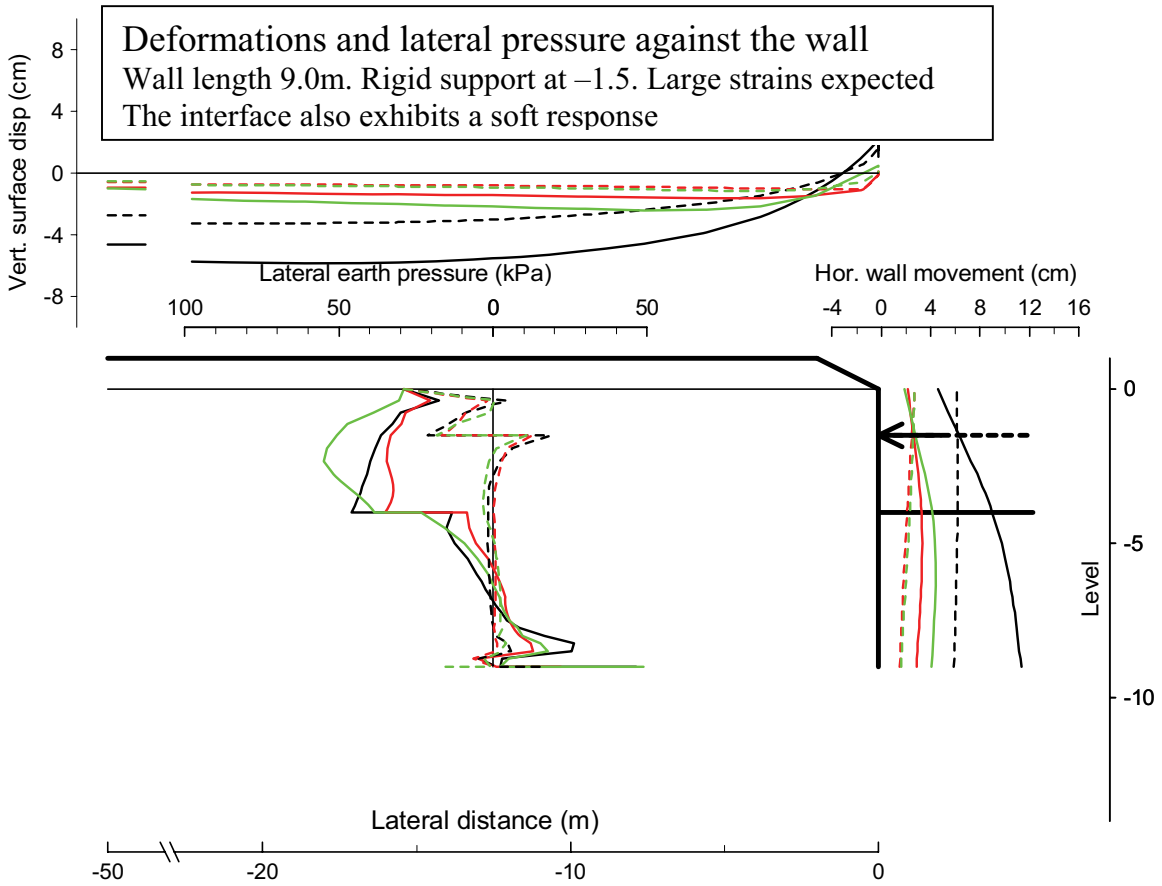

*Figure 9.11: Comparison of the results from three different soil models, embedment 5m with a **rigid** support. Black line: PLEP-MC (large strains expected), Green line: e-ADP, Red line: MIT-S1. Dashed lines represent the response of excavation to –1.5 and solid lines the response of excavation to –4.0*
Note: Different scales to those in previous figure.

The resulting lateral earth pressures from the different calculations are presented in Figure 9.12 to Figure 9.14. These figures illuminate the mobilisation of the strength in the soil, compared with the values obtained by using the relation presented by Rankine (1857).

In Figure 9.12 the developed lateral earth pressures are presented for the rigid and flexible support systems. It is evident that the rigid system prevents movement and therefore mobilization of the strength in the clay. Active pressure develops at a horizontal deformation of approximately 3.2 cm (4 m depth) for the rigid waling system and 3.6 cm (2.5 m depth) for the flexible support. However, during the first excavation stage active pressure developed against the entire length of the wall. At this stage the deformations were approximately 15 mm at the foot of the *SPW*, thus the relation between the deformation and the height was approximately 2‰. Figure 9.12 reveal that the bottom of the excavation is stabilised by negative pore pressure, and it should be noted that no such results can be obtained by means of the total stress based *e-ADP* model.

These negative pore water pressures will dissipate over time, leading to a decrease in shear strength (Lambe, 1970). This dissipation can be quite rapid (Persson, 2004) and should not be neglected when an excavation is open for a longer period of time.

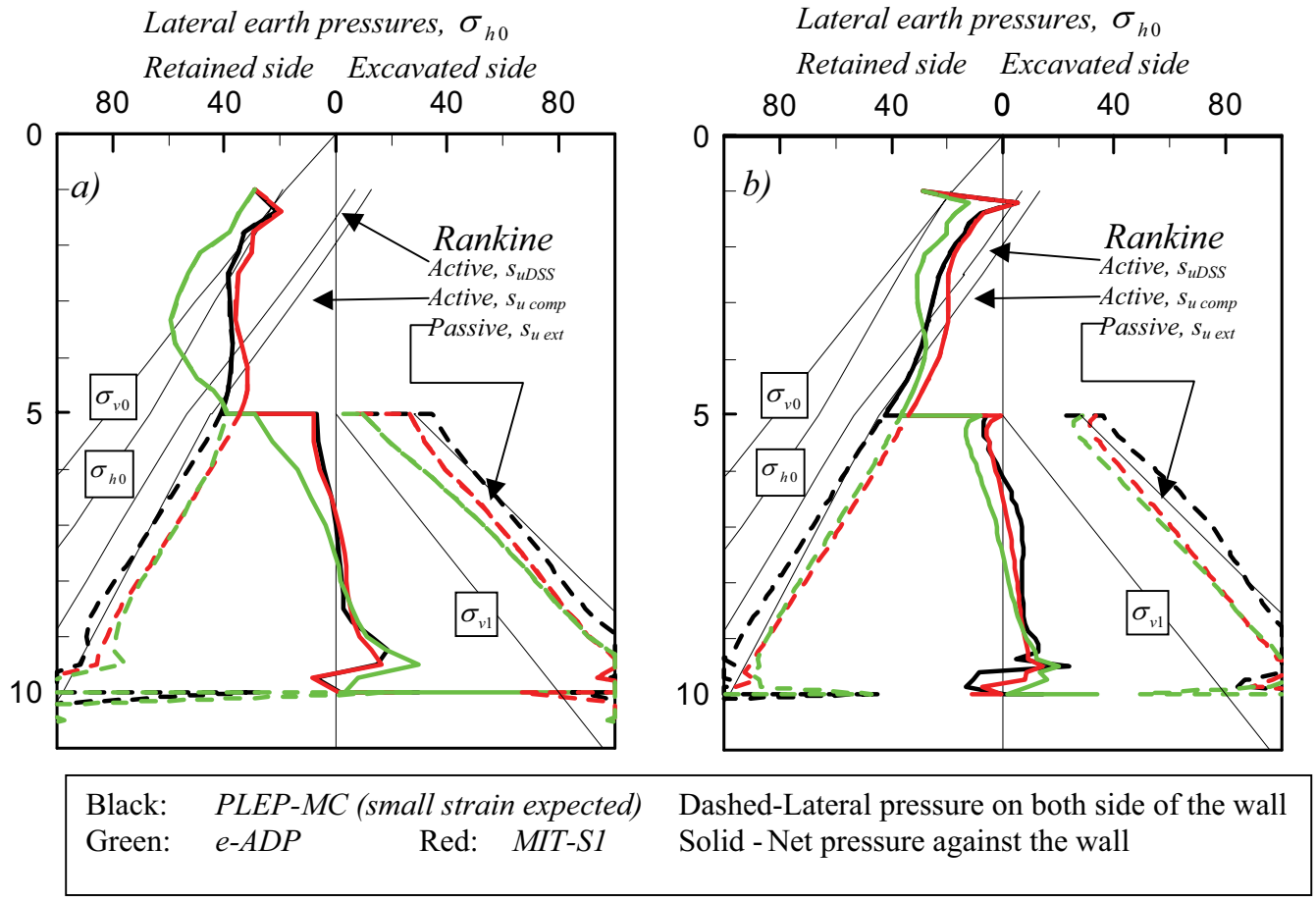

Figure 9.12: Comparison between the three different soil models. Embedding of the wall is 5 m. a) Lateral pressure rigid support b) Lateral pressure flexible support

From Figure 9.12b it is clear that lateral pressure on the retaining side of the *SPW* is negative, which is also an effect of negative excess pore water pressures. During undrained excavation the σ_h decreases on the retained side, while σ_v is constant. Since no volume changes occurred, s' and p' are constant, σ'_h decreases while σ'_v increases. σ'_h cannot be negative unlike σ_h, $(= \sigma'_h + u)$. Many design codes do not permit consideration of negative horizontal stresses, which is wise considering the consolidation process. However, Lambe (1970) reports that the pore water pressure decreases even further during the consolidation process, but that this is probably dependent on the deformation pattern during consolidation. In some design codes, including the Swedish one, the design lateral pressure against the retaining side of the *SPW* should be at least equal to the hydrostatic water pressure from the highest ground water table or from the

top of the highest low permeable layer, Equation (9.6). The reason for using hydrostatic water pressure, $u_{hydro\ stat.}$ is to take possible water filled cracks into account.

$$\sigma_a = \max \begin{cases} \sigma_{vert.} - 2s_u \\ u_{hydrostat} \end{cases} \tag{9.6}$$

There are mixed variants of these two ways of looking at this problem, (Bowles, 1996). However, these will not be delt with here.

None of the undrained numerical analyses known at this point use $u_{hydrostat.}$ as minimum lateral pressure and nor do they comply with the design code. The relation in Equation (9.6) can however be modelled by using a drained interface in combination with undrained properties in the clay. When using the *e-ADP* model this can be done by generating water pressure in the area behind the wall. This is not a major problem when dealing with braced excavations, but the effect needs to be studied when large cantilever movements occur and when using a very flexible support system.

The effects of using reduced strength parameters, calculation F, G and H in Table 9.3, is presented in Figure 9.13. The differences in the way of defining the factor of safety have been discussed in section 9.5 and are visualized in Figure 9.7 and Figure 9.8. Please note that no mechanism has been developed after reduction of the strength parameters in *MIT-S1* by $F_{\phi'}$=1.8. However no convergences where obtained when the strength parameters were further reduced.

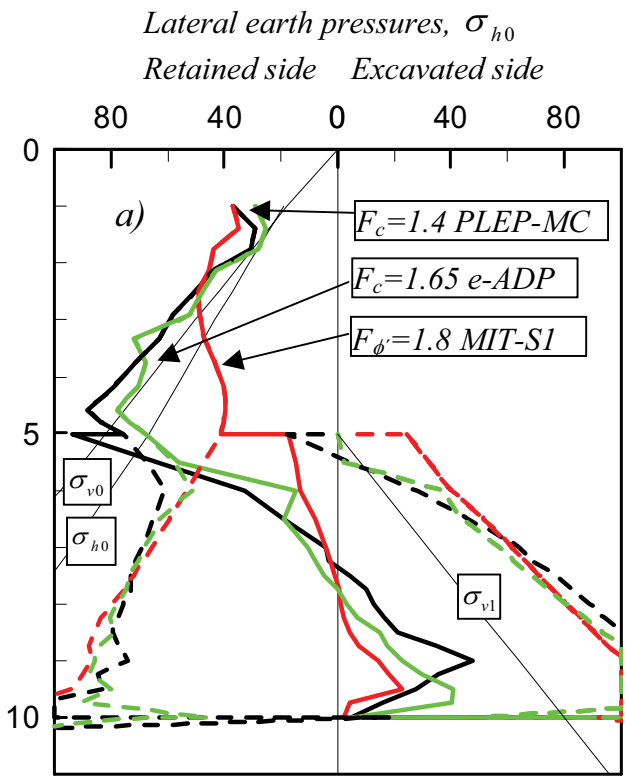

Black:	*PLEP-MC (small strain expected)*		Dashed-Lateral pressure on both side of the wall
Green:	*e-ADP*	Red: *MIT-S1*	Solid - Net pressure against the wall

Figure 9.13: Comparison between three different soil models after reducing the strength, rigid support

When the embedding was reduced as far as possible without stability failure, calculations I, J and K in Table 9.3, and without any strength reduction, it was observed that no embedding was required for such shallow excavations under undrained conditions. The reason for this is the amount of negative pore water pressure within the pit and that an inward movement occurs above the support level during the second excavation phase. This movement will generates large horizontal stresses that act as a balancing force against the rotation.

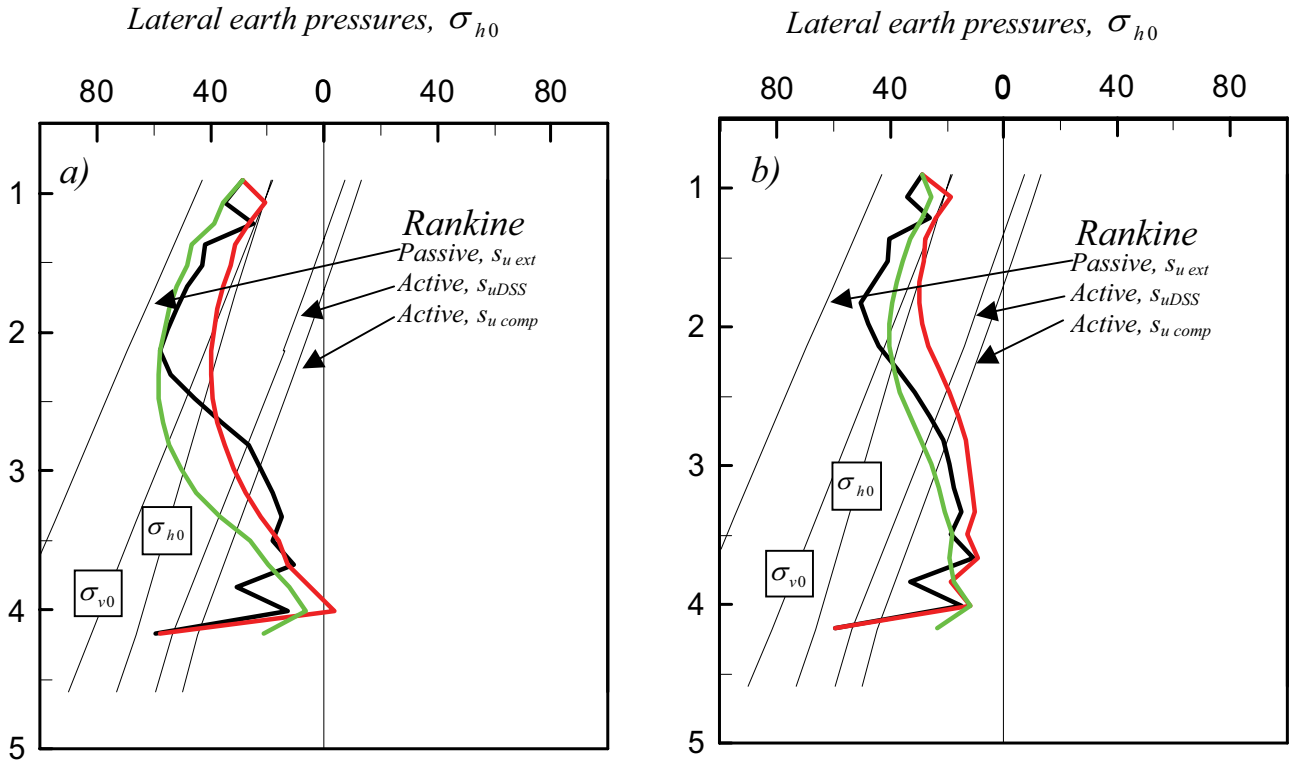

Black:	*PLEP-MC (small strain expected)*		Dashed-Lateral pressure on both side of the wall
Green:	*e-ADP*	Red: *MIT-S1*	Solid - Net pressure against the wall

Figure 9.14: Comparison between three different soil modells. Embedding of the wall 0.0 m. a) Lateral pressure rigid support b) Lateral pressure flexible support

9.5.2 Summary of design values from the different calculations for excavation 1

The outcome of using a rigid support is presented in Table 9.4. and for using a flexible support in Table 9.5. The differences between the three models can be summarized as follows:

- Using a relatively high stiffness in the *PLEP-MC* model yields results more similar to those obtained from *e-ADP* and *MIT-S1* models.
- The support system carries more load when using the *e-ADP* compared to the other two models.
- The stresses and support loads are smallest when using the *MIT-S1*.
- Using anisotropic models increases the factor of safety compared with using an isotropic formulation based on $s_{u\,DSS}$. The *e-ADP* increases the factor of safety, F_c, by approximately 20%.

Table 9.4: Summary of some design parameters from the various calculations using a rigid support.

Calculation	Material model	Factor of safety	Wall length	H_{max} (mm)	M_{max} (kNm/m)	F_{max} (kN/m)
A	*PLEP-MC* large strain	F_c=1.4	9.0	-	-	
B	*PLEP-MC* large strain		9.0	55	99	140
C	*PLEP-MC* small strain		9.0	45	67	131
D	*e-ADP*		9.0	43/44	93/93	179/182
E	*MIT-S1*		9.0	32/33	60/61	116/115
F	*PLEP-MC* small strain	*Phi/c-* reduction	1.41>F_c=**1.4**	840	237	244
G	*MIT-S1*	*Phi/c-* reduction	1.9>F_ϕ>**1.8**	35	87	171
H	*e-ADP*	*Phi/c-* reduction	1.7>F_c=**1.65**	176	219	224
I	*PLEP-MC* large strain	F>1.0	4.0m	98	45	127
J	*MIT-S1*	F>1.0	4.0m	34	32	101
K	*e-ADP*	F>1.0	7.0m	46	57	161

Table 9.5: Summary of some design parameters from the various calculations using a flexible support.

Calculation	Material model	Factor of safety	Wall length	H_{max} (mm)	M_{max} (kNm/m)	F_{max} (kN/m)
A	*PLEP-MC* large strain	F_c=1.4	9.0	-	-	
B	*PLEP-MC* large strain		9.0	116	85	140
C	*PLEP-MC* small strain		9.0	48	62	77
D	*e-ADP*		9.0	52/55	70/72	107/108
E	*MIT-S1*		9.0	36/38	52/53	62/62
I	*PLEP-MC* large strain	F>1.0	4.0m	108	44	112
J	*MIT-S1*	F>1.0	4.0m	57	28	71
K	*e-ADP*	F>1.0	4.0m	56	39	107

9.6 Excavation 2

A deep excavation with several support rows was analysed using the same constitutive models as in the previous section, see Figure 9.6. The work sequence modelled was the installation of the SPW, in the same way as in the "excavation 1" reference calculation. After installation of the retaining wall, the excavation was carried out to level –1.5. Thereafter the excavation continued *h* metres, followed by the installation of a support row at the bottom of the excavation. After that another excavation of h metres was modelled, followed by installation of a support row. This was continued to an excavation depth of 24 metres if failure was not reached. The retaining wall was set to correspond to the stiff combined wall, *HZ 975 D-12/AZ18*[15], with a length of 30 metres. The distance to firm layers was set to 60 metres. The idea was to study how the different methods of modelling clay behaviour affect the behaviour of the wall and the ground surface behind it. The fill layer was treated without any strength, and merely as a load on the clay layer. Since this clay deposit was twice as deep as in excavation 1, another sub layer was introduced in order to match the properties used by *MIT-S1*. The stiffness used in the *e-ADP* and *PLEP-MC* models followed the same concept as in excavation 1, the only difference being that no calculation of the expected high level of strains was performed for the *PLEP-MC* model. Instead, two sets of parameters for the *e-ADP* model were tested with different elastic stiffnesses, one with $G_{e\text{-}ADP} = G_{max}$ and the other with $G_{e\text{-}ADP} = 2/3\ G_{max}$ in order to study the effect on the wall.

The geometry used can be seen in Figure 9.15, where some definitions are provided. L defines the length of the wall and H the excavation depth. The initial unsupported excavation was made to h_u and the vertical spacing between the supports is denoted *h*. The modelled soil profile is presented in Figure 9.16, where some input parameters are given. The parameters used in the *MIT-S1* model are evaluated in Chapter 8 while those applied in the *e-ADP* model are compiled in Table 9.6. The parameters used when modelling the clay with a *PLEP-MC* model coincide with the ones used in *e-ADP* for the strength parameters but with reduced stiffness, as mentioned previously.

[15] For information about this profile please contact the manufacturer

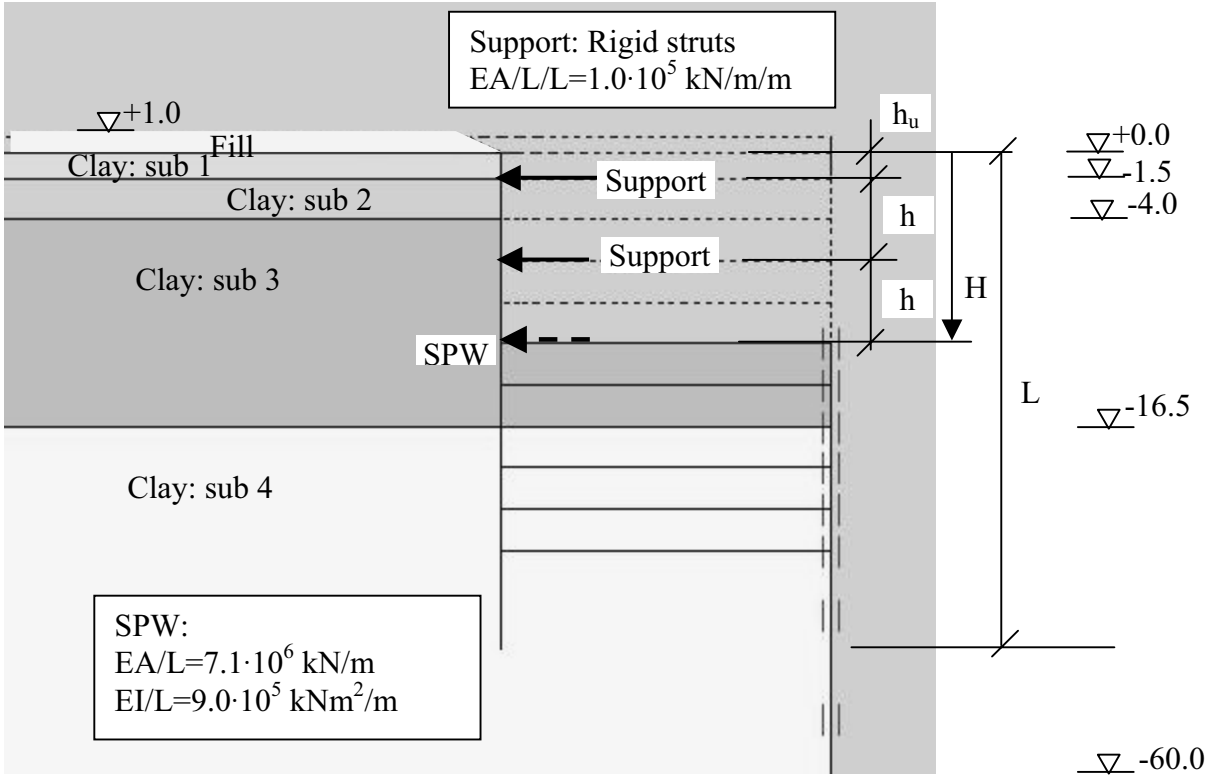

Figure 9.15: Plane strain model of excavation 2.
H=Excavation depth L=Length of wall
h_u=Initial unsupported excavation h=Vertical support spacing

Table 9.6: Parameters used in the e-ADP model with G_{el} approximately equal to G_{max}.

e-ADP	G ($\sigma'_{vert\ initial}$=0) [kPa]	$\frac{\Delta G}{\Delta\sigma'^{initial}_{vert}}$ [-]	μ′ [-]	$\gamma^p_{p\ PS\ comp}$ [%]	$\gamma^p_{p\ PS\ ext}$ [%]	$\gamma^p_{p\ DSS}$ [%]
sub 1	7200	110	0.495	3.8	4.6	2.5
sub 2	8010	80	0.495	2.3	5.1	2.4
sub 3	8640	65	0.495	2.3	5.1	2.4
sub 4	12740	30	0.495	2.3	5.1	2.4

	$\frac{\Delta s^{PS}_{u\ comp}}{\Delta\sigma'^{initial}_{vert}}$ [-]	$\frac{\Delta s^{PS}_{u\ ext}}{\Delta\sigma'^{initial}_{vert}}$ [-]	$\frac{\Delta\tau^{max}_{xy\ DSS}}{\Delta\sigma'^{initial}_{vert}}$ [-]	$s^{PS}_{u\ comp}$ $\left(\sigma'^{initial}_{vert}=0\right)$ [kPa]	$s^{PS}_{u\ ext}$ $\left(\sigma'^{initial}_{vert}=0\right)$ [kPa]	$\tau^{max}_{xy\ DSS}$ $\left(\sigma'^{initial}_{vert}=0\right)$ [kPa]
sub 1	0.19	0.15	0.15	12.1	9.7	9.8
sub 2	0.10	0.08	0.01	14.7	11.7	13.6
sub 3	0.44	0.36	0.34	0.0	0.0	0.0
sub 4	0.44	0.36	0.34	0.0	0.0	0.0

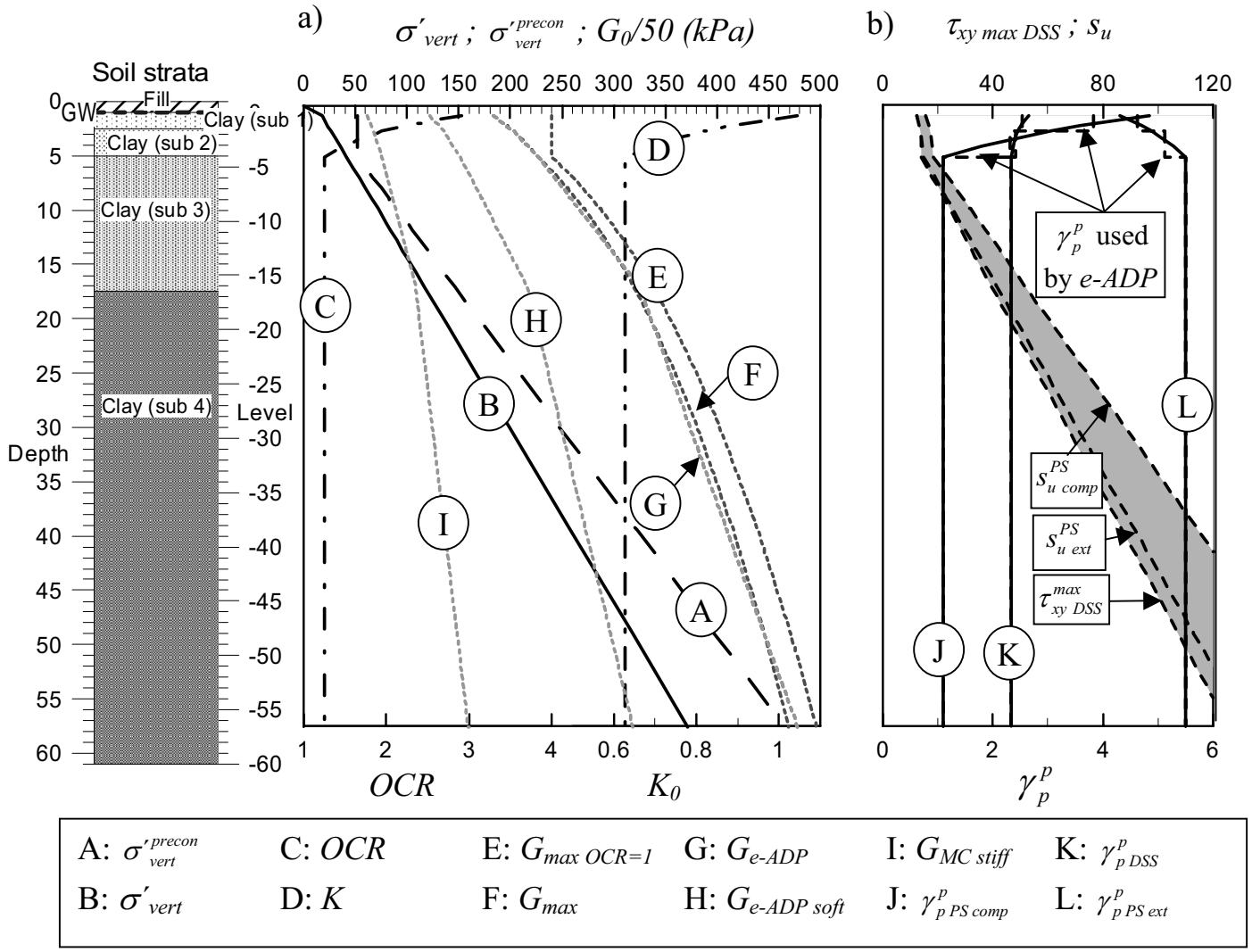

Figure 9.16: Stress situation and shear strength in the profile.
a) Stress situation in the soil profile
b) Undrained shear strength in the profile (grey area). The amount of γ at failure fordiffrent stress paths (solid lines represents the outcome from MIT-S1 and dashed lines the division used by e-ADP.

9.6.1 Effect of vertical support spacing

The distance between the supports will mainly effect the lateral inward movement of the *SPW*. A framework has been developed by Hashash (1992) to estimate the required spacing between the support levels as a result based on the acceptable movement. The empirical relation for movements presented by Hashash (1992) is presented in Equation (9.7). This relation was proposed for excavations where the first support level was installed at the top of the *SPW*.

$$\delta = \left(a \cdot e^{b \cdot h} + \left(c + d \cdot h\right) \cdot H\right) \cdot H \tag{9.7}$$

δ=Maximum deformation (wall deflection, settlement or heave at the excavation floor)
H=Excavation depth
h=Vertical support spacing
a, b, c and *d* are constants dependent on the soil profile and the studied deformation type.

In his work Hashash has shown that movements due to the initial unsupported excavation to depth h_u, have a limited impact on the behaviour of an excavation beyond a particular depth and that cantilever movements are successively eliminated during deeper excavation stages. This behaviour contradicts the findings of several other authors (e.g. O'Rourke, 1981; Clough and O'Rourke, 1990), who report that cantilever movement is additional to those obtained in calculations where h_u=0. This cumulative response was derived from numerical analyses as well as field data, while the work by Hashash is based solely on numerical analyses, albeit performed with the advanced *MIT-E3* model, (e.g. Whittle, 1991), capable of simulating more specific load paths than in previous work. The location of the maximum deformation, e.g. the depth at which the inward movements are largest or the distance from the wall at which the settlements are largest, is not given in the framework suggested by Hashash. Therefore, it is not easy to incorporate the deformations obtained in the unsupported excavation as an additive deformation to the one obtained from Equation (9.7).

The modelled excavation sequence was:

1. Excavation of a trench through the fill layer
2. Installation of the *SPW* (wished in place)
3. Excavation to h_u, cantilever
4. Installation of support at excavation floor.
   Excavation of an additional *h* metres
5. Installation of support at excavation floor.

6. Repetition of work stages 5 and 6 until the excavation reached 24 metres or until numerical collapse.

In order to calibrate the relation given in Equation (9.7) the excavation sequences were performed with h=0[16] and h=5.0 metres respectivly. The results of these two calculations are presented in Figure 9.17 to Figure 9.19, where the last mentioned uses normalized lateral pressure. All pressures in Figure 9.17 and Figure 9.18 were normalized against the initial vertical total stress, $\sigma'^{in\ situ}_{vert}$. This increases the resolution and facilitates the identification of areas where Rankins active or passive pressure has developed. The figure is also complemented by the initial horizontal stress, here denoted initial, and with the vertical stress on the excavated side for the different excavation depths and with the vertical stress on the retained side. These latter curves indicate where $\sigma_h = \sigma_v$.

It is obvious that the support spacing has a major influence on the deformation pattern, which also affects the lateral pressure on the retained side. Active earth pressure, as defined by Rankine, seems to develope at a ratio between lateral movement and excavation depth of approximately 0.5%. The lateral pressure inside the pit appears to be unaffected by the support spacing, which indicates that passive earth pressure develops without any deformation as a consequence of the vertical unloading during excavation. The ability to resist high lateral pressure decreases in line with a decrease in σ_{vert}. If the initial σ_{vert} exceeds this ability, the lateral pressure will decrease to the level of the passive pressure. This allows for full utilization of the undrained shear strength within the soil mass, leading to large deformation if the retaining structure needs the support of stronger layers deeper down.

[16] This was done in two ways: Firstly the sequence modelled was stepwise performing of excavation 2.5 metres without allowing any deformation in this part and above the excavation floor in the SPW. This gives to no movements against the retained side. Secondly which also is more practically. Stepwise excavation with a sliding strut at the bottom, with successive installation of supports at every 2.5 metres. These struts was not allowed to carry tension forces.

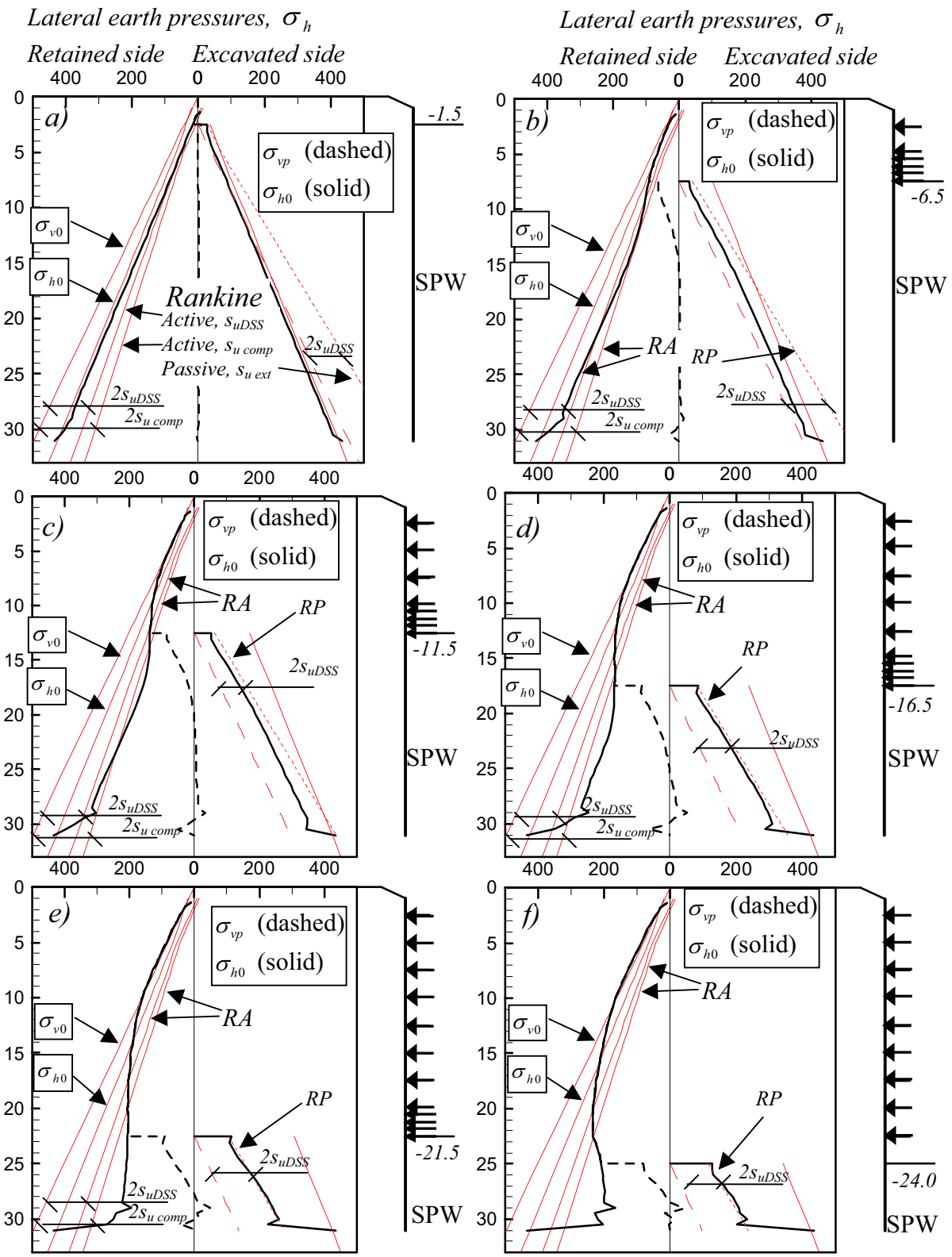

Figure 9.17: Calculatd earth pressures for different excavation stages. (MIT-S1, h_u=1.5 and h=0)
Solid black lines represent the lateral pressure on each side of the wall and the black dashed line is the net pressure. Red lines indicate the vertical stress on each side of the wall as well as Rankines active and passive pressure (RA and RP). The initial horisontal stress on both sides of the wall is also presented.

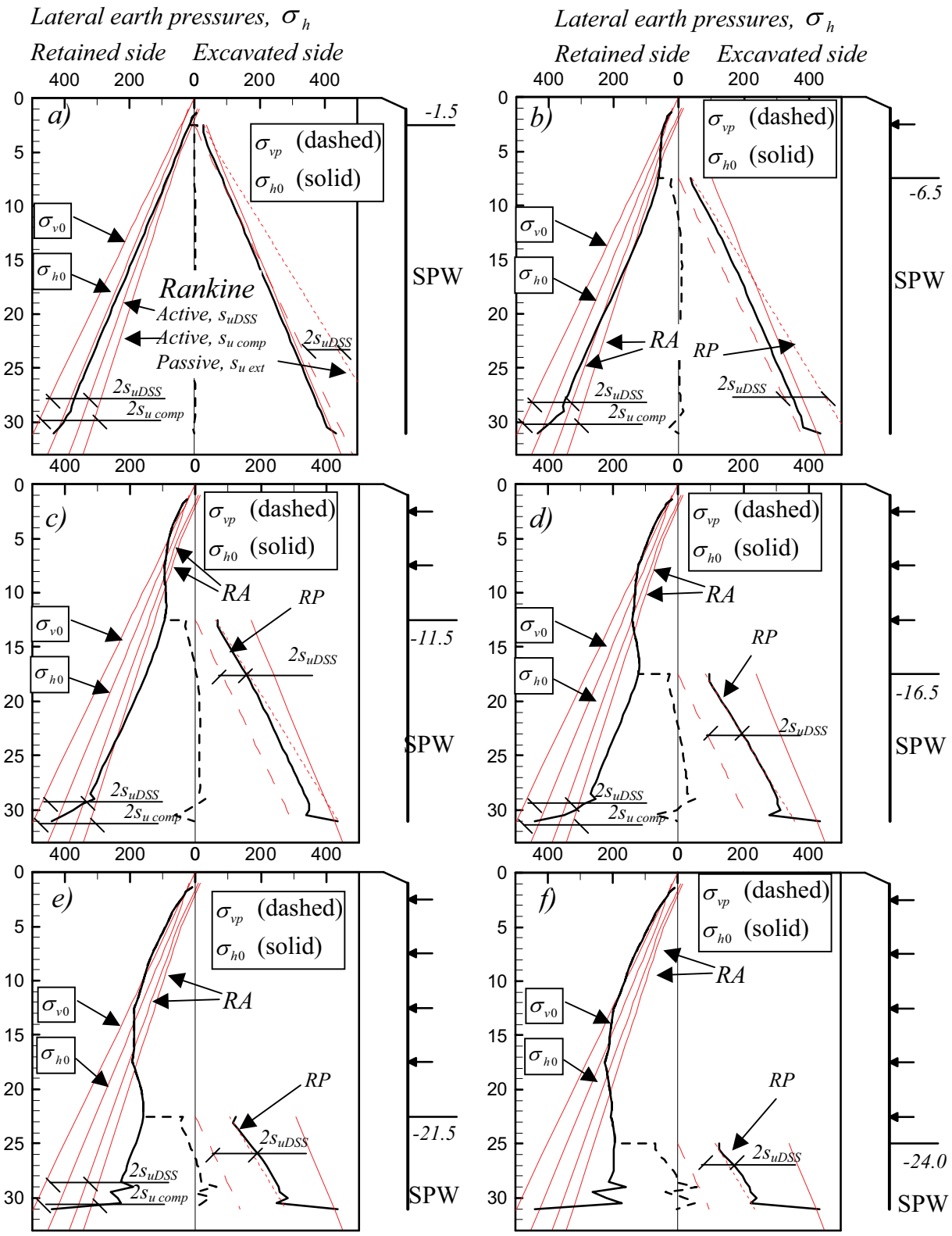

Figure 9.18: Calculatd earth pressures for different excavation stages. (MIT-S1, h_u=1.5 and h=5)
Solid black lines represent the lateral pressure on each side of the wall and the black dashed line is the net pressure. Red lines indicate the vertical stress on each side of the wall as well as Rankines active and passive pressure (RA and RP). The initial horisontal stress on both side of the wall is also presented.

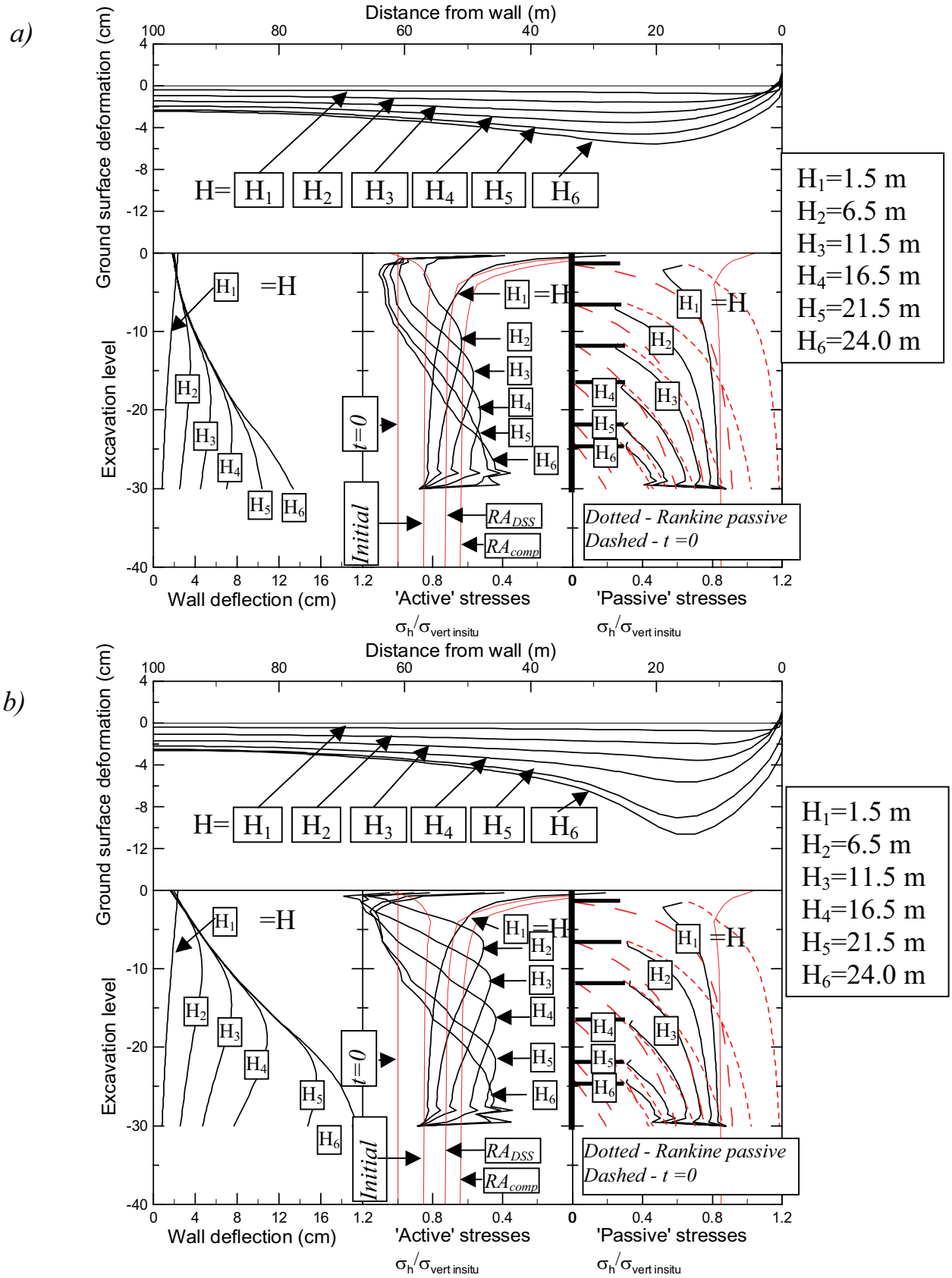

Figure 9.19: Effect of vertical support spacing on deformation patterns and normalized earth pressure acting on both sides of the wall
Wall length =30 m, H denotes excavation depth and h_u=1.5 m
a) spacing between struts, h=0 b) spacing between struts, h=5.0 m

A comparison of the developed passive earth pressures only reveals negligible differences for the various types of support spacing. The lateral pressure at the passive side coincides with the lowest value of the following two scenarios:

- A slight decrease in the initial σ_h depending on the 1D unloading, no specific lateral movements are needed.
- Passive pressure according to Rankine. Large deformations may occur related to the redistribution of the forces acting on the wall when Rankine's passive earth pressure drops below the initial horizontal stress.

The empirical relation from Equation (9.7) is presented in Figure 9.20. As can be seen in Figure 9.20 and Figure 9.19, the decision about the vertical support spacing is also based on economic factors. How much will the deformation cost and on the other hand, how much will the retaining structure cost. Narrow spacing increases not only the amount of steel required, but also leads to a longer construction time and higher building costs. The impact on the surroundings is greater; the disturbance lasts longer with potential traffic problems. If the support system consists of backward anchors the effect of the installation on adjacent constructions (buildings) may be larger if closer as opposed to wider spacing is used, thereby negating the benefit of narrow spacing. Longer construction time and the need for more material in the retaining system will also increase the impact on the global environment.

Ground surface displacement will affect the adjacent buildings and large deformations are to be expected within a distance of 1.5 times the length of the *SPW*. A vertical spacing of 2.5 metres was used when studying how the soil model used affects the behaviour of the *SPW*.

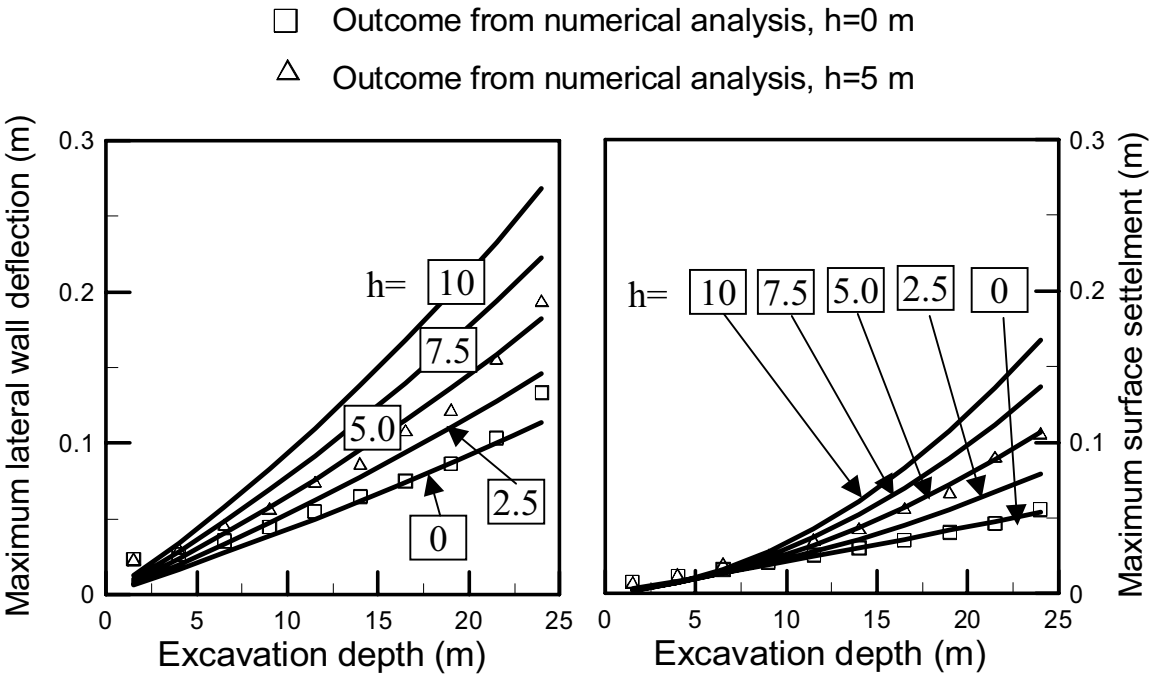

Figure 9.20: Effect of vertical support spacing on the behaviour of the wall and the ground surface. (MIT-S1, h_u=1.5 and Length 30 m), compared with the empirical relation presented in Equation (9.7)

Table 9.7: Effect of vertical support spacing on the maximum bending moments within the SPW

	H=	1.5	4.0	6.5	9.0	11.5	14.0	16.5	19.0	21.5	24.0
h=0	M_{max}=	19	144	261	354	430	486	520	505	395	452
h=5.0	M_{max}=	19	264	589	557	800	762	1070	993	1250	759

9.6.2 Comparison of different soil models, *h*=2.5

In this section the calculated result from using three different models is presented. The models are the same as in Section 9.5, namely the *MIT-S1*, *PLEP-MC* and *e-ADP*. Figure 9.21 presents the result of an excavation to a depth of 16.5 m. Characteristics of the soil profile are provided in Figure 9.16, the unsupported height, h_u, is 1.5 m and the spacing, *h*, is 2.5 m. In Figure 9.21 it should be noted that Case A, in which the *MIT-S1* is used, yields smaller deformations than the other two calculations. When studying the ground surface settlements the calculation with *e-ADP* appear to coincide with the outcome of Case B (*PLEP-MC*) close to the wall, although further away from the excavation the settlement is approximately equal to the ones in Case A. The lateral deformation of the wall is approximately the same for Case B and C, the only difference being that the deformation at the foot of the *SPW* is less in case B. This is due to the fact that the strength used by the *e-ADP* exceeds that employed in the *PLEP-MC* model, $s_{u\ ext}^{PS} > \tau_{xy\ DSS}^{max}$.

When studying active earth pressure it is obvious that in Case A it developed for smaller deformations than in the other two cases and that the horizontal stress increases very quickly from developed active lateral earth pressure to a stress situation where σ_h is approximately equal to σ_v, compare Figure 9.24a. This is an effect of using a constant value, in this case a very high value, of G_{el} and an isotropic hardening function. Very small movements against the retained side are necessary for the development of high horizontal stresses. This phenomena can also be seen in Figure 9.4d.

The strain levels obtained by means of the different calculations are also presented in Figure 9.22 and it is obvious that the stiffness used in the *PLEP-MC* calculation is in range of the obtained strain levels, cf. Figure 10.1. Obtained strain levels are in the range of 0.1 to 0.5%, which corresponds with E_{oed}=625·$s_{u\ DSS}$. However, the strain levels within the pit are slightly higher than 1.0 % which corresponds with E_{oed}=250·$s_{u\ DSS}$. If the strain levels obtained from the calculation using the *MIT-S1* model are deemed to be accurate, the stiffness could have been approximately twice as high on the retained side.

The results from the different excavation stages using the *MIT-S1* and *PLEP-MC* are presented in Figure 9.23. The deformation pattern and the lateral earth pressure against the *SPW* predicted by both models developed as expected during excavation. Empirical calculations run with an *PLEP-MC* model gave unrealistically large settlements at great distances from the *SPW*. The reason for this is shortcomings in the modelling of small strain, which is the case far away from the wall. The calculation using the *PLEP-MC* also had a limitation compared to the *MIT-S1* and the results of field data, which revealed a heave on the ground surface behind the wall. The same excavation sequence is presented in Figure 9.24 where the *e-ADP* model was used with two different stiffnesses. As expected, decreasing the stiffness increased the deformation, while the decrease in lateral earth pressure behind the struts was practically insignificant.

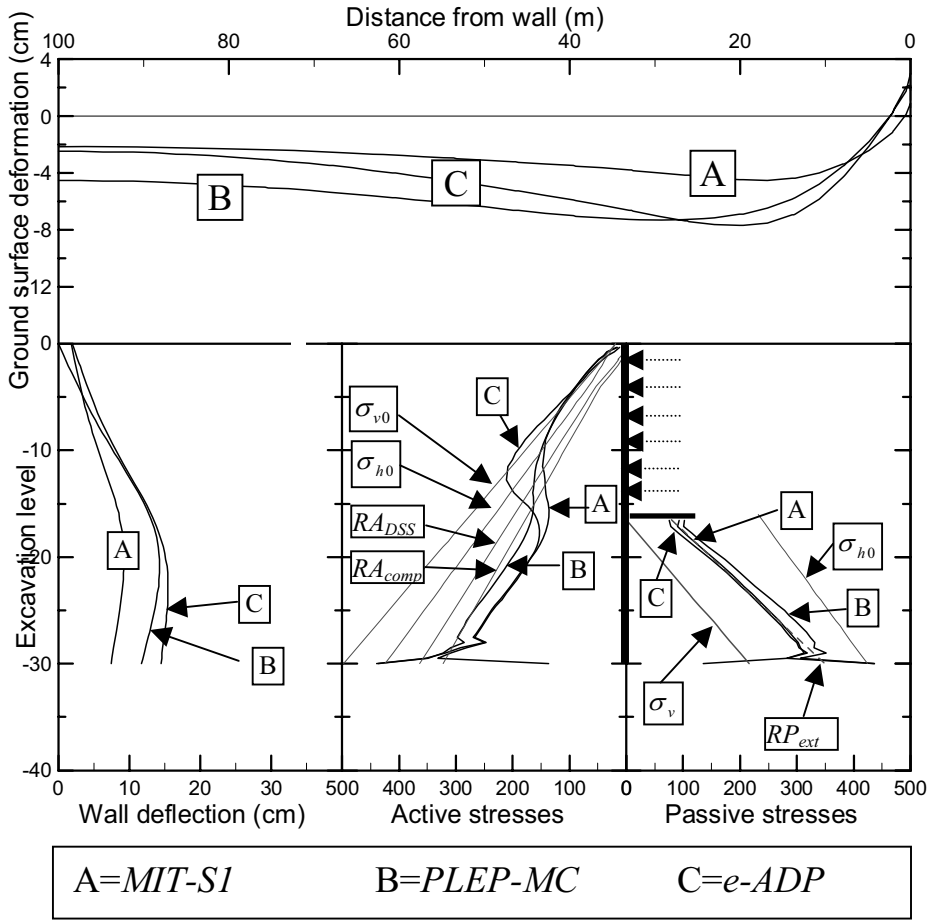

Figure 9.21: Comparison between three different soil models, MIT-S1, PLEP-MC and e-ADP. L=30 m, H=16.5 m, h_u=1.5 m and h=2.5 m.

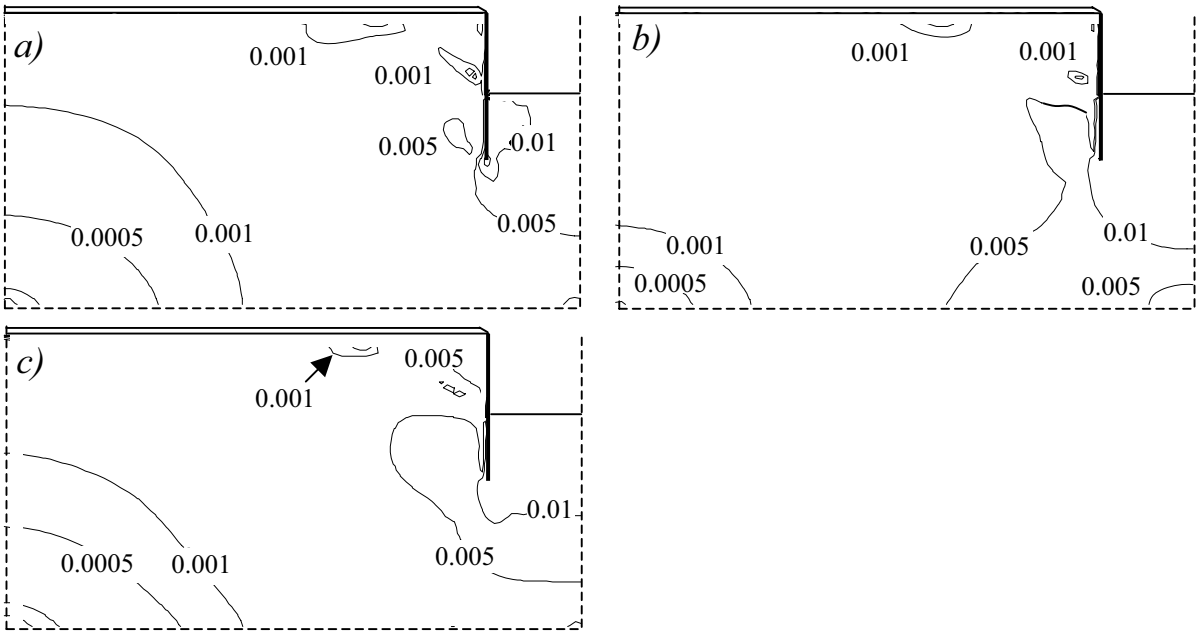

Figure 9.22: Strain levels, γ, for an excavation, H=16.5 m, h_u=1.5 m and h=2.5 m.
a) MIT-S1 b) PLEP-MC c) e-ADP

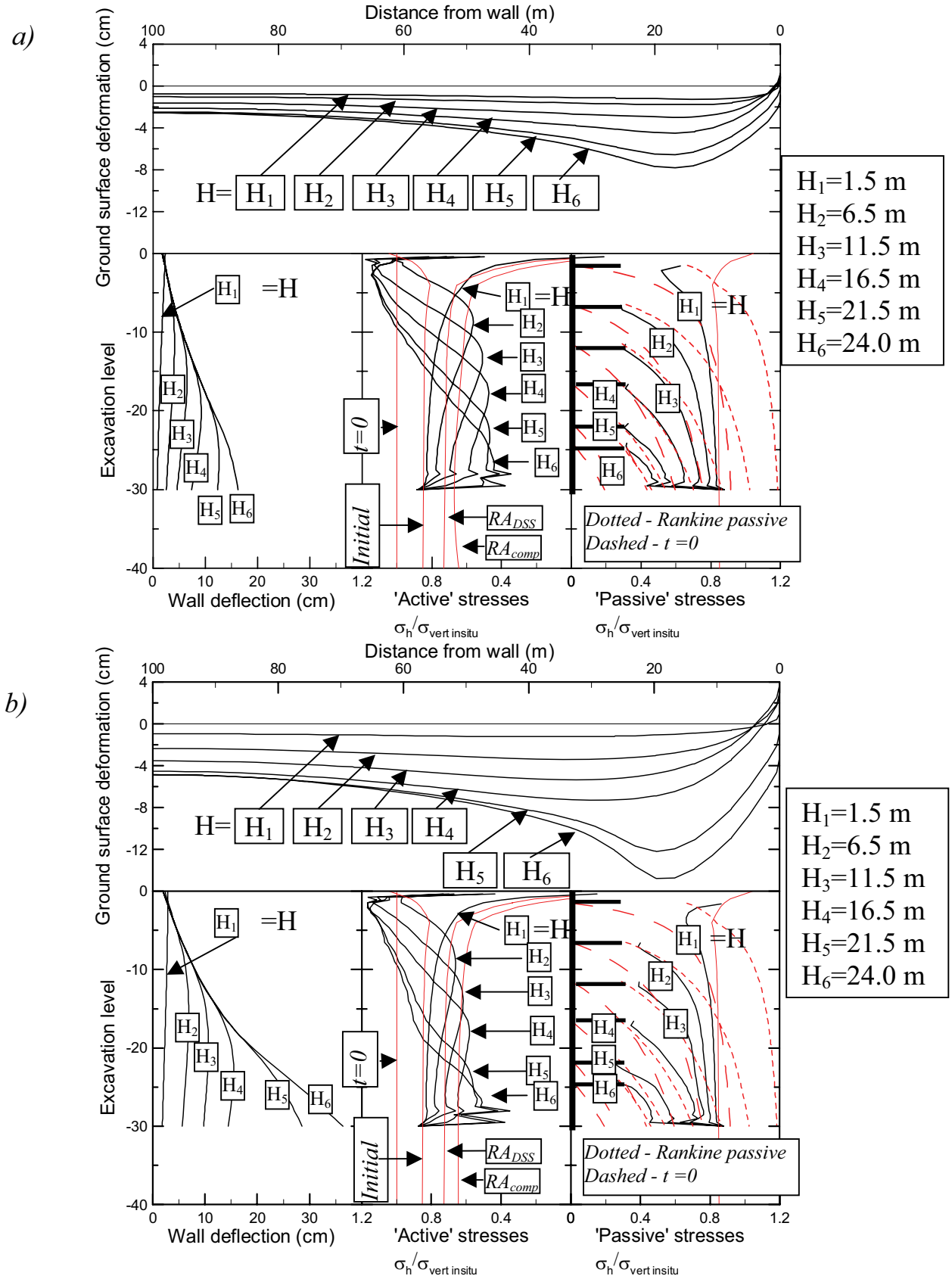

Figure 9.23: Comparison between calculated deformations and pressures against the SPW using a) MIT-S1 and b) PLEP-MC. L=30 m, h_u=1.5 m and h=2.5 m.

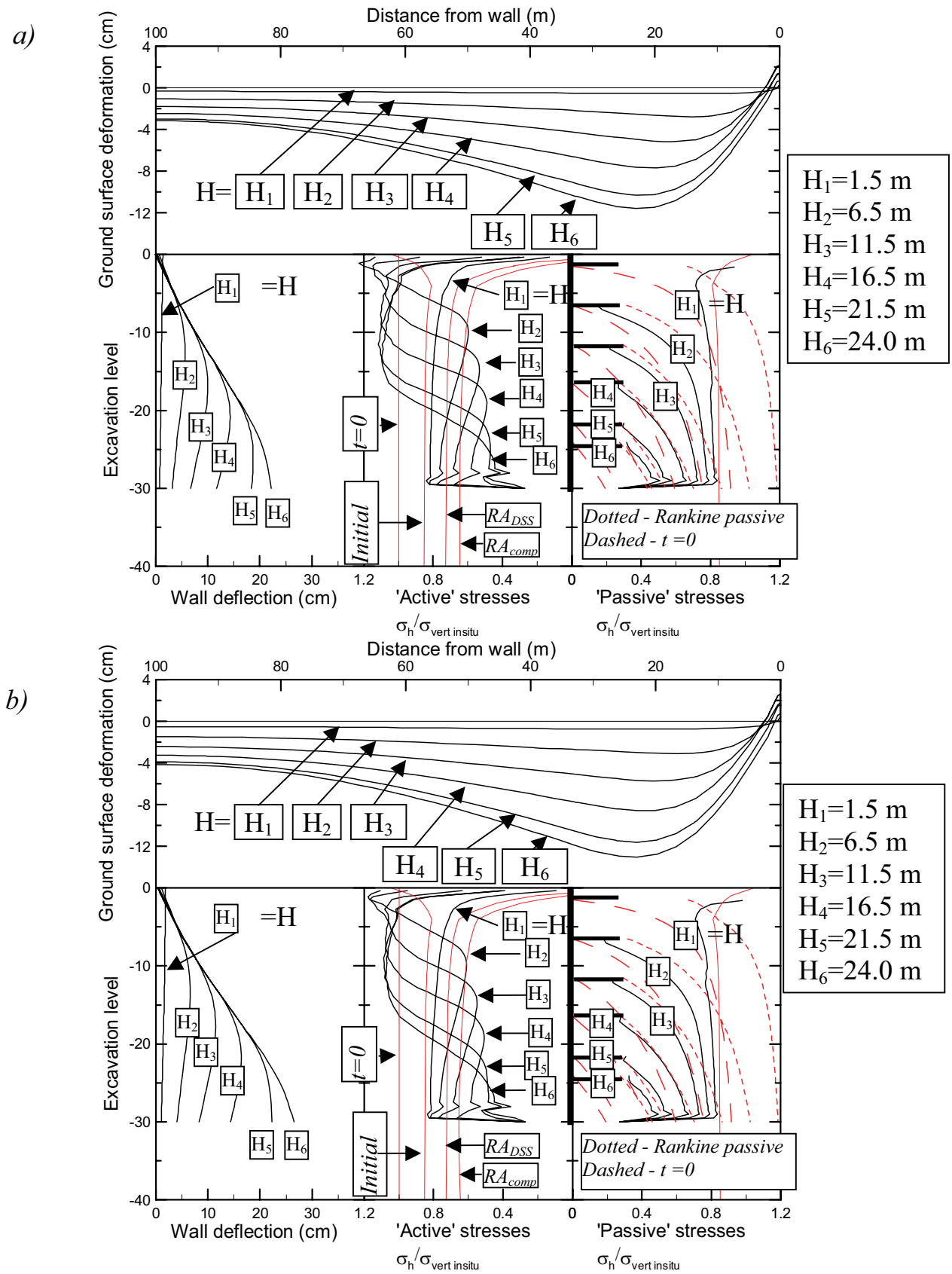

Figure 9.24: Comparison between calculated deformations and pressures against the SPW using a) e-ADP $G_{el}=G_{max}$ and b) e-ADP $G_{el}=2/3 \cdot G_{ma}$. L=30 m, h_u=1.5 m and h=2.5 m.

Studying how the deformation develops for the calculation with *PLEP-MC* during the excavation, it is clear that the deformation accelerates when *H* is increased from 16.5 to 21.5. This is caused by limited support by the embedding, fully developed passive pressure and that the adhesion against the wall is exceeded.

Studying the development of deformation in the *PLEP-MC* calculation during the excavation made it clear that the deformation accelerated when H was increased from 16.5 to 21.5. This was caused by limited support from the embedding, fully developed passive pressure and the fact that the adhesion against the wall was exceeded.

The *MIT-S1* results, see Figure 9.23a, agree well with the framework developed by Hashash (1992). It is likely that this framework can also be used for different widths of support spacing, e.g. using *h*=5 for the first two rows and thereafter *h*=2.5 will probably give a maximum settlement of 8 cm and a maximum lateral movement of 16 cm. This is done by superposition of the estimated deformation for each stage of the excavation.

The differences in earth pressures is reflected in differences in the bending moments in the *SPW* and in the support loads. The maximum bending moments at different excavation stages are presented in Table 9.8 and the support loads in Figure 9.25.

Table 9.8: Effect of soil model on the maximum bending moments in the SPW

	H=	1.5	4.0	6.5	9.0	11.5	14.0	16.5	19.0	21.5	24.0
MIT-S1	M_{max}=	19	264	403	503	602	700	795	870	861	648
PLEP-MC	M_{max}=	29	327	485	589	717	871	1040	1130	869	1360
e-ADP	M_{max}=	8	495	734	896	1040	1050	1230	1260	1210	978

Using the *MIT-S1* instead of the simpler *PLEP-MC* model reduces the maximum bending moments by 36% in this case. Before the *PLEP-MC* calculation loses its embedding support, the decrease is approximately 20%. The *e-ADP* increases the bending moments in all stages with the exception of the last one, where it still mobilizes sufficient embedding support. This increase is an effect of the used combination of stiffness in the *SPW* as well as in the supports. It should be noted that the net pressure against the wall is less below the bottom of the excavation when using the *e-ADP* model compared to the *PLEP-MC* model, but the rotational stiffness around the lowest active support is higher in the latter calculation.

Studying the developed support loads makes it obvious that the utilization of capacity is much better in the *MIT-S1* results than in either of the other two calculations. A comparison of the supports between 4.0 m and 16.5 m reveals that the design load decreases by 10-25% when modelling the clay behaviour with the *MIT-S1* compared with the ordinary *PLEP-MC* model. The degree of utilization in the supports, during the last excavation stage, increases from an average of 80% for *PLEP-MC* to more than 95% for *MIT-S1*.

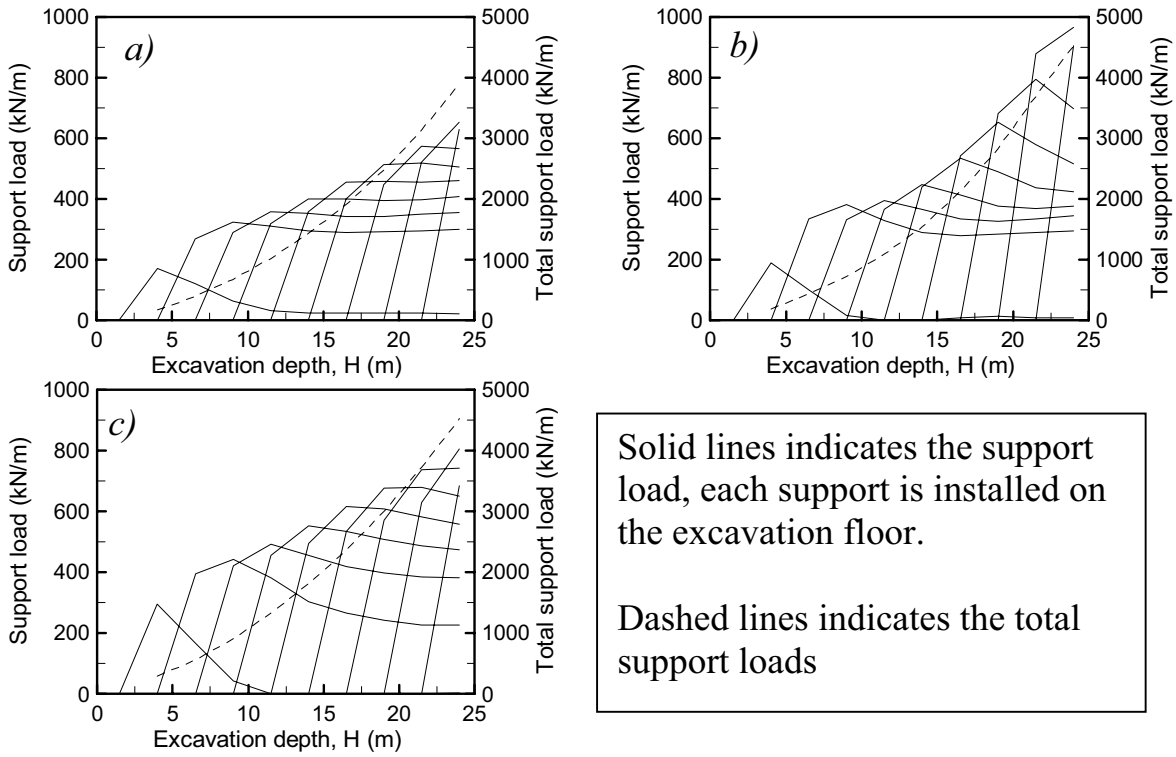

Figure 9.25: Developed support loads during the excavation
a) MIT-S1 b) PLEP-MC c) e-ADP

9.7 Evaluation of empirical methods for estimating ground surface settlement

The literature contains several case studies of the monitoring of ground surface settlement and horizontal wall deflection. Several of these case studies can be found in the database constructed by Long (1999). Based on case studies, several different methods have been proposed to estimate ground surface settlements, some of which are included in Chapter 2. These methods are applied to the sections presented in Chapter 9 and compared with the results obtained from the different ways of modelling clay behaviour.

9.7.1 Excavation 1

The characteristics of this excavation are presented in detail in Chapter 9.5 and briefly summarized here.

The excavation took place in slightly overconsolidated highly plastic clay to a depth of 4m, width (B) 40 m, length (L) 200 m and support system stiffness, $EI/\left(\gamma_w h_{avg}^4\right)$, 116. The factor of safety in relation to basal heave calculated from (Bjerrum and Eide, 1956) was 1.75. Note that semi-empirical methods are defined on the basis of known lateral deformation of the wall obtained from the FE-calculation using the *MIT-S*1 model.

Figure 9.26 illustrates the predicted ground surface settlements when using a rigid support and Figure 9.27 the deformations predicted for the situation when a flexible support system is used. Some methods, such as Peck and *KJHH*, are independent of the horizontal deformation of the wall while others are developed from known maximum lateral deformation and/or the shape of the wall deflection. As can bee seen in Figure 9.26 the scatter is quite large both for the *FE*-calculations and the different empirical methods. From experience it is known that almost no deformations occur at a distance exceeding $4H_e$ from the wall, which is the case for all *FE*-calculations. The main explanation for this behaviour is the assumption of completely undrained behaviour and the lack of small-strain stiffness modelling. However, in this case both the *MIT-S1* and the *e-ADP* model show a stiff response at small strain levels.

The various empirical methods differ from each other and are not completely stringent, i.e. for the flexible support larger inward deformation should lead to larger settlements but this is not a the case in the method proposed by (Clough and O'Rourke, 1990) or by (O'Rourke, 1981), due to the fact that these two methods are dependent on the shape of the lateral deformation of the wall, cf. Eq.(2.15). This shape is defined based on a situation in which no deformation

occurs at the foot of the wall, which was not the case here. It should be noted that the *KJHH* method is out of the range to which it was originally fitted.

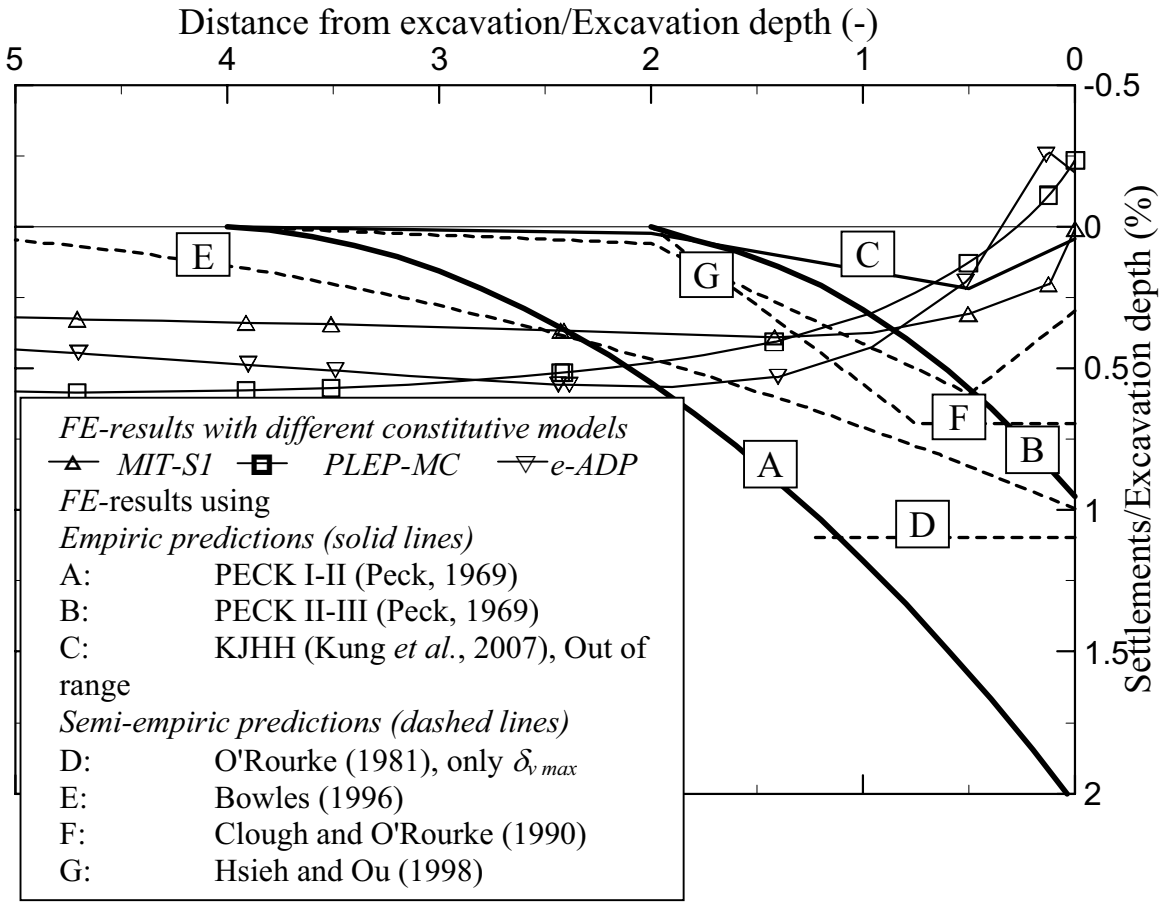

*Figure 9.26: Comparison of ground surface settlements obtained from FE-calculations using different constitutive models with **rigid** support and empirical and semi-empirical methods.*

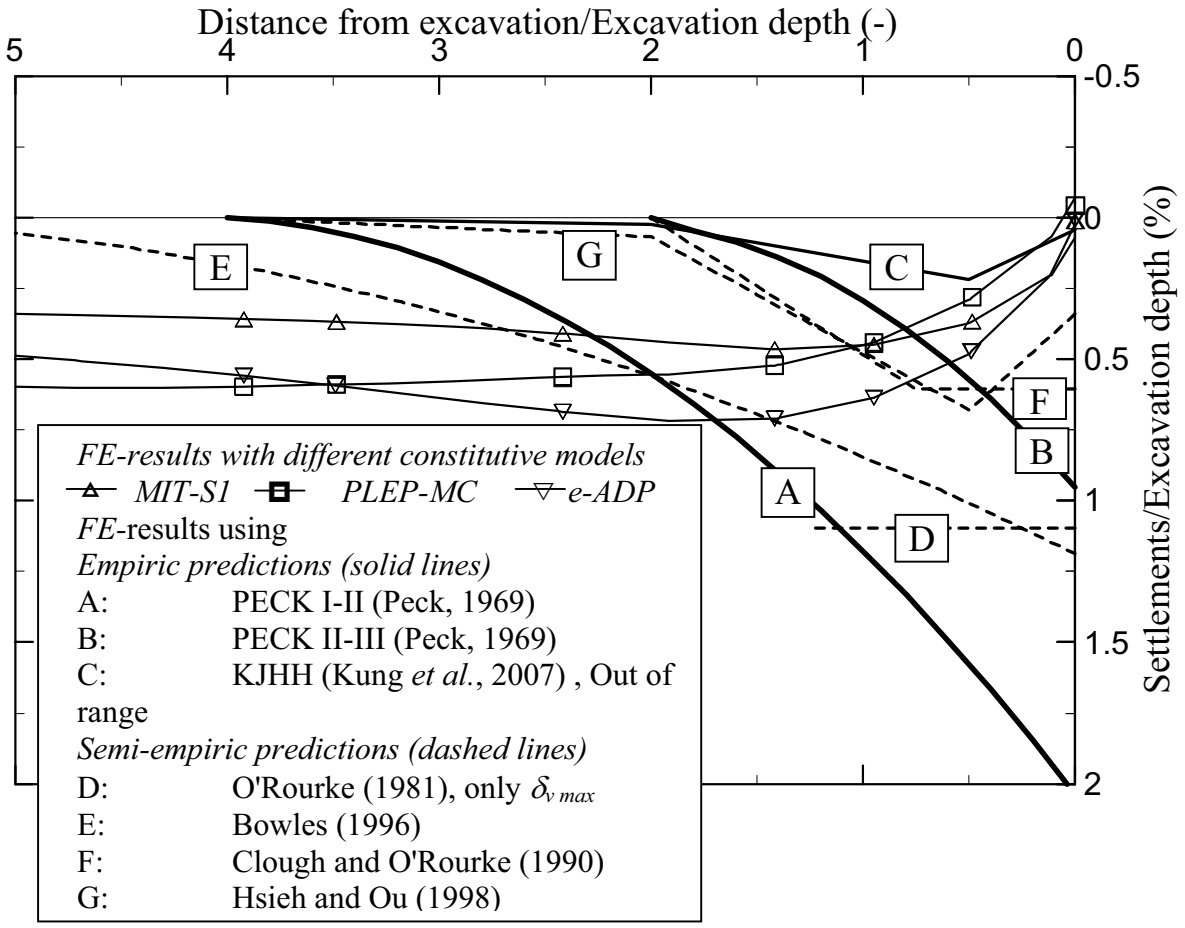

*Figure 9.27: Comparison of ground surface settlements obtained from FE-calculations using different constitutive models with **flexible** support and empirical and semi-empirical methods.*

9.7.2 Excavation 2

The characteristics of this excavation have been provided in Chapter 9.6. In Figure 9.28, Figure 9.29 and Figure 9.30 the predicted ground surface settlements are presented for the three different constitutive ways of describing clay behaviour, *MIT-S1, e-ADP* and *PLEP-MC.* The differences in the estimation of the ground surface settlements are due to differently calculated lateral deformation of the three soil models.

For a deep braced excavation such as the one described above, the consistency of the different methods is better than for the shallow excavation described in the previous section. The semi-empirical methods show better agreement with *FE*-calculations than in the previously mentioned case. However, the *KJHH* method is here assumed to give the best prediction, as it is not affected by the choice of clay behaviour modelling.

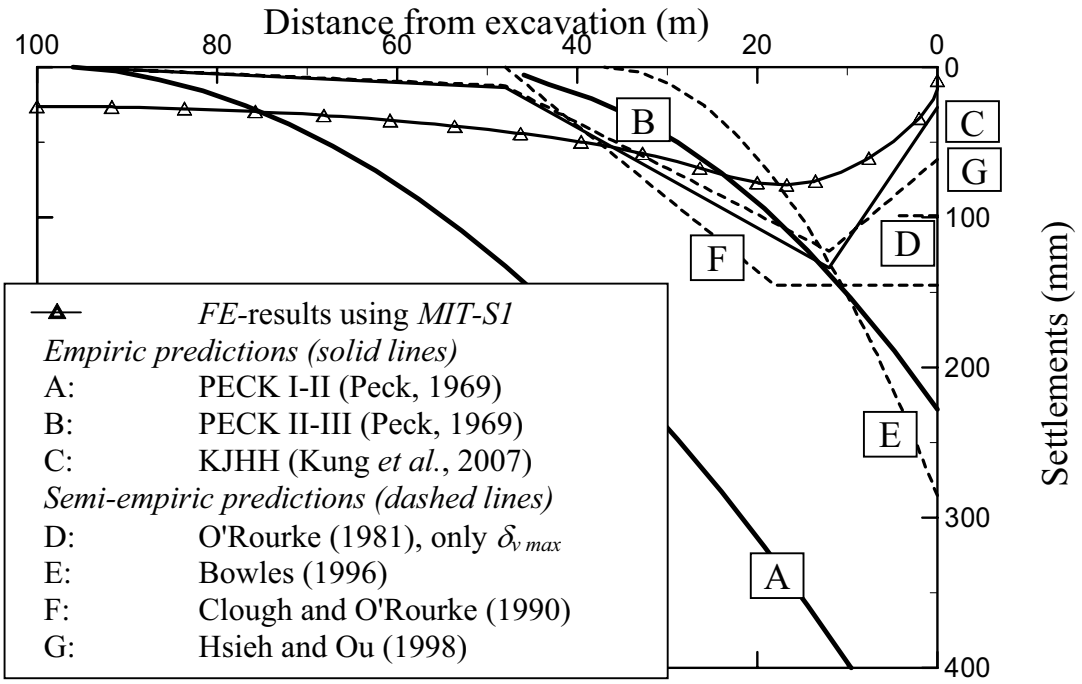

Figure 9.28: Comparison of ground surface settlements predicted by means of FE-calculations using the MIT-S1 model and empirical and semi-empirical methods. H=24 m, B=40 m and L=200 m.

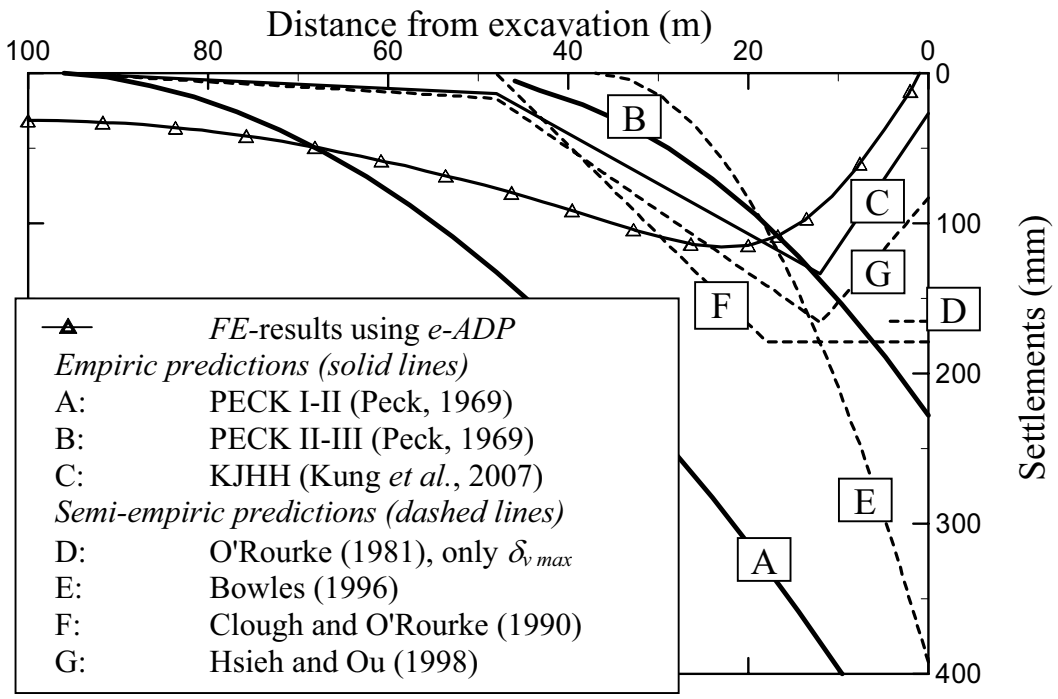

Figure 9.29: Comparison of ground surface settlements predicted by means of FE-calculations using the e-ADP model and empirical and semi-empirical methods. H=24 m, B=40 m and L=200 m.

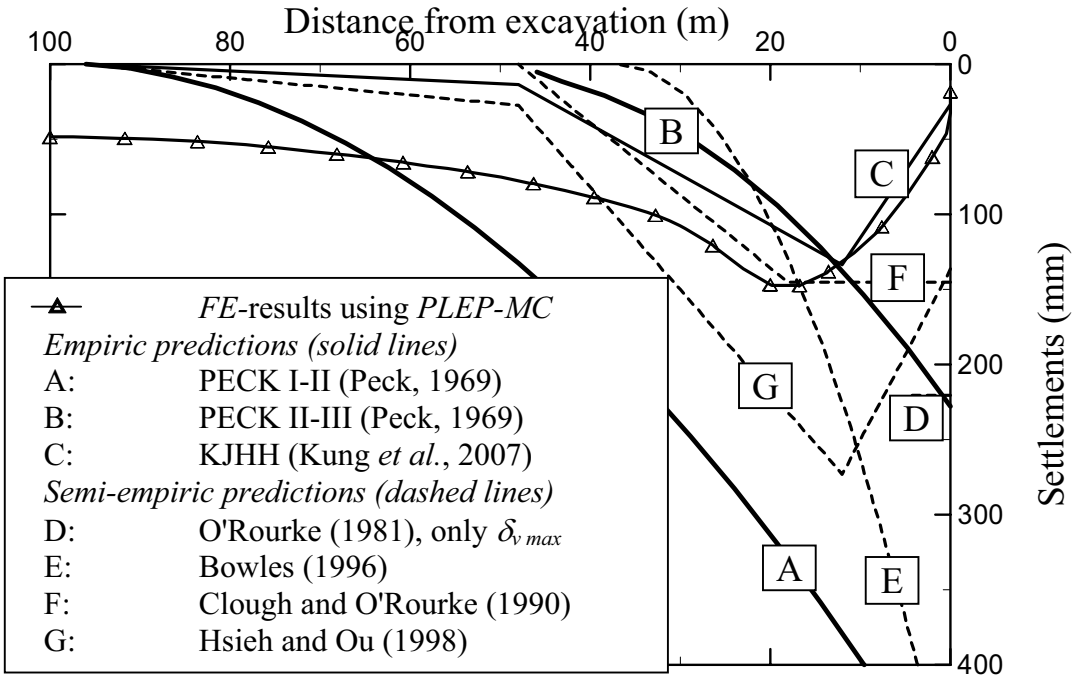

Figure 9.30: Comparison of ground surface settlements predicted by means of FE-calculations using the PLEP-MC model and empirical and semi-empirical method. H=24 m, B=40 m and L=200 m.

The predicted ground surface settlements for some of the various excavation stages are presented in Figure 9.31 and normalized against the excavation depth in Figure 9.32. These two figures have also been complemented by a factor of safety related to basal heave, fosb, in accordance with Bjerrum and Eide (1956) . As can be seen in Figure 9.31, the predicted settlements do not follow the same pattern throughout the different excavation stages. The deformation obtained from the *FE*-calculation shows an increase in ratio between δ_v and H_e when the excavation depth exceeded 16.5 metres. This behaviour is not seen in the empirical prediction; instead, the amount of settlement decreased at each excavation stage.

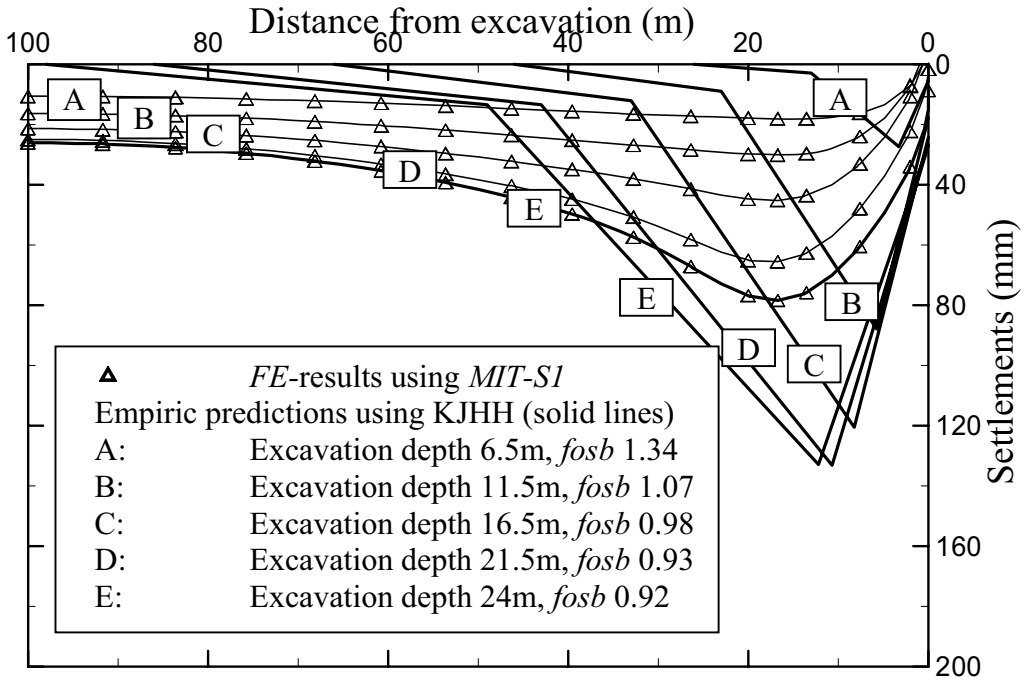

Figure 9.31: Comparison of ground surface settlements predicted by means of FE-calculations using the MIT-S1 model and the KJHH empirical method for different excavation depths in a slightly overconsolidated highly plastic clay. B=40 m, L=200 m $EI/\left(\gamma_w h_{avg}^4\right)$*=2300.*

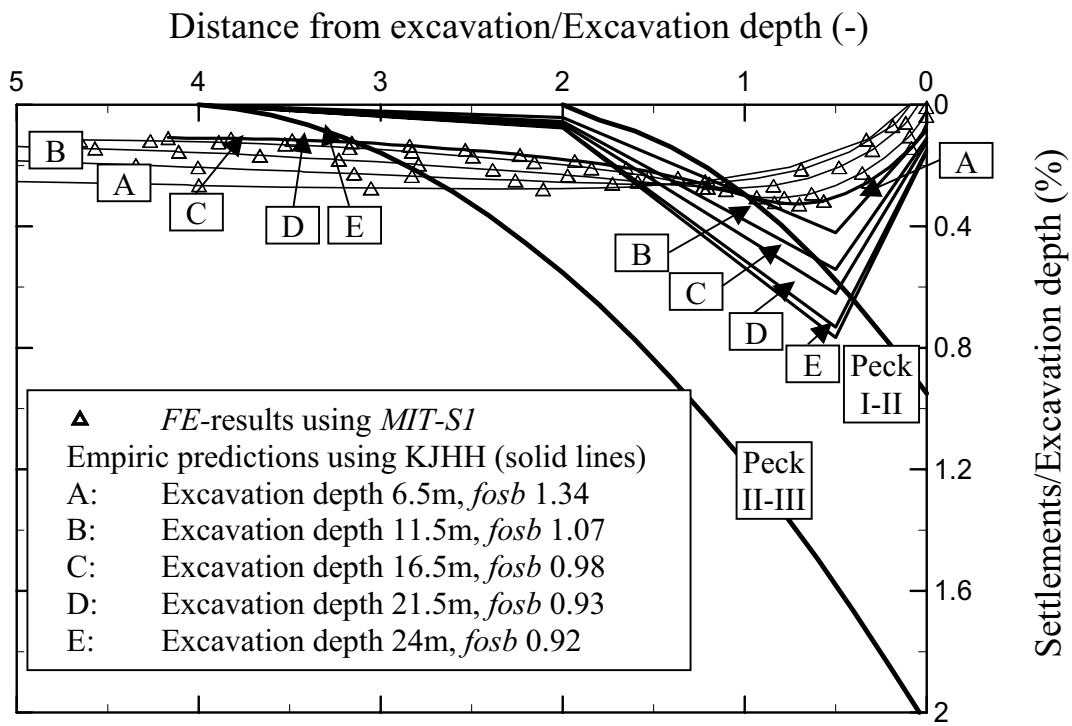

Figure 9.32: Comparison of ground surface settlements, normalized against excavation depth, obtained from FE-calculations using the MIT-S1 model and the KJHH empirical method for different excavation depths in a slightly overconsolidated highly plastic clay. B=40 m, L=200 m $EI/\left(\gamma_w h_{avg}^4\right)$*=2300.*

9.7.3 Empirical ground surface settlements adjacent to a deep excavation, considering three-dimensional effects

The empirical settlements have been illustrated in the previous section. Taking three-dimensional effects into account (Roboski and Finno, 2006) the settlement distribution can be predicted even at the corners of an excavation. In Figure 9.33 the *KJHH* method is used for predicting the two-dimensional settlement distribution, Figure 9.33b, while the method by Roboski and Finno (2006) is used to predict the three-dimensional effects. The assumed geometry is an excavation depth of 24 m and a length of 200 m. The width of the excavation is 40 m but symmetry at the corners has been assumed.

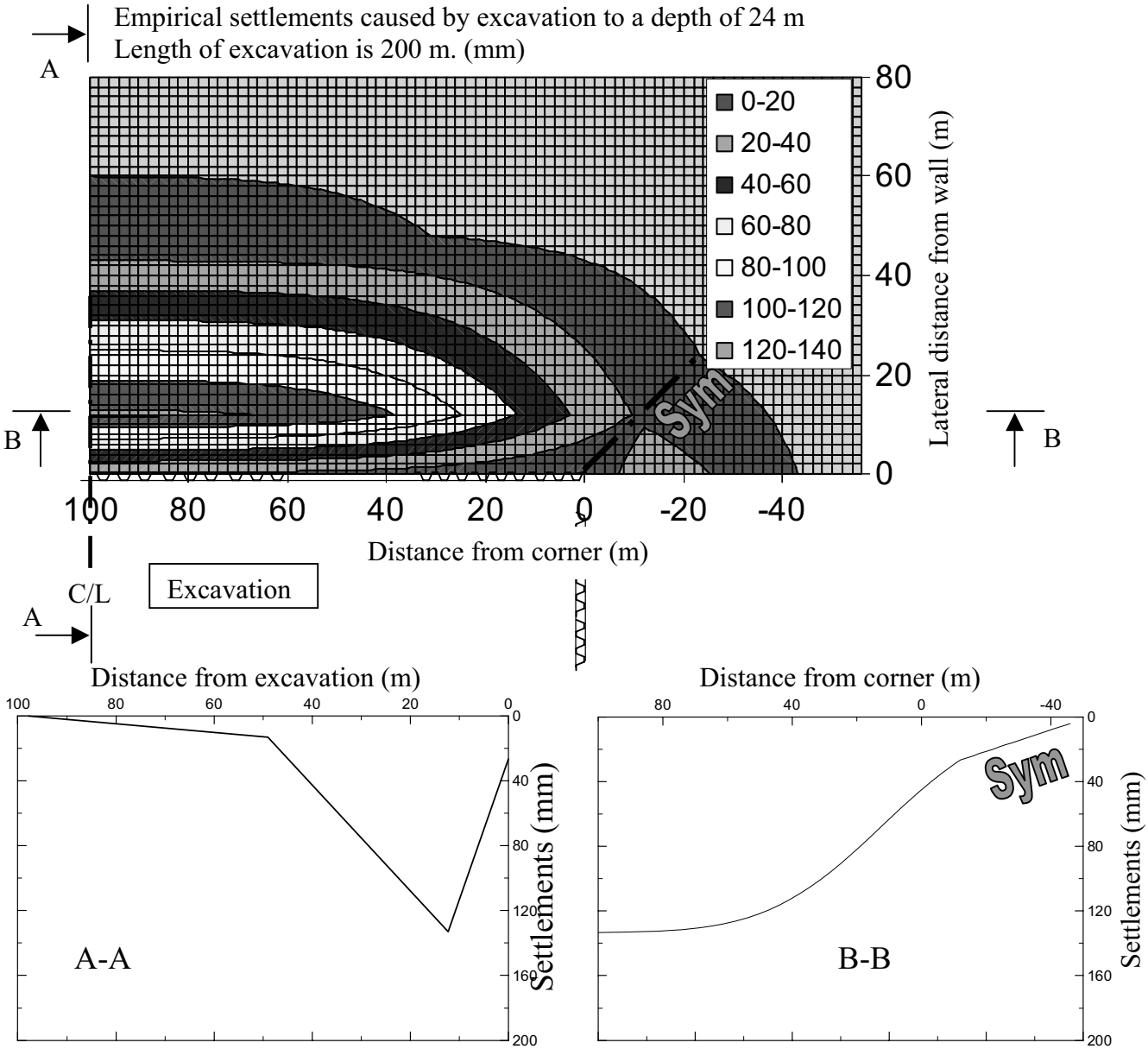

Figure 9.33: Empirical settlements caused by excavation to 24 m depth. The length of the excavation is 200 m. The KJHH method (Kung et al., 2007) was combined with the method proposed by Roboski and Finno (2006). Section 2 in Chapter 9.6

Such predictions also indicate ground surface distortion, which is the major cause of damage to adjacent buildings (Burland and Wroth, 1974; Boscardin and Cording, 1989; Boone, 1996; Aye *et al.*, 2006). Figure 9.34 presents the distortion resulting from the settlement distribution predicted in Figure 9.33. Such a plot makes it relatively easy to judge what buildings are located within the area where damage due to distortion can be expected.

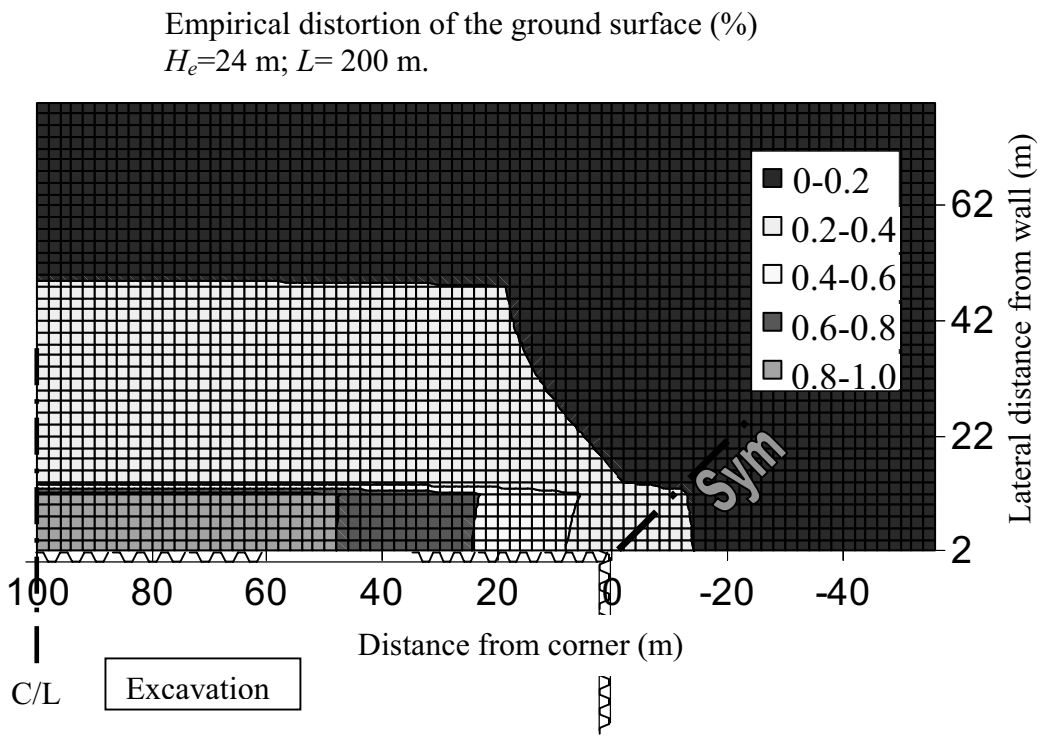

Figure 9.34: Empirical distortion of the ground surface caused by excavation to a depth of 24 m depth.
The length of the excavation is 200 m. The KJHH method (Kung et al., 2007) was combined with the method proposed by Roboski and Finno (2006). Section 2 in Chapter 9.6

10 NUMERICAL ANALYSES OF DEEP EXCAVATIONS AT THE GÖTA TUNNEL

10.1 Introduction

In this section Numerical calculations are presented for section 1/430 north and section 1/470 south. These calculations are divided into 2 different categories:

Class A: Numerical simulations performed based on the soil properties presented by the Swedish Road Administration. Calculations of this kind can be compared with a pre-calculation used to predict the behaviour of the wall system. Numerical pre-calculations were made by the author and colleagues at Skanska before the sheet pile walls were designed. However, the calculations presented here contain the working sequence changes made during construction.

Class B: Numerical simulations, where the clay is represented by the *MIT-S1* constitutive model. The same working sequence as in class A calculations is used, but with a simplified geometry compared with that employed in the previous calculations. The section was simplified due to some limitations in the *USDM*, which were implemented in PLAXIS and contained the *MIT-S1* formulation. This simplified section is also analysed by means of the same constitutive relation as Class A in order to study to what degree the simplification of the geometry affected the results. The latter calculations are not presented here, as the results obtained are almost identical to those of Class A.

The calculations were made undrained, with plane strain (PS) boundary conditions and the algorithm used for solving the *FE*-calculations as described by Brinkgreve (2002). The clay layer was modelled as an undrained material, which can be achieved in different ways. In these calculations, effective soil stiffness was used yielding that undrained stiffness was calculated as a function of the soil stiffness, water stiffness, K_w, and an assumed value of the undrained Poisson´s ratio, μ_u, of 0.495 (Brinkgreve, 2002). Steady state water pressure within the undrained layers was refereed to steady state pressure prior to excavation. This yielded all pore water pressure changes as excess pore water pressure. The resulting pore water pressure was calculated according to Equation (10.1)

$$p_{active} = p_{steady\ state} + p_{excess\ pore\ water\ pressure} \tag{10.1}$$

The adhesion between the wall and the soil was set at 50% of the shear strength. In cases where other soil models were used, the interface along the wall was still addressed with Mohr-Coulomb properties with a strength of 50% of $s_{u\ DSS}$ and a stiffness of $G_{max}/3$. The reason for using a factor of 1/3 was that this value was found to be representative of shear strains in the 0.5% range, see Figure 10.1.

10.2 Class A calculations

In these calculations a linear elasto-plastic constitutive model with a non-associated flow rule, referred to as the *PLEP-MC* model, represented all soil layers. The plastic behaviour was defined by the Mohr-Coulomb (*MC*) failure criteria. The calculation was made on the basis of the parameters set out in the contract between the Swedish Road Administration and the contractor, the only difference being that stiffness was increased in order to model the unloading behaviour.

The given value for the constrained modulus, M_0 or E_{eod}, was a function of the undrained shear strength, s_u, Equation (10.2). The contractor increased the value of E_{eod} by a factor of 2.5 based on the fact that the shear strain around the excavation was excpected to be small.

$$M_0 = 250 \cdot s_u \tag{10.2}$$

Empirical relations for the shear modulus of Swedish clays can be found in (Andreasson, 1979; Larsson and Mulabdic, 1991; Larsson, 1994), The relations given here are based on the work by Hardin and Drnevich (1972) and Andreasson (1979).

Hardin and Drnevich (1972) presented a modified hyberbolic relation for G_{sec} based on the G_0 and the number of load cycles, N. If N equals 1 the relation for G_{sec} will be as in equation (10.4). The initial shear modulus is here based on the work presented by Andreasson (1979), equation (10.3).

$$G_0 = \frac{504}{w_L} \cdot s_{u\ DSS} \tag{10.3}$$

$$G_{\sec} = \frac{G_0}{1 + \frac{\gamma \cdot G_0}{s_{u\ DSS}} \left(1 + e^{-1.3 \frac{\gamma \cdot G_0}{s_{u\ DSS}}} \right)} \tag{10.4}$$

From equation (10.4) the tangent shear modulus can be obtained, equation (10.5) as well as the stress strain relation can be expressed as in equation (10.6)

$$G_{\tan} = \frac{d}{d\gamma_{xy}} \left(\gamma_{xy} \cdot G_{\sec}\left(\gamma_{xy}\right) \right) \tag{10.5}$$

$$\tau_{xy} = \gamma_{xy} \cdot G_{\sec}\left(\gamma_{xy}\right) \tag{10.6}$$

The constrained modulus, E_{eod}, prescribed by the Swedish Road Administration can be transformed into a shear modulus using equation (10.7). The exact value of the effective Poisson´s ratio for the stress paths adjacent to an excavation is

not known, but drained oedometer tests with monitored horizontal stresses have demonstrated that it can vary between 0.1 and 0.35. This variation is used here to verify the strain range for which the prescribed E_{eod} and the E_{eod} used by the contractor was valid. Equation (10.7) was expressed as a strain independent function in equation (10.8), where the proposed value of A was 250 and that used 625.

$$G = \frac{E_{eod}\left(1-2\mu'\right)}{2\left(1-\mu'\right)} \tag{10.7}$$

$$G_{\sec} = \frac{E_{eod\ sec}\left(1-2\mu'_{\sec}\right)}{2\left(1-\mu'_{sec}\right)} = A \cdot s_u \cdot \frac{\left(1-2\mu'_{\sec}\right)}{2\left(1-\mu'_{sec}\right)} \tag{10.8}$$

When the empirical relation for the shear modulus was compared with the proposed linear function of $s_{u\ DSS}$, it was possible to evaluate the strain levels when the shear modulus coincided. This was done in Figure 10.1 for the proposed value of E_{eod} as well as for the values employed. An interval was presented as a consequence in the uncertainties associated with the μ'_0 for stress paths adjacent to the excavation. It should be noted that the shear modulus used for comparison purposes must have secant values, as these describe a mean value of the modulus during strain changes.

Figure 10.1a) makes it quite clear that the constrained value prescribed by the Swedish Road Administration corresponds to a shear strain, γ_{xy}, of approximately 0.8%-1.6% while the straines corresponding to the contractor's stiffness were approximately 0.2%-0.6%. The empirical shear modulus in Figure 10.1a) was valid for a liquid limit, w_L, of 70%. The corresponding values for different w_L are presented in Figure 10.1b). The two different magnitudes of the constrained modulus also correspond to different magnitudes of relative shear stress, Figure 10.1c). The prescribed value corresponds with a relative shear stress of 85%-92%, while those applied correspond to a relative shear stress of 52%-80%. One should bear in mind that this is valid for stress paths coinciding with the one in the CK_0UDSS-test. In the case of active and passive stress paths, the shear modulus, and thus the strain levels, will be almost identical, while the relative shear stress is dependent on the K_0 value, active shear strength, $s_{u\ comp}$, and passive shear strength, $s_{u\ ext}$.

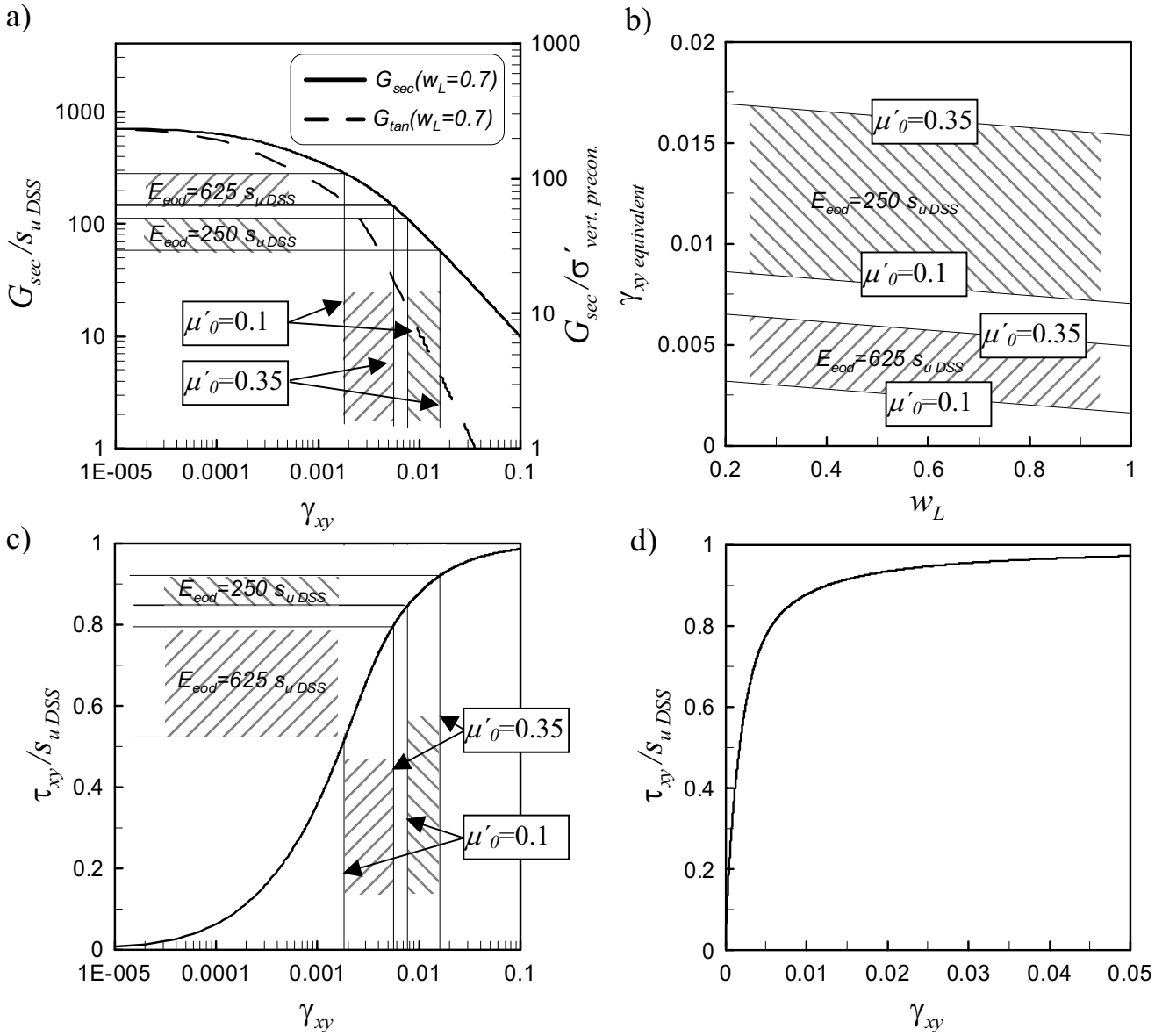

Figure 10.1: Empirical relations for highly plastic Swedish clays in terms of shear modulus compared with strain independent shear modulus as prescribed by the Swedish Road Administration.
a) Empirical relations for the shear modulus (Hardin and Drnevich, 1972; Andreasson, 1979) compared with that used in class A calculations.
b) Equivalent shear strain when a strain independent shear modulus is used compared with empirical relations
c) Empirical relation of the shear stress vs. shear strain compared with coinciding shear strains and shear stresses when using a constant shear modulus value independent of strain level.
d) Empirical relation of the shear stress vs. shear strain, linear scale.

Calculations verified by field measurements presented by Simpson *et al.* (1979) and field measurements presented by Ou *et al.* (2000) indicate that the expected shear strains adjacent to an excavation will be less than 1% and that strain levels decrease rapidly in line with the distance from the excavation. These results

support the increase of the constrained modulus made by the contractor, although the shear strains evaluated in the FE-calculations must be checked against the assumed magnitude of the shear strain by means of a semi iterative process. When using linear elastic, perfectly plastic constitutive models for modelling an excavation, there will always be locations with a variation in strain levels. A time consuming iteration process has to be followed in order to determine the constant value of the modulus, which represents the actual shear strain at all locations in the section. The same kind of process is necessary if one wishes to use different shear strengths due to various stress paths (effects from anisotropy). The important thing is to ensure that the result of the calculation is not out of range compared with the assumptions made when choosing the proper input value for the strengths and the moduli. If the shear strain levels are in the range of 0.1%, the $E_{eod}/s_{u\,DSS}$ can be about 1000, while for shear strain levels of 0.01%, the corresponding value of the $E_{eod}/s_{u\,DSS}$ will be about 1500 to 2500 with the lower value corresponding to μ'_0=0.1 and the higher one to μ'_0=0.35.

The contractor determined the increase in E_{eod} below the preconsolidation pressure by comparing the unloading constrained modulus, M_s, obtained from the empirical relation that $M_{s\,sec} \approx M_{rl}$ is proportional to σ'^{precon}_{vert} with a factor of 90, which differs from that presented in this work, Figure 8.44. This value corresponds well with the unloading and reloading in the range between *OCR* 1.25 and 2.0 based on a value of a_s of 0.8% (Larsson, 1994). For this unloading range, the expected value of μ'_0 should have been approximately 0.2, Figure 8.20b, instead of the value of 0.1 used by the contractor.

The s_u value presented by the Swedish Road Administration makes it obvious that the ratio between s_u and σ'^{precon}_{vert} decreases in line with depth. This remains the case even when changes in *OCR* are taken into account; compare Figure 8.41b. The value of s_u presented by the Swedish Road Administration is mainly based on field vane investigations and the characteristic value is reduced based on the number of tests.

When using a *PLEP-MC* model with failure criteria based on a constant value of s_u, it is of major importance to employ relevant combinations of initial stresses and shear strengths.

10.3 Class B calculations

These calculations were performed by using the *MIT-S1* to describe the clay behaviour. The properties were the ones evaluated in Chapter 8. However, due to certain shortcomings in the implementation of the model in the PLAXIS code, the sections were simplified to horizontal layers, only one of which was described by the *MIT-S1* parameters. The latter limitation means that,

throughout the profile, the clay was described by means of a constant void ratio. This, in combination with increasing preconsolidation pressure with depth, means that no single *LCC*-line was used. The main effect of this simplification is presented in each section containing results from Class B calculations.

10.4 Section 1/430 north

The restrictions regarding deformation in this section were provided by the builder and limited to 100 mm lateral deformation of the *SPW*.

In order to compare the monitored and calculated behaviour, all working stages had to be taken into account. Unfortunately, there is no strict way of analysing the effect of piling on deformation and stress changes. The short-term response to piling is undrained, the clay behaves almost incompressible and the installed volume of concrete causes an uplift of the surface. The uplift pattern is dependent on the surface geometry, installation sequence and the adhesion between the *SPW* and the clay. Furthermore, the effect due to the installation of piles generates excess pore water pressures that gradually decrease as a result of consolidation, as clearly illustrated in Figure 5.11 and Figure 5.12. The dissipation of the excess pore water pressure causes a gradual decrease in surface uplift. However, the dissipation of the excess pore water pressures induced by the piling had not been completed before the start of the excavation within the pit, thus leading to two overlaying deformation processes, which cannot be separated. Nor was the excavation process completely undrained with the result that a full-coupled analysis was required in order to study the behaviour of the soil adjacent to the excavation.

It is impossible to run a "combined analysis"[17] for normal consolidated clay with a simple soil model such as *PLEP-MC*, as it will probably negate the positive outcome of a coupled analysis, allowing consolidation between the different working stages. A more sophisticated model is capable of fulfilling the demands of a combined analysis, but since the primary aim of this study was to compare the outcome of the same calculations using the Mohr-Coulomb and the *MIT-S1* model, the calculation was made for undrained conditions in all work sequences. The calculations took the form of 2D analyses, as this is the most common way of modelling excavations within sheet pile walls.

It is difficult to model soil movements caused by piling, especially in a 2D analysis. It is, however, extremely important to model the effect of piling in one way or another, not only due to deformation but in order to create a stress

[17] A combined analysis is often used in slope stability where the lowest undrained shear strength and the effective shear strength values are used along the slip surface. In most cases the undrained shear strength is used when the *OCR* is below approximately 2.0.

situation as similar as possible to the one in the field. This is crucial when using a stress dependent and stress path dependent stiffness as in *MIT-S1*.

One way of analysing the initial undrained piling response is to model a volume expansion in the area where the piles have been installed. This will, however, generate negative excess pore water pressure in the area subject to expansion under undrained conditions, which creates difficulties when running a time dependent coupled analysis. Several other ways of modelling the effect of piling have been tested, but failed to provide satisfactory results in all respects.

10.4.1 Class A

The contract between the Swedish Road Administration and the contractor set out the parameters to be used, which are presented in Table 10.1. The *OCR* for section 1/430 north is described as 1.2 in the upper part of the clay and a depth of 20 metres, with a range of 1.0 – 1.1 in between. The density of the clay in the area is 17.0 kN/m^3 down to a depth of 9 metres, below which the density is 16.0 to 16.5 kN/m^3. The liquid limit varied between 60 and 70 % to a depth of 9 metres and increased to 75% at 15 metres.

Table 10.1: Characteristics of section 1/430 north

Soil layer	Depth, z [m]	$\gamma_{dry}/\gamma_{wet}$ [kN/m^3]	s_u [kPa]	ϕ'/c' [º/kPa]	M_0 [kPa]	M_L [kPa]
Upper Fill	0-1	20/23	-	30º/0	-	-
Lower Fill	1-2.5	18/18	-	30º/0.1·s_u	-	-
Clay 1	2.5-9	-/17	18+0.54·(z-5)	30º/0.1·s_u	250·s_u	850
Clay 2	9-18	-/16.0	18+0.54·(z-5)	30º/0.1·s_u	250·s_u	850
Clay 3	18-28	-/16.0	25+1.24·(z-18)	30º/0.1·s_u	250·s_u	850+25·(z-20)
Frict layer	28-31	18/20	-	34º/0	-	-

The contract states that the pore water pressure in the clay down to a depth of 10 metres has a groundwater head 2.0 metres below the ground surface, after which it rises and is 0.5 metres below the ground surface at a depth of 20 metres. At 25 metres the groundwater head was found to be at surface level.

A stress situation within the soil strata can be obtained by combining the densities and the pore water pressures, see Figure 10.2 (curve A). An *OCR* variation in accordance with curve C was employed to calculate σ'^{precon}_{vert} (curve B). By using the expression proposed by Schmidt (1966), where $K_0^{nc} = 0.55$ and m=0.6, an expected K_0 was calculated (curve D), from which ratio an initial shear stress was calculated (curve G). As can be seen in Figure 10.2, the initial shear stresses exceeded the recommended shear strength, s_u (curve F). As this is not a realistic stress situation, K_0=0.7 was used as an initial ratio between σ'_{hor}

and σ'_{vert}. By increasing the level of K_0 in the clay to 0.7, the initial shear stresses decreased (curve H). Since the soil strata are not horizontal, the initial stresses have to be generated by gradually increasing the densities in the *FE* calculations by means of a value of μ' in accordance with Equation (10.9). After generation of the initial stresses, the soil parameters are exchanged, in order to better describe the actual problem.

$$\mu'_{initial\ stresses} = \frac{K_0}{K_0 + 1} \tag{10.9}$$

The parameters used in the FE calculations are summarized in Table 10.2 and the initial hydraulic situation set out in the contract is presented in the left section of Table 10.3. A study of the pore water pressure monitored within this research project and the laboratory test from section 1/430 revealed a slightly different pore water pressure situation, which was then used in the FE-calculations presented in the right section of Table 10.3.

Table 10.2: Properties, calculation A

Soil layer	Depth	$\gamma_{dry}/\gamma_{wet}$ [kN/m^3]	ϕ'	s_u [kPa]	G [kPa]	$\mu_{initial}$	$\mu'_{excav.}$
Upper Fill	0-1	20/23	30º	0	10400	0.333	0.2
Lower Fill	1-2.5	18/18	30º	0	10400	0.333	0.2
Clay 1	2.5-9	-/17	0	18+0.54·(z-5)	278·s_u	0.412	0.1
Clay 2	9-18	-/16	0	18+0.54·(z-5)	278·s_u	0.412	0.1
Clay 3	18-28	-/16	0	25+1.24·(z-18)	278·s_u	0.412	0.1
Frict layer	28-31	18/20	34º	0	31250	0.306	0.2

Table 10.3: Steady state pore water pressure as stated in the contract (left) and that obtained in this project (right)

Level	GW head	Gradient	Level	GW head	Gradient
+10.1	+10.1		+10.1	+10.1	
+10.1 - +2.0		+0 m/m	+10.1 - +3.0		+0 m/m
+2.0	+10.1		+3.0	+10.1	
+2.0 - -8.0		+0.14 m/m	+3.0 - -6.0		+0.16 m/m
-8.0	+11.5		-6.0	+11.5	
-8.0 - -13.0		+0.1 m/m	-6.0 - -13.0		+0.07 m/m
-13	+12		-13.0	+12.0	
below –8.0		+0.0 m/m	below –8.0		+0.0 m/m

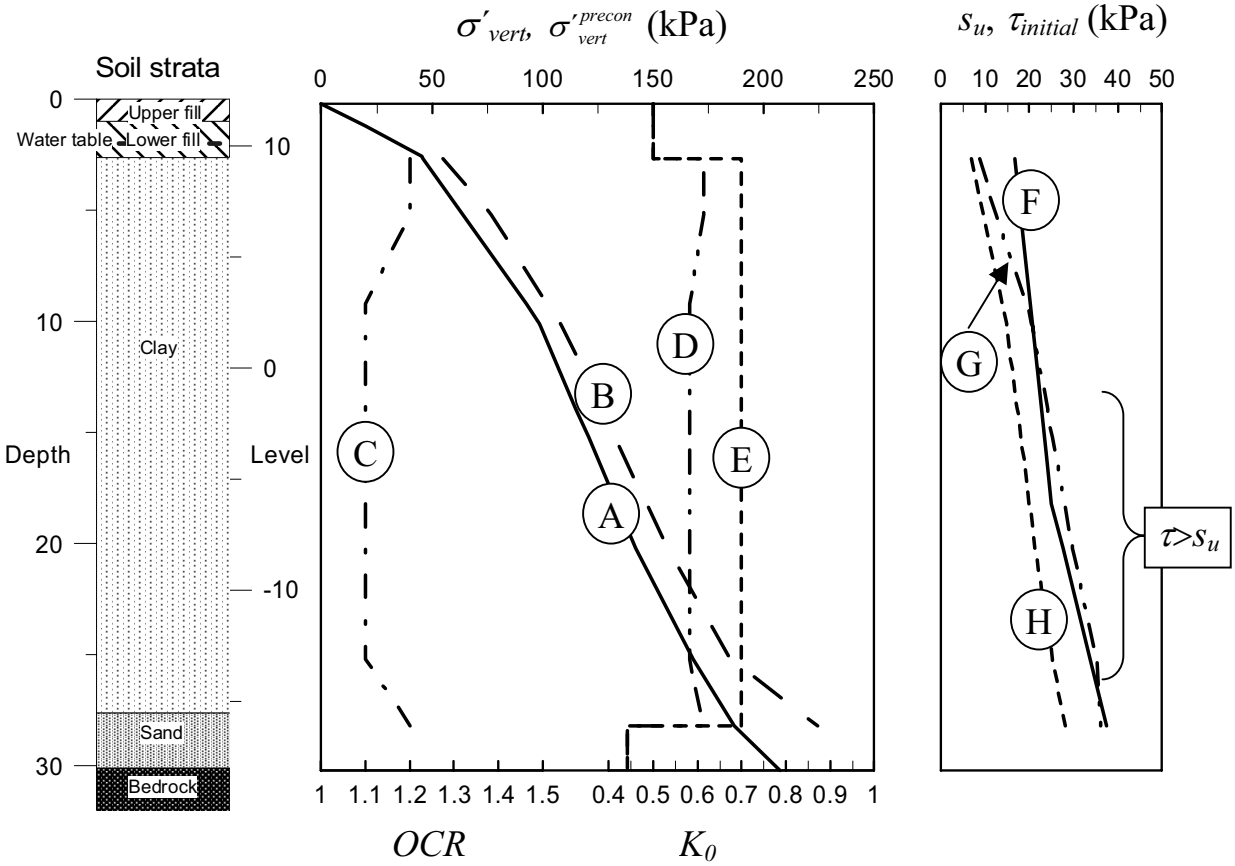

A: σ'_{vert}	C: OCR	E: K_0=0.7 (adjusted)	G: $\tau_{initial}$ from D
B: σ'^{precon}_{vert}	D: K_0=0.55$OCR^{0.6}$	F: s_u (prescribed)	H: $\tau_{initial}$ from E

Figure 10.2: Stress situation in the soil profile used in the Class A calculation. As a result of the failure criteria employed, the empirical relation for K_0 had to be adjusted.

10.4.2 Class B calculations

The clay behaviour is described by the constitutive relations given by the *MIT-S1* formulation. A preconsolidation pressure in accordance with the results presented in Chapter 6 was used in these calculations while the hydraulic situation was the one evaluated in this work. These values, in combination with the limitations described in Chapter 10.3, meant that the most likely stress situation could not be used in the overall soil profile. The main effect of this simplification is presented in G_{max} which can be seen in Figure 10.3, where black lines represent the desired and the red ones are the used ones. Green lines represent Swedish empirical relations for s_u that are dependent on the stress situation, w_L and OCR. The grey field indicates the s_u^{PS} range used in the calculation, which is dependent on the stress path.

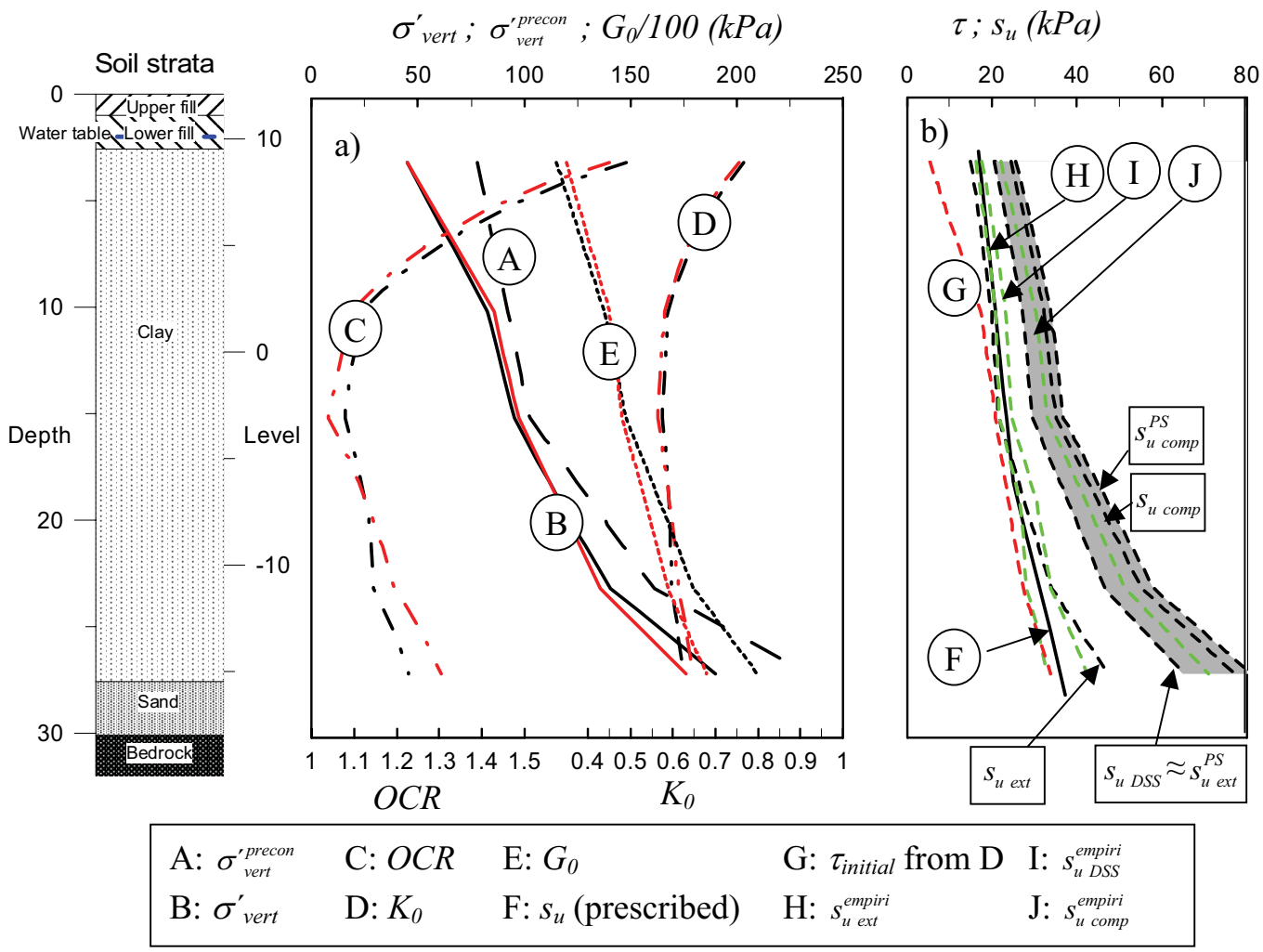

Figure 10.3: Stress situation and shear strength in the Class B calculations.
a) Stress situation in the soil profile (black is the target value and red the obtained value)
b) Undrained shear strength in the profile (dashed black line indicates the outcome of MIT-S1, dashed green line indicates empirical values, dashed red line denotes initial mobilized shear stress, while the solid black line represents the undrained shear strength given by the Swedish Road Administration). The grey area represents the s_u used in the calculations.

G is dependent on the stress history and gradually decreases in line with the "length" along the same stress path. If the stress path vector is changed, the initial response will be stiff again. Although this behaviour is well reported in the litterateur, the stiffness is also depending on the amount of changes in the direction of the stress path. Atkinson et al. (1990) compiled several different laboratory tests showing that the initial shear modulus reaches its maximum value for stress rotations of 180 degrees. A study of the tangential stiffness when unloading from the *LCC*-line in section 1/430 north revealed that it is the same as that presented in Figure 10.4a. The *MIT-S1* model yields a high initial shear modulus, where stress path changes of +90, 180 or 270 degrees do not lead to any differences. Figure 10.4 shows the initial value within the soil profile for different load directions. Note that the stiffness in Figure 10.4b is a function of

the *OCR* value. The -3 level has the lowest *OCR* value and therefore the amount of degradation of *G* in this area is less than in the rest of the profile.

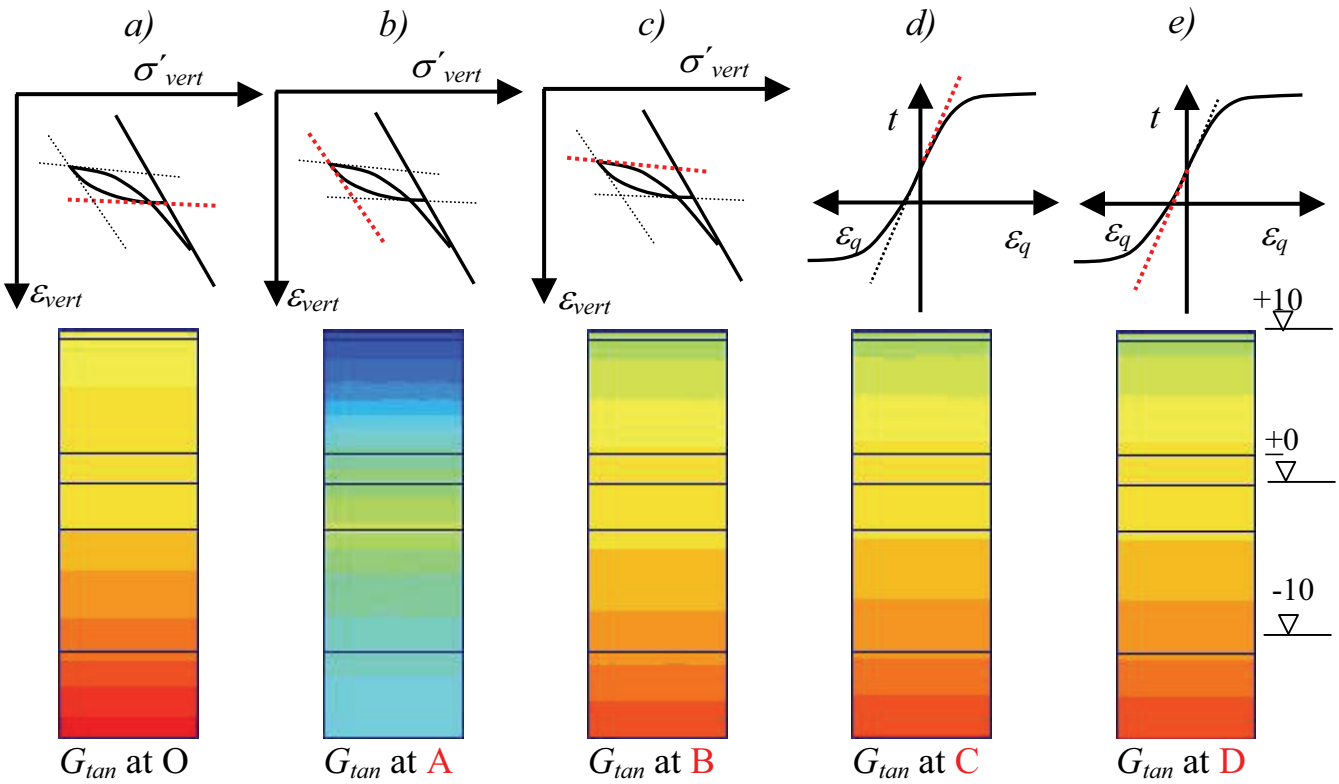

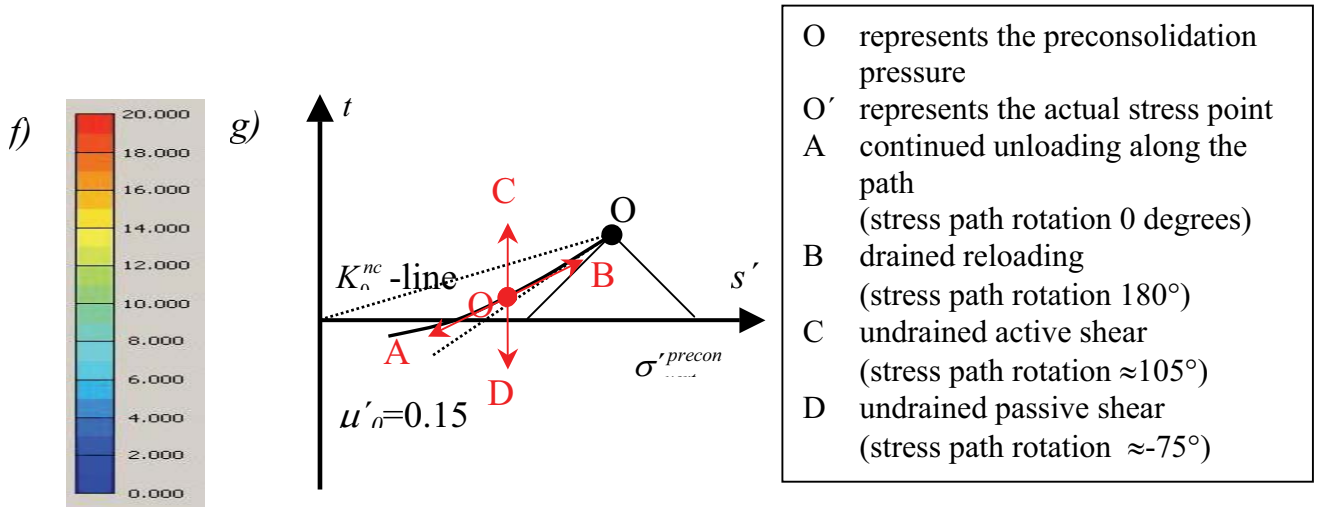

Figure 10.4: Stress path-dependent shear modulus
a) Initial shear modulus, 1D (drained) unloading from O to O′.
b) Shear modulus, 1D (drained) unloading from O′ to A. (strain 10^{-5})
c) Shear modulus, 1D (drained) loading from O′ to B. (strain 10^{-5})
d) Shear modulus, undrained loading from O′ to C. (strain 10^{-5})
e) Shear modulus, undrained loading from O′ to D. (strain 10^{-5})
f) Legend for G_{tan}. (MPa) g) Sketch of different stress paths

During the excavation the shear modulus changed gradually. This is presented in Figure 10.5 for some excavation stages. As can be seen, *G* decreases during excavation.

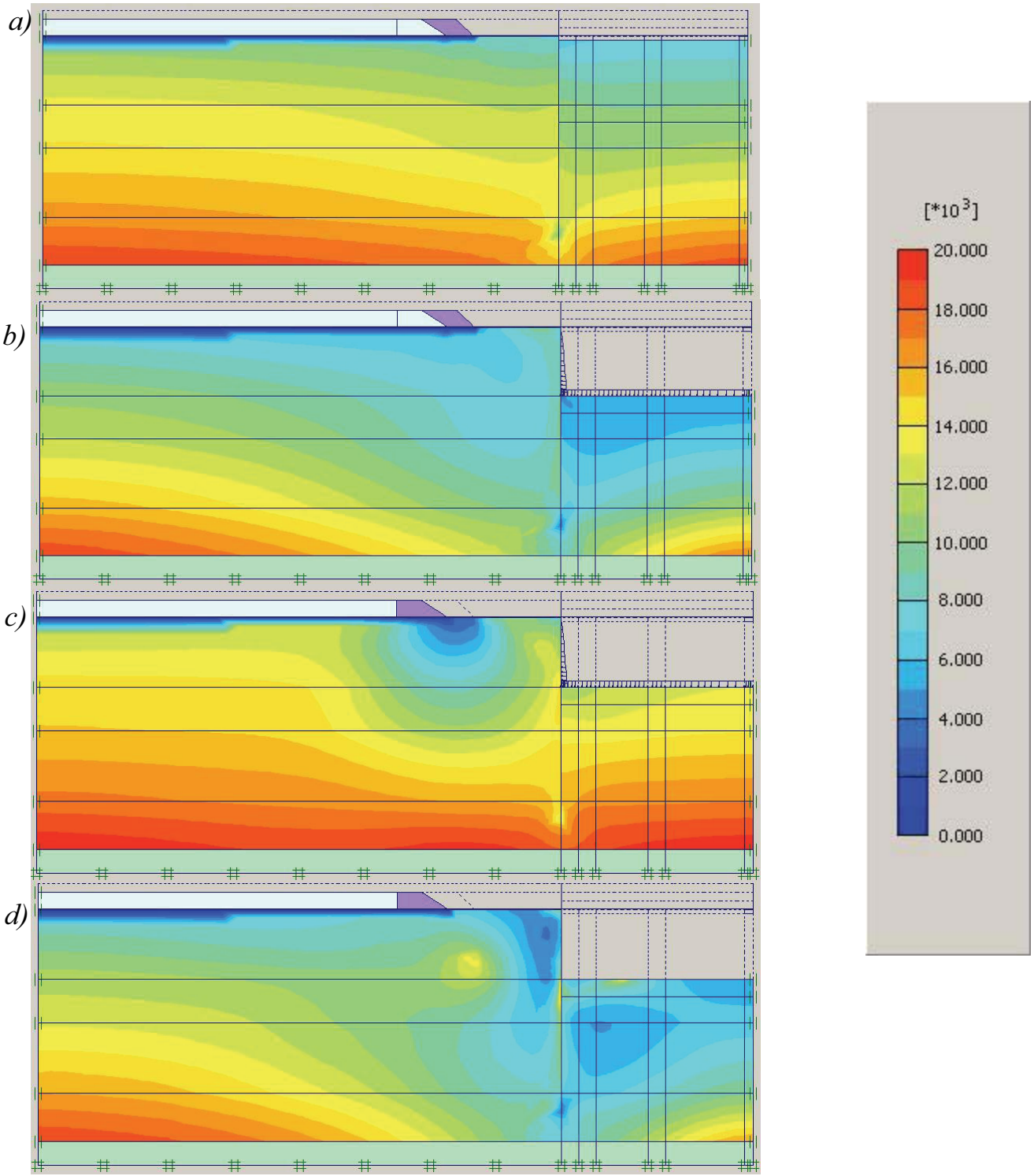

Figure 10.5: Shear modulus at the end of three excavation stages.
a) After unloading to +9.5 within the pit, before piling.
b) After the underwater excavation
c) After an increase of unloading excavation on the retained side
d) After dewatering the pit

Figure 10.5b and c makes it clear that increased unloading excavation outside the pit results in an increase in the shear modulus in some areas and a decrease in others.

10.5 Calculated vs. monitored deformations and earth pressure in section 1/430 north

The results of the Class A and B calculations as well as the monitored deformation and lateral earth pressures for different work stages are presented in Figure 10.6 to Figure 10.8. The black curves represent the monitored deformations/pressures, green curves indicate the results of the Class A and red curves of the Class B calculations.

During the initial work sequences, the deformation pattern as well as the active pressure behind the wall appeared to show a fairly good agreement with both calculations, with the exception of the fact that the observed heave due to the unloading excavation seemed to have been underestimated. The reason for this is probably that the calculated heave was constrained by undrained conditions. When unloading an area, several studies, (e.g. Persson, 2004) have shown that the dissipation of excess pore water pressure due to 1D unloading takes less than a month, with increased heave as a consequence compared with the undrained response. In this case the unloading excavation and the piling were finished within a couple of months.

The deformation pattern of the excavation and dewatering stages within the pit exhibit good agreement with the monitored deformation except for the fact that the Class A calculation had larger horizontal deformations compared to Class B.

The lateral earth pressure, σ_h, is presented in Figure 10.8 and both calculations show excellent agreement with the monitored pressures. The *FE*-calculations do not include hydrostatic pressure as a minimum pressure against the wall as is often the case in classic design and Swedish practice (Ryner *et al.*, 1996). The total earth pressure can even be negative.

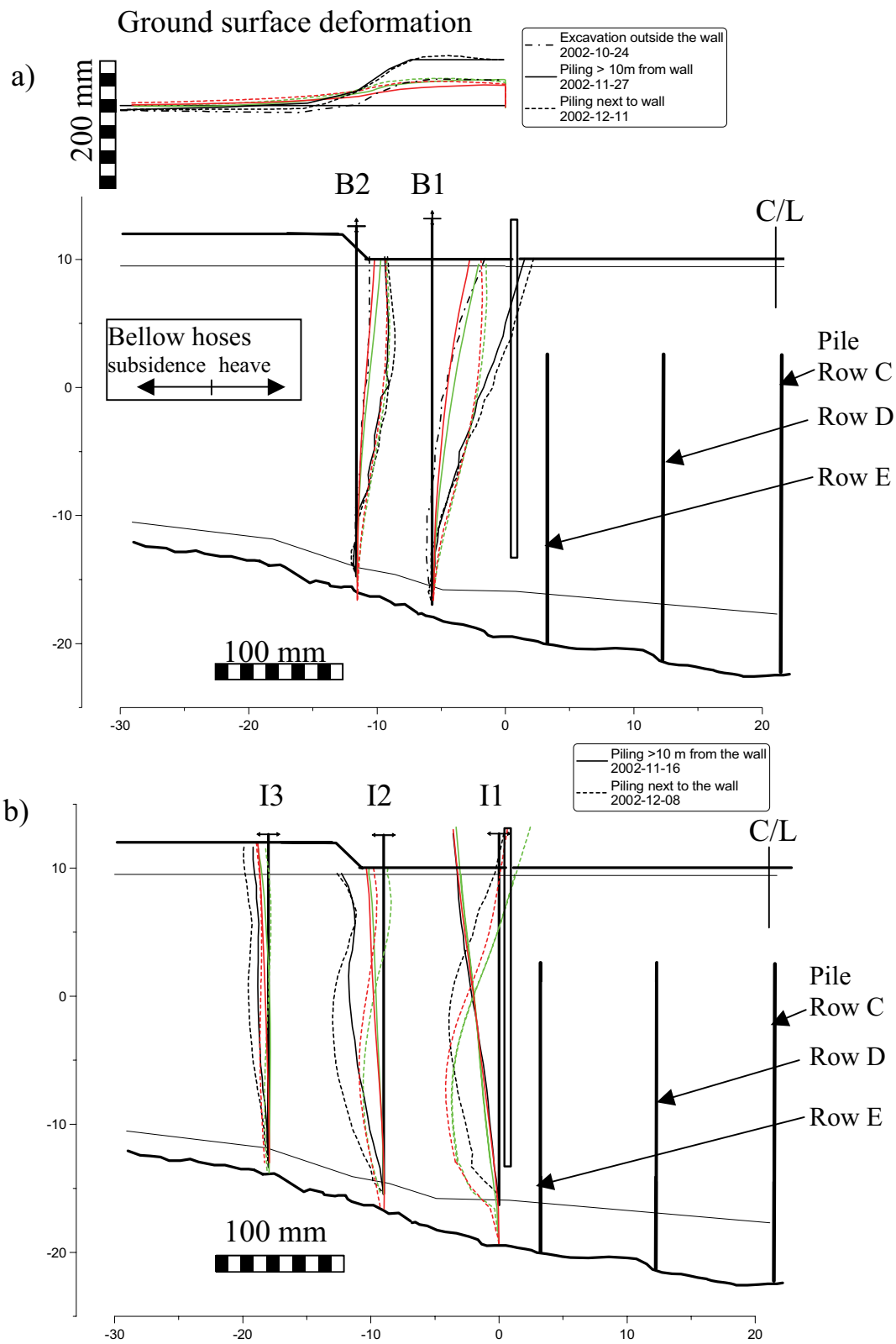

Figure 10.6: Comparison between calculated and monitored deformation, due to piling.
a) Vertical deformations b) Horizontal deformations
Black curves: monitored deformations
Green curves: Class A calculations
Red curves: Class B calculations

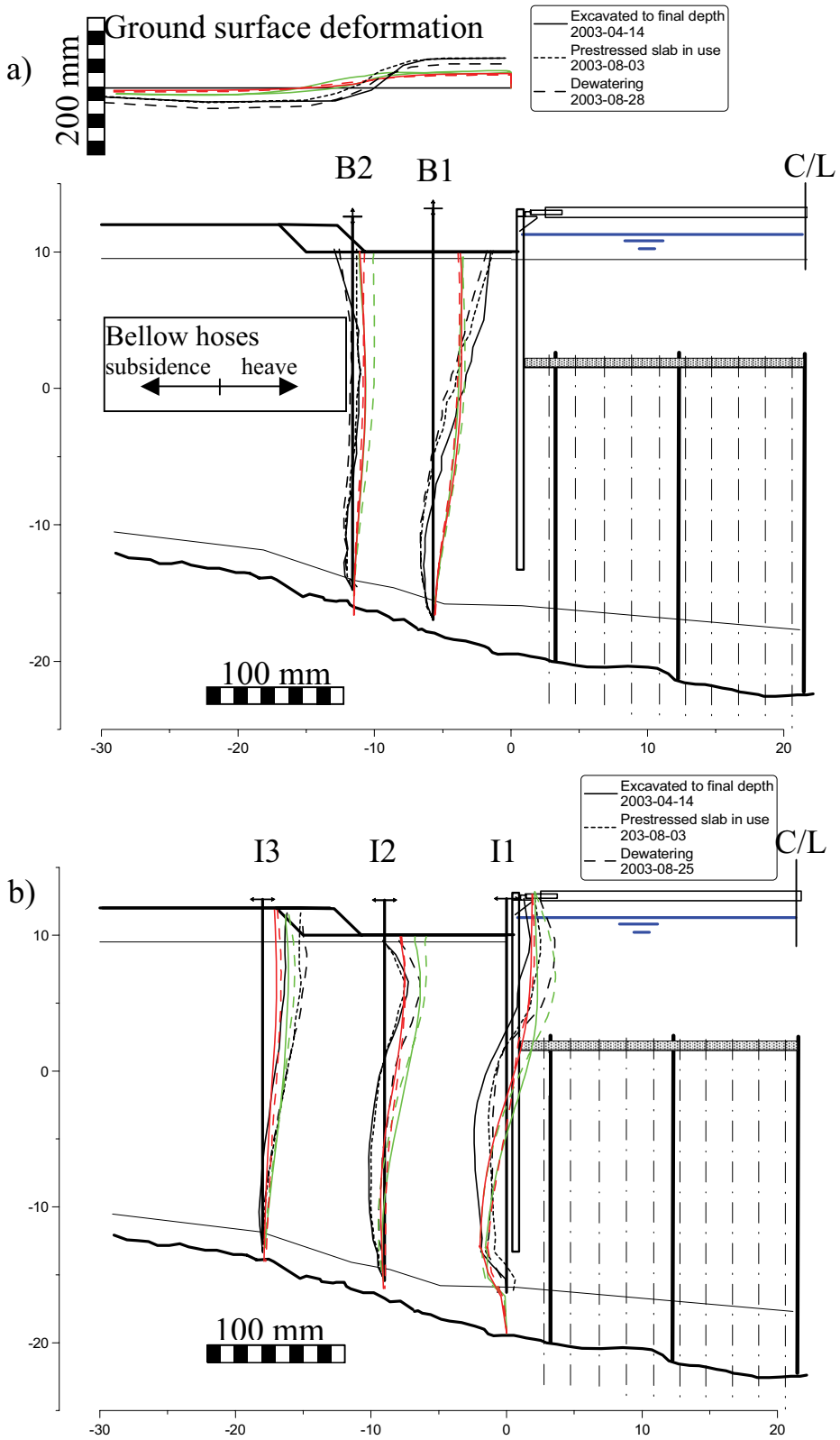

Figure 10.7: Comparison between calculated and monitored deformation, due to excavation and dewatering within the area enclosed by the sheet pile wall.
a) Vertical deformations b) Horizontal deformations
Black curves: monitored deformations
Green curves: Class A calculations
Red curves: Class B calculations

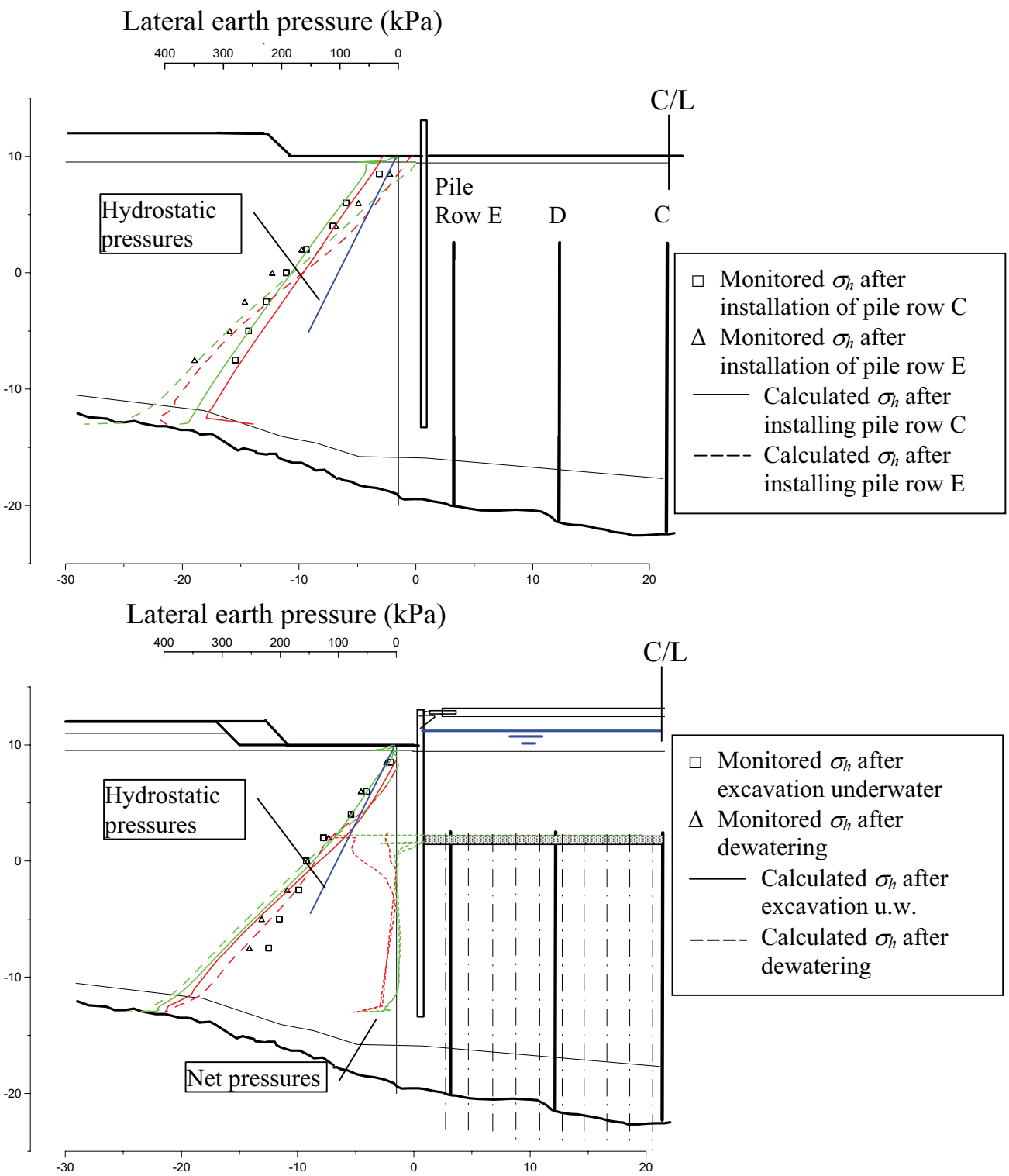

Figure 10.8: Comparison between monitored and calculated σ_h.
a) Lateral pressure due to piling
b) Lateral pressure due to excavation
Black curves: monitored deformations
Green curves: Class A calculations
Red curves: Class B calculations

As previously discussed, the method for simulating the soil displacement due to piling can be questioned, therefore results from calculations that do not include the piles are presented in Figure 10.9and Figure 10.10. It is obvious that the predicted Class A deformations are more than twice the magnitude of the Class B calculation. The shear stiffness used in calculation A is approximately 5 MPa at the top of the clay layer and 10 MPa at the bottom. The corresponding tangent stiffness in/ the Class B calculation is presented in Figure 10.5, which makes it clear why the Class A calculation exhibits larger deformations than Class B.

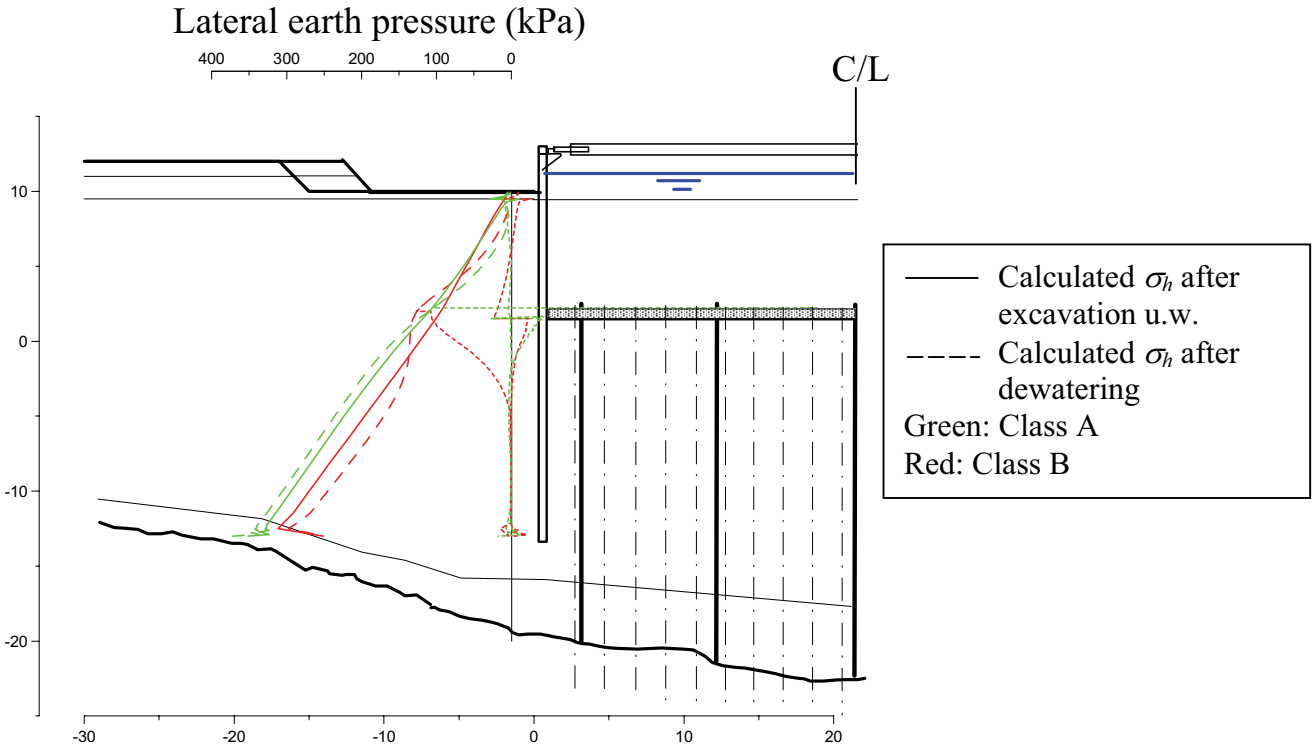

Figure 10.9: Calculated σ_h. Piling effects have been excluded
Green curves: Class A calculations
Red curves: Class B calculations

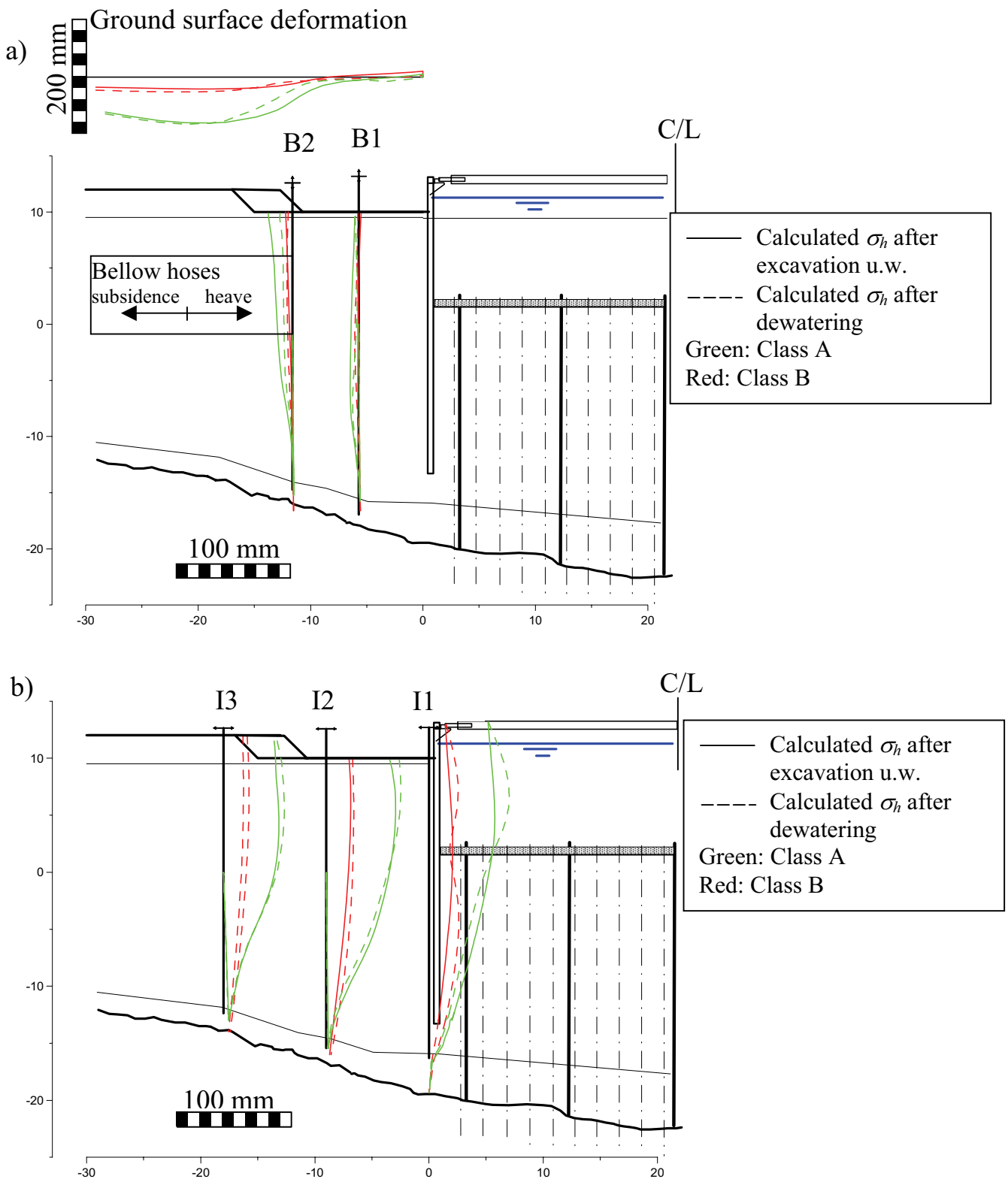

Figure 10.10: Calculated deformation due to excavation and dewatering within the area enclosed by the sheet pile wall. Piling effects have been excluded
a) Vertical deformations b) Horizontal deformations
Green curves: Class A calculations
Red curves: Class B calculations

10.6 Section 1/470 south, class A

The contract between the Swedish Road Administration and the contractor pertaining to section 1/470 south contained the following design parameters, see Table 10.4.

According to the contract, the following properties were to be expected in the soil profile: The *OCR* was described as being 1.2. The density of the clay in the area should be 15.5 kN/m^3 in the upper part, increasing to 17.0 kN/m^3 in the lower part. The liquid limit in the clay should vary between 70 and 60 % with the higher values in the upper partl of the clay. The hydraulic situation in this location was estimated to be hydrostatic with a ground water table at a depth of 2.5 metres.

Table 10.4 Parameters stated in the J2 contract pertaining to section 1/470 south

Soil layer	Depth	$\gamma_{dry}/\gamma_{wet}$ [kN/m^3]	s_u [kPa]	ϕ'/c' [º/kPa]	M_0 [kPa]	M_L [kPa]
Upper Fill	0-1	20/23	-	30º/0	-	-
Lower Fill	1-3.0	18/18	-	30º/0.1·s_u	-	-
Clay 1	3.0-19	-/15.5+0.1·(z-2.5)	15.5+0.833·(z-3)	30º/0.1·s_u	250·s_u	850
Frict layer	19-21	18/20	-	34º/0	-	-

The undrained shear strength, in Table 10.4 is based on field vane and fall cone tests and the values have been adjusted on account of the limited number of tests. These two methods are correlated empirically to the s_u obtained in a DSS-test. A limited number of CPT-tests were also performed at the site. The shear strength and stress history, in combination with the empirical relations of the ratio between σ'_{hor} and σ'_{vert}, indicate that the strength mobilization should be in excess of 100% before any engineering work is started at the site. However, this scenario is not plausible, as anisotropic effects will increase the strength by 30%-50% if no rotation of the principal stresses occurs. Due to the fact that no verified constitutive model capable of describing the anisotropic behaviour was available, the contractor decided to work with a *PLEP* model that used the Tresca failure criteria where s_u was in accordance with the contract. In order to avoid the difficulties associated with full shear strength mobilization, the ratio K_0 was increased in a way that guaranteed a degree of strength mobilization of less than one, f<1. The proposed and the used stress situations are presented in Figure 10.11.

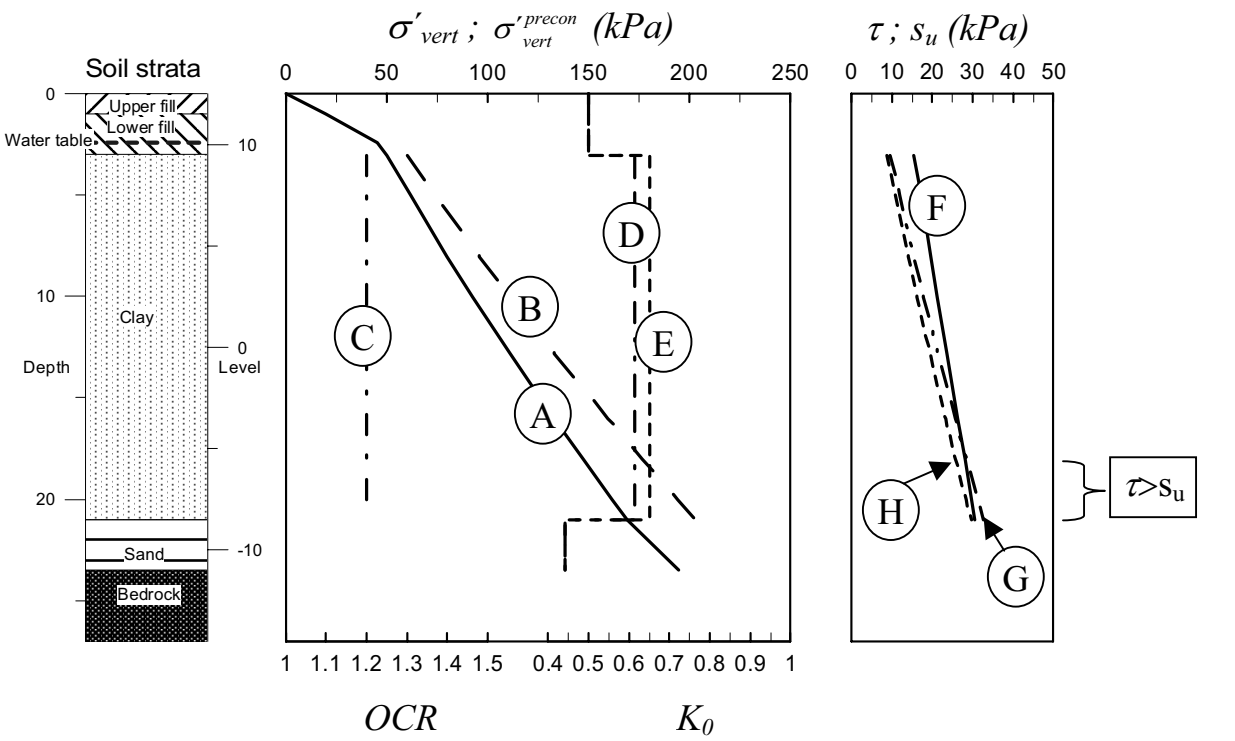

A: σ'_{vert}	C: OCR	E: K_0=0.65	G: $\tau_{initial}$ from D
B: σ'^{precon}_{vert}	D: K_0=0.55$OCR^{0.6}$	F: s_u (prescribed)	H: $\tau_{initial}$ from E

Figure 10.11: Stress situation in the soil profile used in the Class A calculation. According to the failure criteria employed, the empirical relation for K_0 had to be adjusted.

The above is a conservative way of dealing with the numerical problem, provided the increase in K_0 is modest. As a rule of thumb, f should be at least 0.7 to ensure conservative results, even in cases where the problem is dominated by an active zone without stress rotation. This way of handling the problem also had a practical advantage in that the amount of anisotropy did not have to be verified.

10.7 Section 1/470 south, class B

The clay behaviour is described by the constitutive relations derived from the *MIT-S1* formulation and with a stress situation such as that presented in Figure 10.12. In Figure 10.12a, the black curves represent the stress situation in the field, while the red curves represent the model. The grey field in Figure 10.12b compares the s_u used in the calculation with the stipulated s_u and the empirical relations for s_u. When compared with Figure 10.11, it can be seen that the initial mobilized shear stress is lower than in the Class A calculation. The reason for this is that σ'^{precon}_{vert} was found to be somewhat higher than that given by the Swedish Road Administration.

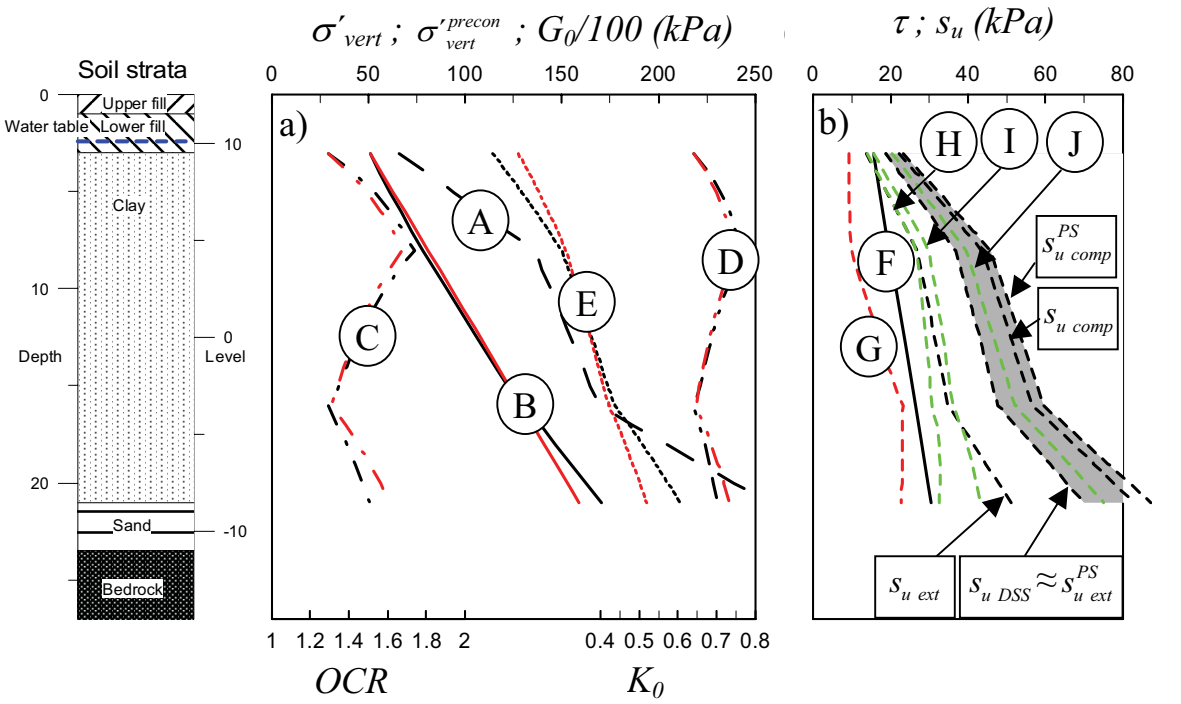

A: σ'^{precon}_{vert}	C: OCR	E: G_0	G: $\tau_{initial}$ from D	I: $s^{empiri}_{u\ DSS}$
B: σ'_{vert}	D: K	F: s_u (prescribed)	H: $s^{empiri}_{u\ ext}$	J: $s^{empiri}_{u\ comp}$

Figure 10.12: Stress situation and shear strength in the Class B calculations.
a) Stress situation in the soil profile (black represents the target while red denotes the value obtained)
b) Undrained shear strength in the profile (the dashed black lines indicate the outcome of the MIT-S1, dashed green lines represent empirical values, dashed red lines the initial mobilized shear stress and solid black lines the undrained shear strength laid down by the Swedish Road Administration). The grey area represents the s_u used in the calculations.

In order to verify the shear modulus output data obtained from the initial calculation phase, is presented in Figure 10.13a, which demonstrates that the numerical calculation results agree with the analytical calculation presented in Figure 10.12. The mobilized shear stress situation, obtained from the calculations with *MIT-S1* model, when simulating the stress history is presented for $\sigma'_{vert} = \sigma'^{precon}_{vert}$ and $\sigma'_{vert} = \sigma'^{insitu}_{vert}$, see Figure 10.13b and c.

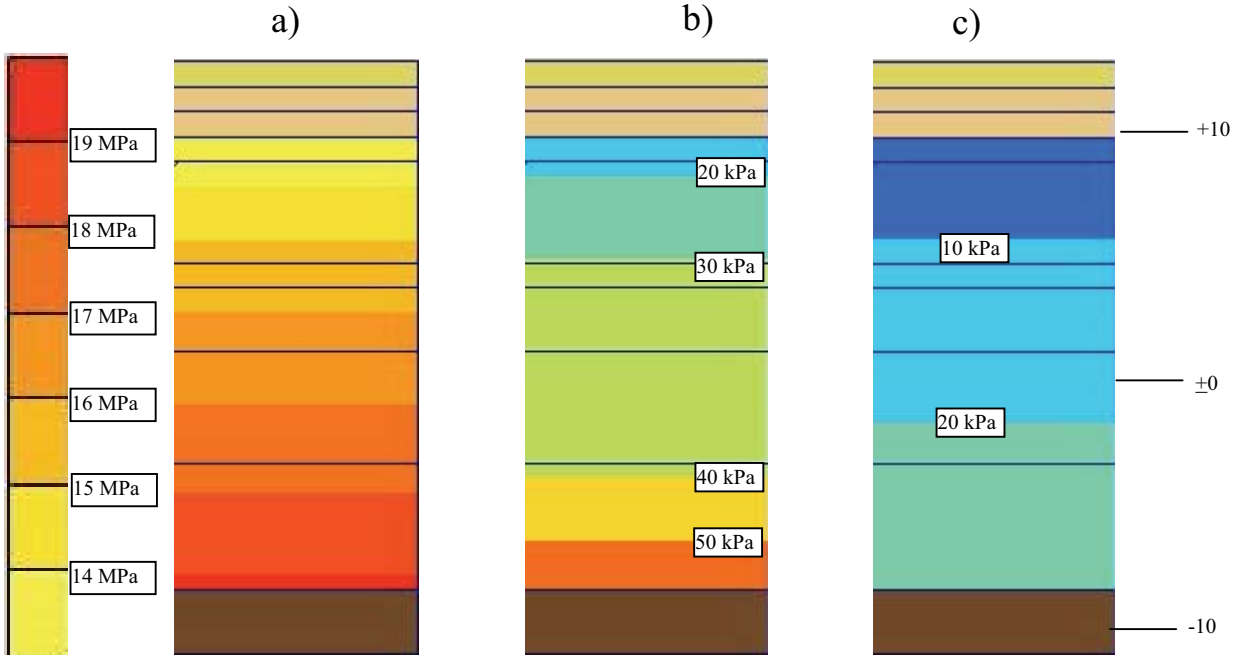

Figure 10.13: Visualisation of the initial shear modulus, G, and the shear stress mobilized after the generation of preconsolidation pressure and unloading to in situ stresses.
a) Initial shear modulus before the start of excavation
b) Mobilized shear stress when $\sigma'_{vert} = \sigma'^{precon}_{vert}$, $K_0^{nc} = 0.55$
c) Mobilized shear stress when $\sigma'_{vert} = \sigma'^{insitu}_{vert}$

In order to visualize the effect of changes in the stress path direction, the actual *G* (tangent value) used is presented for some of the calculation steps. Figure 10.14 illustrates how *G* changed during the excavation and prestressing of anchor row 2. It is clear that the stiffness decreased during the excavation and increased when the anchor was prestressed. During the excavation the stress situation is changed. When stress rotation is neglected, the invariant s_1 will indicate of the amount of shear stress mobilization. Assuming that s_2 and s_3 are small compared with s_1, the mobilized shear stress can be expressed by *t* ($s_1 \cdot \sqrt{6}/4 = t$). Figure 10.15 presents the change in *t* during the excavation of anchor row 2. It is obvious that the soil is approaching active failure behind the wall, although, compared with Figure 10.12b, the mobilized strength is less than 60% of the s_u behind the wall as well as within the excavated area.

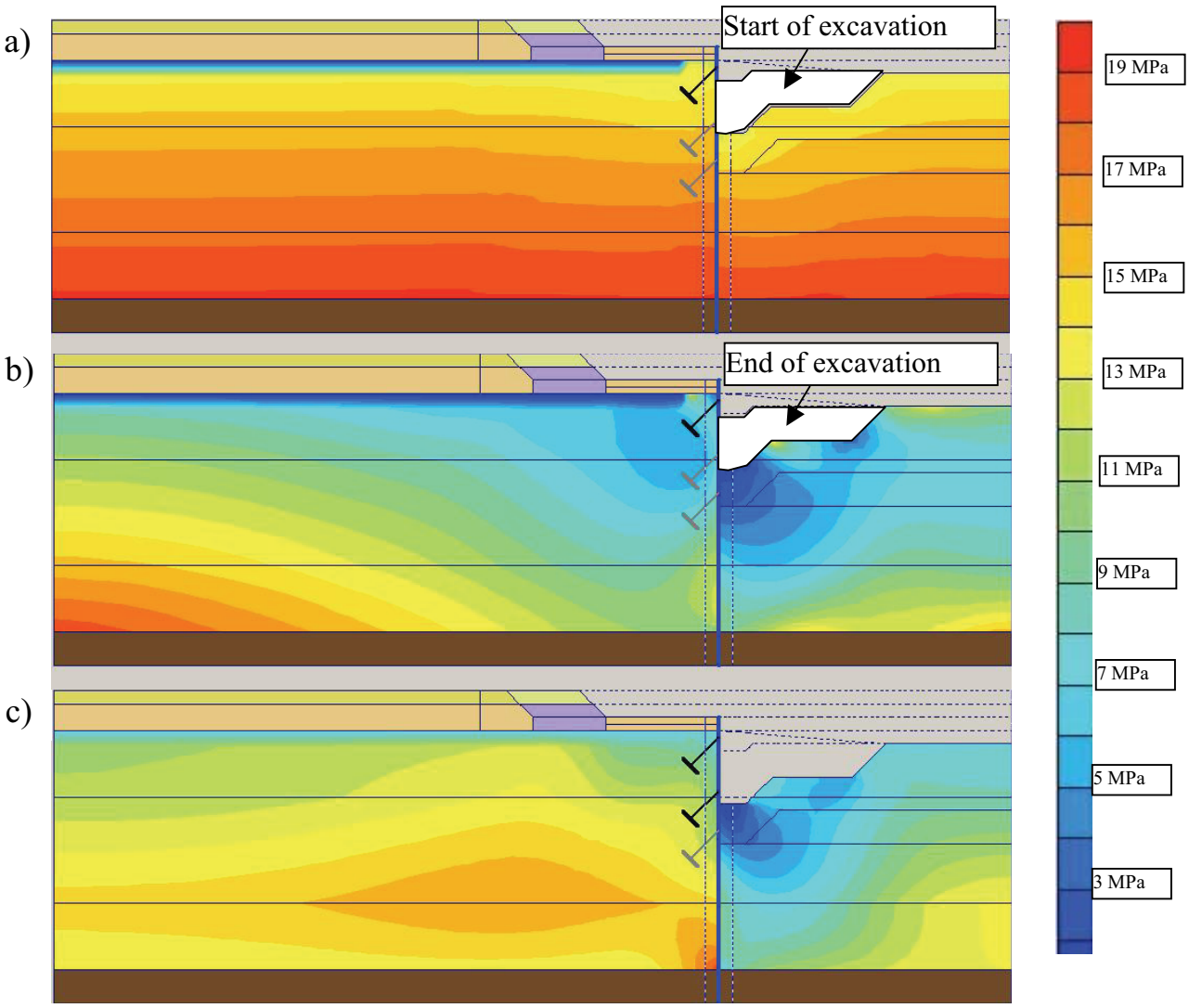

Figure 10.14: Illustration of how G changed during the excavation and prestressing of anchor row 2
a) Initial G during excavation for anchor row 2
b) G at the end of the excavation stage for anchor row 2
c) Initial G when anchor row 2 was prestressed

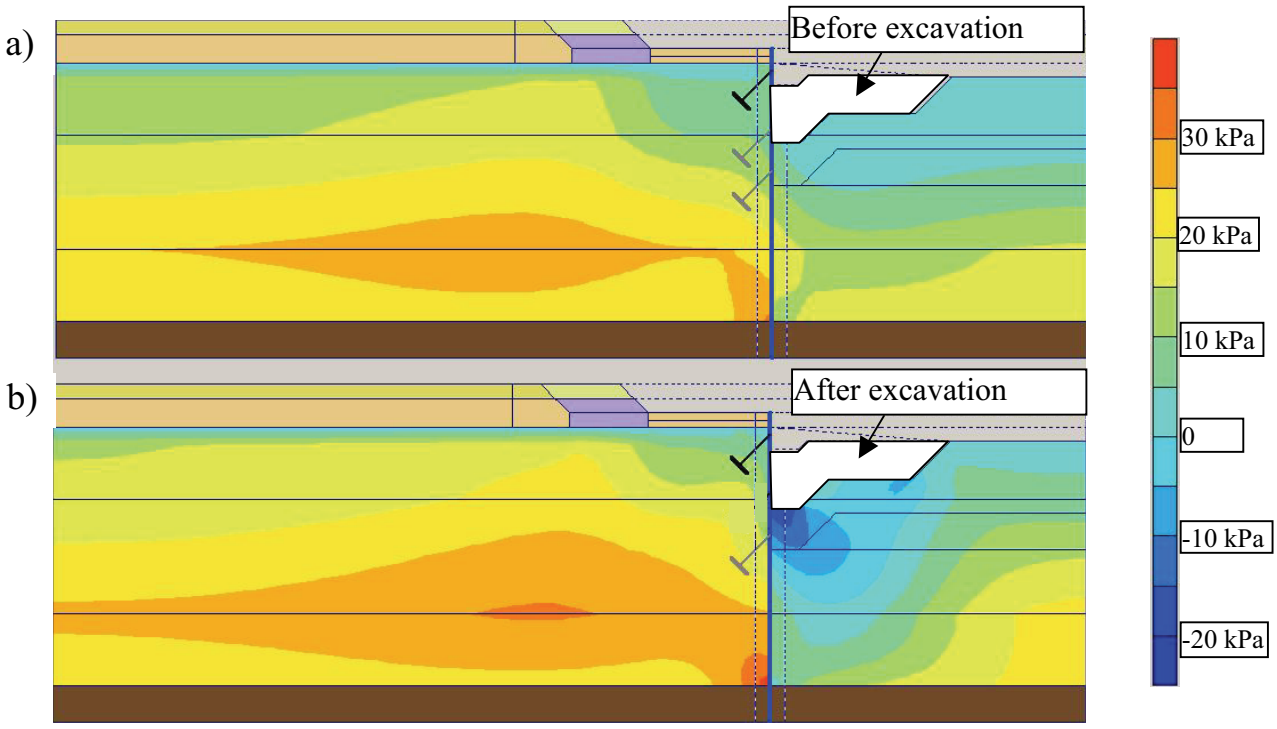

Figure 10.15: Change in t during the excavation for anchor row 2.
a) Mobilized shear stress, t, before the excavation for anchor row 2
b) Mobilized shear stress, t, after the excavation for anchor row 2. It should be noted that anchor row 2 had not yet been installed.

10.8 Calculated vs. monitored deformations and earth pressure in section 1/470 south

The results of the Class A and B calculations are presented in Figure 10.16 to Figure 10.18. Black curves represent the monitored deformations/pressures, green curves the results of Class A and red curves Class B calculations.

From the comparison between the results of class A and B calculations, it is obvious that the first calculation greatly overestimated the monitored deformation. It is important to bear in mind that the monitored vertical deformation is to a great extent caused by volume loss in the underlying sand layer due to the installation of anchors. Neither calculation A nor B models this phenomenon.

The agreement between monitored deformation and the result of the second calculation is excellent.

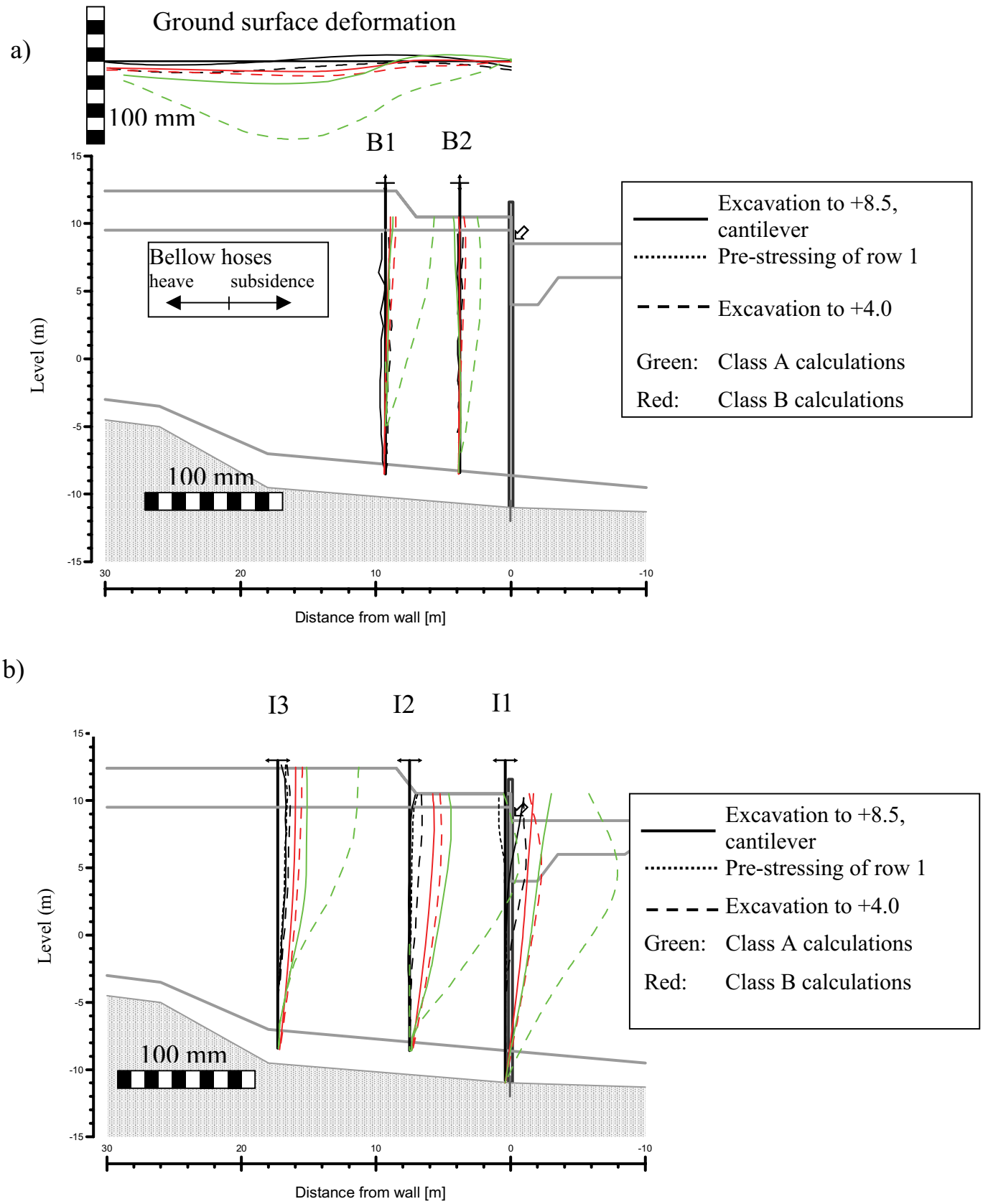

Figure 10.16: Comparison between calculated and monitored deformations caused by the first stages of the excavation
a) Vertical deformations b) Horizontal deformations
Green curves: Class A predictions
Red curves: Class B predictions

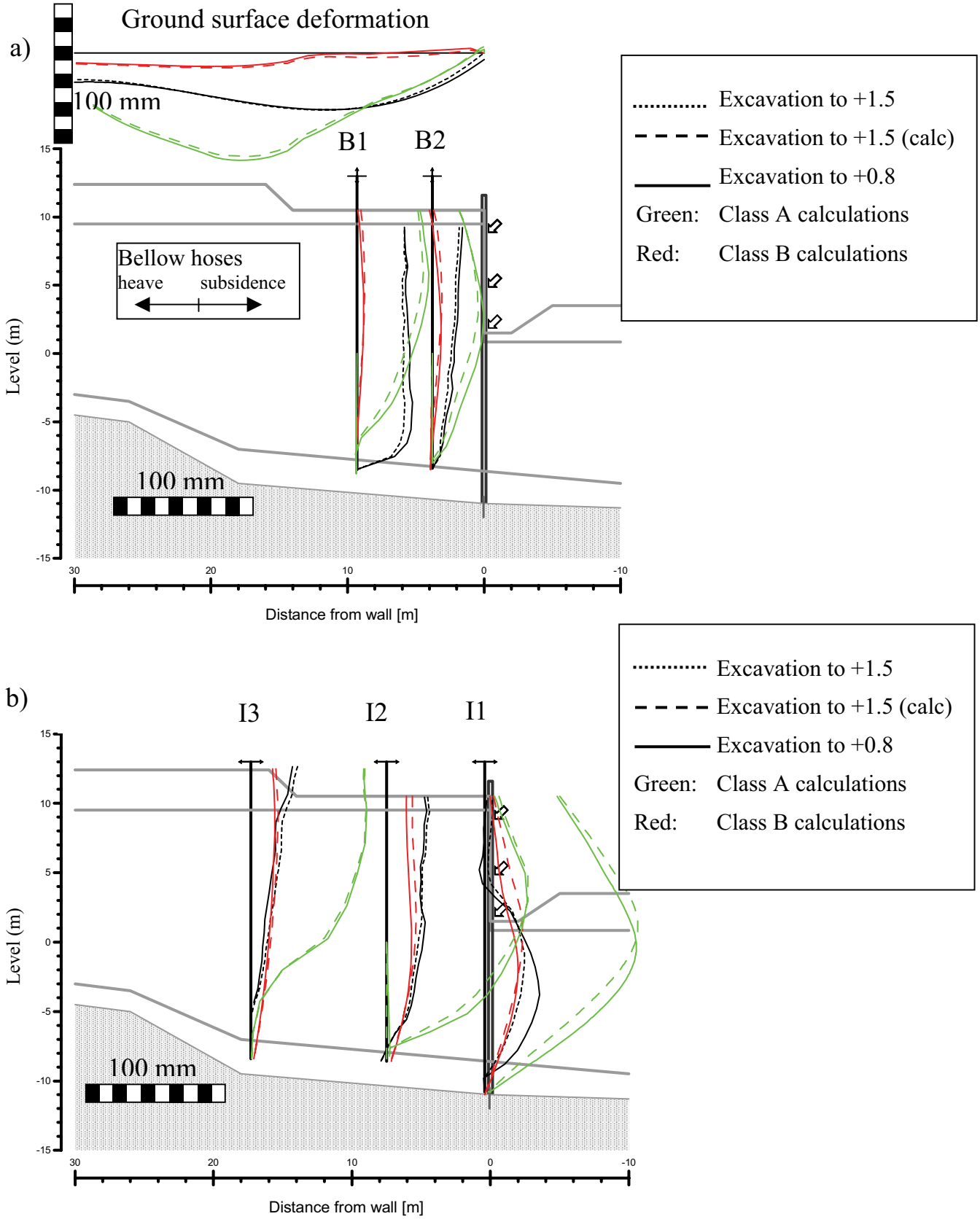

Figure 10.17: Comparison between calculated and monitored deformations caused by the first stages of the excavation
a) Vertical deformations b) Horizontal deformations
Green curves: Class A predictions
Red curves: Class B predictions

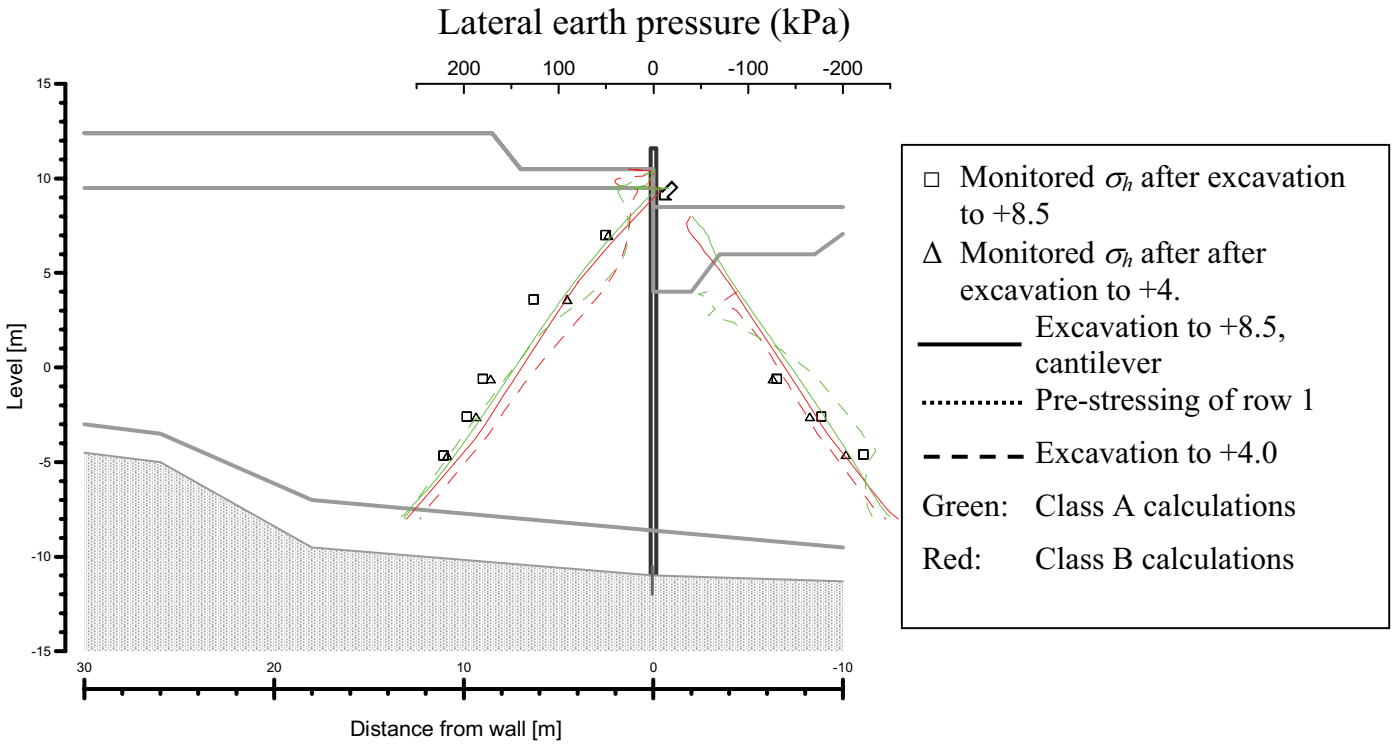

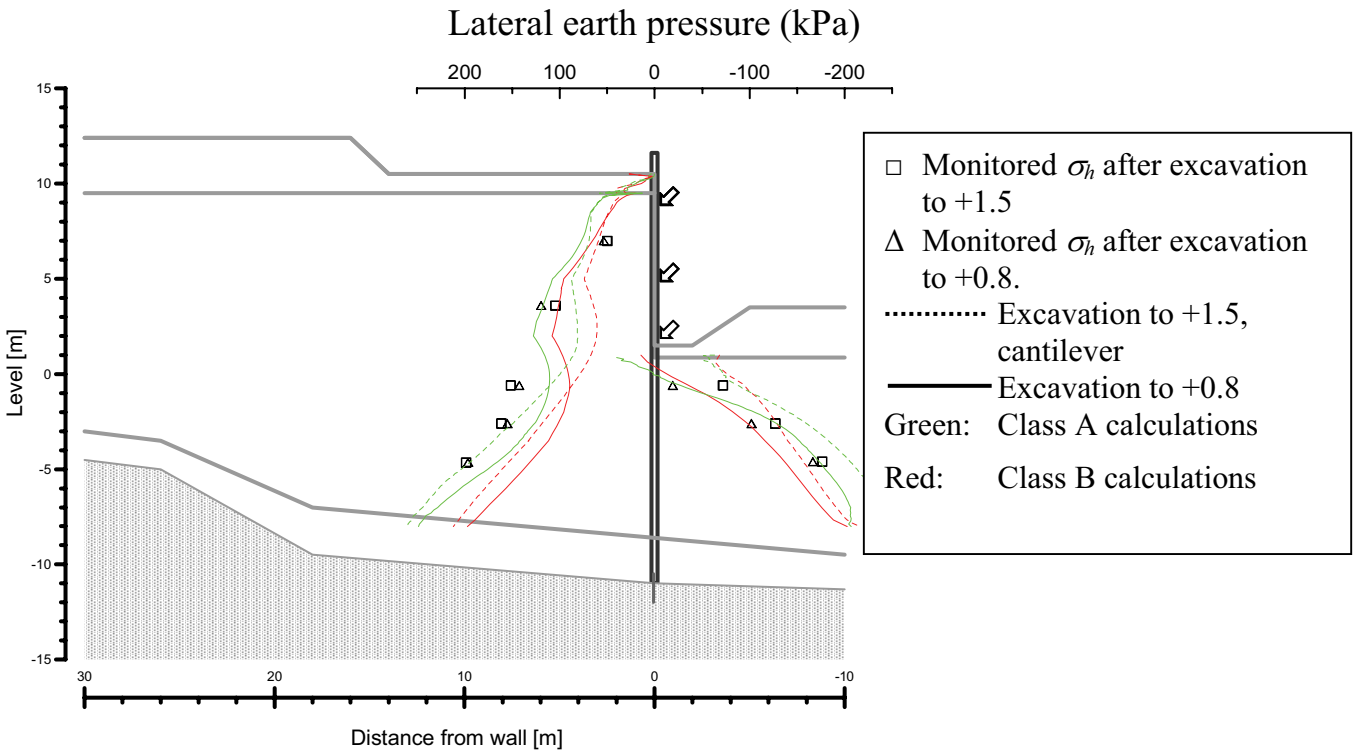

Comparison between monitored and calculated σ_h.
Green curves: Class A calculations
Red curves: Class B calculations

The calculated earth pressure shows excellent agreement with the monitored earth pressure, especially on the passive side.

10.9 Brief comparison between calculated forces on the retaining system

In this section the calculated forces in the support structures and within the area of the wall are compared with each other as well as with the monitored forces in the strut located in section 1/430 north, and in the anchors placed in section 1/470 south. Please note that this situation has nothing whatsoever to do with design, since the values were obtained without any factors of safety. The calculations presented herein were made after the installation of the *SPW*.

The reactions and bending moment in section 1/430 north are listed in Table 10.5. As can be seen, the calculated force in the strut differs by a factor of 4 from the lower value of the calculation using *MIT-S1*. However, none of the calculations yielded the monitored value in the strut. The shape of the wall, see Figure 10.7, confirms the high value that was monitored in the strut. As can be seen in Figure 10.8b and Figure 10.9, none of the calculations take the hydrostatic water pressure as a minimum lateral pressure. The values in brackets are from the calculation where no effort was made to simulate the soil movements caused by piling. Although these values seem to be more trustworthy, they are still too low compared with the monitored strut force.

Table 10.5: Comparison of calculated and monitored reactions in the support system from two different calculations and from field measurements in section 1/430 north

	Class A calculation		Class B calculation		Monitored forces
Working stage	Maximum bending moment (kN/m)	Strut load (kN)	Maximum bending moment (kN/m)	Strut load (kN)	Strut load (kN)
Piling completed	119		125		
Under water excavation	96 (82)		74 (74)		
Dewatering	255 (247)	371 (394)	252 (278)	82 (365)	600

As can be seen in the compilation of the reaction in section 1/470 south, all reactions are lower in Class B compared to Class A calculations. The agreement between the forces monitored in the anchors and those obtained by means of the class B calculation is excellent, although bearing in mind the result presented in Figure 10.18, true bending moments in the wall could be expected to be slightly higher than those derived from class B calculation.

As can be seen in Table 10.6, the agreement between the Class B calculation and the monitored anchor forces was far better than that obtained in the Class A calculation. The sudden increase in anchor force on 2003-01-03 has been discussed previously and shown to be caused by something other than excavation work within the pit. When using *MIT-S1*, the results show less variation in the anchor forces than when employing the *PLEP-MC* model. If this holds true for other excavations with a different soil profile and geometry, there will be an economic reason for using the *MIT-S1* model instead of the *PLEP-MC* model. The degree of utilization will be higher in subsequent excavation stages. If the anchor forces show better agreement in calculation B, the true bending moment within the *SPW* will probably be closer to the result obtained in the Class B calculation. This leads to a reduction of approximately 50% in the required sectional modulus, *W*, within the *SPW*. Decreasing the stiffness of the wall will, of course, change not only the stress distribution against the wall but also the bending moments.

Table 10.6: Compilation of calculated and monitored reactions in the support system from two different calculations and from field measurments in section 1/470 south.

	Class A calculation				Class B calculation				Monitored forces			
Working stage	M_{max}	Anchor force			M_{max}	Anchor force			Anchor force			Date
		Row 1	Row 2	Row 3		Row 1	Row 2	Row 3	Row 1	Row 2	Row 3	
Excavation for row 1	49	-	-	-	14	-	-	-				
Prestressing of row 1	51	1000			70	1000			1000			2002-11-20
Excavation for row 2	342	**1505**			172	**1090**			1194 1330			2003-01-02 2003-01-03
Prestressing of row 2	307	1321	1125		144	979	1125		1118	1125		2003-01-09
Excavation for row 3	**489**	1431	**1482**		**208**	969	**1193**		1129	1030		2003-09-10
Prestressing of row 3	440	1356	1304	1150	178	917	1070	1150	1115	970	1150	2003-09-12
Final excavation	488	1375	1363	**1281**	204	923	1089	**1187**	1077	1001	1100	2003-11-03

301

11 CONCLUSIONS AND PRACTICAL ASPECTS

11.1 Overall conclusion

There is a large empirical base in the literature, in addition to local knowledge of how different geological areas are affected by excavation, which should be used in the early stages of a design process

Soil mechanical issues are characterised by complex interaction between loads, deformation and utilized shear strength. Excavations within a retaining support system are probably among the most complex, as the interaction between the soil and structure as well as the interplay of internal forces and deformation in the retaining system has to be taken into account. In the classic design process where only the ultimate limit state is studied, the unknown factors are limited to load and the shear strength employed. Nevertheless, several failure mechanisms require study. In the case of deep excavations, it is more important to study the true behaviour of the support system and how the excavation work may affect adjacent constructions. Calculation in the serviceability limit state increases the number of unknown parameters since the deformation has to be incorporated into the design. At present, the *FE*-method has proved invaluable. However, it demands deep understanding of soil mechanics pertaining to true soil behaviour, mathematical modelling of the observed phenomena and simplification of reality in a conceptual model.

Detailed *FE*-modelling is, however, not sufficient. Close collaboration between the geotechnical consultant and the contractor is necessary in order to ensure a reliable construction that behaves in an acceptable manner. Monitoring, continuous follow up and comparison between monitored and calculated behaviour are essential and offer the possibility to make adjustments in the design if necessary.

The constitutive *MIT-S1* model has been found to be very powerful for describing almost all rate independent behaviours observed both in the field and in the laboratory. The model has been evaluated and compared with the behaviour of Gothenburg clay. This parameter set has thereafter been verified against the empirical knowledge of the clay behaviour when it comes to undrained shearing, unloading and reloading and the agreement was found to be excellent.

11.2 Crucial aspects in soil behaviour

It has been shown that soil behaviour is very complex and that models capable of reproducing this behaviour on a laboratory scale also predict the behaviour

adjacent to a deep excavation better than less complex models. Some crucial aspects of soil behaviour are listed below.

The predictions of a model capable of reproducing the non-linear response in shear loading have been found to be more trustworthy than those of models that do not take this behaviour into account.

The ability to reproduce the proper initial stresses is of the utmost importance. In many cases, consideration of anisotropic behaviour is necessary in order to model the actual stress situation otherwise the *FE*-calculation may start with a shear strength mobilization ratio that is too high.

The non-linear response during unloading may be important depending on the amount of unloading, cf. the differences between the *MIT-S1* model and the *e-ADP* model. In the case of the *e-ADP* model, some sort of kinematic hardening function would have been preferable.

The hysteretic behaviour observed as a permanent deformation caused by a closed unloading reloading cycle may be important when the stress path changes direction more than ones, e.g. a retaining system with prestressed anchors.

The small strain behaviour is very important when predicting deformations and can be modelled by some sort of kinematic hardening function or by degradation in the shear modulus along a specific stress path, as in the *MIT-S1* model. Small strain behaviour should be able to reproduce different initial shear moduli depending on the amount of change in the stress path direction.

In order to study time effects, it is vital to have a model capable of reproducing shear induced excess pore water pressure in combination with an algorithm capable of allowing dissipation of excess pore water pressures.

Rate dependent shear strength is not the most important factor when an excavation is studied. If for some reason the loading is fast, e.g. anchor or strut failure, the higher strength will be capable of distributing the increase in load, but only for a short time. The eventual failure will temporarily slow down and result in a reduction of strength, thus rendering the soil incapable of distributing the load, which may lead to progressive failure.

Two-dimensional effects increase the undrained shear strength compared to the result of the triaxial test, as has been shown by several authors over the years.

11.2.1 Laboratory study

The *SHANSEP* concept is suitable for evaluating the stress path during 1D unloading and thus the proper consolidation procedure can be used for the different shear tests. The *SHANSEP* concept may result in the loss of some information, due to destructuring of the sample when preconsolidation pressure is exceeded. However, a combination of 1D tests performed with unloading after more than 10% compression and tests unloaded from stresses slightly below the preconsolidation pressure will verify the accuracy of *SHANSEP*.

1D tests are commonly used for establishing the stress history and studying the uniformity within the soil layer, e.g. the creation of sub layers. However, the 1D test result should be presented as void ratio vs. effective stress in order to evaluate the sub layers and the *SHANSEP* outcome.

1D CRS tests provide the true stress response for stresses higher than σ'_L. Below this point the stress path does not fully follow that in the field for the same boundary conditions. The stress history of the deposits as well as for subsequent unloading, reloading and/or creep is not reconstructed in the standard CRS test.

It has been shown that *NSP*, the normalized soil parameter concept, provides a very good prediction of the shear strength profile. A modification of the ordinary *NSP* concept was introduced by Pestana (1994) for the shear modulus. This modification normalized the modulus against the inverse of the porosity divided by the mean stress to the power of 1/3. The technique has shown good agreement with the clay at Järntorget, but if it is to be applied to all sites, the commonly used relation between s_u and G requires modification.

The method proposed by Ladd *et al.* (1977) used to connect the s_u for different *OCR*s has been shown to produce realistic results. From the analysis using the outcome of test simulation with the constitutive *MIT-S1* model, a slightly different expression was found that somewhat better describes the degradation in s_u normalized against σ'^{precon}_{vert} with an increased *OCR*.

Triaxial tests have proved invaluable when it comes to understanding the behaviour of an 1D compression test with unloading and reloading cycles.

The *DSS* test provides valuable information about the shear modulus. However, the obtained strength values τ^{peak}_{hor} and τ^{res}_{hor} do not represent the true value of $s_{u\,DSS}$, as they are slightly smaller and provide results on the safe side.

Some special CRS tests were performed in order to minimize the effect of creep when the sample was unloaded. Such tests may provide the same information as

the ordinary stepwise oedometer test, but in a different form. However, more research is needed in order to establish whether or not creep behaviour can be predicted by this test.

It has been shown that the s_u estimated from field vanes and fall cone tests almost consistently yields lower values than those obtained from CK_0DSS-tests.

The need to account for anisotropy is important, thus a design incorporating the initial stress situation is necessary.

Idealized stress paths have been presented in order to deepen the knowledge among geotechnical engineers. The outcome of different types of laboratory test performed in the triaxial cell has been presented as well as the value of using these tests. Depending on the conceptual model studied, the need of more advanced laboratory tests than the CRS tests may be needed

11.3 Capability of different soil modelling approaches

Different constitutive models used for describing soil behaviour will often provide somewhat different results. Three different approaches were used and evaluated. The ability of the *e-ADP* and the *MIT-S1* models compared to the more commonly used *PLEP-MC* model is summarized below. However, some brief comments about the perfect linear elasto-plastic model will be provided. These simple models are truly linear elastic until the failure criterion is fulfilled. Plastic deformation occurs when the stresses coincide with the criterion, but can be controlled in such at way that it can simulate dilatation or contraction.

11.3.1 Failure criterion

A three-dimensional approach with a different failure criterion than Mohr-Coulomb yields a higher undrained shear strength than that obtained from triaxial testing, with the exception of the case when two principal stresses are equal. The size of the increase depends on the stress path and boundary condition. The Drucker-Prager failure criterion that defines a symmetrical cone in the principal stress space is another commonly used method, which, however, does not describe the observed behaviour in the soil any better than the Mohr-Coulomb failure criterion. Several different failure criteria have been proposed in the literature. Those proposed by Lade (1975) and by Matsouka and Nakai (1974) have proved both realistic when it comes to describing soil behaviour and mathematically easy to handle.

11.3.2 Short comments of the *MIT-S1* model

The *MIT-S1* soil model uses the Matsuoka and Nakai (1974) failure criterion, which has the ability to model the effect of the intermediate principal stress as

well as shear induced excess pore water pressure and small strain behaviour. It can model almost all known behaviour observed in soil, with the sole exception of rate dependency behaviour. Therefore, it is currently one of the most effective models for simulating excavations.

11.3.3 Short comments of the *e-ADP* model

The *e-ADP* model is very simple to use and all parameters are easy to evaluate, although it requires triaxial testing or preferably plane strain compression tests and extension tests. This constitutive model can only describe total stress changes and not development of excess pore water pressure, which makes it unsuitable for drained situations. Another shortcoming compared to the *MIT-S1* model is that the soil strata have to be divided into sub layers in order to model the different behaviours that occur when the *OCR* differs in the profile. It is defined similar to the empirical relations used in Sweden, the only difference being that the s_u is normalized against σ'_{vert} and not σ'^{precon}_{vert}. The model is capable of describing anisotropic behaviour, which in many cases is needed to accurately describe the soil behaviour. The anisotropic behaviour is generated by applying a simple Tresca failure criterion as a function of the rotation of the principal stresses. The model is also capable of describing the non-linear response during first time shear and capturing the stiff unloading reloading behaviour. However, the model uses an isotropic hardening function with a constant stiffness in the elastic region, which makes it unsuitable for modelling large unloading and reloading changes. Introducing a kinematic hardening function would increase the accuracy when modelling unloading reloading problems.

11.4 Empirical methods

Some of the empirical methods applied to the idealized excavations have been presented, of which the *KJHH* method appears to provide the most likely distribution for deep excavations. This, in combination with an *FE*-calculation, may produce relatively accurate ground surface settlement distributions. Three-dimensional effects can be taken into account in order to produce predictions for the entire area adjacent to an excavation.

11.5 Deformation pattern adjacent to an temporary excavation in soft clay

Several empirical and semi-empirical methods for describing ground surface settlements have been reviewed and compared. Some of these methods also indicate the magnitude of the wall deflection. However, they provide limited information about the deformation within the soil mass. When such information is important, numerical analysis is necessary.

11.5.1 Ground surface settlements

Ground surface settlements monitored at different sites generally exhibit two types of profile: sprandrel and concave. Sprandrel mainly occurs when the top of the retaining wall has limited support and the retained soil is non-cohesive.

When simulating a shallow and a deep excavation in cohesive soil, the settlement profile mainly depends on the factor of safety against basal heave, the location of the top support and the friction between the wall and the soil mass.

A low factor of safety against basal heave increases the settlements. When combined with a rough wall surface, the maximum settlements occur at a distance from the wall defined as half the width of the excavation. In earlier stages when the factor of safety against basal heave is sufficient, the maximum settlements tend to appear at a distance equal to the excavation depth.

The location of the top support is the dominant factor for the development of settlements close to the wall. In cases when the factor of safety against basal heave is sufficient, the settlements are mainly controlled by the inward bulging of the retaining wall.

The roughness of the wall will affect the settlement profile, which is dependent on the vertical movement of the wall relative to the vertical movements within the soil mass. For a braced wall, high roughness contributes to the development of a concave ground surface settlement profile. A retaining system consisting of e.g. backward anchoring with a vertical downward component in combination with insufficient vertical stability and high roughness will create a sprandrel shaped settlement profile.

The absolute value of the true roughness is, in most cases, unknown in the design situation, thus it is recommended to vary it within the possible range. Introducing roughness in the calculation may generate slender and shorter walls when the vertical stability is sufficient but, on the other hand, if that is not the case, introducing roughness will have the opposite effect. The use of numerical tools such as the *FE*-method makes it possible to study these effects.

The field monitoring at the Göta tunnel revealed that the main vertical settlements in the monitored sections were primarily caused by engineering work other than excavation, for example the installation of anchors undermined the clay layer while installation of piles caused a ground surface uplift.

11.5.2 Wall deflection

A wall deflection is required when performing deep excavations where the equilibrium is dependent on additional mobilization of the shear strength within the soil on the retained side (decreased lateral pressure from in situ values to active pressure). In order to avoid deformation, an infinite stiff support system is necessary. However, a stiff diaphragm wall heavily braced and fixed below the excavation grade will keep this deformation to a minimum. It should be noted that the installation of such walls also generates some disturbance.

In the literature the support system stiffness, $EI/\gamma_w h_{avg}^4$, and the flexibility number, $EI/\ h_{avg}^5$, are often used in the design on the assumption that the same values of these relations will generate the same wall deflection. This may be the case if
1) all combinations of the anchors and/or struts exhibit the same overall force–deformation relation (e.g. a narrower distance between the rows requires a softer response from each support).
2) the cantilever deformation is the same when the first support level is installed.
3) the factor of safety against basal heave is the same[18].
4) the horizontal deformation below the excavation grade is the same.
Although these requirements are rarely fulfilled, the support system stiffness or flexibility number may be very useful when comparing different retaining wall systems in the early design stages.

When comparing the three different ways of describing clay behaviour, it has been stated that the *MIT-S1* model predicted less deformation than the other two. As can be seen from the case study, the results obtained using the *MIT-S1* model are superior to those from the *PLEP-MC* model, even when quite high stiffness was applied to the clay. When using the *e-ADP* model, the predicted inward deformation is approximately the same as when using the *PLEP-MC* model, assuming strains of a magnitude of 0.1% in the clay.

11.5.3 Developed strain

Strain must develop in order to mobilize the strength in the soil. The soil stiffness will decrease in line with increasing strain, making it crucial to have a stress or strain dependent stiffness when modelling excavation problems. However, if a constant stiffness is used when modelling an excavation, the calculation must be performed with adequate stiffness in relation to the amount of strain. From Figure 9.22 it is obvious that the strain levels are between 0.1% and 0.5% in the retained soil and 0.5% to 1.0% under the excavation grade.

[18] The stability number is affected by the wall stiffness up to a critical value (Ukritchon, B. *et al.*, 2003)

A soil model incapable of accurately describing small strain effects will increase the strain level under the excavation grade. From Figure 10.1 it is clear that the strain levels exceed those assumed within the pit while, on the other hand, the strain levels fall below those assumed in the retained soil. Accurate assumptions of the oedometer modulus using the *PLEP-MC* model would have been $1000s_{u\,DSS}$ in the retained soil and $100s_{u\,DSS}$ within the upper part of the soil below the excavation grade. However, these values are not constant during the excavation sequence and can therefore not be presented as true values for an excavation problem modelled by means of a *PLEP-MC* model.

11.6 Earth pressure

The field measurements reveal that reasonably reliable lateral earth pressures have been monitored on the retained side of the wall as well as within the excavation area. It has been stated that consolidation effects have to be taken into account when different engineering activities overlap. It has also been found that stiff supports such as struts, slabs and prestressed anchors increase lateral earth pressure compared with the active lateral earth pressure according to Rankine. In deep excavations carried out in several stages, it is very important to include the deformation pattern in the prediction of lateral earth pressures.

The numerical back calculation shows that the difference between the *MIT-S1* model and the *PLEP-MC* model is a smaller lateral earth pressure when using the former due to the incorporation of anisotropic strength behaviour. However, no increase in accuracy compared to monitored lateral earth pressure was observed. In fact, the simpler calculation had slightly better agreement. If all engineering activities and workmanship could have been incorporated into the numerical modelling, the agreement would have been better with the *MIT-S1* than with the simpler models. When the monitored support forces were compared with the calculated ones, the more advanced calculation using the *MIT-S1* model showed far better agreement than the simpler calculation performed with the *PLEP-MC* model.

The idealized excavation performed with the three different constitutive relations, *PLEP-MC*, *e-ADP* and *MIT-S1* makes the effect of incorporating anisotropic strength and different stiffness in unloading and reloading quite clear. The introduction of anisotropic strength reduces the active lateral pressure, while the introduction of various moduli for different types of loading greatly affects the lateral pressure when the wall is pressed against the retained side.

11.7 Appropriate requirements and restrictions on deformations

In many projects unrealistic and/or uneconomical restrictions are placed on wall deformation values. In most cases these restrictions are intended to limit

deformations in adjacent constructions. The reason for restricting wall deformation instead of e.g. ground surface deformation is that wall deformation is generally easier to monitor. However, more effort should be placed on estimating the permissible vertical and horizontal deformation as well as inclinations in each adjacent building.

11.7.1 Wall in need of embedment support

A retaining wall in need of embedment support is mainly used in deep deposits of soft soil. The embedment support is based on the fact that the lateral earth pressure inside the wall exceeds the lateral earth pressure on the retained side. This requires deformations inwards the pit, which may vary in line with the embedment length and strength of the soil etc. In the idealized sections, it can be seen that a wall deformation of at least 0.5% of the excavation depth is needed to obtain equilibrium. This calculated ground surface settlement is somewhat less then the horizontal wall deformation, 0.3%. Depending on the factor of safety it may even increase. According to the empirical base, the maximum ground surface settlement will be somewhat smaller than the maximum lateral wall deflection when the upper part of the wall is well supported (concave settlement profile) and up to 50% larger when the upper part of the wall has limited support (sprandrel settlement profile). When a concave settlement profile is assumed, the maximum settlement is expected to occur at a distance of 50-75% of the excavation depth. At distances greater than twice the excavation depth, the settlements are less than 10 % of the maximum settlement. At a distance of four times the excavation depth, the settlement caused by the excavation is negligible.

11.7.2 Walls supported, not only by earth pressure, below the excavation grade

Retaining walls supported below the excavation grade can be designed in a way that limits the soil deformation to almost zero. However, this requires a very stiff wall and rigid support system. The embedment support can take the form of installation of the wall in the bedrock, cross walls or reinforced slabs installed between the retaining walls (Eide *et al.*, 1972; Wunsch, 2003; Magnus *et al.*, 2005). However, installation of a support system below the final excavation grade will affect the surroundings, which effects have to be compared with the increased deformation that occurs if the support is dependent on the mobilization of the shear strength within the soil. An underground support system always involves some uncertainties in terms of its function, and an extensive monitoring program is usually required. It is important to remember that the strength mobilization deformation is only one component of the effects on the environment adjacent to an excavation.

11.8 Short guidelines for the use of *FE*-calculations in the study of deep excavations

One of the main purposes of this project was to increase the understanding of how to use numerical tools when designing retaining systems for deep excavations in soft soils. However, at this stage it was not possible to present a complete manual for designing retaining walls by means of the *FE*-method. Some short guidelines will be presented here but it should be noted that a design using a numerical tool requires a good knowledge of soil behaviour as well as of soil-structure interaction. The numerical tool should not be treated as a magic box which always produces reliable results. The *FE*-method, with current commercial constitutive models, complements the design process and is a valuable tool for estimating deformations adjacent to an excavation. It is also superior for analysing the reason for damage or non-tolerable deformations as well as invaluable during the construction process when combined with the observational method where it offers the possibility to introduce proper changes into the design.

Good knowledge of soil behaviour, a greater number of more advanced laboratory tests and a high level of empirical knowledge are necessary in order to obtain reliable results from an *FE*-calculation. Soil behaviour relevant to the actual problem must be identified, as most of the available constitutive models have limitations. The necessary laboratory tests can be chosen on the basis of the relevant soil behaviour. The drainage situation, whether it is possible to treat the problem as undrained or fully drained or whether the consolidation effect should be taken into account must be known. The stress history has to be studied as well as how adjacent structures may affect the interaction between the soil and the retaining system.

CPT-soundings are a valuable means of investigating the hydraulic condition. These soundings can also be used to decide from which depth samples should be taken.

When establishing the stress history, a CRS-test is the most valuable method. The standard CRS-test will produce a vertical preconsolidation pressure profile and good estimates of the compression behaviour above σ'^{precon}_{vert}. Hydraulic conductivity can also be evaluated from CRS-tests.

The initial stress situation is crucial for advanced numerical simulation involving soil behaviour, especially when the shear strength within the soil is a dominant feature, as in the case of deep excavations. In normal and slightly overconsolidated clays, the mobilized shear strength in situ may exceed the

strength observed in fall cone tests and field vane soundings[19]. This implies that shear strength anisotropy must be taken into account. A simple model that is only capable of reproducing strength, independent of the shear direction, will require some modification of the initial stress state. Such a modification will, however, affect the outcome of the calculations and has to be considered when the results of the simulation are evaluated. The K_0-test is a valuable source of obtaining the accurate stress situation. First, an ordinary 1D-compression test, maintaining a constant diameter, is performed to at least 20% compression. The same properties are derived from this test as from the CRS-test. In addition to these characteristics, K_0^{nc} can be derived as well as the behaviour for stresses below the preconsolidation pressure. Secondly, an unloading K_0-test is performed from a stress situation on the *LCC*. This unloading can be carried out after compression of the first sample, and the results are thereafter scaled in accordance with the *SHANSEP* concept, or on a second sample consolidated to a vertical stress equalling σ'^{precon}_{vert} and a horizontal stress of $K_0^{nc} \cdot \sigma'^{precon}_{vert}$. In order to obtain the relation between horizontal and vertical stress, the unloading is performed to the same *OCR* as in the field. In the numerical simulation, the stress situation and preconsolidation pressure have to be modelled somewhat differently, depending on the constitutive model used. In a situation where the *OCR* is constant throughout the soil profile, the stress generation is fairly straightforward. If the *OCR* varies in the clay layer and the soil model used is incapable of reproducing the change in μ′ through the unloading, the clay layers must be subdivided. In such cases the relation presented in Figure 8.20 can be used.

After generation of the proper initial conditions, the different stress paths expected around the excavation have to be identified. In a typical temporary excavation in low permeable clay, three different shearing zones can be expected; one active zone on the retained side of the soil, one exposed to direct shear and one passive zone under the excavation grade. In normally consolidated or slightly overconsolidated clay, these three zones will be able to withstand different amounts of shear. Therefore, a soil model capable of reproducing this behaviour is recommended, as otherwise care has to be taken when choosing the proper soil strength.

Accounting for anisotropic shear strength will increase the factor of safety compared with using only the shear strength obtained from field vane tests, fall cone tests or simple direct shear tests. Numerical modelling of an excavation with a simple model that is incapable of reproducing the anisotropic shear strength can, however, be made by assigning different shear strengths to

[19] The estimated s_u from CK_0DSS-tests may even be too low due to one of the shortcomings of the method, $s_u \neq \tau^{max}_{hor}$.

different areas of the soil around the retaining wall. However, it is not possible to provide uniform recommendations about where to use the different strengths, as it depends on the deformation pattern and rotation of the principal stresses, both of which have to be studied in each individual case. The following recommendations service as a general guideline.

- $s_{u\ comp}$ may be used above the excavation grade if the factor of safety against basal heave is sufficient
- $s_{u\ ext}$ should be used within the pit above the foot of the retaining wall
- $s_{u\ DSS}$ is the most representative strength below the excavation grade on the retained side and below the embedding.
- When the factor of safety against basal heave is low, it may be more suitable to assign an undrained shear strength equal to the one obtained from direct simple shear tests in the area where a vertical failure surface may develop.

The areas where different strengths should be assigned change during the excavation sequence in a deep excavation performed in several stages.

11.9 Theoretical behaviour vs. real behaviour

It has been shown that activities which are not included in the conceptual model can have a major influence on the outcome, both in terms of load on the retaining system and in particular on deformations adjacent to the excavation. Changes in the excavation sequence may lead to completely different behaviour than that for which the retaining system was designed. All changes associated with the excavation sequence or different constructional solutions at the site must be checked against the original design and verified by a geotechnical consultant. Poor workmanship can ruin the best design, making it essential to advise every employee of the importance of adhering to the design and prescribed work sequence. For example, a deficiency in the performance of the waling in combination with struts may decrease the stiffness of the props used in the *FE*-design down to 2% (O'Rourke, 1981).

In cases when calculations made by means of rough constitutive models, such as linear elastic or *PLEP* models, show better agreement with the observed behaviour compared to calculations made with advanced models e.g. the *MIT-S1* model there is probably at least two errors in the calculation. Poor workmanship, carelessness, and/or non-modelled activities generate larger deformations than necessary. The deformation predictions made with a model that is incapable of simulating small-strain stiffness and shear strength anisotropy exceed those made by a model that takes such phenomena into account. This can mean that back-calculations made without knowledge of the true working sequence/activities and level of workmanship may reproduce smaller deformations with an advanced soil model compared to the monitored ones,

while back-calculations with a simpler model show better agreement with the measurements.

11.10 Practical outcome

Use of the *FE*-method will probably increase in the future and models capable of reproducing anisotropic behaviour and small strain stiffness will hopefully be available in commercial programs. This work has highlighted the need for these models as well as the potential economic benefit of using them in the design process. The deep excavation simulated with the *MIT-S1* model yielded a more economical design compared to the others, as well as predicting less deformation. More comparative calculations are required to establish if this is the general case. However, when a model like the *MIT-S1* is used, understanding of the behaviour increases, which in turn improves the sensitivity of the chosen design.

The numerical tools require qualified laboratory tests in order to obtain reliable numerical analysis results. Increased use of the observational method, which is likely when numerical tools become the primary design tool, will require the presence of geotechnical engineers at construction sites

When it comes to field measurements, the possibility of reliably monitoring earth pressures has been presented as well as results from bellow hose measurements and inclinometers at different locations from the wall. The monitoring is very time consuming but necessary when part of the design is based on the observational method. The monitoring program and installation of the devices and gauges should commence prior to the installation of the retaining wall, so that no information is lost.

12 FUTURE RESEARCH

12.1 Numerical analyses

The use of numerical tools will become more common in the design process. The understanding derived from using these tools in full-coupled analyses under transient conditions may be a future research area.

12.2 Constitutive modelling

The accuracy of the *MIT-S1* constitutive model will increase if rate dependency and small strain stiffness dependent on the amount of change in the stress path direction are incorporated. Rate dependency could be incorporated as a visco-elastic part in the model and/or by allowing the boundary surface to expand over time. Small strain stiffness may be addressed by introducing another set of internal state variables bearing in mind the second last stress reversal point. The initial shear modulus could thereafter be calculated as a function dependent on the level of variation in the stress change direction.

The *e-ADP* model has shown good agreement under undrained loading conditions compared to laboratory tests and simulations using the *MIT-S1* model. However, some shortcomings were identified in the unloading reloading situation. The *e-ADP* model is incapable of modelling softening behaviour which may be incorporated in the same manner as in the *ANISOFT* model (Andresen and Jostad, 1999). At present, efforts are being made by the developer of the *e-ADP* model to create a model based on effective stresses. Hopefully this new model will be as user friendly as the *e-ADP* model is today.

12.3 Laboratory testing

Monitoring the time dependent decrease in σ'_{vert} for a constant deformation in the oedometer may be a way of estimating creep behaviour in clay. However, it requires an extensive parallel testing program comprising traditional creep tests exposed to a constant load, as opposed to merely keeping the deformation constant. These tests will probably have to include continuous monitoring of the horizontal as well as the vertical stress and the vertical deformation. It is also recommended to perform them in accordance with the *SHANSEP* concept, with a compression to at least 10-15% before the time effects are studied.

The rate dependency of the parameter K_0^{nc} should be investigated in detail as well as how K_0 changes due to creep.

A large amount of special tests were performed within this work and it would be of great benefit if all phenomena observed therein could be used in the future.

12.4 Field monitoring

Within this work, numerous piezometers were used to identify stress changes in the clay. However, the data have not been analysed in terms of consolidation. These data could be a valuable source of information in the future.

REFERENCES

Aas, G. (1985). "Stability problems in a deep excavation in clay." Publikasjon-Norges Geotekniske Institutt(156): 1-9.

Addenbrooke, T., Potts, D. and Dabee, B. (2000). "Displacement Flexibility Number for Multipropped Retaining Wall Design." Journal of Geotechnical and Geoenvironmental Engineering **126**(8): 718-726.

Alén, C. and Jendeby, L. (1996). Heave caused by unloading - Case study Ullevi (In Swedish). *Proc. of* Nordiska Geoteknikermötet, 12, NGM-96: Interplay between geotechnics and environment, Reykjavik: 353-358.

Altabba, B. and Whittle, A. (2003). "Finite element analysis of the combined effects for adjoining braced excavations." Civil Engineering Practice **18**(1): 5-24.

Al-Tabbaa, A. and Wood, D. (1989). An experimentally based "bubble" model for clay. *Proc. of* International symposium on numerical methods in geomechanics 3, (NUMOG III), Niagara Falls, Canada: 91-99.

Andreasson, B. (1979). Deformation characteristics of soft, high-plastic clay under dynamic loading conditions. Geotechnical department. Chalmers Chalmers University of Technology, Gothenburg: 242 pp.

Andresen, L. and Jostad, H. (1999). Application of an Anisotropic Hardening Model for Undrained Response of Saturated Clay. *Proc. of* Num. Mod. Geomech. – NUMOG VII, Graz: 581-585.

Athanasiu, C. (1999). Proposal for an anisotropic, soft clay model to be incorporated in future developments in Plaxis. *Proc. of* International symposium on beyond 2000 in computational geotechnics. 10 years of PLAXIS international, 1, Amsterdam, A.A. Balkema: 271-280.

Atkinson, J., Richardson, D. and Stallebrass, S. (1990). "Effect of recent stress history on the stiffness of overconsolidated soil." Geotechnique **40**(4): 531-540.

Aye, Z., Karki, D. and Schulz, C. (2006). Ground Movement Prediction and Building Damage Risk-Assessment for the Deep Excavations and Tunneling Works in Bangkok Subsoil. *Proc. of* International Symposium on Underground Excavation and Tunnelling, Bangkok: 281-297.

Becker, D., Crooks, J., Been, K. and Jefferies, M. (1987). "Work as a criterion for determining in situ and yield stresses in clay." Canadian Geotechnical Journal **24**(4): 549-564.

Bell (1915). The lateral pressure and resistance of clay, and the supporting power of clay foundations. A century of soil mechanics. ICE. London: 93-134.

Bengtsson, P.-E. and Sällfors, G. (1996). Geo-group for the Göta tunnel: Proposed method for statistical representation of properties. Contractual document for the Göta tunnel project (In Swedish) 9 pp.

Bjerrum, L. and Aitchison, G. (1973). Problems of soil mechanics and construction on soft clays and structurally unstable soils. *Proc. of* International conference on soil mechanics and foundation engineering, Moscow: 111-190.

Bjerrum, L. and Eide, O. (1956). "Stability of strutted excavations in clay." Geotechnique **6**(1): 32-47.

Bjerrum, L., Eide, O. (1956). "Stability of strutted excavations in clay." Geotechnique **6**(1): 32-47.

Bjerrum, L., Frimann-Clausen, C. and Duncan, J. (1972). "Earth Pressures on Flexible Structures-A State-of-the-Art Report." General Report, 5th ECSMFE, Madrid: 169-196.

Boone, S. (1996). "Ground-Movement-Related Building Damage." Journal of Geotechnical Engineering **122**(11): 886-896.

Borin, D. L. (1989). WALLAP - computer program for stability analysis of retaining walls, GEOSOLVE.

Boscardin, M. and Cording, E. (1989). "Building Response to Excavation-Induced Settlement." Journal of Geotechnical Engineering **115**(1): 1-21.

Bowles, J. (1996). Foundation analysis and design, McGraw-Hill: 1003 pp.

Bozozuk, M. and Fellenius, B. H. (1979). "The bellow-hose settlement gauge." Can. Geotech. J. **16**(1): 233-235.

Brinkgreve, R. and Bakker, H. (1991). "Non-linear finite element analysis of safety factors." Proc. 7th Int. Conf. on Comp. Methods and Advances in Geomechanics, Cairns, Australia: 1117-1122.

Brinkgreve, R. B. J. (2002). PLAXIS, Finite Element Code for Soil and Rock Analyses: 635 pp.

Burland, J. and Wroth, C. (1974). "Allowable and differential settlement of structures, including damage and soil-structure interaction." Settlement of Structures, Proceedings of the Conference of the British Geotechnical Society, Cambridge. Pentech Press, London, UK: 611-764.

Casagrande, A. (1936). The determination of the pre-consolidation load and its practical significance. *Proc. of* 1st Int. Conf. Soil Mechanics and Foundation Engineering, Harvard: 60-64.

Chen, J., Yin, J. and Lee, C. (2004). "Rigid finite element method for upper bound limit analysis of soil slopes subjected to pore water pressure." ASCE. Journal of Engineering Mechanics **130**(8): 886-893.

Chen, W. F. (1975). "Limit analysis and plasticity." Development in Geotechnical Engineering **7**.

Claesson, P. (2003). Long term settlements in soft clays. Department of Geotechnical Engineering. Chalmers University of Technology, Gothenburg: 197 pp.

Clough, G. and Hansen, L. (1981). "Clay Anisotropy and Braced Wall Behavior." Journal of the Geotechnical Engineering Division **107**(7): 893-913.

Clough, G. and O'Rourke, T. (1990). "Construction induced movements of insitu walls. Design and Performance of Earth Retaining Structures." ASCE Geotechnical Special Publication **25**: 439-470.

Coulomb, C. A. (1776). "Essai sur une Application des Regles de Maximis et Minimis a Quelques Problèmes de Statique, Relatifs a l'Architecture." Memoires de Mathematique et de Physique, Présentés, à l'Academie Royale des Sciences **3**(38).

Dafalias, Y. F. and Popov, E. P. (1975). "A model of nonlineary hardening materials for complex loading." Acta Mech **21**: 173-192.

Dellatre, L. (2001). "A century of design methods for retaining walls-The French point of view."

Drucker, D., Gibson, R. and Henkel, D. (1957). "Soil mechanics and work hardening theories of plasticity." Trans. ASCE **122**: 338-346.

Drucker, D. and Prager, W. (1951). Soil Mechanics and Plastic Analysis Or Limit Design, Division of Applied Mathematics, Brown University.

Dugan, J. J. and Freed, D. (1984). Ground heave due to pile driving. *Proc. of* International conference on case histories in geotechnical engineering, St. Louis: 117-122.

Duncan, J. and Chang, C. (1970). "Nonlinear analysis of stress and strain in soils." ASCE. Soil Mechanics and Foundations Division. Journal **96**(SM5): 1629-1653.

Edstam, T. and Jendeby, L. (1992). Sheet Pile Wall used for a deep excavations in soft clay. (Original title, Spont i anslutning till djup schakt i lös lera. Fältmätningar av jordtryck och spontrörelser. Datorsimulering med hjälp av FLAC) (In Swedish). Department of Geotechnical Engineering at Chalmers University of Technology, Gothenburg**:** 85 pp.

Eide, O., Aas, G. and Josang, T. (1972). Special application of cast-in-place walls for tunnels in soft clay. *Proc. of* 5th European Conf. on Soil Mechanics and Foundation Engineering, Madrid, Spain: 485–498.

Ekenberg, M. (2004). Deep excavations, in deep deposits of clay, associated with the construction of the Göta Tunnel (Original title, Djupa schakter i mäktiga lerlager vid utbyggnad av Götatunneln, entreprenad J2) (In Swedish). *Proc. of* NGM 2004. Nordic Geotechnical Meeting, 14, Ystad, SWEDEN.

Faheem, H., Cai, F. and Ugai, K. (2004). "Three-dimensional base stability of rectangular excavations in soft soils using FEM." Computers and Geotechnics **31**(2): 67-74.

Faheem, H., Cai, F., Ugai and K, H., T (2003). "Two-dimensional base stability of excavations in soft soils using FEM." Computers and Geotechnics **30**(2): 141-163.

Finno, R., Blackburn, J. and Roboski, J. (2007). "Three-Dimensional Effects for Supported Excavations in Clay." Journal of Geotechnical and Geoenvironmental Engineering **133**: 30-36.

Fredriksson, A. and Stille, H. (1979). *FE*-analysis of anchored sheet pile walls (Original title, Analys av forankrade sponter med finita elementmetoden) (In Swedish). Stockholm: 116 pp.

Germaine, J. T. (1982). Development of the directional shear cell for measuring cross-anisotropic clay properties. Department of Civil and Environmental Engineering. Massachusetts Institute of Technology, Cambridge.

Grimstad, G. (2005). A constitutive model for undrained anisotropic behaviour of clays. Department of Civil and Transport Engineering. The Norwegian University of Science and Technology, Trondheim.

Grimstad, G., Nordal, S. and Athanasiu, C. (2006). A constitutive model for undrained anisotropic behaviour of clays. *Proc. of* European conference on numerical methods in geotechnical engineering, 6, Graz, Taylor & Francis: 19-25.

Hamza, M., Ata, A. and Roussin, A. (1999). "Ground Movements Due to the Construction of Cut-and-Cover Structures and Slurry Shield Tunnel of the Cairo Metro." Tunneling and Underground Space Technology **14**(3): 281-289.

Hanna, T. H. (1985). Field Instrumentation in Geotechnical Engineering: 843 pp.

Hardin, B. and Drnevich, V. (1972). "Shear modulus and damping in soils: part 1: measurement and parameter effects; part 2: design equations and curves." ASCE. Soil Mechanics and Foundations Division. Journal **98**(part 1: 7; part 2: 8): part 1: 603-624; part 2: 667-692.

Hashash, Y. (1992). Analysis of deep excavations in clay. Department of Civil and Environmental Engineering. Massachusets Institute of Technology, Cambridge: 337 pp.

Hashash, Y., Marulanda, C., Ghaboussi, J. and Jung, S. (2006). "Novel Approach to Integration of Numerical Modeling and Field Observations for Deep Excavations." Journal of Geotechnical and Geoenvironmental Engineering **132**: 1019-1031.

Hashash, Y. and Whittle, A. (1996). "Ground Movement Prediction for Deep Excavations in Soft Clay." Journal of Geotechnical Engineering **122**(6): 474-486.

Hashash, Y. and Whittle, A. (2002). "Mechanisms of Load Transfer and Arching for Braced Excavations in Clay." Journal of Geotechnical and Geoenvironmental Engineering **128**(3): 187-197.

Hashiguchi, K. (1977). An expression of Anisotropy in a Plasitic Constitutive Equation of Soils. *Proc. of* International conference on soil mechanics and foundation engineering, Tokyo: 302-305.

Holtz, R. and Kovacs, W. (1981). Introduction to geotechnical engineering, (Prentice-Hall) Englewood Cliffs, NJ: 733 pp.

Hsieh, P. and Ou, C. (1998). "Shape of ground surface settlement profiles caused by excavation." Canadian Geotechnical Journal **35**(6): 1004-1017.

Jamiolkowski, M., Ladd, C., Germaine, J. and Lancellotta, R. (1985). New developments in field and laboratory testing of soils. *Proc. of* International conference on soil mechanics and foundation engineering, 11, San Francisco: 57-153.

Jan, J. C., Hung, S. L., Chi, S. Y. and Chern, J. C. (2002). "Neural Network Forecast Model in Deep Excavation." Journal of Computing in Civil Engineering **16**: 59-65.

Janbu, N. (1957). Earth pressure and bearing capacity calculations by generalized procedure of slices. *Proc. of* the 4th International Conference, International Society of Soil Mechanics and Foundation Engineering, London: 207-213.

Janbu, N. (1972). Earth pressure computations in theory and practice. *Proc. of* European conference on soil mechanics and foundation engineering, 5, Madrid: 47-54.

Janbu, N. (1973). Shear strength and stability of soils. The applicability of the Coulombian material 200 years after the ESSAI. Norsk Geoteknisk Forening, Oslo**:** 47 pp.

Johansson, B. and Jendeby, L. (1998). Generation of excess pore water pressure due to piling, and the effect on slope stability (Original title, Portrycksökningar till följd av pålslagning och dess betydelse för stabiliteten) (In Swedish). Department of Geotechnical Engineering, Chalmers University of Technology, Gothenburg**:** 40 pp.

Johansson, B. and Jendeby, L. (1999). Changes in total stresses and pore water pressures during piling. *Proc. of* European conference on soil mechanics and geotechnical engineering, Amsterdam: 553-558.

Jonsson, J. and Kristiansson, A. (2004). Displacement due to pile driving in soft clay (In Swedish). Department of Civil and Environmental Engineering. GeoEngineering. Chalmers University of Technology, Gothenburg: 74 pp.

Jumikis, A. R. (1962). Soil Mechanics. Princeton, Van Nostrand Co.

Karlsrud, K. (2003). Technical note 2G-201- Deformation characteristics to use in geotechnical calculations (Original title, Teknisk notat 2G-201 - Deformatjonsparametere for bruk i geotekniske beregeninger) (In Norwegian). Norwegian Geotechnical Institute, Oslo.

Karlsrud, K. and Aas, G. (1995). Norwegian practice related to design of braced excavations. *Proc. of* Int. Symp. on Underground Construction in Soft Ground, New Dehli: 49-52.

Karlsrud, K. and Andresen, L. (2005). "Loads on Braced Excavations in Soft Clay." International Journal of Geomechanics **5**: 107-113.

Kavvadas, M. (1982). Non-Linear Consolidation around Driven Piles in Clays. Dept. of Civil Engineering. Massachusetts Institute of Technology, Cambridge: 666 pp.

Kim, J. and Salgado, R. (1999). "Limit analysis of soil slopes subjected to pore-water pressures." ASCE. Journal of Geotechnical and Geoenvironmental Engineering **125**(1): 49-58.

Kulhawy, F. (1992). Some thoughts on the evaluation of undrained shear strength for design. *Proc. of* Predictive soil mechanics. Wroth memorial symposium, Oxford: 394-403.

Kung, G. T. C., Juang, C. H., Hsiao, E. C. L. and Hashash, Y. M. A. (2007). "Simplified Model for Wall Deflection and Ground-Surface Settlement Caused by Braced Excavation in Clays." Journal of Geotechnical and Geoenvironmental Engineering **133**(6): 731-747.

Ladd, C. (1991). "Stability Evaluation During Staged Construction." Journal of Geotechnical Engineering **117**(4): 540-615.

Ladd, C. and Foott, R. (1974). "New design procedure for stability of soft clays." ASCE. Geotechnical Engineering Division. Journal **100**(GT7): 763-786.

Ladd, C., Foott, R., Ishihara, K., Schlosser, F. and Poulos, H. (1977). Stress-deformation and strength characteristics. *Proc. of* International conference on soil mechanics and foundation engineering, 9, Tokyo: 421-494.

Lade, P. (2005). "Overview of constitutive models for soils." Soil constitutive models: Evaluation, selection, and calibration: 1-34.

Lade, P. and Duncan, J. (1975). "Elastoplastic stress-strain theory for cohesionless soil." ASCE. Geotechnical Engineering Division. Journal **101**(GT10): 1037-1053.

Lade, P., Duncan, JM (1975). "Elastoplastic stress-strain theory for cohesionless soil." ASCE. Geotechnical Engineering Division. Journal **101**(GT10): 1037-1053.

Lambe, T. (1970). Braced excavations. *Proc. of* Lateral stresses in the ground and design of earth retaining structures, New York, Ithasca: 149-218.

Lambe, T. W. and Whitman, R. V. (1969). Soil mechanics. New York, Wiley.

Larsson, R. (1977). Basic behaviour of Scandinavian soft clays. Swedish Geotechnical Institute, Linköping**:** 108 pp.

Larsson, R. (1981). Drained behaviour of Swedish clays. Swedish Geotechnical Institute, Linköping**:** 157 pp.

Larsson, R. (1986). Consolidation of soft soils. Swedish Geotechnical Institute, Linköping**:** 174 pp.

Larsson, R. (1994). Deformation characteristics in soil (Original title, Deformationsegenskaper i jord) (In Swedish). Department of Geotechnical Engineering, Gothenburg**:** 81 pp.

Larsson, R. (1995). CPT test. Equipment, testing, evaluation. An in situ method for determination of stratigraphy and properties in soil profiles. Swedish Geotechnical Institute, Linköping**:** 77 pp.

Larsson, R., Bergdahl, U, Eriksson, L (1984). Evaluation of shear strength in cohesive soils with special reference to Swedish practice and experience. Swedish Geotechnical Institute, Linköping**:** 32 pp.

Larsson, R. and Mulabdic, M. (1991). Shear moduli in Scandinavian clays. Measurement of initial shear modulus with seismic cones. Empirical correlations for the initial shear modulus in clay. Statens Geotekniska Institut, Linköping**:** 127 pp.

Larsson, R. and Sällfors, G. (1981). Hypothetical yield envelope at stress rotation. *Proc. of* International conference on soil mechanics and foundation engineering, 10, Stockholm, June 1981: 693-696.

Larsson, R., Sällfors, G (1985). "Automatic continuous consolidation testing in Sweden." ASTM Special Technical Publication **892**: 299-328.

Leung, E. and Ng, C. (2007). "Wall and Ground Movements Associated with Deep Excavations Supported by Cast In Situ Wall in Mixed Ground Conditions." Journal of Geotechnical and Geoenvironmental Engineering **133**: 129-143.

Liedberg, N., Axelsson, G. and Ekenberg, M. (2003). Optimization of retaining structures and foundations by the use of the observational method - two case histories. *Proc. of* European conference on soil mechanics and geotechnical engineering, 13, Prague: 583-588.

Lindström, M. and Matsoukatidis, S. (2003). Retaining wall in deep excavation in clay – comparison between calculated and measured horizontal displacements. Department of Geotechnical Engineering, Chalmers University of Technology, Gothenburg: 77 pp.

Long, M. (1999). "Database for Retaining Wall and Ground Movements due to Deep Excavations." Journal of Geotechnical and Geoenvironmental Engineering **127**(3): 203-224.

Magnus, R. R., Teh, C. I. and Lau, J. M. (2005). Interim report of the Committee of Inquiry into the incident at the MRT Circle Line Worksite that led to the collapse of Nicoll Highway on 20 April 2004 Singapore. <http://www.mom.gov.sg/MOM/CDA>.

Mana, A. and Clough, G. (1981). "Prediction of movements for braced cuts in clay." ASCE. Geotechnical Engineering Division. Journal **107**(6): 759-777.

Matsuoka, H. and Nakai, T. (1974). "Stress-Deformation and Strength Characteristics under Three Diffrent Principal Stresses." Proc. Japanese Society of Civil Engineers **232**: 59-70.

Mayne, P. and Kulhawy, F. (1982). "K_0-OCR (At rest pressure - Overconsolidation Ratio) relationships in soil." ASCE. Geotechnical Engineering Division. Journal **108**(GT6): 851-872.

Mesri, G. and Castro, A. (1987). "$C\alpha/C_c$ Concept and K_0 During Secondary Compression." Journal of Geotechnical Engineering **113**(3): 230-247.

Nash, D. (1987). Chapter 2: A comparative review of limit equlibrium methods of stability analysis. Slope stability by Nash, D., Anderson, MG and Richards, KS, John Wiley & Sons.

Nicholson, D. P. (1987). The design and performance of the retaining wall at Newton Station. *Proc. of* Mass Rapid Transit Conference, Singapore: 147-154.

Nordal, S. (1983). Elasto-plastic Behaviour of Soils Analyzed by the Finite Element Method. Geotechnical Division, Norwegian Institute of Technology, University of Trondheim.

Nordal, S. (2004). Soil Modeling. Norwegian University of Science and Technologhy, Geotechnical Division, Trondheim.

O´Neill, D. (1985). Undrained shear strength anisotropy of an overconsolidated thixotropic clay. Department of Civil and Environmental Engineering. Massachusetts Institute of Technology, Cambridge.

Ochiai, H. and Lade, P. (1983). "Three-dimensional behavior of sand with anisotropic fabric." ASCE. Journal of Geotechnical Engineering **109**(10): 1313-1328.

Oner, M. (1997). Deep Dark Secrets of Geotechnical Engineering, ejge.

O'Rourke, T. (1981). "Ground movements caused by braced excavations." ASCE. Geotechnical Engineering Division. Journal **107**(9): 1159-1178.

O'Rourke, T. (1993). Base stability and ground movement prediction for excavations in soft clay. Retaining Structures. Clayton. London, Thomas Telford: 131-139.

Oskarsson, R. and Thorén, T. (2004). A study of 3-dimensional side effects during stepwise excavation in the Götatunneln project, J2 (In Swedish). Department of GeoEngineering. Geology and Geotechnical Engineering. Chalmers University of Technology, Gothenburg: 74 pp.

Osman, A. and Bolton, M. (2004). "A new design method for retaining walls in clay." Canadian Geotechnical Journal **41**(3): 451-466.

Osman, A. and Bolton, M. (2007). Back analysis of three case histories of braced excavations in Boston Blue Clay using MSD method. *Proc. of* Soft Soil Engineering, London, Taylor & Francis: 755-764.

Ou, C., Hsieh, P. and Chiou, D. (1993). "Characteristics of ground surface settlement during excavation." Canadian Geotechnical Journal **30**(5): 758-767.

Ou, C., Liao, J. and Cheng, W. (2000). "Building response and ground movements induced by a deep excavation." Geotechnique **50**(3): 209-220.

Ou, C. and Shiau, B. (1998). "Analysis of the corner effect on excavation behaviors." CAN GEOTECH J **35**(3): 532-540.

Pappin, J., Simpson, B., Felton, P. and Raison, C. (1986). "Numerical analysis of flexible retaining walls." Symp. on Computer Applications in Geotechnical Enginering, the Midland Geotechnical Society: 789-802.

Peck, R. (1969). "Advantages and limitations of the observational method in applied soil mechanics (Ninth Rankine Lecture)." Geotechnique **19**(2): 171-187.

Peck, R. (1969). Deep excavations and tunneling in soft ground. *Proc. of* Seventh international conference on soil mechanics and foundation engineering, Mexico: 225-290.

Peck, R. B. (1943). "Earth pressure measurements in open cuts, Chicago subway." Trans. ASCE **108**: 1008-1036.

Persson, J. (2004). Unloading modulus of soft clay: A field and laboratory study. Department of GeoEngineering. Geology and Geotechnical Engineering. Chalmers University of Technology, Gothenburg: 127 pp.

Persson, J. (2007). Hydrogeological Methods in Geotechnical Engineering: Applied to settlements caused by underground constructions. Department of Civil and Environmental Engineering. Chalmers University of Technology, Gothenburg: 185 pp.

Perzyna, P. (1963). "The constitutive equations for rate sensitive plastic materials. Q." Appl. Math **20**(4): 321-332.

Pestana, J. (1994). A unified constitutive model for clays and sands. Department of Civil and Environmental Engineering. Massachusetts Institute of Technology, Cambridge: 473 pp.

Pestana, J. M. and Whittle, A. J. (1999). "Formulation of a unified constitutive model for clays and sands." International Journal for Numerical and Analytical Methods in Geomechanics **23**(12): 1215-1243.

Pestana, J. M., Whittle, A. J. and Gens, A. (2002). "Evaluation of a constitutive model for clays and sands: Part II - Clay behaviour." International Journal for Numerical and Analytical Methods in Geomechanics **26**(11): 1123-1146.

Potts, D., Axelsson, K., Grande, L., Schweiger, H. and Long, M. (2002). Guidelines for the Use of Advanced Numerical Analysis, Thomas Telford: 177 pp.

Potts, D. M. and Zdravkovic, L. (1999). Finite element analysis in geotechnical engineering. [Vol. 1] : Theory, Thomas Telford,: 440 pp.

Potts, D. M. and Zdravkovic, L. (2001). Finite element analysis in geotechnical engineering. [Vol. 2] : Application, Thomas Telford: 427 pp.

Rankine, W. (1857). "On the stability of loose earth." Philosophical Transactions of the Royal Society of London **147**.

Roboski, J. and Finno, R. (2006). "Distributions of ground movements parallel to deep excavations in clay." Canadian Geotechnical Journal **43**(1): 43-58.

Roscoe, K. and Burland, J. (1968). "On the generalized stress strain behaviour of wet clay." Engineering Plasticity **3**: 539-609.

Rowe, P. (1952). "Anchored sheet pile walls." Proc. Instn Civ. Engrs **1**(1): 27-70.

Runesson, K. (1978). On Non-linear Consolidation of Soft Clay: A Numerical Approach with Special Emphasis on Plasticity and Creep, Department of Structural Mechanics, Chalmers University of Technology.

Ryner, A., Fredriksson, A. and Stille, H. (1996). Handbook for design of sheet pile walls (Original title, Sponthandboken. Handboken för konstruktion och utformning av sponter) (In Swedish). Stockholm: 154 pp.

Sahlström, P., Stille, H (1979). Anchored sheet pile walls (Original title, Förankrade sponter) (In Swedish). Stockholm: 128 pp.

Schmidt, B. (1966). "Earth pressures at rest related to stress history. Discussion." Can. Geotech. J. **3**: 239-242.

Schmidt, B. (1967). "Lateral stresses in uniaxial strain." Danish Geotechnical Institute Bulletin No.23, Denmark.

Schmidt, B. (1969). Settlements and Ground Movements Associated with Tunneling in Soil. University of Illinois.

Schweckendiek, T. (2006). Structural reliability analysis of deep excavations-coupling reliability methods with finite elements. Section Hydraulic and Geotechnical Engineering. Delft University of Technologhy, Delft: 213 pp.

Schweckendiek, T. and Courage, W. (2007). Structural reliability analysis of deep excavations. PLAXIS Bulletin: 9-13.

Simpson, B., O'Riordan, N. and Croft, D. (1979). "Computer model for the analysis of ground movements in London Clay." Geotechnique **29**(2): 149-175.

Skempton, A. W. (1951). The bearing capacity of clays. *Proc. of* Bldg Res. Cong., London: 180-189.

Skredkommissionen (1995). Guidelines for slope stability investigations (Original title, Anvisningar för släntstabilitetsutredningar) (In Swedish). Royal Swedish Academy of Engineering Sciences, Linköping**:** 194 pp.

Smith, I. M. and Griffiths, D. V. (2004.). Programming the finite element method. Chichester, Wiley: 628 pp.

Stallebrass, S. and Taylor, R. (1997). "The development and evaluation of a constitutive model for the prediction of ground movements in overconsolidated clay." Geotechnique **47**(2): 235-253.

Stille, H. (1976). Behaviour of anchored sheet pile walls. Department of soil and rock mechanics. The Royal Institute of Technology, Stockholm: 192 pp.

Sällfors, G. (1975). Preconsolidation pressure of soft, high-plastic clays. Geotechnical department. Chalmers University of Technology, Gothenburg: 231 pp.

Sällfors, G. (2003). Consistent answers from a soil sample. *Proc. of* International workshop on geotechnics of soft soils. Theory and practice, Noordwijkerhout, The Netherlands: 79-88.

Tavenas, F. (1979). "The behavior of embankments on clay foundations: state of the art." Proc. 32nd Can geotech Conf. 9 Canadian Geotechnical Society.

Tefera, T. (2004). Large scale model study and numerical investigation of sheet pile wall. Department of Civil and Transport Engineering / Norges teknisk-naturvitenskapelige universitet, NTNU. Institutt for bygg, anlegg og transport. Doktor ingeniöravhandling 2004:138. Norwegian University of Science and Technology, Trondheim: 174 pp.

Terzaghi (1943). Theoretical soil mechanics. New York, Wiley: 510 pp.

Terzaghi, K. and Peck, R. (1967). Soil mechanics in engineering practice. New York, Wiley: 566 pp.

Ukritchon, B., Whittle, A. and Sloan, S. (2003). "Undrained Stability of Braced Excavations in Clay." Journal of Geotechnical and Geoenvironmental Engineering **Aug 2003**.

Wager, O. (1972). Bälgsättningsmätare för mätning av vertikalrörelser i jord. *Proc. of* Nordisk Geoteknikermöte, Trondheim, Norway: 95-98.

Vaid, Y. and Campanella, R. (1974). "Triaxial and plane strain behavior of natural clay." ASCE. Geotechnical Engineering Division. Journal **100**(3): 207-224.

Wang, Z., Ng, C. and Liu, G. (2005). "Characteristics of wall deflections and ground surface settlements in Shanghai." Can. Geotech. J **42**(5): 1243-1254.

Ward, W. H. (1955). "Experiences with some sheet-pile cofferdams at Tilbury." Geotechnique **5**(4): 327-330.

Vermeer, P. and Borst, R. (1984). "Non-associated plasticity for soil, concrete and rock." Heron **29**(3): 1-64.

Vermeer, P. and Neher, H. (2000). A soft soil model that accounts for creep. *Proc. of* Proceedings of Beyond 2000 in Computional Geotechnics: 249-261.

Whittle, A. and Kavvadas, M. (1994). "Formulation of MIT-E3 constitutive model for overconsolidated clays." ASCE. Journal of Geotechnical Engineering **120**(1): 173-198.

Whittle, A. J. (1987). A constitutive model for overconsolidated clays with application to the cyclic loading of friction piles. Department of Civil Engineering. Massachusetts Institute of Technology, Cambridge: 641 pp.

Whittle, A. J. (1991). MIT-E3: A constitutive model for overconsolidated clays. *Proc. of* Computer Methods and Advances in Geomechanics, Rotterdam.

Whittle, A. J. (1993). "Evaluation of a constitutive model for overconsolidated clays." Geotechnique **43**: 289-313.

Wong, K. and Broms, B. (1989). "Lateral Wall Deflections of Braced Excavations in Clay." Journal of Geotechnical Engineering **115**(6): 853-870.

Wood, D. (2004). Geotechnical modelling: 488 pp.

Wroth, C. (1975). In situ measurement of initial stresses and deformation characteristics. /State-of-the-art review/. *Proc. of* Conference on in situ measurement of soil properties, North Carolina State University: 181-230.

Wunsch, R. (2003). "Construction of deep excavations in soft clay with regard to bottom heave - shown by the" Lilla Bommen Tunnel" project in Gothenburg." Bautechnik **80**(9): 580-585.

Yu, H., Salgado, R., Sloan, S. and Kim, J. (1998). "Limit analysis versus limit equilibrium for slope stability." ASCE. Journal of Geotechnical and Geoenvironmental Engineering **124**(1): 1-11.

Zhou, C., Yin, J., Zhu, J. and Cheng, C. (2005). "Elastic Anisotropic Viscoplastic Modeling of the Strain-Rate-Dependent Stress-Strain Behavior of K_0-Consolidated Natural Marine Clays in Triaxial Shear Tests." International Journal of Geomechanics **5**: 218-232.

Zienkiewicz, O. and Taylor, R. (2000). The Finite Element Method, Butterworth-Heinemann: 687 pp.

APPENDICES

Statistical analysis of the data presented by the builder

Introduction

Based on the data presented by the builder (the Swedish Road Administration), the undrained shear strength in one of the four subareas at site J2 was studied.

Two different methods of statistical analysis are compared (Bengtsson and Sällfors, 1996). The first is a stringent evaluation. Every metre of depth was analysed separately in terms of mean value and standard deviation, after which the undrained shear strength was reduced due to the limited number of tests.

The second is a more practical but somewhat subjective method. A rough estimate is that the lower quintile (5% quantile) and the upper quintile (95% quantile) can be obtained by estimating the boundaries of the scattered data and only allowing some extreme values outside these boundaries. The mean value is estimated to be in the middle of the boundaries and the standard deviation can be calculated as the distance between the two lines divided by 3.3, assuming a normal distribution. For comparison purposes, the upper and lower quintiles from method 1 were used as boundaries in method 2. A normal distribution has been assumed and the analyses were conducted according to the codes in use before the start of the project. Since then, new codes (Eurocode) have been adopted and uncertainties are handled slightly differently.

Notations and equations (Bengtsson and Sällfors, 1996)

$\bar{x}$	Mean value
x_i	Test value number i
n	Number of values in a sample
σ	Standard deviation for a population
V_c	Coefficient of variation
$\bar{x}_{\inf}$	Reduced mean value accounting for the limited number of tests.
$\bar{\sigma}$	Mean standard deviation for a number of sample
σ_{red}	Reduced standard deviation with regard to the fluctuation distance
$\bar{\sigma}_{\inf}$	Mean standard deviation for a number of samples
S	Vertical fluctuation distance in the soil
L	Vertical length of the failure zone
γ_m	Partial factor
α_i	Sensitivity factor
β	Reliability index

$$\bar{x} = \frac{\Sigma x_i}{n} \text{ (mean value)} \tag{A.1}$$

$$\sigma = \frac{\Sigma(\bar{x} - x_i)^2}{(n-1)} \text{ (standard deviation)} \tag{A.2}$$

$$\bar{x}_{\inf} = \bar{x} - \frac{\sigma}{\sqrt{n}} \cdot 1.65 \text{ (reduced mean value)} \tag{A.3}$$

$$\bar{\sigma} = \frac{\Sigma n_i \cdot \sigma_i}{\Sigma n_i} \text{ (mean standard deviation)} \tag{A.4}$$

$$V_c = \frac{\bar{\sigma}}{\bar{x}} \text{ (Coefficient of variation)} \tag{A.5}$$

$$\sigma_{red} = \frac{\sigma}{\sqrt{\frac{L}{S}}} \text{ (reduced standard deviation)} \tag{A.6}$$

$$\gamma_m = \frac{1}{1 - \alpha_i \cdot \beta \cdot V_c} \text{ (Partial factor as a function of } \beta\text{, normal distribution)} \tag{A.7}$$

$$V_c = \frac{\sigma}{\bar{x}} \text{ (Coefficient of variation)} \tag{A.8}$$

The standard deviation obtained can be reduced if the assumed failure in the soil greatly exceeds the distance of fluctuation, Equation (A.6). Bengtsson and Sällfors (1996) recommend to avoid reducing the standard deviation by more than 50%, that is equal to S not less than 75% of L. The partial factor can be calculated according to Equation (A.7) for a normal distribution. β is the reliability index and α_i the sensitivity factor of the studied parameter. Note that $\Sigma(\alpha_i^2)=1$.

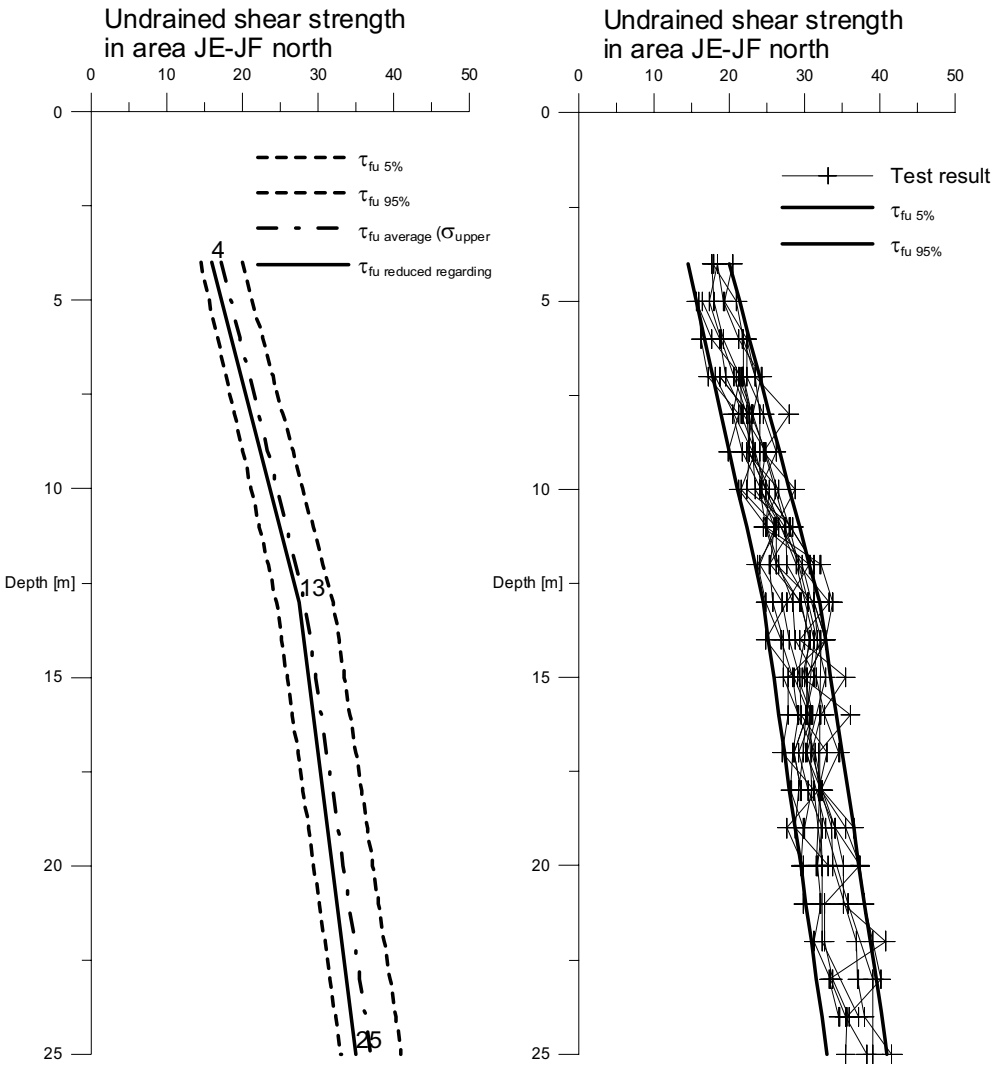

Figure A.1: Undrained shear strength in sub area JE-JF north
a) Evaluated mean value, lower and upper quintile and a reduced mean value due to the limited number of data points. Method number 1.
b) All data from field vane tests with the assumed boundaries representing the lower and upper quintile. Method number 2.

In a normal case, α_i is assumed to be 0.9 for s_u since it is considered to be the most critical parameter when retaining systems are designed in soft clay. According to BKR99, the index against safety, β, should at least represent the values given in Table A.1 in order to fulfil the demands on safety in the category to which the construction belongs.

Table A.1: Required safety index in different safety classes and the partial factors used to increase the safety index from safety class 1.

Safety class	β	γ_n
1	3.7	1.0
2	4.3	1.1
3	4.8	1.2

In this case it is recommended that β for safety class 1 is used when γ_m are calculated, while the demand for higher safety in different situations is taken into account by factor γ_n.

In the ultimate limit state, γ_n varies according to Table A.1, and in the serviceability limit state γ_n=1.0.

The parameter used in the calculations is given by the following expression

$$p_d = \frac{p_k}{\gamma_m \bullet \gamma_n} \tag{A.9}$$

p_k Characteristic value of parameter p, mean value.
p_d Design value of parameter p.

In Table A.2 the data shown in Figure A.1 are compiled into statistical data. It is obvious that the two different approaches to estimating the standard deviation yield similar results. The partial factors were calculated after reduction to compensate for the fact that the soil mass exceeded the fluctuation distance. Since the reduction was limited to 50%, the partial factor varied between 1.12 and 1.25. The prescribed value was 1.25.

Table A.2 Statistic data from area JE-JF north.

Layer	Depth	$s_{u,\,trend}$	Standard deviation, $\bar{\sigma}$	Coefficient of variation, V_c (%)	Reduced standard deviation, σ_{red} (S=1, L=15)	Reduced coefficient of variation, $V_{c\,red}$	Partial factor, γ_m (S=1, L=15, α=-0.9)
Stringent							
Upper part	4	17.5	2.0	11.4	0.52 (1.00)	2.9 (5.7)	1.11 (1.25)
	13	28.9		6.9		1.8 (3.5)	1.06 (1.13)
Lower part	13	28.5	2.5	8.8	0.65 (1.25)	2.2 (4.4)	1.08 (1.17)
	25	37.3		6.7		1.7 (3.4)	1.06 (1.24)
Subjective							
Upper part	4	17.3	2.0	11.6	0.52 (1.00)	3.0 (5.8)	1.11 (1.24)
	13	28.2		7.1		1.8 (3.5)	1.07 (1.13)
Lower part	13	28.2	2.3	8.2	0.59 (1.15)	2.1 (4.1)	1.08 (1.16)
	25	37.0		6.2		1.6 (3.1)	1.06 (1.12)

* Values in brackets are derived assuming a maximal reduction o the standard deviation of 50%.

The influence of different parameters such as V_c and α is shown in Figure A.2a. In order to establish representative partial factors it is crucial to have good input data that describe the variation in the soil, e.g. V_c and it is also important to use a proper value for the sensitivity factor, α. The latter parameter will, however, differ depending on the failure criterion adopted, cf. Chapter 9.5. It is also highly dependent on the choice of distributions for different parameters as well as the variation of the parameters. In Figure A.2b only two parameters were assumed to be involved in a hypothetical conceptual model. The same standard deviation was assumed and the partial factors for each of the parameters are presented depending on the sensitivity factor for parameter 1.

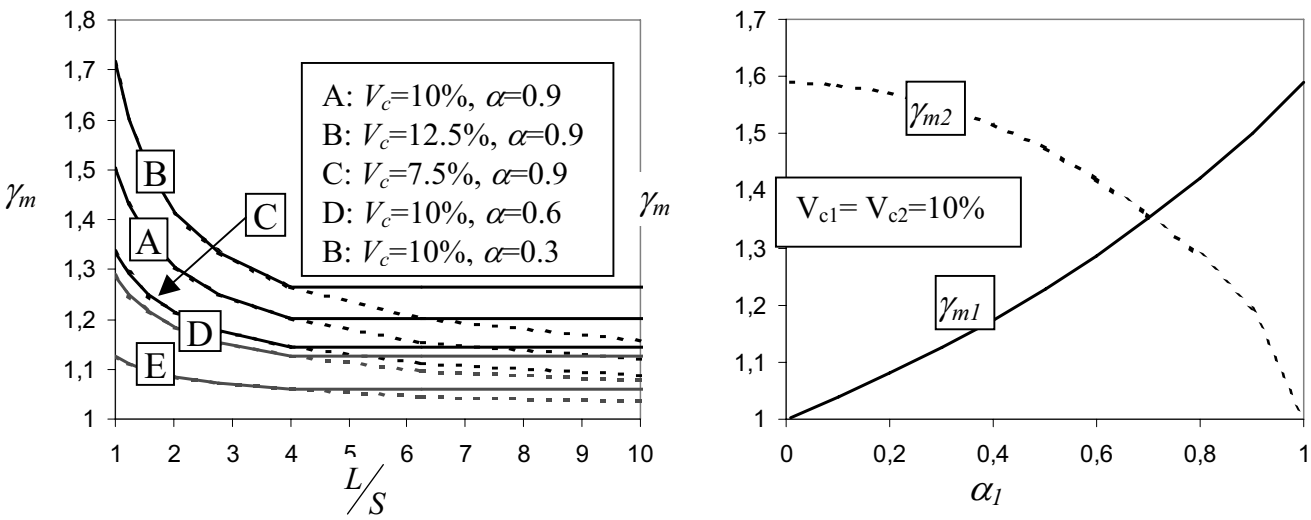

Figure A.2: Visualization of the partial factor, γ_m, safety class 1.
a) Reduction of γ_m due to involved soil mass. Solid lines: Reduction of σ is restricted to 50%. Dashed lines: No restriction of the reduction.
b) Effect of the sensitivity parameter α. Solid line: γ_m for parameter 1, as a function of α. Dashed lines: Effect on γ_m for parameter 2, as a function of α_1 assuming only two parameters.

A representative length of the soil mass had to increase by four times the fluctuation distance in order to reach the maximum reduction of the partial factor. Figure A.3 shows the possibility of reducing γ_m based on the involved soil volume. Even in this case, it is important to have good knowledge of the scatter of the parameter and its level of impact on the analysis.

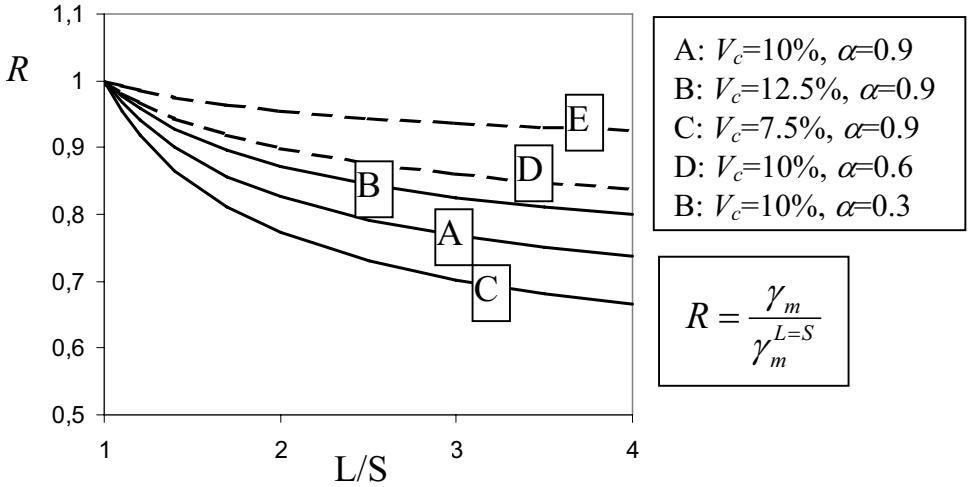

Figure A.3: Visualization of the possibility to reduce the partial factor, γ_m, based on the involved soil volume. Safety class 1 is assumed.

The values in the design codes where R can be reduced to a minimum of 0.8 seem to be a fairly good recommendation but are dependent on V_c and α, whether the soil volume is large and that no reduction of the scatter was used when establishing γ_m.